Department of Mechanical Engineering
The University of Adelaide
South Australia

AN INVESTIGATION OF THE FORMATION OF HOLLOW BEAD DEFECTS IN PIPELINE FIELD WELDS

G. M. DELPHINE CANTIN

A Thesis submitted for the Degree of Doctor of Philosophy

October 1997

TABLE OF CONTENTS

ABSTRACT ix

ACKNOWLEDGMENTS xi

STATEMENT OF ORIGINALITY xiv

NOMENCLATURE xv

CHAPTER 1

GENERAL INTRODUCTION 1

1.1 INTRODUCTION 1

1.2 LITERATURE REVIEW 5

1.2.1 Introduction 5

1.2.2 Description of the Hollow Bead Pore 6

1.2.3 Field Welding of Pipeline Welds using Stove Pipe Welding 7

1.2.4 Survey of Hollow Bead Occurrence on Pipeline Projects 14

1.2.5 Effect on Mechanical Properties 15

1.2.6 Variables Associated with Hollow Bead Formation 15

1.2.6.1 Effect of Welding Parameters 15

1.2.6.2 Effect of Welding Consumables 19

1.2.6.3 Effect of Parent Metal Composition 20

1.2.6.4 Effect of Joint Geometry 21

1.2.7 A General Description of Elongated Gas Pores 22

1.2.8 Gas - Metal Reactions and Detailed Investigations of Porosity in Welding 28

1.2.8.1 Gas -Metal Reactions in Arc Welding and Melting 29

1.2.8.2 Detailed Investigations of Porosity in Welding 34

1.2.8.2.1 The Nucleation of Gas Bubbles 34

1.2.8.2.2 The Effect of Welding Parameters on the Formation of Porosity 42

1.2.8.2.3 The Effect of Parent Metal Composition on the Formation of Porosity 52

1.2.9 Solidification Mechanics and Microstructure in Fusion Welds 55

1.2.10 The Role of Segregation in the Formation of Gas Pores 66

1.2.11 Conclusions 67

CHAPTER 2

EXPERIMENTAL WORK 69

2.1 INTRODUCTION 69

2.2 SURVEY OF THE INCIDENCE OF HOLLOW BEAD ON THE SOUTH WEST QUEENSLAND PIPELINE PROJECT 70

2.2.1 Introduction 70

2.2.2 Results and Discussion 71

2.3 EXPERIMENTAL TECHNIQUES 79

2.3.1 Equipment 79

2.3.2 Materials 83

2.3.3 Joint Geometry 86

2.4 PRELIMINARY EXPERIMENTS 87

2.4.1 Introduction 87

2.4.2 Common Practices used for the Field Welding of the Root Pass of Pipeline Girth Welds using the Stove Pipe Technique 87

2.4.3 Experimental Conditions and Results 93

2.4.4 Discussion 95

2.5 WELDING OF PIPE SAMPLES 96

2.5.1 Introduction 96

2.5.2 Equipment 96

2.5.3 Experimental Conditions 96

2.5.4 Results 98

2.5.5 Discussion 101

2.6 AN INVESTIGATION OF THE EFFECTS OF WELDING VARIABLES ON THE FORMATION OF HOLLOW BEAD DEFECTS 107

2.6.1 Introduction 107

2.6.2 Experimental Conditions 107

2.6.3 Results 108

2.6.4 Discussion 108

2.7 AN INVESTIGATION OF THE EFFECT OF BOHLER ELECTRODES ON HOLLOW BEAD FORMATION 123

2.7.1 Introduction 123

2.7.2 Materials 123

2.7.3 Results 123

2.7.4 Discussion 125

2.8 AN INVESTIGATION OF THE EFFECT OF THE FLUX MOISTURE CONTENT OF HOLLOW BEAD FORMATION 126

2.8.1 Introduction 126

2.8.2 Experimental Conditions 127

2.8.3 Results 128

2.8.4 Discussion 128

2.9 EXPERIMENTS TO TEST THE EFFECT OF THE JOINT GEOMETRY ON HOLLOW BEAD FORMATION 130

2.9.1 Introduction 130

2.9.2 Experimental Conditions 130

2.9.3 Results 131

2.9.3.1 Statistical Analysis 132

2.9.4 Discussion 135

2.10 EXPERIMENTS ON THE EFFECT OF JOINT PREPARATION SURFACE CONTAMINATION 138

2.10.1 Introduction 138

2.10.2 Materials 138

2.10.3 Welding Conditions 138

2.10.4 Results 139

2.10.5 Discussion 139

2.11 EXPERIMENTS ON THE EFFECT OF PARENT METAL COMPOSITION 141

2.11.1 Introduction 141

2.11.2 Materials 141

2.11.3 Welding Conditions 143

2.11.4 Results 143

2.11.4.1 Statistical analysis 149

2.11.5 Discussion 154

2.12 OCCURRENCE OF HOLLOW BEAD DEFECTS AT THE START OF WELDS 160

2.12.1 Introduction 160

2.12.2 Analysis and Results 160

2.12.3 Discussion 160

2.13 FILMING OF THE WELD KEYHOLE 163

2.13.1 Introduction 163

2.13.2 Equipment 163

2.13.3 Welding Conditions 164

2.13.4 Results 164

2.13.5 Discussion 175

2.14 ANALYSIS OF GASES PRESENT INSIDE HOLLOW BEAD PORES 177

2.14.1 Introduction 177

2.14.2 Procedure 178

2.14.3 Results 178

2.14.4 Dimensions of Hollow bead used in the Analysis and Welding Conditions 179

2.14.5 Discussion 179

2.15 ANALYSIS OF THE DIFFUSIBLE HYDROGEN CONTENT OF THE WELD METAL 180

2.15.1 Introduction 180

2.15.2 Procedure 180

2.15.3 Welding Conditions and Results 182

2.15.4 Discussion 182

2.16 SUMMARY OF EXPERIMENTAL RESULTS 183

CHAPTER 3

METALLOGRAPHIC CHARACTERISATION OF HOLLOW BEAD 185

3.1 INTRODUCTION 185

3.2 MACRO EXAMINATION 185

3.3 SOLIDIFICATION MICROSTRUCTURES 190

3.3.1 Solid State Transformation 190

3.3.2 Primary Solidification Microstructure 195

3.3.2.1 Materials 196

3.3.2.2 Experimental Conditions 197

3.3.2.3 Metallography 197

3.3.2.4 Discussion 198

3.4 THE INFLUENCE OF MACROSEGREGATION 206

3.5 THE INFLUENCE OF WELDING CONDITIONS ON THE SIZE OF THE WELD BEAD 212

3.6 DISCUSSION 223

3.7 SCANNING ELECTRON MICROSCOPY 225

3.7.1 Scanning Electron Microscopy of Hollow Bead Pores 225

3.7.2 Scanning Electron Microscopy of Wormhole Pores 283

3.7.2.1 Introduction 283

3.7.2.2 SEM Microscopy 284

3.8 DISCUSSION 291

CHAPTER 4

FINITE ELEMENT MODELLING OF WELD POOLS 295

4.1 INTRODUCTION 295

4.2 BACKGROUND AND THEORY 295

4.3 MODELLING THE WELD POOLS PRODUCED BY MMA STOVE PIPE WELDING 298

4.3.1 Double Ellipsoid Heat Source 298

4.3.2 Cylindrical Heat Source 298

4.3.3 Results and Discussion 299

CHAPTER 5

A MODEL FOR THE FORMATION OF HOLLOW BEAD 309

5.1 INTRODUCTION 309

5.2 THE MODEL 309

5.2.1 Overview 309

5.2.2 Hydrogen as the Principle Agent in Hollow Bead Formation 310

5.2.3 Mechanism of Hydrogen Absorption in the Molten Weld Pool 312

5.2.3.1 Introduction 312

5.2.3.2 The Absorption of Hydrogen from Cellulosic Electrodes 317

5.2.3.2.1 Introduction 317

5.2.3.2.2 Analytical work 318

5.2.3.2.3 Results 319

5.2.3.2.4 Discussion 324

5.2.4 Nucleation of Gas Bubbles in the Weld Pool 330

5.2.5 Factors Influencing the Location of Porosity in the Weld Pool 335

5.2.6 Formation of Hollow Bead or an Elongated Gas Pore at the Solidification Interface 342

5.3 SUMMARY 348

CHAPTER 6

6.1 SUMMARY AND CONCLUSIONS 349

6.2 FUTURE WORK 357

6.2.1 Introduction 357

6.2.2 The Influence of Silicon 357

6.2.3 The Modelling of the Weld Pool 359

6.2.4 Characterisation of the Plasma and Determination of Hydrogen Absorbed by the Weld Pool 360

REFERENCES **361**

PUBLICATIONS ORIGINATING FROM THIS THESIS WORK 371

APPENDIX A

TABLES OF EXPERIMENTAL WELDING CONDITIONS AND RESULTS 372

APPENDIX B

DETERMINATION OF PERCENTAGE DILUTION OF BASE METAL 410

APPENDIX C

REPORT ON TRAINING PROGRAMME 411

APPENDIX D

TRACES OF WELDING CURRENT, VOLTAGE AND ELECTRODE FORCE FROM DATA LOGGER 443

APPENDIX E

MACROGRAPHS OF HOLLOW BEAD IN X80 STEEL 445

APPENDIX F

GRAPHS OF THE OCCURRENCE OF HOLLOW BEAD AGAINST HEAT INPUT AT CONSTANT WELD TRAVEL SPEED 448

ABSTRACT

The root pass of pipeline girth welds is made using the manual metal arc stovepipe technique using cellulosic electrodes. This technique remains the most cost effective, accessible and productive method of welding Australian pipelines, which tend to be of small diameter and small wall thickness. The sporadic appearance of epidemics of hollow bead defects during the construction of pipelines has been responsible for increasing the cost and time required for completion of a number of projects in many parts of the world.

Hollow bead which forms in the root pass of pipeline welds is an elongated linear pore aligned with the weld axis. The inability to identify the cause of this defect has been one of the major obstacles in attempting to reduce its occurrence. As a result of this situation, following an important pipeline construction project which was seriously disrupted by problems with hollow bead, a number of Australian companies contributed to a major three year programme of research undertaken by the Cooperative Research Centre for Materials Welding and Joining.

An automated manual metal arc welding machine capable of simulating the stovepipe welding technique has been used to reproduce hollow bead under controlled and monitored conditions. This has enabled the factors contributing to the formation of this phenomenon to be critically reviewed and quantified. A systematic study of the effects of a range of parameters including welding variables, parent metal composition, joint geometry and surface condition and welding consumables has been undertaken. The data obtained has been used to ascertain their influence on the occurrence of hollow bead pores, and to provide guidelines for field welding

practice which provide a high level of confidence that hollow bead can be eliminated as a practical problem in pipeline construction.

The experimental results have clearly identified the parameters which affect the formation of hollow bead and these are summarised below.

1. High levels of welding current and travel speed were found to have a major influence on hollow bead.
2. The silicon content of the parent metal and the flux moisture content of the electrode had a minor effect on the occurrence of the defect.
3. The dimensions of the joint geometry, the presence of rust and paint on the joint and the concentration of aluminium and carbon in the parent metal had no significant effect.

The work has also led to the development of a model for the formation of the hollow bead pore using detailed metallurgical characterisation in conjunction with the established parametric correlations.

ACKNOWLEDGMENTS

The work reported herein was undertaken as part of a Research Project of the Cooperative Research Centre for Materials Welding and Joining. It was initiated and supervised by the Australian Pipeline Industry Association/Welding Technology Institute of Australia (Core Partner of the Cooperative Research Centre for Materials Welding and Joining) joint Research Panel 7 and benefited from substantial cash and in-kind support from the Panel and especially BHP Steel, Tubemakers of Australia, The Lincoln Electric Company, Epic Energy, Gas and Fuel Corporation, EAPL, AGL, Böhler Steel, SECWA and Mc Connell Dowell.

I would like to thank my supervisors John V. Bee (University of Adelaide - Core Partner of the Cooperative Research Centre for Materials Welding and Joining), Leigh Fletcher (Cooperative Research Centre for Materials Welding and Joining) and Graham Powell (CSIRO - Division of Manufacturing Science and Technology - Core Partner of the Cooperative Research Centre for Materials Welding and Joining) for much help and support, and for all their efforts in reading this thesis.

I received much guidance from members of the joint Panel 7 (Pipelines) of the Australian Pipeline Industry Association and the Welding Technology Institute of Australia (Core Partner of the Cooperative Research Centre for Materials Welding and Joining) through discussions at quarterly meeting for four years. I am grateful to the following companies for the materials they provided continuously during the project, and to their delegate who organised the supplies. BHP - Slab and Plate Products Division (Core Partner of the Cooperative Research Centre for Materials Welding and Joining) (Frank Barbaro and Graham Bowie), The Lincoln Electric Company (Bob Sim and Bob Tainsh), BHP - Pipelines (formerly Tubemakers of Australia) (John Piper), Böhler (Brian Johnston) and Epic Energy (Hans Borek).

Throughout the entire duration of the project I received much help and many ideas for the research from a lot of people. I am greatly appreciative of this support.

Frank Barbaro (BHP - Slab and Plate Products Division) provided much help with the analysis of the data and also participated in some of the experiments, as well as organising the supply of steel and laboratory melts. BHP - SPPD supplied most of the steel for the project as well as

the analytical services. The preparation of special melts of steel with controlled composition is a very expensive and extremely difficult to obtain service. I am extremely privileged as a student to have been given access to resources of this nature.

I am grateful to Jim Kwiatkowski from Mc Connell Dowell, who organised my trip to Western Australia and was closely involved in some of the experiments.

I would like to thank Bob Morrison at Tubemakers of Australia - Pipelines Research Centre who refurbished the automated welding machine used for all experiments and for all his advice and help.

I am very appreciative of the support I received from Ian Henderson and for his close participation and useful input to the project.

I was very fortunate to meet John Lowke from CSIRO - Division of Applied Physics in a late stage of the project and his contribution with the analytical study of the arc composition was invaluable.

I would like to thank Roger Wills who spent two days welding pipe samples and reproducing hollow bead pores.

I am grateful to Malcolm Gray from Microalloying Inc. and David Howden from the Ohio State University for spending much time organising my trip to the USA as well as for their discussions of the project. I would like to thank John Balch at the National Pipeline Welding School in Tulsa where I was given a one week intensive training in stovepipe welding.

I was fortunate to be able to perform some of the work at CSIRO (Division of Manufacturing Science and Technology) and I constantly used the library and laboratory facilities. I would like to thank the following people whose help was invaluable: Peter Lloyd with whom I had many useful discussions and who helped with the scanning electron microscopy, Mike Painter who spent much time generating the finite element models. I also received a lot of assistance with welding, metallography and experiments from Tom Gordon, Gunther Herfurth, Laurie Jarvis, Peter Knott, Trevor Kenyon, Mike Pullen and Ken Barton.

I received constant help from the members of the engineering workshop at The University of Adelaide, Craig Price, Ron Jaeger and Anthony Sherry. I also like to thank Ian Brown, Silvio de Ieso and Graham Kelly for their assistance with my experiments, and William Buttery for

his assistance with preparing test plates and with metallography. I also thank Dr. Krishnan from the Department of Mechanical Engineering at The University of Adelaide for his helpful discussions.

I would like to acknowledge the participation of TWI, and especially Sheila Stevens, who performed the analyses.

I am extremely grateful for the support of my mother and sister, and especially my best friend Gareth Bridges for his constant help and brilliant ideas.

STATEMENT OF ORIGINALITY

To the best of my knowledge and belief all of the material presented in this thesis, except where otherwise referenced, is my own original work and has not been presented previously for the award of any other degree or diploma in any University. If accepted for the award of the Degree of Doctor of Philosophy, I consent that this thesis be made available for loan and photocopying.

G. M. Delphine Cantin

Nomenclature

AS	Australian Standard
API	American Petroleum Institute
AWS	American Welding Society
A_f	Work of formation of a nucleus
bcc	Body centred cubic
C_e	Equilibrium molar concentration of solute at the solidification interface
C_S	Composition of the gas phase
C_L	Composition of the liquid phase
C_o	Nominal alloy composition
C^o_{liq}	Initial concentration of gas in the liquid phase
C^o_{sol}	Initial concentration of gas in the solid phase
C^r_{liq}	Concentration of gas at the supersaturation point
$C_{liq(x)}$	Concentration of gas in the liquid phase
$C_{sol(x)}$	Concentration of gas in the solid phase
C^r_{liq}	Standard gas solubility at the melting point
D	Diffusivity
DC(+)	Direct Current Electrode Positive
DC(-)	Direct Current Electrode Negative
ERW	Electrical Resistance Welding
g	Gravitational acceleration
G	Thermal gradient
R	Growth rate

fcc	Face centred cubic
GMA	Gas Metal Arc
GTA	Gas Tungsten Arc
h	Depth of weld pool
H_o	Null hypotheses in statistical test
I	Thermodynamic probability
k	Equilibrium partition coefficient
K	Equilibrium constant
MMAW	Manual Metal Arc Welding
n_1 and n_2	Size of groups I and II in Wilcoxon Rank Sum statistical test
N_a	Avogadro's number
P	Pressure
P_b	Gas pressure inside a bubble
P_{lib}	Liberation pressure
P_o	Atmospheric pressure
P_{H_2}	Pressure of hydrogen
q	Convective heat loss
Q_{in}	Total energy input from arc
r	Radius of gas bubble
r_f and r_b	Factors used in finite element calculations to represent the partitioning of heat at the front and back of the weld poll
r_c	Critical radius of gas bubble
r_g	Gas bubble radius
R	Gas constant
R^2	Coefficient of determination (in regression analysis)
R.F	Root Face

R.G	Root Gap
R_1 and R_2	Sum of ranks for groups I and II in Wilcoxon Rank Sum statistical test
SEM	Scanning Electron Microscope
t	Time
TWI	The Welding Institute
V	Volume
V_r	Solidification rate
x	Distance from solidification interface
α	Significance level in statistical test
δ	Thickness of layer of gas-forming solutes at solidification interface
ΔG^o	Standard Gibb's free energy
η	Arc efficiency
ϕ	Diameter
μ	Population mean in statistical test
θ	Angle of gas nucleus with solidification interface
ρ	Density
σ_l	Surface tension of liquid metal
$\sigma_{l.g}$	Surface tension at the liquid-gas interface
$\sigma_{l.s}$	Surface tension at the liquid-solid interface
$\sigma_{g.s}$	Surface tension at the gas-solid interface
Ω	Growth constant
[H]	Concentration of hydrogen

Chapter 1

GENERAL INTRODUCTION

1.1 Introduction

In Australia the network of cross-country transmission pipelines represents a major component of the industrial infrastructure by which oil and gas are delivered from remote mining areas to distribution centres near the capital cities. The Australian pipeline industry is entering a phase which will see millions of dollars invested in the development and expansion of transmission grids. The cost of constructing a pipeline is approximately at 50% of the total project cost (for a gas pipeline) (Venton, 1995) with girth welding considered as the critical component. In addition the overall progress of the welding operation is determined by the deposition of the root pass. In Australia and in the USA the root pass is welded using the manual metal arc stovepipe technique which employs cellulosic electrodes. This technique provides a cost effective, accessible and highly productive method of welding Australian pipelines which tend to be of small diameter and wall thickness.

The planning of the construction of new transmission pipelines in Australia requires welding procedures that will minimise cost and increase productivity. The occurrence of defects in welds which require repairs or cut-outs, and thus results in delays, can dramatically increase the construction costs of a pipeline. A defect which forms in pipeline welds is the hollow bead pore which is commonly defined as an elongated linear porosity located in the root pass of a pipeline girth weld. The sporadic appearance of high numbers of hollow bead defects during

the construction of pipelines has been responsible for increasing the cost and time required for completion of a number of projects. The inability to identify the cause of the severe incidence of this defect has been one of the major obstacles in attempting to reduce its occurrence. Prior to this research program, knowledge of the factors which influence its formation was limited. This is the result of several factors, namely that the severe incidence of hollow bead defects is sporadic, pipelines are constructed in remote areas and because it is generally considered to be a welder-induced defect.

A definitive study into the factors which influence the formation of hollow bead was thus initiated. A collaboration between the Australian pipeline industry, through the joint Welding Technology Institute of Australia/Australian Pipeline Industry Association (Panel 7 - Pipelines), and the Cooperative Research Centre (CRC) for Materials Welding and Joining was formed. The aims of the three year research program were detailed in a project proposal approved by Panel 7 and the CRC for Materials Welding and Joining and are described below.

The purpose of the proposed research was:

(i) to determine the effects of welding and metallurgical variables on the formation of hollow bead;

(ii) to perform a detailed study of the characteristics of hollow bead in order to understand the mechanism of formation; and

It was proposed that, following a review of the literature and industrial experience on hollow bead, sections of welds containing hollow bead would be acquired and a detailed metallographic investigation of their principal features would be undertaken. There appeared, at that stage, to be little information on the characteristics of the defect itself.

The subsequent stage would consist of setting up an automated manual metal arc welding machine capable of simulating the stovepipe welding technique to deposit welds under controlled conditions while monitoring the operating variables. This machine would then be used to carry out a systematic study of the effects of a range of parameters including welding parameters, parent metal composition, joint geometry and welding consumables. All welds would be radiographed and the defects found would be characterised metallographically.

The experimental program was envisaged to be an iterative process where progress would be decided on go/no go criteria based on the results of successive experiments. In that way some suggested influential factors would be eliminated while others would be identified as requiring further more detailed investigation.

The automated manual metal arc welding machine has therefore been used to reproduce hollow bead under carefully controlled and monitored conditions. This has enabled the factors contributing to the formation of this phenomenon to be critically reviewed and quantified.

The effects of operational variables, such as welding current, travel speed and heat input have been studied to ascertain their influence and provide data on acceptable ranges of those variables for the avoidance of hollow bead. The handling characteristics of the cellulosic electrode have also been investigated by monitoring performance under varying operational conditions, by varying the moisture content of the flux and by comparing cellulosic electrodes produced by different manufacturers.

The effect of joint geometry has been estimated by a study of two variables, root gap and root face. The influence of the condition of the surface of the joint preparation and adjacent areas has also been investigated.

In order to determine whether the composition of the parent pipe has any appreciable effect on the formation of the defects, experimental studies have examined pipeline steels containing "high" and "low" concentrations of three alloying elements: silicon, aluminium and carbon. Existing literature on hollow bead suggested that these three elements could be influential factors.

A detailed metallurgical characterisation of hollow bead defects and their solidification microstructures has been performed so that, together with the study of the variables mentioned above, a model for the formation of the hollow bead defect could be developed.

Training in the areas of steelmaking, metallurgy, the manufacture of linepipe and welding electrodes and pipeline construction was undertaken at two stages during the project. The first programme looked at Australian industries including BHP - Slab and Plate Products Division (Port Kembla), BHP - Pipelines (formerly Tubemakers of Australia Ltd.) (Kembla Grange), Tubemakers of Australia Kwinana Submerged Arc Welding Line Pipe Plant (Western Australia), Tubemakers of Australia Pipelines Research Centre (Melbourne), the Shaw Coating Plant (Port Kembla), The Lincoln Electric Company (Sydney) and Mc Connell Dowell. Information on the welding and construction practices of the pipeline industry in the USA was obtained during the second stage. The latter included visits to the National Pipeline Welding School (Tulsa, Oklahoma), pipeline construction sites in Florida, the Ohio State University and the Edison Welding Institute. A survey of industrial experience with the hollow bead defect was also carried out during these visits. A report detailing the activities undertaken during these training programmes has been included in Appendix C.

1.2 Literature Review

1.2.1 Introduction

The field welding of pipelines is a complicated process where many set-up, operating and metallurgical variables could influence the production of hollow bead defects. Unfortunately, very little literature exists directly concerning hollow bead and there have been no controlled scientific studies carried of this specific phenomenon. Only one experimental study has been reported (Barkow, 1973) in which the effects of welding parameters on the formation of hollow bead in a fully killed steel is discussed.

In this review, therefore, the literature is presented together with some more general references on similar types of defects for which the mechanisms of formation are more clearly understood. It has also been found that few of the fundamental research studies on porosity deal with manual metal arc welding and cellulosic electrodes. In fact, much of the literature is concerned with gas metal arc and gas tungsten arc welding of aluminium. This material has been identified as highly susceptible to hydrogen porosity. Since hydrogen is the principal component of the shielding gas in cellulosic electrode welding, it was considered relevant to consider these studies here.

The mechanisms for the formation of porosity are concerned primarily with the theory of solidification of metals and the resulting microstructures. A review of the principles of solidification such as macrosegregation and microsegregation, mode of growth and weld pool shape are thus presented.

1.2.2 Description of the Hollow Bead Pore

In the Australian Standard 2885.2-1995 for the Welding of Gas and Petroleum Pipelines, hollow bead is defined as an elongated linear porosity that occurs in the root pass of pipeline welds.

Hollow bead was described by Barkow (1973) as an elongated void in the root (or stringer) bead which could be found anywhere around the circumference of the pipe. In that study hollow bead was frequently found to have a very thin wall at the surface of the root bead on the inside of the pipe and could even be open towards the inside. A schematic of a cross section of a root bead with a hollow bead pore in the reinforcement region is shown in Figure 1.1. The hollow bead pores were also observed to be generally cylindrical in shape and to have considerable dimension in the circumferential axis of the weld. In some cases the defect was also pear-shaped, leading up into the weld itself, and even showed a small crack extending radially inwards.

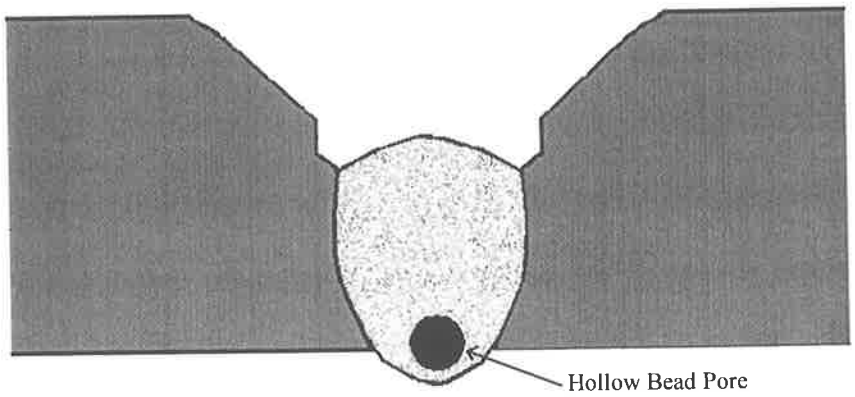

Figure 1.1: Schematic of the cross section of a weld with a hollow bead pore at the bottom of the bead.

1.2.3 Field Welding of Pipeline Girth Welds using the Stovepipe Welding Technique

In Australia and in the United States of America (USA) transmission oil and gas pipelines are most commonly welded using a manual metal arc welding technique called stovepipe welding. Cellulosic electrodes are used and welding is performed vertically downwards (the 5G multiple position welding). The cellulosic electrode develops an atmosphere of hydrogen, resulting in a fierce arc, which gives deeper penetration (Svensson, 1994) and allows high weld travel speeds and hence high welding productivity rates to be achieved. This type of electrode is suited to pipe welding for the following reasons: drying is not required, a high volume of shielding gas is evolved giving good protection against atmospheric contamination when welding in the open and the small amount of slag produced enables the weld to be made downwards (downward welding being faster than upward welding) (Lancaster, 1992). This type of electrode is described in more detail below and in Section 1.2.6.2.

The standard end preparation for pipes used in Australia is the single vee butt weld (see Figure 1.2). The standard AS 2885.2 - 1995 specifies the following limits, a root face (R.F) of 1.6 +/- 0.8mm and a bevel angle (Φ) of 30^{o} $+5^{o}$ /- 0^{o}. The dimensions of the root gap (R.G) are usually specified in welding procedures of particular pipeline projects.

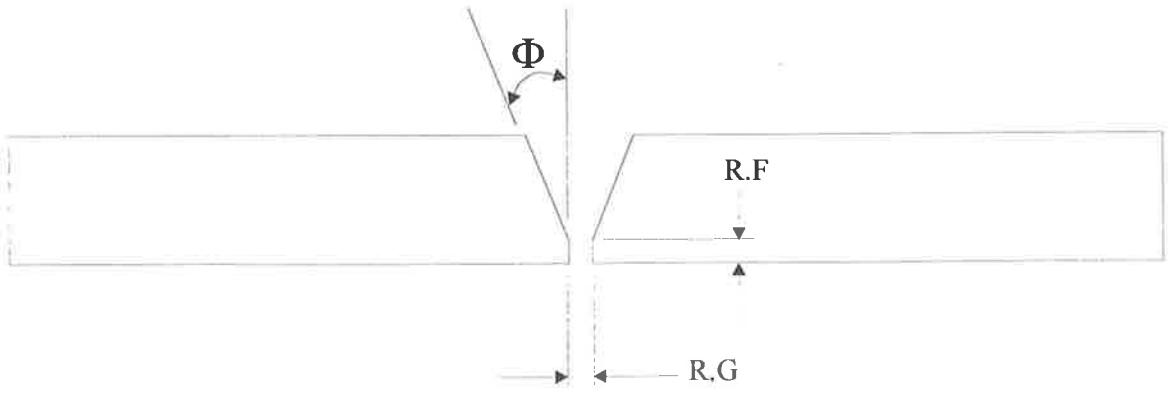

Figure 1.2: Schematic diagram of a standard end preparation of a pipe.

In the field welding of pipelines the joint is clamped using an internal line-up clamp which aligns the pipes and keeps them in place. The welders of the root pass (usually two for pipe diameters greater than 200mm and up to four on large diameter pipelines), working on either side of the pipe and opposite to each other, then start welding towards the bottom of the pipe. After completion, or part completion (a minimum of 70%), of the root pass the clamp is removed and the hot pass is made, followed by the filler and capping passes.

The technique used by pipeline welders when welding with cellulosic electrodes is to insert the electrode into the joint preparation and hold it under pressure against the bevel (see Figure 1.3). The electrode coating, which burns after the metal core, rests on the bevel as the electrode is dragged downhill (without a weaving motion) around the circumference. The electrode is usually held at a tilt angle of about 10 to 15^{o} from the radial axis of the pipe. The arc force and pressure of the shielding gases create a keyhole, about the size of the electrode core wire, below the weld pool. The keyhole is usually kept small to obtain a good root bead. A large keyhole, due to high welding current, root gap and tilt angle, may produce undercut.

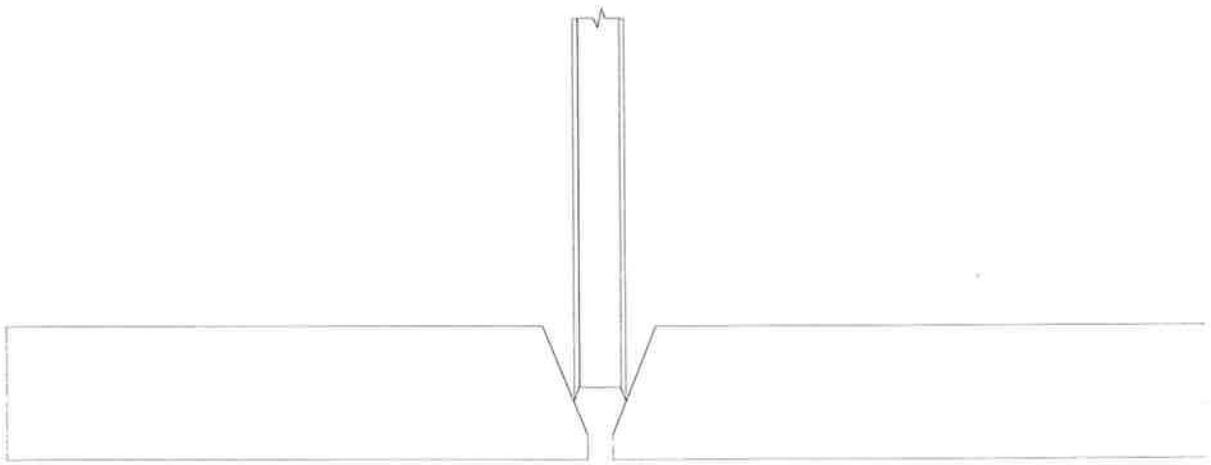

Figure 1.3: Schematic showing the position of the electrode in the weld preparation.

Although detailed descriptions of the operations which occur during the construction of pipelines are given in Appendix C, a summary of the processes is given here. The first phase in the construction process is the establishment of a right-of-way, which is a strip of land where the pipeline is built and which allows the movement of vehicles. Ahead of the welders, the linepipe is unloaded from trucks onto the right-of-way, the linepipe is bent where required, the trench where the pipeline will be buried is dug and the pipe ends are cleaned. The root pass is then welded, followed after a short interval (usually within five minutes) by the hot pass and later by the filling and capping passes. The welded joints are visually and radiographically inspected, and are then cleaned and coated. The pipe strings which are approximately one kilometre long are lowered into the trench and are tied-in by welders. Finally the pipe is covered with a backfill of earth. Hydrostatic testing and the installation of cathodic protection constitute the final stages

Some background information and terminology regarding the type of electrode and the steels used for linepipe is given in the remainder of this section.

The cellulosic electrode is classified as an EXX10 electrode under the American Welding Society (AWS) system and this convention has been used in this thesis. The "E" indicates an arc welding electrode, the first two numbers indicate the tensile strength of the weld (all weld metal) in 1000psi, the third number, "1", indicates an all position electrode and the last number, "0", indicates a covering high in cellulose. The equivalent terminology in metric units for the AWS E6010 electrode is the Australian Standard AS 1553.1 E4110 where the "41" indicates a tensile strength of 410MPa. The strength of cellulosic electrodes vary from the lower strength electrode AWS E6010 (AS 1553.1 E4110) to the medium strength electrodes AWS E7010 (AS 1553.2 E4810) to E8010 (E5510) and to E9010 (E6210). The

metric designations have never been adopted by the pipeline industry in Australia, and this is the reason the non-metric designations are used in this thesis.

Steels for the manufacture of linepipe for cross country pipelines carrying oil and gas are classified under the American Petroleum Institute (API) standard 5L X specifications (for example API 5L X60), where "5L" is the specification for linepipe and "X" is the grade designation for high test line pipe. The two numbers following the "X" are the first two digits of the minimum yield strength (in 1000psi). The steels grades are (with the corresponding yield strength in MPa given in brackets) X42 (290), X46(317), X52(359), X56(386), X60 (414), X65(448), X70(483) and X80(552).

In Australia linepipe is most commonly manufactured using the electric resistance welding (ERW) process which suits the practice of using small diameter pipelines (typically in the 150 to 450mm range) (see Appendix C for a brief description of the operations used in the manufacturing of linepipe using the ERW process). The steel grade for ERW linepipe has progressed from API 5L X42/X46 to the present X70 and the maximum operating pressures have increased from 6.8 to 15.3 MPa (Figure 1.4). The typical compositions for these grades (ERW pipe) have been given in Table 1.1 and combine data from various sources since the composition of some grades have varied with time.

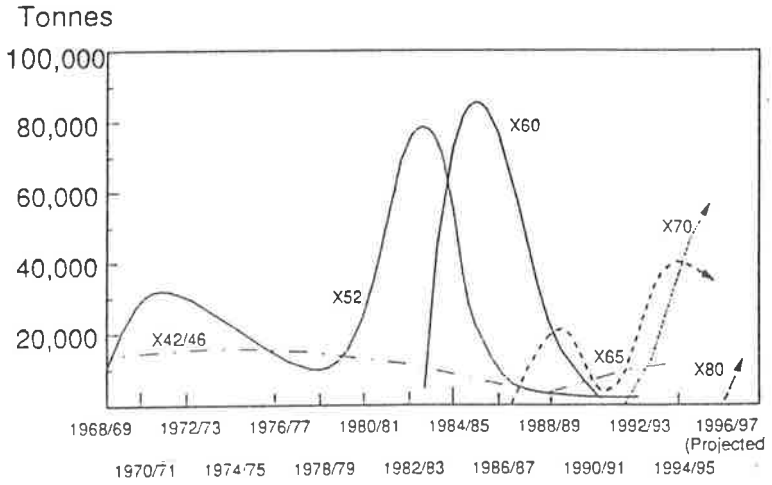

Figure 1.4: ERW linepipe grade lifecycle in Australia (Williams et al., 1996)

API Grade	C	Mn	Si	P	S	Ni	Cr	Cu	Al	Nb	V	Mo	Ti	N	Ca
X42[1]	0.19	0.50	0.055	0.010	0.023										
X42[2]	0.135	0.66	0.130	0.013	0.004	0.023	0.014	0.007	0.038	<0.005	<0.003	0.002	<0.003		
X46[3]	0.22	0.83	0.050	0.009	0.016										
X46[4]	0.12	0.68	0.30	0.010	0.019				0.040	0.025					
X46[5]	0.08	1.15	0.12	0.017	0.004				0.025				0.013	0.005	0.0030
X52[6]	0.09	0.80	0.13	0.018	0.004				0.027	0.025			0.025	0.007	0.0025
X60[7]	0.080	1.25	0.12	0.021	0.004	0.025	0.027	0.018	0.018	0.041	<0.002	0.002	0.012		
X65[8]	0.080	1.40	0.14	0.016	0.003				0.030	0.035	0.035		0.012	0.006	0.0030
X70[9]	0.095	1.55	0.33	0.016	0.001				0.030	0.040	0.060		0.013	0.0045	0.0008
X70[10]	0.060	1.35	0.32	0.012	0.005				0.030	0.060		0.23	0.014	0.0050	0.0008
X80[11]	0.075	1.59	0.31	0.018	0.001				0.026	0.057		0.22	0.013	0.0060	0.0011

Table 1.1: Typical ERW linepipe steel composition (Percentage of elements by mass).

[1] Stewarts and Lloyds (Australia) Pty. Ltd. (1967)

[2] Tubemakers of Australia Ltd. (1993)

[3] Stewarts and Lloyds (Australia) Pty. Ltd. (1968)

[4] Tubemakers of Australia Ltd.(Stewarts and Lloyds Division) (1975)

[5, 6, 8] Williams, (1987)

[7] Tubemakers of Australia Ltd.(Steel Pipe Division) (1985)

[9, 10, 11] Williams et al., (1996) (ERW pipe from full width strip)

Modern linepipe steels can be characterised by low levels of carbon (<0.08%) and impurities. The strength reduction caused by lower carbon contents has been compensated by appropriate additions of manganese (the Mn content has increased from 0.50 to 1.6% in X80 steels), nickel and copper, as well as optimised microalloying additions in conjunction with disciplined controlled rolling practices (Williams, 1987). The impurities are controlled using processes such as liquid iron desulphurisation, calcium silicide ladle injection (which converts harmful alumina clusters to globular calcium aluminates and modifies the shape of sulphides for improved toughness transverse to the rolling direction) and vacuum degassing, which reduces the risk of oxidation and nitrogen pick-up and decreases the hydrogen levels. The control of strength levels and improved fracture toughness (while controlling the levels of microalloying elements to meet weldability requirements) has also been achieved through better controlled rolling practices. The objective has been to obtain a very fine and uniform grain size as well as maximum strengthening potential from Nb(C,N) without resorting to excessive levels of Nb (Williams, 1987).

The silicon content has increased from about 0.05% in semi-killed steels to 0.30% in killed steels. The controlled use of microalloying elements (niobium, vanadium, titanium and more recently molybdenum) to increase the strength of pipe steels is evident from Table 1.1.

To further improve the strength of X70 and X80 steels, at lower carbon equivalents which permit safe preheat-free field welding with cellulosic electrodes, Mo has been used. The more conventional Nb-V alloy system requires correspondingly higher carbon equivalent designs (Williams et al., 1996). A further description of the steelmaking and strip making processes are given in Appendix C.

In the next paragraph some consideration is given to the choice of the strength of the cellulosic electrode for welding pipeline steels API 5L X56 through to X80.

The girth welds of pipeline steels up to and including grade X56 are best welded only with low strength electrodes (E6010) which will result in very ductile and tough welds. For X60 steels the girth welds, up to the filler passes, are best welded again with low strength E6010 electrodes. A contribution of strength from the reinforcement in the cap pass is needed to ensure the weld is stronger. With the linepipe steel grades X65 and X70, the root and hot passes should be welded with low strength electrodes and the subsequent passes with higher strength electrodes (preferably E7010 for X65 and E8010 for X70) in order to achieve adequate weld strength (Bilston et al., 1995). Welding of the root and hot passes with low strength electrodes is common practice in Australia, though may not be necessarily used elsewhere.

The choice of appropriate methods and consumables to weld X80 grade steel is still the subject of ongoing research. The maximum available consumable strength level is, for X80 steel, marginal with respect to strength matching for the pipe (Barbaro et al., 1995). In the case of thin walled high strength X80 linepipe where there are only a few passes (for example 3 passes, a root, a hot and a cap pass, are required for a wall thickness of 5mm), and the available cellulosic consumable specified minimum strength level (up to E9010) slightly undermatches that of the pipe, the importance of the root bead weld strength becomes important with regard to the overall strength of the weldment. However, increasing the strength level of the root bead pass to maximise weld joint strength would increase the susceptibility to cracking. These issues constitute the basis of current research since it has been suggested that the conventional welding procedure, which includes cellulosic electrodes,

may need to be maintained in order to achieve the economic benefits of higher strength linepipe in Australia (Barbaro et al., 1995).

1.2.4 Survey of Hollow Bead Occurrence on Pipeline Projects

A survey was carried out by C. W. Pope & Associates Pty Ltd (Biddle, 1993) to assess the incidence of hollow bead on the Junee to Griffith Gas pipeline. One thousand consecutive pipeline welds were surveyed to determine the variation in the length, height and position of all nominated areas of hollow bead. The pipe grade was API 5L X42, the outside diameter was 168.3mm and the wall thickness varied from 4.6 to 6mm.

The welders were in this instance welding an average of 200 welds in a 10 hour day. No welds, however, were rejected as a result of the incidence of hollow bead outside the limits of Australian Standard AS 2885 - 1987. The maximum length of hollow bead was found to be 10mm and the maximum width, estimated from the contrasting density of the discontinuity on the radiograph, was less than 1.2mm.

When the position of hollow bead was plotted on a diagram of a circumferential weld, it was found that in all cases the hollow bead discontinuity coincided with stop or start areas of the weld, and 94% of hollow bead were found at the bottom of the pipe between the 8 o'clock and 6 o'clock position. A relationship between position and length of hollow bead was not observed and only very rarely was there more than one length of hollow bead present in any one weld.

1.2.5 Effect on Mechanical Properties

The investigation undertaken by Barkow (1973) was the most thorough study done on hollow bead. The results of the mechanical tests performed are given below.

Of the 48 transverse joint tensile tests made, three fractured in the weld metal at approximately the same tensile strength as the parent metal. One of the three was due to a hollow bead defect. The remainder fractured in the parent metal.

All the face-bend tests were bent to 160^{o} without failure.

Of the root bend tests, two broke because of internal undercut. However, 20 of the specimens showed evidence of hollow bead defects in the root. It should be noted, however, that the Australian Standard AS 2885.2 - 1995 does not require any root bend tests to be performed.

Of the nick-break tests made, four specimens showed hollow bead defects.

Barkow also found that hollow bead was more prevalent where a large reinforcement bead existed at the root, but concludes, however, that the size of this reinforcement bead is not a factor which affects the mechanical properties.

1.2.6 Variables Associated with Hollow Bead Formation

1.2.6.1 Effect of Welding Parameters

In 1973, Barkow (1973) reported that the appearance of hollow bead defects in pipeline welds was the result of the introduction of fully killed, high strength and high toughness pipeline steels. Although it was suggested that the formation of hollow bead could be the result of higher silicon content, it was also mentioned that hollow bead was occasionally found with semi-killed steels. The experiments performed by Barkow used 5 different samples of API 5L X65. The composition of the steel samples show a silicon content between 0.28 and 0.35%, a

carbon content in the range 0.15 to 0.20%, a manganese content of 1.31 to 1.40% and small microalloying additions: niobium (0.03%), zirconium (0.04 to 0.10%) and vanadium (0.05 to 0.07%). The aluminium level varied between 0.02 to 0.04%.

The conclusions made by Barkow (1973) were that weld travel speed and current were the main contributing factors to the formation of hollow bead and that a welder could avoid its occurrence by changing his technique. Barkow found that increasing the welding current, voltage and travel speed increased the possibility of the formation of this defect. He also stated that the real cause of hollow bead was the weld travel speed. It was proposed that a high welding speed reduced the volume of metal being deposited due to the decrease in heat input and as a result the amount of molten metal available was not sufficient to fill the entire root gap. Since solidification was from the outside in, voids were created at the centre of the weld bead. However, when the welding speed was lower more heat was introduced into the weld area and more metal was deposited. As a result the weld pool remained molten longer and the molten metal had more time to fill the entire gap. It was also recognised by Barkow that with a "low carbon" fully killed pipeline steel the weld pool would be slightly more fluid, which the welders would compensate for by employing higher travel speeds.

Wright (1993) has mentioned, however, that the above hypothesis proposed by Barkow does not fully explain the rounded nature of hollow bead which suggests some contribution from entrapped gas, but that nevertheless any such contribution would probably be exacerbated by high travel speeds.

It was also observed by Barkow that as the welding current increased, hollow bead defects became more numerous and larger. It was suggested that a soaking type technique (which employs a low travel speed) with a welding current and voltage below 170A and 28V

respectively and a maximum travel speed of 330mm/min should be used to avoid their formation.

In The Lincoln Electric Company handbook on the Welding of Pressure Pipelines and Piping Systems (1991) and in the article by Hinkel (Lincoln Electric Company, 1984) it has been stated that hollow bead is aggravated by excessive travel speeds and high currents and that the stringer bead should be welded with 5/32inch (4mm) electrodes at 130 - 165A DC(+) and at a travel speed of 10 to 12 in/min (250 to 305mm/min) to minimise its occurrence. It has also been mentioned that DC(-) together with lower currents should be used when hollow bead defects are a problem.

A paper by The Welding Institute (TWI) (Wright, 1993), which has reviewed published literature and carried out a survey of industrial experience related to hollow bead, has reported from its survey of various companies that the primary causes of hollow bead are high levels of weld travel speed and current.

In an investigation on the effects of long keyhole and convection on weld defect formation in gas tungsten arc (GTA) welds, Lin and Eagar (1983) suggested that the strong eddy motion behind the arc was responsible for tunnel pore defects. The effect of varying the welding current was studied and showed that when the current was increased from 250A to 300A, a sharp increase in the penetration depth caused the formation of a tunnel cavity. It was suggested that the disappearance of the tunnel pore at even higher currents is a result of the greater volume of liquid metal available in the 350A weld which fills the cavity formed by the long keyhole. These welding currents cannot be compared with the ones used in stovepipe welding and neither can the current densities in this case as the diameter of the welding electrode has not been given by Lin and Eagar. However, the effect of an increase in welding

current on the formation of the tunnel cavity and the theory put forward to explain the formation of hollow bead have been considered here.

They postulated that the eddy motion was due to the unbalanced distribution of current flow. Since the solid metal has a higher electrical conductivity than that of the liquid metal, most of the current entering the pool will flow to the front and sides of the arc, while less current passes through the elongated weld pool behind the arc (see Figure 1.5).

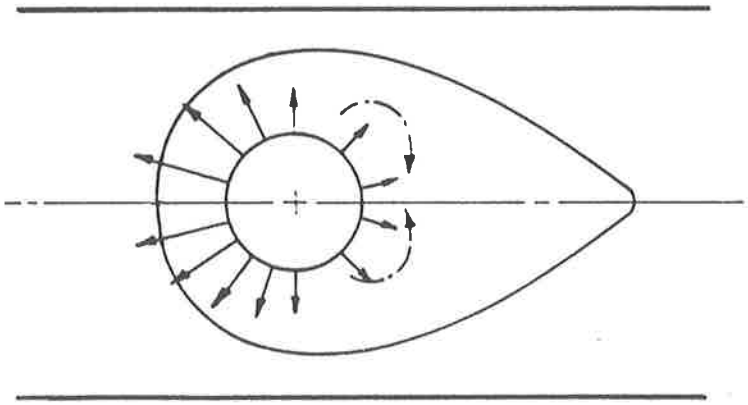

Figure 1.5: Schematic representation of the unbalanced distribution of current in the weld pool which produces unbalanced electromagnetic forces (Lin and Eagar, 1983).

The circumferential eddy motion which forms at the top of the weld prevents metal from filling the bottom of the depressed keyhole resulting in tunnel porosity along the base of the weld bead. They indicated that a similar mechanism could account for the formation of hollow bead in stovepipe welding where a deep depression or keyhole was formed by the expanding gases produced by the decomposition of the electrode coating. A circumferential flow could be induced which would inhibit metal from "sinking" to the root of the weld in a manner similar to that described above.

This mechanism, however, cannot explain the observed formation of some hollow bead defects at the top of the weld bead.

1.2.6.2 Effect of Welding Consumables

Okuda (1987) has studied the characteristics of welding consumables and has described cellulosic electrodes as ones generating a large quantity of gases such as CO, CO_2, H_2 and H_2O, as well as allowing a high level of hydrogen in the weld metal which could cause cold cracking and blow-holes.

Cellulosic electrodes contain a high percentage (about 35%) of cellulose (Böhler Welding Technology)) which breaks down at temperatures typically around 200 - 300°C to develop an atmosphere of hydrogen (about 50% of the shielding gas (Boniszewski, 1992)), as well as generating large amounts of carbon monoxide, carbon dioxide and some water vapour. The other constituents are typically rutile (20-60%), quartz (15-30%), carbonates (0-15%) and ferromanganese (5-10%) (Svensson, 1994)

The volume and composition of the gas liberated by one 5.0 ϕ x 350mm long cellulosic electrode has been given by Lancaster (1992) as consisting of 2.3 STP L of CO and CO_2, 1 STP L of H_2 and 2 STP L of H_2O. The gases which are generated provide a reducing atmosphere around the arc and shield it from atmospheric gases. The volume flow rate of the shielding gas is high at 5.4L/min compared with 1.4L/min for basic low hydrogen electrodes (Boniszewski, 1992). Their high ionisation potentials result in a high arc voltage and, therefore, high arc energy which is responsible for rapid burn-off and deep penetration (Houldcroft, 1967). The moisture content of the electrode is high, from 3 to 6% (Svensson, 1994). The weld metal hydrogen content is also high, usually in the range of 30-60mL/100g. Cellulosic electrodes will, however, yield weld metal with the lowest nitrogen content among

all the covered electrodes due to the effectiveness of the voluminous gas shield in protecting the weld metal from the atmosphere (Boniszewski, 1992).

The slag from cellulosic electrodes is moderately viscous and fast-freezing and is produced in small volumes to prevent it from running down into the arc. The slag is also thin and brittle and is therefore easily removed from the surface between weld runs (Böhler Welding Technology).

The telephone survey done by TWI (Wright, 1993) has identified the handling characteristics of consumables as a contributing factor to the formation of hollow bead. It was suggested that an inadequate moisture content of the electrode flux influences the formation of these defects by reducing the volume of shielding gas around the arc, hence allowing more atmospheric gases to enter the weld pool.

1.2.6.3 Effect of Parent Metal Composition

As mentioned in Section 1.2.6.1 Barkow first suggested in 1973 that silicon was an influential factor in the formation of hollow bead, despite the fact that hollow bead had previously been reported in semi-killed steels.

In reviewing the claim made in the Lincoln Electric Company handbook "Welding of Pressure Pipelines and Piping Systems" (1991) that hollow bead generally occurs with pipe steels containing over 0.1% silicon, the report by TWI (Wright, 1993) mentioned that the role of silicon in the parent material in directly promoting the formation of hollow bead had never been proved. In The Lincoln Company handbook it has been suggested that welders could increase the welding speed to sufficiently high levels to result in hollow bead due to their inexperience of welding fully killed steels, where the weld pools are slightly more fluid.

However, silicon contents of linepipe are now commonly between 0.25 and 0.35 % and hollow bead does not often occur in pipeline welds outside the limits specified in the pipeline welding code. Wright (1993) found that during an extensive investigation on hydrogen cracking of cellulosic welds in API 5L X60 pipe (with a silicon content of 0.38%), carried out by TWI in 1969, no problems with hollow bead were reported.

The same article by TWI also reported an internal research project undertaken by Böhler in 1972, which suggested that high aluminium contents (greater than 0.04%) could be linked with hollow bead.

Furthermore, the telephone survey of industrial experience undertaken by TWI (Wright, 1993) revealed that in the area of parent metal composition, aluminium and silicon were again suggested as contributing factors, as well as very low sulphur levels. The survey has indicated however, that these factors were thought to be minor compared to welding technique.

1.2.6.4 Effect of Joint Geometry

The Lincoln Electric Company handbook (1991) states that hollow bead can be avoided if the root gap is increased and (although no supporting reference is given) that hollow bead generally occurs in thin walled pipes.

In his experimental study, Barkow (1973) found that when a large root face of approximately 3.2mm was used with a root gap of 1.6mm, a high welding current could be used in conjunction with a relatively low travel speed which resulted in good penetration without the formation of hollow bead defects. When the same parameters were used with a narrower root gap, lack of penetration resulted.

1.2.7 A General Description of Elongated Gas Pores

In this literature review a broad study of elongated gas pores has first been undertaken to characterise their typical features and shape, the location of their nucleation and direction of propagation, as well as to obtain a general understanding of the mechanism of their formation and the gases involved.

Elongated pores are commonly known as worm holes or tunnel pores. The elongated shape is due to pore formation between the growing dendrites during solidification, and growth at the same speed and direction as the solidification front (Svensson, 1994). Elongated pores follow the solidification pattern and nucleate either near the fusion line or near the centre of the weld and grow lengthways, sometimes increasing in diameter at the same time.

Lancaster (1993) has stated that tunnel porosity is associated with hydrogen and has explained that its formation is the result of the formation of a region immediately adjacent to the solidification front which becomes enriched in gas-forming solutes. He has also mentioned that practical experience has shown that steel can be welded with rutile or cellulosic electrodes, the latter of which can produce a shielding gas that contains up to 50% hydrogen, without any porosity. In addition, he has suggested that when there is a significant amount of hydrogen present in the arc (greater than approximately 10%) there is vigorous bubbling of gas such that at the rear of the weld pool the hydrogen is not far from the solubility limit and solidification takes place without further gas evolution. It is possible to freeze this zone, and this may occur owing to irregular movement and at stops and starts of welding. Otherwise in steel the weld pool purges itself of the hydrogen (Lancaster, 1993).

Other authors have made similar comments. A continuous supply of gas from the surrounding liquid, either by discontinuity of solubility at the solidification interface or by a reaction

producing a gaseous discharge, allows a pore to form and grow (Granjon, 1991). The growth of the gas bubble from the initial nucleus is controlled by the transportation of gas dissolved in the molten metal to the dividing boundary between the gas and the liquid (Lundin, 1984).

Devletian and Wood (1983) have explained that in welding bubbles nucleate heterogeneously on external nuclei such as the solidification interface, slag inclusions and external contaminants which reduce the energy of formation of the gas nucleus. It was noted that in high purity aluminium alloys having virtually no heterogeneous nuclei available, high levels of supersaturation of hydrogen could be obtained but little porosity would result. However, when substantial quantities of oxides and other inclusions were available to act as nuclei, much less supersaturation and greater porosity occurred during solidification. It was also mentioned that the interstices between cellular dendrites could provide localised regions in which bubbles could grow, in which case, however, detachment and flotation into the molten weld pool was less likely (Devletian and Wood, 1983).

Devletian and Wood (1983) commented further on the growth of pores and proposed that the interdendritic pores were controlled by the growth substructure, whereas spherical pores were controlled by surface tension. Also, elongated pores would grow provided that the length and growth rate of secondary dendrite arms were insufficient to block the lengthening growth of the bubble. They suggested that mechanical entrapment of bubbles did not distort their shape because the portion of cellular dendrites that contacted the bubble wall would freeze in place. The internal surface of the pore was likely be uneven due to the numerous parts of the primary and secondary cellular dendrite arms that formed the wall (Figure 1.6).

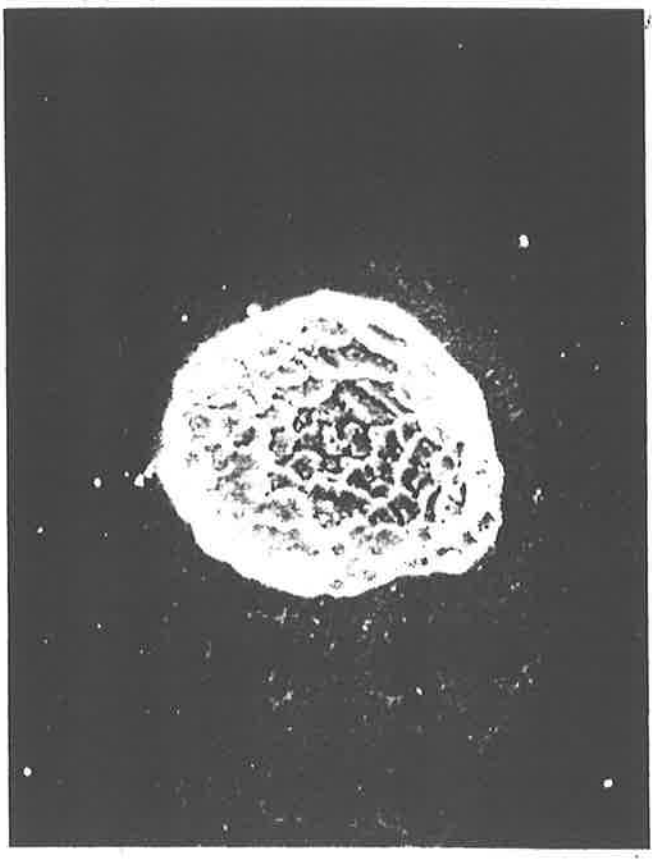

Figure 1.6: Spherical pore in an aluminium alloy weld showing primary and secondary cellular-dendritic arms that have terminated along the pore wall (x500) (Devletian and Wood, 1983).

Svensson (1994) has suggested that the growth rate of a pore is dependent on factors such as the diffusion rate of porosity-forming gases (hydrogen and nitrogen), the overall gas concentration in the molten weld metal (particularly that of hydrogen) and the concentration of stable nuclei for pore formation.

The gases responsible for the formation of pores have been identified as hydrogen, nitrogen and carbon monoxide, as well as carbon dioxide when welding non-killed steels (Svensson, 1994). The sources of the oxygen which enters the weld pool are oxides in the filler wire or parent metal, oxygen compounds in the electrode flux and oxygen from the atmosphere (Lundin, 1984). Water vapour, from the reaction between oxygen and hydrogen, may also be entrapped during solidification. Furthermore the water vapour may be dissociated by the reaction with metal ions (for example iron) to form hydrogen (Ibarra and Olson, 1995). The water vapour released by surface contaminants such as moisture, oil and grease can dissociate in the arc and allow hydrogen to be absorbed into the weld pool (Harris, 1988). The glossy inside surface of elongated pores found in steel welds has been attributed to the reducing character of the gases, hydrogen or carbon monoxide, which cause their formation (Granjon, 1991).

An alternative mechanism for the growth of elongated pores has been proposed invoking the diffusion of hydrogen to form bubbles and their subsequent coalescence. This process is said to be a function of the time within which the weld pool remains molten and the velocity of the bubbles. In this model, heterogeneous nucleation occurs away from the solid-liquid interface allowing a large percentage of freshly nucleated bubbles to float and grow freely. Subsequently, the continuous growth of pores occurs as the rising bubbles collide (Devletian and Wood, 1983).

Howden and Yen (1986) have described worm hole pores in austenitic stainless steel welds as originating at the fusion line adjacent to the parent metal and then growing in a direction perpendicular to the solidification front at the centreline of the weld. Growth was at either upward or downward angles to the horizontal centreline of the weld, depending on the heat

flow and solidification direction. The cross section of the pores was observed to be round. These experiments used the gas tungsten arc (GTA) welding process with an argon shielding gas to which additions of hydrogen up to 15% by volume were made. The weld travel speeds ranged from 1.5 to 2.5mm/s (90 to 150mm/min) and welding currents from 60 to 100A with an arc length of 2mm. The results revealed that the diameter of individual worm hole pores increased (up to 2mm) with increasing current, travel speed and hydrogen partial pressure in the arc. The number of pores also increased with increasing hydrogen pressure.

A model was proposed to show that the worm hole pore could propagate by hydrogen flow from the solidifying weld metal by a solid state diffusion process, rather than from the molten metal. This model was based on previous research on the behaviour of hydrogen in arc weld pools (Howden and Milner, 1963) which showed that hydrogen gas absorbed into the pool, according to Sievert's relationship, was retained in the weld metal on solidification.

In a review of the formation of gas pores in weld metal, Trevisan (1990) summarised the findings of various papers on this subject. On the influence of welding parameters the results show that the amount of porosity decreases with increasing travel speed and increases with increasing welding current. The first effect is proposed to arise from the reduced time available for pore formation since the metal remains in the molten state for a shorter period and is not related to a change in the rate of hydrogen absorption. The second effect is explained as a consequence of the increase in surface temperature of the weld pool which enlarges the area of the hot zone over which hydrogen absorption takes place, thus increasing the rate of gas pick up.

On the subject of elongated pores, the texts "Metallurgy of Welding" (Lancaster, 1980) and "Welding Fabrication" (Tweedale, 1969), have briefly explained the causes of tunnel porosity

observed in gas metal arc (GMA) welding in which large discontinuous cavities or large continuous holes may occur due to the use of excessive currents. The tunnelling defect (long continuous holes) in the GMA welding of aluminium has been attributed to excessive currents which causes turbulence in the weld pool. Excessive stirring was also mentioned as a reason for tunnelling, by allowing the metal to be driven away from the root of the run and causing it to solidify as an arch over the gap.

Elongated pores made using a solid-gas eutectic solidification technique, which involves melting a solid in a hydrogen atmosphere and then cooling through the eutectic point (Simone and Gibson, 1996 and 1997), have shown features which are similar to ones seen with hollow bead pores. This technique is applicable to various metals including copper, nickel, iron and aluminium. At the eutectic, solidification of the metal and nucleation of pores, resulting from diffusion of gaseous hydrogen out of the melt as it freezes, occur simultaneously. The volume fraction of the gaseous hydrogen phase, or the porosity, of the resulting material, can be controlled by manipulation of the pressure of the hydrogen atmosphere in the casting chamber, since the position of the eutectic point depends on the pressure of the system. Directional solidification yields pores that are elongated in the direction of movement of the solidification front since the hydrogen gas tends to diffuse to pores that have already nucleated on the solidification front.

The pores produced using this technique (Simone and Gibson, 1996 and 1997) are cylindrical, their size and shape vary within the longitudinal position, and they grow intermittently along the length of a particular specimen. The experimental conditions which affect the structure of the pores are not mentioned. Photographs of longitudinal samples containing pores show that

the diameter at the start is small and then gradually increases with growth. In some cases the diameter of the pores also varies along their length.

These two features as well as the discontinuous growth in the direction of solidification (many pores rather than one long single pore form) are comparable to the characteristics of hollow bead.

1.2.8 Gas - Metal Reactions and Detailed Investigations of Porosity in Welding

The general study on gas pores in the previous section has revealed the importance of hydrogen in the formation of porosity. It can thus be concluded that hydrogen is a dominant factor in the formation of gas pores due to its prevalence in welding arcs and weld pools, its high rate of diffusion (the diffusivity, D, of hydrogen in liquid steel is approximately 3×10^{-7} m^2/s (Lancaster, 1992)) and its reduction in solubility with solidification and decreasing temperature (see Figure 1.7 which illustrates the case of the equilibrium solubility of hydrogen in iron with temperature). A survey was made, therefore, of the mechanism of the absorption of gas into the molten weld pool and the effect of welding variables on the absorption characteristics. In addition a more thorough study of porosity in welds was undertaken.

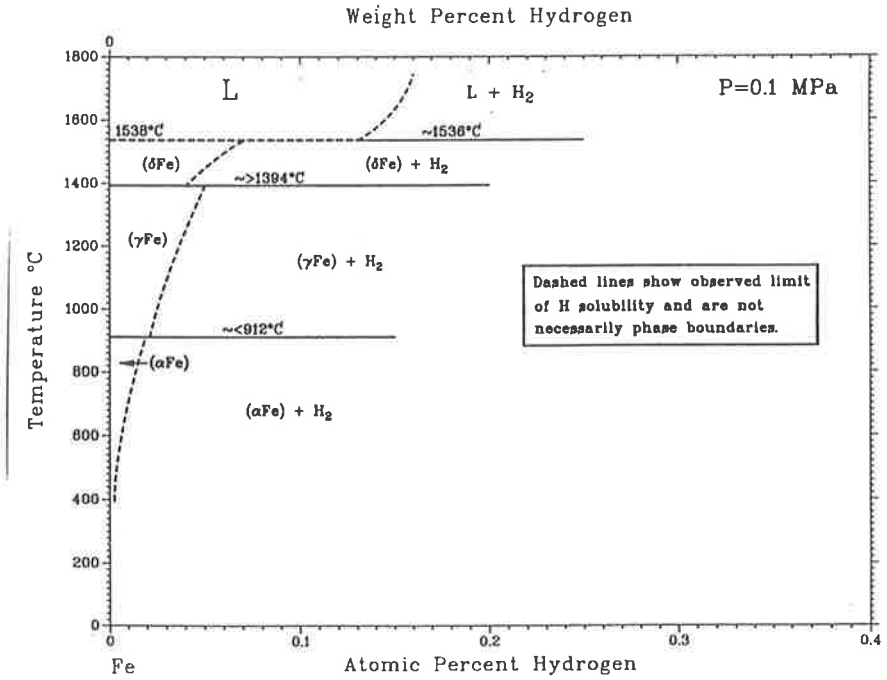

Figure 1.7: Diagram showing the solubility of hydrogen in iron with temperature for a pressure of 1atm (San-Martin and Manchester, 1993).

1.2.8.1 Gas -Metal Reactions in Arc Welding and Melting

Howden and Milner (1963) have dealt with the factors influencing, and mechanisms of, hydrogen absorption in arc melting. The results deal with absorption in the molten metal, rejection on cooling and retention in the solid.

The experiment involved striking an arc, between a fixed non-consumable tungsten cathode and a movable copper anode containing a depression which housed the metal test sample, to melt a metal button in a closed chamber containing an argon/hydrogen mixture at atmospheric pressure. Analysis of the hydrogen content of the gas before and after melting the metal

sample allowed the determination of the amount of gas dissolved within the molten sample. The amount of hydrogen evolved during cooling of the sample was also measured. The hydrogen content of the gas in the chamber was determined using a katharometer (or thermal conductivity gauge).

It was reported that the concentration of hydrogen in the molten pool was equal to the solubility of hydrogen in a zone close to the arc where the temperatures are above the melting point of the metal. This region was termed the hot zone and it was found that its effective temperature was dependent on current and time. As the current was increased the temperature was observed to increase allowing more gas to be absorbed. There was a critical hot zone temperature at which a maximum quantity of gas was absorbed. Above this critical hot zone temperature the boiling point of the metal was approached and the absorption of gas decreased due to vaporisation of the metal.

Investigating the effects of welding parameters, impurities and alloying additions on iron, it was found that arc length had no measurable effect on the hydrogen content. There was, however, an increase in the gas content of the specimen with an increase in arc current, in the range 100 - 200A, and a decrease when the current was raised to 250A.

In the current experimental investigation on hollow bead pores, the welding current was varied from about 130 to 220A. The electrodes used (Lincoln Fleetweld 5P+) have a recommended current rating of 90 to 175A. It was found that above 220A the electrode would catch fire towards the end of the run. The current densities could not be compared as the diameter of the tungsten electrode was not given by Howden and Milner.

It was reported that an austenitic stainless steel which has a higher equilibrium hydrogen solubility than ferritic steels (since the interstices in the fcc lattice are larger than those in a

bcc lattice) absorbed more gas than iron and mild steel by a factor of 1.2 at 100A and a factor of 1.6 at 250A. It was also mentioned that with iron it was impossible to attain a solubility of more than 1.6 times the melting point solubility due to the vaporisation of the metal.

In addition the experimental data showed that for ferrous metals the hydrogen solution pressure, which is the driving force for diffusion of hydrogen from the solidified metal either into the atmosphere or into the adjacent base metal, was much greater for ferritic structures (above 10^4 atm) than for austenitic structures (about 10^2 atm).

Salter (1963) has also studied the absorption of hydrogen by arc melted steel. The effect of the shielding gas composition and the arc variables on the gas absorption pattern were examined. The influence of a slag "blanket" and moisture content in the argon on the quantity of gas retained in the metal were also measured in an attempt to correlate the work more closely with welding problems.

The experimental work involved melting mild steel buttons using a tungsten electrode under an argon arc. The hydrogen absorbed by the metal in an atmosphere of argon/hydrogen or argon/water vapour was examined as a function of hydrogen partial pressure, arc current, arc length and specimen size. The quantity of hydrogen retained in the specimen as well as that evolved from the specimen after extinguishing the arc were measured.

The nett rate of absorption of hydrogen by the steel buttons was found to increase with arc current and also with the hydrogen partial pressure of the surrounding atmosphere. The equilibrium solubility of hydrogen in the molten steel increased with arc current, decreasing specimen size, and also increased according to the square root of the hydrogen partial pressure. The time for the hydrogen content to reach equilibrium was mostly dependent on specimen size, increasing with increasing specimen size. The hydrogen contents at

equilibrium were higher (for a particular experiment approximately 0.9 - 1.3 times higher) than those predicted by Sievert's law (equation 1.1), for metal melted under molecular hydrogen at the specimen temperature measured:

$$[H] = K \sqrt{P_{H_2}} \qquad (1.1)$$

where [H] is the concentration of hydrogen, P_{H_2} is the partial pressure of hydrogen and K is the equilibrium constant which is dependent on temperature.

This difference appeared to be due to the rapid absorption of atomic hydrogen over a small high temperature zone beneath the arc and the proportion of the specimen surface covered by this zone. This hot zone was found to increase in size rapidly as the current was increased from 110 to 200A. It was also found that the hot zone has approximately the same area for different specimens size, thus covering a greater proportion of the surface area of the smaller specimens than of larger ones. It was postulated that as hydrogen is absorbed, the specimen first approaches and then exceeds the equilibrium hydrogen content with regard to the cooler molecular gas and hydrogen is then desorbed over the area of exposed surface outside the hot zone.

The proportion of hydrogen retained by the specimen on cooling to room temperature was largely controlled by the surface area to weight ratio of the specimen and its environment. The environment of the specimen surface had an influence on the rate of hydrogen loss on cooling: the presence of hydrogen in the atmosphere, or slag on its surface inhibited desorption. The absorption of hydrogen from atmospheres of argon/water vapour closely followed that from argon/hydrogen atmospheres if the available hydrogen was considered to be equivalent to the volume of water vapour.

Similar results were obtained in a recent study by Hooijmans and den Ouden (1996). Arc melting experiments were carried out under stationary arc conditions in an argon-hydrogen atmosphere on small samples of pure iron. Immediately after the arc was switched off, the sample was cooled by a gas flow originating from holes in a metal ring around the sample. The cooling rate was varied by changing the composition of the gas from pure argon to pure helium. After solidification and cooling to room temperature, the samples were placed in a container filled with liquid nitrogen until analysis by gas chromatography. The amount of hydrogen in the shielding gas varied from 0 to 40%.

In all of the experiments the measured hydrogen concentration in the sample was found to increase rapidly from zero to a saturation value dependent on the hydrogen partial pressure in the shielding gas. The hydrogen concentration in the sample was found to increase with an increasing concentration of hydrogen in the shielding gas from about 0.0003 weight% at 2volume% of hydrogen in the shielding gas to 0.00085weight% at 40volume%.

The influence of the cooling time on the hydrogen concentration in the iron samples was also investigated. It was established that the measured amount of hydrogen was not equal to the amount present in the liquid metal at the moment the arc was extinguished since hydrogen would escape through the surfaces of the weld. The hydrogen content of the samples was therefore strongly dependent on the cooling rate after the extinction of the arc. The results showed a decrease in the hydrogen content with increasing cooling time, which was defined as the time interval between the extinction of the arc and the moment the sample reaches a temperature of 300°C. For example, a variation in cooling time from 4 to 10s resulted in a decrease in hydrogen concentration from 0.00045 to 0.00020 weight%. The initial hydrogen concentration in each sample was calculated from the measured hydrogen concentration and

the cooling history of the sample using a finite element method. It was found that a significant amount of the hydrogen absorbed in the sample (between 40 and 60%) disappeared during cooling.

The influence of the welding conditions on the hydrogen absorption is explained by two mutually independent processes: inflow of hydrogen through the interface between the arc and the liquid metal and outflow of hydrogen through the entire surface of the liquid metal.

1.2.8.2 Detailed Investigations of Porosity in Welding

1.2.8.2.1 The Nucleation of Gas Bubbles

The formation of a gas bubble requires that the gas pressure inside the bubble (P_b) exceeds the sum of the external atmospheric pressure (P_o), the hydrostatic pressure (ρgh), and the surface pressure ($2\sigma/r$):

$$P_b > P_o + \rho gh + 2\sigma/r \qquad (1.2)$$

where ρ is the density of the liquid metal, g is gravitational acceleration, h is the depth of the bubble below the surface of the weld pool, σ is the surface tension of the liquid metal and r is the radius of the bubble.

The hydrostatic pressure term is usually neglected for normal welding conditions as the depth of weld pools is small. The gas pressure inside the bubble then becomes:

$$P_b > P_o + 2\sigma/r \qquad (1.3)$$

Rakhmanov (1978) has evaluated the work of formation required for the nucleation of a gas nucleus in welds. He used the thermodynamic probability, I, of the simultaneous separation of gas molecules for the formation of a stable nucleus with a radius greater than the critical radius:

$$I = Ce^{\frac{-A_f}{kT}} \qquad (1.4)$$

where A_f is the work of formation of a nucleus, k is Boltzmann's constant, T is absolute temperature and C is a constant which is identical for all gases. As the formula is not sufficiently accurate it was used to evaluate approximately the effect of various factors on the formation of nuclei. To compare the thermodynamic probability, I, for various values of A_f, it was noted that the inequality $A_1 > A_2$ always gives $I_1 > I_2$. Therefore, only the variation of the corresponding work of formation of the nucleus was examined. A formula for A_f was derived:

$$A_f = 4\pi r_c^2 \sigma_{l.g} - \frac{4}{3}\pi r_c^3 (P_{lib} - P_o) \qquad (1.5)$$

where r_c is the critical radius, $\sigma_{l.g}$ is the surface tension at the liquid-gas interface, P_{lib} is the liberation pressure (which is discussed below) and P_o is the atmospheric pressure.

The critical radius is given by:

$$r_c = \frac{2\sigma_{l.g}}{P_{lib} - P_o} \qquad (1.6)$$

where P_{lib} is the pressure that can be produced by the gas released from solution in liquid metal at the melting temperature and has been termed the liberation pressure. This quantity is given by:

$$P_{lib} = \left(\frac{C_g}{S_{g.l}} \right)^2 \qquad (1.7)$$

where C_g is the concentration of gas in liquid metal and $S_{g.l}$ is the solubility of the gas in liquid metal at the melting point and for a pressure of 1atm above the liquid metal.

Rakhmanov (1978), found, using this procedure, that the homogeneous formation of nuclei in liquid metal in arc welding was not possible.

The nucleation of a bubble on a flat, horizontal boundary between the solid and liquid phases was investigated assuming that the concentration of the gas in the liquid phase including the layer of liquid metal adjacent to the interface is constant. A bubble nucleated on a surface has the form of a spherical segment with wetting angle θ and three components of surface tension due to the presence of three phases in the system (Figure 1.8):

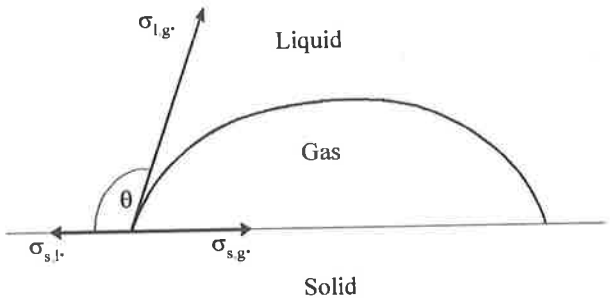

Figure 1.8: Schematic of a gas nucleus on a solid surface in a melt.

The relationship between the components of surface tension and θ is given by

$$\sigma_{s.g} - \sigma_{s.l} = \sigma_{l.g} \cos\theta \qquad (1.8)$$

where $\sigma_{s.g}$ is the surface tension at the solid-gas boundary, $\sigma_{s.l}$ is the surface tension at the solid-liquid boundary and $\sigma_{l.g}$ is the surface tension at the liquid-gas boundary. The work of formation for such a system is given by

$$A_f = \frac{4\pi\sigma_{l.g}^{\ 2}}{3(P_{lib} - P_o)^2} (1+\cos\theta)^2 (2-\cos\theta) \qquad (1.9)$$

An increase in the wetting angle will decrease the work of formation of a nucleus. An evaluation of this system, however, revealed that the wetting angle is acute and thus the work of formation, A_f, was not considerably lower than the work required for homogeneous nucleation. It was thus concluded that other factors were controlling the formation of gas nuclei in welds.

As a result the effect of non-metallic inclusions, which would increase the wetting angle, was investigated and it was found that the work was reduced, but not markedly. It was concluded that the presence of inclusions was not the only controlling factor determining the possibility of pore formation.

The effect of the solidification conditions on the concentration of gas in a layer of liquid metal adjacent to the liquid phase and the work of formation of a nucleus in this layer was also studied.

Rakhmanov (1978) proposed the following. At the high solidification rates observed in arc welding, the amount of gas that remains in the solidifying metal is greater than the equilibrium distribution. The concentration of the gas in the layer of the solid phase adjacent to the interface rapidly increases and becomes almost equal to the initial concentration of the gas in the liquid phase, C^{o}_{liq} . At the same time a concentration "condensation" forms in the layer of liquid metal adjacent to the solidification interface. In this layer the concentration of the gas becomes equal to C^{o}_{liq} /k (where k is the equilibrium partition coefficient) characterising a rapid change in solubility. The mean thickness of the layer, δ, is proportional the diffusion coefficient of the gas in the liquid, D_L, and the solidification rate, V_r:

$$\delta = \frac{D_L}{V_r} \qquad (1.10)$$

The variation in the gas concentration in the layer at the solidification interface will depend mainly on the solidification rate, the number and duration of delays (which are due to the discontinuous nature of solidification in welding) and the diffusion rate of the gas in the solid and liquid phases. Even if it is assumed that the concentration condensation does not exist during solidification, it must form during the interruption. In areas where solidification fronts meet the local content of the gas may be even higher. It was thus concluded that gas nuclei were most likely to form at the solidification interface due to the formation of a layer of highly concentrated gas solutes.

In a recent study by Redchits and Froloc (1996), the derivation of a new criterion to characterise the stages of nucleation of bubbles and their growth in the molten weld pool used the assumption that the conditions for the nucleation of gas bubbles would improve as the susceptibility of the metal to supersaturation with hydrogen increased because a larger amount of hydrogen would evolve from solution.

Grigorenko (1970) also studied the distribution of gas solutes at the solidification interface to explain the mechanism by which gas pores formed in welds even when the concentration of gas in the molten weld pool was lower than the standard solubility of the gas in the liquid at the melting point.

Equations 1.11 and 1.12 were used to elucidate the mechanism. At the start of solidification the amount of gas solutes which migrate into the solid phase, $C_{sol.(x),}$ is governed by the product of the gas content of the liquid phase and the discontinuity in solubility, $k\ C^{o}_{liq}$, where k is the equilibrium partition coefficient and C^{o}_{liq} is the initial gas concentration in the liquid phase. The concentration in the solid then gradually increases in accordance

with Equation 1.11. The gas content of the liquid ahead of the solidification interface, $C_{liq.(x)}$, increases according to Equation 1.12.

$$C_{sol.(x)} = k\, C^{o}_{liq} + C^{o}_{liq}\,(1 - k)(1 - e^{\frac{-kVx}{D_L}}) \qquad (1.11)$$

$$C_{liq.(x)} = C^{o}_{liq} + C^{o}_{liq}\left(\frac{1-k}{k}\right)(1 - e^{\frac{-kVx}{D_L}}) \qquad (1.12)$$

where C^{o}_{liq} is the initial gas concentration in the liquid, k is the equilibrium partition coefficient, V is the velocity of the solidification front, x is the distance from the fusion line and D_L is the diffusion coefficient in the liquid phase.

This causes a layer enriched in gas-forming solutes at the interface. The concentration in the liquid away from the interface drops to the initial concentration, C^{o}_{liq}, of the gas in the liquid phase. It was proposed that gas bubbles would form at the interface only if the concentration of gas in the liquid was greater than the standard solubility of the gas in the liquid at the melting point, C^{r}_{liq}. This is illustrated in Figure 1.9. When the concentration of gas at the interface exceeds this standard solubility a state of supersaturation is achieved (the concentration is then equal to C^{p}_{liq}) and a bubble is able to nucleate. The concentration, C^{p}_{liq}, is dependent on the work of formation of a bubble and is therefore lower when a bubble forms in the depression of growing grains as opposed to a planar surface. Grigorenko has thus suggested that as the weld solidifies and the mean curvature of the growing grain front decreases (the dendrites become wider as a result of the growth of secondary branches), the value of C^{p}_{liq} increases.

After the formation of the bubble the concentration of gas in the liquid would drop again to the standard solubility. It would also stabilise at that value since the gas which is rejected enters the pore and causes it to grow instead of accumulating at the interface (region **bc** in Figure 1.9).

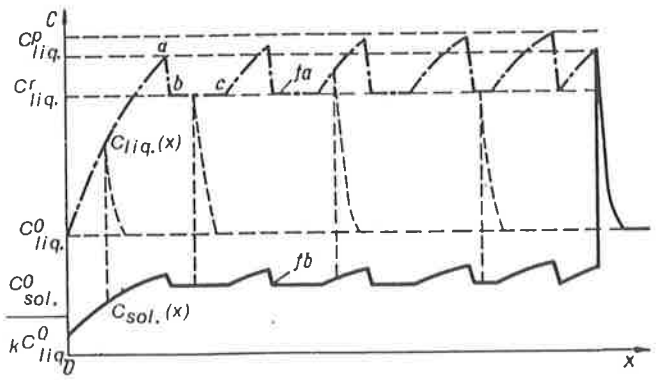

Figure 1.9: Schematic representation showing the distribution of an impurity in metal during the solidification of a weld, taking into account the work of formation of bubbles of gas (Grigorenko, 1970).

Pokhodnya and Demchenko (1980) have mentioned that, although the model proposed by Grigorenko (1970) assumes no convective flows in the weld pool and does not calculate the gas concentration between the dendrites at the interface, it works well in the enriched layer in front of a solidification interface. They developed a similar model for the distribution of gas in the solid and liquid phases at a cellular dendritic interface.

The numerical analysis showed the enrichment of the liquid with dissolved gas was mainly localised in the liquid between the cellular-dendrites, while the concentration of gas in the liquid phase above the liquidus was almost uniform. The variation of hydrogen concentration

in the completely solidified segments of the cellular-dendrites was shown to be negligible due to the relatively high diffusion rate of hydrogen in the solid phase.

The role of the distribution of hydrogen in the weld pool was then related to the growth of gas bubbles in the weld pool. It was concluded that the condition required for the formation of the gas nucleus was that the saturation of the gas in the weld pool exceeded the equilibrium solubility and that the higher the supersaturation the smaller the critical radius required for the growth of a bubble. The growth rate of the gas bubble was found to be highly dependent on the initial hydrogen concentration in the weld pool with the rate increasing at higher concentrations. The rate of growth also varied with time, the maximum being observed in the initial stage of growth. The growth rate then decreased and stabilised to the rate of solidification of the weld pool, while the gas pressure in the bubble decreased. A gas-depleted layer in the liquid, which moved with the bubble, was formed as a result of gas diffusion to the bubble.

Lancaster (1993) has also suggested that gas bubbles can form at the interface and the formation of a tunnel pore is possible, even when convective flow in a weld pool is considered, due to the existence of a boundary layer at the interface with a thickness in the order of 10^{-4}m. The boundary layer is defined as a region at the interface within which the flow velocity varies from zero at the interface to that of the bulk liquid. The thickness of the enriched layer at the interface was calculated using equation 1.12 and assuming that its extent could be taken as that over which the concentration falls to one-tenth that at the interface. The following values were also assumed, V = 3mm/s, $D_L = 1 \times 10^{-7}m^2/s$ and k = 13/25.2 = 0.512. A value of 7.2×10^{-5}m was obtained for the thickness of the enriched region which can thus be accommodated within the boundary layer.

The expression given in Equation 1.12, which describes the distribution of the concentration of hydrogen in the liquid metal at the solidification interface, has also been used by Suga (1987) to study the conditions for the growth of a gas nucleus. The equation which governs the formation of a gas bubble (Equation 1.2) and Sievert's law (Equation 1.1) were also used to derive an expression for the critical radius of a nucleus which when exceeded will allow a nucleus to stabilise and grow.

$$r_c = \frac{2\sigma_l}{(C^{\circ}_{liq}{}^2/k^2K^2 - \rho d - P_o)} \qquad (1.13)$$

where σ_l is the surface tension of the liquid metal, C°_{liq} is the initial concentration of the gas in the liquid metal, k is the equilibrium partition coefficient, K is the equilibrium constant in Sievert's law, ρ is the density of the liquid metal, d is the depth from the weld surface to the gas pore and P_o is the atmospheric pressure. It was deduced that the size of the nucleus had to be smaller than the thickness of the enriched layer at the interface in order for it to grow. A model was also developed to analyse the growth of a bubble attached to the solidification front and the effect of the initial hydrogen concentration and the solidification rate on the growth rate of the bubble were determined. The main conclusions were that the growth rate of a bubble increased and the critical radius decreased with an increase in the initial concentration of hydrogen in the melt and with a decrease in the solidification rate.

1.2.8.2.2 The Effect of Welding Parameters on the Formation of Porosity

Willgoss and Atthey (1980) have studied the formation of the tunnel pore in stainless steel during GTA welding. They attributed the formation of these to excess gases such as hydrogen, water vapour and nitrogen dissolved in the weld metal.

It is worthwhile to note that the tunnel pores described by Willgoss and Atthey have similar characteristics to the worm hole pores discussed in Howden and Yen (1986), and is also common to the hollow bead pore. Both tunnel and worm hole pores show evidence of cellular dendritic growth aligned with the growth direction on the internal surface. The merging of two pores into a single one is also characteristic to both.

The effects of factors such as workpiece edge preparation, a low surface to volume ratio of the weld pool, the welding procedure (downhand/horizontal-vertical) and hydrogen content in the shielding gas were also investigated.

It was observed that a narrower edge preparation (or groove angle) and the presence of hydrogen in the shielding gas increased the probability of creating tunnel pores. The latter was explained by observing that the weld pool became saturated with gas under the arc and that the solubility of hydrogen decreased rapidly during metal solidification. The gas was thus rejected at the solidification boundary at the back of the pool into a propagating void. The ratio of surface area to volume of the weld pool was found to be critical in determining the rate of venting of hydrogen gas from the weld metal: the smaller the area of the liquid surface (both front and back face) at the start of the weld, the more tunnel pores were initiated in the weld pool.

It was also stated that the start-up conditions of the weld determined whether or not a tunnel pore could remain stable and grow.

Willgoss and Atthey (1980) have also proposed a model for the formation and growth of tunnel pores. They derived an equation for the number of gas molecules in a pore from the pressure of gas within it, and were thus able to predict the growth rate of a pore by comparing

the rate of change of the number of molecules in the pore to the rate at which the atoms diffuse across the liquid/gas surface.

Solutions were obtained for the pore shape as a function of heat input and the quotient ε/α, where ε is the gas efflux and α is the traverse speed. They found that the pore size was a function of ε for constant α and that the pore diameter decreased and the length of the pore increased with increasing heat input. The model also predicts the shape of the pore for a particular set of welding variables.

Willgoss (1980) further investigated the factors which cause porosity in GTA welding of stainless steels. The effects of joint geometry and shielding gas composition were considered and the mechanisms for pore formation correlated with experimental results.

Willgoss considered two models for the nucleation of pores in welding: homogeneous and heterogeneous nucleation, but suggested that a welding situation was an unlikely environment to encourage cavitation by homogeneous nucleation. He proposed that the formation of pores could instead be modelled using the principle of heterogeneous nucleation where the pore formed from an external nucleus such as a microbubble, slag inclusion or surface debris. Refractory materials in the form of slag could absorb small quantities of any gas present in the weld pool and on cooling act as void nucleation sites. Bubbles of any size (up to 100μm diameter) were potential nucleation sites of larger globular pores or tunnel pores. Any bubbles which existed for periods of time as long as a few seconds could possibly be swept into contact with a solidifying boundary. A bubble would also readily attach itself to a solid boundary reducing its internal energy by an expansion which results in a decrease in the surface tension component of pressure.

From his experiments he was able to conclude that as the workpiece edge preparation (or the bevel angle) decreased and the hydrogen content of the shielding gas increased the probability of creating tunnel pores increased. High levels of hydrogen in the shielding gas resulted in two or three pores propagating simultaneously. Pores were observed to nucleate at the weld start close to the fusion boundaries on the sides of the weld and then grow normal to the solidification front. The diameter of the pore then increased with growth. At low levels of hydrogen in the argon shielding gas initiation of pores usually took place at the weld start, whereas at high levels nucleation took place along the full length of the weld.

In an investigation on hydrogen absorption and porosity in aluminium alloys, Woods (1974) has looked at the welding and compositional factors influencing hydrogen absorption and hydrogen solid solubility. The susceptibility to weld porosity, for a particular alloy, was determined by the initial material hydrogen content, the effective solid solubility of hydrogen in the metal, the value of the hydrogen absorption coefficient and the rate at which gas bubbles escape. It was assumed that the total hydrogen in the weld metal was composed of the hydrogen before the weld was made and the hydrogen introduced during welding, and that on solidification, a portion of the volume of hydrogen was retained in solid or supersaturated solid solution in the weld, and the remainder of the gas was potentially available to form porosity.

The experiments consisted of producing bead-on-plate welds in the overhead position using the GTA and GMA techniques. The gas content of the metal, consisting of the gas absorbed by the weld metal from the arc (both in solid solution and porosity forms), was measured.

The measurements of hydrogen absorption, at constant arc hydrogen levels, showed that the gas content of the weld metal decreased as the weight of fused metal increased. When the

level of hydrogen in the arc was varied, the trend was for the level of porosity to increase with increasing arc hydrogen. The rate of hydrogen absorption was found to increase initially with increasing weld pool size and then reach a constant value. It was suggested that there was a limit in the size of the weld pool where any further increase will not significantly influence the area over which absorption takes place.

On the influence of welding variables, the rate of hydrogen absorption and thus porosity increased with welding current. It was proposed that increasing the current raised the average surface temperature of the weld pool, enlarging the area of the hot annular zone over which absorption takes place (in the centre of this annulus the temperature of the pool surface is at or near the boiling point of the metal and consequently gas absorption is low). This would result in an overall increase in the rate of gas pick-up as current increases. Increases in weld travel speed were found to reduce the weld porosity, although the rate of hydrogen absorption was unaffected by a change in travel speed. This led to the conclusion that the reduction in porosity at increasing travel speeds was a consequence of the reduced time available for gas pick-up due to the increase in solidification rate.

It was concluded that the rate of hydrogen absorption was dependent on the volume of the molten metal in the weld pool. An increase in the size of the weld pool would allow better desorption of the gas and also improve the opportunity for bubble growth and escape.

It has been established that as the welding current is increased, when welding with rutile coated electrodes, the hydrogen content of the weld metal increases (Pokhodnya and Yavdoshchin, 1969). The experiments performed in that study measured the diffusible hydrogen content of fillet welds using eudiometers and a glycerine solution, and the residual hydrogen content using a vacuum melting method. The results revealed that as the welding

current was increased, from 170 to 290A for a 5mm diameter electrode, the total hydrogen content increased from 26cm^3/100g of deposited weld metal to 32cm^3/100g. An increase from 220 to 360A for a 6mm diameter electrode, increased the total hydrogen content from 28 to 32cm^3/100g. The results for the 4mm diameter electrode showed an increase in total hydrogen content from 27 to 38cm^3/100g on increasing the current from 150 to 190A.

Experimental data obtained by The Lincoln Electric Company (1986) also shows an increase in the diffusible hydrogen content of welds made at higher current levels with (unspecified) coated electrodes (10mL/100g at 180A, 12mL/100g at 215A and 17mL/100g at 300A), but only when expressed as a function of deposited metal. No effect of welding current was observed when the diffusible hydrogen was expressed as a function of fused metal. A similar observation was reported by Kiefer (1996).

White et al. (1992) have studied the effect of welding parameters on diffusible hydrogen levels in steel welds produced during cored electrode welding, with 1.2mm diameter flux-cored and metal-cored electrodes. The diffusible hydrogen content was measured by collecting the evolved hydrogen over mercury at room temperature. After complete evolution the volume of hydrogen was corrected to standard temperature and pressure.

For the rutile flux-cored consumable (type AWS E71T-1), lower hydrogen levels were obtained by decreasing the welding current: from 8.7mL/100g of deposited metal at 210A to 7.1mL/100g at 160A. For the basic flux-cored consumable (type AWS E71T-5) a reduction in hydrogen levels was also observed with decreasing current: from 3.5mL/100g at 260A to 2.4mL/100g at 210A and 1.8mL/100g at 160A. The results for the metal-cored electrode (type AWS E71T-G) were quite high since the fused metal weights were much greater for this consumable due to increased penetration. The hydrogen contents are thus also given in terms

of both deposited and fused metal (in brackets) for comparison. The hydrogen levels varied by a small amount at high currents - from 5.6(3.3)mL/100g at 240A to 6.3(2.9)mL/100g at 280A. At those two currents spray transfer was suggested to occur. However, a reduction in hydrogen level was observed at 160A (2.0(1.6)mL/100g) when the dip mode transfer was proposed to occur. White et al. believe that the major cause was a limitation of the transfer of hydrogen to the much larger droplets which had a lower surface to volume ratio compared with those in spray mode.

The influence of the weight of deposited metal was also investigated for the rutile flux-cored consumable. Earlier work had suggested that an increase in deposit weights resulted in a reduction in diffusible hydrogen content. In this investigation, the weight of deposited metal was varied from 2 to 10g by varying the welding speed only. The weight of deposited metal in the lower part of that range appears very small and may be dominated by the start and stop regions of the weld although the authors do not comment on this. Two welding conditions were used which produced high and low hydrogen levels (using two welding currents). At the higher hydrogen level condition, a decrease in hydrogen content was found as the deposit weight increased - from 12mL/100g of deposited weld metal for the 2g deposit to 5mL/100g for the 10g deposit. This was attributed to a slower cooling rate of the larger weld pool allowing more time for hydrogen to escape. A trend was not observed, however, for the lower hydrogen level where the diffusible hydrogen content remained at approximately 4mL/100g for all weights of deposited metal. The residual hydrogen content was found to increase with decreasing weight of deposited metal, from approximately 0.7mL/100g of deposited metal at 2g to approximately 0.4mL/100g at 8g.

Lundin et al. (1992) studied the effect of the coating moisture content and found an increase in diffusible hydrogen in welds, made in duplex stainless steels using a manual metal arc welding consumable. For DC(+) electrodes (type Thyssen 2209), the diffusible hydrogen increased from approximately 25mL/100g at 0.5% moisture to 34mL/100g at 3.2% moisture.

It has also been determined, for basic flux coated electrodes and submerged-arc flux, that increasing the flux moisture content increases the diffusible hydrogen content of the weld metal (Lancaster, 1992).

The weld bead shape has also been identified as a significant variable controlling the amount of porosity (Harris, 1988). Welds which are narrow and have a high crown tend to trap porosity, since individual pores must rise a long distance before escaping from the surface. A weld pool moving vertically down traps hydrogen bubbles (and other porosity-forming gases such as nitrogen) due to a long escape path.

Harris (1988) has also reported that in GTA welding of mild steel an increase in welding speed or solidification rate may reduce the amount of porosity if the bulk gas concentration of the molten weld pool lies between the solubilities of the gas in liquid and solid metal. When the bulk gas concentration is more than the gas solubility in liquid metal, an increase in the welding speed may increase the amount of porosity. The major cause of porosity was found to be hydrogen rather than nitrogen as the diffusivity coefficient of hydrogen is higher than that of nitrogen and the bulk hydrogen concentration for bubble formation is lower than that for nitrogen.

Howden (1982) has investigated the behaviour of hydrogen in weld pools during arc welding. He studied the transport of hydrogen dissolved in a stationary arc-melted pool into the surrounding metal.

In all cases concentration of hydrogen in the metal was greater than the hydrogen partial pressure in the arc. It was postulated that the pool creates a "pumping" action, due to repeated solidification and remelting of the metal in the outer layers of the pool, which forces the hydrogen from the liquid pool into the surrounding solid metal. The investigation suggested that much of the hydrogen was not rejected by the solid metal in the solidification process, and that for welding conditions with a moving weld pool and high solidification rates, the initial hydrogen content of the solidified weld metal was probably equal to that of the molten pool. It was thus concluded that the traditional explanation of porosity formation by rejection of hydrogen at the solidification front would need to be re-evaluated.

Saperstein et al. (1964) have studied the causes of porosity in aluminium welds. The importance of factors such as the dewpoint of the shielding gas, contamination of the parent and filler metals and welding variables in the formation of porosity was evaluated.

Bead-on-plate welds were automatically deposited using the GMA welding process with type 1100 filler metal and 3003 base metal. Control measures were taken to avoid moisture contamination resulting from leaks in the electrode holder and from contaminated gas lines.

The shielding gas dew point was monitored at the inlet of the electrode holder assembly with a radiation cloud chamber type dew point meter of the continuous flow design. To investigate shielding gas moisture contamination, controlled quantities of water were added by saturating a portion of the total gas flow through a water bubbler. Three methods were used to measure the volume fraction of porosity in the welds, namely, radiography, microscopy (visual) and gravimetric measurements in order to rate their relative accuracies. The x-ray method was found to give the smallest error and was thus chosen for the experiments.

A series of control welds showed that porosity was found only at the start of all of the welds with no porosity downstream. Variations in travel speed between 10 and 40 inches per minute (ipm) (250 and 1016mm/min) did not affect these results.

When a shielding gas preflow was included in the experiment the start porosity was reduced (but not eliminated) suggesting that one of the causes was contamination of the shielding gas by the ambient atmosphere. No definite reasons were given for the start-up porosity which persisted even with preflow. One cause which was advanced was hydrogen in solid solution in the filler or base metals or surface absorbed moisture.

The effect of surface contamination was studied by observing the influence of oxide layers (obtained by submerging the base and filler metal in aerated water for 24 hours) and the combined effect of residue from acetone and grease which was applied liberally on the surface. The results demonstrated that porosity both at the start and downstream were not affected by these contaminants. It was proposed that the welding heat volatilised the plate contaminants such as hydrocarbons and water ahead of the arc thus minimising dissociation in the arc atmosphere.

A method was established to generate porosity reproducibly whereby the shielding gas was contaminated with water. Porosity was in this way distributed uniformly along the length and randomly across the width. The start-up porosity was also denser apparently due to the sudden initial surge of gas which produced excess contamination at the start. The results showed an exponential increase in porosity as the dew point increased above a threshold value of -40^{o}F. Results on the effect of welding conditions demonstrated a significant influence of variations in travel speed; very little porosity was observed at 10ipm (250mm/min), gross porosity at 25ipm (635mm/min) and moderate porosity at 40ipm (1016mm/min). The size of the

individual pores varied from fine at the highest travel speed to coarse at the lower speeds suggesting that the distribution and sizes of pores was governed by the time available for pore nucleation and growth when the weld deposit is solidifying. The same correlations were observed when dry molecular hydrogen was substituted for water in the shielding gas, indicating that hydrogen caused the porosity in both cases.

1.2.8.2.3 The Effect of Parent Metal Composition on the Formation of Porosity

Willgoss (1980) has reported that porosity is commonly associated with carbon in the parent metal due to the formation of carbon monoxide and is increased by the primary formation of ferrite rather than austenite in the solidifying weld metal.

Diffusion of gases is slower in a fcc lattice (austenite) than a bcc lattice (ferrite) as the interstices are larger in the former structure.

Pokhodnya and Yavdoshchin (1969, 1972) investigated the effect of deoxidising agents such as silicon, carbon and aluminium in welds and found that these agents tend to increase porosity. The principal role of hydrogen in the formation of porosity was established and the increase in pore formation with the presence of the deoxidising agents was investigated. A series of experiments was conducted to determine the role of silicon in particular on the formation of porosity in welds. The silicon content of the weld pool was increased by adding ferrosilicon in varying amounts into the coating of rutile-based electrodes. The results showed that this increased the total and residual concentration of hydrogen in the weld metal and reduced the diffusible hydrogen content of the weld. It was thus proposed that silicon (and potentially other surface active agents) decreased the rate of hydrogen evolution from the

weld pool and thus increased the degree of supersaturation of gases during solidification and the formation of porosity.

Elements such as oxygen, sulphur, calcium and silicon are surface active relative to iron because they will lower the surface tension of iron even when added in very small concentrations to the melt (Kudrin, 1985). In this process the concentrations of these elements in surface layers (for example at the boundaries between metal and slag and molten metal and growing crystal during solidification) increases.

Data on the effect of silicon content on the diffusivity of hydrogen (at room temperature) in iron reveal that an increase in the concentration of silicon can slow down hydrogen diffusivity markedly (Boniszewki, 1992).

Material	**Diffusivity at 25°C (cm^2/s)**
Pure α iron	1.6×10^{-5}
Fe-1.06%Si	1.2×10^{-6}
Fe-1.85%Si	3.5×10^{-7}

At higher temperatures the change in the rate of hydrogen diffusion with increasing silicon content is not as pronounced (see Figure 1.10) (Smialowski, 1962). The rate of hydrogen evolution from steel at room temperature has also been reported to decrease at higher silicon content (Smialowski, 1962). There are no data, however, available for lower silicon contents.

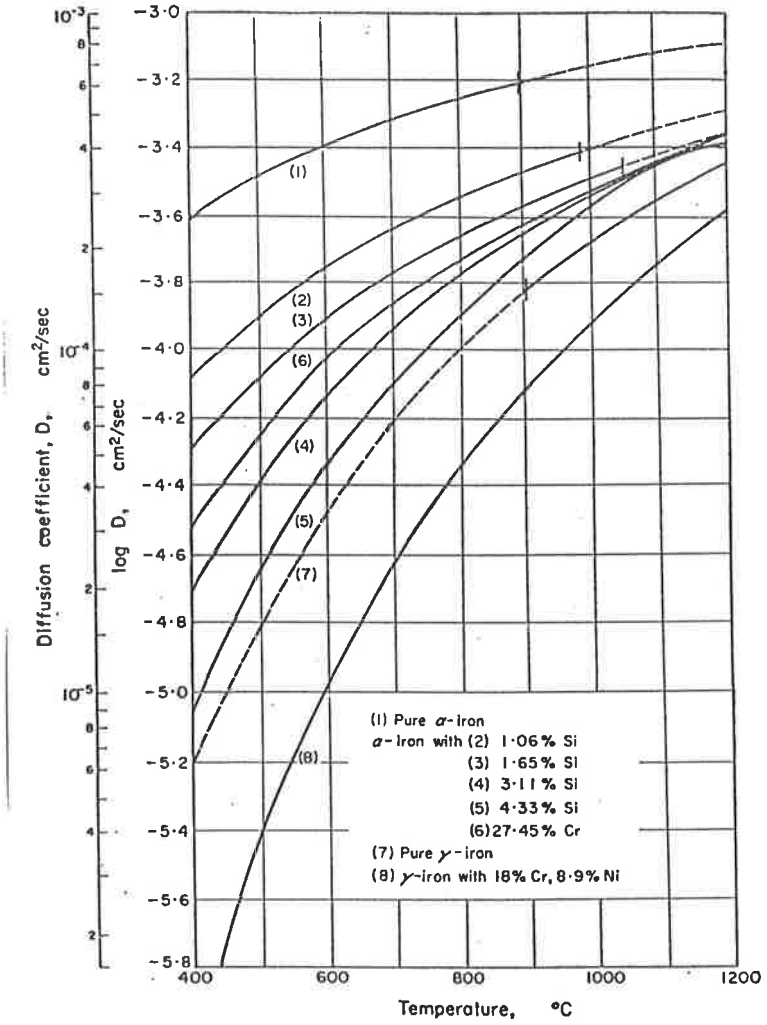

Figure 1.10: Diffusion coefficient of hydrogen in ferrous alloys. Influence of the temperature, lattice structure and composition (Smialowski, 1962).

The effect of metal composition on hydrogen solubility was studied by Weinstein and Elliot (1963) who measured the solubility of hydrogen in liquid pure iron and in a number of liquid binary alloys using a Sievert's type apparatus. The solubility of hydrogen at 1atm pressure and 1592°C in liquid pure iron was found to be equal to 27.2cm^3/100g (average of fifteen measurements). The alloying elements Al, B, C, Co, Cu, P, S and Sn decrease the solubility of hydrogen in iron while Nb, Cr, Mn and Ni increase it. Unfortunately no values were given for silicon. Figure 1.11 shows the effect of these alloying elements on the solubility of hydrogen in liquid iron at 1592°C.

The effect of these elements on the solubility of hydrogen in liquid iron was correlated with the free electron concentration of the alloying element. An element with a larger effective number of free electrons than pure iron decreased the solubility of hydrogen in liquid iron, while the elements with a smaller number of free electrons increased it.

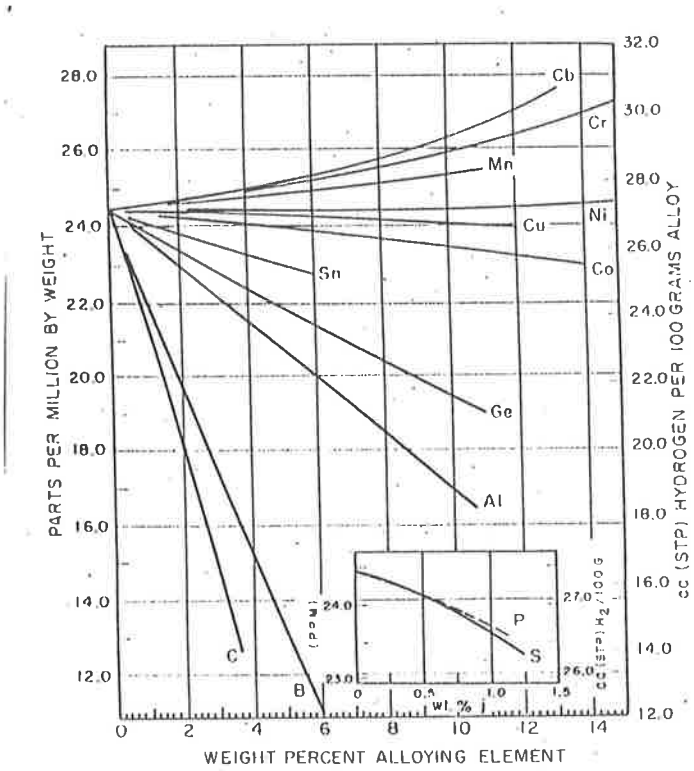

Figure 1.11: Solubility of hydrogen at 1atm pressure in binary iron alloys at 1592°C (Weinstein and Elliot, 1963).

1.2.9 Solidification Mechanics and Microstructure in Fusion Welds

A study of the solidification microstructure associated with hollow bead is an essential part of the formulation of a theory for the mechanism of formation of these defects. A review of weld solidification mechanics and its application to the understanding of elongated gas pores in welds is therefore presented in this literature survey.

Savage and Aronson (1966) have related the shape of the weld pool to the grain orientation produced during weld metal solidification. Macroscopic growth is governed by a process

known as competitive growth whereby the grains oriented by chance having the preferred easy growth direction (the <100> direction for fcc and bcc metals) nearly parallel to the maximum temperature gradient will be favoured. Hence they will tend to grow in the liquid more rapidly, expanding in cross section at the expense of their less favourably oriented neighbours. During welding the maximum thermal gradient is perpendicular to the solid-liquid interface at all points on the boundary

The two extreme types of weld geometry normally encountered during welding are the tear-drop shaped and the elliptical-shaped weld pools (Figures 1.12 (a) and (b)) (Savage, Nippes and Erickson, 1976).

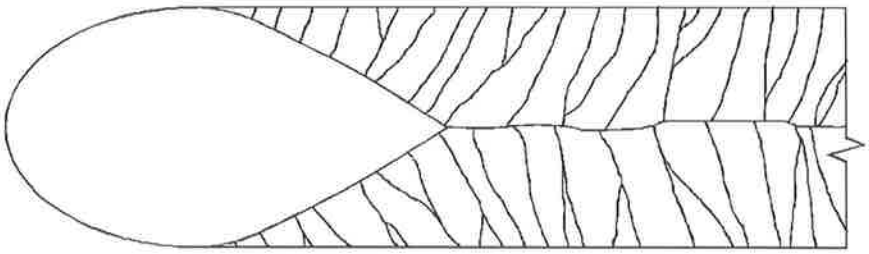

Figure 1.12(a): Schematic representation of a tear drop shaped weld pool.

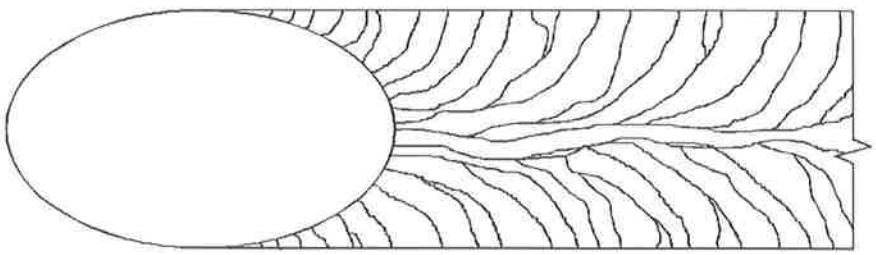

Figure 1.12(b): Schematic representation of a elliptical shaped weld pool.

A tear-drop shaped puddle is elongated along the centreline due to the inability of the system to extract heat fast enough in this direction. It has an almost invariant maximum temperature gradient at all points on the pool edge. As a result any grain favourably oriented for growth at the fusion boundary is able to grow at optimum speed and expand at the expense of the less favourably oriented grains. In the case of an elliptical shaped weld puddle the direction of the maximum thermal gradient at the pool boundary changes continuously from the fusion line to the weld centreline. Therefore no single grain is in a favoured growth situation for any extended period and very many more than the previous case survive to reach the centre of the weld. This geometry is formed at either lower weld travel speeds or higher welding currents.

Each individual columnar grain exhibits a substructure consisting of a parallel array of dendrites or cells which, in the case of mild and low alloy steel weld metals, will be masked by the austenite to ferrite transformation (Grong and Matlock, 1986).

In fusion welds in fcc and bcc metals the solid forms by epitaxial nucleation on partially melted base metal grains followed by growth along the <100> preferred growth direction (Savage, Nippes and Miller, 1976). The liquid-solid interface will initially grow in a planar mode. The stability of the solidification front is controlled by the extent of constitutional supercooling ahead of the advancing interface, and is therefore influenced by factors such as the total amount of alloying and impurity elements present, the growth rate R and the thermal gradient G in the weld pool. The solidification front will be dendritic at low $G/R^{1/2}$ ratios (high degree of constitutional supercooling), cellular-dendritic at medium $G/R^{1/2}$ ratios and fully cellular at high $G/R^{1/2}$ values (low degree of constitutional supercooling). For steel welds, the ratio of the temperature gradient to the growth rate ($G/R^{1/2}$) close to the fusion line is generally large enough to promote cellular-dendritic solidification (Grong and Matlock,

1986). This is a dendritic type of substructure where the formation of secondary arms is suppressed because of a relatively small temperature gradient in the transverse direction compared to the longitudinal direction.

The growth mode of solidification can be explained therefore in terms of constitutional supercooling which can in turn be explained as result of segregation, or the variation in solute concentration ahead of the moving solid-liquid interface. Segregation is the result of the rejection of solute (or solvent) at the interface during solidification.

For a simple single-phase binary alloy within the solidification temperature range, the intersection of a temperature isotherm with the liquidus defines the composition of the liquid phase, C_L, while the intersection with the solidus defines the composition of the solid phase, C_S (see Figure 1.13). The distribution coefficient, k, is defined as the ratio of C_S to C_L for any temperature at which solid and liquid phases coexist. The values of k can be either greater or less than 1.0.

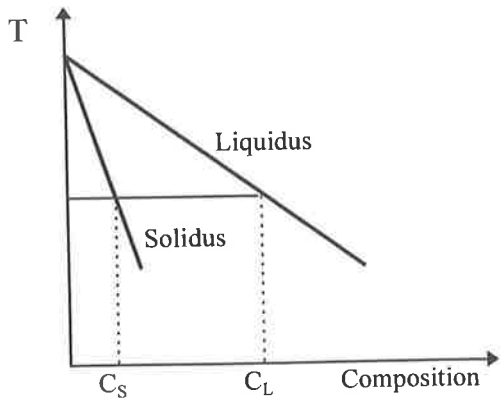

Figure 1.13: Schematic phase diagram of temperature (T) versus composition showing solidus and liquidus compositions in equilibrium.

It is assumed in the following discussion that during solidification redistribution of solute in the liquid phase is by diffusion only and that there is no diffusion of solute in the solid phase. This case is more appropriate for describing morphological stability and microstructural development in welds since it allows for the build-up of a solute boundary ahead of the solid-liquid interface.

The first solid to form exhibits the composition kC_o where k is the distribution coefficient and C_o equals the nominal composition of the alloy. Thus, for $k < 1.0$ the excess solute rejected by the first solid to form increases the concentration of the solute in the adjacent liquid. On the other hand, for $k > 1.0$, the liquid at the solid-liquid interface is depleted of solute in order to produce the first solid which is solute enriched. For the first case, $k < 1.0$, the temperature of the interface is lower than the liquidus temperature of the bulk liquid, and constitutional supercooling can occur even if the temperature of the liquid is everywhere above that of the interface. As steady state conditions are reached, the solid composition approaches that of the nominal alloy composition, C_o, while the liquid composition at the interface is C_o/k.

During growth, morphological stability of the planar solid-liquid interface is determined by the thermal and compositional gradients that exist at the interface. If the actual temperature gradient is steeper than the gradient in the equilibrium liquidus temperature at the interface, any perturbation at the plane front will remelt since the actual temperature is above the liquidus temperature. Therefore the planar front will remain stable. If, however, the thermal gradient is smaller than the liquidus temperature gradient, the liquid ahead of the solidification front is supercooled. Any accidental protuberances penetrating this region could then dissipate latent heat to the surrounding constitutionally supercooled liquid. As the protuberance penetrates the liquid, the liquid in contact with the tip becomes progressively richer in solute

thus raising the solute content of the solid forming the tip. At the same time the solute rejected laterally by transverse growth near the base of the protuberance is added to a liquid already enriched with solute thus further depressing the liquidus near the base of the protuberance and restricting the extent of transverse growth. This in turn tends to produce a convexity in the interface at a distance slightly removed from the base which promotes more protuberances clustered about the first until each grain on the entire interface is covered by a family of similarly orientated cells of roughly hexagonal cross section.

For a given growth rate, the thermal gradient producing cellular-dendritic growth would not be as steep as that associated with cellular growth. Hence, with this solidification mode the distance a protuberance penetrates into the liquid is greater than with cellular solidification. Since the protuberance is enveloped in supercooled liquid, branched growth can develop (Savage, Nippes and Miller, 1976).

Powell and Lloyd (1995) have applied weld metal solidification mechanics, as summarised above, in the correlation of the appearance of elongated pores in the light microscope and scanning electron microscope (SEM) with the cellular-dendritic growth mode and resulting microsegregation as well as banding due to macrosegregation.

They produced welds using welding electrodes containing high levels of nickel and manganese to enable microsegregation to be revealed by etching in Le Pera's reagent. Nickel and manganese segregate to cellular-dendritic boundaries due to their small equilibrium partition coefficients.

The SEM micrograph of two elongated gas pores (Figure 1.14) show white ridges on the internal surface which are aligned with the direction of growth of the gas pores. The substructure surrounding the gas pore was also etched in Le Pera's reagent. Darker etching

areas representing regions of microsegregation as a result of cellular-dendritic growth were confirmed by energy dispersive x-ray analysis in the SEM to contain increased levels of nickel and manganese in these areas.

The distance between the white ridges on the internal surface (see Figure 1.15) was found to be the same as the darker etching cellular-dendritic boundaries: approximately 20 microns. This indicated that the ridges aligned in the direction of solidification occurred as a result of solute-enriched liquid in the cellular-dendritic solidification boundary solidifying after protrusion into the pore.

The initiation and increase in diameter of the gas pores was explained in terms of solute banding, indicated in Figure 1.16 by the darker bands numbered 1, 2 and 3. Solute banding in a weld was explained to be common due to frequent variations in heat input in arc welding. Consequently, an increase in the growth rate produces an increase in the solute content of the weld metal. An increase in gas-forming solutes (carbon, oxygen and hydrogen) at the solute band 1 resulted in the initiation of the pore and at solutes bands 2 and 3 produced an increase in diameter (Powell and Lloyd, 1995).

Chalmers (1964) provided a similar explanation for the shape of gas bubbles in terms of the relative rates of growth of the bubble and the speed of advance of the solidification front. An elongated or cylindrical bubble will experience stable growth when the bubble growth rate and the weld solidification rate coincide. He also observed worm holes formed in ice cubes produced by freezing water containing dissolved air. He attributed the oscillations in diameter of these worm holes to periodic changes in the rate of solidification caused by intermittent operation of the compressor of the refrigerator and suggested that the process was essentially the same in a solidifying metal.

These solute bands, surrounding gas pores, have also been observed by Suga and Hasui (1986). The bands were described as special solidification lines which occur around the elongated pores and in their periphery. The mechanism of formation of the elongated pore was explained in this case as a repetitive growth and rising up process of a bubble at the solidification front. This process was said to form the special solidification lines around the pore. The composition of the gas in the elongated pores was also obtained. The analysis showed hydrogen as the main gas component, at around 96%, with small quantities of CO and CO_2.

The study by Powell and Lloyd (1995) has, however, shown that these lines are the result of macrosegregation and that the accumulation of gas-forming solutes at these intervals are conducive to the nucleation and the increase in diameter of gas pores.

A study of blow holes in shielded metal arc and submerged arc welding of steel in the Fractographic Atlas of Steel Weldments (1982) has revealed similar features on the internal surface of gas pores as described above. Figures 1.17 and 1.18 show low and high magnification images of the internal surface of a blow hole formed during the shielded metal arc welding of steel. This surface has been described as comparatively featureless and smooth. Protuberances due to the cellular dendrites are present on the surface, but are not clearly visible.

The interior of a worm hole, found in a submerged arc welded mild steel pipe weld, is shown in Figure 1.19. Here the directionality and protuberances of cellular dendrites are clearly recognisable.

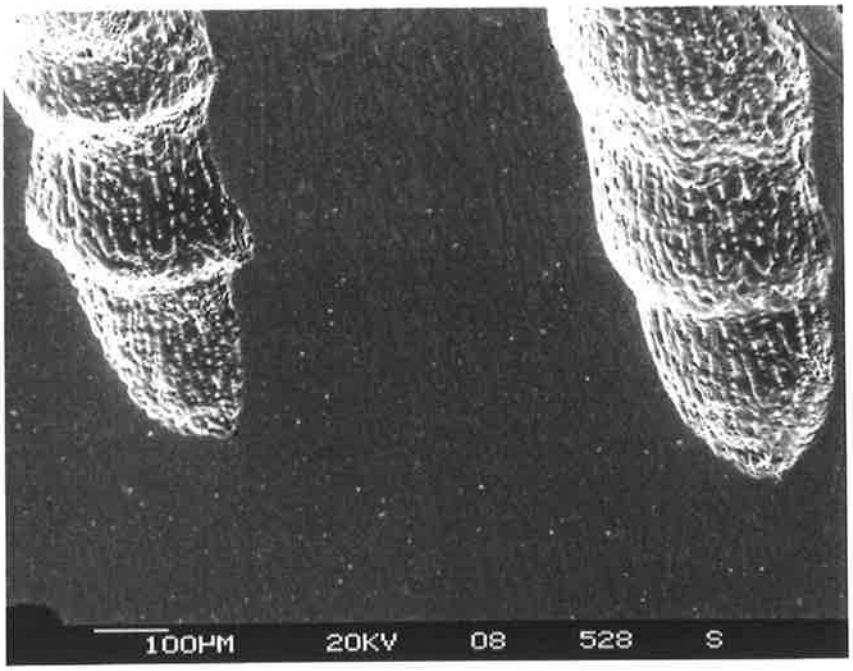

Figure 1.14: SEM micrograph of elongated pores in a steel (Powell and Lloyd, 1995).

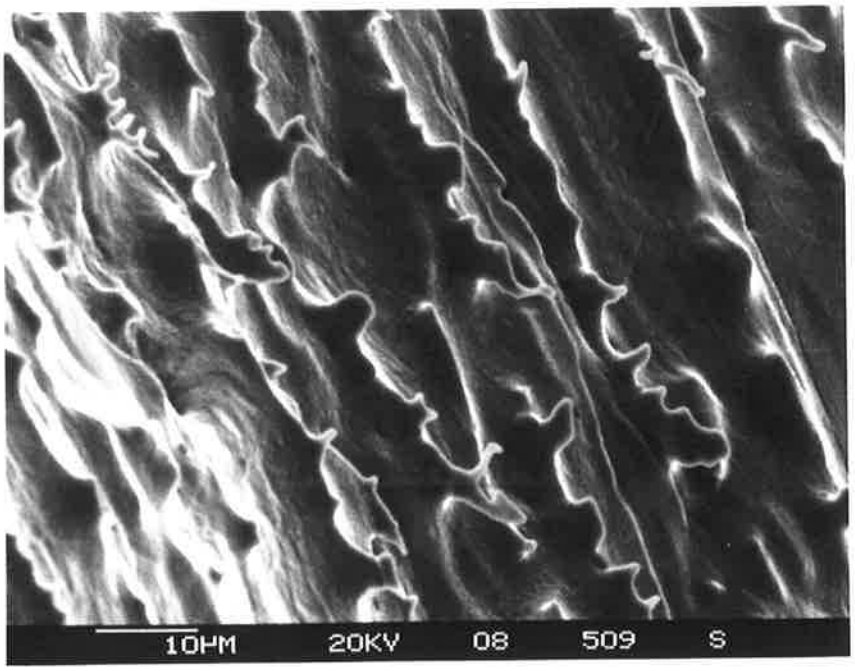

Figure 1.15: SEM micrograph of the internal surface of elongated gas pores (Powell and Lloyd, 1995).

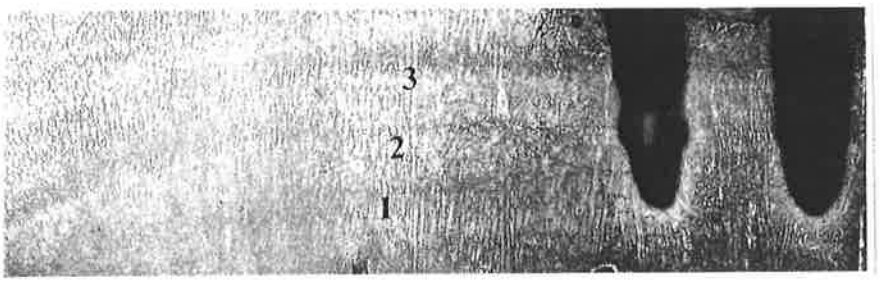

Figure 1.16: Light micrograph showing transverse solute banding (numbered) resulting from an increase in growth rate (Powell and Lloyd, 1995).

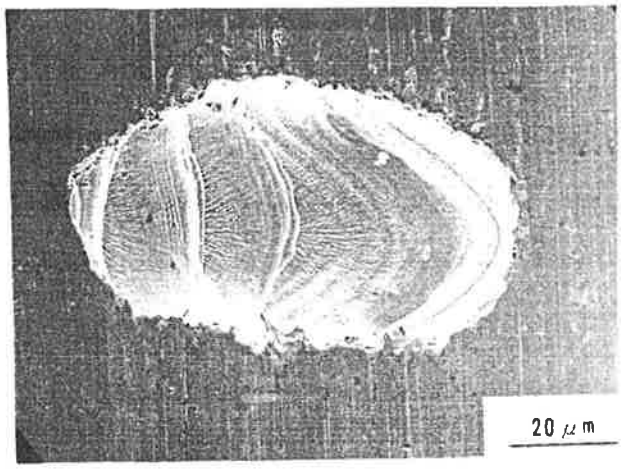

Figure 1.17: Appearance of a blow hole at low magnification (Fractographic Atlas of Steel Weldments, 1982).

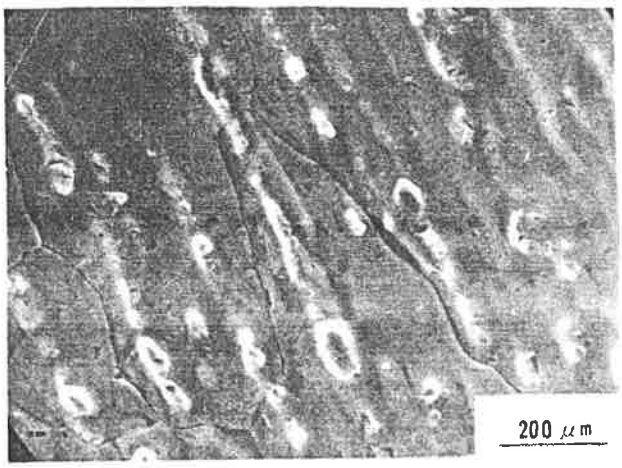

Figure 1.18: Appearance of the interior of the blow hole in Figure 1.17 at high magnification (Fractographic Atlas of Steel Weldments, 1982).

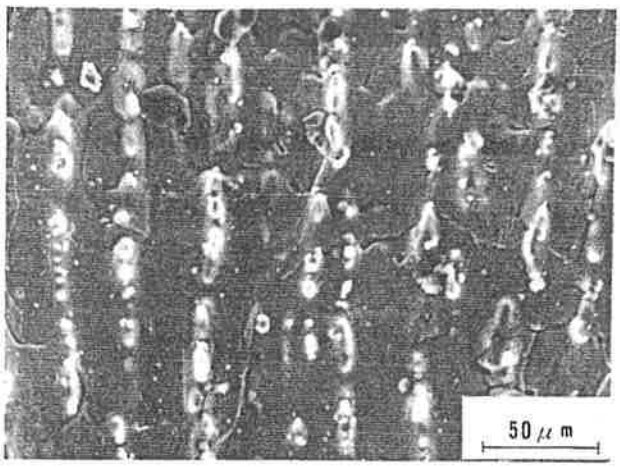

Figure 1.19: High magnification of the interior of a worm hole (Fractographic Atlas of Steel Weldments, 1982).

1.2.10 The Role of Segregation in the Formation of Gas Pores

As discussed above porosity is usually associated with macrosegregation, or solute banding. Solute banding is commonly observed as periodic regions of solute enrichment or depletion and is revealed on etching a weld surface as light or dark curved lines marking successive positions of the advancing interface (Davies and Garland, 1975). Macrosegregation has been explained as cyclic changes in the rate of solidification resulting from thermal fluctuations in the weld pool (D'Annessa, 1966). These bands are normal to the direction of solidification, and represent regions of solute enrichment due to a sudden increase in growth rate or regions of solute diminution due to a sudden decrease in growth rate. The growth rate fluctuations which lead to banding are observed in weld pools made without any periodicity in the power source (Davies and Garland, 1975). In this case fluctuations are explained to be the result of uncontrollable variations in arc stability resulting in variations in heat input to the weld pool and in turn periodic variations in the temperature gradient of the liquid at the solid-liquid interface (D'Annessa, 1966).

D'Annessa has also explained weld porosity formation as a result of the transverse solute banding phenomenon. The solute enriched band structure resulting from periodic increases in growth rate was explained to be regions where the degree of microsegregation was greater than the degree of microsegregation in the less rich adjacent structure. The short range partitioning of gas element solute was also maximum in the banded regions. The formation of porosity was thus the result of interdendritic microsegregation of the gas element (hydrogen) during the slow growth rate interval in which there was sufficient time to permit accumulation of molecular hydrogen to form pores.

The formation of a solute rich band along the centreline of the weld is another manifestation of macrosegregation in welds. During dendritic growth in welds significant diffusion of solute

down the concentration gradient in the mushy zone may occur and lead to a build up of solute in the last region to solidify at the weld centreline. Further, the weld pool may continuously build up in solute, transporting elements like sulphur and hydrogen large distances along the weld centreline (David and Vitek, 1989).

1.2.11 Conclusions

There has been no systematic investigation of hollow bead defects in the root pass of pipeline joints welded using the stovepipe technique. It has been necessary therefore to study the theories for elongated pores in general. These investigations have dealt mostly with tunnel and worm hole pores in gas metal arc welding with little information pertaining to manual metal arc welding and cellulosic electrodes. It can be assumed, however, that aspects of the mechanisms put forward to explain the absorption of hydrogen in a weld pool, the role of solidification and the influence of welding parameters on the formation of pores are applicable to this welding process.

It must be pointed out, however, that the tunnel and worm hole pores have different characteristics from the hollow bead pore. The former nucleate at the fusion line and then propagate perpendicular to the solidification front along the centreline of the weld. These pores can grow at an angle from the horizontal weld centreline, either rising to the top of the weld or dipping to the weld root. These types of pores are also observed to merge to form a single pore. These characteristics are not observed with hollow bead defects. The hollow bead nucleates and grows in the longitudinal direction of the weld. The current study has also found that pores are found at either the root or the bottom of the weld bead, with a thin outer wall, and grow as singular pores always parallel to the direction of welding.

Since there is so little literature dedicated to the hollow bead defect per se, a detailed investigation was undertaken to determine the effects of welding parameters, joint geometry and surface condition, parent metal composition and type of electrode on its formation. Furthermore, a detailed study of the microstructural characteristics of the hollow bead defect was performed. Together these studies are designed to provide a model for the mechanism of formation of hollow bead.

Chapter 2

Experimental Work

2.1 Introduction

A major part of the research consisted of a systematic and thorough experimental programme. In the absence of any previous controlled studies, the main objective was to identify the possible factors responsible for the formation of hollow bead.

The experimental programme was designed to determine the effect of welding and metallurgical variables on the occurrence of hollow bead. The welding variables included welding current and voltage, travel speed, joint geometry and surface condition, electrode type and flux moisture content. The effect of the composition of the parent plate was investigated by the examination of steels containing high and low concentrations of carbon, silicon and aluminium.

The first section of this chapter deals with a survey of the incidence of hollow bead defects during the construction of a pipeline. This was done in an attempt to identify some of the factors which might cause the formation of hollow bead. The information obtained was subsequently used in preliminary experiments which were performed on a welding machine capable of automating the stovepipe welding process. The main objective was to reproduce hollow bead in order to establish an initial set of conditions under which it would form and to obtain samples of the defect for metallographic examination. The remainder of the chapter is

devoted to the systematic study of the effect of welding and metallurgical variables on the formation of hollow bead.

2.2 Survey of the Incidence of Hollow Bead on the South West Queensland Pipeline (SWQ) Project

2.2.1 Introduction

This project involved the construction of a gas pipeline from the Moomba gas fields in central Australia to Jackson in South West Queensland. The pipe was grade API 5L X70, with an outside diameter of 406.4mm and a wall thickness of 9.9mm. The severe occurrence of hollow bead, outside the limits specified in the Australian Standard 2885 - 1987, seriously disrupted the construction of this pipeline.

These problems with the hollow bead defect subsequently led the pipeline industry to conceive and sponsor a three year research project to investigate the phenomenon. As mentioned in the Introduction (Section 1.1) the project was initiated through the Welding Technology Institute of Australia (Research Panel 7 Pipelines) and obtained the collaboration and support of the Cooperative Research Centre for Materials Welding and Joining.

It was important to conduct a survey of the occurrence of hollow bead defects on the South-West Queensland pipeline project in an attempt to highlight factors possibly linked with the formation of hollow bead. Twenty nine radiographs of welds most severely affected by hollow bead were studied to assess the length and number of the defects at specified locations around the pipe circumference.

2.2.2 Results and Discussion

The results presented in Table 2.1 are a detailed record of the survey showing the length of all indications of hollow bead with respect to location around the pipe circumference for all thirty welds. The locations which did not contain any hollow bead defects are absent from the table. The total number and length of defects have also been included. In addition, an indication of the width of the hollow bead pores is given in terms of the symbols (s) for small for a width less than 1mm, (m) for medium for a width of 1 to 1.5mm and (l) for large for a width of about 2mm. The diagram in Figure 2.1 shows the system used to define location with the outline of pipe cross section (looking downstream) divided in thirteen areas. The results from this survey have also been recorded in the form of histograms, as shown in Figures 2.2a and b, which combine the results from all radiographs. In Figure 2.2a the total number of hollow bead with lengths between 4 and 13mm (inclusive) has been plotted at each section around the pipe circumference, and in Figure 2.2b the number of hollow bead with lengths greater than 13mm has been plotted. The hollow bead pores with lengths less than and equal to 3mm were not considered very significant. A length of hollow bead exceeding 13mm is important as under the Tier 1 Acceptance Criteria of the Australian Standard 2885.2 1995, a hollow bead pore with a length greater than 13mm is deemed unacceptable and requires the weld to be repaired. No hollow bead was found in positions 400-500, 500-600, 600-700, and 700-800.

The field welding of transmission pipelines using the stovepipe welding technique has been described in Section 1.2.3 of the Literature Review. The welding procedure for the SWQ pipeline project required two welders for the welding of the root pass. Two welders, working opposite each other, are usually employed for pipe diameters greater than 200mm to increase the rate of progression. Referring to the diagram in Figure 2.1 the sequence of welding operations is as follows. One welder starts near the 1 o'clock position and welds anticlockwise

to the 9 o'clock position, while at the same time the second welder starts near the 3 o'clock position and welds to 7 o'clock position. The joint is then completed by welding the two remaining quadrants, from near top dead centre to the 3 o'clock position and from the 9 o'clock to near the bottom dead centre.

The type of electrode used to weld the root pass in this project was a Lincoln Electric Fleetweld 5P (E6010) 4.0mm in diameter.

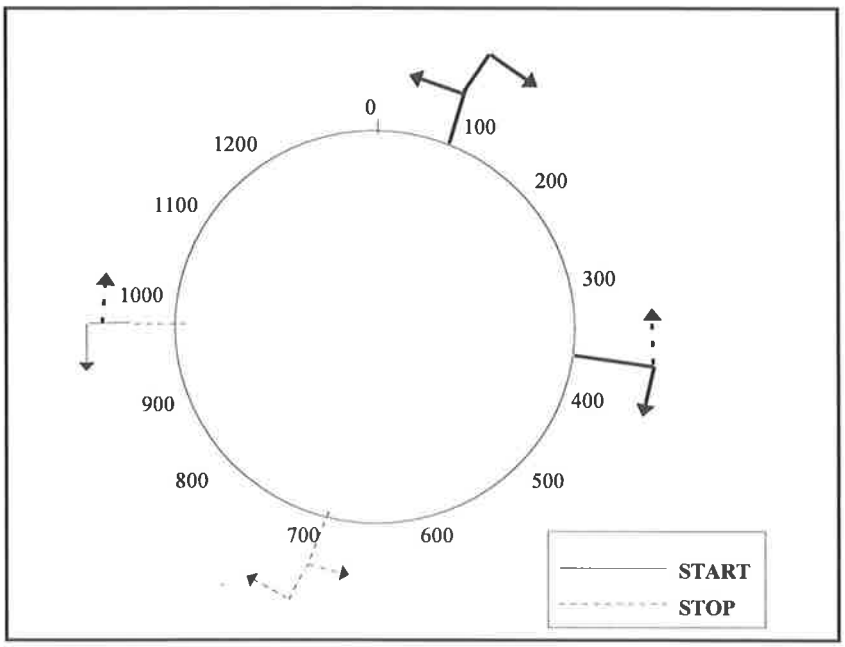

Figure 2.1: Schematic diagram of pipe cross section looking downstream.

Weld Number	Position	Individual Length of Hollow Bead (mm)	Total Number of Hollow Bead	Total Length of Hollow Bead	Width of Hollow Bead (mm)
134	0-100	10, 12, 3	3	25	m
134	100-200	7, 3	2	10	s
134	200-300	4, 3, 1, 3, 9, 5, 3, 2	8	30	s
135	1100-1200	10, 9	2	19	m
135	0-100	6, 8	2	14	s
135	100-200	7, 13, 3, 5	4	28	s
135	200-300	2, 13, 7	3	22	s
141	0-100	3, 9, 3, 6	4	19	m
141	100-200	3.5	1	3.5	m
141	200-300	4, 10, 2, 2, 1, 3	6	22	s
152	0-100	2, 4, 3.5, 4, 2, 5, 2.5, 2	8	25	m
152	100-200	2, 2, 2, 2, 3, 2, 3	7	16	m
152	200-300	5, 2, 2, 9, 4, 4, 2	7	28	m
152	300-400	3, 3, 11	3	17	m
178	200-300	10, 2, 1	3	13	s
178	300-400	4, 3.5	2	7.5	s
178	1000-1100	13, 3, 5, 2, 6, 8	6	37	s
178	1100-1200	2	1	2	s
178	1200-0	2, 3	2	5	m
191	0-100	6, 9	2	15	m
191	200-300	2, 7, 2, 2, 6, 12, 2, 2	8	35	s
191	300-400	6, 1, 2, 2, 2	5	13	s
213	0-100	25, 5, 4	3	34	l
213	1000-1100	10, 4, 13, 4, 15	5	46	s
213	1100-1200	9, 2, 3, 4, 3	5	21	s
213	1200-0	10, 9, 5, 12	4	36	l
219	800-900	20	1	20	s
219	1000-1100	11, 4	2	15	m
219	1100-1200	5, 13, 2, 10	4	30	m
219	1200-0	12, 1, 4, 4, 7	5	28	m
226	0-100	6, 2, 11, 9, 5	5	33	l
226	100-200	4, 5, 3, 6	4	18	m
226	900-1000	5, 8, 3, 3	4	22	s
226	1000-1100	2, 4, 4, 7, 2, 3	6	22	s
226	1100-1200	4, 6, 7, 3, 16, 16, 8, 2	8	62	m
226	1200-0	19, 5, 5, 18, 5	5	52	m, l

Table 2.1: Results of Survey of the Occurrence of Hollow Bead on the SWQ Pipeline.

Weld Number	Position	Individual Length of Hollow Bead (mm)	Total Number of Hollow Bead	Total Length of Hollow Bead	Width of Hollow Bead (mm)
228	900-1000	11, 4, 4, 3	4	22	s
228	1000-1100	7, 3, 2, 4, 3, 10	6	29	s
228	1100-1200	2, 6, 4, 2, 6, 7, 9	7	36	s, m
228	1200-0	2, 4, 3.5, 3, 5, 7	6	24.5	m
230	900-1000	6, 11, 15	3	32	s
230	1000-1100	4, 12, 4, 1	4	21	s
230	1100-1200	4, 4, 11, 3, 8	5	30	s
230	1200-0	4, 9, 6, 5, 4, 1, 1, 3	8	33	m
248	0-100	10, 7, 8, 4	4	29	m
248	1000-1100	3, 4, 1, 2, 7, 4	6	21	s
248	1100-1200	3, 3.5, 4, 6, 3, 2	6	21.5	m
248	1200-0	4, 6, 3, 3, 5, 6, 4	7	31	m
256	0-100	7, 20, 6	3	33	l
256	800-900	17, 2, 12	3	31	s
256	900-1000	4, 9, 2, 6	4	21	s
256	1000-1100	11, 2	2	13	s
258	1000-1100	3, 9, 4, 3, 4, 4, 6, 2, 1	9	36	s
258	1100-1200	9, 1, 3.5	3	13.5	m
258	1200-0	4, 4, 4, 10, 10, 13, 3, 4.5	7	48.5	m
264	0-100	17, 2, 3, 4	4	26	m, l
264	1200-0	3, 6, 10, 4, 3, 4, 2	7	32	m
264	900-1000	30, 2, 2, 2, 3, 2, 3	7	44	s
264	1000-1100	2, 3	2	6	s
271	900-1000	18, 2, 2	3	22	s
271	1200-0	7, 3, 7, 4, 5, 6, 1, 9, 5	9	51	m
271	0-100	5, 6, 4, 5, 8, 9, 4, 4	8	45	m
272	900-1000	2, 4, 8, 3	4	17	s
272	1100-1200	4, 3, 3	3	10	m
272	1200-0	5, 6, 8, 3, 5, 5, 10, 2	8	44	m
272	0-100	3, 4, 6, 17, 4, 5	6	39	l
279	1000-1100	9, 5, 7, 4, 1, 4, 1, 4, 3, 4	10	42	s
279	1200-0	3, 10, 7, 10	4	30	m
279	0-100	2.5, 10, 3, 3, 4	5	22.5	l
283	900-1000	17, 4	2	21	m
283	1000-1100	1, 3, 7, 3, 12	5	36	m
283	1100-1200	3, 1, 2, 3, 7, 3, 4, 8	8	31	m
283	1200-0	8, 5, 7, 17, 7, 8	6	51	l
283	0-100	4, 8, 7, 6, 3	5	28	l

Table 2.1(cont.): Results of Survey of the Occurrence of Hollow Bead on the SWQ Pipeline.

Weld Number	Position	Individual Length of Hollow Bead (mm)	Total Number of Hollow Bead	Total Length of Hollow Bead	Width of Hollow Bead (mm)
286	1100-1200	2, 1, 6, 9, 3, 8	6	29	m
286	1200-0	4, 2, 6, 13, 4, 4, 8	7	41	l
286	0-100	7, 12, 1, 11, 10, 10, 7	7	58	l
288	0-100	11, 4	2	15	m
288	1000-1100	3, 4, 4, 4, 9, 6, 5, 2, 7	9	44	s
288	1100-1200	8, 1.5, 2, 4, 19, 7, 18	7	59.5	m, l
288	1200-0	20, 18, 4.5, 5	4	47.5	m, l
289	900-1000	6, 2, 6, 1, 4	5	23	s
289	1000-1100	3, 2, 2, 2, 6, 3, 2, 3	8	23	s
289	1100-1200	1, 3, 12, 3	4	19	m
289	1200-0	1, 2, 8, 2.5	4	13.5	m
289	0-100	6, 6, 7, 11, 10	5	40	m
300	0-100	3, 8, 15, 14, 4, 7	6	51	m, l
300	1000-1100	14, 6, 2, 6, 3, 3, 9	7	43	s
300	1100-1200	1, 3, 3, 7, 5, 3, 2, 10	9	39	s
300	1200-0	3, 7, 1, 4, 7, 13, 9	7	44	m
304	1100-1200	5, 3.5, 4, 11, 2, 6	6	31.5	m
304	1200-0	6, 3, 7, 8, 6, 16	6	46	m
304	0-100	3, 21 ,12, 6	4	42	l
304	900-1000	6, 7	2	13	s
306	1000-1100	3, 2, 12, 2, 5, 1, 2.5	7	s	27.5
306	1100-1200	4, 10, 9, 3.5, 4, 1.5, 2, 1.	8	s	35
306	1200-0	22, 10, 4, 10, 24	5	m	70
306	0-100	2, 10, 18, 14, 5	5	m, l	49
308	1000-1100	6, 7, 2, 6, 2, 2.5, 5	7	30.5	s
308	1100-1200	10, 2, 4, 6, 8, 4	6	42	m
308	1200-0	6, 2, 9, 3, 2.5, 10, 1, 2, 5	9	40.5	m
308	0-100	9, 3, 18, 3, 5	5	38	m
312	1100-1200	5, 7, 5, 5, 1, 2, 5	7	30	m
312	1200-0	4, 8, 4, 11, 9	5	36	m
312	0-100	17, 8, 5, 5	4	35	l
313	0-100	8, 3, 7, 5	4	23	m
313	900-1000	3, 10, 5, 2, 4	5	24	s
313	1000-1100	1, 1, 1, 4, 1, 1, 2, 1, 1	9	13	s
313	1100-1200	3, 20, 5, 6, 2, 5	6	41	m
313	1200-0	6, 5, 6	3	17	m
314	0-100	1, 4, 4, 9, 3	5	21	m
314	100-200	1, 3, 8	3	12	s
314	900-1000	10, 7	2	17	s
314	1000-1100	5, 1, 3, 8, 2.5, 7	6	26.5	s

Table 2.1(cont.): Results of Survey of the Occurrence of Hollow Bead on the SWQ Pipeline.

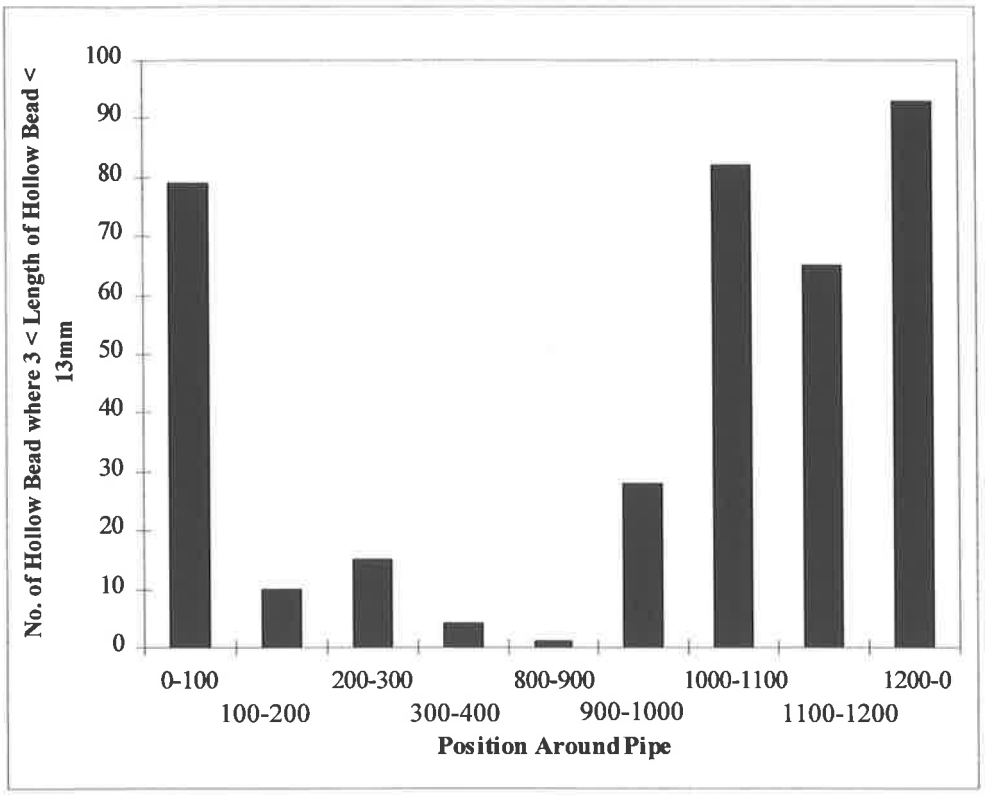

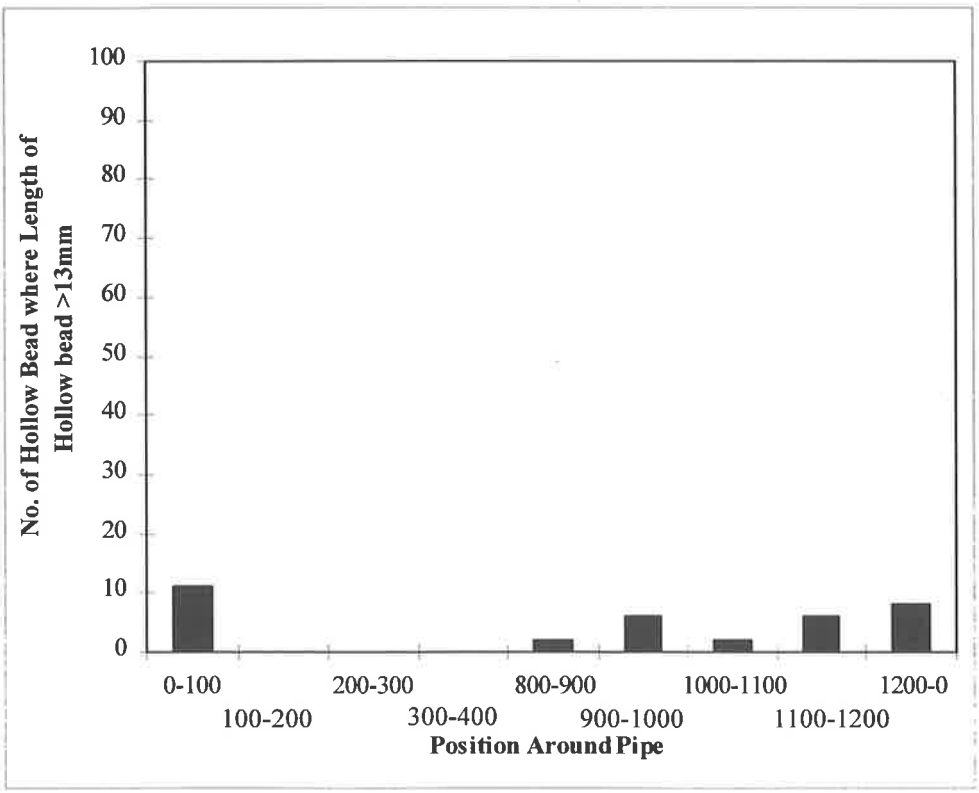

Figure 2.2(a) and (b): Histograms of the number of hollow bead defects at different areas around the pipe circumference, for (a) lengths of hollow bead between 4 and 13mm inclusive and (b) lengths of hollow bead greater than 13mm. Survey of 30 radiographs. The pipe grade was API 5L X70, the diameter was 406.4mm and the wall thickness 9.9mm.

The welding code used on this project was the Australian Standard 2885 - 1987. The criteria of acceptance for hollow bead for a production weld specified in this standard are as follows. Hollow bead which exceeds the following limits shall be unacceptable and reported as defects:

Hollow bead pores with a height or depth equal to a quarter of the nominal thickness of the thinner parent metal (mm).

Hollow bead pores longer than 10mm and with a height or depth between one tenth and one quarter of the nominal thickness of the thinner parent metal (mm), the length of an individual indication of hollow bead or the aggregate length of hollow bead exceeds 50mm in any 300mm of weld.

The severity of the incidence of hollow bead is highlighted by examining the data in Table 2.1. The length of each of each individual segment in Figure 2.1 (that is 0 -100, 100 - 200 etc.) is approximately 98mm. In all cases, therefore, the incidence of hollow bead in these welds well exceeded the acceptance limits specified in AS 2885 - 1987. Many welds also had individual lengths of hollow bead greater than 10mm, up to 25mm.

Hollow bead was observed to be more prevalent in the top half of the pipe and especially at the start of welds (areas 0-100 and 1200-0) and the stop/start region between 900-1200 and 0 - 100 where the longest pores occurred. The width of the defects were also largest in these areas. Overall the number and length of defects were consistently higher in one particular quadrant of the pipe (900-0 and 0-100) suggesting a possible link with the technique and welding variables used by a particular operator. The histograms also show that in all cases the most common lengths of hollow bead are between 3 and 5mm and that the maximum length for a hollow bead in this survey is 25mm.

Other information, speculative in nature, was obtained from people involved in the construction of the pipeline. It was suggested that the severe incidence of hollow bead occurred where the root face was towards the higher end of the dimensional range (around 2.4mm) such that higher welding currents were required to be employed to obtain adequate penetration. The welding procedure qualification record for this project, based on the standard AS 2885 - 1987, specified joint dimensions and tolerances for a single vee butt weld preparation of 1.6 +1.0/-0.8mm for the root face and 1.5 +1.0/-0.5mm for the root gap. A root face of 2.4mm was, therefore, at the high end of the range but not over the specified limit. Hollow bead was also noted to be more prevalent on the side of a particular welder (900-0 and 0-100) who had allegedly used high welding currents.

Based on this survey, it appeared that hollow bead could be produced in an X70 steel and using high welding currents. These conditions were used as the basis for the preliminary laboratory experiments.

2.3 Experimental Techniques

The equipment and materials used in the majority of experiments are described here. Where different materials have been used, the relevant details of the materials and equipment are included in the appropriate section.

2.3.1 Equipment

The experiments in this study, except for the welding of the pipe samples (segments of pipe 200mm in length), have been performed on an automated stick electrode welding machine designed to simulate the manual method of making root beads: the stovepipe welding technique.

The automated manual metal arc welding machine is illustrated in Figures 2.3-2.4. It was designed to allow the welding operation to be done under monitored conditions, with parameters such as weld travel speed and electrode force or voltage kept constant during welding runs. The machine was originally built by Tubemakers of Australia Ltd. in 1976 and was in 1993 modified and refurbished by Bob Morrison at Tubemakers of Australia Pipelines Research Centre for the purposes of this project on hollow bead defects.

The stovepipe welding technique involves the use of cellulosic stick electrodes which are forced into the joint bevel. The cone made by the electrode coating rests on the bevel as the electrode is dragged down around the pipe circumference. The force of the electrode on the bevel is, therefore, a more appropriate parameter than arc voltage in simulating this welding technique. As a result the automated system was designed to function under a force control mode, although a voltage control mode was subsequently added. The latter mode is required during start-up and in cases where the machine is needed to simulate other welding techniques.

Figure 2.3: Photograph of the automated stick electrode welding machine, welding generator and data logging computer. The large screen at the back of the machine was used to protect the equipment during filming of the process.

Figure 2.4: Photograph of work table showing the clamping arrangement and the position of the electrode inside the joint preparation prior to welding.

The equipment consists of a large work table which can be rotated within a 180^{o} range, from horizontal down-hand through vertical to horizontal overhead. The table contains guides for a work carriage to which flat test plates are attached and which is driven by a variable speed electric motor. Weld travel speed is adjusted by varying the speed of the work carriage and ranges from 140 to 690 mm/min.

The electrode feeder is attached to the work table and consists of an insulated electrode holder which is driven by means of a re-circulating ball bearing screw system. The screw is driven through a rubber belt by a D.C. servo-motor. The electrode force ranges from 1 to 50N. A series of tests to establish the maximum normal electrode force which might be expected in manual metal arc stovepipe welding operations was carried out by researchers at Tubemakers of Australia Pipelines Research Centre in Melbourne (Morrison, 1993). There the actual force exerted by a qualified pipeline welder was measured using extreme joint geometry conditions such as a tight root gap. The force recorded during welding ranged from approximately 10 to 40N and it was concluded that the range of 1 to 50N would be adequate for the automated machine.

The electronic controller controls and coordinates the work carriage drive, the electrode feeder system and the welding generator. It also displays, on digital panels, the welding current and voltage and the force acting on the electrode. The electrode force and arc voltage levels are preset on the controller.

A personal computer with the Snapshot software program was connected to the recorder output of the controller to log data on welding current, voltage and electrode force. A sample rate of 20 points per second was used with a maximum sweep time of 50 seconds. Examples

of the traces obtained from the data logger for the welding current and voltage and the electrode force during a particular welding run have been included in Appendix D.

The welding process is started by placing a small ball of steel wool on the test plate underneath the electrode tip. When a voltage from the generator is applied to the electrode, a current starts to flow which causes the steel wool ball to melt and an arc to be created. The flow of current in the welding circuit is detected by the controller and a time delay circuit is activated. This delay was set to 0.5 seconds so that the arc is allowed to stabilise before the electrode feeder and work-table travel start. Initially welding progresses under the voltage control mode for 1.5 seconds, again to allow the arc to become better established. The work piece then moves upwards under the electrode feeder and the servo motor drives the electrode holder to maintain the force applied to the level set on the controller.

Welding in the laboratory was carried out using the vertical down technique under force control, using flat plate samples. The work table was held in the vertical position and the electrode holder adjusted to a trailing angle of 15^{o} above the horizontal. The travel speed was kept constant throughout each weld run.

2.3.2 Materials

The test plates and pipe samples used in all the experiments performed in this project, except for the alloys used in the study on parent metal composition, were prepared from 8.3mm thick API 5L X70 steel plates, which has the nominal composition given in Table 2.2. It is a relatively low carbon, fully killed, microalloyed steel with a very low sulphur content.

C	P	Mn	Si	S	Ni	Cr	Mo	Cu	Al	Nb	Ti	V
.09	.016	1.56	.33	.001	.022	.017	.002	.008	.03	.04	.012	.056

Table 2.2: API 5L X70 steel composition. Percentage concentration by mass. Analysis by atomic emission spectroscopy.

Cellulosic electrodes made by manufacturers such as Böhler and Thyssen are widely used in industry, although the Lincoln Electric Fleetweld 5P+ and 5P are the most popular choice for the root pass.

The Lincoln Fleetweld 5P+ electrodes (E6010/E4110) 4.0mm in diameter, were chosen for all experiments (except for the study of the influence of electrodes from an alternate manufacturer - Section 2.7) on the basis that the 5P+ type is an improved version of the Lincoln 5P electrode. Although the 5P type is still widely used in industry it is being rapidly replaced by the 5P+. The electrodes had a moisture content of 2.3% and were supplied in batches of 12 electrodes in sealed packs. These packs were specially prepared for this project by The Lincoln Electric Company so that all the experiments could be performed using one batch of electrodes with a controlled level of moisture.

Only unopened packs were used during a particular experiment with any remaining electrodes being discarded. The compositions of the electrode core wire and flux coating are given in Tables 2.3 and 2.4 respectively.

The typical weld metal compositions of the 5P and 5P+ electrodes are given in Table 2.5.

	C	P	Mn	Si	S	Ni	Cr	Mo	Cu	Al	Nb	Ti	V	N	O
5P	0.075	0.008	0.39	0.015	0.011	0.018	0.021	0.004	0.014	0.003	<.005	<.003	<.003	.0017	.0019
5P+	0.080	0.012	0.32	0.075	0.007	0.018	0.019	0.002	0.010	0.008	<.005	<.003	<.003	.0020	.0017

Table 2.3: Composition of the electrode core wire of the 5P and 5P+ electrodes. Percentage concentration by mass.

	Fe	SiO_2	Al_2O_3	CaO	Mn	MgO	P	K_2O	TiO_2	Zn	S	Cu	Ni	V	Na	Cr	F	LOF
5P	3.9	19.7	1.6	0.25	5.2	1.9	.014	0.05	14.8	.016	<.005	.050	.023	0.03	4.0	.044	<.1	43.9
5P+	15.7	14.4	0.21	4.6	5.4	0.20	.010	0.02	15.3	.018	<.005	.058	.030	0.01	3.1	.048	<.1	31.3

Table 2.4: Composition of the electrode flux of the 5P and 5P+ electrodes. Percentage concentration by mass. Analysis by x-ray fluorescence spectrometry. LOF indicates the percentage concentration lost on fusion.

	C	P	Mn	Si	S	Ni	Cr	Mo	Cu	Al	Nb	Ti	V
5P	.115	.014	1.05	.28	.005	.028	.018	.003	.01	.015	.025	.018	.031
5P+	.125	.013	1.06	.24	.011	.025	.018	.003	.01	.013	.023	.016	.016

Table 2.5: Weld metal composition. Percentage concentration by mass.

2.3.3 Joint Geometry

The dimensions of the root face and bevel angle used in the experiments (Figure 2.5) were kept within the limits specified in the Australian Standard 2885 Part 2 - 1995 for the Welding of Gas and Petroleum Pipelines. These limits have been mentioned in Section 1.2.3.

The joint geometry dimensions could not be fixed as a wide range of heat inputs were tested. At high heat inputs and a small root face and/or a wide root gap burn-through becomes a problem, while at low heat input lack of penetration results from a large root face and/or a narrow root gap. The dimensions of the joint geometry, however, remained within the specifications set in the AS 2885.2 - 1995 and were recorded for each weld made. The range for these dimensions were as follows.

Root Face, R.F = 1.6 - 2.1mm

Root Gap, R.G = 1.3 - 1.6mm

Bevel angle, $\Phi = 30^{o}$.

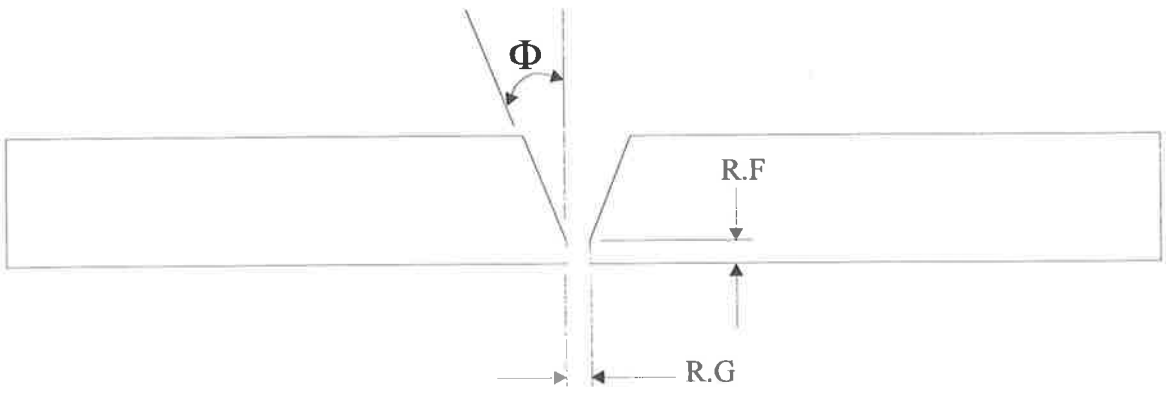

Figure 2.5: Schematic of the joint geometry.

2.4 Preliminary Experiments

2.4.1 Introduction

The design of these preliminary experiments and all subsequent ones have been based primarily on the welding parameters used for the field welding of the root pass of pipeline girth welds by the stovepipe technique. Initially the welding practices used both in Australia and the USA were established by studying actual welding procedures and through measurements during field trips (see Appendix C for details on the latter). These practices have been compiled in the next Section 2.4.2.

The objectives of the preliminary experiments were to assess the ability of the automated manual metal arc welding machine to reproduce the hollow bead defect and to obtain an initial range of conditions under which the defect forms. In addition, samples of hollow bead were required for metallographic studies due to the inability to obtain defects from field welds. These are usually repaired in the field by grinding a portion of the weld. It was therefore decided to concentrate in these experiments on the conditions which would produce the maximum number of hollow bead defects.

2.4.2 Common Practices used for the Field Welding of the Root Pass of Pipelines Girth Welds using the Stovepipe Technique.

The Procedure Qualification Record for the South West Queensland pipeline project (Kwiatkowski, 1993) (see also Section 2.2) was studied initially to obtain an indication of the welding parameters used for the welding of the root pass by the stovepipe technique. The Procedure Qualification Record specified the following parameters for the welding of the root pass with Lincoln 5P electrodes, 4.0mm in diameter; a welding current range of 175 - 180A (direct current electrode positive DC(+)), a welding voltage range of 32V and an average weld

travel speed of 320mm/min. The current density range corresponding to a welding current range of 175 - 180A for an electrode 4mm in diameter is 13.8 - 14.3A/mm^2. In the following discussion the corresponding current densities have been included in brackets.

It was recommended, however, that higher welding currents and travel speeds be used in conjunction with a large root face (around 2.4mm) and small root gap (around 1.0mm) (Kwiatkowski, 1993).

During the field trip to the Tubridgi Pipeline in Western Australia in 1993, which has been described in Appendix C, the welding parameters used by the welders of the root pass were noted. The linepipe for this project was API 5L X70, with an outside diameter of 273mm and a wall thickness of 5mm. The electrode used for the root pass was the Lincoln 5P+, 3.25mm in diameter. The welding parameters used by the two root pass welders on a particular day were measured by the inspector using a tong tester. The welding current was 115A (13.9A/mm^2) for one welder and 120A (14.5A/mm^2) for the other, and the welding voltage for both was 26V. The welding procedure for this project specified a welding current between 110 (13.3A/mm^2) and 120A (14.5A/mm^2) and a welding voltage between 26 and 28V. The current density values are comparable to the ones for the 4mm diameter electrode mentioned in the Procedure Qualification Record for the SWQ project.

The survey carried out by C. W. Pope & Associates Pty Ltd (Biddle, 1993) on the Junee to Griffith Gas pipeline, described in the Literature Review (Section 1.2), has also provided details of the welding parameters. The dimensions and tolerances of the joint geometry were 1.5mm +/-0.5mm for the root gap and 1.6mm +/-0.8mm for the root face. The electrode specified for the root pass was the Lincoln 5P, 3.25mm in diameter, and the ranges for the

welding current and voltage were 90 - 140A (10.8 - 16.9A/mm^2) (DC+) and 25 - 35V respectively.

The Weld Procedure Specification for the Whyalla (in South Australia) pipeline project (Tenneco Energy, 1988) details the materials and parameters used for the construction of this pipeline. The linepipe was API 5L X52, with an outside diameter of 219.1mm and a wall thickness of 4.3mm The dimensions and tolerances of the joint geometry were 2 - 3mm (maximum) for the root gap and 1 - 1.5mm for the root face. The electrodes specified for the root pass were Lincoln 5P, 3.25mm in diameter, and the welding current and voltage ranges were 65 - 130A (7.8 - 15.7A/mm^2) DC(+) and 25 - 35V respectively. The Test Weld Record shows a weld travel speed of 300mm/min.

Three welding procedures for pipelines constructed in the USA were also obtained from the National Pipeline Welding School in Tulsa, Oklahoma (see Appendix C Training Programme). The information from two Pipe Welding Procedures from the All-American Pipeline Company and one from the Williams Pipe Line Company have been summarised in Table 2.6. Only the details pertaining to the parameters for the welding of the root pass have been included. The dimensions and tolerances of the joint geometry were, for all welding procedures, 1.6mm +/- 0.8mm for both the root face and root gap.

Procedure	Grade API 5L	Outer Diameter (mm)	Wall Thickness (mm)	Electrode Type 4.0mm Diameter	Welding Current (A) DC(+)	Welding Voltage (V)	Weld Travel Speed (mm/min)*
1[1]	Grade B (or X42)	304.8	6.4	Lincoln 5P+	130 - 160	20 - 25	152-356
2[2]	X65 to X70	762	7.1 - 8.7[#]	Lincoln 5P+	135 - 160	22 - 26	229-381
3[3]	X42	406.4	6.4	Lincoln 5P+	150 - 175	22 - 26	229-381

Table 2.6: Information from welding procedures from the companies listed below. Information on the welding parameters for the root pass only are given.

[1] (All-American Pipeline Company Pipe Weld Procedure AAPL-5A, 1993).

[2] (All-American Pipeline Company Pipe Weld Procedure AAPL-24, 1993).

[3] (Williams Pipe Line Company Pipe Welding Procedure 1C-S, 1988).

[#] The joint design shows that pipe of these different thicknesses are to be joined together.

* The weld travel speeds have been converted to mm/min from inches/min.

Information obtained from field trips to pipeline construction sites in the USA is also given in Table 2.7 and 2.8. These field trips have been described further in Appendix C.

Two pipeline construction sites in Florida, USA, were visited in 1994. The information on the parameters for welding of the root bead was gathered for both spreads and is presented in Tables 2.7 and 2.8. An average weld travel speed was obtained by recording the time taken by the welders to weld each bead which was approximately equal to a sixth of the pipe circumference (three electrodes were used by each welder to weld one half of the pipe. The average welding current and voltage were measured using a tong tester.

Location	Type of Electrode	Weld Travel Speed Range (mm/min)	Average Weld Travel Speed (mm/min)	Average Welding Current (A)	Average Welding Voltage (V)
Spread 7	Lincoln 5P+ 4.0mm Diameter	330 - 405	365	175	26

Table 2.7: Details of the welding parameters for the root pass on Spread 7.

As well as measuring the welding current and travel speed on Spread 7, information on these parameters was obtained from the daily inspection sheets. The inspections sheets showed that higher travel speeds between 18 and 22in/min (457 - 559mm/min) were used and the welding current and voltage varied between 140 and 180A and 23 to 33V respectively.

Location	Number of Welders	Type of Electrode	Weld Travel Speed Range (mm/min)	Average Weld Travel Speed (mm/min)	Average Welding Current (A)	Average Welding Voltage (V)
Spread 8	2	Lincoln 5P+ 4.0mm Diameter	399 - 480	456	170	28

Table 2.8: Details of the welding parameters for the root pass on Spread 8.

A welding procedure for the construction a 435km oil pipeline built in Iran between 1976 and 1978 has been described by Mathias (1980). A summary of the procedure is given here as the welding process was the stovepipe technique. It was found to be similar those described above.

The linepipe was to API 5L X60 specification with diameters of 762 and 813mm and a wall thickness of 7.14mm. The welding procedure and specifications for the joint geometry and other parameters were designed to the API Standard 1104. The parameters for the welding of the in-line welds are recorded in Table 2.9.

Pass	Electrode	Welding Voltage (V)	Welding Current (A)	No. of Welders
Root	Fleetweld 5P 4mm diameter	24 - 28	140 - 180	3
Hot	Shield-Arc 85 4mm Diameter	26 - 28	200 - 220	2
Filling	Shield-Arc 85 5mm Diameter	26 - 29	170 - 220	2
Capping	Shield-Arc 85 5mm Diameter	26 - 28	160 - 210	2

Table 2.9: Stovepipe welding procedure for Marun-Esfahan Pipeline in Iran (Mathias, 1980).

Notes
1. Preheating to 100°C when ambient temperature is below 5°C.
2. Clamp removed after completion of 75% of the root pass.
3. Time lapse between root and hot pass is 5 mins.
4. All welds completed the same day.
5. Joint bevel angle: 60°
6. Root gap: 1.5-3mm.
7. Root face: 0.8-1.5mm
8. Interpass cleaning: brushing and grinding.

It is worthwhile to note the recommended range of welding current for the Lincoln 5P and 5P+ electrodes from their manufacturer's guide (The Lincoln Electric Company (Australia) Pty. Ltd., 1986) (Table 2.10).

Electrode	Diameter and Current Ranges	
	3.2mm	4.0mm
Fleetweld 5P	75 - 130A	90 - 175A
Fleetweld 5P+	65 - 130A	90 - 175A

Table 2.10: Recommended welding current range for Lincoln 5P and 5P+ electrodes.

When comparing the recommended welding current range and the ones specified in the welding procedures, mentioned above, as well as the ones actually used, it can seen that the

current levels used in practice are at the extreme end of the range recommended by the manufacturer and higher. A possible reason for this is that the root pass welders try to maximise the number of welds done per day, and thus employ high weld travel speeds (above 400mm/min) which require high welding currents (above 175A) to maintain an adequate level of heat input.

2.4.3 Experimental Conditions and Results

The dimensions of the joint preparation and the levels of welding current and weld travel speed were initially chosen from values which, from practical experience, were thought to produce hollow bead. These values were obtained principally from the welding procedure used for the construction of the South West Queensland pipeline. As previously mentioned in Section 2.2 the dimension of the root face of some of the pipes used during construction was towards the upper end of the specified limit, to a maximum of 2.4mm. It was thus speculated that the larger root face was one of the contributing factors to the high incidence of hollow bead on this pipeline since higher welding currents were employed. A root face of 2.5mm was therefore selected to assess this factor. Two sets of experiments were carried out. A larger root gap was used in Set 2 to determine the effect of higher weld travel speeds. The bevel angle was set at 30^{o}. In Set 1 of the experiments, the welding data was not successfully logged due to a computer malfunction. The data on welding current and voltage recorded in Table 2.11 were therefore obtained by noting the values from the digital displays of the controller during welding.

In Set 2, data were successfully logged by the computer. The average values for the welding conditions were calculated using functions available in the software.

In Set 1, the hollow bead defects were found by random sectioning of the welds using a cut-off wheel. Although hollow bead was detected it was not possible to assess exactly their total number and length in the welds. In Set 2, data on the location and dimensions of the hollow bead defects were determined from radiographs and have been recorded in Table 2.11.

In this thesis the heat input refers to the arc energy, or the welding current times the voltage divided by the weld travel speed. Heat input is strictly the arc energy factored by the arc efficiency factor for the welding process concerned. However, in the literature this definition is commonly termed the heat input. In addition since only one process was used in this investigation the efficiency can be considered constant. Therefore the values quoted allow direct comparison of the effect of both heat input and arc energy.

					Average					
	Plate No	**Root Face (mm)**	**Root Gap (mm)**	**Travel Speed (mm/min)**	**Current (A)**	**Voltage (V)**	**Heat Input (kJ/mm)**	**No. of Hollow Bead**	**Total Length of Hollow Bead (mm)**	**Average Length of Hollow Bead (mm)**
Set 1	1a	2.5	0.4	300	190	N/A	N/A	N/A	N/A	N/A
	1b	2.5	0.6	300	190	N/A	N/A	N/A	N/A	N/A
	2a	2.5	0.4	300	190	N/A	N/A	N/A	N/A	N/A
	2b	2.5	0.6	300	190	N/A	N/A	N/A	N/A	N/A
	3a	2.5	0.7	350	190	N/A	N/A	N/A	N/A	N/A
	3b	2.5	0.5	350	190	N/A	N/A	N/A	N/A	N/A
	4a	2.5	0.4	350	190	N/A	N/A	N/A	N/A	N/A
	4b	2.5	0.3	300	190	N/A	N/A	N/A	N/A	N/A
Set 2	1a	2.5	1.5	350	190	25	0.78	4	27	7
	1b	2.5	1.5	515	N/A	N/A	N/A	3	12	4
	2a	2.5	1.5	515	189	25	0.53	2	5	2.5
	2b	2.5	1.4	515	219	28	0.71	2	23	12
	3	2.5	1.5	650	190	22	0.39	3	7	2
	4	2.5	1.4	515	196	23	0.53	4	16	4

Table 2.11: Experimental conditions for preliminary experiments. N/A: not available.

2.4.4 Discussion

Hollow bead defects were found to be present in all the welds confirming the ability of the automated system to produce the defect. A range of conditions within which hollow bead occurs was established; high welding currents from 190 to 220 A and a wide range of weld travel speeds from 300 to 650 mm/min. Samples of the defect from these preliminary experiments were used in the metallographic characterisation of hollow bead (Chapter 3).

2.5 Welding of Pipe Samples

2.5.1 Introduction

This experiment was a preliminary investigation into the influence of the welding parameters on the formation of hollow bead in the root pass under field conditions. Welds were prepared on X70 grade pipe samples with an outside diameter of 406.4mm and a wall thickness of 8.5mm by a qualified pipeline welder using the manual stovepipe technique in the vertical down position. These welds were also used as a reference to assess the validity of the results from the automated equipment. The reproduction of hollow bead pores allowed the metallographic characterisation of the defect. The microstructure of the welds and characteristics of the hollow bead pores from the manual and automated techniques were compared.

2.5.2 Equipment

A Lincoln AS 400 diesel driven generator was used. Welding current and voltage were measured using a tong tester and the mean weld travel speed was determined using a stop watch and noting the individual stops and starts of the weld runs.

2.5.3 Experimental Conditions

The pipes were welded using both Lincoln 5P and 5P+ electrodes because it was proposed that the performance of the 5P could have an influence on promoting the formation of hollow bead. The 5P is more difficult to handle especially when the dimensions of the joint preparation are not ideal.

The outline of the pipe circumference showing the division of the pipe into quadrants, the locations of the stops and starts and the sequence of the weld runs are shown in Figure 2.6.

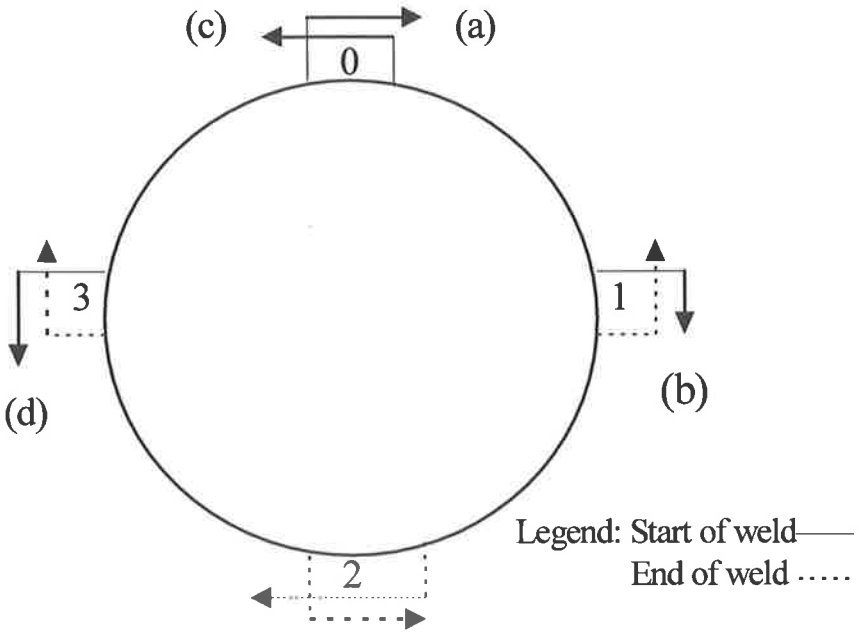

Figure 2.6: Schematic showing division of the pipe circumference into quadrants and showing the location of the starts and stops of the weld runs.

The sequence of welding runs is as follows:

(a) The first run starts before the "0" position and finishes slightly after the "1" position.

(b) The second run starts before the "1" position, on the previous run, and finishes past the "2" position.

(c) The third run starts just before the "0" position, on the first run, and finishes just after the "3" position.

(d) The fourth run starts before the "3" position, on the previous run, and finishes after the "2" position.

2.5.4 Results

The trials were successful in achieving the aim of reproducing hollow bead; only one welded joint was completely free of hollow bead defects.

The radiographs of the welds were examined to obtain information on the dimensions and location of the defects. The length and diameter of each defect were measured and the information recorded in Tables A1 and A2 (Appendix A) together with the total number, total length, average length and maximum length of the defects at each location around the pipe circumference.

The parameters used in welding each joint, including root face, root gap, electrode type, travel speed, welding current and voltage for each quadrant around the pipe have been recorded in Table 2.12.

Pipe Number	Position	Root Face	Root Gap	Electrode Type	Travel Speed	Welding Current	Welding Voltage	Weld Passes	Total Number of Hollow Bead	Total Length of Hollow Bead	Average Length of Hollow Bead
		(mm)	(mm)	(Lincoln)	(mm/min)	(A)	V			(mm)	(mm)
P1	0-1	2.2	0.95	5P	456	N/A	N/A	ROOT/HOT	4	12	3
	1-2	2.2	0.95	5P	376	N/A	N/A	ROOT/HOT	3	10	3.3
	2-3	2.2	0.95	5P	415	N/A	N/A	ROOT/HOT	3	9.5	3.2
	3-0	2.2	0.95	5P	454	N/A	N/A	ROOT/HOT	6	15.5	2.6
P2	0-1	1.8	0.85	5P+	454	N/A	N/A	ROOT/HOT	0	0	
	1-2	1.8	0.85	5P+	464	N/A	N/A	ROOT/HOT	4	8.5	2.1
	2-3	1.8	0.85	5P+	434	N/A	N/A	ROOT/HOT	3	4.5	1.5
	0-3	1.8	0.85	5P+	N/A	N/A	N/A	ROOT/HOT	0	0	
P3	0-1	2	1.4	5P	430	N/A	N/A	ROOT/HOT	7	19	2.7
	1-2	2	1.4	5P	N/A	N/A	N/A	ROOT/HOT	0	0	
	2-3	2	1.4	5P	N/A	N/A	N/A	ROOT/HOT	2	10.5	5.3
	3-0	2	1.4	5P	500	N/A	N/A	ROOT/HOT	4	21	5.3
P5	0-1	2.3	1.3	5P	555	N/A	N/A	ROOT/HOT	3	4.5	4.5
	1-2	2.3	1	5P	707	N/A	N/A	ROOT/HOT	1	5	
	2-3	2.3	1.2	5P	600	N/A	N/A	ROOT/HOT	9	4.5	4.5
	3-0	2.3	1.3	5P	570	N/A	N/A	ROOT/HOT	7	24	3.4
P6	0-1	2	1.1	5P	670	N/A	N/A	ROOT/HOT	5	18.5	3.7
	1-2	2	1.1	5P	670	N/A	N/A	ROOT/HOT	8	15.5	5.4
	2-3	2	1.1	5P	460	N/A	N/A	ROOT/HOT	4	11	2.8
	3-0	2	1.1	5P	561	N/A	N/A	ROOT/HOT	2	7	3.5
P7	0-1	1.8	0.6	5P	634	N/A	N/A	ROOT/HOT	4	16	4
	1-2	1.8	0.6	5P	585	N/A	N/A	ROOT/HOT	3	22	7.3
	2-3	1.8	0.6	5P	413	N/A	N/A	ROOT/HOT	4	17.5	4.4
	3-0	1.8	0.6	5P	551	N/A	N/A	ROOT/HOT	3	13.5	4.5
P8	0-3	1.7	1.2	5P+	417	N/A	N/A	ROOT/HOT	0	0	

Table 2.12: Welding conditions and results for the experiments using pipe samples+A50 (N/A: not available).

Pipe Number	Position	Root Face (mm)	Root Gap (mm)	Electrode Type (Lincoln)	Travel Speed (mm/min)	Welding Current (A)	Welding Voltage V	Weld Passes	Total Number of Hollow Bead	Total Length of Hollow Bead (mm)	Average Length of Hollow Bead (mm)
P10	0-1	1	0.5	5P	440	N/A	N/A	ROOT/HOT	1	2	
	1-2	1	0.5	5P	475	N/A	N/A	ROOT/HOT	5	24	4.8
	2-3	1	0.5	5P	400	N/A	N/A	ROOT/HOT	0	0	
	3-0	1	0.5	5P	424	N/A	N/A	ROOT/HOT	5	15	3
P11	0-1	1.8	1	5P	354	145	27	ROOT	1	10	
	1-2	1.8	0.4	5P	523	175	29	ROOT	6	25	4.2
	2-3	1.8	1.4	5P	440	175	31	ROOT	2	10	5
	3-0	1.8	1	5P	390	155	29	ROOT	1	3.5	
P12	0-1	1.7	1.6	5P+	320	130	30	ROOT	0	0	
	1-2	1.7	1	5P+	450	160	30	ROOT	2	6	3
	2-3	1.7	1.1	5P+	382	140	28	ROOT	2	4	2
	3-0	1.7	0.8	5P+	428	158	29	ROOT	1	5	
P13	0-1	2.5	1.4	5P	556	175	31.5	ROOT	6	17.5	2.9
	1-2	2.5	1	5P	523	185	31.5	ROOT	15	56.5	3.8
	2-3	2.5	1.2	5P	528	185	31.5	ROOT	15	58	3.9
	3-0	2.5	1.2	5P	512	180	31	ROOT	6	32	5.3
P14	0-1	2.5	1.2	5P+	500	180	33	ROOT	3	5	1.7
	1-2	2.5	1.2	5P+	555	170	32.5	ROOT	1	12	
	2-3	2.5	1.2	5P+	417	174	31	ROOT	3	4	1.3
	3-0	2.5	1	5P+	511	180	33	ROOT	2	5	2.5

Table 2.12(continued): Welding conditions and results for the experiments using pipe samples (N/A: not available).

2.5.5 Discussion

The following discussion is based on observation of the data obtained from the radiographs. The proportion of hollow bead pores which occurred at the start of weld runs compared to the end of weld runs was assessed by determining the number and length of defects 50mm from the start and stops for all welds. In most cases the total number and length of hollow bead is only slightly higher at the end of weld runs such that a significant trend in these results does not appear to exist. Any increase in hollow bead at the end of a weld run could be due to an increase in the welding current due to a decrease in the length and thus the resistance of the electrode. Hollow bead defects were found in all pipe quadrants and again no significant relationship between their occurrence and location in a particular quadrant could be noted. There is therefore no clear evidence from this set of data to suggest that the location around the circumference of the pipe is a factor influencing the formation of hollow bead.

The results of the survey of the occurrence of hollow bead on the South West Queensland pipeline, reported in Section 2.2, showed that the defect was more prevalent in particular quadrants around the pipe. It was pointed out, however, that the reason for this may have been due to the technique and welding parameters employed by the welder at those locations.

Although the data on the welding conditions is not complete, some comments can be made on the effect of welding current and weld travel speed on the occurrence of hollow bead in the pipe welds. The total number and total length of hollow bead in the welds were used to

compare the influence of welding variables on the pipe welds P11, 12, 13 and 14. It is observed that at low welding current and travel speeds the incidence of hollow bead decreases.

The contrast in the radiographs from the pipe samples precluded the production of adequate photographic prints. However visual comparison between the radiographs of samples prepared by both automated and manual welding revealed no obvious differences. Figures 2.7 and 2.8 are radiographs of welds made using the automated process; examples of short hollow bead are shown in Figure 2.7 and longer ones in Figure 2.8.

Figures 2.9 and 2.10 show cross sections of welds produced using the manual and automated methods. The shape of the beads and the growth microstructure are similar - both showing columnar grain growth towards both top and bottom surfaces. These features are discussed later in more detail (Chapter 3). The appearance of the weld beads is similar; both contain "wagon-tracks" on the sides of the bead and the heat affected zones are comparable in size and shape. The shape of the two welds are slightly different as the joint geometry and heat input used were different.

Samples of hollow bead obtained from both welding types were also studied in the SEM and again no differences were noted. Figures 2.11 and 2.12 are SEM micrographs of the interior surface of typical hollow bead pores obtained from welds made manually and with the automated process. Both examples show the characteristics which have been found to be

particular to hollow bead pores. Briefly, these features are a "cusp" formed at the initiation point of the pores (marked A in the figures), an oxidised surface containing slag inclusions and ripples (or steps) on the surface where the diameter of the pores changes. These and other detailed observations are discussed more thoroughly in Chapter 3.

This investigation has confirmed the ability of the automated system to reproduce hollow bead defects comparable to those found in field welding.

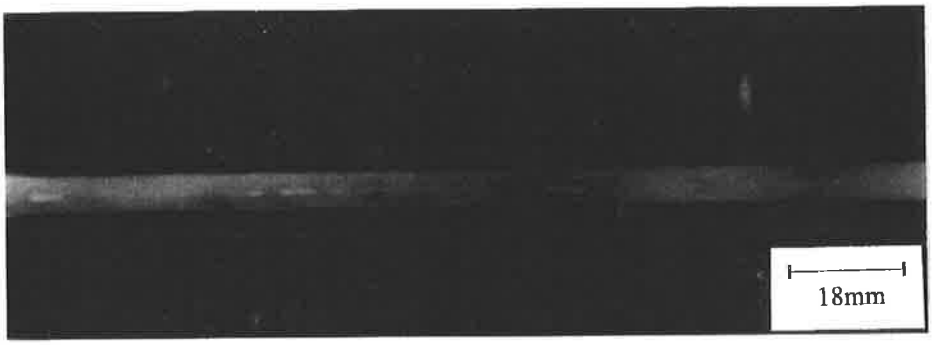

Figure 2.7: Radiograph of a root pass weld made using the automated equipment showing examples of short hollow bead defects.

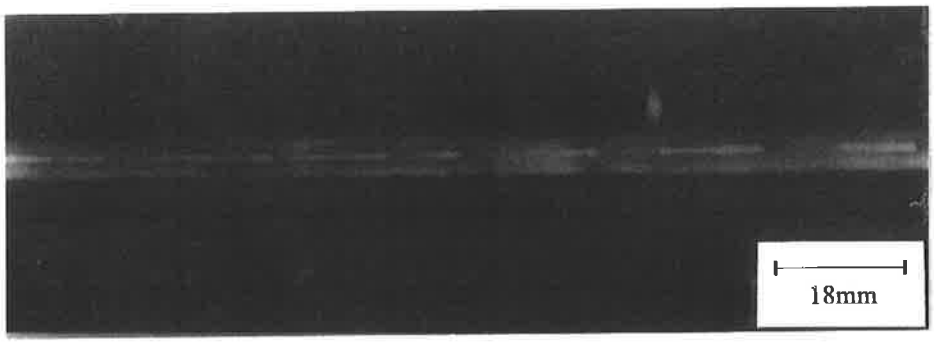

Figure 2.8: Radiograph of a root pass weld made using the automated equipment showing examples of long hollow bead defects.

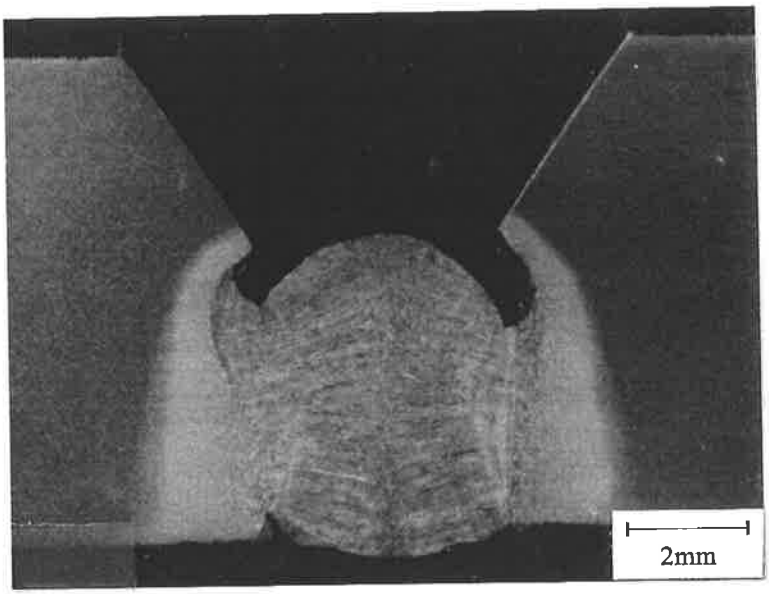

Figure 2.9: Micrograph of the cross sections of the root pass weld made manually.

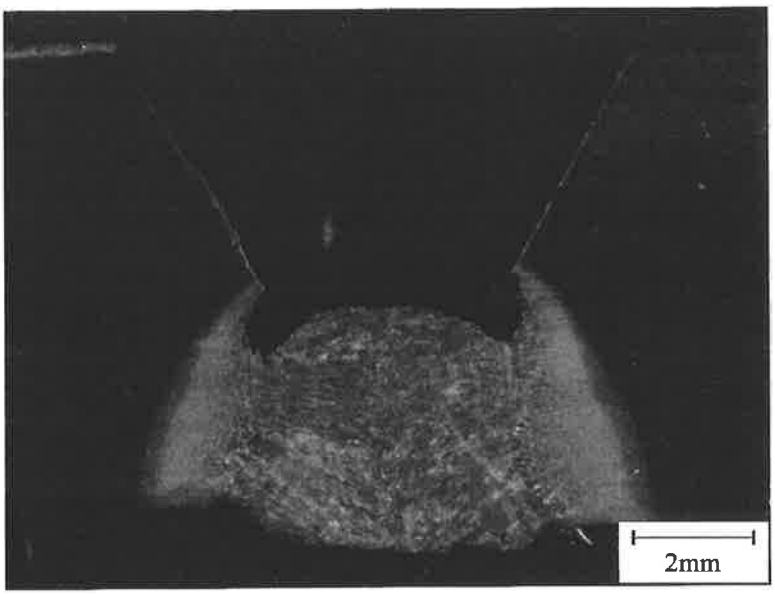

Figure 2.10: Micrograph of the cross section of the root pass weld made using the automated equipment.

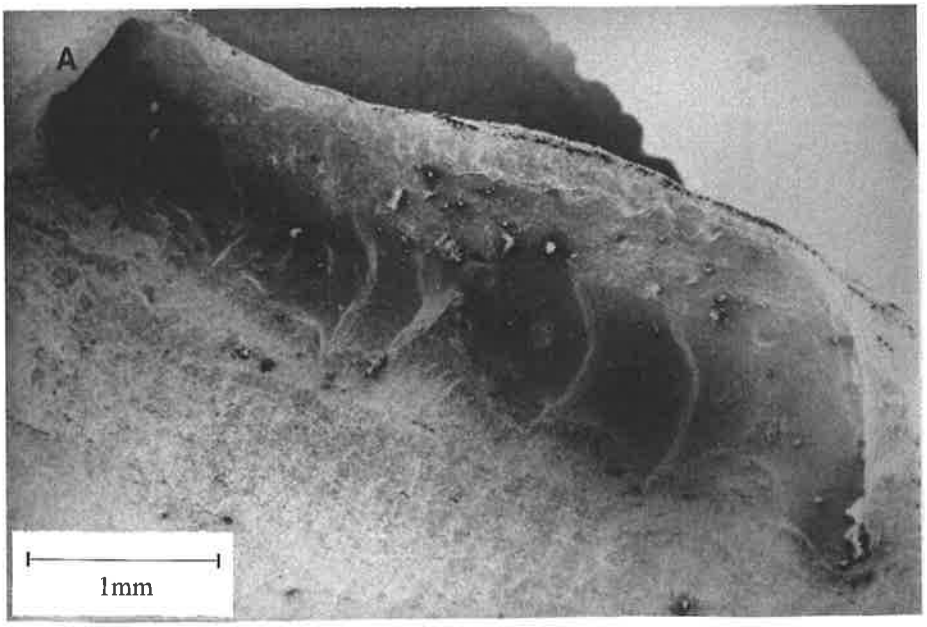

Figure 2.11: SEM micrograph of the internal surface of a pore from a pipe sample weld.

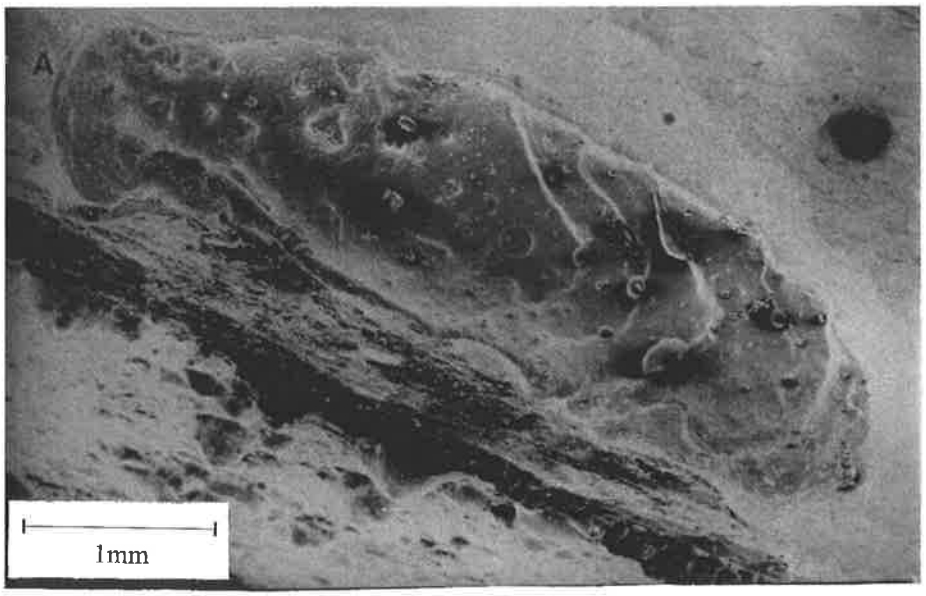

Figure 2.12: SEM micrograph of the internal surface of a pore from a weld made using the automated equipment.

2.6 An Investigation of the Effects of Welding Variables on the Formation of Hollow Bead Defects

2.6.1 Introduction

This series of experiments was designed to determine the precise influence of welding parameters, namely welding current, weld travel speed and heat input on the formation of hollow bead defects. The information found in the review of the literature indicated that the formation of porosity was strongly dependent on welding parameters as they have an effect on the heat input, solidification rate, the absorption and desorption of gases, the shape of the weld pool and the solidification mode.

The results obtained in these experiments have provided a definitive range of welding operational conditions under which hollow bead is produced. The sets of conditions where hollow bead is either formed in various degrees of severity or is completely avoided were used in other experiments.

The effects of changes in heat input in the range from 0.5 to 1.2 kJ/mm; the influence of weld travel speed, from 250 to 600 mm/min, at constant welding current; and the effects of welding current, from 120 to 240A, at constant speed were studied.

The range of welding currents used in these experiments encompasses a wider range of values than those commonly used in practice. Lincoln Fleetweld 5P+ electrodes, 4.0 mm in diameter, have a current rating of 90A to 175A. In the field, for standard joint preparations and an electrode 4mm in diameter, the average welding current is around 175A.

2.6.2 Experimental Conditions

The experimental conditions and results have been recorded in Table A3 (Appendix A).

During a welding run, except for the start, the welding conditions were maintained at stable levels. Welds were discarded if they were made under conditions that were too unstable.

2.6.3 Results

All the welds were radiographed to determine the occurrence of hollow bead defects. Although the length of the welds were typically between 200 and 230mm the total number and length of hollow bead were determined in 170mm of weld. This is because the region coinciding with the start of the welds, where the welding conditions were unstable, was not included.

The results have been plotted in Figures 2.13, 2.14 and 2.15. In most cases each condition was repeated three times to assess the statistical validity of the results.

Measurements of the diameter of hollow bead pores are presented in Table 2.13. The data in this table pertain to samples obtained from experiments on the effect of welding current at constant travel speed. The measurements were made from radiographs of the welds. In the cases where the diameter of the pore varies with length the minimum (usually at the start) and the maximum (usually at the end) diameters are given. The diameters of individual pores are separated by a comma and the change in diameters by a dash.

2.6.4 Discussion

The graphs in Figure 2.13a-j represent the change in the occurrence of hollow bead (total length, total number and average length of the defects) with welding current at constant weld travel speed.

The trend observed in all cases (for all weld travel speeds) is an increase in the total number, total length and average length of hollow bead with increasing welding current. It is also

evident from Figures 2.13a-j that the travel speed is an influential factor; the total length of hollow bead at 250 and 300mm/min are of comparable magnitudes at similar current levels. The total length then increases at 400mm/min, and remains similar at 500mm/min. The increase in the total number of hollow bead with increasing travel speed is less pronounced, although it tends to increase more rapidly from 250 and 300mm/min to 400 and 500mm/min. An extreme condition is observed at 600mm/min where the total length of hollow bead has increased significantly. The total number remains at a similar magnitude to that at 500mm/min at increasing current levels implying that the increase in travel speed has had a major influence on the length of individual pores. The repeated data points at all conditions are in good agreement with each other and the trends are reproducible at all travel speeds suggesting that a valid set of data has been obtained.

Figure 2.14a-h represent the change in the occurrence of hollow bead with weld travel speed at constant current. A general observation of the results suggests the weld travel speed has a secondary effect on the formation of hollow bead compared to the welding current, except at high speeds (500 and 600mm/min). At 140 and 160A (which is within the range recommended by The Lincoln Electric Company) hollow bead does not form except at 600mm/min. Hollow bead appears and increases in length from 170 to 186A (which is outside the range recommended by The Lincoln Electric Company) as predicted by the previous results on the effect of welding current. For a constant current of 170A there is a slight increase in the total length at 550 and 600mm/min. The increase is more pronounced at 186A, and especially at 600mm/min where the total length has increased significantly. Therefore the conclusions made in the previous paragraph, that increasing welding current and very high weld travel speeds are dominant factors in the formation of hollow bead, also apply to this set of results.

Although it is possible from the graphs in Figures 2.13a-j and 2.14a-h to comment on the effect of the heat input and thus cooling rate and weld pool shape on the occurrence of hollow bead, for clarity, all the data obtained in the experiments on the effect of welding current and travel speed have been combined and plotted in Figures 2.15a-f. The effect of heat input at constant current on the total length and total number of hollow bead is shown. It is evident that at the lowest heat input, which correspond to the highest travel speed, the total length of hollow bead is highest and increases more rapidly as the welding current increases. The total number of hollow bead also increases with decreasing heat input. However the rate of increase is less for the total length and there is little change in the magnitude of this parameter at the levels of welding current studied. This again suggests the major influence of the welding current on the length of the pores.

The diameters of hollow bead pores at varying current levels and for constant weld travel speeds are presented in Table 2.13 and show that there does not appear to be a correlation between the diameter and welding conditions. For a particular welding current and travel speed, the diameter of pores can range from 0.5 to 1mm. This is in fact the case at most welding conditions.

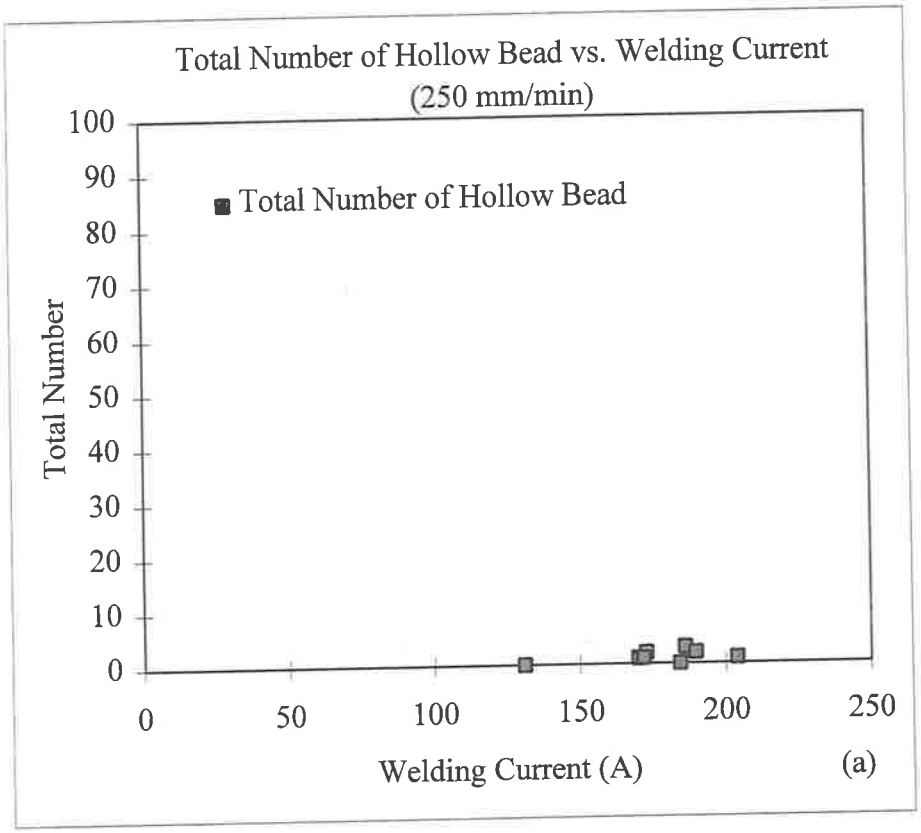

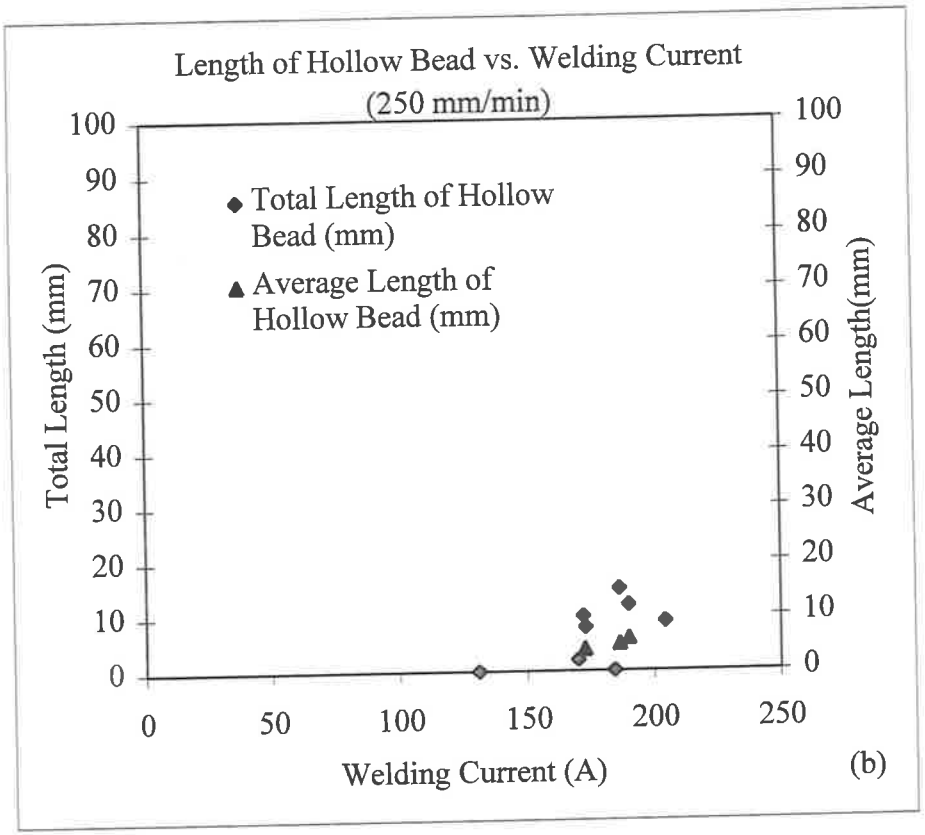

Figure 2.13a,b: The effect of welding current at a constant weld travel speed of 250mm/min on the occurrence of hollow bead.

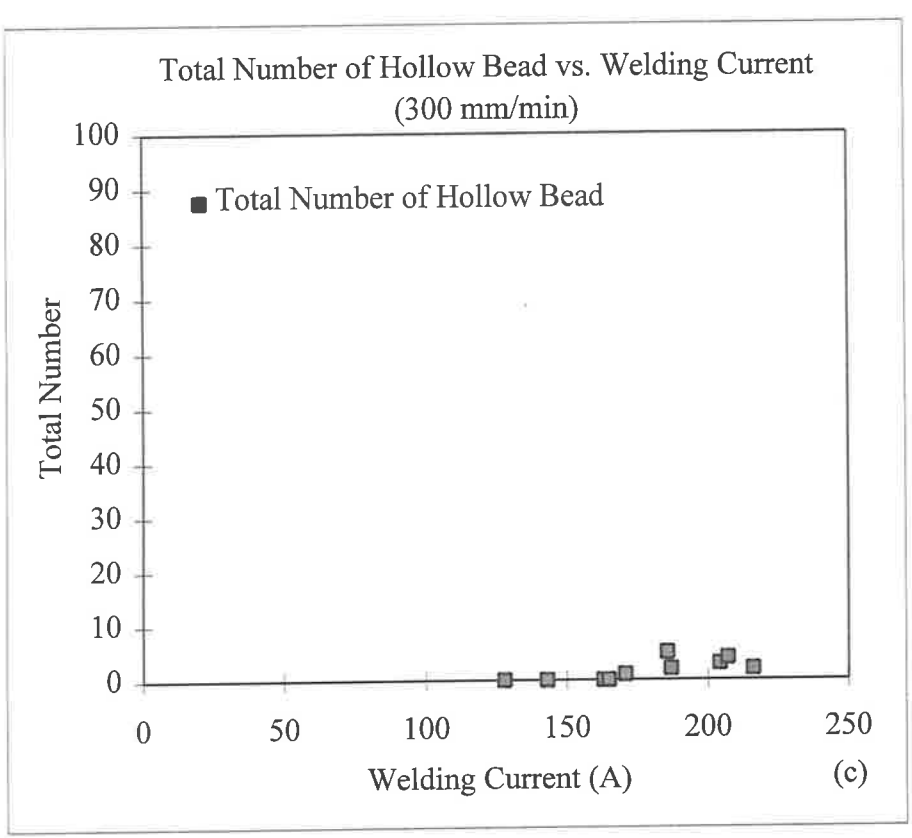

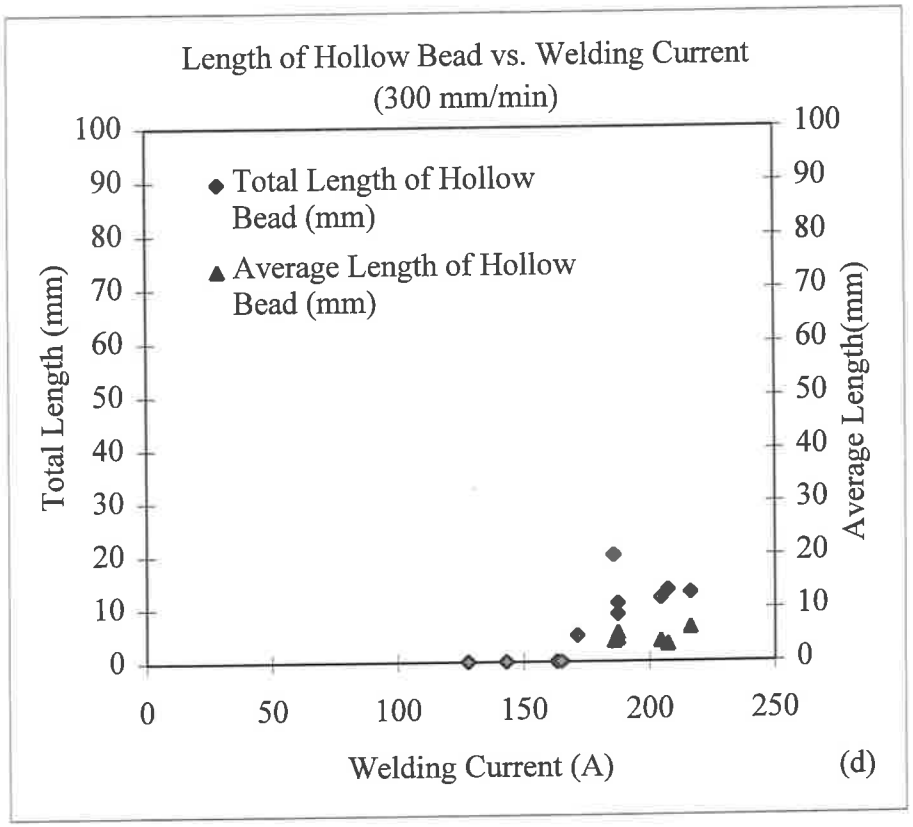

Figure 2.13c,d: The effect of welding current at a constant weld travel speed of 300mm/min on the occurrence of hollow bead.

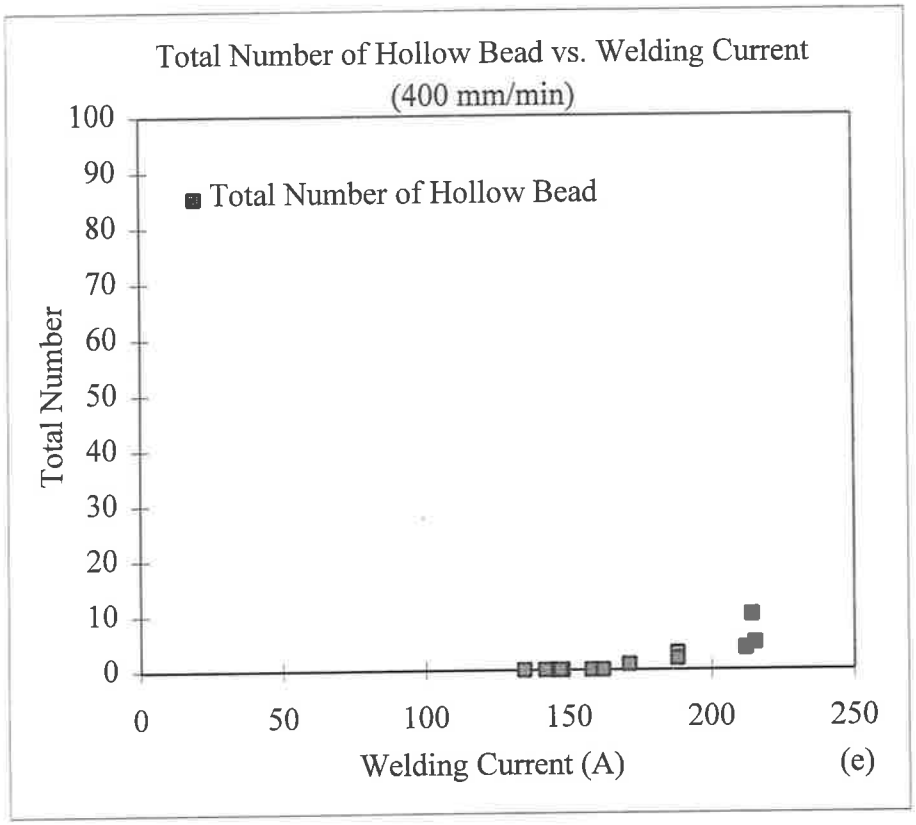

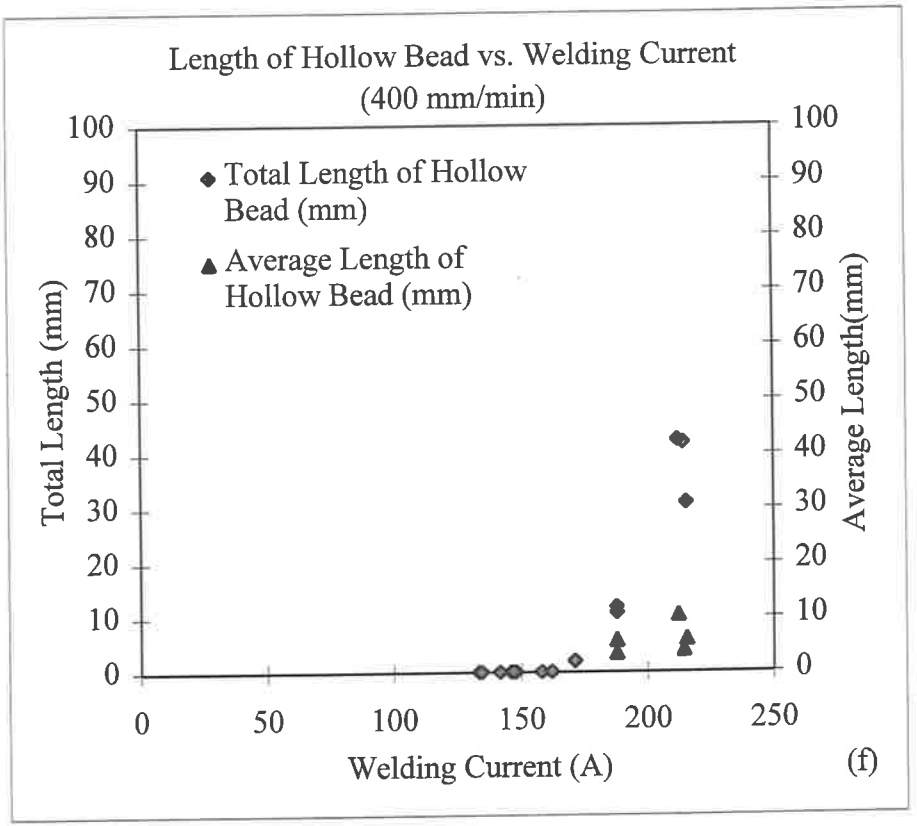

Figure 2.13e,f: The effect of welding current at a constant weld travel speed of 400mm/min on the occurrence of hollow bead.

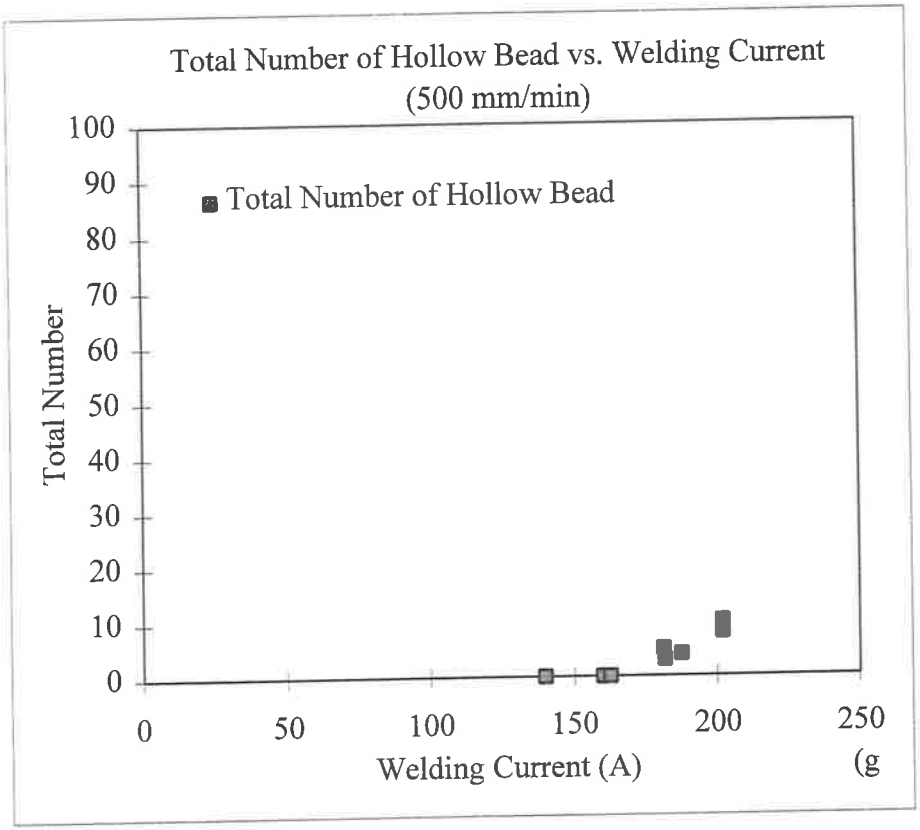

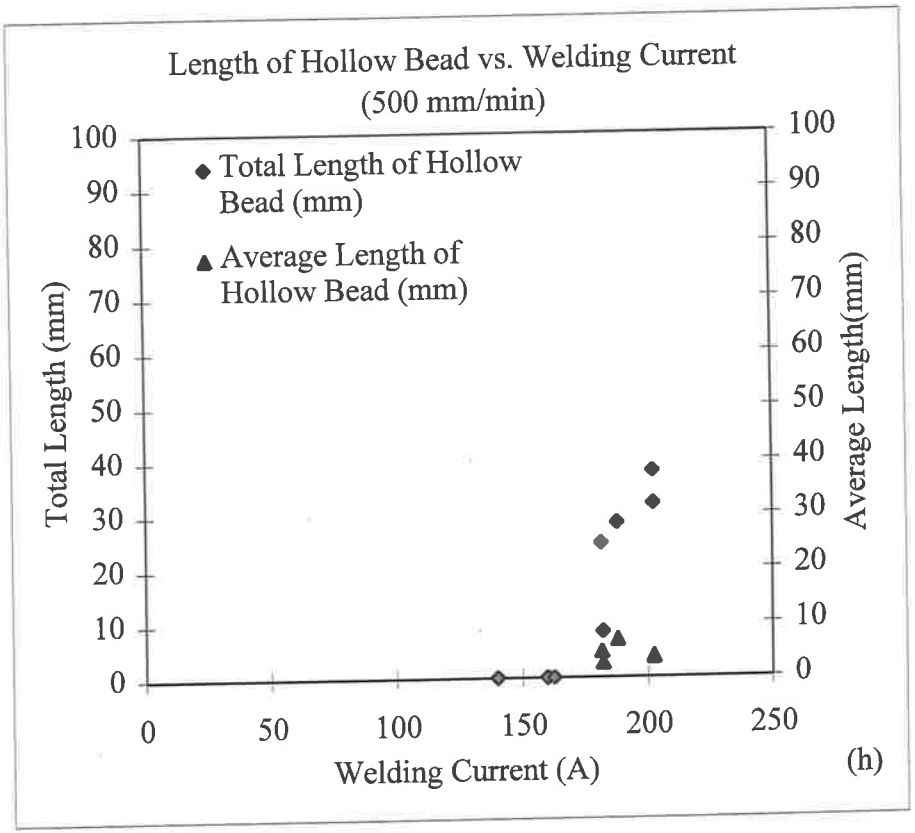

Figure 2.13g,h: The effect of welding current at a constant weld travel speed of 500mm/min on the occurrence of hollow bead.

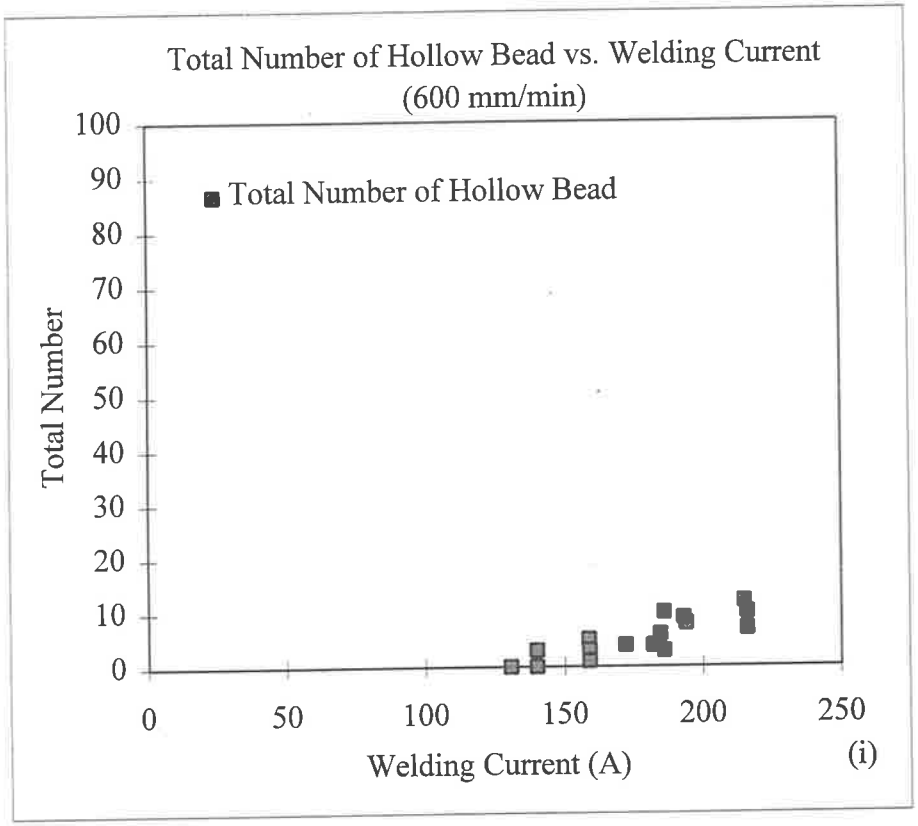

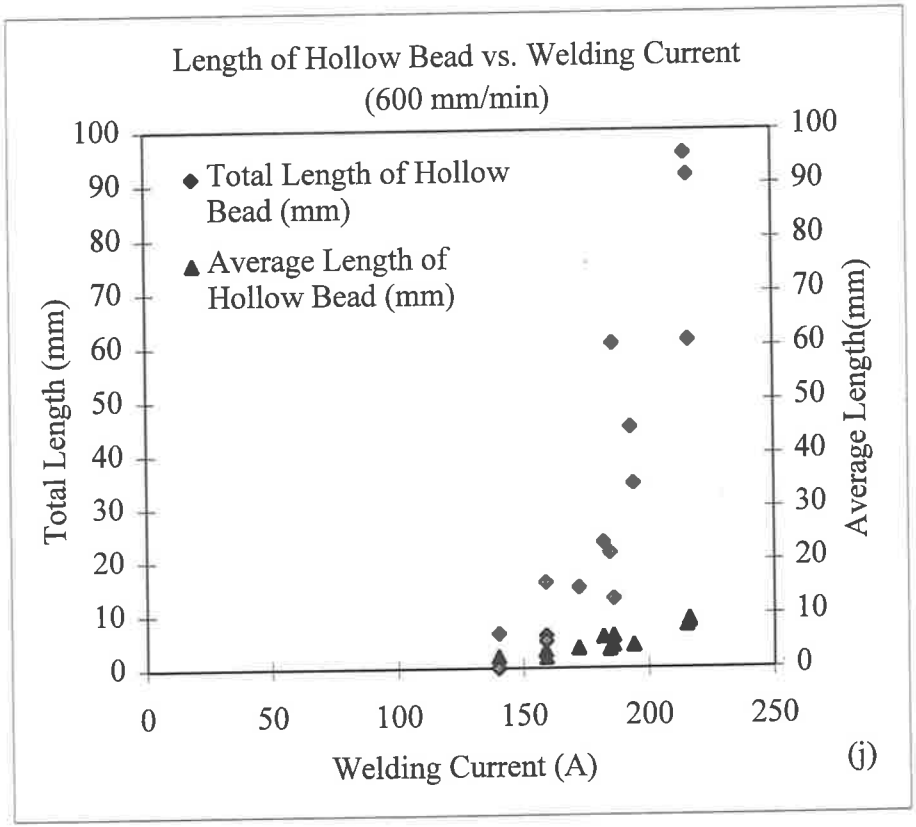

Figure 2.13i,j: The effect of welding current at a constant weld travel speed of 600mm/min on the occurrence of hollow bead.

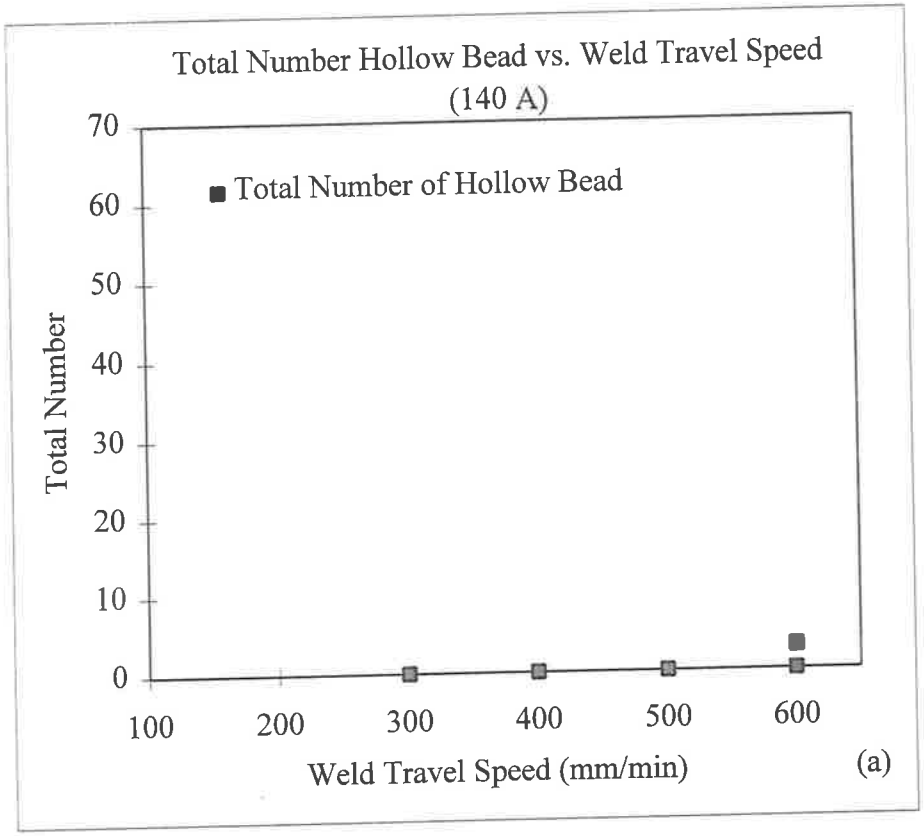

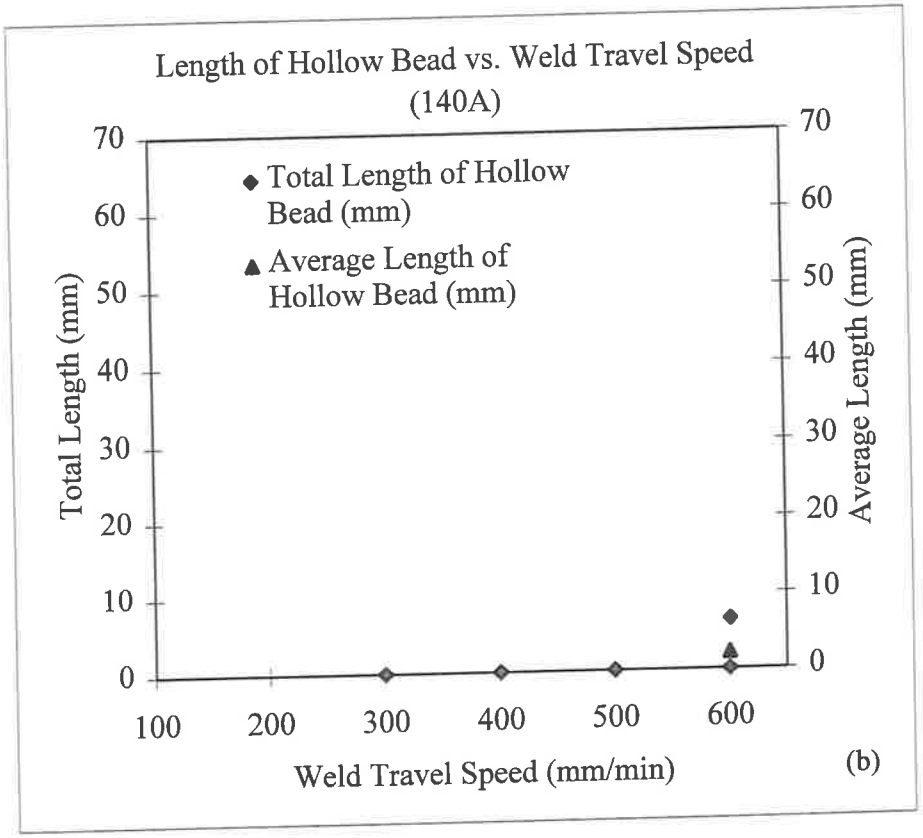

Figure 2.14a,b: The effect of weld travel speed at a constant current of 140A on the occurrence of hollow bead.

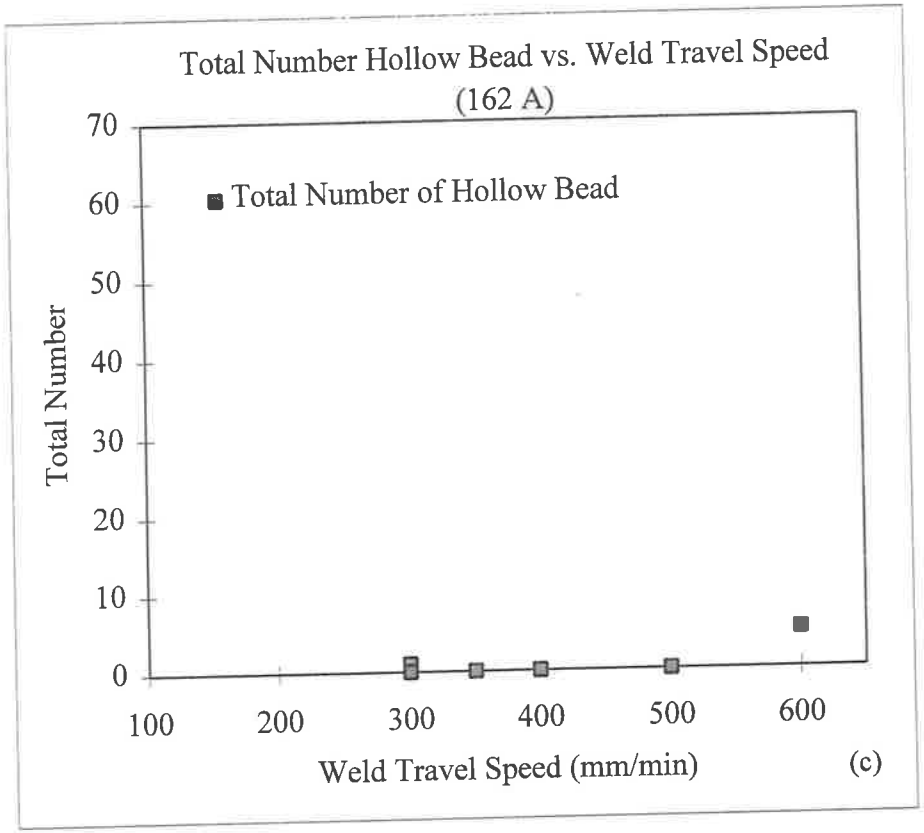

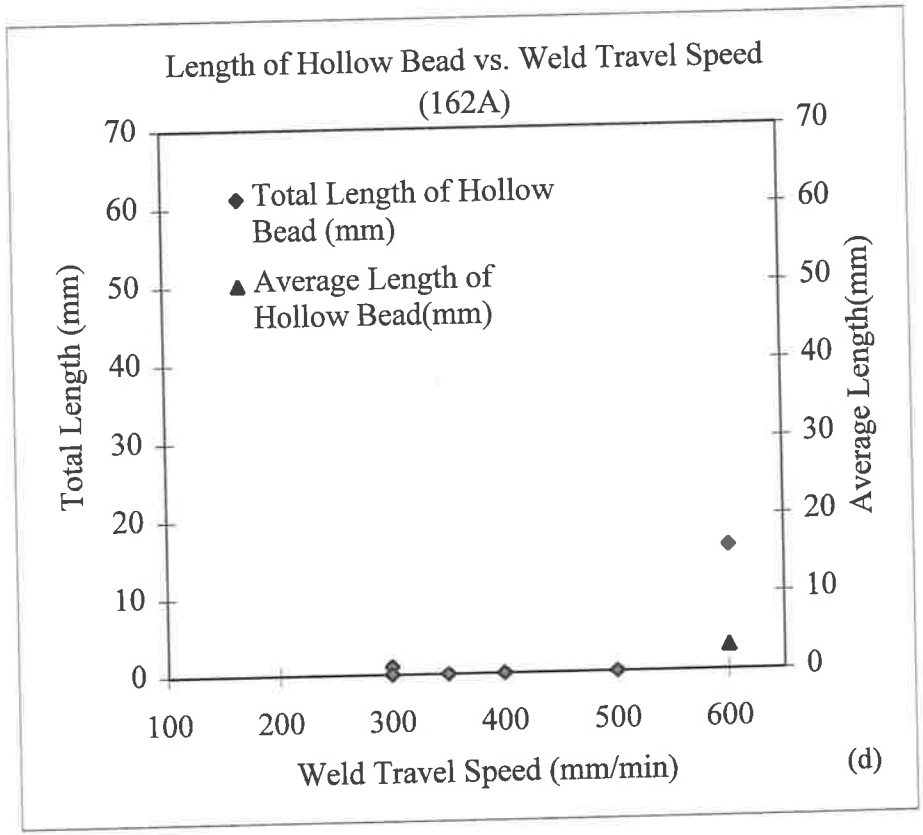

Figure 2.14c,d: The effect of weld travel speed at a constant current of 162A on the occurrence of hollow bead.

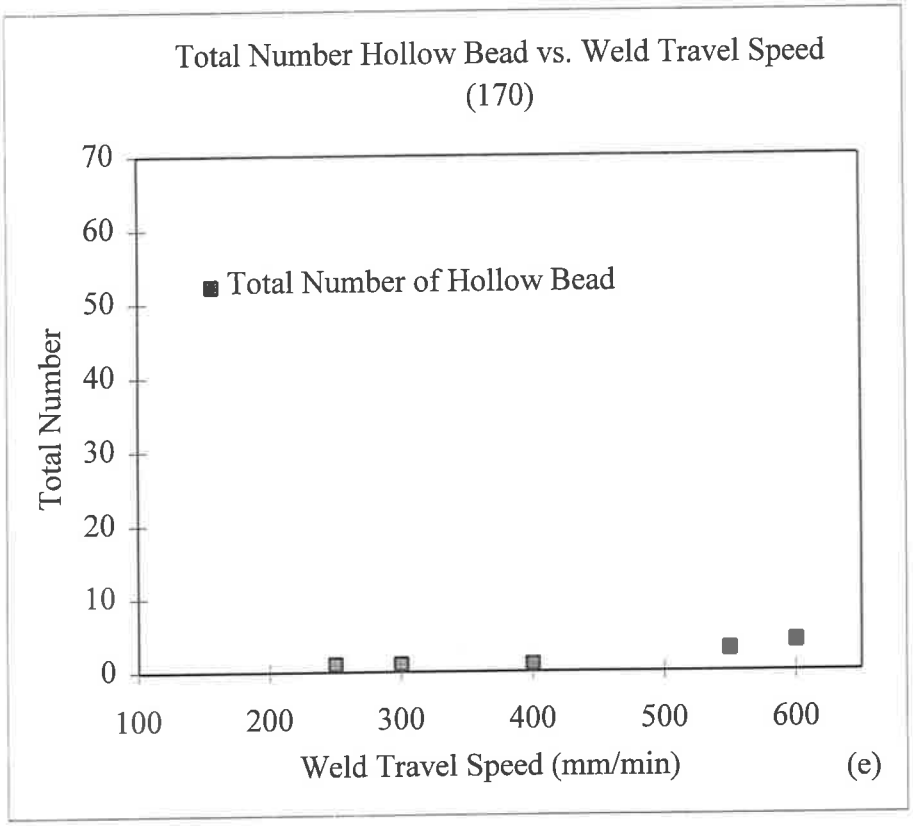

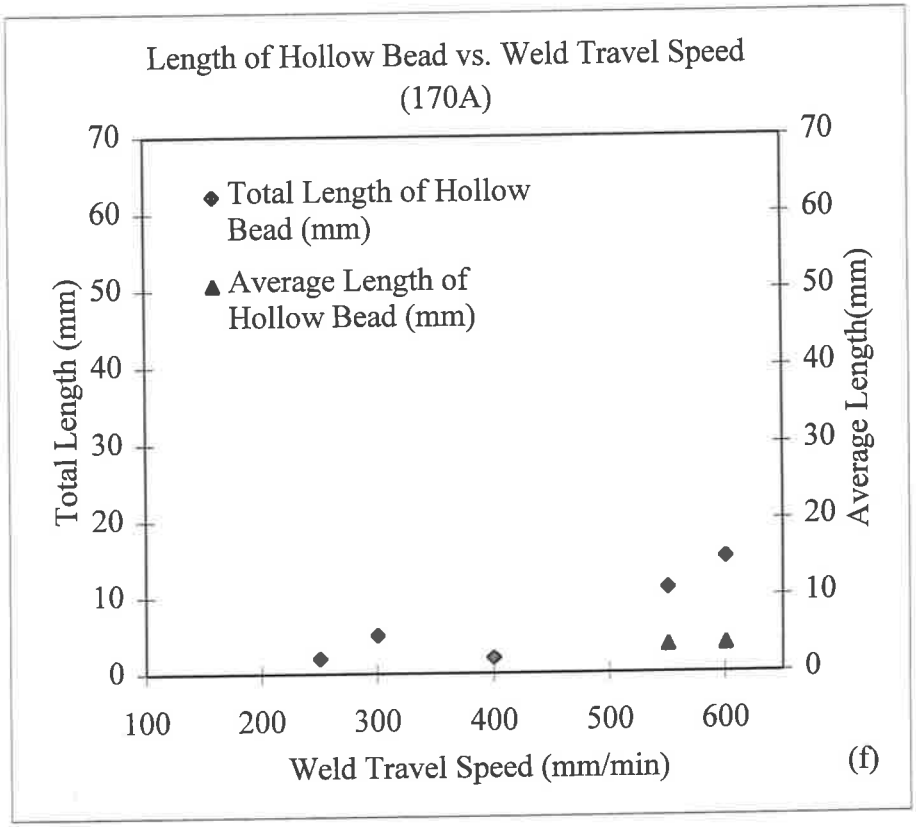

Figure 2.14e,f: The effect of weld travel speed at a constant current of 170A on the occurrence of hollow bead.

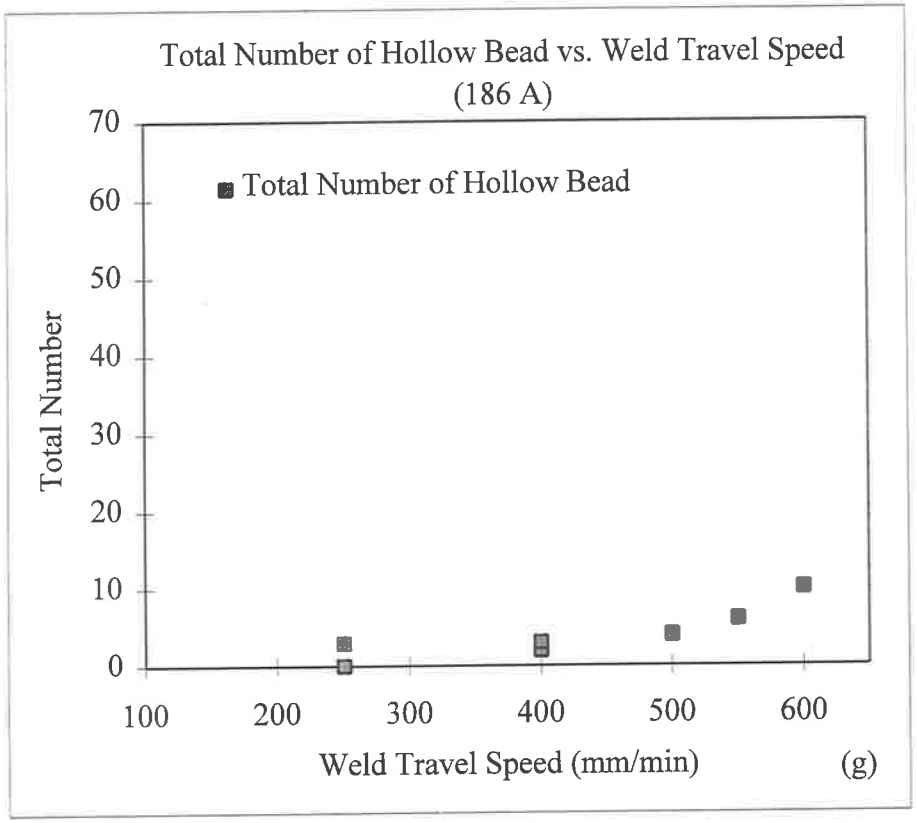

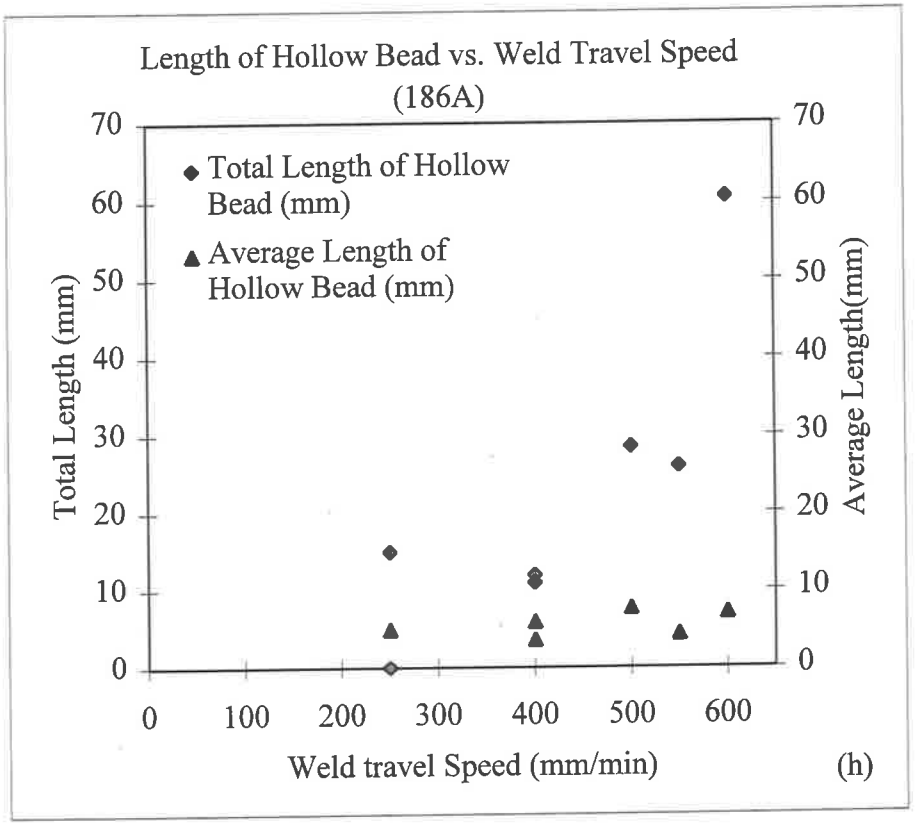

Figure 2.14g,h: The effect of weld travel speed at a constant current of 186A on the occurence of hollow bead.

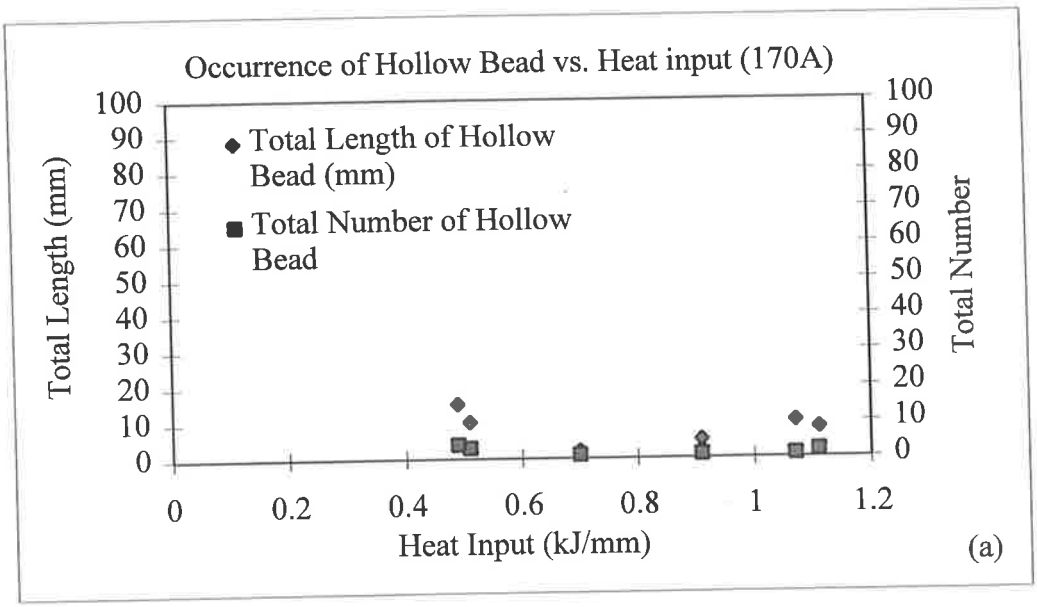

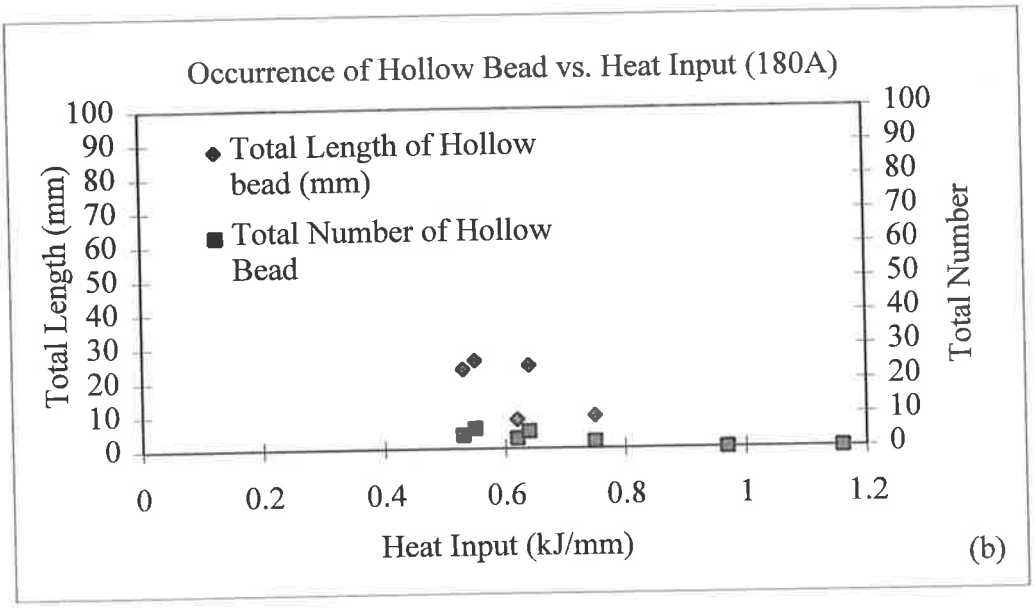

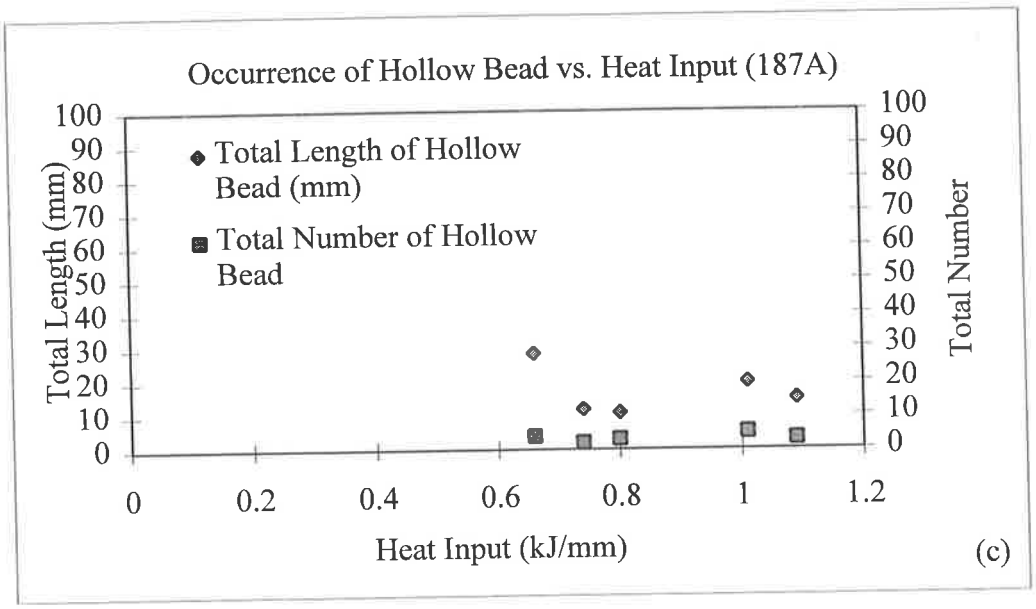

Figure 2.15a-c: The effect of heat input on the occurrence of hollow bead at constant welding currents.

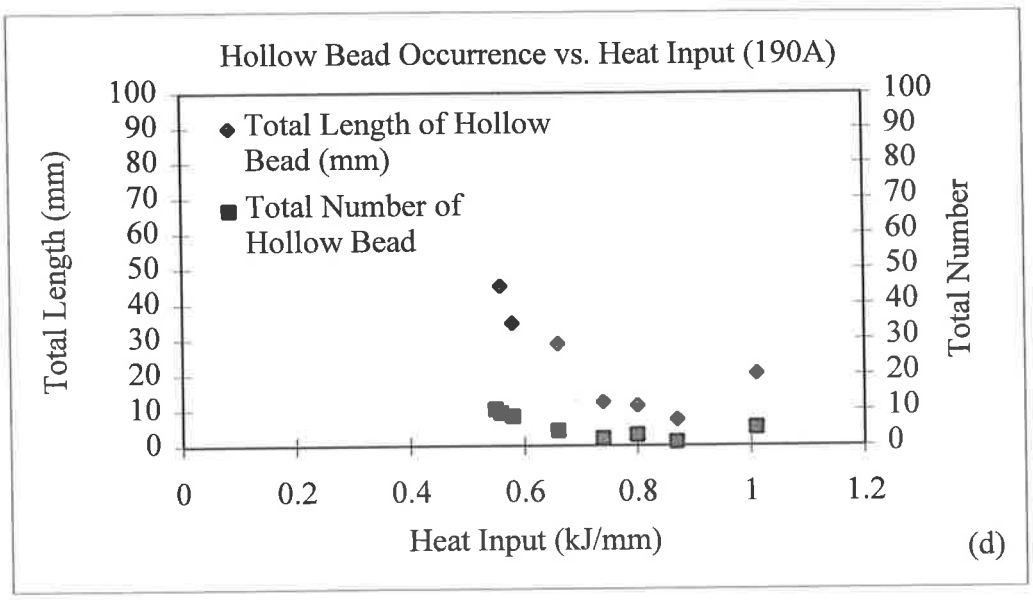

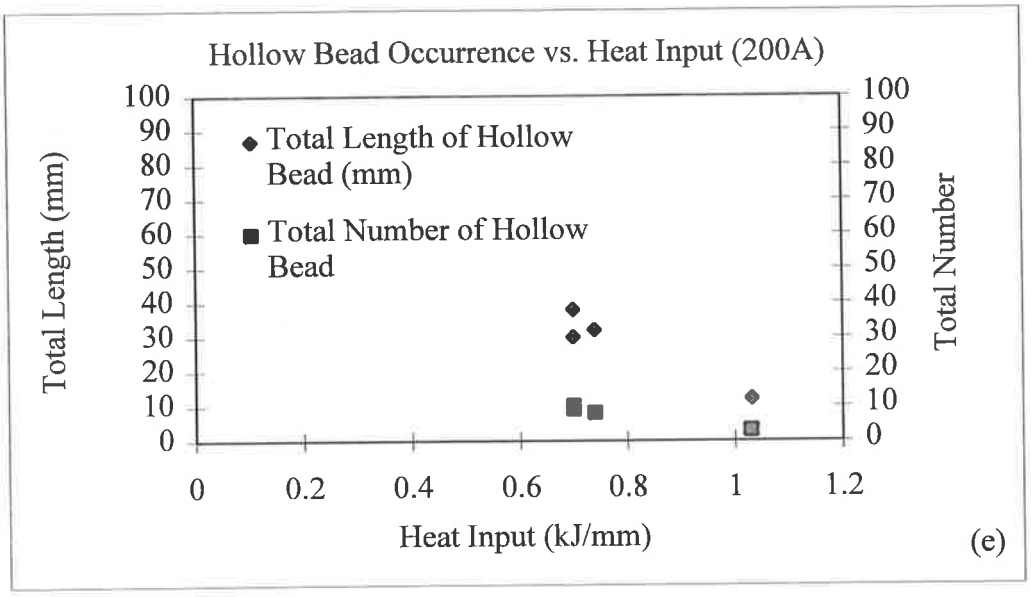

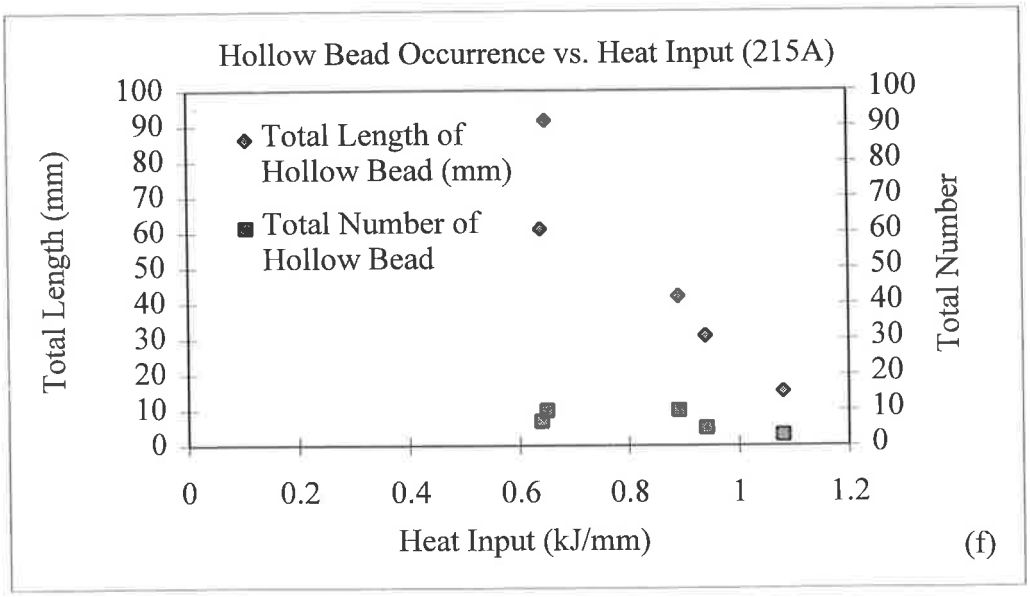

Figure 2.15c-f: The effect of heat input on the occurrence of hollow bead at constant welding currents.

Travel Speed (mm/min)	Current (A)	Diameter of Hollow Bead (mm)	Travel Speed (mm/min)	Current (A)	Diameter of Hollow Bead (mm)
250	186	0.8, 0.8, 1	500	202	0.8, 0.5, 0.8, >0.5,
	170	0.8			0.8-1, 0.8, 1, 0.5, 0.5
	173	1, 1		202	0.5, 0.5, 0.5, 0.5-1,
	204	1			0.8, 0.5-0.8, 0.8, 1
				181	0.5, 0.8, 1, 0.5, 0.5-0.8
300	204	0.5, >0.5, 1		188	0.5, 0.5, 1, 0.8
	187	1, 1, 1.2, 0.5-1, 1.2-0.8		182	0.5, 1, 0.5
	187	0.5-0.8, 0.5-1.5			
	216	0.8, 0.8	600	159	0.5-1, 0.5, 0.5, 0.8, 0.5
				193	0.5-1, 0.8, 1, 1-1.2, 0.8, 0.8, 0.5-0.8, 1
400	214	0.5, 0.8, >0.5-1, 0.5-1, 1,1,		186	1, 1, 0.8, >0.5-1, 0.5-1, 0.5-1, 0.5-0.8, 0.8, 1-0.5, 0.8
		>0.5-1, >0.5-0.5, 0.5-0.8, 0.5		216	1, 1, 0.8, >0.5-1, 0.5-1, 0.5-1, 0.5-0.8, 0.8, 1-0.5, 0.8
	188	0.8		140	>0.5, 0.5, 0.5
	188	1-1.2, 0.5-0.8		172	>0.5, 0.5, 0.8, 0.8
	215	1-2, 1.2, 0.8, 0.8, 0.5		182	>0.5-0.8, 0.5, 0.8, 0.8
	171	0.5		185	1, 0.5, 0.8, >0.5, >0.5, 0.5-1,0.8
	212	0.8, 0.8-1, 0.8-1, 1		159	0.8, 0.8-1, 0.8-1, 1, 0.8, 1
				186	0.8, 0.5-1, 0.5
				159	0.8
				216	1, 1, 0.8, 0.5, 1, 0.8-1.2, 0.8

Table 2.13: Diameter of individual hollow bead pores at varying welding current and constant weld travel speed.

2.7 An Investigation of the Effect of Böhler Electrodes on Hollow Bead Formation

2.7.1 Introduction

Experiments were performed to study the influence of cellulosic electrodes from an alternate manufacturer, Böhler. A set of welding conditions was chosen from the previous experiments with Lincoln Electric electrodes and the experiments were repeated using Böhler electrodes.

2.7.2 Materials

Böhler Fox Cel electrodes, 4.0mm in diameter, were used in these experiments.

2.7.3 Results

All results and experimental conditions have been recorded in Table A4 in Appendix A. The results have been also presented in Figure 2.16a-c. The curves obtained from the previous experiments with Lincoln Electric electrodes as well as some additional data (pertaining to the performance of Lincoln Electric electrodes) obtained during these experiments have been added to these graphs for comparison.

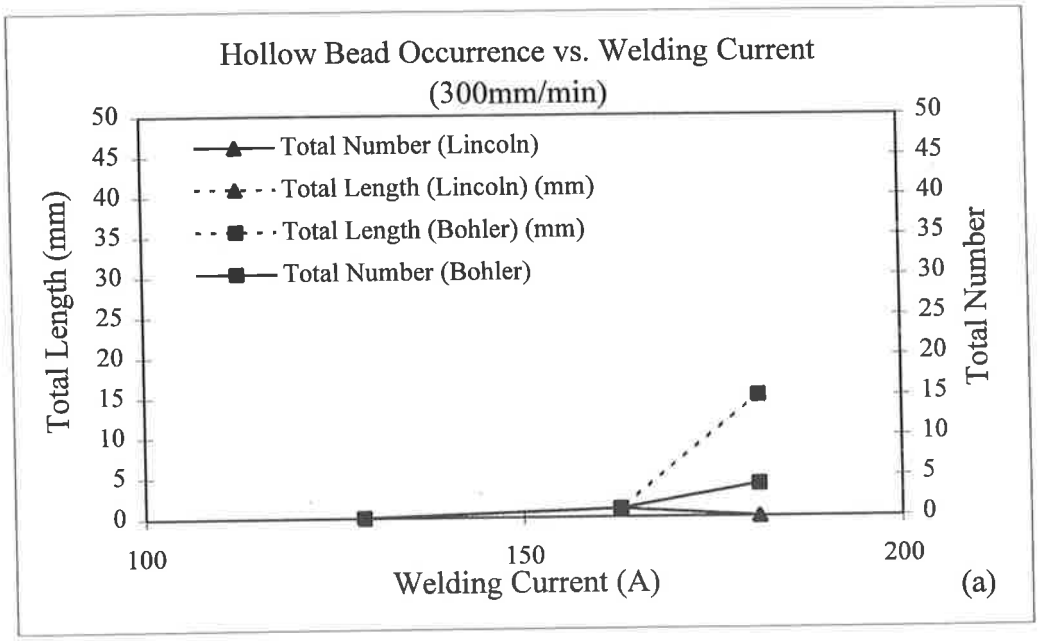

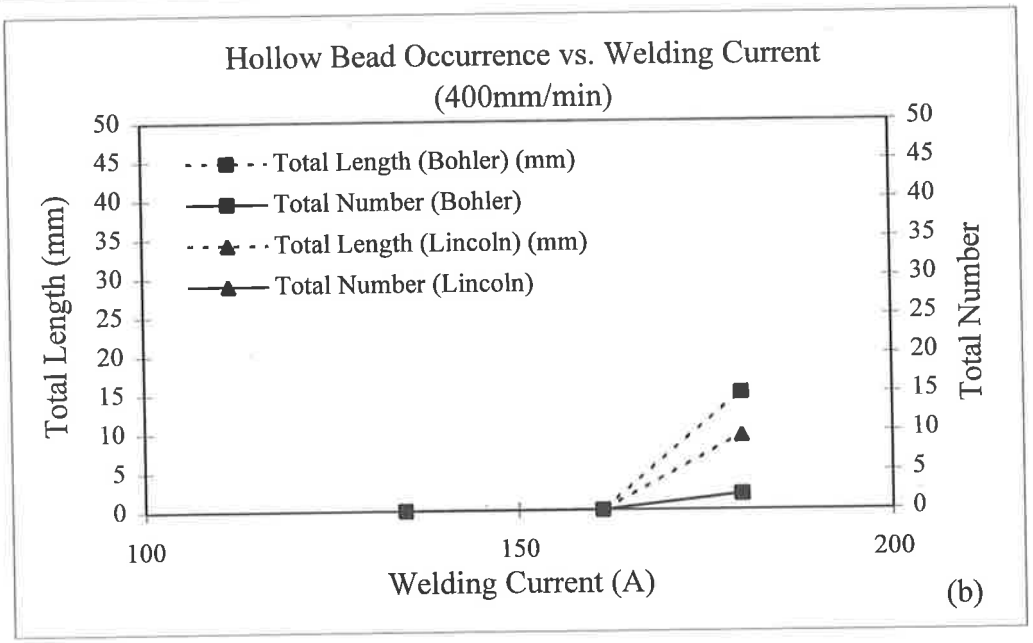

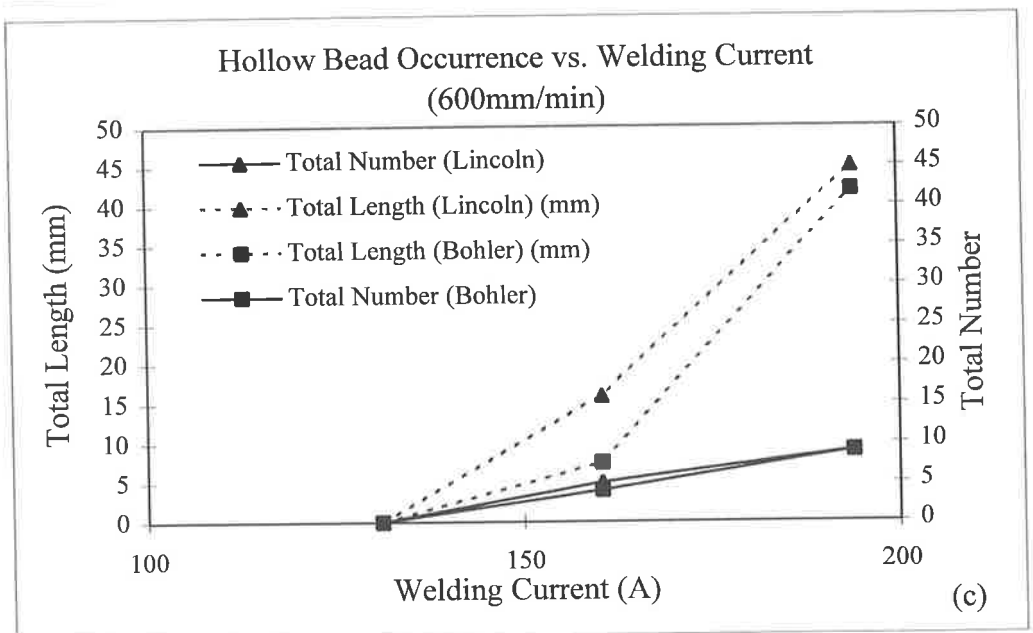

Figure 2.16a-c: The effect of welding current and electrode brand on the occurrence of hollow bead at constant weld travel speed.

2.7.4 Discussion

The graphs in Figure 2.16a-c show the effect of the welding current, at constant weld travel speeds of 300, 400 and 600mm/min, on the total length and total number of hollow bead. Overall the results indicate a similar performance between the two different electrodes, with only small variations occurring in the total length of hollow bead. In most cases there is no or a very small difference in the number of pores, except at the point coinciding with 300mm/min and 180A, for the Lincoln Electric electrode, where hollow bead did not occur. This particular result is probably due to a statistical fluctuation. The data in Figure 2.16b which is for the same weld travel speed shows that close to 180A the total length of hollow bead is on average approximately 15mm which is similar to the value obtained with the Böhler electrode.

2.8 An Investigation of the Effect of the Flux Moisture Content of Hollow Bead Formation

2.8.1 Introduction

The cellulose flux contains high levels of carbon due to a wood flour mixture and has a tendency to absorb a high percentage of moisture. During the welding process, the gaseous products released due to the combustion of the cellulose and moisture are carbon monoxide, carbon dioxide, oxygen, hydrogen and water vapour. The relatively high levels of hydrogen in the arc increases the voltage across the arc, due to its high ionisation potential, and thus increases the penetration and burn-off rate of the electrode. The hydrogen content of the weld is also very high.

These experiments were designed to determine the influence of a change in moisture content of the flux coating on the occurrence of hollow bead. The moisture content of the coating of the electrodes can be quite variable, and the effect of variations were thus required to be determined.

The moisture in the electrode coating may be present in various forms (McKeown, 1985): free moisture present as water molecules and which is readily removed at around 100°C, moisture present as structural hydroxyl groups in organic substances such as cellulose which decompose and release hydrogen at around 200 to 300°C, water of crystallisation and colloidally absorbed moisture present in minerals which is released at temperatures around 300°C and above, and moisture retained by the silicate binders during initial drying which can be held to temperatures as high as 400°C.

2.8.2 Experimental Conditions

The moisture content was varied in two different ways; by immersing the electrodes in water and by baking the electrodes. Three electrode conditions were tested:

Control - in the "as-received" condition (in sealed packages) from Lincoln Electric with a 2.3% moisture content.

Reduced moisture content - the electrodes were dried in an oven at 150°C for 45 minutes. A higher temperature would have decomposed the cellulose in the flux. The moisture which was removed was therefore only in the form of free moisture absorbed in the coating. The resultant moisture levels were calculated using a gravimetric technique, assuming an initial moisture content of 2.3%. The levels obtained were close to 0%. That is, the free moisture was entirely removed from the electrodes.

Increased moisture content - the electrodes were immersed in water for 8 minutes. A longer immersion time would have degraded the integrity of the flux. The moisture content was calculated approximately, assuming an initial moisture content of 2.3%, using a gravimetric technique. A moisture content of about 6% was obtained.

The welding conditions were chosen which had previously been found to promote the formation of hollow bead. The weld travel speed and the welding current were maintained at 400mm/min and 180A respectively, which is a condition giving an average incidence of hollow bead. A condition where the incidence is more severe, that is a higher welding current, would have masked the effect of the change in moisture content. The experiments were repeated three times for each flux moisture condition.

2.8.3 Results

Figure 2.17 is a graph of the occurrence of hollow bead, in terms of the total length and total number of hollow bead, versus the flux moisture content. A regression analysis has been performed on the data and the regression lines and the coefficient of determination R^2 have been included in the figure.

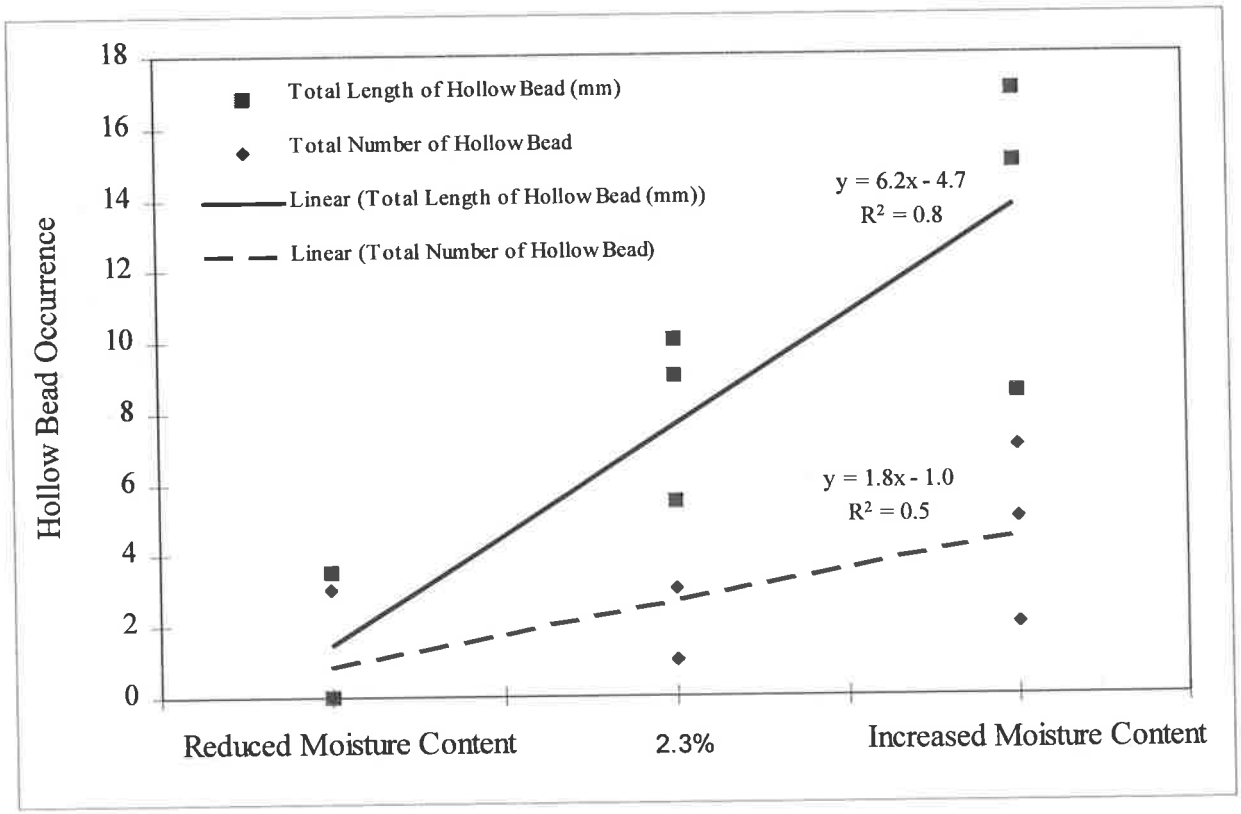

Figure 2.17: The effect of flux moisture content on the occurrence of hollow bead.

2.8.4 Discussion

The regression and R^2 analyses reveal that a reasonably good fit has been obtained for the data on the total length of hollow bead, whilst there is more scatter for the data on the total number. The analysis shows that there is an increase in the length of hollow bead as the flux moisture content is increased from 0 to 6%. At a moisture content of close to 0% the occurrence of hollow bead is zero in two out of the three repeats.

As mentioned in the Introduction of this section (Section 2.8.1) the moisture content of electrode coatings can be quite variable, depending on the batch of electrodes and storage conditions such as opened cans. The results of these experiments suggest that a loss of moisture in the coating is likely to reduce the occurrence of hollow bead under the welding conditions used. An increase in moisture content, up to the level of 6% tested in these experiments, is likely to result in an increase in hollow bead. It is expected, however, that the effect of moisture content will be secondary to that of the welding current. Also the changes in moisture content were achieved in these experiments by extreme means. In the case, therefore, of electrodes stored in opened cans, the change in moisture content which would occur when exposed to ambient atmospheric conditions should have only a minor effect on the formation of hollow bead.

2.9 Experiments to Test the Effect of the Joint Geometry on Hollow Bead Formation

2.9.1 Introduction

These experiments were aimed at assessing the influence of changes in the dimensions of the joint geometry. Data obtained in previous experiments were used to predict two welding conditions, one which would promote the formation of hollow bead and one which would not. Four joint preparations, with combinations of high and low root gaps and faces, were tested.

2.9.2 Experimental Conditions

Welding condition 1 (no hollow bead):

Welding current = 150 A

Weld travel speed = 400 mm/min

Welding Condition 2 (hollow bead)

Welding current = 180 A

Weld travel speed = 500 mm/min

The four joint preparation were as follows:

	Root face (mm)	Root Gap (mm)
1	1.6	1.8
2	1.6	1.0
3	1.5	1.6
4	2.4	1.6

Table 2.14: Dimensions of the joint preparation.

2.9.3 Results

A detailed set of experimental conditions and results have been recorded in Table A5 in Appendix A and summarised in Table 2.15.

		Condition 1 400mm/min 150A						Condition 2 500mm/min 180A							
		Hollow Bead Occurrence													
Root Face (mm)	Root Gap (mm)	Total Number			Total Length (mm)			Total Number			Average Number	Total Length (mm)			Average Length
1.6	1.8	0	0	0	0	0	0	8	3	4	5	28	6	21	18.3
1.6	1.0	0	0	0	0	0	0	4	4	5	4.3	14	18.5	12	14.8
1.5	1.6	2	0	0	10	0	0	2	1	5	2.7	8.5	7	10	8.5
2.4	1.6	0	0	0	0	0	0	1	4	3	2.7	8	17	8	11

Table 2.15: Results of joint geometry experiments.

2.9.3.1 Statistical Analysis

A non-parametric test was chosen to analyse the results because it was not possible to determine the distribution of the data and in most cases the data do not follow a normal distribution. The Wilcoxon rank-sum test (also called the Mann-Whitney test) for independent samples was used as it makes no assumptions on the distribution of the sample.

The data was combined and organised in ascending order and given a rank order, Tables 2.16-2.21. When observations with the same value were encountered the mean of the ranks was used. The symbols n_1 and n_2 refer to the size of the two groups I and II of the data under comparison, where $n_1 \leq n_2$, R_1 and R_2 are the sums of the ranks for groups I and II respectively, R_1 is always associated with the smaller sample size. H_o is the null hypothesis.

The changes in joint geometry at the 150A have not had an effect on the occurrence of hollow bead indicating that the welding current is again the most influential factor in the formation of hollow bead. The statistical analysis was performed on the data at the 180A current level. The changes in root gap and root face, as well as total number and length of hollow bead, were compared separately.

1. The root face = 1.6mm and the root gap = 1.0 and 1.8mm.

The null hypothesis states in this case that the change in root gap has no effect on the occurrence of hollow bead. The alternative hypothesis states that the increase in root gap does increase the occurrence of hollow bead, or $\mu_1 < \mu_2$ where μ is the population mean and Group I represents the data for a root gap equal to 1.0mm. The null hypothesis is rejected if R_1 is equal to or less than a critical value for R_1 obtained from tables[1].

[1] Schmidt, M. J., Understanding and Using Statistics Basic Concepts, Table E, Appendix 1, p436.

Total Number	3	4	4	4	5	8
Rank	1	3	3	3	5	6
Group	II	I	I	II	I	II

Table 2.16: Group I and II ranks for the total number of hollow bead.

Total Length	6	12	14	18.5	21	28
Rank	1	2	3	4	5	6
Group	II	I	I	I	II	II

Table 2.17 : Group I and II ranks for the total length of hollow bead.

I 180A RG=1.0	**II 180A RG=1.8**	**I 180A RG=1.0**	**II 180A RG=1.8**
Total Number	**Total Number**	**Total length**	**Total Length**
3	1	2	1
3	3	3	5
5	6	4	6
R_1=11	R_2=10	R_1=9	R_2=12

Table 2.18: Group I and II ranks and their sums for total number and length of hollow bead

The critical value for R_1 at n_1=3 and n_2=3 is 6 at a level of significance α=0.05. The null hypothesis is therefore not rejected, suggesting that the data does not provide sufficient evidence to support the alternative hypothesis which states that the increase in root gap increases the occurrence of hollow bead.

2. The root gap = 1.6mm and the root face = 1.5 and 2.4mm.

The null hypothesis states that the change in root face has no effect on the occurrence of hollow bead. The alternative hypothesis states that the increase in root face does increase the occurrence of hollow bead, or $\mu_1<\mu_2$ where μ is the population mean and Group I represents the data for a root face equal to 1.5mm. The null hypothesis is rejected if R_1 is equal to or less than a critical value for R_1 obtained from tables.

Total Number	1	1	2	3	4	5
Rank	1.5	1.5	3	4	5	6
Group	I	II	I	II	II	I

Table 2.19: Group I and II ranks for the total number of hollow bead.

Total Length	7	8	8	8.5	10	17
Rank	1	2.5	2.5	4	5	6
Group	I	II	II	I	I	II

Table 2.20: Group I and II ranks for the total number of hollow bead.

I 180A RF=1.5 Total Number	**II 180A RF=2.4 Total Number**	**I 180A RF=1.5 Total length**	**II 180A RF=2.4 Total Length**
1.5	1.5	1	2.5
3	4	4	2.5
6	5	5	6
R_1=10.5	R_2=10.5	R_1=10	R_2=11

Table 2.21: Group I and II ranks and their sums for the total number and length of hollow bead.

The critical value for R_1 from the table at $n_1=3$ and $n_2=3$ is 6 at $\alpha=0.05$. The null hypothesis is therefore not rejected, suggesting that the data do not provide sufficient evidence to support the alternative hypothesis stating that the increase in root face increases the occurrence of hollow bead.

2.9.4 Discussion

The analysis of the data suggests that no correlation exists between variations in joint geometry and hollow bead porosity. The large variations in the data are partly responsible for this result. Previous studies (Harris, 1988, Willgoss and Atthey, 1980 and Willgoss, 1980) have shown that the edge preparation does affect the formation of porosity such that a narrow bevel angle and welds which have a high crown promote porosity due to a reduction in the effectiveness of venting gases from the weld pool. Some reasons can be put forward to explain the discrepancy between the results obtained in this experimental investigation and the above observations. The differences in root gap and root face may have to be set at more extreme dimensions for significant changes in the occurrence of hollow bead to be observed. It was, however, not possible to experiment with other dimensions because a larger root face and smaller root gap result in a lack of penetration and a smaller root face and wider gap in blow-through.

The cross sectional weld profiles were studied to assess the changes in shape at the various joint geometries by polishing weld cross sections and etching in 2% nital (see Figure 2.18a-d). When comparing Figures 2.18a and b, it is clear that changing the root face has had an effect on the weld bead profile; the welds were all made at the same welding conditions (a welding current of 180A and a weld travel speed of 500mm/min) and as expected for a similar root gap the extent of penetration of the weld is greater with a smaller root face. The result is a wider and flatter profile. Whereas with a high root face a narrow and high profile is observed due to

reduced degree of penetration. The change in root gap at constant root face (Figures 2.18c and d) has had a less pronounced influence.

Overall the profiles in Figures 2.18b, c and d show small variations in overall shape and size. The weld bead in Figure 2.18a is higher and has a smaller bottom surface compared to the other three beads. However, these differences are small, for example the change in height between the beads in (a) and (d) is only 1.3mm, and the narrow bottom surface in (a) is compensated by a wide top surface. It can thus be suggested that the changes in width of the top and bottom did not vary sufficiently from one geometry to another to affect the incidence of hollow bead. The height of weld bead has also remained similar at all but one of the joint geometries which means that the length of the escape path for the desorption of hydrogen also remained approximately constant.

Overall there no significant evidence that the joint geometry will have a direct influence on the formation of hollow bead within the range of dimensions specified in the SA 2885.2 - 1995.

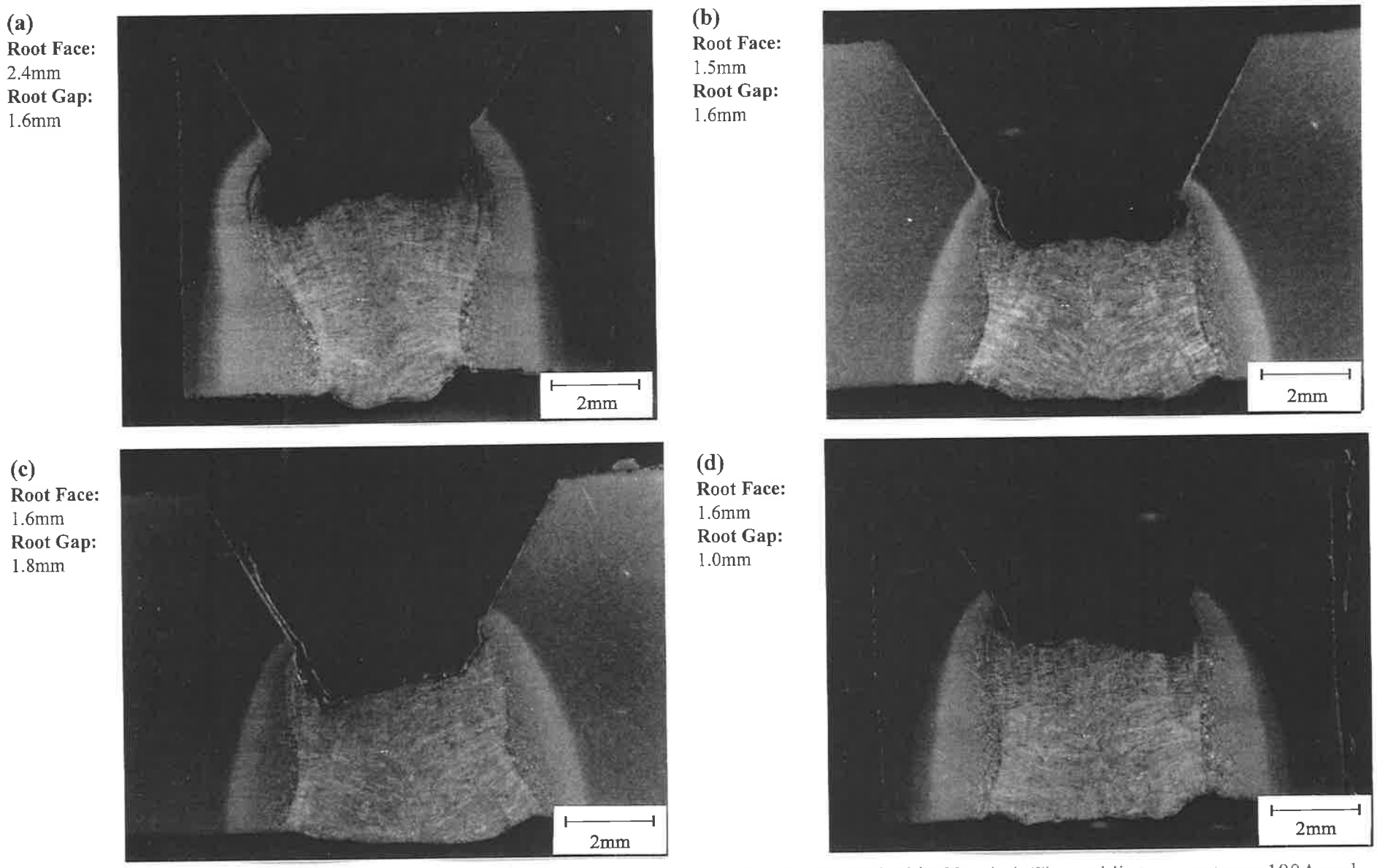

Figure 2.18a-d: Micrographs of weld cross sections made at varying root face and root gap. Etched in 2% nital. The welding current was 180A and the weld travel speed was 500mm/min.

2.10 Experiments on the Effect of Joint Preparation Surface Contamination

2.10.1 Introduction

Contaminants on the surface of the joint preparation have been shown to contribute to an increase in the hydrogen content of weld metal due to the evolution of water vapour from the hydrocarbons (Powell and Lloyd, 1995 and Harris, 1988) and their dissociation in the arc to form gases, particularly hydrogen. The contaminants can also increase the number of inclusions in the weld and thus increase the potential sites for the nucleation of pores.

2.10.2 Materials

The effects of rust and paint were investigated. A rusty layer was obtained by leaving the plates outdoors for a period of two weeks. After this time a uniform layer of rust formed on the surface of the joint preparation. The paint used was an water based acrylic paint. A thick layer of moist paint was applied to the joint surfaces prior to welding. Control welds were also made where the joint preparation was thoroughly cleaned, using alcohol and a wire brush, prior to welding.

2.10.3 Welding Conditions

The experiments tested the effect of the contaminants on the incidence of hollow bead in welds made at three current levels (140, 180 and 200A). The weld travel speed was kept constant at 500mm/min.

2.10.4 Results

All experimental conditions and results have been recorded in Table A6 in Appendix A and are summarised in Table 2.22.

Welding Condition	500mm/min 140A		500mm/min 180A		500mm/min 200A	
Surface Condition	Total Number	Total Length (mm)	Total Number	Total Length (mm)	Total Number	Total Length (mm)
Control	0	0	3	8.5	9	30
Rust	0	0	3	8	8	33
Paint	0	0	4	14	9	33

Table 2.22: Results of experiments on the effect of surface condition.

2.10.5 Discussion

The contaminants on the joint preparation clearly have had little effect on the occurrence of hollow bead with only very small variations in the results between the different surface conditions. The welding current is again seen to be the dominant factor in the formation of hollow bead.

Some previous authors who have assessed the effect of material contamination on porosity have also reported minor effects. Saperstein et al. (1964) investigated surface contamination in the welding wire and on the parent plate. Three types of tests were conducted. One consisted of extensive corrosion on the parent plate, one employed filler metal also contaminated with rust and the third looked at the effects of residual acetone solvent and grease (heavily contaminated with iron oxide particles). The grease was spread liberally on the plate surface prior to welding. These measures did not produce significant amounts of porosity. One reason given for this was the possibility of the welding heat volatilising the

plate contaminants such as hydrocarbons and moisture ahead of the arc, thus minimising dissociation in the arc atmosphere. In the case of surface corrosion on the filler metal, it was suggested that the concentration of absorbed moisture on the surface may have been too low to produce an above threshold hydrogen concentration in the arc atmosphere.

The effect of rust has also been investigated by Pokhodnya and Yavdoshchin (1972). Amounts of rust varying from 270 to 3080mg per 100mm of weld metal were tested using submerged arc and cored electrode wire welding processes. Two methods of introducing the rust in the weld were studied. The first employed a special cored wire which contained the powdered rust and which was placed in the weld groove. The second method employed powdered rust which was poured into the groove (the weld preparation did not have a gap between the edges). The former method of introducing the rust produced more pores as the metal shell prevented moisture from being initially removed from the rust and also prevented the rust from blowing out. Pores were initiated at lower levels of rust (345mg/10mm of weld) with the submerged arc welding process compared with the cored electrode wire process where pores appeared at 1540mg/100mm of weld metal.

This investigation suggests that rust can be blown out by the arc without entering the weld pool and causing porosity, and that depending on the process (in this case the flux cored wire process) the amount of rust required to form porosity is high (1540mg/100mm of weld metal).

The results from these two investigations and the current one suggest that contamination of the surface of the parent plate can have no effect on porosity in welds when the contaminants are volatilised by the heat and gases from the arc and therefore do not enter the arc atmosphere where they can dissociate and enter the weld pool.

2.11 Experiments on the Effect of Parent Metal Composition

2.11.1 Introduction

The effect of parent metal composition has been examined by changing the concentration of three alloying elements, silicon, aluminium and carbon. Silicon was identified by Barkow (1973) and The Lincoln Electric Company (1991) as a possible cause for the occurrence of hollow bead. It was suggested that hollow bead had become a prominent problem since the introduction of fully killed steels with comparatively higher silicon contents. The problem was attributed to the increase in the fluidity of the weld pool at higher silicon contents such that the welder had to increase the weld travel speed to maintain control of the weld pool. Aluminium was identified as another potential contributor to hollow bead formation by a survey of the literature and industrial experience by Wright, (1993), although in this case no explanation is given.

A higher level of carbon may also increase the formation of elongated pores by increasing the concentration of carbon in the weld metal and thus increasing the chance of forming porosity due the evolution of carbon monoxide. However, silicon and aluminium are strong deoxidisers and will react with oxygen in the weld thereby reducing the risk of porosity due to carbon monoxide formation.

2.11.2 Materials

Both laboratory melts and pipe steels [1-10] were selected to study the influence of these elements. The compositions of the 10 steels are given in Table 2.23. Compositions 5 and 10, which have a higher carbon content, represent the typical composition used in pipelines in the 1960's prior to the practice of deoxidising with higher levels of silicon. The required test plates of these steels were obtained from flattened pipe samples.

Composition No.	C	P	Mn	Si	S	Ni	Cr	Mo	Cu	Al	Ti	Nb	V	N	O
1	**0.13**	0.004	1.52	0.13	0.004	0.012	0.007	0.011	0.016	0.015	0.017	0.043	0.061	0.0045	0.0010
2	0.060	0.004	1.51	**0.37**	0.004	0.005	0.007	0.004	0.004	**0.008**	0.02	0.038	0.063	0.0028	0.0010
3	0.065	0.004	1.52	0.12	0.004	0.005	0.007	0.004	0.004	**0.053**	0.015	0.041	0.065	0.0066	0.0017
4	0.060	0.003	1.61	0.14	0.004	0.005	0.007	0.004	0.004	0.032	0.018	0.044	0.068	0.0024	0.0011
5	**0.23**	0.012	0.68	0.13	0.003	0.024	0.016	0.002	0.012	0.041	<.003	<.003	<.003	N/A	N/A
6	0.055	0.004	1.51	**0.36**	0.003	0.009	0.008	0.003	0.003	**0.025**	0.012	0.041	0.065	0.0040	0.0025
7	0.055	0.005	1.52	**0.36**	0.003	0.009	0.009	0.003	0.004	**0.018**	0.012	0.041	0.066	0.0040	0.0020
8	0.060	0.003	1.54	**0.36**	0.003	0.008	0.009	0.003	0.003	**0.012**	0.015	0.040	0.064	0.0018	0.0020
9	0.060	0.003	1.54	**0.35**	0.003	0.008	0.010	0.003	0.003	**0.008**	0.016	0.041	0.063	0.0022	0.0050
10	0.185	0.023	1.17	0.22	0.016	0.014	0.019	0.004	0.030	0.023	0.002	<.003	<.003	0.0029	0.0030

Table 2.23: Compositions of laboratory melts and pipe samples. Percentage concentrations by mass. Analysis by atomic emission spectroscopy. Nitrogen and oxygen by inert gas fusion.

Initially only the first four compositions were used in the experiments with composition 4 as the control composition. Composition 1 has a higher carbon content, composition 2 a higher silicon content and composition 3 a higher aluminium content. Compositions 5 and 10 were chosen to study the effect of an even higher carbon content as well as changes in the silicon content. Compositions 6 to 9 were added to the experimental programme later to further study the combined effect of silicon and aluminium content. The silicon content of these four steels are constant while the aluminium content changes from 0.008 to 0.025%.

2.11.3 Welding Conditions

In the first set of experiments a welding current of 180A and a weld travel speed of 400mm/min were used for compositions 1 to 5 and three repeats were done.

Three welding conditions were chosen subsequently: the weld travel speed was maintained at 400mm/min but welding currents of 150, 180 and 200A were used. The experiments were repeated between 2 and 5 times for particular welding conditions. Since no hollow bead pores formed at a welding current of 150A after two repeats, no further experiments were performed for that condition.

A detailed set of experimental conditions and results have been recorded in Table A7 in Appendix A.

2.11.4 Results

In the first set of experiments two types of porosity not previously observed in this project were detected. Small spherical gas pores were observed close to the fusion line as well as worm holes near the weld centreline. The worm holes could be differentiated from hollow bead pores since the former nucleated close to the fusion line (see Figure 2.19) and then changed direction and grew at the weld centreline. It was noticed that the test plates used in

these first experiments were covered with a thick, loose oxide layer. In subsequent experiments this oxide was removed from the region of the weld preparation by grinding an area 40mm wide and exposing the metal. Under these conditions gas pores and worm holes were not observed. The results from these first experiments have been presented separately in Table 2.24.

The remainder of the results are presented in Tables 2.25 and 2.26. The total number and length of hollow bead presented in Table 2.26 have been calculated for a length of weld equal to 100mm. Initially these parameters were evaluated for a length of weld equal to 170mm (see Table 2.25), however the test plates made from the steels 6 to 9 were of a smaller size which thus reduced the length of weld made. The actual length of weld used to measure the occurrence of hollow bead has been recorded in Table A7 (Appendix A) for all welds.

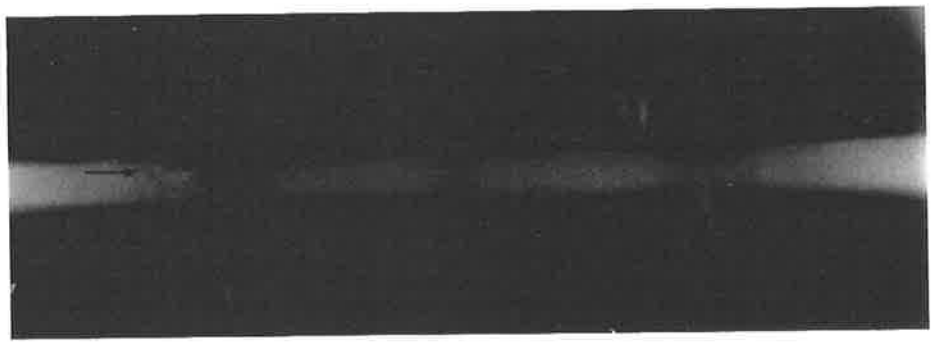

Figure 2.19: Photo of a radiograph of a weld containing a worm hole pore (indicated by an arrow on the photo).

Some of the welds made from the first five compositions and the three welding conditions were selected for weld metal analysis. The weld metal was cut from the test plates near the fusion line using a cut-off wheel. The samples were then ground on all sides to remove the slag as well as any portion of the parent metal. About 10 grams of weld metal was used for analysis by atomic emission spectroscopy. The weld metal compositions are recorded in Table 2.27.

Composition	Hollow Bead		Worm Holes		Gas Pores
Number	Total Number	Total Length (mm)	Total Number	Total Length (mm)	Total Number
4	1	5	2	7.5	9
0.06% C	7	35.5	0	0	8
0.14% Si	3	10	0	0	3
0.032% Al					
3	3	10	1	2	8
0.065% C	2	11.5	0	0	3
0.12% Si	3	9	3	11.5	15
0.053% Al					
2	1	8	2	14	14
0.060% C	3	18	2	10	15
0.37% Si	2	5	2	9	7
0.008% Al					
1	3	14.5	0	0	5
0.13% C	0	0	0	0	0
0.13% Si	0	0	0	0	0
0.015% Al					

Table 2.24: Results of the first set of experiments on effect of the parent metal composition on the occurrence of hollow bead.

Welding	400 mm/min		400 mm/min		400 mm/min	
Condition	150 A		180 A		200 A	
	Total	Total	Total	Total	Total	Total
Composition	Number	Length	Number	Length	Number	Length
No.		(mm)		(mm)		(mm)
4	0	0	0	0	5	17
0.06% C	0	0	2	2	1	1
0.14% Si			0	0	1	4
0.032% Al			0	0	4	13
			0	0		
3	0	0	0	0	1	6
0.065% C	0	0	6	6	1	3
0.12% Si			0	0	2	10
0.053% Al			1	3	1	10
			0	0		
2	0	0	4	12	10	30.5
0.060% C	0	0	4	11.5	7	30
0.37% Si			10	21.5	4	26
0.008% Al			2	7.5	6	29
			5	13	9	30.5
1	0	0	0	0	2	4
0.13% C	0	0	0	0	0	0
0.13% Si			1	1	0	0
0.015% Al			0	0		
			0	0		
5	0	0	1	1	0	0
0.23% C	0	0	0	0	1	3
0.13% Si			0	0	0	0
0.012% Al			0	0		
			1	2.5		
			1	2		

Table 2.25: Results of experiments on the effect of the parent metal composition on the occurrence of hollow bead (170mm of weld).

Composition Number	Welding Current	C	P	Mn	Si	S	Ni	Cr	Mo	Cu	Al	Sn	Nb	Ti	V	N	O
2	200A	0.105	0.007	1.03	0.28	0.008	0.012	0.011	0.003	0.007	<0.003	0.002	0.018	0.016	0.039	0.0043	0.0380
2	183A	0.120	0.009	1.06	0.29	0.009	0.014	0.013	0.004	0.008	0.005	0.004	0.026	0.014	0.037	0.0048	0.0410
2	150A	0.105	0.011	1.14	0.30	0.011	0.017	0.016	0.006	0.009	0.003	0.006	0.033	0.016	0.038	0.0034	0.0420
API 5L X70	150A	0.125	0.017	1.09	0.26	0.010	0.030	0.019	0.005	0.012	0.012	0.004	0.023	0.0 17	0.032	0.0048	0.0515
API 5L X70	188A	0.130	0.015	1.15	0.28	0.008	0.029	0.017	0.003	0.010	0.009	0.002	0.021	0.035	0.033	0.0047	0.0450
API 5L X70	215A	0.110	0.016	1.46	0.34	0.005	0.031	0.014	0.004	0.010	0.026	0.003	0.034	0.010	0.040	0.0060	0.0415
4	201A	0.125	0.007	1.07	0.16	0.010	0.013	0.013	0.004	0.007	0.009	0.003	0.022	0.031	0.040	0.0045	0.0550
4	183A	0.105	0.007	1.17	0.16	0.009	0.012	0.012	0.004	0.007	0.013	0.003	0.026	0.040	0.043	0.0050	0.0550
4	150A	0.135	0.010	1.16	0.19	0.012	0.016	0.016	0.007	0.010	0.015	0.006	0.034	0.039	0.040	0.0039	0.0535
3	180A	0.095	0.008	1.07	0.13	0.009	0.013	0.013	0.004	0.007	0.021	0.004	0.023	0.020	0.039	0.0070	0.0560
3	200A	0.115	0.009	1.06	0.15	0.010	0.015	0.013	0.005	0.007	0.017	0.004	0.021	0.020	0.039	0.0063	0.0550
1	183A	0.145	0.006	1.09	0.17	0.008	0.014	0.012	0.006	0.018	0.009	<0.002	0.025	0.021	0.036	0.0055	0.0420
1	183A	0.145	0.008	1.00	0.13	0.009	0.018	0.012	0.008	0.017	0.005	0.003	0.023	0.020	0.034	0.0060	0.0490
5	202A	0.230	0.017	0.61	0.15	0.010	0.025	0.018	0.004	0.014	0.028	0.005	0.005	0.019	0.004	0.0060	0.0540
5	181A	0.220	0.018	0.61	0.15	0.011	0.028	0.020	0.005	0.014	0.018	0.006	0.005	0.019	0.004	0.0057	0.0540

Table 2.27: Composition of the weld metal of welds produced in the experiments on the effect of theparent metal composition.

2.11.4.1 Statistical analysis

The Wilcoxon rank sum test described in Section 2.9 was used to analyse the data obtained in this experiment for the first five compositions. The aim of the analysis was to determine whether there are significant differences in the incidence of hollow bead between the control and the other four steels.

The results obtained from the aluminium, silicon, carbon and 0.2% carbon melts have been compared with the control composition (composition 4 in Table 2.23). The data for the total number and length (at the 200A current level) have been considered separately. At the 150A and 180A current levels the occurrence of hollow bead is zero in most cases and thus cannot be used in the test. Hollow bead has occurred with the high silicon composition at 180A and it can be stated, just by observation of the data, that the increase in silicon resulted in a significant increase in the incidence of hollow bead.

1. The control and the silicon composition.

The data has been combined and organised in ascending order and given a rank order, Tables 2.28-2.38. When observations with the same value were encountered the mean of the ranks was used. The symbols n_1 and n_2 refer to the size of groups I and II where $n_1 \leq n_2$, R_1 and R_2 are the sums of the ranks for groups I and II respectively, and R_1 is always associated with the smaller sample size. H_0 is the null hypothesis which in this case states that the increase in silicon content does not have an effect on the occurrence (total length or number) of hollow bead. The alternative hypothesis states that the increase in silicon content does increase the occurrence of hollow bead, or $\mu_1<\mu_2$ where μ is the population mean. The null hypothesis is

rejected if R_1 is equal to or less than a critical value for R_1 obtained from tables[1] at a level of significance, α=0.05.

Total Number	1	1	4	4	5	6	7	9	10
Rank	1.5	1.5	3	4	5	6	7	8	9
Group	I	I	I	I	II	II	II	II	II

Table 2.28: Group I and II ranks for the total number of hollow bead.

Total Length	1	4	13	17	26	29	30	30.5	30.5
Rank	1	2	3	4	5	6	7	8.5	8.5
Group	I	I	I	I	II	II	II	II	II

Table 2.29: Group I and II ranks for the total length of hollow bead.

I 200A Control	**II 200A Silicon**	**I 200A Control**	**II 200A Silicon**
Total Number	**Total Number**	**Total length**	**Total Length**
1.5	5	1	5
1.5	6	2	6
3	7	3	7
4	8	4	8.5
	9		8.5
R_1=10	R_2=35	R_1=10	R_2=35

Table 2.30: Group I and II ranks and their sums.

[1] Schmidt, M. J., Understanding and Using Statistics Basic Concepts, Table E, Appendix 1, p436.

The critical value for R_1 from the table at n_1=4 and n_2=5 is 11 at α=0.05. The null hypothesis is therefore rejected suggesting that the data provides sufficient evidence to conclude that the mean for the occurrence (total number and length) of hollow bead at the higher silicon content is greater than the mean for the occurrence at the control composition.

2. The control and the carbon composition (0.13% C).

The null hypothesis in this case states that the higher carbon content does not have an effect on the occurrence of hollow bead. The alternative hypothesis states that the higher carbon content decreases the occurrence of hollow bead, or $\mu_1<\mu_2$. Group I represents the carbon composition since it has the smaller sample size.

Total Number	0	0	1	1	2	4	5
Rank	1.5	1.5	3.5	3.5	5	6	7
Group	I	I	II	II	I	II	II

Table 2.31 Group I and II ranks for the total number of hollow bead.

Total Length	0	0	1	4	4	13	17
Rank	1.5	1.5	3	4.5	4.5	6	7
Group	I	I	II	I	II	II	II

Table 2.32 Group I and II ranks for the total length of hollow bead.

I 200A Carbon	II 200A Control	I 200A Carbon	II 200A Control
Total Number	**Total Number**	**Total length**	**Total Length**
1.5	3.5	1.5	3
1.5	3.5	1.5	4.5
5	6	4.5	6
	7		7
R_1=8	R_2=20	R_1=7.5	R_2=20.5

Table 2.33: Group I and II ranks and their sums.

The critical value for R_1 from the table at n_1=3 and n_2=4 is 6 at α=0.05. The null hypothesis is therefore not rejected, suggesting that the data does not provide sufficient evidence to support the alternative hypothesis which states that the higher carbon content decreases the occurrence of hollow bead.

3. The control and the 0.2% carbon composition.

The null hypothesis in this case states that the higher carbon content does not have an effect on the occurrence of hollow bead. The alternative hypothesis states that the higher carbon content decreases the occurrence of hollow bead, or $\mu_1<\mu_2$. Group I represents the carbon composition since it has the smaller sample size.

Total Number	0	0	1	1	1	4	5
Rank	1.5	1.5	4	4	4	6	7
Group	I	I	I	II	II	II	II

Table 2.34 Group I and II ranks for the total number of hollow bead.

Total Length	0	0	1	3	4	13	17
Rank	1.5	1.5	3	4	5	6	7
Group	I	I	II	I	II	II	II

Table 2.35 Group I and II ranks for the total length of hollow bead.

I 200A Carbon	**II 200A Control**	**I 200A Carbon**	**II 200A Control**
Total Number	**Total Number**	**Total length**	**Total Length**
1.5	4	1.5	3
1.5	4	1.5	5
4	6	4	6
	7		7
R_1=7	R_2=21	R_1=7	R_2=21

Table 2.36: Group I and II ranks and their sums.

The critical value for R_1 from the table at n_1=3 and n_2=4 is 6 at α=0.05. The null hypothesis is therefore not rejected, suggesting that the data does not provide sufficient evidence to support the alternative hypothesis which states that the higher carbon content decreases the occurrence of hollow bead.

4. The control and the aluminium composition.

The null hypothesis in this case states that the higher carbon content does not have an effect on the occurrence of hollow bead. The alternative hypothesis states that the higher aluminium content decreases the occurrence of hollow bead, or $\mu_1<\mu_2$. Group I represents the aluminium composition and group II the control composition. Only the total length is compared in this case as there are too many values which are tied in the data for the total number.

Total Length	1	3	4	6	10	10	13	17
Rank	1	2	3	4	5.5	5.5	7	8
Group	II	I	II	I	I	I	II	II

Table 2.37 Group I and II ranks for the total length of hollow bead.

I 200A Al	**II 200A Control**
Total length	**Total Length**
2	1
4	3
5.5	7
5.5	8
R_1=17	R_2=19

Table 2.38: Group I and II ranks and their sums.

The critical value for R_1 from the table at n_1=4 and n_2=4 is 11 at α=0.05. The null hypothesis is therefore not rejected, suggesting that the data does not provide sufficient evidence to support the alternative hypothesis which states that the higher aluminium content decreases the occurrence of hollow bead.

2.11.5 Discussion

The composition of the parent plate is an important consideration when using the stovepipe welding technique because the percentage of dilution from the parent plate is high (up to 58%) (the calculations have been included in Appendix B).

The statistical analysis was performed for the first five steels only, where compositions 1, 2, 3 and 5 have been compared with the control composition number 4. The results of these initial experiments are shown in Table 2.25 where the occurrence of hollow bead has been measured in a 170mm length of weld. The analysis, as well as direct observation of the results, suggests that silicon (at levels of 0.37% in the parent metal corresponding to about 0.30% in the weld) is a contributing factor to the formation of hollow bead, while the other elements, up to 0.23% carbon and up to 0.053% aluminium in the parent metal (corresponding to 0.22% carbon and 0.021% aluminium in the weld metal) have not produced significant variations.

The results also show that welding current is again the most powerful factor contributing to the formation of hollow bead pores. Hollow bead defects do not appear at 150A regardless of the parent metal composition, whereas they are present at 180A and become more prevalent at 200A. This applies to all the results obtained in these experiments (see Table 2.26)

As mentioned earlier the first set of experiments produced other types of porosity which had not previously been observed. The results, recorded in Table 2.24, are difficult to explain. The data shows large variations both within each composition and between the compositions and thus does not provide any conclusive information on the effect of the three elements. This data has not been included in Tables 2.25 and 2.26. There is not enough information to put forward a definite explanation for the occurrence of the worm holes and gas pores. However, the presence of the oxide layer on the plate next to the joint preparation has probably had a role to play. The exact reason for the appearance of gas pores and worm hole pores in these experiments is not known. The experiments which studied the effect of rust on the joint preparation on the occurrence of hollow bead showed that this contaminant was not an

influential factor. Here, however, the presence of the oxide appears to have had an effect on hollow bead. It is possible that the higher thickness of this oxide layer may have been a factor.

Further experiments were conducted to test the combined effect of the silicon and aluminium as composition number 2 was found to have a very low aluminium content (0.008%). Another pipe steel, with a higher silicon content (0.22%) than the one in composition number 5 and a high carbon content (0.185%), was also added in an attempt to determine the critical silicon content which increases the incidence of hollow bead. The results from the experiments on the effect of the welding current done on an API 5L X70 steel (with a 0.33% Si content) have been added to Table 2.26 for comparison.

A silicon content of 0.36% in compositions 6 to 9 has produced an incidence of hollow bead slightly higher than the one for composition number 2, while the change in aluminium content (from 0.008 to 0.025%) has had no noticeable influence. The composition number 10 (the pipe steel with 0.185% carbon and 0.22% silicon) has produced similar results to composition number 5 which has a lower silicon content at 0.13%, as well as a higher carbon content at 0.23% . The incidence of hollow bead in the X70 steel is comparable to the incidence in the high silicon melts (numbers 2 and 6 to 9) although the welding current (shown in brackets in the Table 2.26) is higher. This increase in welding current would be expected to increase the occurrence of hollow bead slightly. Further experiments are now required to determine the threshold silicon content which promotes the increase in hollow bead. At this stage it can only be said that the value will lie between 0.2 and 0.36%.

Some consideration is now given to the effect of the solidification microstructure from the liquid to solid transformation. The compositions of the steels studied in these experiments, including the API 5L X70 steel but excluding the pipe steels with compositions 5 and 10,

have a carbon content up to 0.13%, a manganese content up to 1.61% and a nickel content up to 0.022%. The corresponding weld metal compositions include a carbon content up to 0.15%, a manganese content up to 1.46% and a nickel content up to 0.031%.

The iron-carbon phase diagram shows that δ-ferrite is the stable phase for the liquid to solid transformation microstructure for carbon contents less than 0.18% (Svensson, 1994), and that above this solidification occurs as austenite. Under equilibrium conditions, a carbon content of 0.18 to 0.55% results in δ-ferrite as the first solid to form which subequently decomposes at the peritectic to form austenite. The effect of high colling rates, however, on this portion of the phase diagram is to favour the formation of austenite. Nevertheless, in this study there is microstructural evidence which indicates that in the steels under consideration δ-ferrite is the first solid phase to form. Alloying with manganese in concentrations of 0.5 to 2weight% does not change the solidification mode, whereas alloying with high concentrations of both manganese and nickel might form austenite (Svensson, 1994).

Sugden and Bhadhesia (1988) have observed the location of inclusions in the microstructure of welds to predict their primary solidification microstructures. It was found that a weld metal with a carbon and manganese content of 0.29weight% and 0.76weight% respectively (made on an parent plate with 0.68% carbon, and in the austenitic state before welding, with a low carbon electrode) solidified with austenite as the primary phase. This was said to follow from the fact that weld pool solidification occurred by epitaxial growth of grains at the fusion boundary, and it was the crystallographic structure of those which determined the solidification mode. A weld metal with a carbon and manganese content of 0.19weight% and 1.40weight% respectively, made on a low carbon parent plate with a medium carbon electrode, was found to solidify with δ-ferrite as the primary phase.

It can therefore be assumed that the welds made from the compositions 1 to 4 and 6 to 9 and the X70 steel which have a carbon content lower than 0.18%, a manganese content up to 1.17% and a nickel content up 0.031% solidified with δ-ferrite as the primary phase.

Etching the weld in nital does not reveal the original δ-ferrite microstructure since it is masked by the subsequent transformation to austenite during cooling. Special etching techniques are required to reveal the ferrite microstructure so that it can be compared with the solid state microstructure (this is also discussed in Chapter 3 Section 3.3.2). If the weld first solidified as ferrite, then the δ-ferrite boundaries will be neither parallel nor coincident with the prior austenite grain boundaries since the heat source is not stationary in welding, and thus the direction of the thermal gradient continuously changes during cooling (Sugden and Bhadhesia, 1988).

As is described in more detail in Chapter 3, Section 3.3.2, it was attempted in this work to reveal the δ-ferrite microstructure by etching the welds in Le Pera's reagent, a solution of picric acid and sodium metabisulphite, which highlights the segregation at the cellular dendritic boundaries. This technique, however, was not successful due the relatively low levels of alloying elements such as manganese and nickel, and as a result the segregation at the cellular dendritic boundaries was not clearly revealed. It was also attempted to observe the primary solidification microstructure by chemical microanalysis using an energy dispersive x-ray spectrometer, and then to compare it with a scanning electron micrograph of the microstructure at the same location etched in nital. The distribution of manganese in the weld was analysed. Again the segregation in the weld could not be clearly observed.

It is a reasonable assumption, however, that the welds made in compositions 1 to 4 and 6 to 9 and the API 5L X70 steel solidified with δ-ferrite as the primary phase due to the level of

carbon below 0.18% and the low levels of manganese and nickel. On the other hand solidification of the welds made from compositions 5 and 10 could have occurred with austenite as the primary phase. An accurate assessment is difficult for composition 10, however, without a study of the microstructures because the carbon content is just above 0.18% and the manganese and nickel content of both compositions are relatively low.

The higher carbon content in composition 5 does not appear to have significantly affected the formation of hollow bead. Composition 5 (the weld metal composition is given in brackets) has a carbon content of 0.23% (0.23%), a silicon content of 0.13% (0.15%) and an aluminium content of 0.041% (0.023% average). When comparing the occurrence of hollow bead which resulted from this composition with the one from composition 1, which has a lower carbon content at 0.13%, similar silicon content but lower aluminium, it can be seen that there is no significant difference (see Table 2.25). The aluminium content was shown previously not to be an influential factor.

2.12 Occurrence of Hollow Bead Defects at the Start of Welds

2.12.1 Introduction

It was mentioned in an earlier section that the welding conditions at the start of the weld were unstable and thus the initial portion of the weld was not considered when analysing the results. It was noticed, however, that in many cases a hollow bead had formed in this initial part even at welding conditions which did not produce any pores in the remainder of the weld. A survey of 122 radiographs, from the experiments described in the previous Sections 2.6 to 2.9, was thus undertaken to study this occurrence.

2.12.2 Analysis and Results

The radiographs of welds from the experiments on the effects of welding parameters, parent metal composition, joint geometry and flux moisture content were chosen. The incidence of hollow bead pores in or near the start crater (including hollow bead pores which started within 5mm of the crater) and the welding current in that location were determined. The results have been recorded in Table A8 in Appendix A which also includes the length of the hollow bead at the start, the total number and length of hollow bead in 170mm of the remainder of the weld and the average welding current for the weld run (excluding the start). The survey revealed that 54% of the welds studied contained one hollow bead at the start of the weld.

2.12.3 Discussion

The results of this survey show that when a hollow bead occurred at the start, the welding current in that location was higher than the average current for the remainder of the weld in 50% of cases. It was also found, however, that hollow bead occurred at the start of welds even

when the welding conditions initially should not have been conducive to its formation, and no hollow bead was detected in the rest of the weld.

An example of a typical trace of welding current versus time obtained from the data logger is shown in Figure 2.20. The trace shows the major instabilities in welding current at the start of the run (between 2 and 10 seconds). In this particular case the average welding current is 188A while the current at the start increases rapidly to about 200A. The fluctuations in the parameters are partly because the current is controlled manually during welding and also due to the sequence of operations at the start. When the process is started the machine operates under voltage control for about 2.5 seconds to allow stabilisation, and for the first 0.5 second the table does not move. After this delay the force control mode is activated and the electrode is forced into the joint. At that stage the welding current tends to increase suddenly as seen in Figure 2.20 until the current can be decreased and stabilised by manual adjustment of the motor generator controls. The fluctuations and rapid increases in current tend to be more pronounced at high currents, from about 180A. The hollow bead pores which form at the start have been found to have the same characteristics as all the others examined. It is possible that when major fluctuations in welding conditions occur at the start of the welding process, these have considerable influence on the formation of hollow bead. This is discussed further the next section (Section 2.13) and in Chapter 5.

The radiographs of the pipe sample welds were also studied but the porosity at the start of the weld was observed only in 7 cases out of 39 welds with hollow bead pores (Section 2.5). It is likely that the welder had greater control at the start welding than the automated machine which would prevent the occurrence of the sharp increase to very high current levels and any major instabilities.

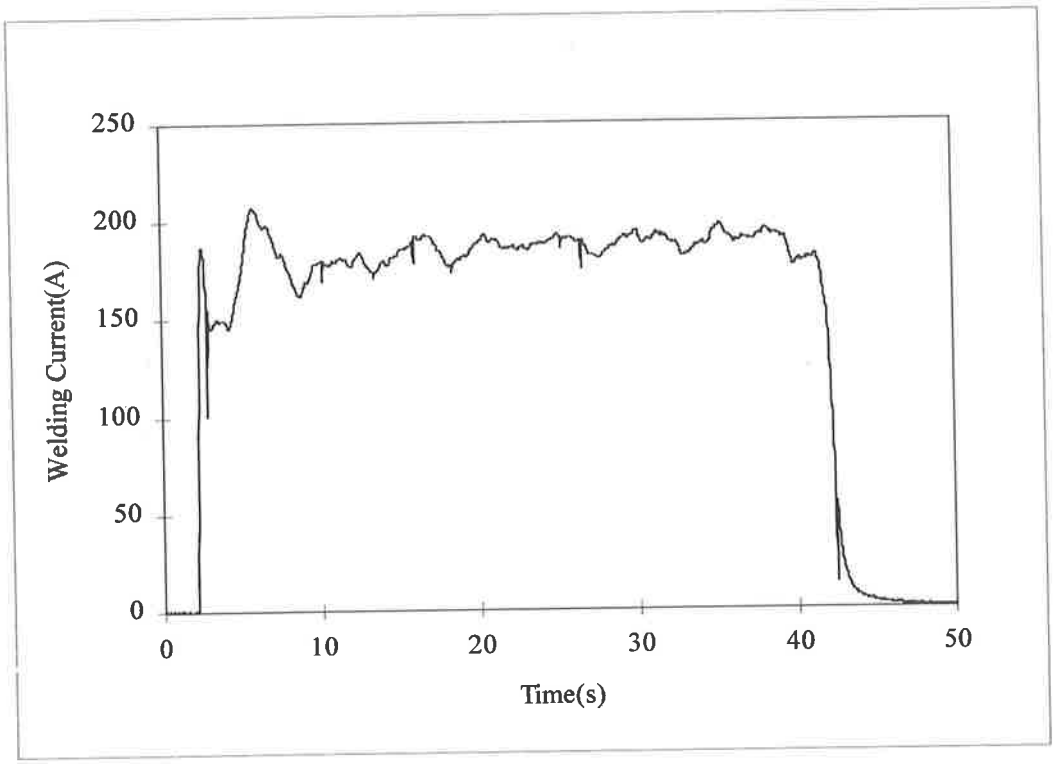

Figure 2.20: Trace of welding current versus time during a weld run.

2.13 Filming of the Weld Keyhole

2.13.1 Introduction

In stovepipe welding, the keyhole is a window which is formed by the pressure of the expanding gases evolving from the electrode and by the force of the arc itself. The geometry of the keyhole is expected to give an indication of the shape of the weld pool. It is an important parameter for the manual welder who controls the dimensions of the keyhole by varying the welding current, weld travel speed and the force and angle of the electrode in order to control the shape of the weld bead. In this project the keyhole was filmed in an attempt to correlate the shape of the weld pool, as determined by the geometry of the keyhole, and the formation of porosity.

High speed filming carried out in previous experimental work using the same automated manual metal arc welding machine (Fletcher and Morrison, 1977) indicated that the keyhole geometry varied rapidly throughout the welding process. A short segment of this high speed film obtained from Bob Morrison (Tubemakers of Australia, Pipelines Research Centre, Melbourne, Australia) was studied in this work. Still frames from the film have been reproduced and presented later in Figure 2.23. It was thought that similar variations would occur with the weld pool and as a result have an influence on the solidification rate which is in turn related to macrosegregation and porosity.

2.13.2 Equipment

A black and white video camera was used. Two polarising filters in a crossed configuration were attached to the lenses to reduce the intense light from the arc. An infra-red filter, which discriminates light from the weld pool which is at a cooler temperature than the arc, was also used. The iris on the camera was adjusted during a trial welding run. Filming was done from

the back of the plate, that is on the side opposite that from which welding was being conducted.

2.13.3 Welding Conditions

Filming took place during experiments on the effect of welding conditions and parent metal composition (described in Sections 2.6 and 2.9).

2.13.4 Results

Figures 2.21 and 2.22 are still frames from the films made during two welding runs at different welding conditions. The first was recorded at low travel speed and low welding current and the other at a high travel speed and high welding current.

Additional features such as metal transfer and the turbulence around the keyhole were observed from the high speed film and then analysed. The third set of Figures (Figure 2.23) show still frames from the high speed film obtained from Tubemakers of Australia. Although the orientation of the keyhole is horizontal in this figure welding still took place with the work table of the machine in the vertical position.

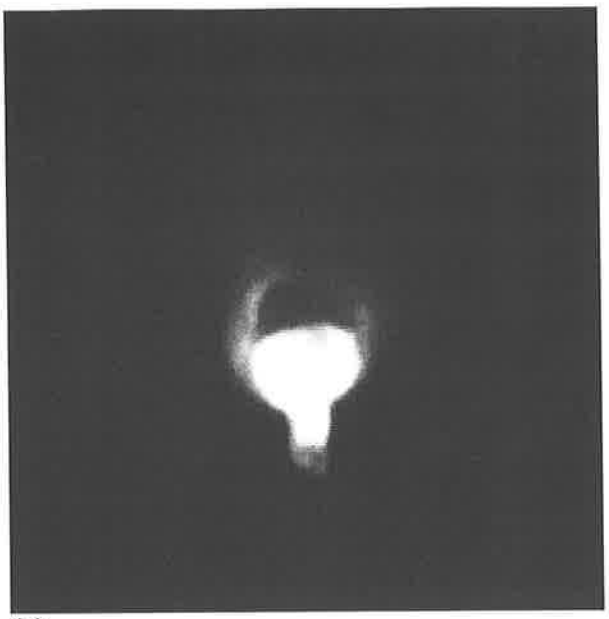

(a)

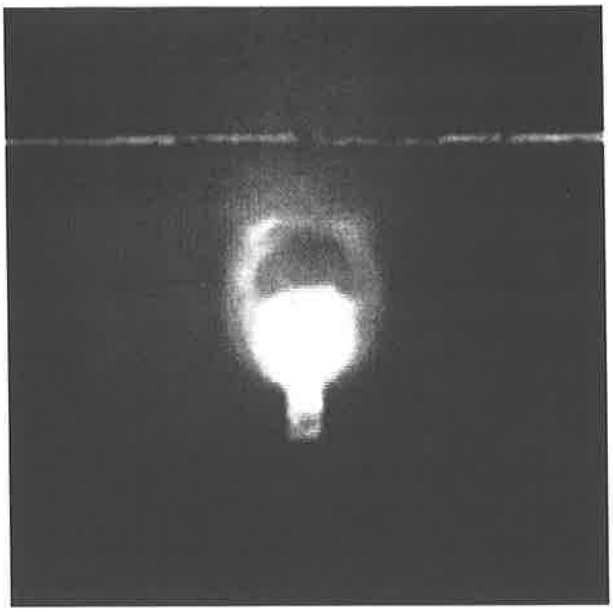

(d)

(b)

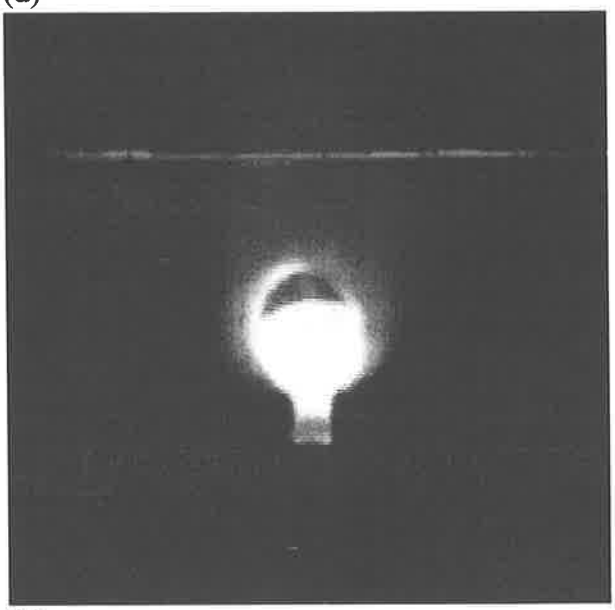

(e)

(c)

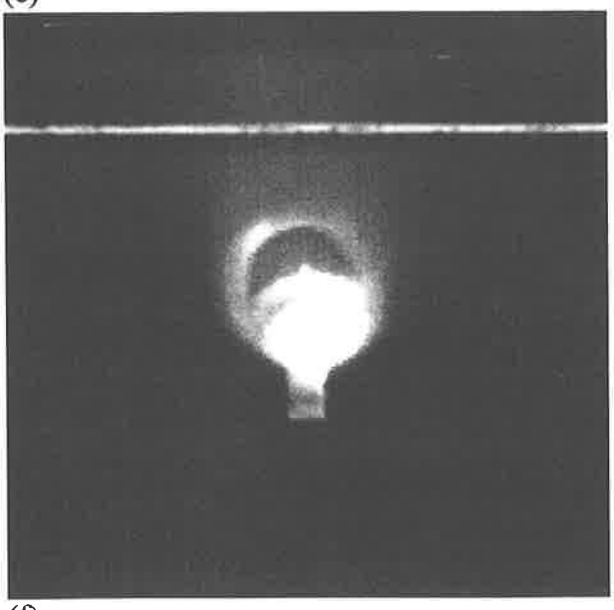

(f)

Figure 2.21a-f: Still frames from the film of a weld run made at 160A and 300mm/min [x3.2].

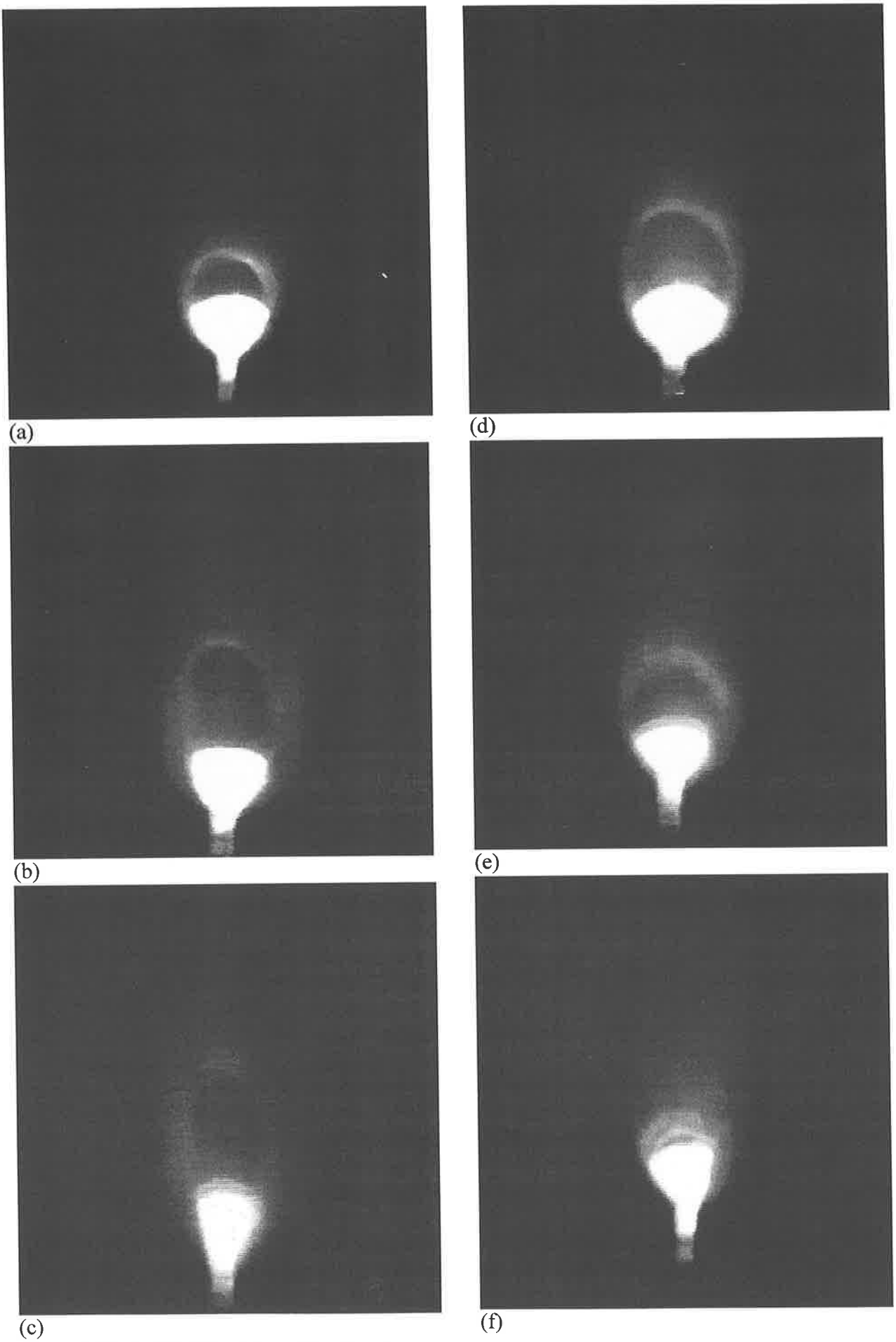

(a) (d)

(b) (e)

(c) (f)

Figure 2.22a-f: Still frames from the film of a weld run made at 216A and 600mm/min [x2.9]

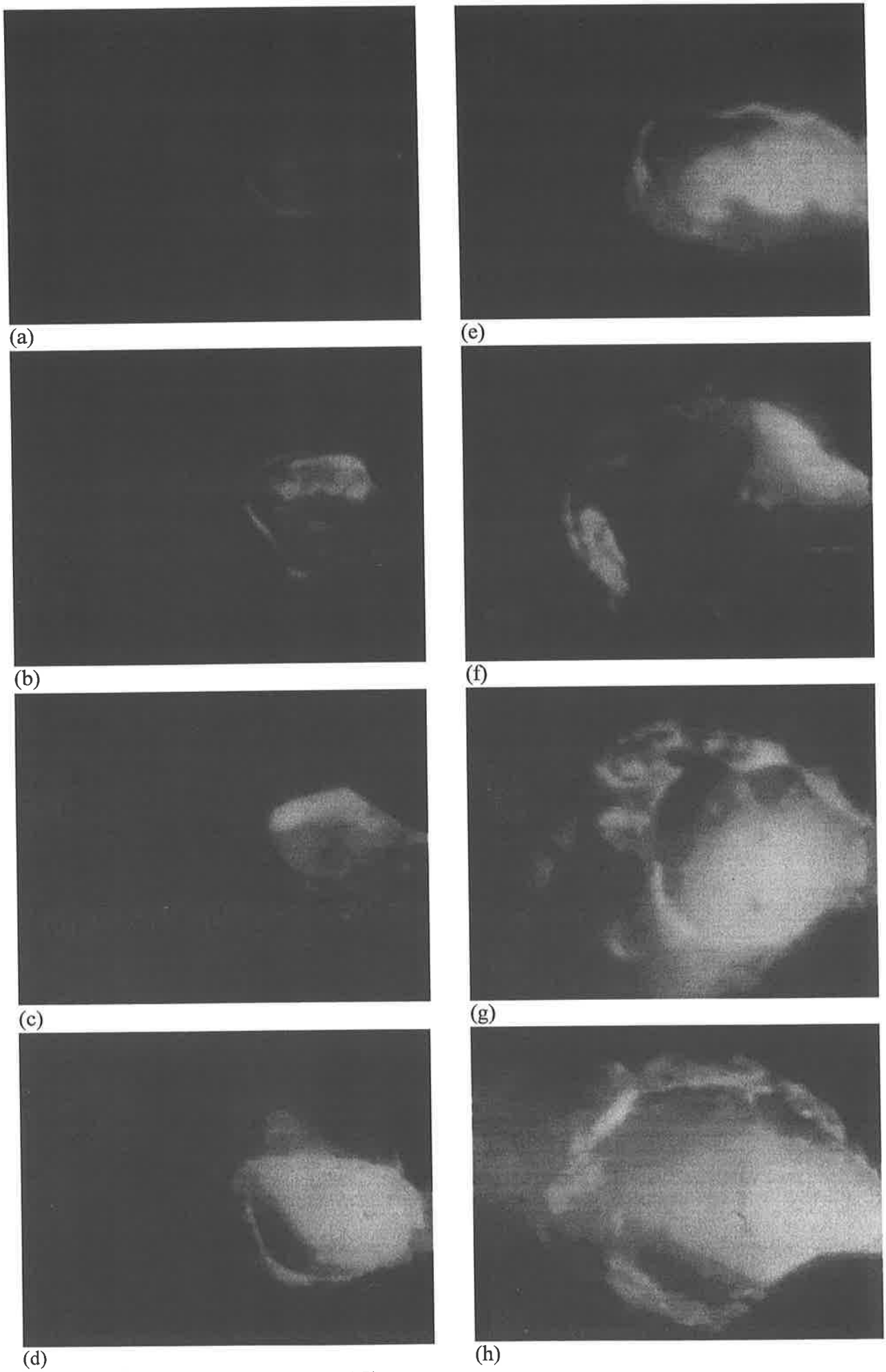

Figure 2.23a-h: Still frames from high speed film (film courtesy of Tubemakers of Australia).

The average length and width of the keyhole were determined for particular welding runs by taking measurements from approximately 20 still frames within a one second period (see Table A9 in Appendix A). Two to five different time periods were considered for each individual welding run. The periods were chosen to corresponded to the region within the 170mm length of weld where the occurrence of hollow bead was measured. The area of the keyhole was estimated using the formula for the area of an ellipse, $\pi ab/4$, where a and b are the length and width respectively (see Figure 2.24).

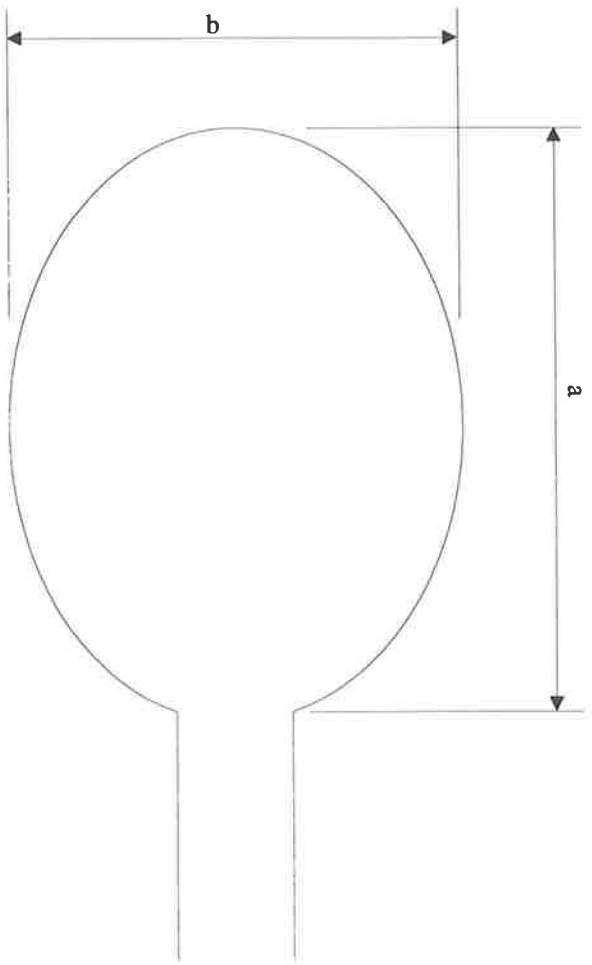

Figure 2.24: Schematic of the keyhole geometry.

The standard deviation was also evaluated and was used as a measure of the variation in the geometry. The results have been presented in Table 2.39 and in the graphs in Figure 2.25a-d

and Figure 2.26a-k. The graphs in Figure 2.25 have been produced to find which parameters describing the geometry of the keyhole can be correlated with the occurrence of hollow bead. In Figure 2.26, the variation in the area of the keyhole with time for all of the welding runs filmed are represented as well as the average of the measurements, indicated by a single horizontal line. The first four graphs represent conditions where hollow bead did not occur, the next three graphs represent conditions where the occurrence of hollow bead was very low and the remainder conditions where hollow bead occurred.

Plate No.	Welding Current (A)	Travel Speed (mm/min)	Total Number of Hollow Bead	Total Length of Hollow Bead (mm)	Average Length of Key Hole (mm)	Standard Deviation	Area (mm^2)	Standard Deviation
WTS1	140	400	0	0	4.1	0.8	12.3	3.6
WTS2	170	400	1	2	5.0	0.8	16.1	2.7
WTS3	170	300	1	5	5.7	0.6	21.5	4.1
WTS4	186	500	4	28.5	5.5	0.9	17.0	4.4
WTS5	140	500	0	0	4.5	0.9	12.2	3.7
WTS6	140	600	3	6.5	4.6	1.3	10.9	3.0
WTS7	186	600	4	23.5	5.4	1.2	15.7	4.8
WTS8	170	600	4	15	4.8	1.2	14.0	4.7
WTS9	162	300	0	0	5.0	0.7	17.3	4.6
WC1	216	600	10	91.5	7.7	2.1	27.4	7.3
WC3	143	300	0	0	5.0	0.7	16.5	3.0

Table 2.39: Results of measurements of average length and area of the keyhole.

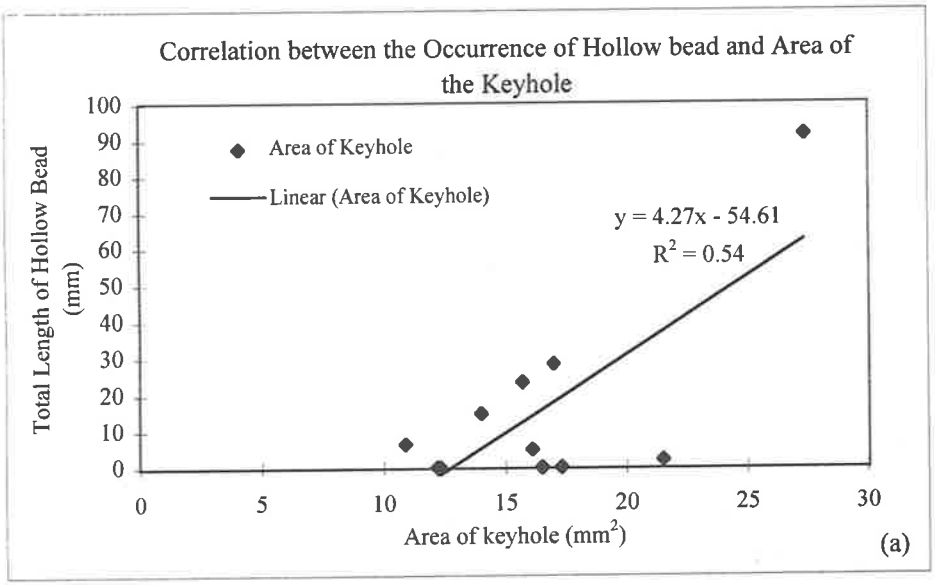

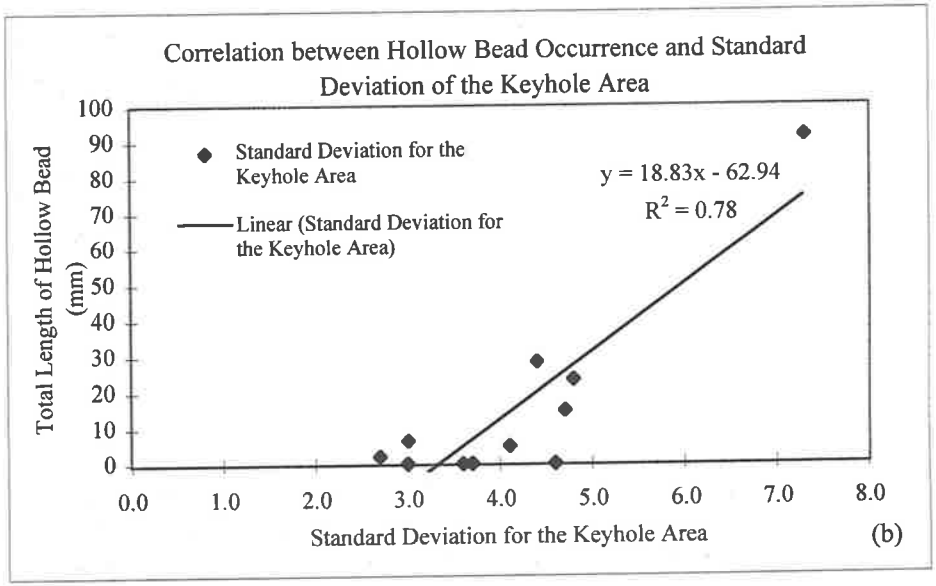

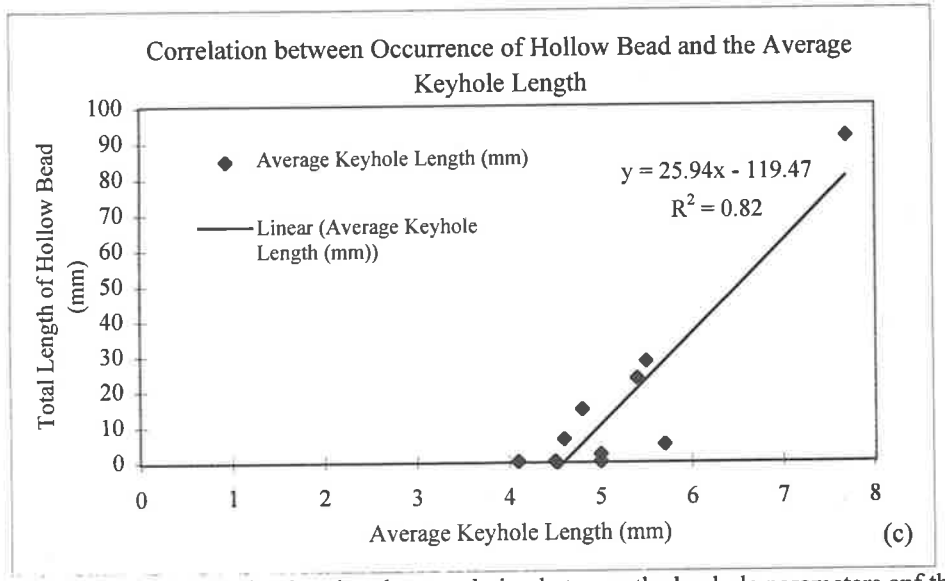

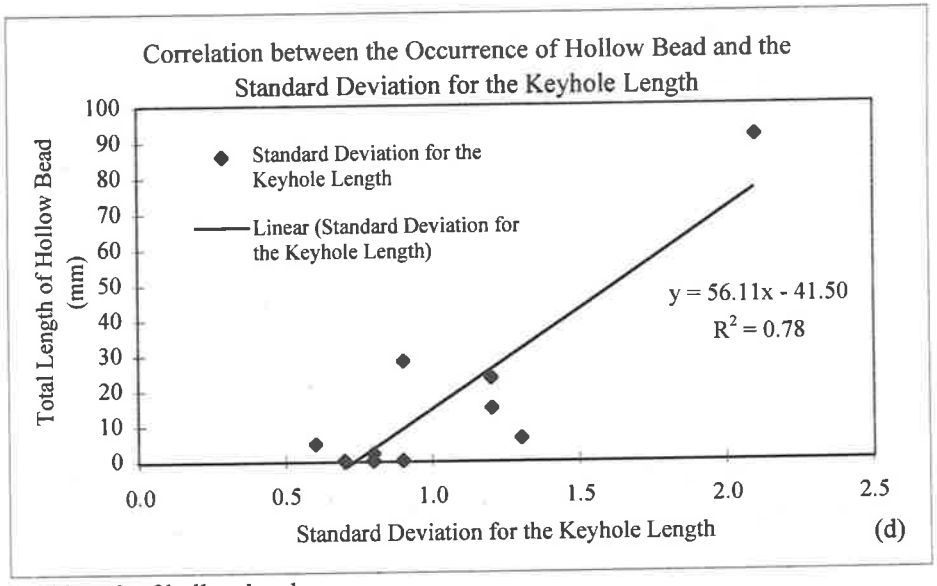

Figure 2.25a-d: Graphs showing the correlation between the keyhole parameters anf the total length of hollow bead.

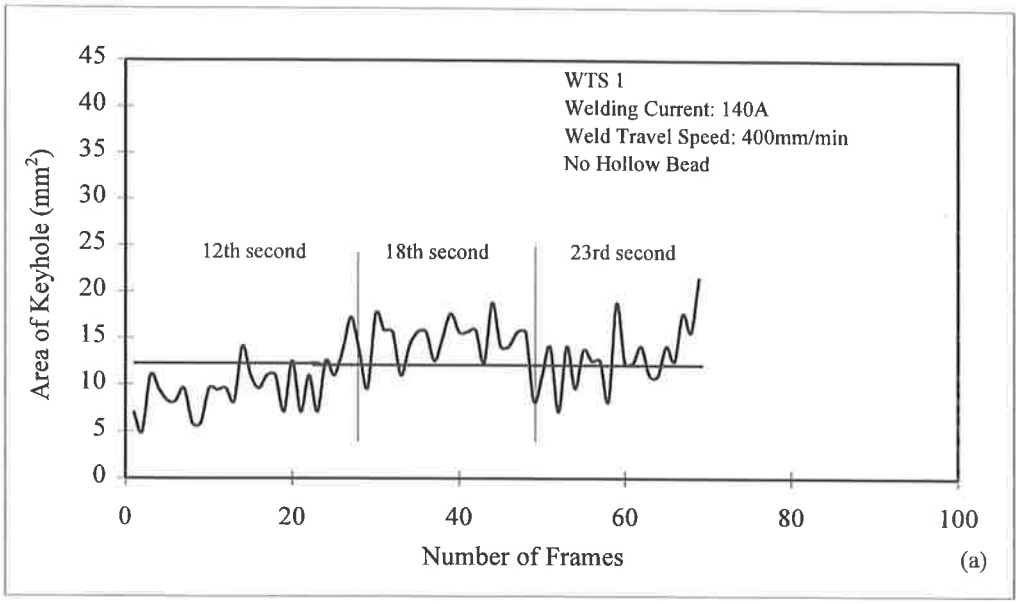

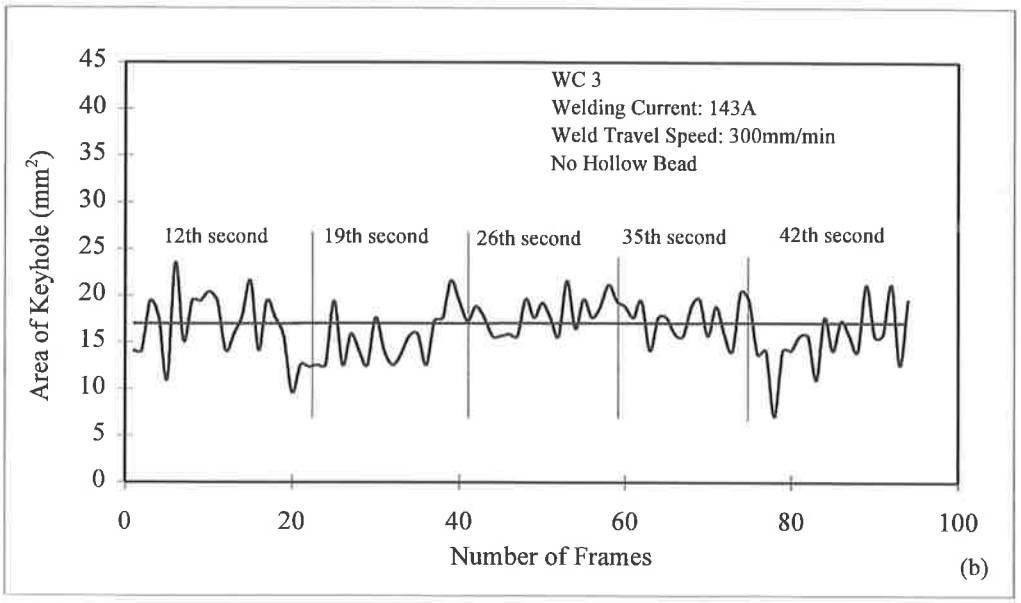

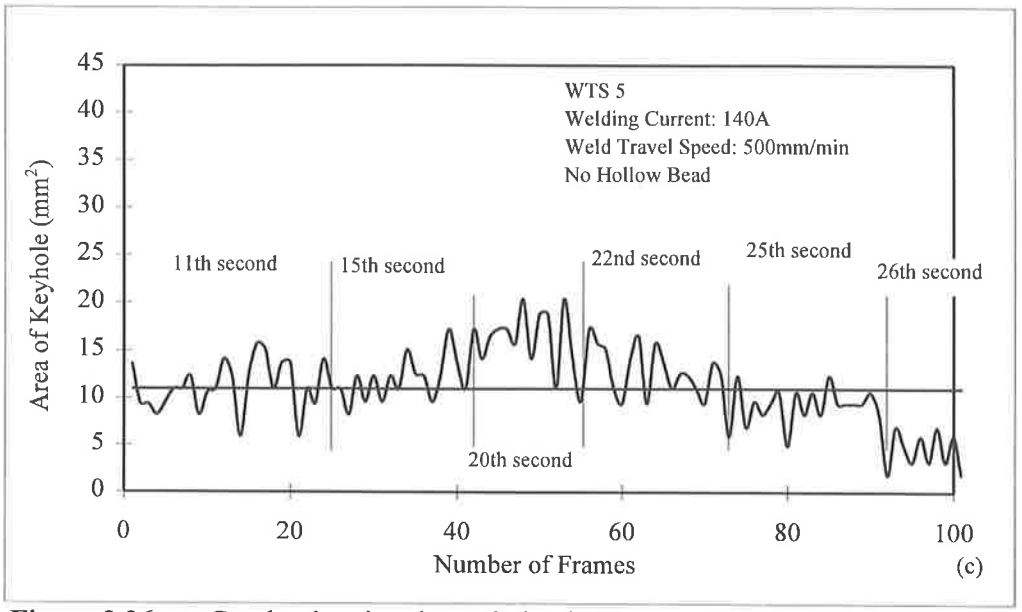

Figure 2.26a-c: Graphs showing the variation in the area of the keyhole.

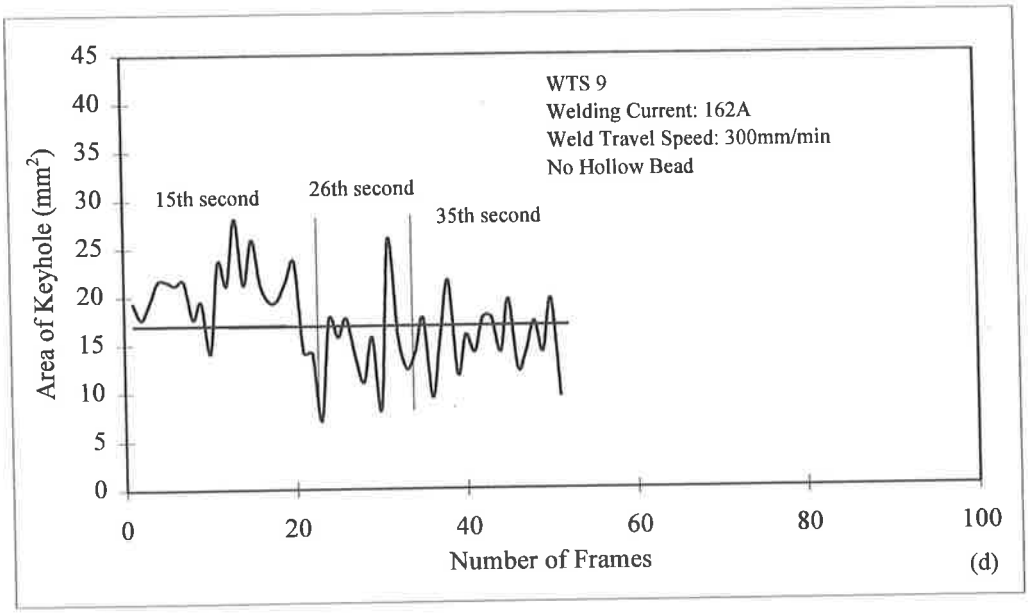

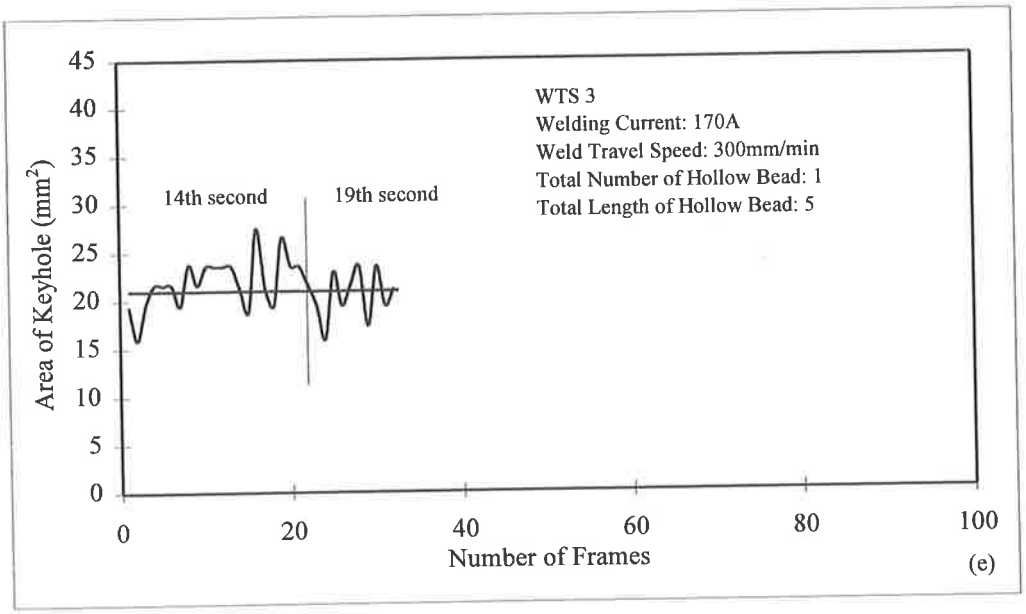

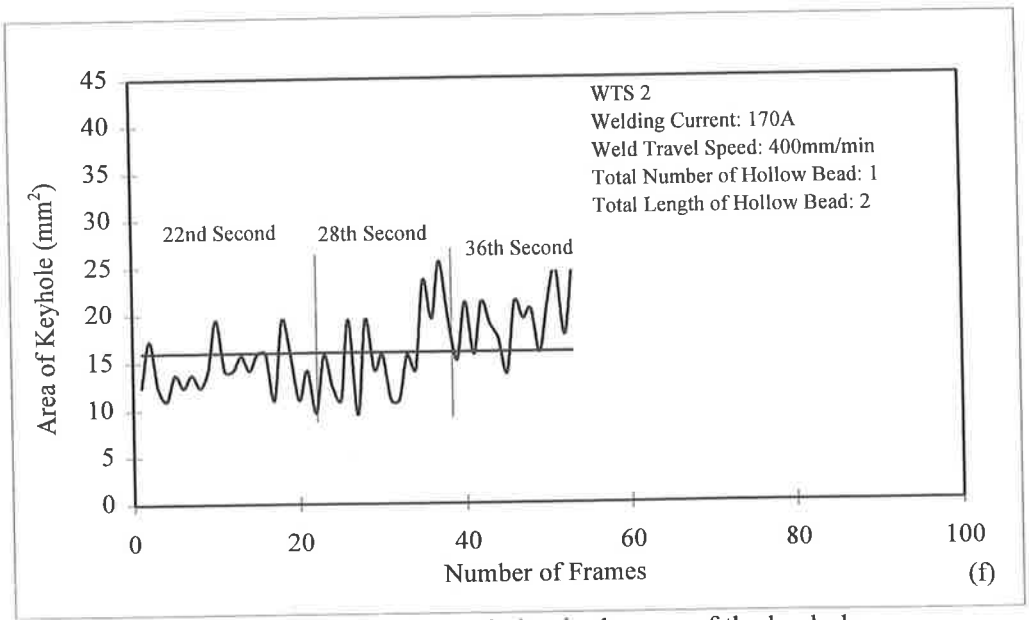

Figure 2.26d-f: Graph showing the variation in the area of the keyhole.

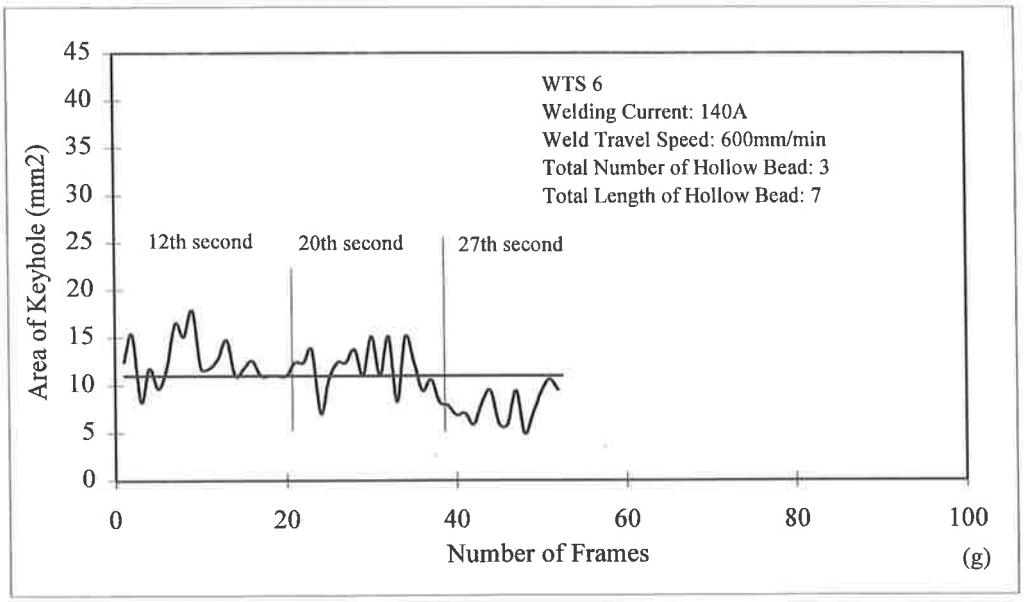

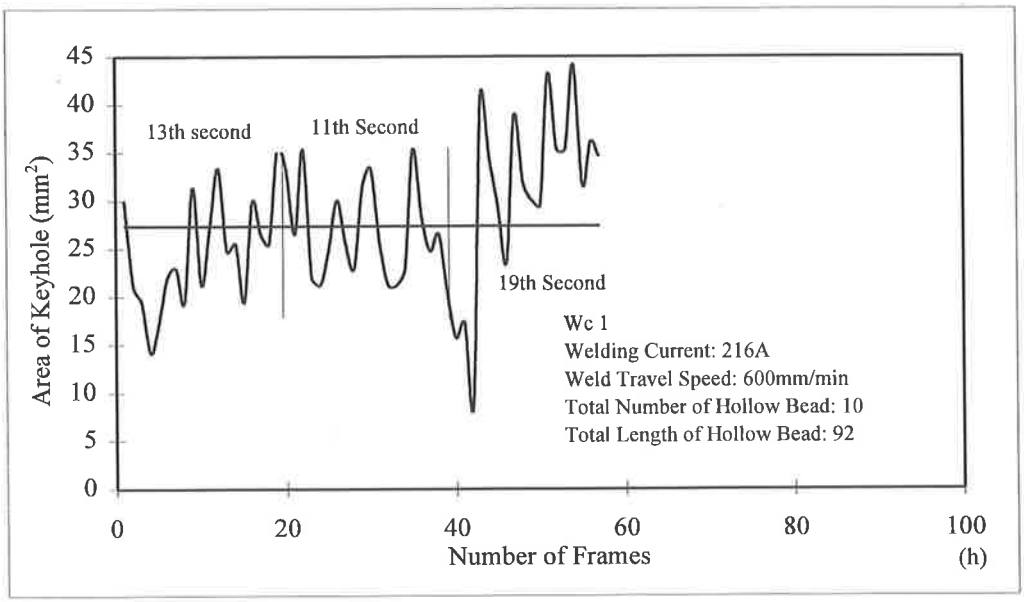

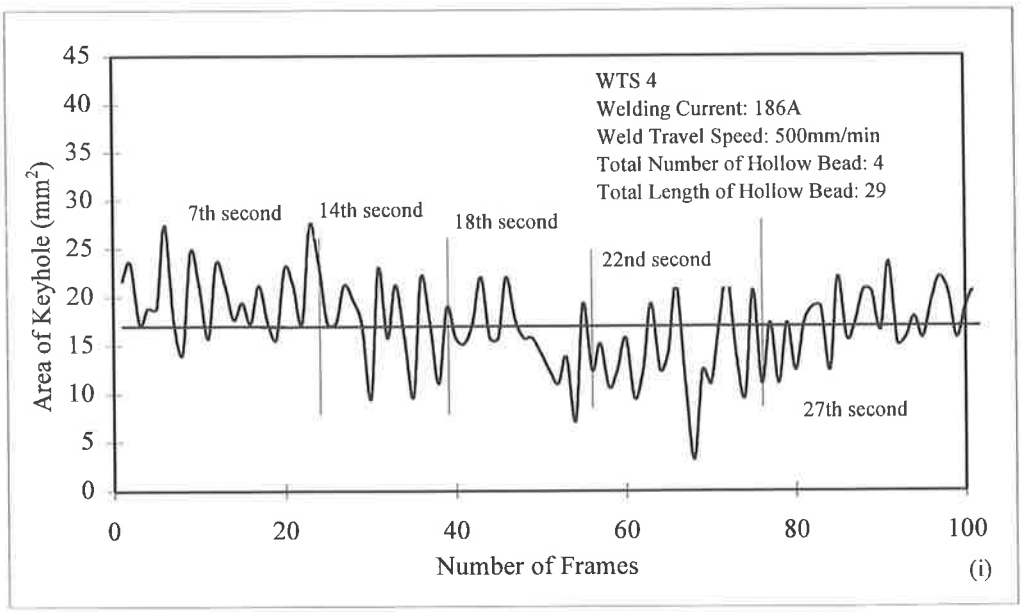

Figure 2.26g-i: Graph showing the variation in the area of the keyhole.

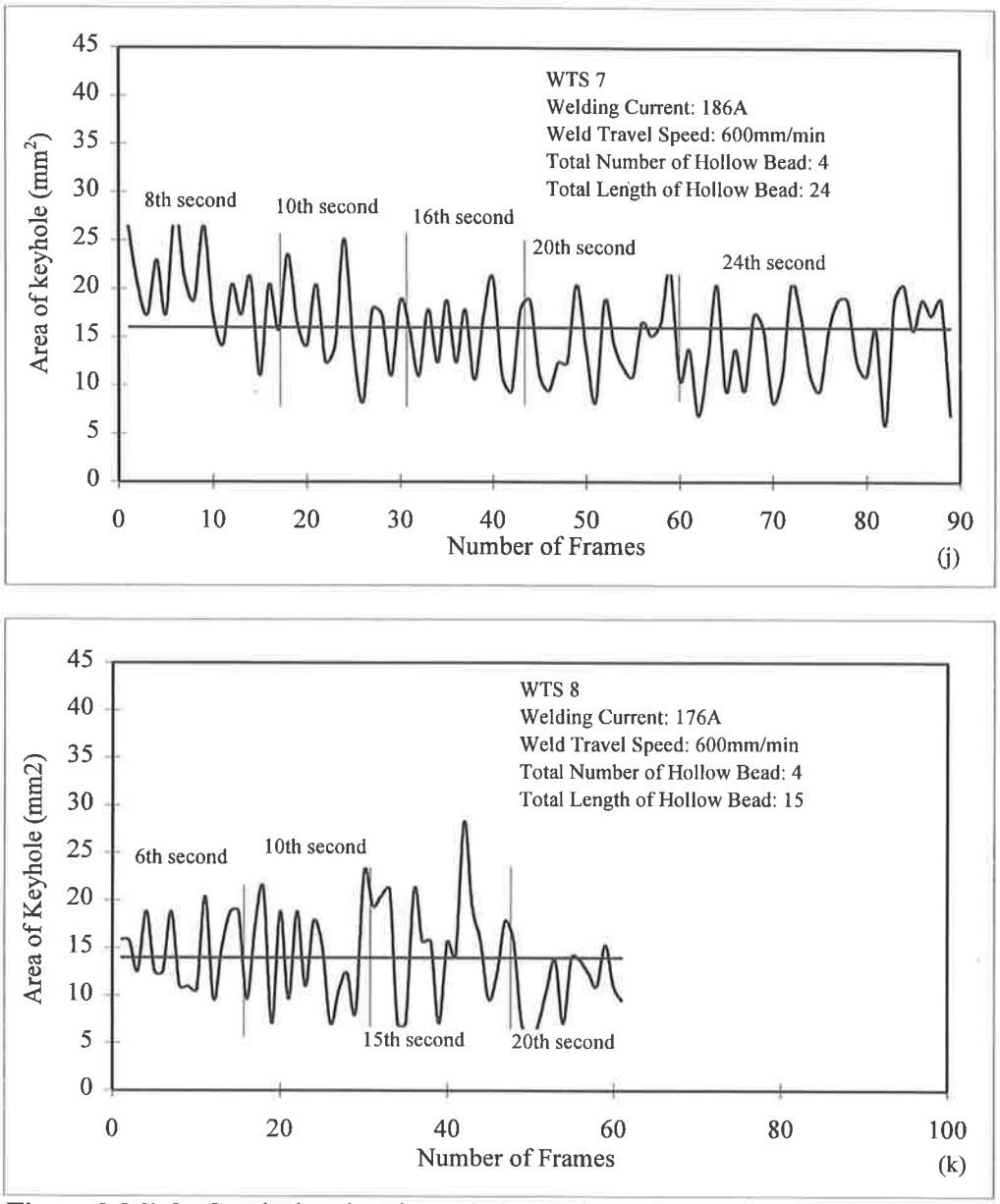

Figure 2.26j, k: Graph showing the variation in the area of the keyhole.

2.13.5 Discussion

The results have been summarised in Table 2.39 and in Figures 2.25. Regression analyses were performed on the data plotted in Figure 2.25 to find a correlation between the keyhole parameters and the change in the total length of hollow bead in the welds studied. The correlation coefficients, R^2, for the plots were calculated and have been included in the graphs. The regression analyses and these coefficients reveal that a reasonably good fit has been obtained for the data of the total length of hollow bead against the length and the standard deviation of the length and area measurements, while there is more scatter for the data on the area of the keyhole. Only the total length of hollow bead was considered as the previous experiments showed that this parameter was more sensitive to changes in the welding variables than the total number of hollow bead.

The effect of the variation in the length and area of the keyhole on the occurrence of hollow bead is now discussed. The analyses of the results have indicated that an increase in the variation of the dimensions of the keyhole (measured by the standard deviation) is conducive to an increase in the total length of hollow bead. The data in Table 2.39 reveal that at the highest speed and current (where the total length of hollow bead is also highest) the variation in the area of the keyhole is much higher than at lower speeds and currents. At the low welding current and travel speed the variations in the size of the weld pool are small, whereas at the high welding current and travel speed the changes in keyhole dimensions are larger. This is also evident from the graphs in Figure 2.26. In the first three cases where hollow bead did not occur (Figure 2.26a-c) and the three where the occurrence was very small (Figure 2.26e-f) the magnitude of the oscillations are smaller than in the cases where the incidence of hollow bead is higher (Figure 2.26h-k). A portion of the graph in Figure 2.26d, representing a condition where hollow bead did not occur, shows oscillations which are larger than expected

considering the observation in Figures 2.25a-c, e-f. The variability in the size of the keyhole can also be observed from high speed filming (Figure 2.23).

The keyhole is formed by the pressures of the arc and of the expanding shielding gases acting against the molten weld pool. Consequently its dimensions will fluctuate with arc voltage and current, and hence heat input. The fluctuations are evidently aperiodic and apparently random. There are a number of contributing factors to this variation such as uneven joint preparation, external air currents, mechanical vibration, variations in electrode and flux diameter and composition, and heating of the parent metal. All of these factors will cause variations in the arc/electrode impedance which the welding generator responds to in a non-instantaneous fashion. The entire system is extremely complex and contains a number of non-linear components. This, in combination with the random and uncontrollable nature of some of these factors is the likely cause of the apparently chaotic variation in keyhole dimension observed. An extremely useful future project in the field of hollow bead formation could be to model the electro-mechanical system of this welding technique to determine which are the most significant factors in keyhole variation. Controlling this variation may allow hollow bead to be eliminated whilst retaining the economical advantages of high welding speeds at high currents.

Solute banding (macroscopic variations in composition) visible in the weld microstructure has been associated with changes in the rate of solidification which have further been related with uncontrollable variations in the heat input and stability of the arc known to occur in welding (David and Vitek, 1989 and Davies and Garland, 1975).

In this case, the larger fluctuations in heat input, seen at the higher speed and also higher currents, would be expected to increase these variations in solidification rate. As the rate of

solidification increases, so does the concentration of gas-forming solutes at the solidification interface. Their solubility decreases as the metal solidifies causing them to accumulate at the interface and it has been shown that porosity is related to this banding (Powell and Lloyd, 1995 and Harris, 1988). The correlation of hollow bead to fluctuations in the keyhole could thus be due to a similar mechanism.

Barkow (1973) noted in his work on hollow bead that the length of the keyhole could be correlated with the incidence of hollow bead, such that if the length of the keyhole was kept below a quarter of an inch (6.4mm), hollow bead would not occur. As mentioned above, in these experiments the data have also shown a good correlation between the length of the keyhole and the total length of hollow bead. Although an explanation for the effect of the fluctuations of the area and length of the keyhole on the formation of hollow bead has been given, the influence of the length of the keyhole is not known at this stage.

2.14 Analysis of Gases Present Inside Hollow Bead Pores

2.14.1 Introduction

The Literature Review (Chapter 1) reviewed the theories of gas pore formation in welds. The type of gas or gases expected to be found in a pore depends on the mechanism by which it forms and propagates. In the present study it was observed that in most cases the start of hollow bead pores was less oxidised that the termination end. It was proposed that the nucleating gas could therefore be a reducing gas and that the oxidation was caused by secondary reactions once the pore was initiated. Understanding the mechanism of formation of hollow bead and being able to explain its features therefore requires a knowledge of the gases present inside the pores.

In this work, the analysis of gases in the pores was performed by The Welding Institute (TWI) which has a dedicated system for this purpose. Three weld samples containing hollow bead pores, of different lengths, were used in the tests.

2.14.2 Procedure

The gases were analysed using a HAL100 quadrupole mass spectrometer attached to a purpose built system which enables the pore to be pierced, releasing the gas into a high vacuum system. The pressure in the sample chamber before fracturing the pore was around $1x10^{-7}$ torr, and after fracturing the samples, this rose to at least $1x10^{-2}$ torr. The mass spectrometer was calibrated with certified gas mixtures to establish the sensitivity factors for the various gases.

2.14.3 Results

The results of the gas analysis received from TWI (TWI References 621205 S/96/160) are given in Table 2.40.

	HB1	HB2	HB3
CH_4	< 1	< 1	< 1
CO_2	< 1	< 1	< 1
Ar	< 1	< 1	< 1
O_2	< 1	< 1	< 1
CO	2	1	9
H_2	94	95	80
N_2	4	3	10
He	<1	<1	<1

Table 2.40: Results of pore gas analysis in % (partial pressure).

The samples used in the analysis were subsequently sectioned and their dimensions measured in the SEM. The total gas pressure inside the pore was also calculated using the ideal gas law, (pressure x volume = constant, at constant temperature), and knowing the pressure of the gas inside the sample chamber after piercing the welds from the measured volume of the chamber and the pore itself. These results, as well as the welding conditions used to make the welds, are given in Table 2.41.

2.14.4 Dimensions of Hollow Bead Pores used in the Analysis and Welding Conditions used to Produce the Welds.

	Hollow Bead 1	Hollow Bead 2	Hollow Bead 3
Length (mm)	10.1	7.8	5.7
Average Diameter	1mm	0.8mm	0.9mm
Gas Pressure inside Pore (atmosphere)	1	1.4	1.5
Welding Current (A)	215	194	215
Welding Voltage (V)	600	600	600

Table 2.41: Information on the dimensions, gas pressure and welding conditions of hollow bead pores used in the analysis of the composition of the gas.

2.14.5 Discussion

The results in Table 2.40 above clearly show that hydrogen is the major gas inside hollow bead pores. It must be emphasised that the composition of the gas during the formation of hollow bead could be different from the composition analysed approximately one month after welding when the analyses were conducted. For example hydrogen in the weld could diffuse into the pore and oxygen and carbon monoxide would combine with iron to form oxides. It is expected, however, from these results that hydrogen will be the major gas responsible for the

propagation of hollow bead. The presence of nitrogen indicates that there is some contamination of the shielding gas with atmospheric gases during welding. Detailed descriptions of the internal surface of the pores are given in Chapter 3.

2.15 Analysis of the Diffusible Hydrogen Content of the Weld Metal

2.15.1 Introduction

Previous work, as cited in the Literature Review (Section 1.2), has clearly demonstrated the role of hydrogen in the formation of porosity in welds. An increase in the weld metal hydrogen content, due to higher welding currents and levels of hydrogen in the arc, and in some cases surface contaminants, have been shown to increase the amount of porosity. In this study, experimental results have shown that the occurrence of hollow bead is strongly dependent on the welding current and independent of weld travel speed up to a certain limit. As it had been established that the major gas responsible for the formation of hollow bead pores is hydrogen, data on the concentration of hydrogen in welds produced using cellulosic electrodes and the variation in concentration with welding current and travel speed were required.

2.15.2 Procedure

The procedure for the determination of weld metal hydrogen followed that outlined in the Australian/New Zealand Standard AS 3752 - 1996 Welding - Methods for determination of the diffusible hydrogen content of ferritic weld metal produced by arc welding. This standard sets out the sampling and analytical procedures for the determination of diffusible hydrogen in weld metal arising from the welding of ferritic steel using arc welding processes with consumable electrodes.

The automated welding machine, with a similar set up to the one described for previous experiments, was used to perform the welding. The test pieces were clamped and aligned in a copper welding jig which served as a heat sink. The degassed test pieces, consisting of the test specimens and the run-on and run-off pieces, were ground prior to the tests to remove the surface oxide. The test pieces were then identified and weighed. Single bead on plate welds were deposited on the test pieces using the welding parameters listed in Table 2.42.

Within 5 seconds of extinguishing the arc the test pieces were removed from jig and agitated in a bath of icy water for about 20 seconds and then immersed in liquid nitrogen for storage. The storage time of the test pieces in the liquid nitrogen was between 2 and 3 hours (the standard specifies a maximum time of 3 days). The welded test specimens were separated from the run-on and run-off pieces and brushed to remove the slag. Care was taken to ensure that during these operations the test specimen did not reach $0^{o}C$ by not allowing the specimen to remain out of the bath for more than 15s.

The test specimens were then agitated in a bath of cool water until the ice skin melted, dried using compressed air and inserted in the capsules which formed part of the gas chromatograph equipment used to measure the volume of hydrogen. The capsules containing the specimens were placed in an oven at $48^{o}C$ for 72 hours to allow the hydrogen to diffuse out of the welds. The concentration of hydrogen was calculated using the data from the gas chromatograph and the weight of the welds (which was calculated by subtracting the weight of the original test pieces from the welded specimens). The data are given in terms of diffusible hydrogen content per 100g of deposited metal.

2.15.3 Welding Conditions and Results

Welding Conditions		Diffusible Hydrogen Content (mL/100g)
Weld Travel Speed (mm/min)	**Welding Current (A)**	**mL/100g of deposited metal**
300	140	30.4
300	180	46.9
300	200	54.5
500	140	41.3
500	180	48.0
500	200	54.1

Table 2.42: Results of experiments on the effect of welding conditions on the diffusible hydrogen content of welds. Average of four measurements.

2.15.4 Discussion

Overall the results demonstrate an increase in the diffusible hydrogen content with increasing welding current. This result is not unexpected since previous research on the absorption of hydrogen by metals such as iron and aluminium has shown that an increase in the welding current will increase both the rate of absorption of hydrogen and its concentration in the weld metal. The measurement of the diffusible hydrogen content of welds made using coated electrodes (White et al., 1992, Pokhodnya and Yavdoshchin, 1969 and The Lincoln Electric Company, 1986) show a similar trend.

It must be stated, however, that there is some disagreement regarding the way the diffusible hydrogen data from MMA welds are expressed, either in terms of deposited or fused metal. It has been reported that when the results of diffusible hydrogen content of welds made using

MMA welding are expressed as a function of the weight of fused metal (rather than deposited metal) the welding conditions including current are not observed to have an effect (The Lincoln Electric Company, 1986, Kiefer, 1996).

The work undertaken by White et al. (1992) using 1.2mm tubular wire consumables, both flux cored and metal cored, found that the diffusible hydrogen contents measured as a function of the weight of fused metal increased with welding currents ranging from 160 to 280A. Although this work was not carried out using MMA welding, an increase in penetration occurred with the metal cored wire which thus caused an increase in the weight of fused metal. Despite this increase in weight a reduction in diffusible hydrogen content (expressed both in terms of deposited and fused metal) with decreasing welding current, from 160 to 280A as mentioned above, was observed.

In the study performed by The Lincoln Electric Company (1986) the welding current ranged from 180 to 300A. It could therefore be possible that the narrower current range in the latter study could be responsible for the trend observed.

An explanation of these results is discussed in Chapter 5 in terms of the influence of an increase in the welding current on the temperature of the arc plasma and hence the degree of dissociation of hydrogen. Since the rate of absorption of monatomic hydrogen from the plasma will be higher than diatomic hydrogen, it is expected that a higher dissociation fraction will increase the hydrogen content of the weld pool.

2.16 Summary of Experimental Results

The experimental work has formed a large part of this research and has been successful in identifying the key variables responsible for the formation of hollow bead. An overall assessment of the entire set of results clearly shows that the welding current is the major

factor affecting hollow bead. The influence of factors such as the weld travel speed, joint geometry, brand of electrode, surface condition of the joint preparation and parent metal composition were all tested for various welding currents. The results of these experiments show that the welding current was in all cases the most influential factor; at low welding currents (around 150A) hollow bead did not occur and its incidence was not affected by changes in the other variables.

There is experimental evidence, however, that some of the variables listed above play a secondary role in promoting hollow bead. These factors are high weld travel speeds around 500 and 600mm/min, a silicon content greater than 0.33% in the parent metal and an increase in the flux moisture content.

It was observed that the high travel speeds are associated with rapid and aperiodic fluctuations in the area of the keyhole which can be related to the movement of the weld pool and hence of the solidification interface. Furthermore it appears that the formation of hollow bead at the start of the welds could be related to instabilities in the welding conditions during that period.

A silicon content between 0.33 and 0.37% silicon in the parent metal was found to increase the occurrence of hollow bead at welding currents of 180 and 200A. Hollow bead pores did not occur in most of the welds made from plates with a silicon concentration below 0.22% silicon.

An increase in the moisture content of the electrode flux was found to increase the occurrence of hollow bead, while a decrease had the opposite effect. Variations in the dimensions of the joint geometry, the brand of electrode and the presence of rust and paint on the joint preparation did not significantly contribute to the formation of hollow bead.

Analyses of the composition of the gas present inside hollow bead pores have revealed that hydrogen is the predominant gas, while carbon monoxide and nitrogen are present in small amounts. This composition may not however be the same as that present during the formation of the pore. These findings have been further discussed in Chapter 5 in correlation with a proposed model for the formation of hollow bead.

Chapter 3

METALLOGRAPHIC CHARACTERISATION OF HOLLOW BEAD

3.1 Introduction

A detailed microstructural characterisation of the hollow bead defect has formed an essential component of the modelling of the solidification process which gives rise to hollow bead. In this study the defects have been characterised in terms of their principal features such as exact location in the weld, size, shape, internal surface appearance and solidification microstructure. The following observations apply to hollow bead samples obtained from both plate and pipe welds.

3.2 Macro Examination

Cross sections of the root pass were polished and etched in 2% nital for macro-examination. A typical example is shown in Figure 3.1a. The coarse columnar microstructure in the weld zone, and the heat affected zone in the parent plate are clearly visible, as well as the "wagon tracks" (undercut regions on both sides of the top surface of the weld which contain slag inclusions). A hollow bead defect is evident close to the surface at the root of the weld.

The position, size and cross sectional shape of hollow bead were studied from optical macrographs produced from cross sections of samples of the root pass as shown in Figures

3.1a-e.

Hollow bead defects are most commonly found in or close to the reinforcement part of the root pass as shown in Figure 3.1a (Wright, 1993, Hinkel, 1984, Barkow, 1973). In these circumstances where they do not reduce the weld thickness to less than that of the adjacent parent metal they should therefore have little or no effect on the structural performance of the weld. In this study, however, similar defects have been found at the near the root surface of the root bead even with no reinforcement present as shown in Figures 3.1b. This weld was produced using a high welding current, of the order of 190A and above, and the slightly concave appearance of the bottom surface is typical of welds produced at these currents.

The thickness of the ligament at the root of the bead is typically quite small. In the Figure 3.1b it is of the order of 0.2 - 0.4 mm. The diameter of the hollow bead will in many cases change along the axis of the weld and can become quite large. The diameter of individual hollow bead pores in the welds made to study the effect of the welding conditions have been recorded in Table 2.6 (Chapter 2) and illustrate the typical values and ranges. The diameter of pores has been observed to vary from 0.5 to 1.5mm. The range for increase in diameter along the length of individual pores is between the following values, 0.5 to 1mm, 0.8 to 1mm, 0.8 to 1.2mm and 0.5 to 1.5mm.

Prior to this research, hollow bead was thought to occur only near the root surface of the root bead, usually in the reinforcement. In this study, however, defects have also been found near the top surface of the root bead as shown in Figure 3.1c. These defects display the same microstructural characteristics as those found near the root surface. A comparison of the internal surfaces of pores from near the root and top surfaces of the root bead was done in the SEM and also revealed qualitatively similar features. The macrograph in Figure 3.1d shows a

weld with evidence of porosity near both root and top surfaces of a single root bead.

The defects near the top surface of the root bead will not present any problems in pipeline construction since they will be repaired by the hot (second) pass. Figure 3.1e shows a weld with a root and a hot pass. The hot pass has melted a large portion of the root bead such that a pore located near the top surface of the first pass would be melted. The hollow bead situated near the root surface of the root bead has, however, remained intact.

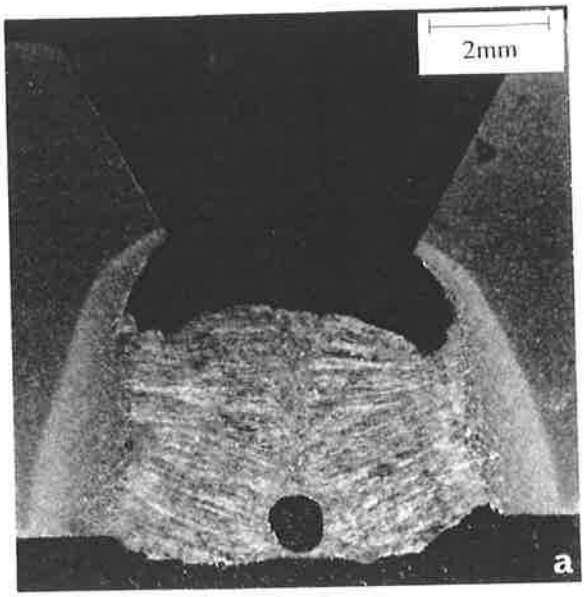

Figure 3.1a: Macrograph showing the typical appearance of hollow bead in the reinforcement part of the weld bead. Welding conditions: weld travel speed 515mm/min, welding current 190A, welding voltage 25V. Root gap 1.4mm and root face 2.5mm.

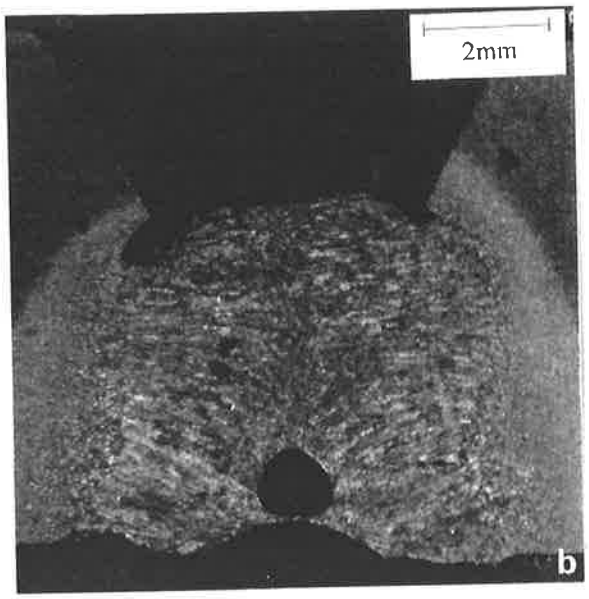

Figures 3.1b: Macrograph of a weld showing a hollow bead pore near the root surface of the root bead with no reinforcement. Welding conditions: weld travel speed 350mm/min, welding current 190A, welding voltage 25V. Root gap 1.5mm and root face 2.5mm.

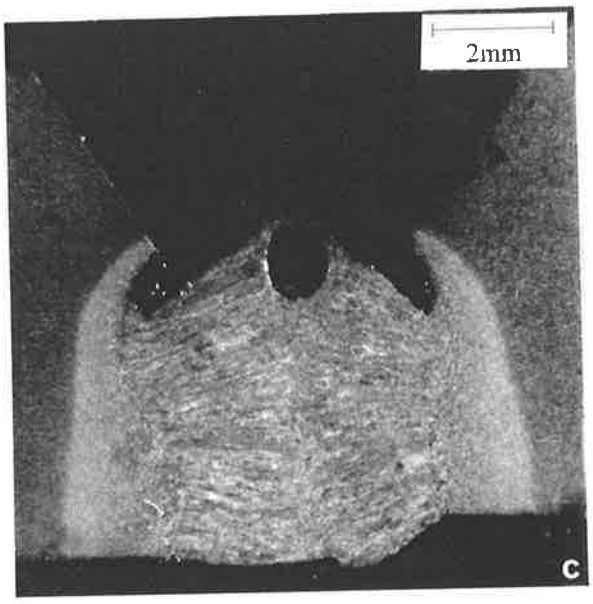

Figure 3.1c: Macrograph of a weld with a hollow bead pore located near the top surface of the weld bead. Welding conditions: weld travel speed 520mm/min, welding current 185A, welding voltage 25V. Root gap 1.0mm and root face 2.5mm.

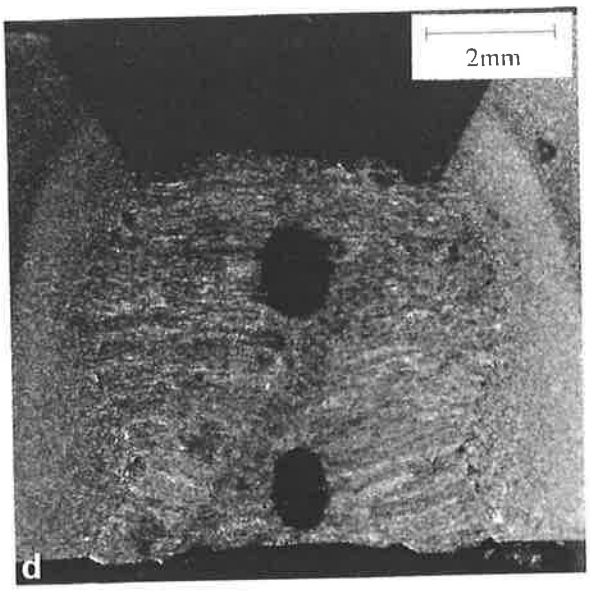

Figure 3.1d: Macrograph of a weld with hollow bead pores located near both root and top surfaces of the weld. Welding conditions: weld travel speed 300mm/min, welding current 190A(the voltage was not recorded). Root gap 0.5mm and root face 2.5mm.

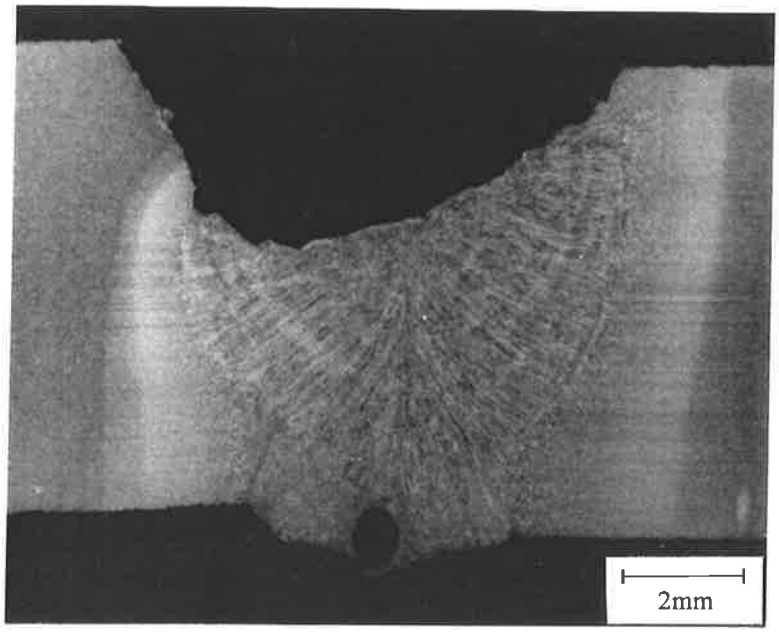

Figure 3.1e: Macrograph of a weld showing the root and hot passes with a hollow bead in the reinforcement. Welding conditions: weld travel speed 410mm/min (the welding current and voltage were not recorded), root gap 0.6mm and root face 2.5mm.

Further examples of hollow bead pores have been obtained from a research project of the Cooperative Research Centre for Materials Welding and Joining on "Weld Metal Cracking in Thin Walled X80 Pipeline Steels (Project Number 96.33)" currently being carried out at the University of Wollongong, Australia by Professor Druce Dunne and Dr. Nazmul Alum. Macrographs of these hollow bead pores have been included in Appendix E. The welds were made during WIC (Welding Institute of Canada) cracking tests using 8.5mm thick plates made from an API 5L X80 steel and cellulosic electrodes, 4.0mm in diameter and with a E9010 classification. The root face and root gap were both 1.5mm. The tests were conducted at room temperature and with no preheating.

In all cases the pores are located near the root of the beads. In some cases the pores are further away from the root surface, with the ligament between the surface of the weld and the surface

of the pore being quite thick. It was mentioned by Dr. Alum that hollow bead was observed only in the preliminary part of the experiments when stable welding conditions could not be achieved. The power source used for welding was a Migatron power source designed for GTA welding and difficulties were initially encountered in obtaining stable welding currents and voltages during manual metal arc welding.

The hollow bead pores, which formed in the welds made using the automated equipment and manually on pipe samples, typically showed a thinner ligament between the pore and weld surfaces as in Figure 3.1. The cross section of the weld beads made with the X80 steels also show in some cases a larger reinforcement than that observed in the work on hollow bead.

3.3 Solidification Microstructures

3.3.1 Solid State Transformation

The macrograph in Figure 3.2 of the cross section of a weld etched in 2% nital shows the solidification macrostructure.

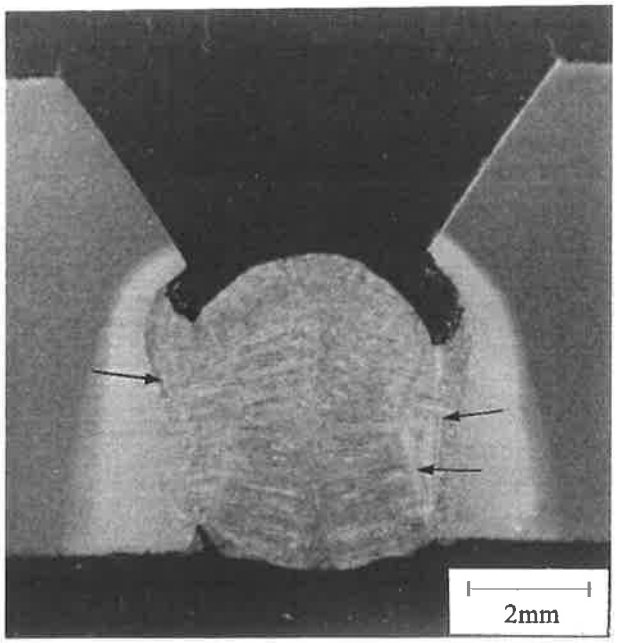

Figure 3.2: Macrograph of a weld cross section etched in 2% nital. Welding conditions: a weld travel speed of 530mm/min, welding current 185A and welding voltage 32V, root gap 1.2mm and root face 2.5mm.

The columnar microstructure is shown in more detail in Figure 3.3 and at higher magnification in Figure 3.4. The morphology at the grain boundaries consists of allotriomorphic ferrite (grain boundary ferrite in International Institute of Welding (IIW) terminology) and within the grains of Widmanstätten ferrite (ferrite with aligned second phase in IIW terminology) and acicular ferrite. The formation of the columnar grains is observed to proceed from the fusion line to the centreline and also towards the root and top surfaces. In this example the growth direction is towards the top surface in the top half of the bead and towards the root surface in the bottom half. The macrostructure of the weld in Figure 3.1d, for example, has the same growth direction characteristic. In some cases a large portion of the grains will tend to grow towards the root surface. Welds which have a much wider root surface than top surface and those which have a high width to height ratio tend to have a greater proportion of the grains growing towards the root surface (see Figures 3.24, 3.25, 3.28. 3.30, and 3.31). An explanation for these observations is given in Chapter 4 - Finite Element Modelling of Welds Pools.

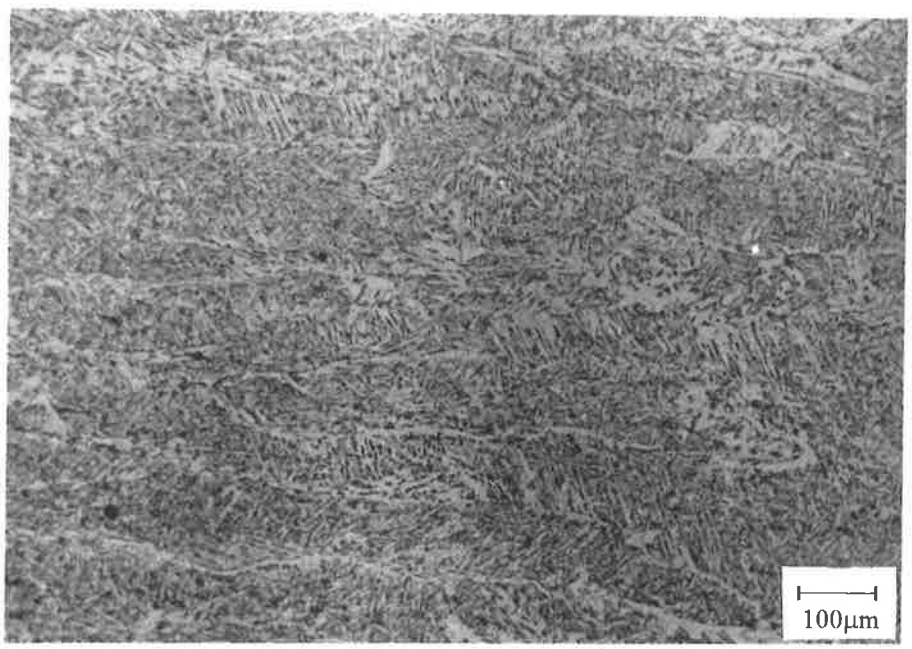

Figure 3.3: Micrograph of a weld cross section etched in 2% nital showing the columnar microstructure.

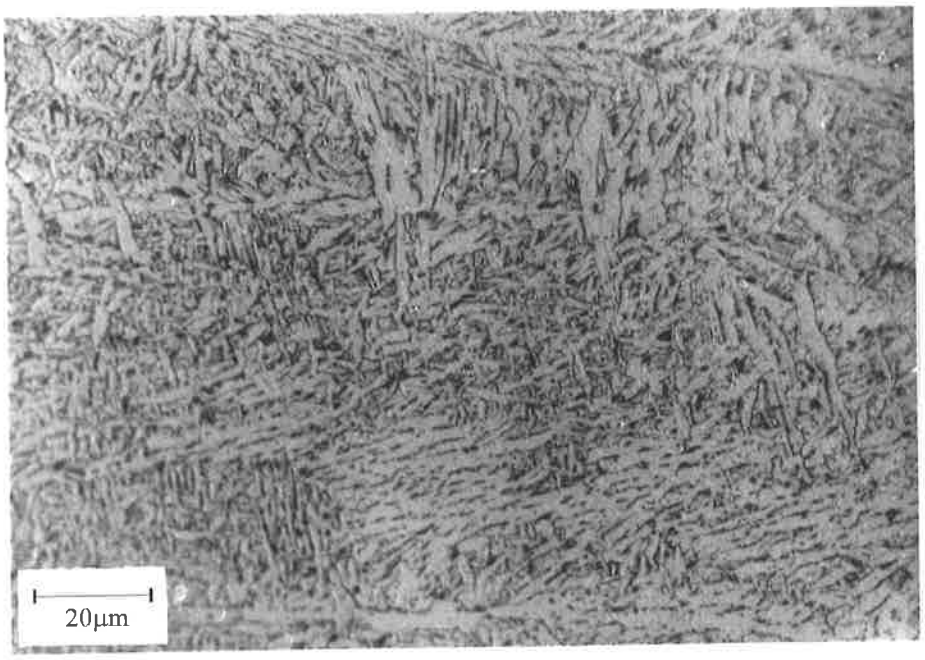

Figure 3.4: Micrograph of a weld cross section etched in 2% nital showing the columnar microstructure at higher magnification.

A different structure from the columnar one is observed around the weld centreline (Figure 3.5). This feature is explained from the microstructure seen in a longitudinal horizontal section where at the weld centreline the direction of growth becomes parallel to the welding direction. Therefore, at the centreline of a weld cross section the ends of grains are seen.

Bands of macrosegregation have produced alternate dark and bright lines (arrowed in Figure 3.2) near the fusion line and perpendicular to the direction of growth. These bands which are initially vertical close to the fusion line then move towards the top and root surfaces reinforce the view that solidification proceeds towards these surfaces.

Another common characteristic of all the weld beads is the "tapering" of the bead thickness towards the middle height of the bead. This produces a typical hour-glass shape.

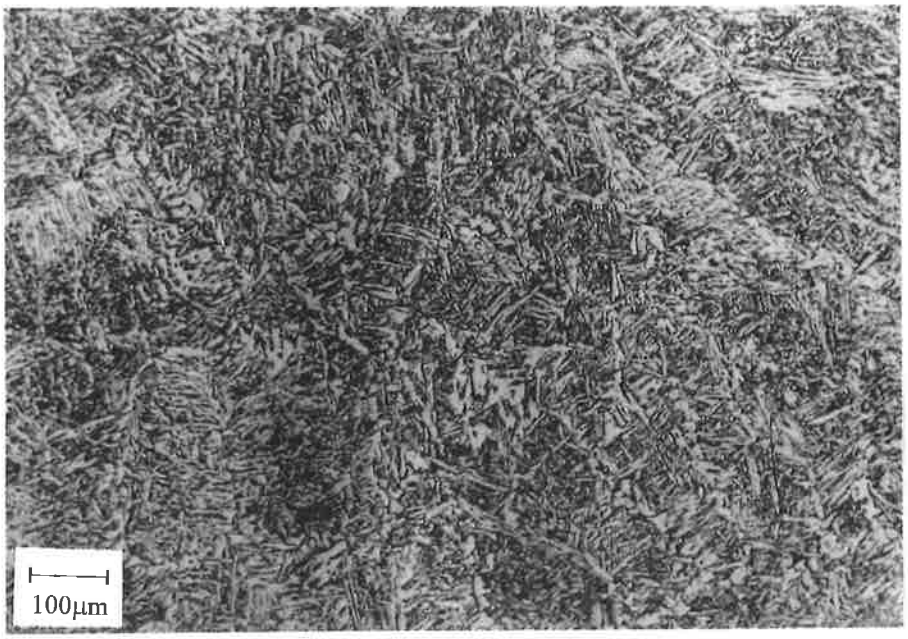

Figure 3.5: Micrograph of a weld cross section etched in 2% nital showing the microstructure at the centreline.

The direction of grain growth observed from a longitudinal horizontal section of a weld etched in 2% nital is shown in Figure 3.6. A change in the growth direction of the grains from perpendicular, at the edge of the weld pool to parallel with the welding direction toward the weld centreline is evident. This micrograph also shows a hollow bead pore (marked A in Figure 3.6) which has nucleated and propagated at the weld centreline. This centreline region would coincide with the region of highest concentration of gas-forming solutes such as hydrogen, carbon, nitrogen and oxygen, capable of nucleating gas pores. This is discussed in more detail in Section 3.4 which deals with macrosegregation in the weld.

A longitudinal horizontal section from a weld made at conditions which does not produce any hollow bead defects is shown in Figure 3.7. Again the change of growth direction is clearly seen toward the weld centreline.

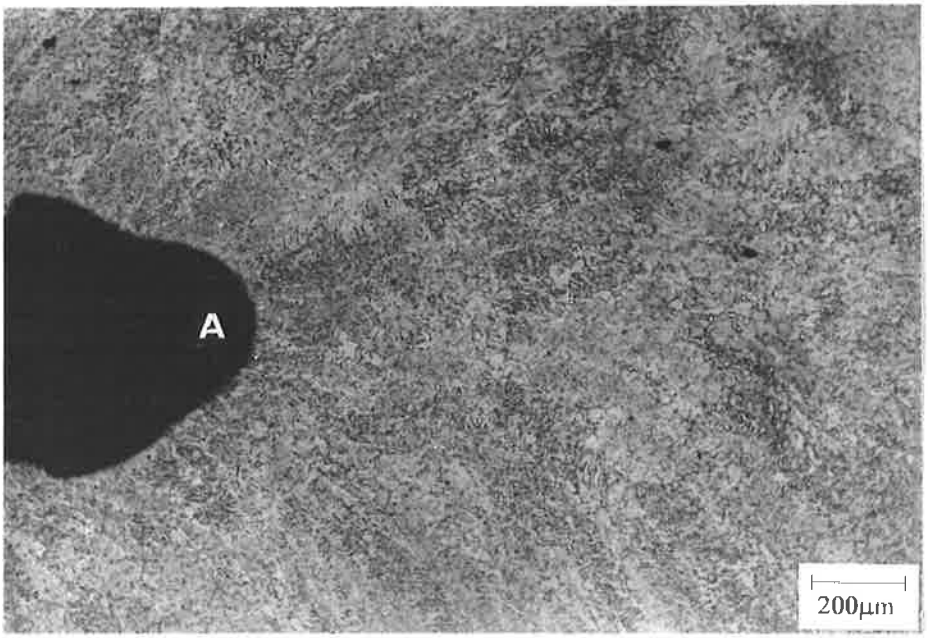

Figure 3.6: Optical micrograph of a longitudinal horizontal section of a weld, etched in 2% nital. A hollow bead pore is shown to nucleate and propagate at the weld centreline. Welding conditions: weld travel speed 400mm/min and welding current 180A, root gap 1.3mm and root face 2.0mm.

Figure 3.7: Optical micrograph of a longitudinal section of weld without hollow bead, etched in 2% nital. Welding conditions: weld travel speed 400mm/min, welding current 130A and welding voltage 20V, root gap 1.5mm and root face 1.6mm.

microstructures the prior austenite grains boundaries were observed to cross the original δ-ferrite solidification boundaries.

On the basis of these observations it can be assumed that, although the cellular dendrites are not coincident with the prior austenite grain boundaries, the direction of growth of the δ-ferrite grains will be similar to the secondary austenite grains. The work described below attempted to verify this assumption.

As explained in Section 2.11.5 the composition of the weld metal was too low in alloying elements for the primary microstructure to be revealed clearly when etching with Le Pera's reagent. To study the primary solidification microstructure welds were prepared, therefore, using electrodes high in nickel and manganese. Both elements segregate at the cellular-dendritic boundaries due to their small equilibrium partition coefficients. The concentration of nickel was further increased in some welds by the addition of nickel shims to the joint preparation. Le Pera's reagent, which is a solution of picric acid, sodium metabisulphite and water, was then used to reveal the microsegregation and thus enable the observation of the primary solidification mode.

3.3.2.1 Materials

Test plates were prepared from 5mm and 8.3mm API 5L X70 steel plates.

The Lincoln Electric Company manufactured 2 types of electrodes with special alloying additions, namely high levels of nickel and manganese. The details of the chemistry of the electrode are given in Table 3.1.

Individual nickel shims, of 99.0% purity and 0.15mm thick, were held in place on the root face by gluing the ends to the two ends of the plates. The concentration of nickel in the weld

metal was varied by changing the number of nickel shims placed in the joint preparation. 5P+ electrodes were used to make these welds. The concentration of nickel in the welds was verified using microprobe analyses and showed an average concentration of about 3%.

It was recognised that increasing the concentration of nickel in the weld could change the primary solidification phase as nickel is a strong austenite former. However, the objective of this work was to determine whether the primary solidification microstructure had an approximately similar pattern as the solid state microstructure, that is a change in growth direction at the weld centreline. Since the direction of dendritic growth of ferrite and austenite are the same, the <001> direction (Chalmers, 1962), then cellular dendrites having either a bcc or fcc structure will grow with the same preferred growth direction, <001>, closely aligned with the direction of the maximum thermal gradient in the weld pool. The pattern of the primary solidification microstructure is thus expected to be the similar for both ferrite and austenite.

Electrode	P	S	C	Si	Mn	Ni	others
FW5P-Ni	0.019	0.021	0.110	0.090	0.300	1.070	trace
FW5P-Ni/Mn	0.020	0.023	0.150	0.150	0.930	1.080	trace

Table 3.1: Composition of all-weld metal in percent by mass.

3.3.2.2 Experimental Conditions

The joint geometry used was a root face of 1.6mm, a root gap of 1.0-1.5mm and bevel angle of 30^{o}.

3.3.2.3 Metallography

The specimens for this study were prepared by grinding and polishing cross sections of welds

and then etching with Le Pera's reagent. This etchant enables the primary solidification microstructure to be revealed by staining the regions of microsegregation of nickel and manganese at the cellular dendritic boundaries to a lesser degree(see also the work by Powell and Lloyd, 1995 described in Section 1.2.9). These regions, therefore, appear as bright lines on the microstructure when viewed in an optical microscope.

3.3.2.4 Discussion

Optical micrographs of cross sections etched with Le Pera's reagent are shown in Figures 3.8 to 3.10. The bright lines on the microstructure represent areas of microsegregation at the cellular-dendritic boundaries, and therefore reveal the primary solidification microstructure. The distance between these lines, which is approximately 20 microns, gives an indication of the diameter of the cellular dendrites.

At the weld centreline an "apparent equiaxed" region is observed and represents the cross section of cellular dendrites as they are seen “end on” at the weld centreline where the direction of growth changes (Figure 3.10).

Figure 3.8: Micrograph of a weld cross section etched with Le Pera's reagent showing microsegregation in the cellular dendritic microstructure.

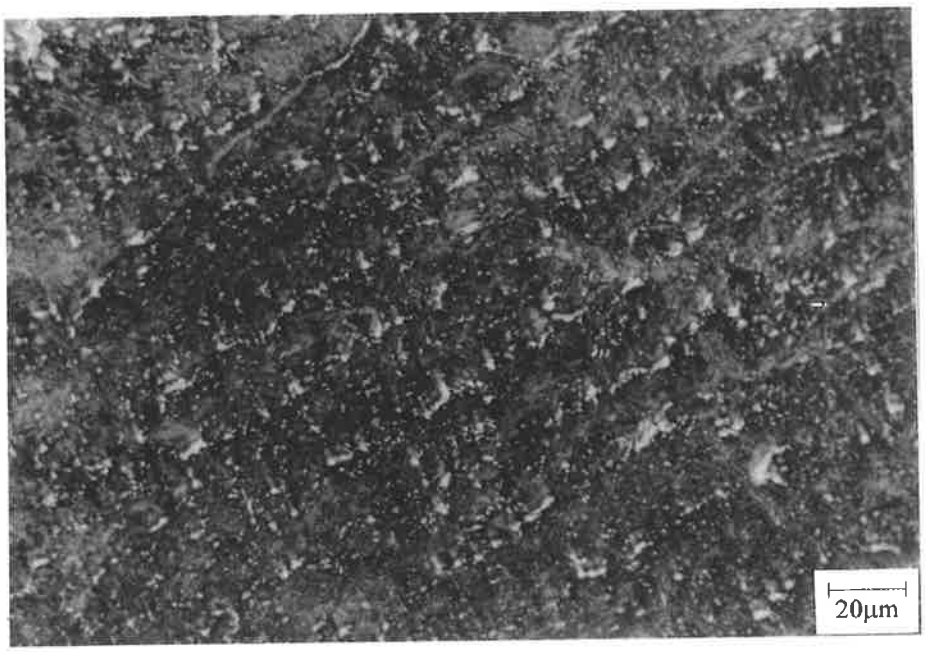

Figure 3.9: Higher magnification micrograph of the microstructure in Figure 3.8.

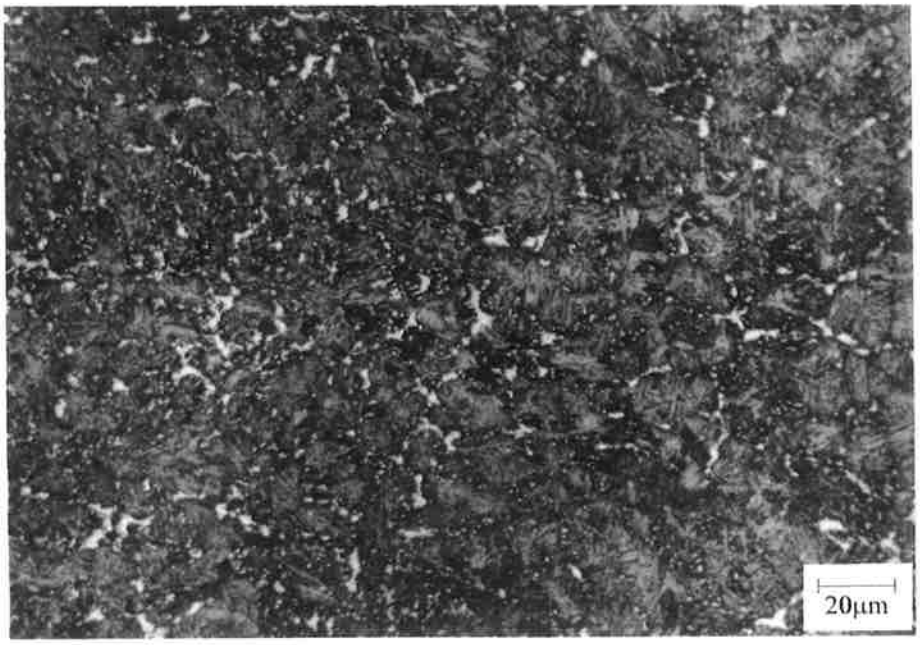

Figure 3.10: Micrograph of the microstructure at the centreline region of the weld.

The micrographs in Figures 3.11 to 3.18 are from a longitudinal horizontal section of a weld which contains 3% nickel. Figure 3.11 is macrograph of the weld showing a hollow bead pore at the centreline. The change in growth direction at the weld centreline to parallel with the welding direction, which is typical of the welds studied in this work, is evident. The weld was etched in 2% nital after etching in Le Pera's reagent. The primary microstructure is more clearly seen in this sample due to the higher concentration of nickel.

The microstructure shown in Figure 3.12 shows the primary growth structure in a region adjacent to the start of the hollow bead (marked A in Figure 3.11). The boundaries of the cellular dendrites are seen as orange lines about 20 - 25 microns apart and the prior austenite grain boundaries as white lines. The two microstructures are seen more clearly at higher magnification in Figure 3.13. Both microstructures curve and follow a similar direction as growth proceeds towards the weld centreline. It was mentioned previously that this weld could have solidified with austenite as the primary phase, but that the direction of cellular

dendritic growth would be similar to that for δ-ferrite. It can thus be assumed that the primary solidification microstructure will have a similar pattern as the solid state transformation microstructure. Some evidence which points to the formation of austenite as the primary solidification phase is the coincidence of the boundaries of the cellular dendrites and those of the prior austenite grains and which are shown by arrows in Figures 3.13 and 3.14.

The microstructure shown in Figures 3.14 and 3.15 are from areas marked B and C respectively in Figure 3.11. The microstructure in Figure 3.14 is not curved as it is in an area which is close to the fusion line where the grains have not yet changed direction. The microstructure in the area marked C again shows the change in growth direction at the weld centreline.

The primary microstructure adjacent to the hollow bead pore is shown in Figures 3.16 and 3.17 (marked D in Figure 3.11). The cellular dendrites grow to the surface of the pore (the black region at the top of the micrograph) which explains the features observed on the internal surface of the pores detailed in Section 3.7 - Scanning Electron Microscopy of Hollow Bead Pores. Also apparent in the microstructure are bands (marked by arrows) representing areas of macrosegregation. One of the bands is seen at higher magnification in Figure 3.18. The concentration of solutes in the band appears to have increased, resulting in a dense bright region. The effect of macrosegregation on the formation of porosity has been discussed in the Literature Review (Section 1.2) and has also been studied in more detail in this research (Section 3.4).

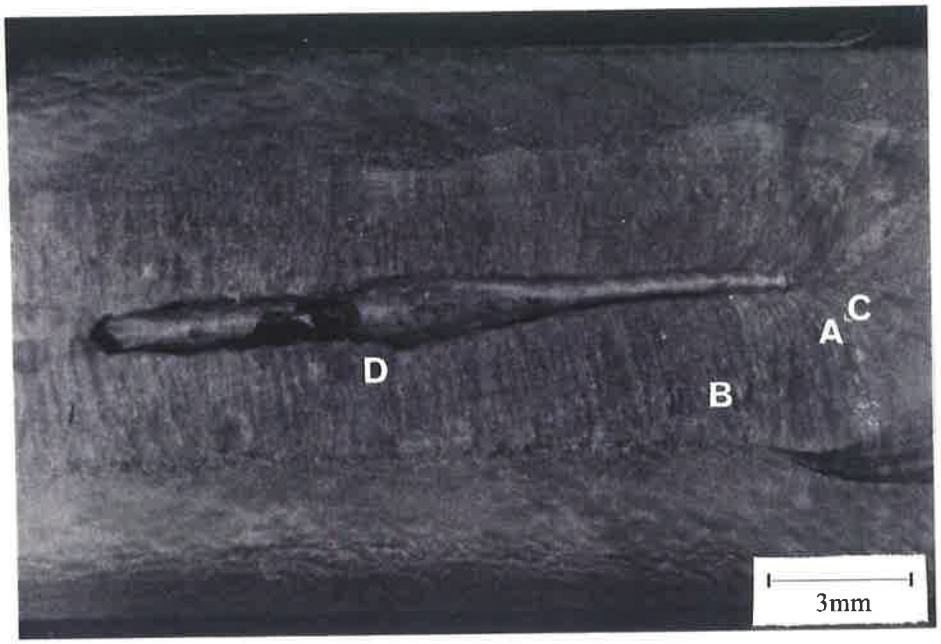

Figure 3.11: Macrograph of the longitudinal horizontal section of the weld etched in nital. Welding conditions: a weld travel speed of 400mm/min and a welding current of 180A. The root gap was 1.5mm and the root face was 2.0mm.

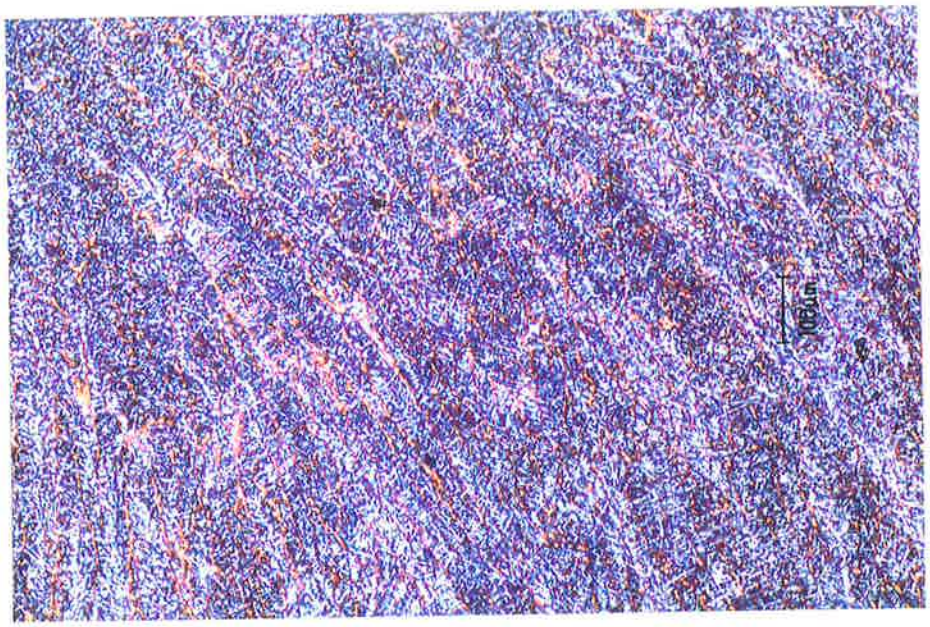

Figure 3.12: Micrograph of an area at the start of the weld (marked A) which has been etched in Le Pera's reagent.

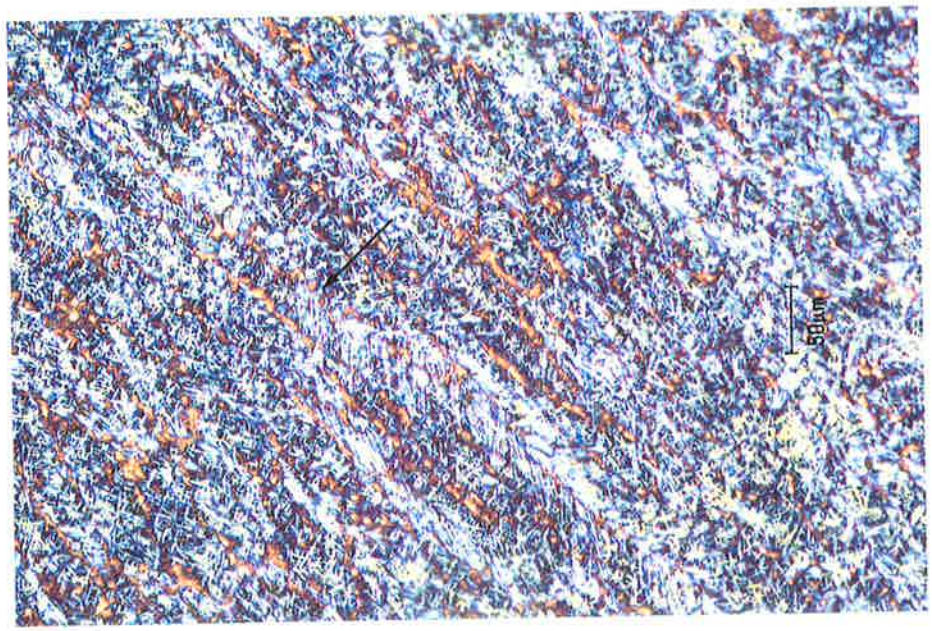

Figure 3.13: Higher magnification micrograph of Figure 3.12 showing both the α-ferrite and primary microstructures.

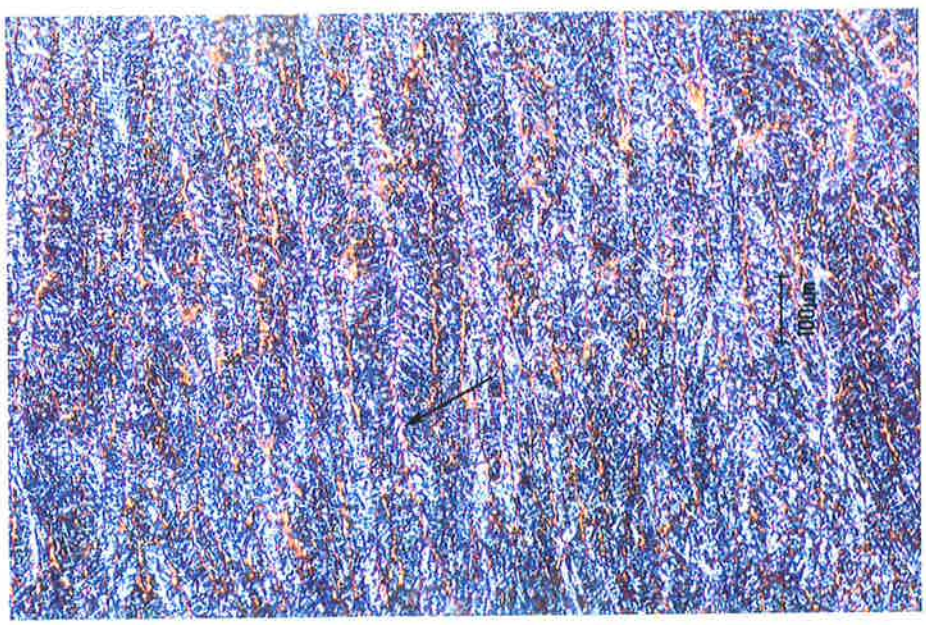

Figure 3.14: Micrograph of the area of the weld marked B. Etched in Le Pera's reagent.

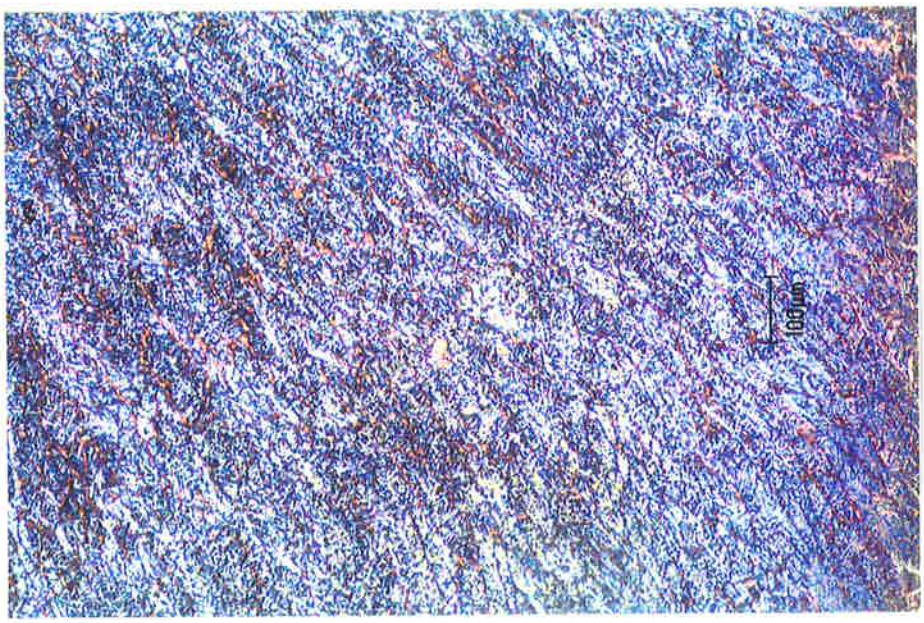

Figure 3.15: Micrograph of the area of the weld marked C. Etched in Le Pera's reagent

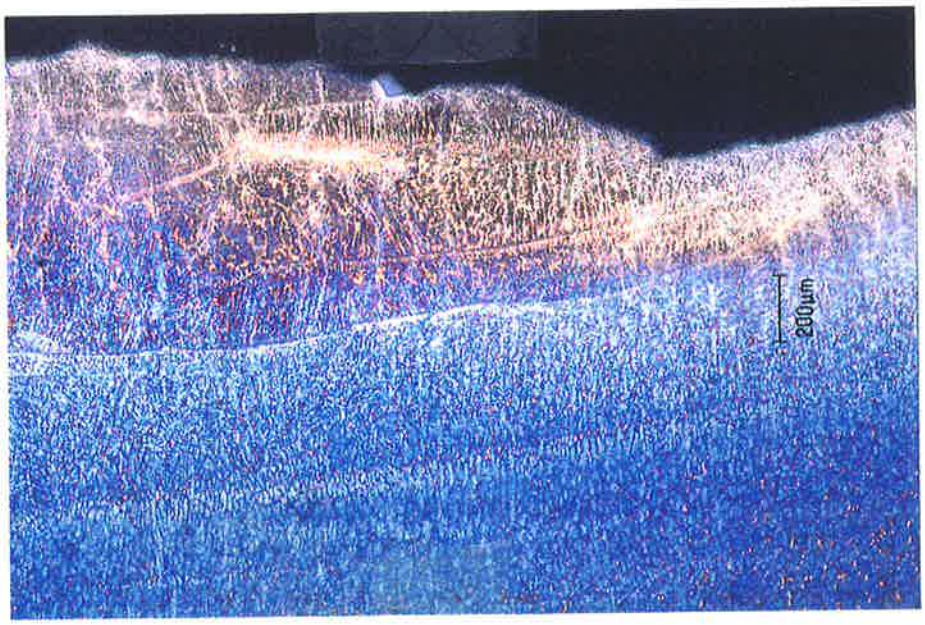

Figure 3.16: Micrograph of an area of the weld next to the hollow bead pore (marked D in Figure 3.11). Etched in Le Pera's reagent.

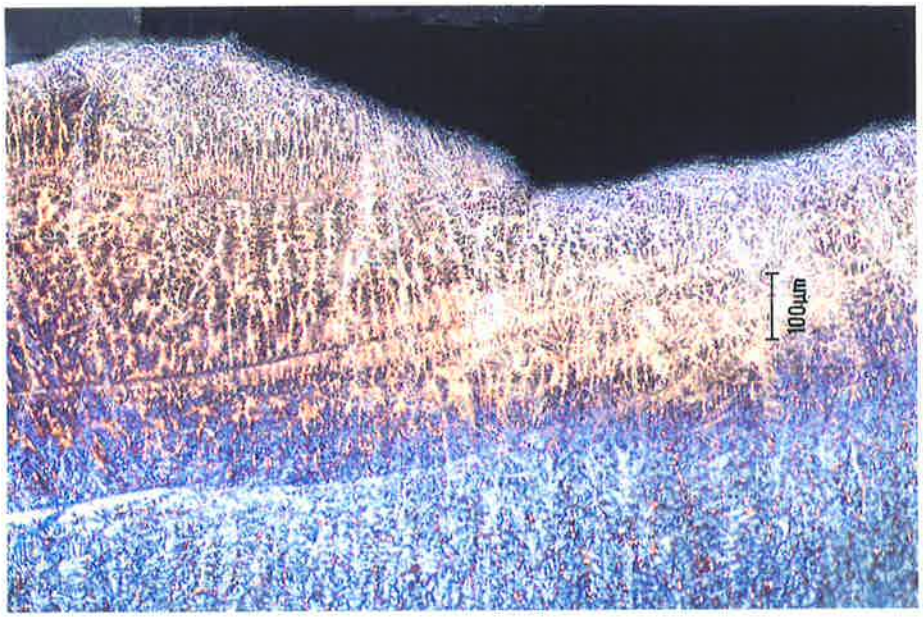

Figure 3.17: Higher magnification micrograph of the area of the weld near the pore seen in Figure 3.16. Etched in Le Pera's reagent.

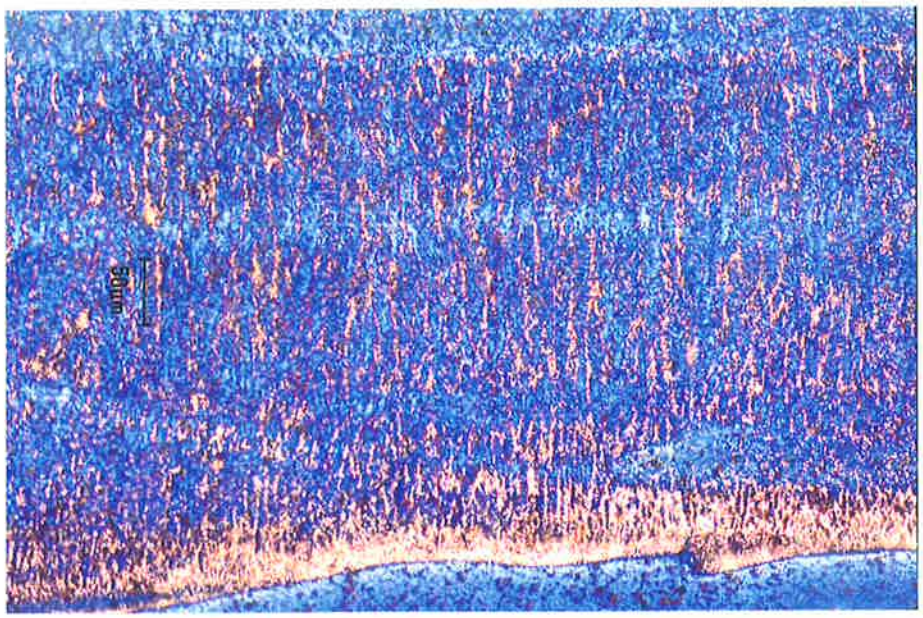

Figure 3.18: Higher magnification micrograph of the bands seen in Figure 3.17 where macrosegregation has occurred.

3.4 The Influence of Macrosegregation

In the Literature Review the role of macrosegregation in the formation of porosity was described (David and Vitek, 1989, Davies and Garland, 1975, D'Annessa, 1966). In previous research fine globular porosity has been observed along solutes bands where the concentration of elements less soluble in the solidifying metal, including gases, increased due to a sudden rise in solidification rate. In these regions the concentration of gases increases sufficiently for gas pores to nucleate. Powell and Lloyd (1995) have also shown that elongated pores nucleate where solute banding occurs and that the diameter of the pore increases at subsequent solute bands. This suggests the nucleation and growth of elongated gas pores as well as the resulting shape (which exhibits continuous irregularities in the pore diameter) is not likely to be due to the coalescence of bubbles. Instead the likely mechanism is the sudden increase of gas-forming solutes at the solidification interface (due to macrosegregation).

In this work a study of the variations of elemental concentrations in welds was carried out using electron microprobe analysis to gain a better understanding of segregation in the welds used in this research. The technique produced maps of the distribution of manganese in the weld microstructure from cross sections and longitudinal horizontal sections. The variation in concentration of manganese is indicated by the change in colours in the map. A colour scale is shown on the right hand side which ranges from 0 (black) to 2% (white) manganese. Macrosegregation of this element is clearly seen at high and low magnification in Figures 3.19 - 3.21, while microsegregation is apparent, but not clear, at high magnification in Figure 3.22. The maps in Figures 3.19 - 3.21 give a quantitative distribution of manganese in the welds.

The map in Figure 3.19 is from a longitudinal horizontal weld section with the centreline located at the centre of the map (indicated by arrow). The welding direction is from right to left. The blue band at the bottom left hand corner is a pen mark which was drawn on the sample to indicate the region to be analysed.

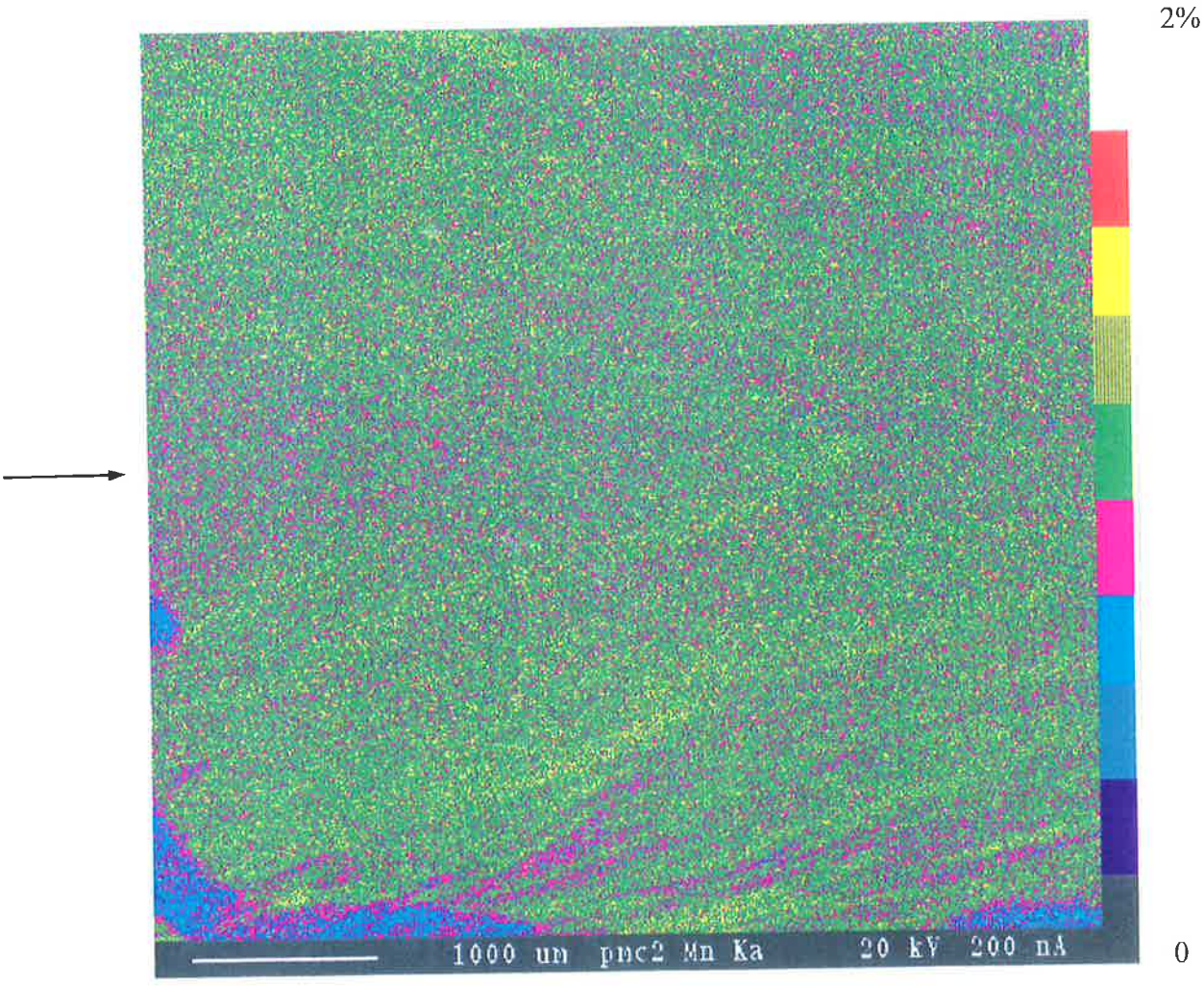

Figure 3.19: Elemental map from the microprobe showing the macrosegregation of manganese in a longitudinal horizontal section of a weld. The centreline of the map corresponds approximately to the weld centreline of that section. Welding conditions: weld travel speed 400mm/min and welding current 180A. Weld metal composition: 0.105%C, 1.17%Mn and 0.16%Si. Weld size: 6mm wide.

Figure 3.20 is another longitudinal horizontal section with the start of a hollow bead pore seen as a purple circular section at centre on the left side.

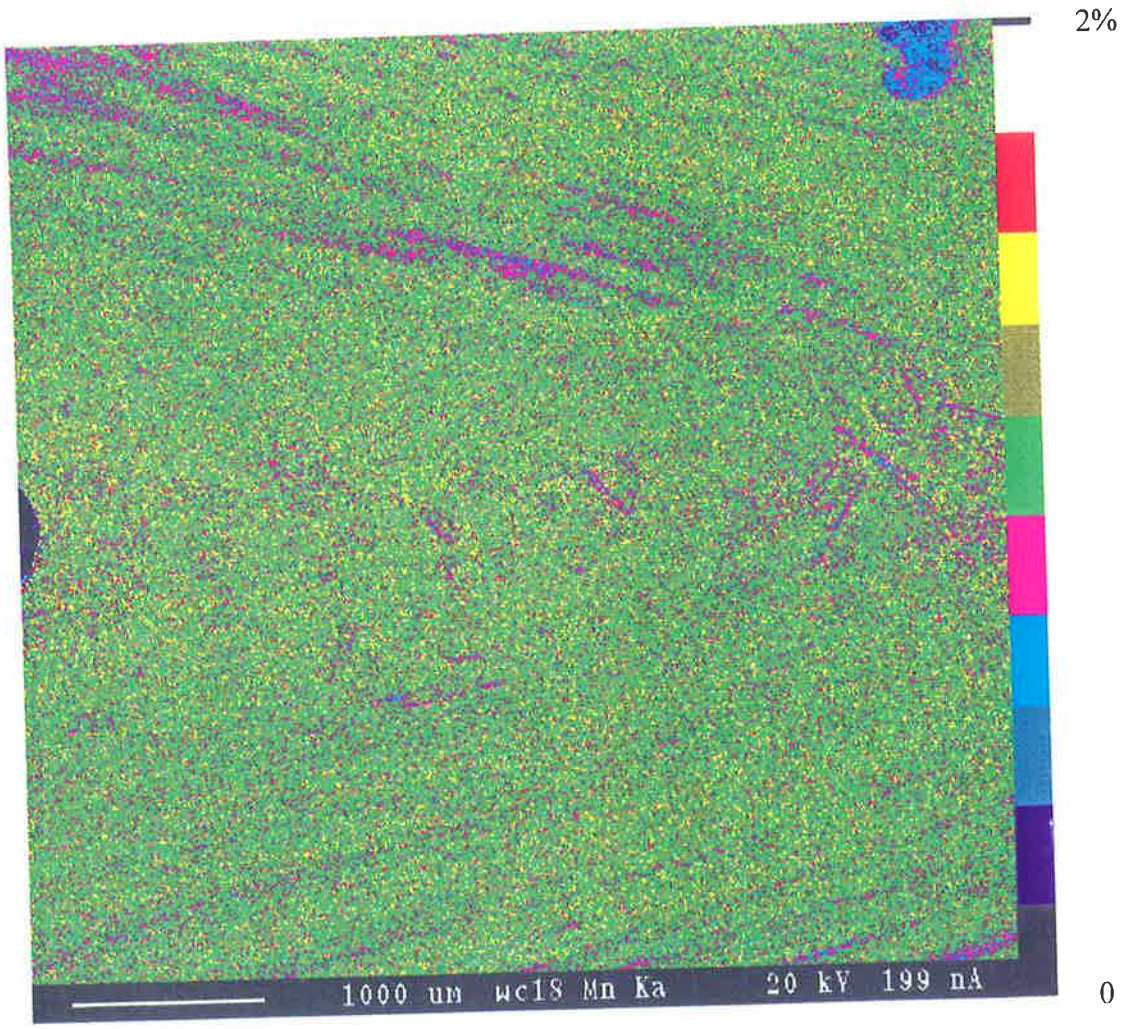

Figure 3.20: Elemental map from the microprobe showing the macrosegregation of manganese in the longitudinal horizontal section of a weld in a region before the start of a hollow bead pore. The centreline of the map corresponds approximately to the weld centreline of that section. The purple circular section at the centreline on the left hand side of the map is the start of the pore. Welding conditions: weld travel speed 400mm/min and welding current 180A. Weld metal composition: 0.122%C, 1.46%Mn and 0.34%Si. Weld size: 5mm wide.

A map of the region at the top centre portion of a weld cross section is shown in Figure 3.21. A pen mark is again seen as a blue band on the top right hand corner of the map.

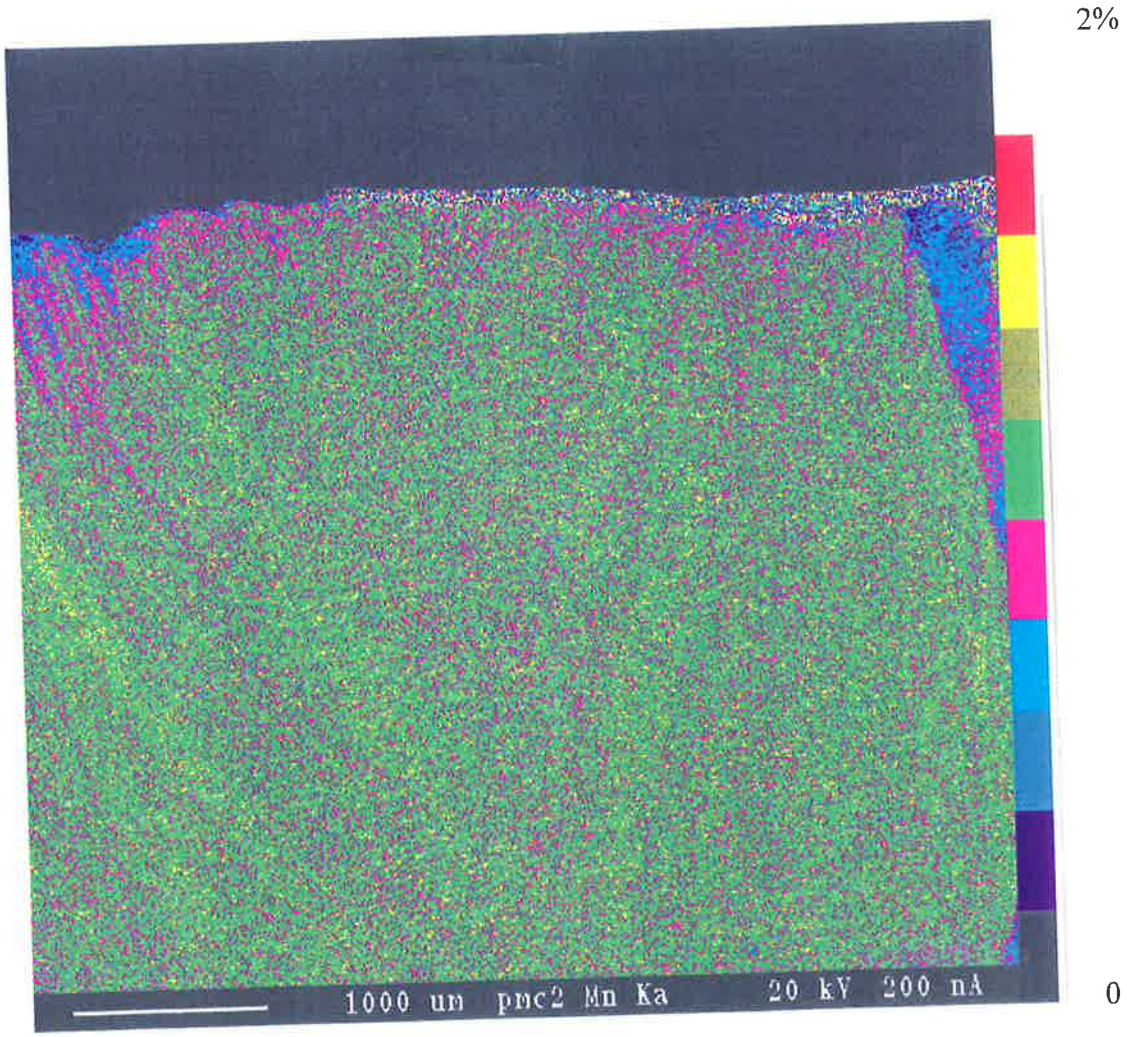

Figure 3.21: Elemental map from the microprobe showing the macrosegregation of manganese in a weld cross section. The centreline of the map corresponds approximately to the weld centreline of that section. Welding conditions: weld travel speed 400mm/min and welding current 180A. Weld metal composition: 0.105%C, 1.17%Mn and 0.16%Si. Weld size: 6mm wide cross section.

Higher magnification maps of a longitudinal horizontal weld section are shown in Figure 3.22. These maps only give qualitative information on the distribution of manganese. The map on the left shows a portion of the parent metal and the weld fusion line and the map on the right an adjacent segment of the weld. The conditions used to produce the welds, their composition and size are given in the figure captions.

These maps reveal an important characteristic in the way the weld solidifies; banding due to macrosegregation occurs throughout the weld (from the fusion line to the centre of the weld).

Welds etched in 2% nital suggest that banding is only prominent close to the fusion line (for example the lines arrowed in Figure 3.2) where the density of bands is highest. The distribution of manganese in Figure 3.22 shows this feature; in the map on the left hand side the (red) bands representing locations high in manganese near the fusion line are very close together. Although these bands become further apart they are still present at the centre of the weld.

The map of the weld cross section also shows that banding occurs up to the weld centreline (indicated by arrow in Figure 3.21). The slope of these bands indicates that grain growth, which is perpendicular to the bands, is in the direction of the top surface as previously deduced from the micrographs in Section 3.3. It is therefore possible that gas-forming solutes can segregate in high concentrations at the weld centreline and near the root and top surfaces and hence contribute to the formation of gas bubbles.

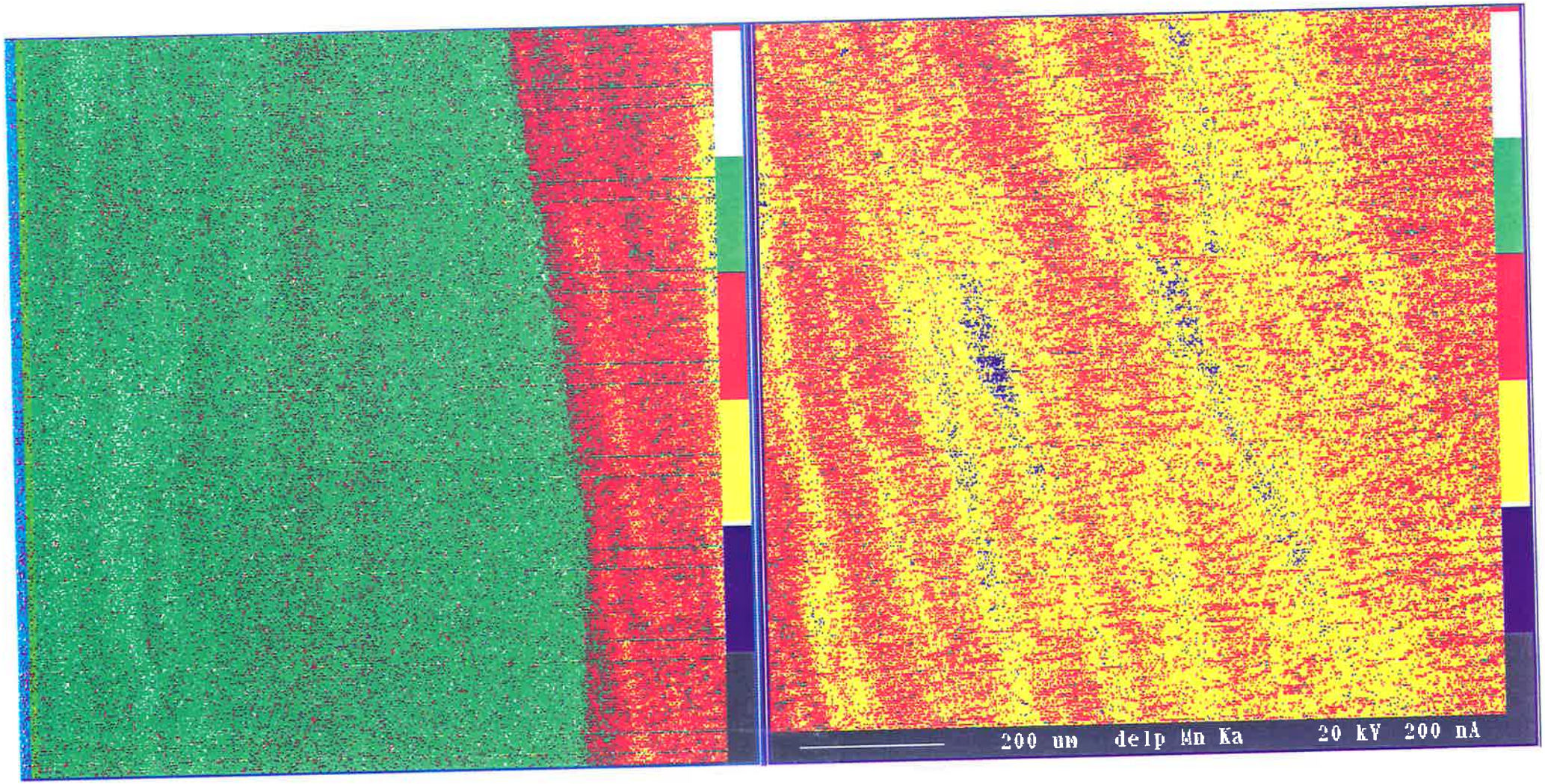

Figure 3.22: Higher magnification elemental maps showing macrosegregation of manganese close to the fusion boundary of a weld. Welding conditions: weld travel speed 400mm/min and welding current 180A. Weld composition: 0.145%C, 1.00%Mn and 0.13%Si.

3.5 The Influence of Welding Conditions on the Size of the Weld Bead

The relationship between the occurrence of hollow bead and the size of the weld pool at various welding conditions has been studied from cross sections and longitudinal horizontal sections of welds. The sections were polished and then etched in 2% nital.

Considering first the weld cross sections obtained at various levels of current at constant weld travel speeds, Figures 3.23-3.25 show welds produced at a constant travel speed of 300mm/min with the current increasing from 130A to 214A. As the heat input increases the volume of the weld bead increases as does the width of the surfaces at the root and top of the weld bead. The greater volume of weld metal formed as the welding current increases is expected to result in an increase in the absorption of hydrogen and other gases. However, the rate of desorption of gases will also increase as the size of the bead and hence the weld pool also increases. Similar comments apply for travel speeds of 400 and 600mm/min (Figures 3.26 - 3.28 and 3.29 -3.21 respectively).

The effect of travel speed can be assessed by comparing the weld beads in Figures 3.23 - 3.25 and 3.29 -3.31. At both low (300mm/min) and high speeds (600mm/min) the volume of the weld bead and both surfaces at the top and root of the welds increase with increasing current. The volume of weld metal at the lower weld travel speed of 300mm/min is greater for all values of welding current compared to the volume of weld metal at 600mm/min since the heat input is greater. When comparing the areas of the cross sections at these two weld travel speeds, it is observed that the increase in area with increasing current is greater at 300 than 600mm/min. It is possible therefore that the concentration of hydrogen is higher in the smaller weld pools made at this high travel speed. As described in the Literature Review (Section 1.2), previous studies on the absorption of hydrogen in weld pools found that a decrease in the weight of metal deposited resulted in an increase in the concentration of hydrogen (White et al., 1992, Woods, 1974, Salter, 1963).

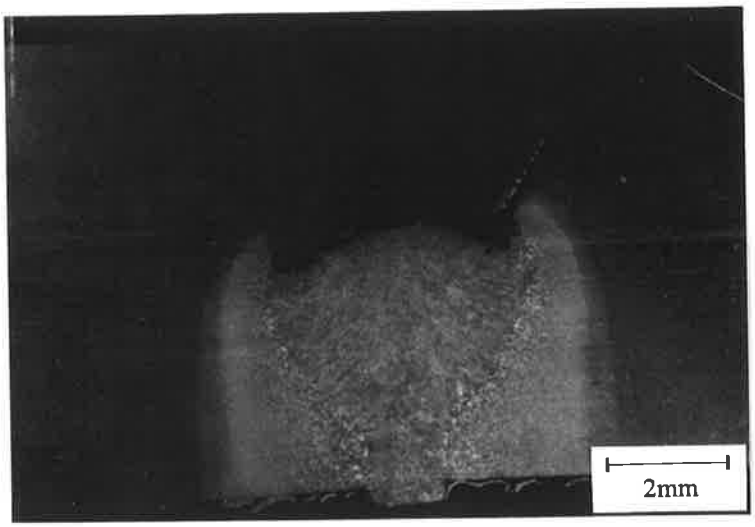

No hollow bead formed in this weld. The calculated area is 11mm^2.

Figure 3.23: Cross section of a weld made at 300mm/min and 143A (heat input equal to 0.57kJ/mm).

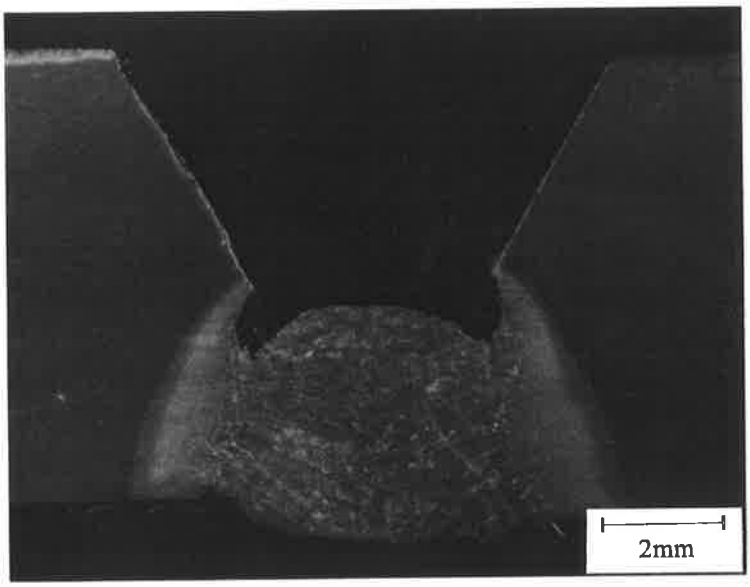

In this weld the total number of hollow bead is 1 and the total length is 1mm.
The calculated area is 1135mm^2.

Figure 3.24: Cross section of a weld made at 300mm/min and 163A (heat input equal to 0.70kJ/mm).

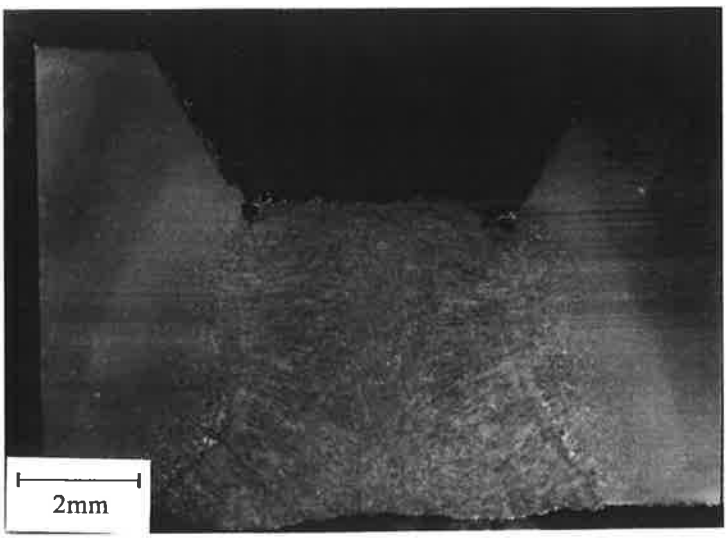

In this weld the total number of hollow bead is 5 and the total length is 20mm.
The calculated area is 1740mm^2.

Figure 3.25: Cross section of a weld made at 300mm/min and 187A (heat input equal to 1.0kJ/mm).

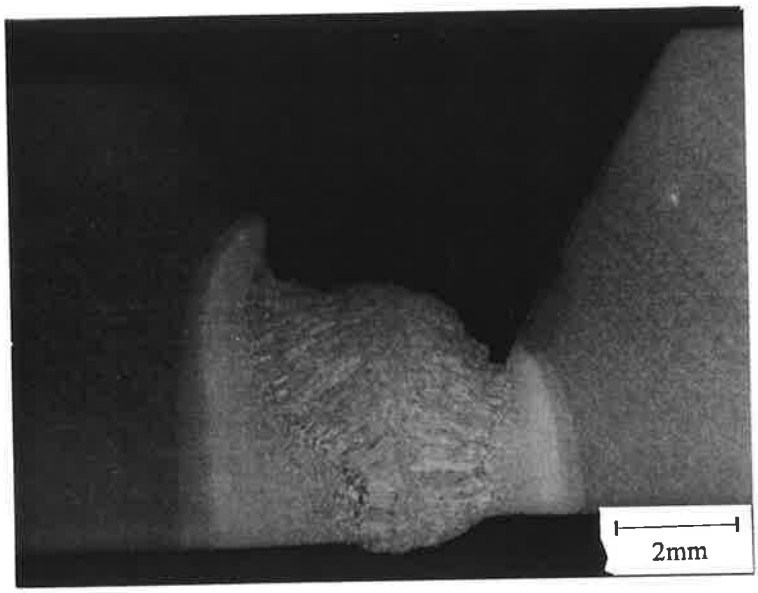

No hollow bead formed in this weld. The calculated area is 812mm^2.

Figure 3.26: Cross section of a weld made at 400mm/min and 130A (heat input equal to 0.44kJ/mm).

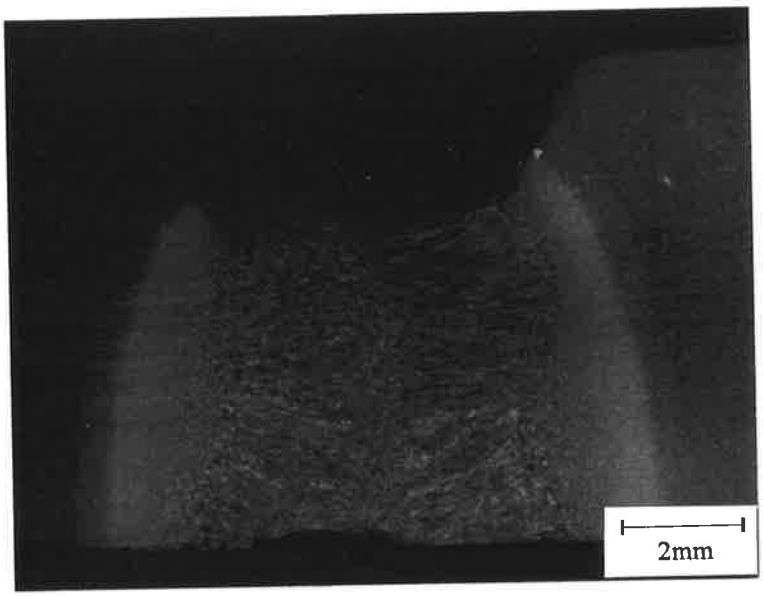

In this weld the total number of hollow bead is 2 and the total length is 12mm.
The calculated area is 1784mm^2.

Figure 3.27: Cross section of a weld made at 400mm/min and 185A (heat input equal to 0.74kJ/mm).

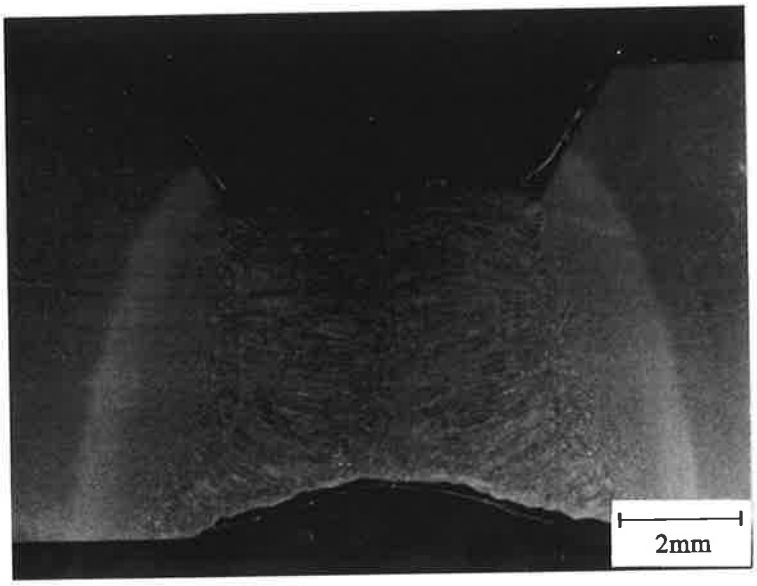

In this weld the total number of hollow bead is 10 and the total length is 42mm.
The calculated area is 1832mm^2.

Figure 3.28: Cross section of a weld made at 400mm/min and 214A (heat input equal to 0.89kJ/mm).

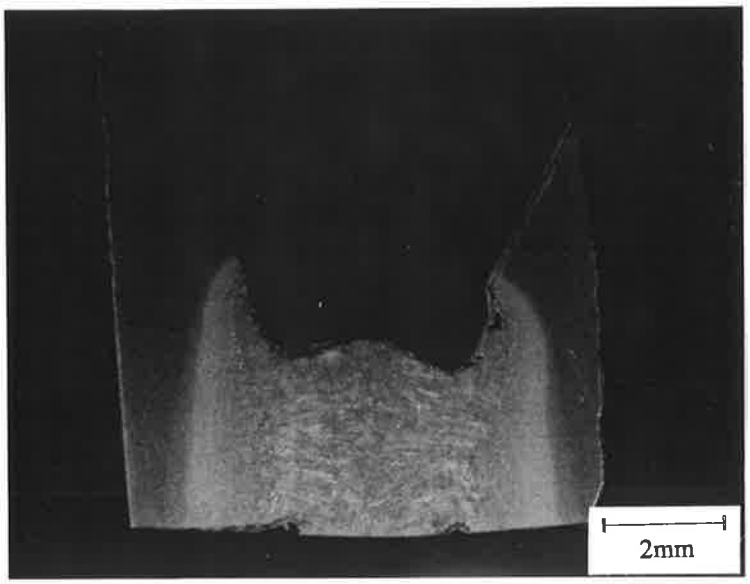

No hollow bead formed in this weld. The calculated area is 698mm^2.

Figure 3.29: Cross section of a weld made at 600mm/min and 130A (heat input equal to 0.32kJ/mm).

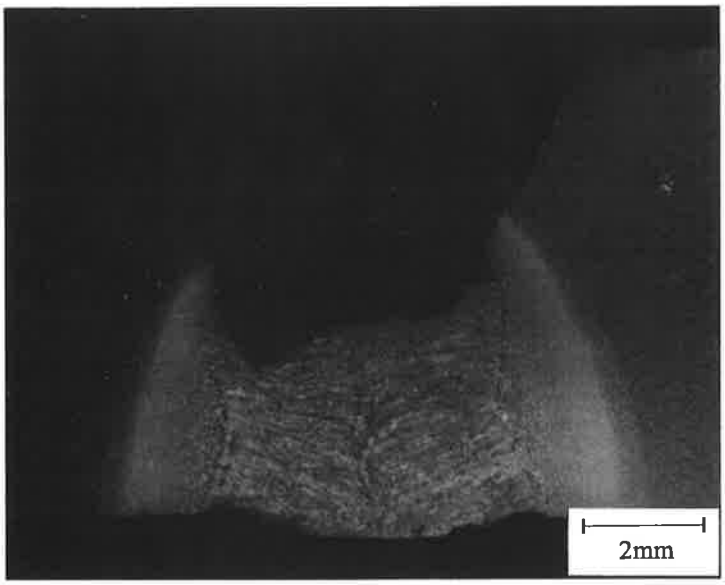

In this weld the total number of hollow bead is 5 and the total length is 16mm.
The calculated area is 1009mm^2.

Figure 3.30: Cross section of a weld made at 600mm/min and 159A (heat input equal to 0.42kJ/mm).

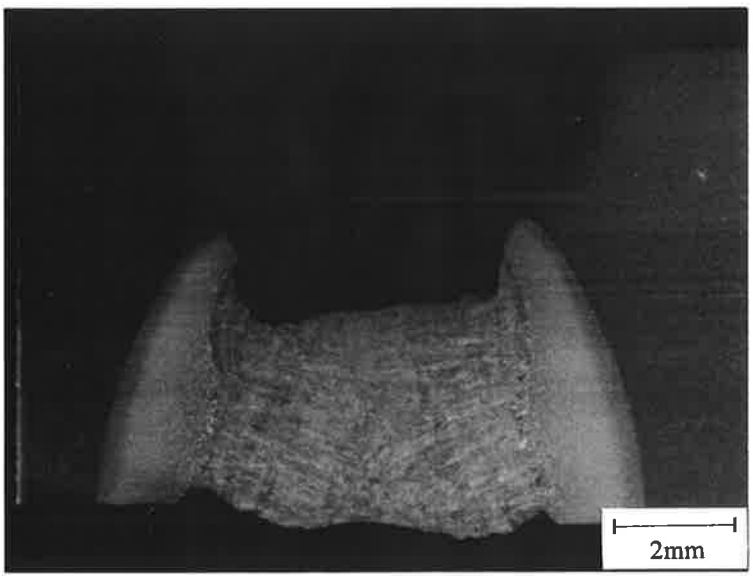

In this weld the total number of hollow bead is 9 and the total length is 45mm.
The calculated area is 1209mm^2.

Figure 3.31: Cross section of a weld made at 600mm/min and 193A (heat input equal to 0.56kJ/mm).

Figures 3.32 - 3.43 are longitudinal horizontal sections of welds, etched in 2% nital, which have been arranged to show the changes in weld bead shape and size as the current increases at constant weld travel speed. The macrographs in Figures 3.33, 3.34, 3.36, 3.38 and 3.40 show undercuts near the fusion zones. These were not removed during polishing as they extended deeply into the weld and it was desired to study the structure close to the root surface of the weld bead.

Also apparent on these macrographs are solute bands due to macrosegregation. These bands are perpendicular to the direction of growth and appear more numerous and more closely distributed close to the fusion line. At the very low currents (around 130A) where hollow bead never occurs solute bands are less apparent suggesting a more uniform solidification rate and thus less segregation of solutes with low equilibrium coefficients. This observation can be correlated with the findings made from the filming of the keyhole (Section 2.13). The high variations in the area of the keyhole associated with conditions which promote the formation of hollow beads point to the fact that large and rapid changes in solidification rates are partly responsible for the formation of hollow bead pores.

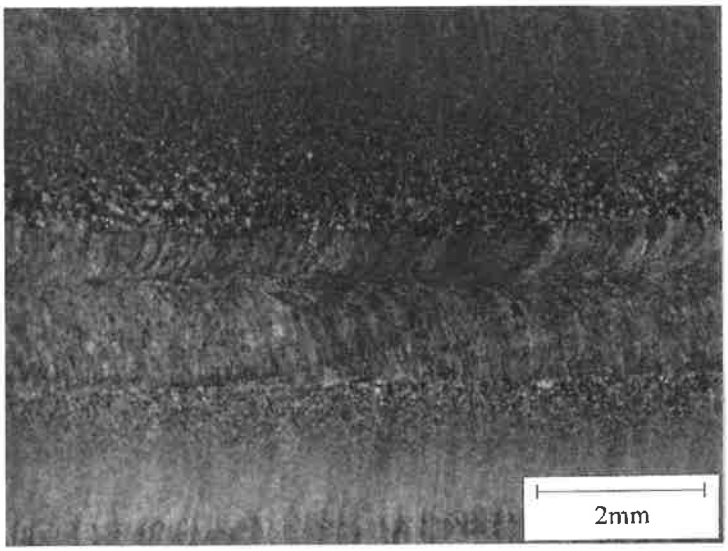

Figure 3.32: Longitudinal horizontal section of a weld made at 300mm/min and 128A (heat input equal to 0.64kJ/mm. No hollow bead formed in this weld.

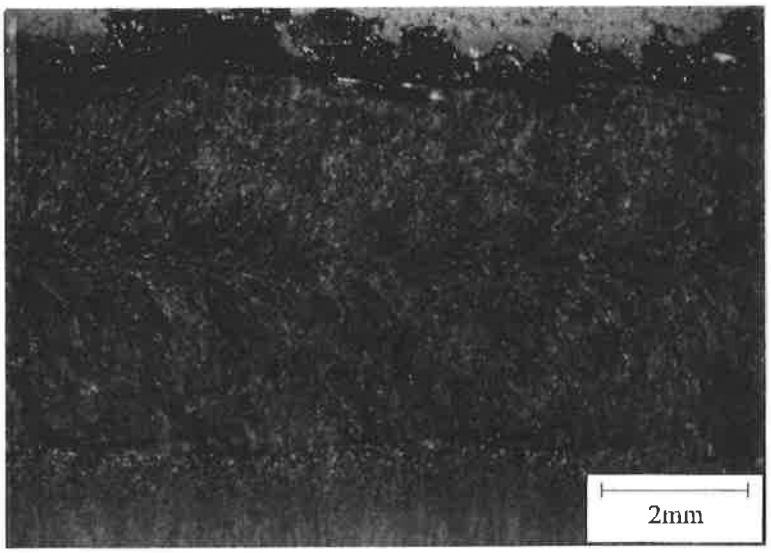

Figure 3.33: Longitudinal horizontal section of a weld made at 300mm/min and 142A (heat input equal to 0.71kJ/mm). No hollow bead formed in this weld.

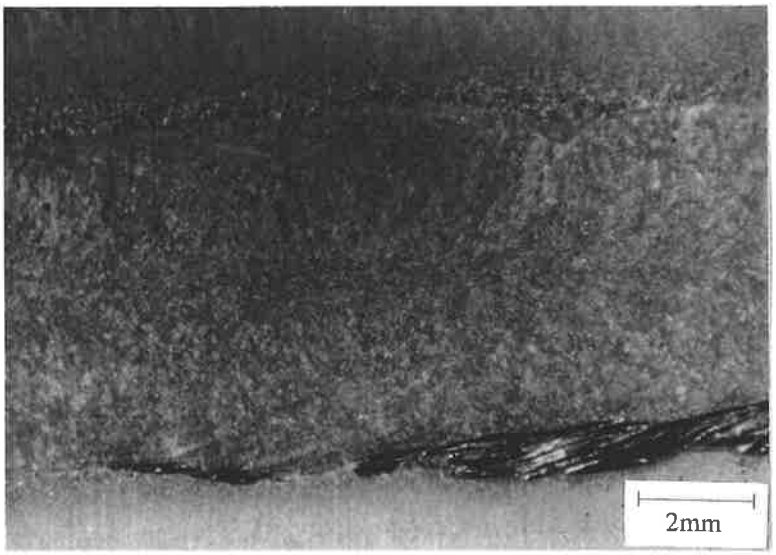

Figure 3.34: Longitudinal horizontal section of a weld made at 300mm/min and 163A (heat input equal to 0.70kJ/mm). In this weld the total number of hollow bead is 1 and the total length is 1mm.

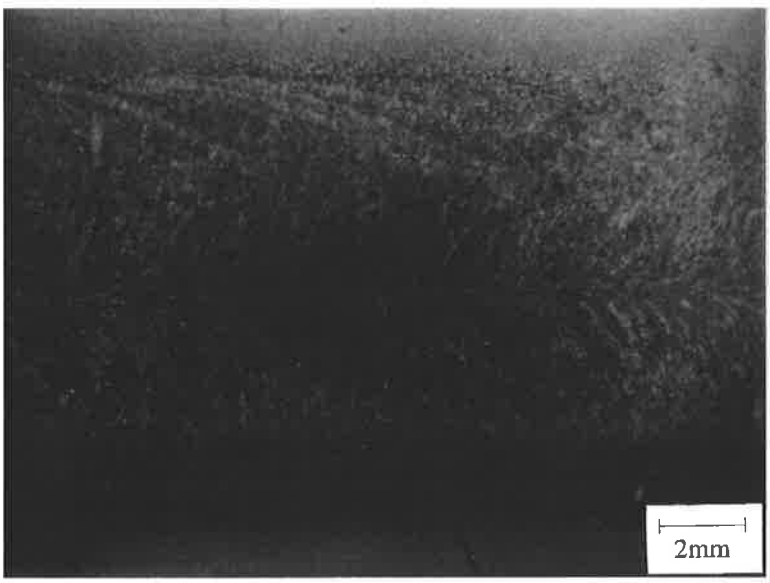

Figure 3.35: Longitudinal horizontal section of a weld made at 300mm/min and 204A (heat input equal to 1.0kJ/mm). In this weld the total number of hollow bead is 3 and the total length is 12mm.

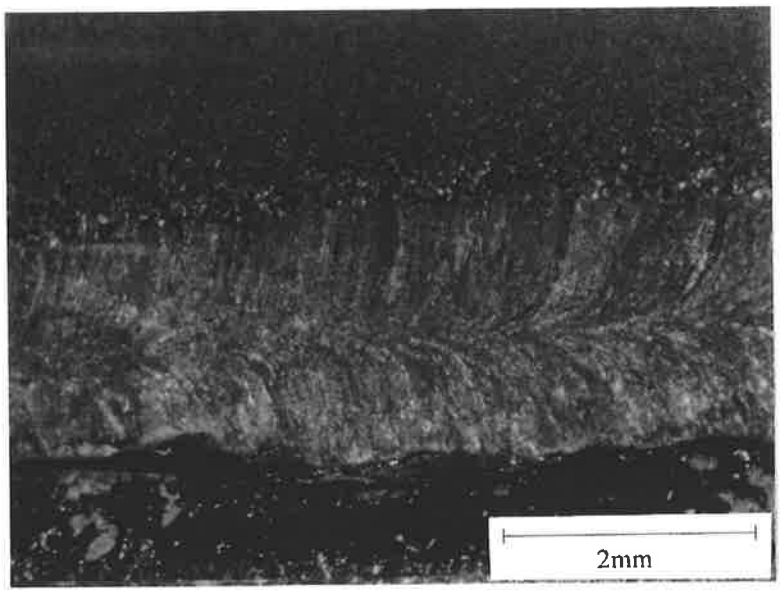

Figure 3.36: Longitudinal horizontal section of a weld made at 400mm/min and 133A (heat input equal to 0.44kJ/mm). No hollow bead formed in this weld.

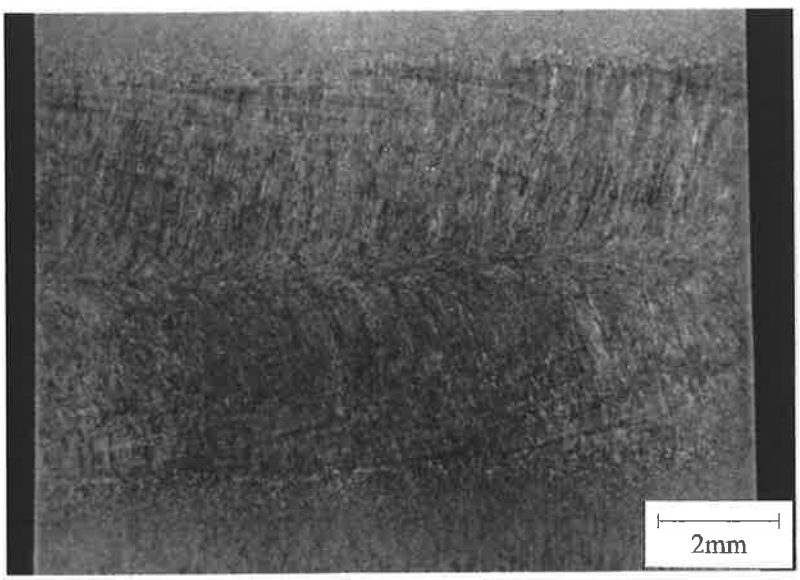

Figure 3.37: Longitudinal horizontal section of a weld made at 400mm/min and 188A (heat input equal to 0.74kJ/mm). In this weld the total number of hollow bead is 2 and the total length is 12mm.

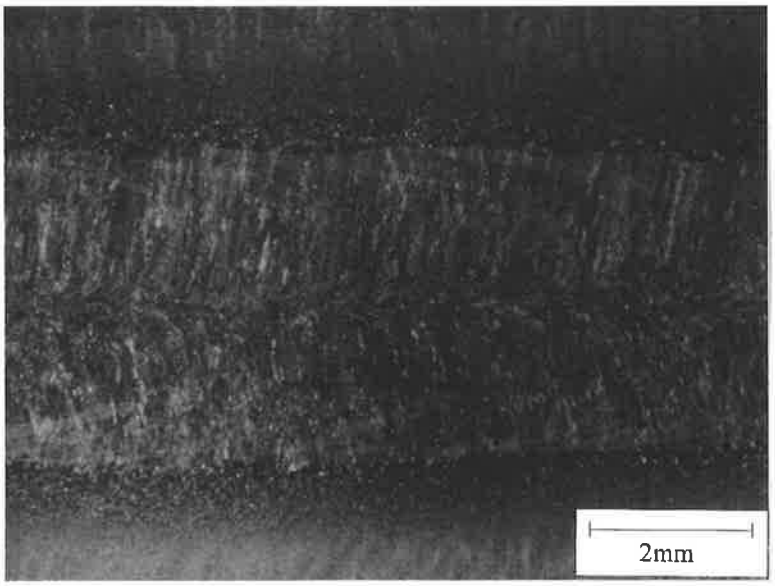

Figure 3.38: Longitudinal horizontal section of a weld made at 550mm/min and 150A (heat input equal to 0.39kJ/mm). No hollow bead formed in this weld.

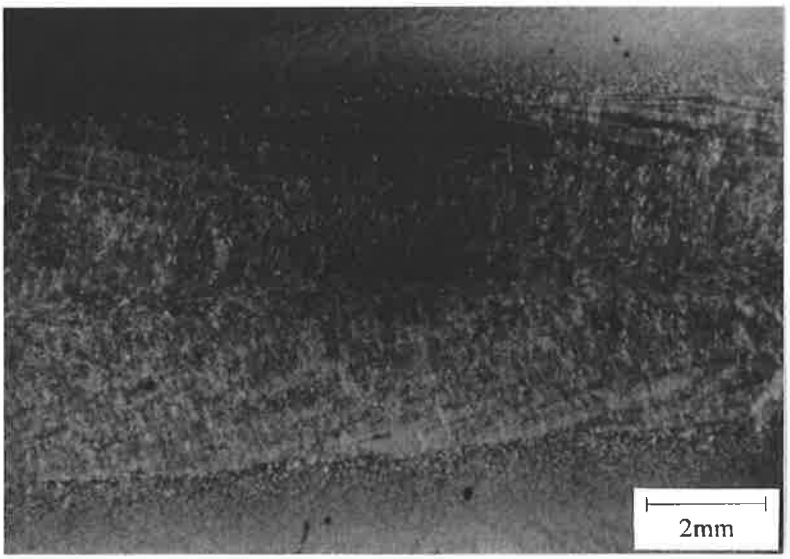

Figure 3.39: Longitudinal horizontal section of a weld made at 550mm/min and 170A (heat input equal to 0.51kJ/mm). In this weld the total number of hollow bead is 3 and the total length is 11mm.

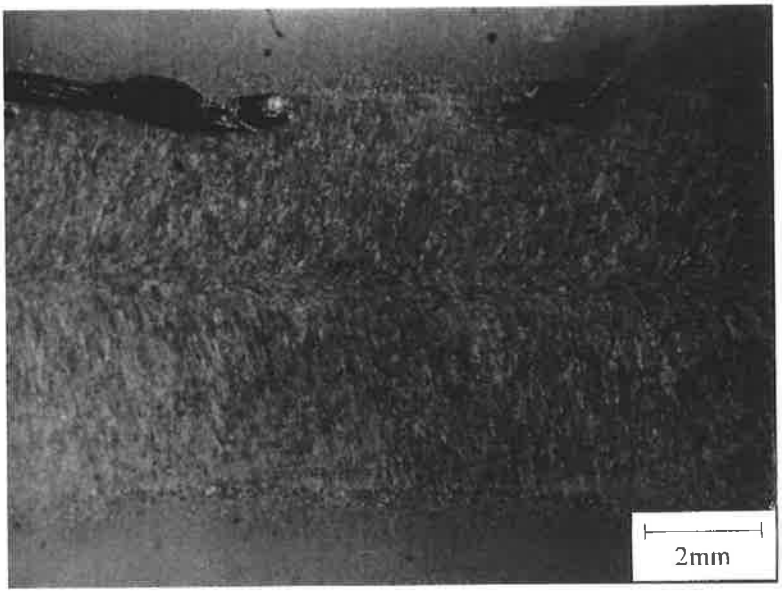

Figure 3.40: Longitudinal horizontal section of a weld made at 550mm/min and 184A (heat input equal to 0.55kJ/mm). In this weld the total number of hollow bead is 6 and the total length is 26mm.

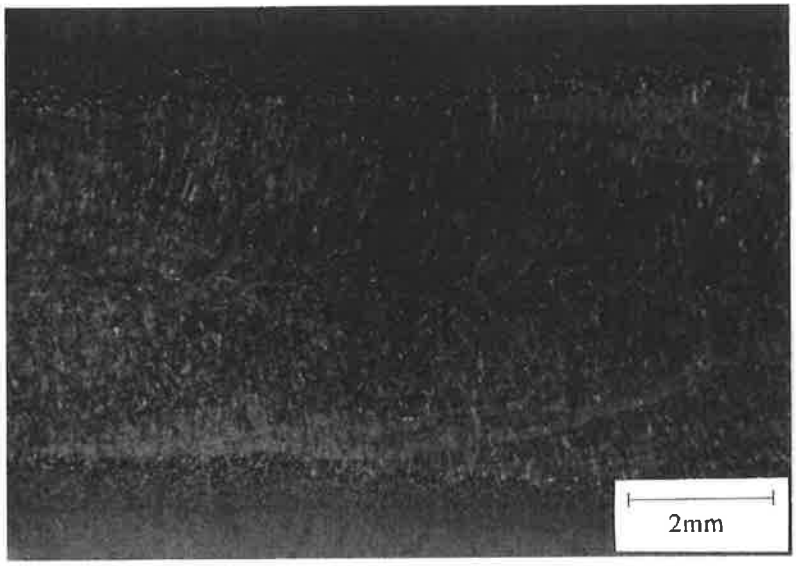

Figure 3.41: Longitudinal horizontal section of a weld made at 600mm/min and 159A (heat input equal to 0.42kJ/mm). In this weld the total number of hollow bead is 5 and the total length is 16mm.

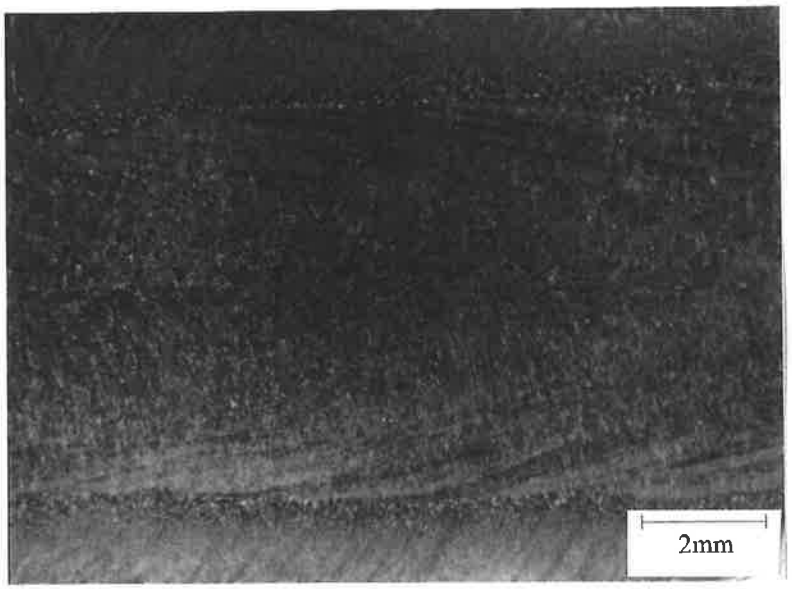

Figure 3.42: Longitudinal horizontal section of a weld made at 600mm/min and 193A (heat input equal to 0.56kJ/mm). In this weld the total number of hollow bead is 9 and the total length is 45mm.

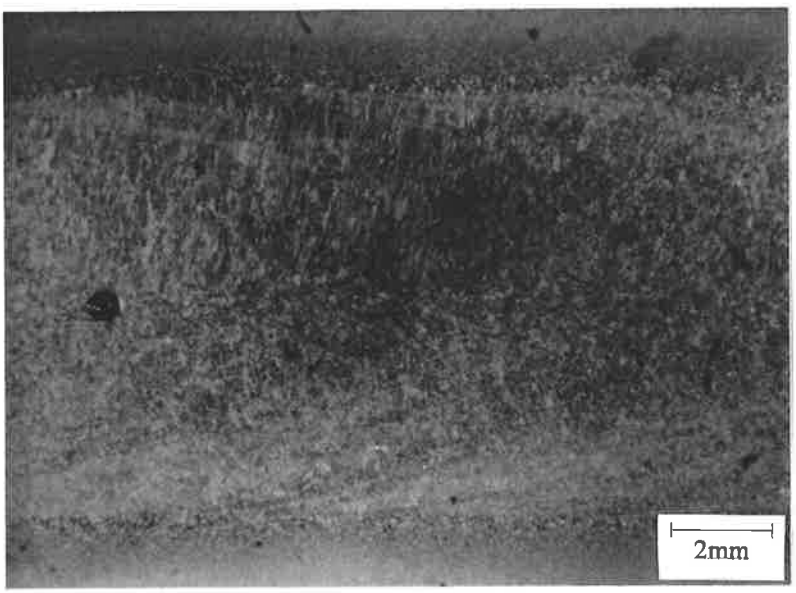

Figure 3.43: Longitudinal horizontal section of a weld made at 600mm/min and 216A (heat input equal to 0.64kJ/mm). In this weld the total number of hollow bead is 7 and the total length is 61mm.

3.6 Discussion

It has been shown that hollow bead pores nucleate and propagate at the top or the root of the weld bead close to the surfaces. It had been previously observed that hollow bead only occurred near the root surface of the weld bead. It has been established in this work, however, that in practical field welding conditions the hot pass will melt a large portion of the root bead and hence any pores situated at the top will disappear.

The shape of the macrostructure of the root beads produced using the stovepipe welding technique has been studied. In general, "wagon-tracks" are formed on both sides of the top part of the weld, and the beads tend to taper midway along the height. The microstructure consists of allotriomorphic ferrite (grain boundary ferrite in International Institute of Welding (IIW) terminology) at the grain boundaries and of Widmanstätten ferrite (ferrite with aligned second phase in IIW terminology) and acicular ferrite within the grains. The microstructure seen in a weld cross section shows that the direction of columnar growth proceeds from the fusion line to the weld centreline and towards the top and root surfaces. The microstructure seen at the weld centreline of a weld cross section and the one seen in a longitudinal horizontal section shows that the direction of growth changes from perpendicular to parallel to the welding direction at the weld centreline. The shape of the heat affected zone which is narrower near the top of the weld than the bottom suggests that the maximum temperature gradient is towards the top surfaces of the parent plates where the volume of material is greatest. This is discussed further in Chapter 4 - The Finite Element Modelling of Weld Pools. It can thus be suggested that, based on a model where gas-forming solutes are rejected at the solidification interface due to their decrease in solubility with decreasing temperature and can be pushed by the solidification interface, the centreline as well as the top and root regions of

the welds will have the highest concentration of these solutes.

The shape of the microstructure explains the direction of growth of hollow bead; because a hollow bead pore nucleates at the weld centreline, it will grow in the direction of solidification which for these welds is in the direction of welding.

All these observations relate to the microstructure resulting from the solid state transformation. Since a pore will nucleate during the liquid to solid transformation the primary solidification microstructure had to be studied. This was done by etching weld samples high in nickel and manganese and looking at the microsegregation at the cellular dendritic boundaries. It has been established that the primary δ-ferrite microstructure has a similar direction of growth to the α-ferrite structure, which validates the previous statements made regarding the influence of the direction of solidification on the location of hollow bead in the welds.

The shape and the size of the welds pools have been further studied to determine the effect of welding conditions. As expected an increase in the heat input increases the volume of the welds. At the same welding current, the increase in the area (volume) of the weld is lower at 600mm/min than at 300mm/min. The concentration of hydrogen could thus be higher in the smaller weld pools made at 600mm/min, a condition where the occurrence of hollow bead was found to be highest.

3.7 Scanning Electron Microscopy

3.7.1 Scanning Electron Microscopy of Hollow Bead Pores

The internal surface features of hollow bead were characterised by examining a large number of pores in the SEM. Common factors have been identified and described in this work.

For the examination of the inside surfaces, longitudinal vertical sections of hollow bead were prepared by cutting the weld to within about 2mm of the pore using a jeweller's saw and then prising the sample open. This technique provided 2 sections of each defect which were studied in a Philips XL20 scanning electron microscope. Another method used involved grinding the outside surface of the weld until the hollow bead pore was exposed. An EDAX energy dispersive spectrometer (EDS) was used for qualitative elemental analysis.

Figure 3.44 is an SEM micrograph of the internal surface of a hollow bead pore 15mm in length which initiated at point A. This pore was exposed by grinding the outside surface of the bead from a longitudinal horizontal section. The optical micrograph of the same pore, shown in Figure 3.11, has been used in the correlation of the columnar microstructure surrounding the pore and the cellular dendritic structure evident on the internal surface of the pore. The curvature of the columnar grains towards the weld centreline, discussed in Section 3.3.2, is clear at the area marked A on the optical micrograph (the initiation point of the pore).

The SEM micrograph, in Figure 3.45, shows the initial segment of the pore where irregularities in growth at the start are observed as well as an increase in width. The brighter ridges, in Figures 3.45 and 3.46, are aligned with the curved columnar grains which can seen in the microstructure at the weld centreline (see Figure 3.6).

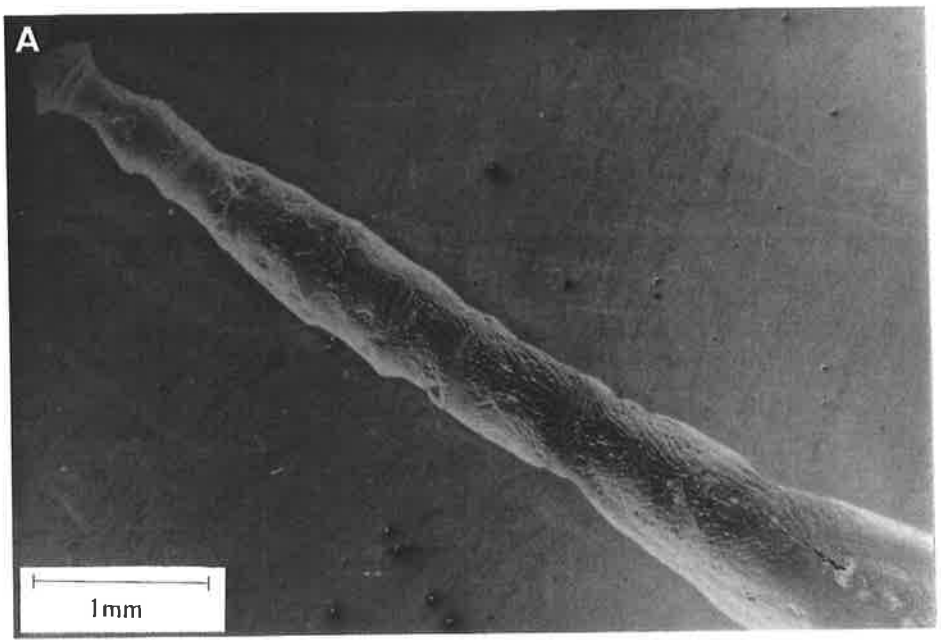

Figure 3.44: SEM micrograph of the internal surface of a hollow bead pore.

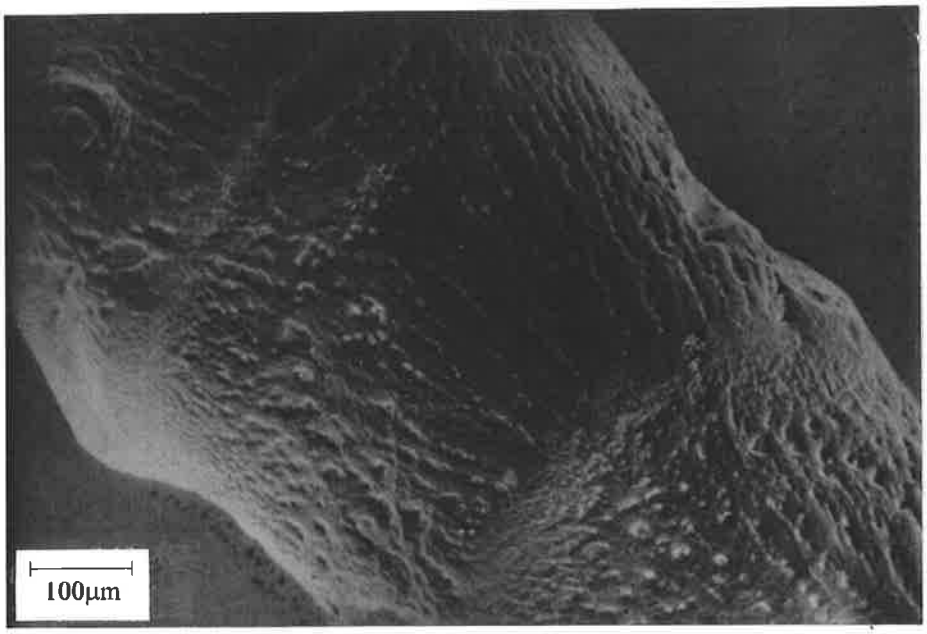

Figure 3.45: SEM micrograph of ridges aligned with the growth direction in a region close to the start of the pore.

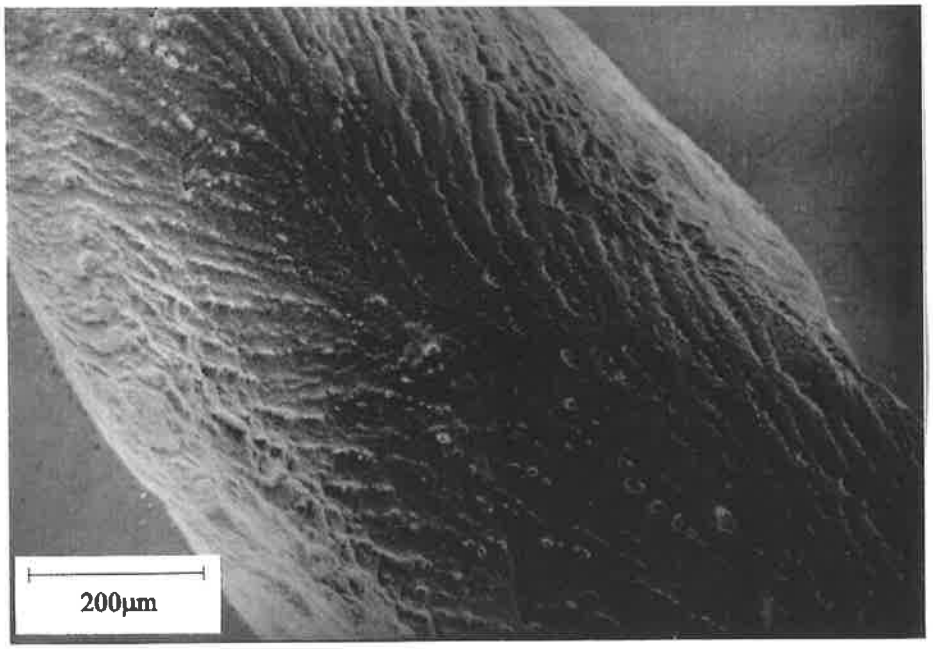

Figure 3.46: Another example of the ridges on the surface aligned with the growth direction.

The ridges, also seen in Figure 3.47 at higher magnification, are similar to the ones described in the Literature Review (see Figures 1.7 and 1.8) and their formation is explained in terms of microsegregation whereby solute-enriched liquid in the cellular-dendritic solidification boundary solidifies after protrusion into the pore (Powell and Lloyd, 1995). The distance between these ridges is approximately 20 to 25 microns, the same value as measured by Powell and Lloyd (1995). These ridges are also observed to follow the direction of growth as observed from the longitudinal horizontal weld sections; the grains grow initially perpendicular to the welding direction and then proceed parallel to the travel direction near the weld centreline. This also confirms the correspondence between the shape and direction of growth of the primary transformation microstructure and solid state transformation microstructures.

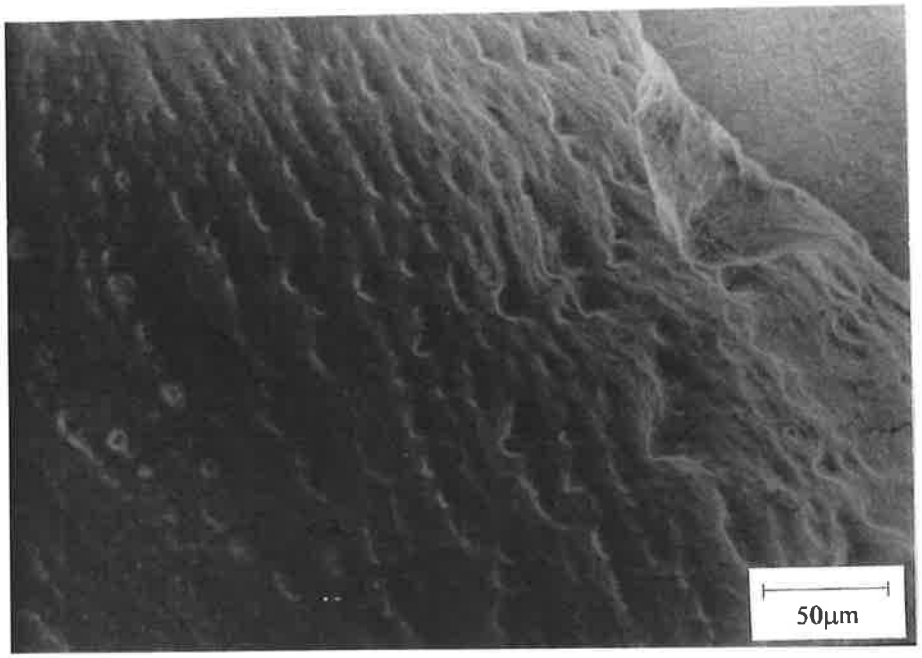

Figure 3.47: Higher magnification micrograph of the ridges.

It has been found that the most convenient method of exposing the internal surface of pores for examination is to fracture welds in the longitudinal vertical direction as explained previously in this section. As a result the remainder of this section on SEM microscopy deals with longitudinal vertical sections of hollow bead pores. The nucleation point of all of the pores has been marked A and the termination end marked B.

The next example deals with a short hollow bead pore (Figure 3.48). It has been studied in some detail as it reveals clear evidence of cellular dendritic growth inside the pore. The solidification pattern at area C, seen at higher magnification in Figure 3.49, is similar to the one described in the previous example. It consists of ridges, due to microsegregation, aligned in the direction of growth.

At area D in Figure 3.48, the diameter of the pore increases, and the surface appears very smooth with no ridges present.

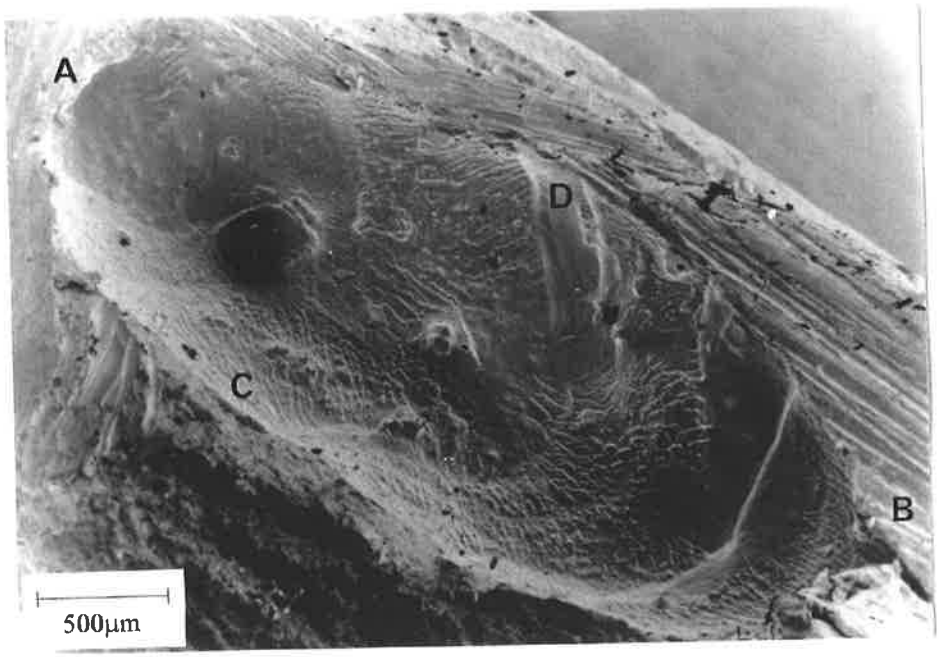

Figure 3.48: SEM micrograph of the internal surface of a hollow bead pore, which initiated at point A and terminated at point B.

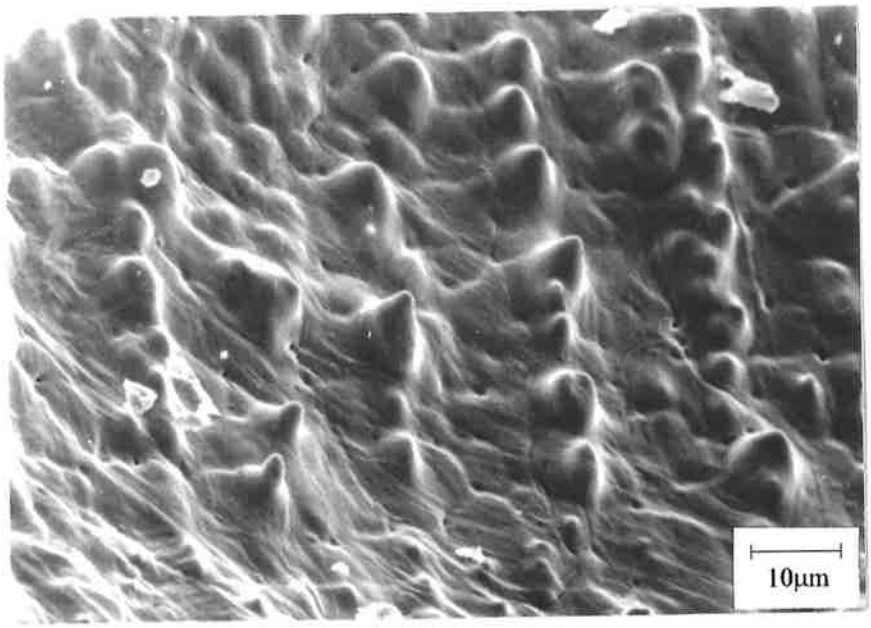

Figure 3.49: Higher magnification micrograph of the microstructure showing microsegregation at cellular dendritic boundaries at area C (seen as bright ridges).

At higher magnification again there is evidence of a dendritic microstructure (Figure 3.50). These rounded features, approximately 10 microns in diameter, are thought to be the secondary arms of cellular dendrites. As mentioned in the Literature Review the growth morphology in the weld is dependent on both the thermal gradient, G and the solidification rate, R. The combined variable $G/R^{1/2}$ is considered when determining the stability of an interface such that a high ratio tends to produce a planar microstructure while a low ratio tends produce a dendritic microstructure. In the case considered here it can be assumed that the thermal gradient during the growth of a pore, for similar welding conditions, will be approximately constant. It is known, however, that the solidification rate fluctuates constantly and rapidly due to frequent variations in heat input. When the solidification rate increases macrosegregation, an increase in the solute content at the solidification interface, results. Also associated with the increase in solidification rate is an increase in the degree of supercooling ahead of the solidification interface which encourages a more dendritic microstructure where secondary branches grow from the main cellular branches. The increase in diameter of the pore can be explained by the higher levels of gas-forming solutes at the solidification interface, due to macrosegregation, which can form gases which diffuse into the growing pore.

In Figure 3.51, similar dendritic arms can be seen, at E, although in this region their surface and the adjacent smooth area appear to be covered by a thin film (marked F). This film has been identified using EDS analysis as a layer of iron oxide (see Figure 3.52). There is also evidence of globules (marked G) associated with this film. EDS analysis showed that the globules contained mixed oxides of silicon, aluminium, manganese and titanium typical of a slag inclusion (see Figure 3.53). The small spherical globules were also of this type.

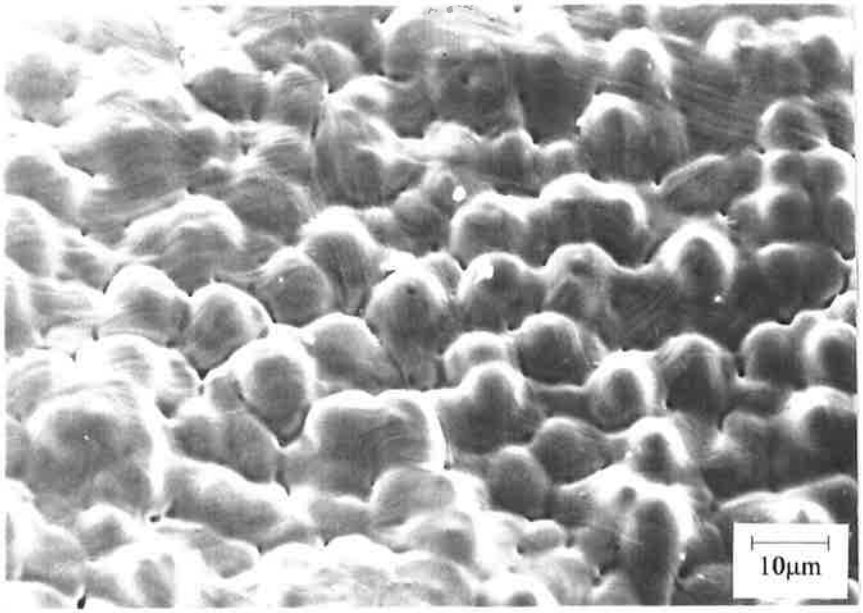

Figure 3.50: Solidification microstructure consisting only of the side arms of cellular dendrites.

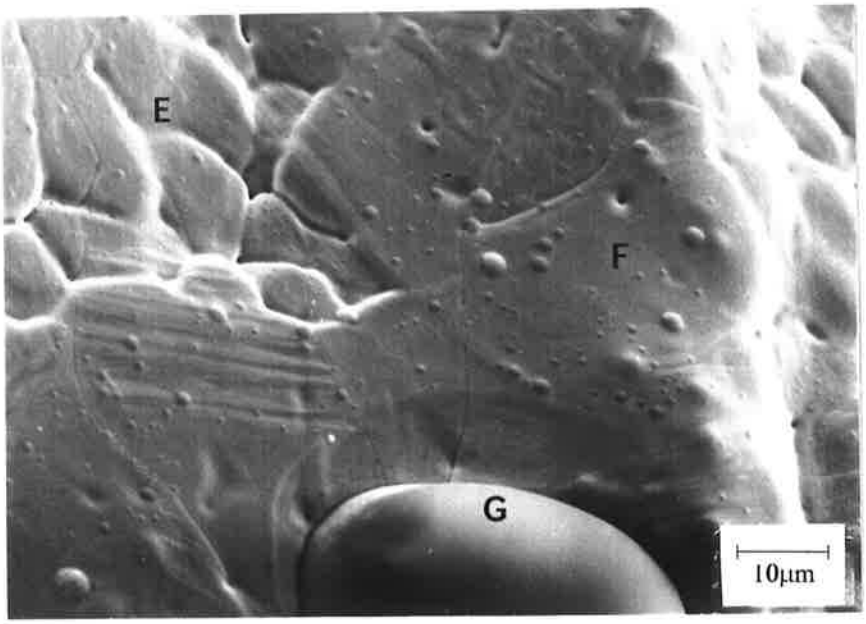

Figure 3.51: Micrograph showing the oxide layer partially covering the solidification microstructure.

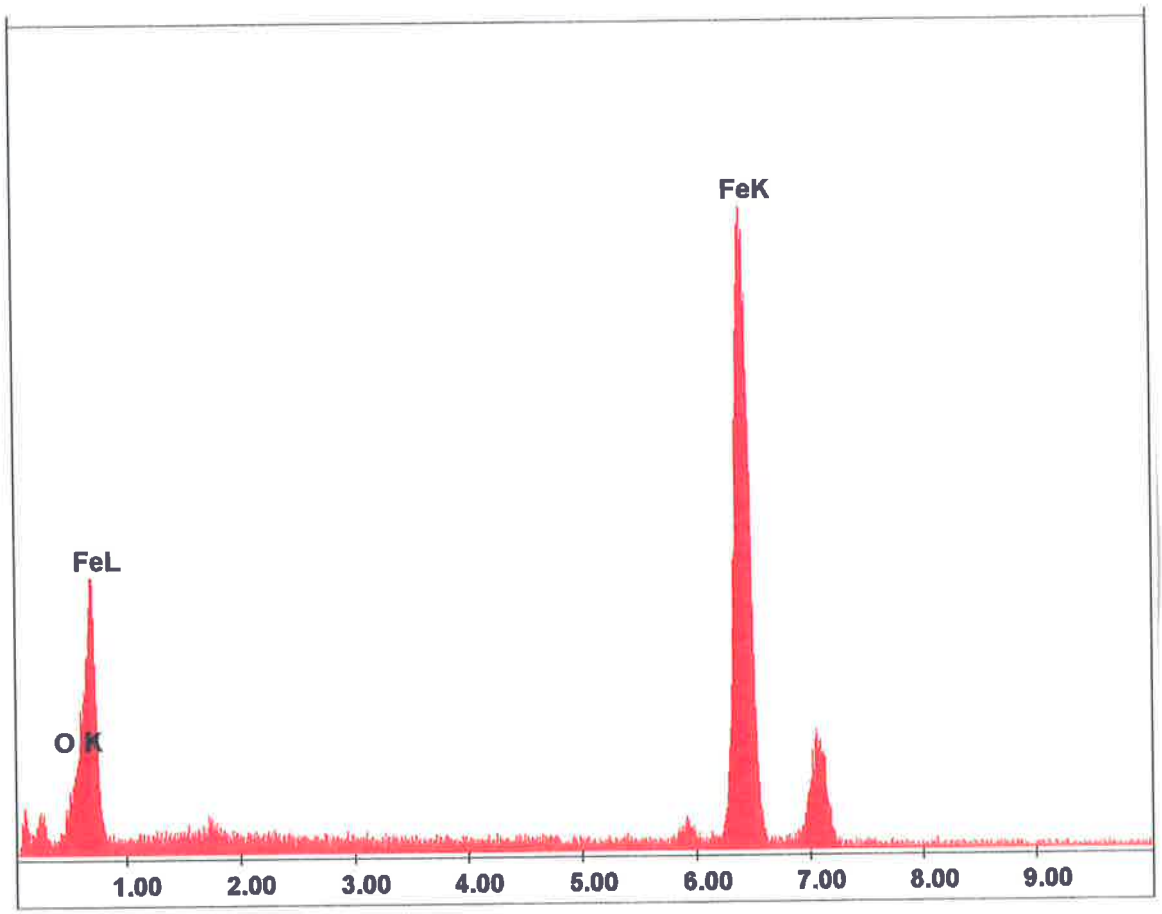

Figure 3.52: X-ray spectrum of the oxide layer at the area marked F in Figure 3.51.

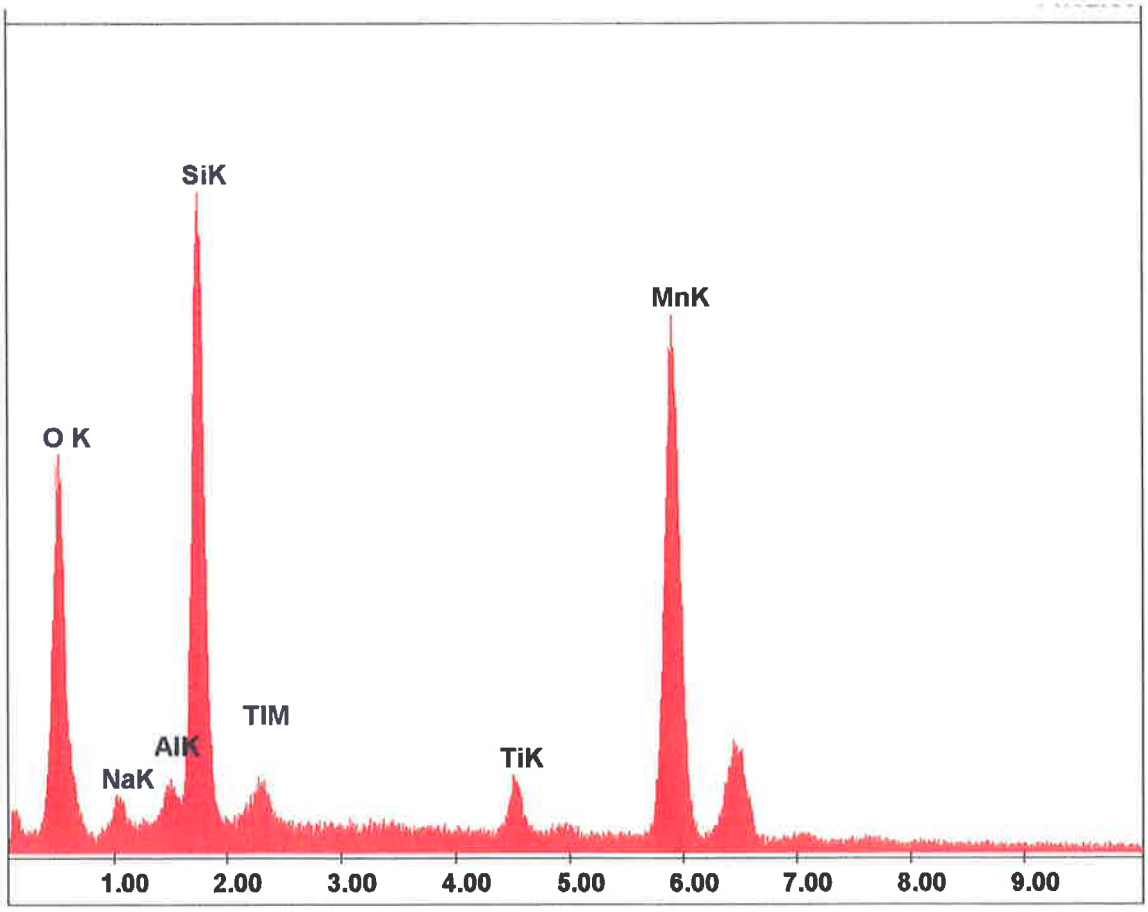

Figure 3.53: X-ray spectrum of the globules on the oxide layer in Figure 3.51.

In this investigation, several features were identified which are common to all the hollow bead pores examined. The initiation point (marked A in the relevant micrographs) was identified from radiographs and the direction of welding. In each case this area exhibited a typical morphology which has been termed a "cusp".

The hollow bead pores also in many cases increased in diameter during growth, and all the pores contained slag particles and oxide surface layers to some extent. These features are illustrated in the following micrographs (Figures 3.54- 3.133).

In the hollow bead defect shown in Figure 3.54 the cusp (at A) is clearly visible but the ridges associated with cellular dendritic growth are not obvious. This was found to be due to a layer of iron oxide covering the inside surface. At the cusp, the oxide layer is thin and only partially covers the solidification structure (Figure 3.55). The identity of this layer was confirmed using EDS analysis (Figure 3.56). The extent of oxidation changed with the growth of the pore. Further into the pore, marked H in Figure 3.54, the solidification structure is almost completely obscured by a thicker oxide film (Figure 3.57). Near the end of the pore the oxide layer appears even thicker and is associated with spherical particles (Figure 3.58). These were again identified as fragments of mixed oxide slag. At the termination end of the pore (marked B), there are angular fragments (Figure 3.59). These were identified as oxides rich in titanium, aluminium, manganese and silicon, again typical of slag inclusions. All the hollow bead samples studied in this project show evidence of slag at the termination end of the pore. The x-ray spectrum shown in Figure 3.60 is typical of all the slag fragments found in all the defects. The size and shape of the slag varies from one pore to another.

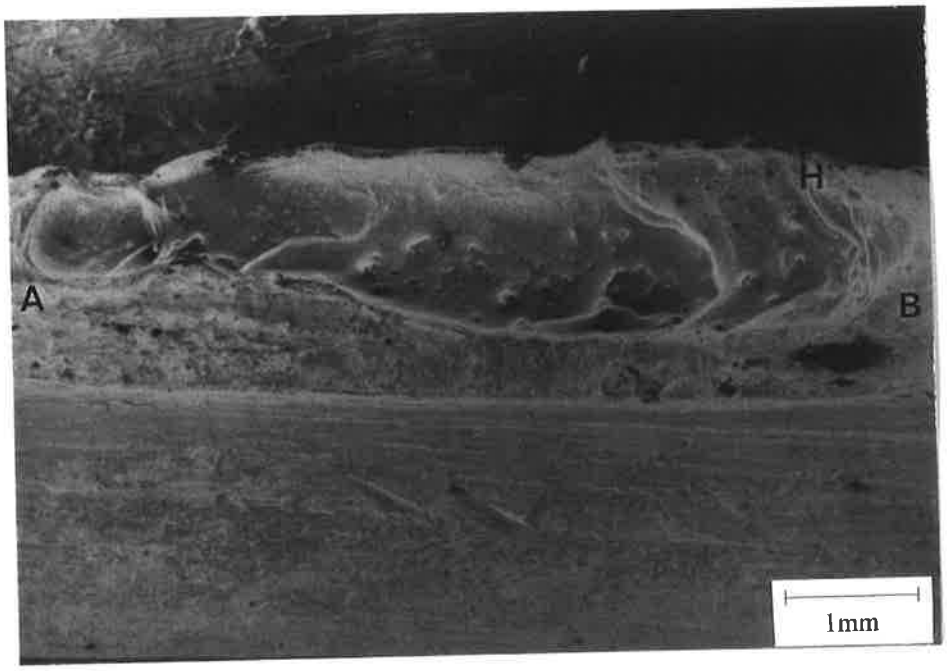

Figure 3.54: Scanning electron micrograph of a hollow bead pore. The pore initiated at the cusp (marked A) and terminated at (B).

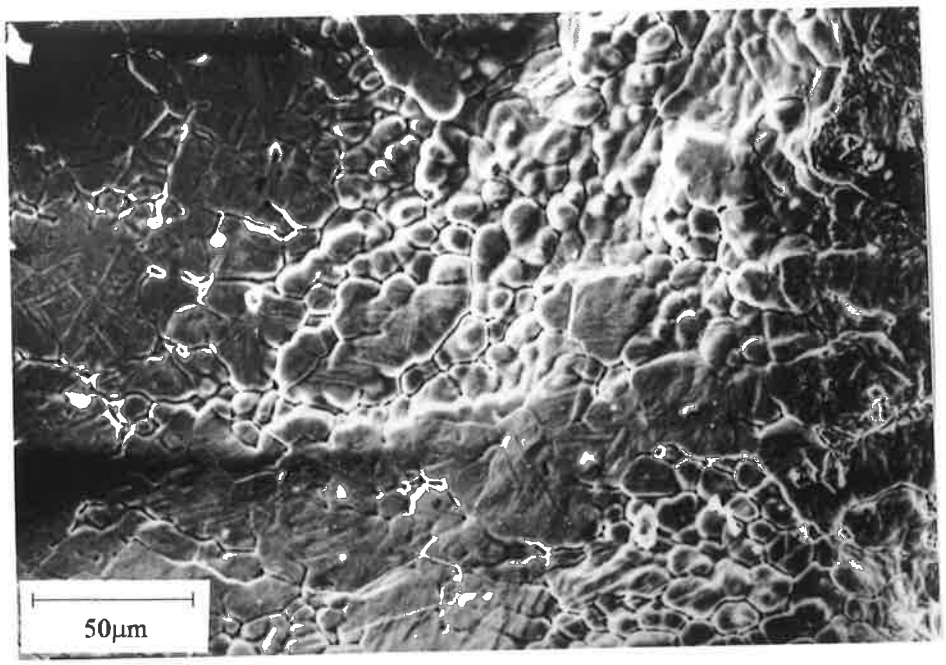

Figure 3.55 : Micrographs of the solidification microstructure of the initial cusp region. The oxide layer partially covers the microstructure.

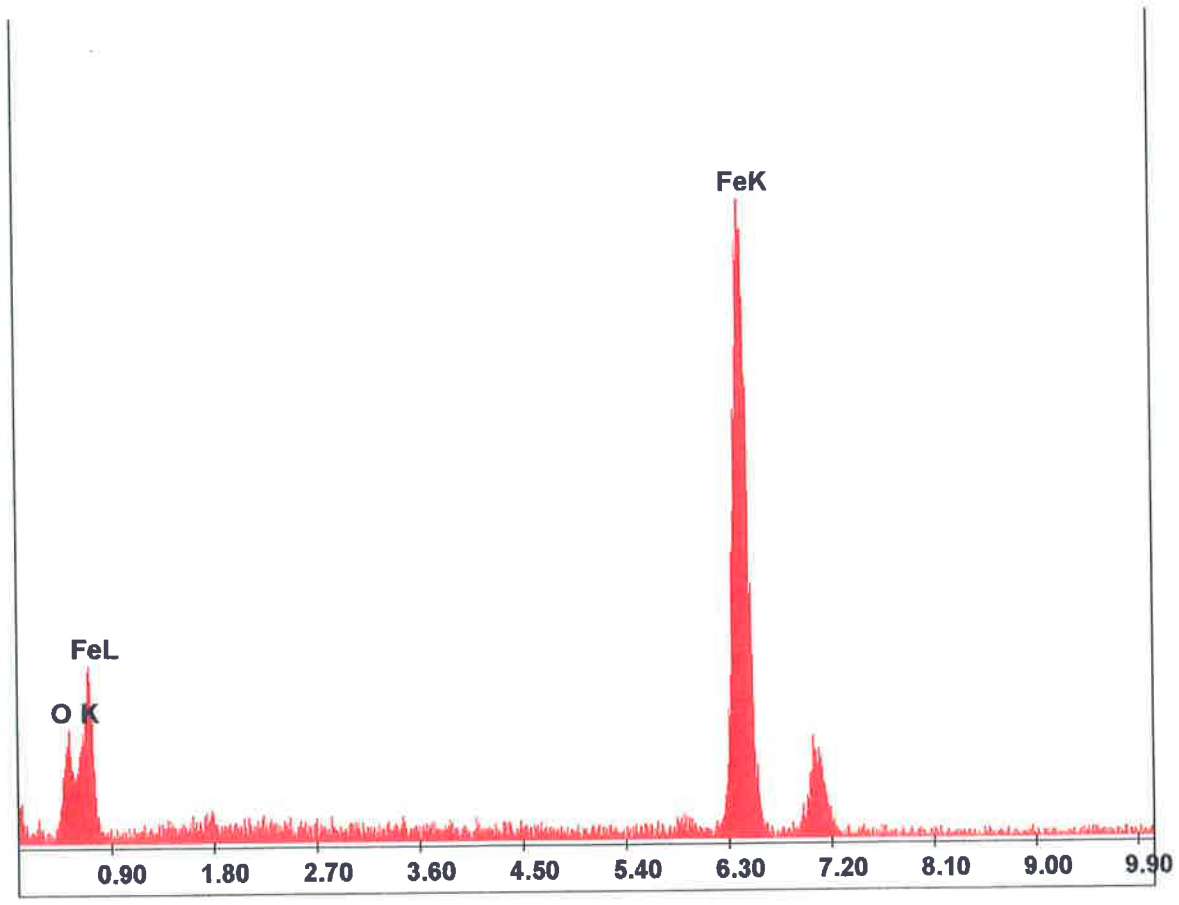

Figure 3.56: Typical x-ray spectrum of an oxide layer.

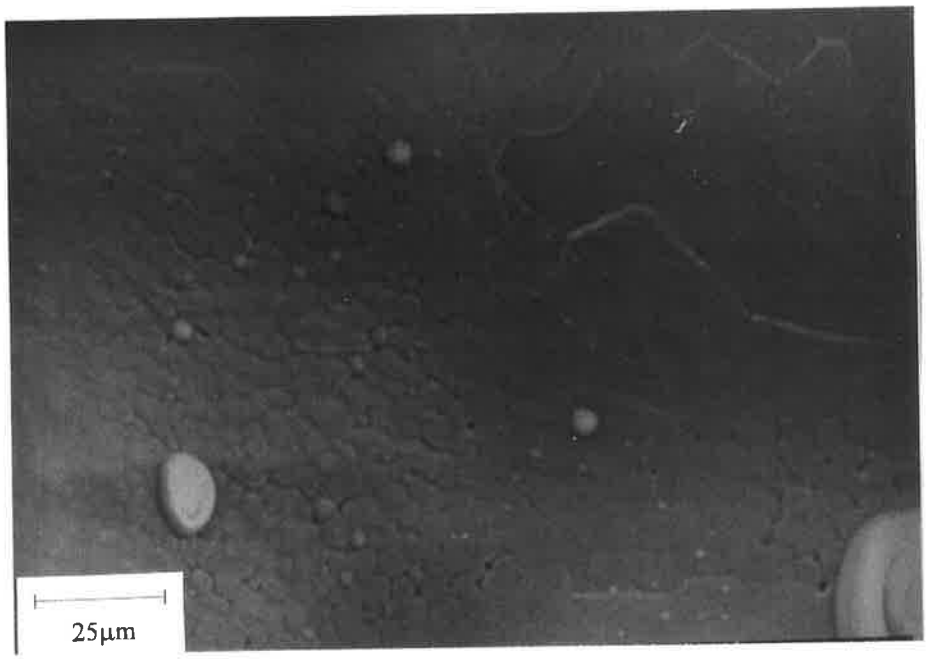

Figure 3.57: SEM micrograph showing the oxide layer partially covering the solidification microstructure (marked H).

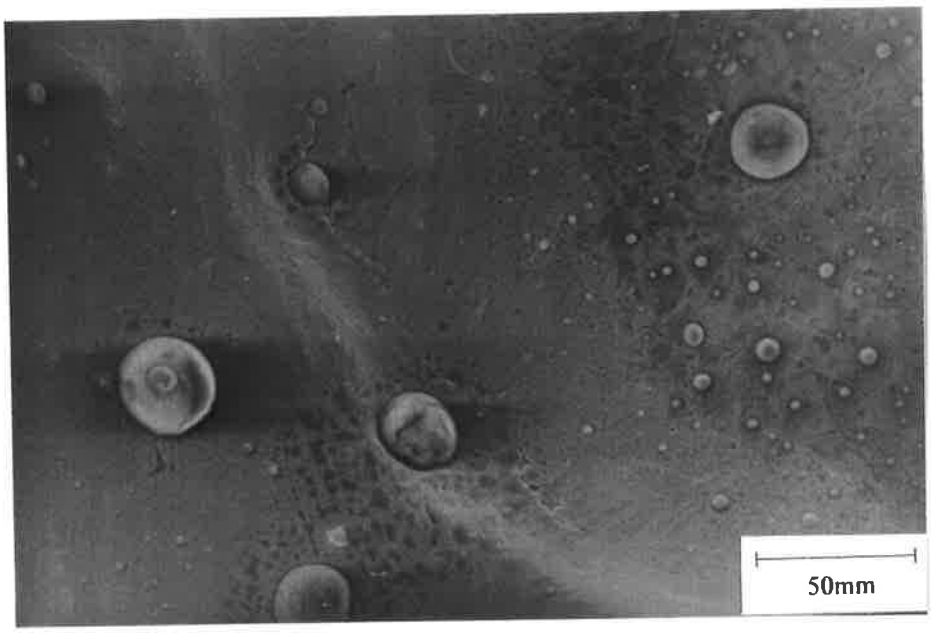

Figure 3.58: Micrograph of a thicker oxide layer near the end of the pore. Slag fragments can also be seen on the surface.

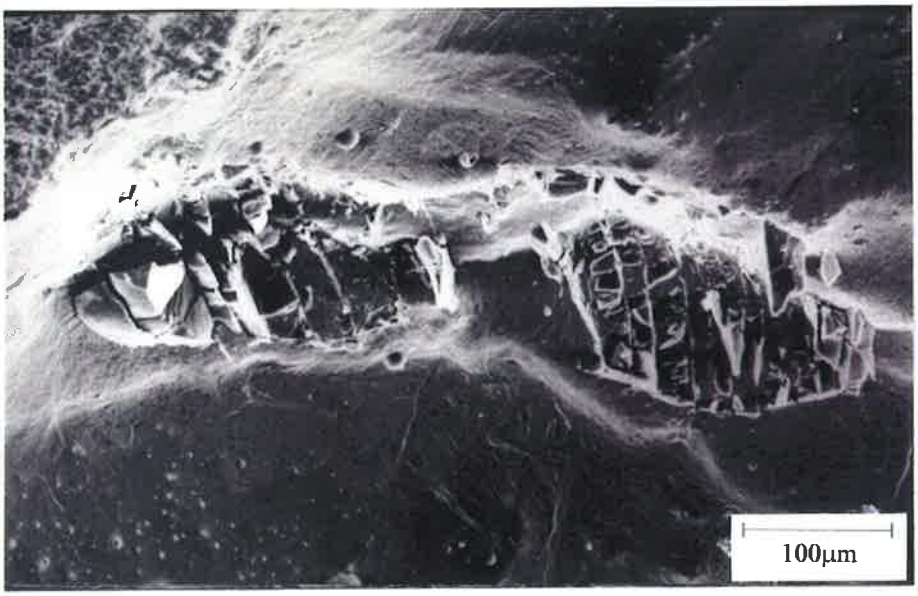

Figure 3.59: Angular particles at the termination end of the pore.

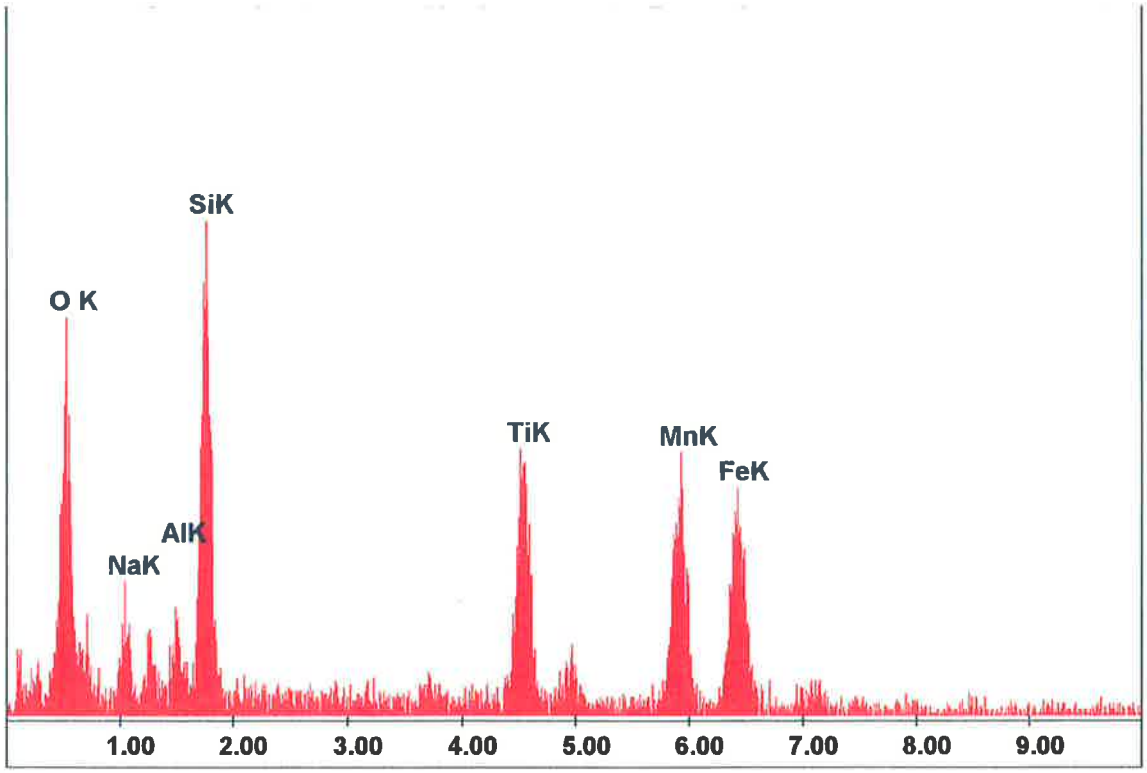

Figure 3.60: Typical x-ray spectrum of a slag inclusion.

Further examples of hollow bead pores are presented in the remainder of this section. The section has been divided such that the typical features of hollow bead are presented first. Hollow bead pores with particular characteristics are considered separately. A study of long hollow bead pores is then presented and their features compared with the ones found in smaller pores. The hollow bead samples used in the analysis of the gas composition are also described.

In the initial part, micrographs showing the entire length of hollow bead pores are presented first (Figures 3.61-3.64), followed by micrographs of cusps (Figures 3.65-3.68), the typical solidification microstructures observed in the cusp region (Figures 3.69 and 3.70), typical types of oxide films found along the length of the pores (Figures 3.71 and 3.72), and slag particles and the adjacent surface at the termination end of the pores (Figures 3.73-3.78).

The hollow bead pore in Figure 3.61 has a cusp at the initiation point (marked A) and a diameter which increases continuously along its length. A slight decrease in the diameter is observed at the end of the pore (marked B).

The diameter of the hollow bead in Figure 3.62 is more discontinuous and the cusp is not well defined. Its surface also appears more oxidised and contains many slag globules. This same form of slag is also visible on the surface of the pores in Figures 3.63 and 3.64. The diameter of the pore in Figure 3.63 also exhibits discontinuities as well as an increase in diameter in the growth direction. The cusp of the hollow bead in Figure 3.64 is better defined due to a small decrease in diameter after its formation.

The degree of oxidation of the internal surface varies from one pore to the next. The general trend, however, is for the cusp to be slightly oxidised, such that the solidification microstructure is visible (Figure 3.65), and for the level of oxidation to increase with growth. In some cases, for example the pore in Figure 3.62, the entire surface is oxidised even the region in the cusp (Figure 3.66). Evidence of oxidation is also observed in the cusps in Figures 3.67 and 3.68.

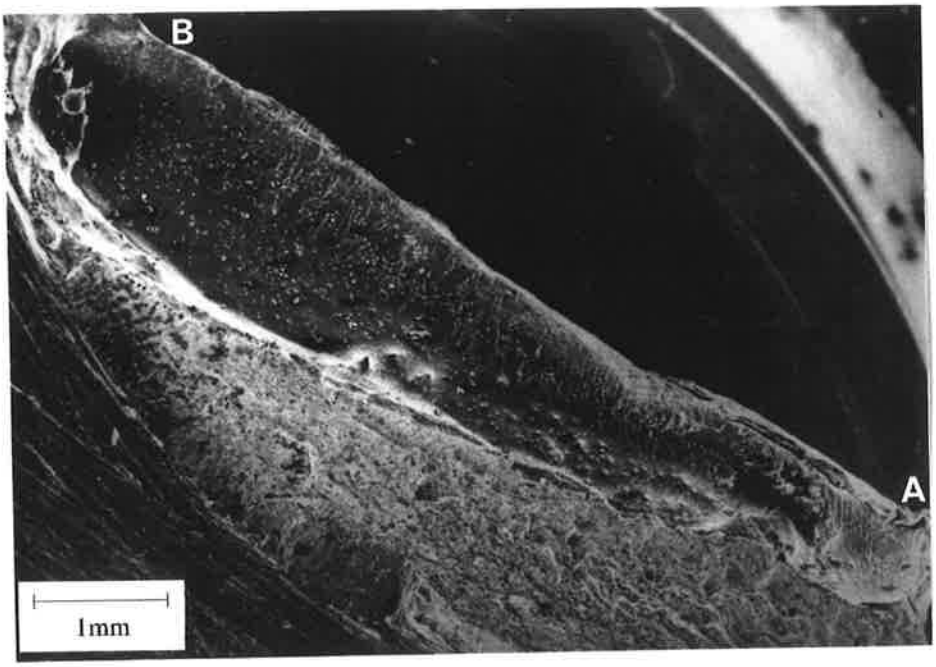

Figure 3.61 : Scanning electron micrograph of a hollow bead pore. The pore initiated at the cusp (marked A) and terminated at (B).

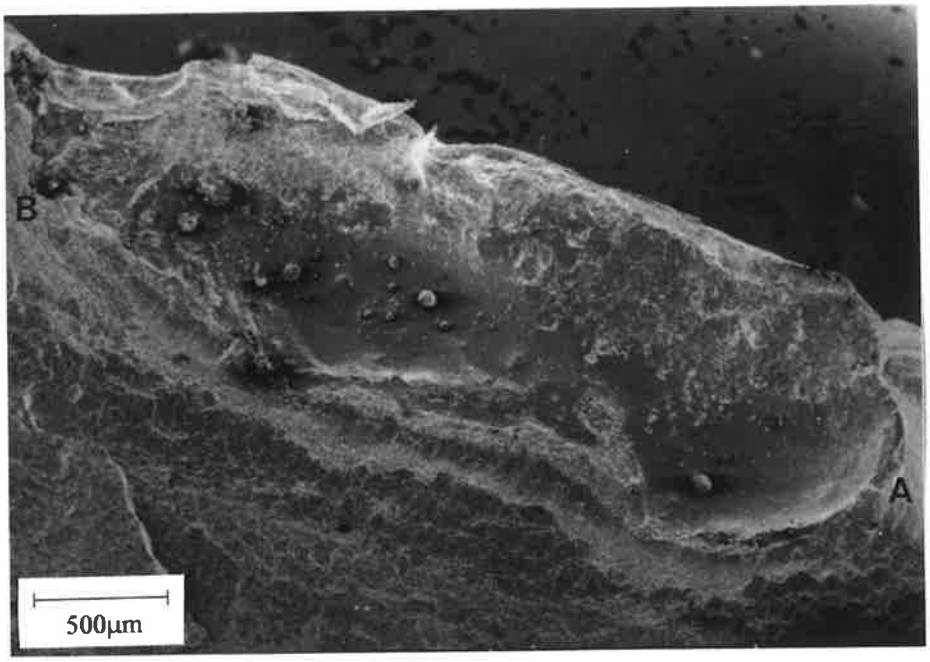

Figure 3.62 : Scanning electron micrograph of a hollow bead pore.

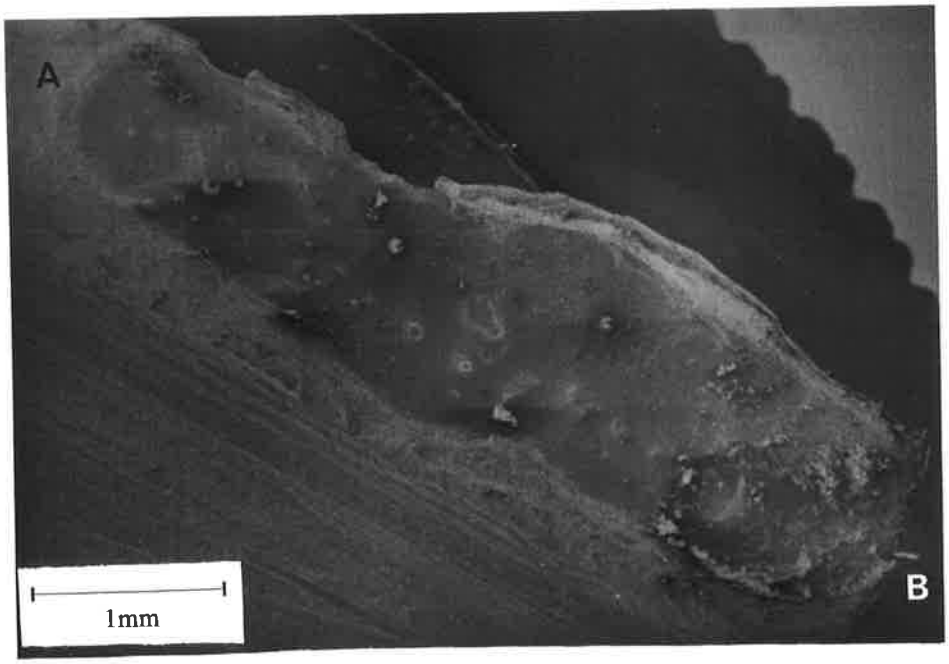

Figure 3.63 : Scanning electron micrograph of a hollow bead pore.

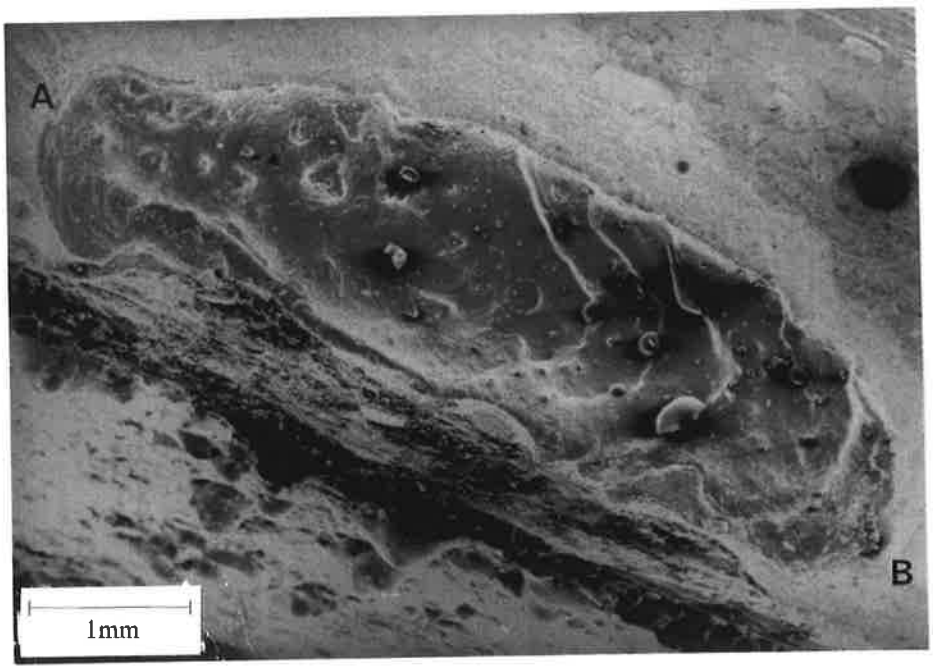

Figure 3.64 : Scanning electron micrograph of the hollow bead defect. Ripples are evident on the pore surface.

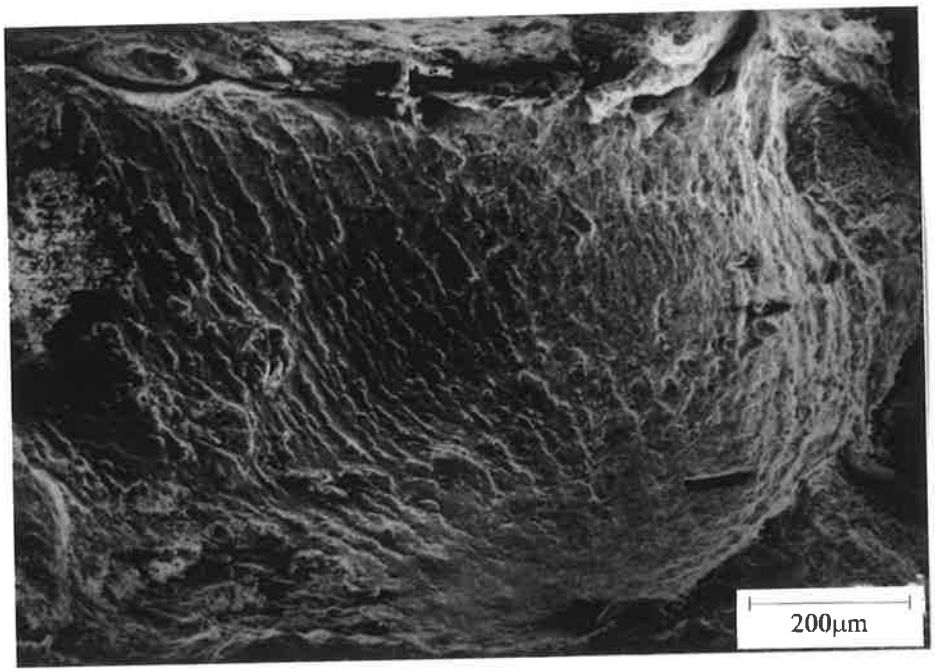

Figure 3.65: Higher magnification micrograph showing the cusp at (A) in Figure 3.61.

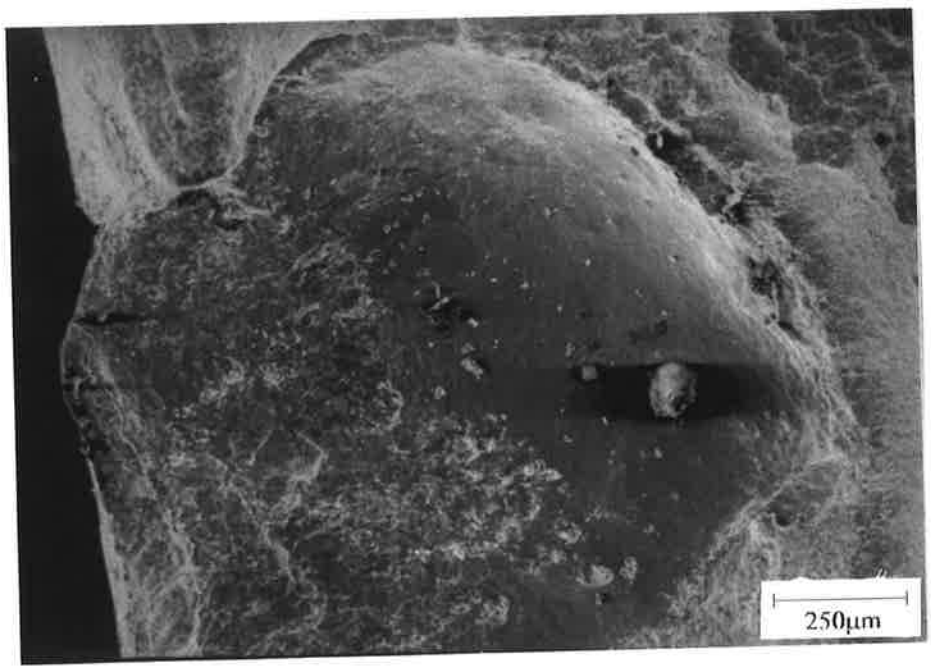

Figure 3.66: Higher magnification micrograph showing the cusp at (A) in Figure 3.62.

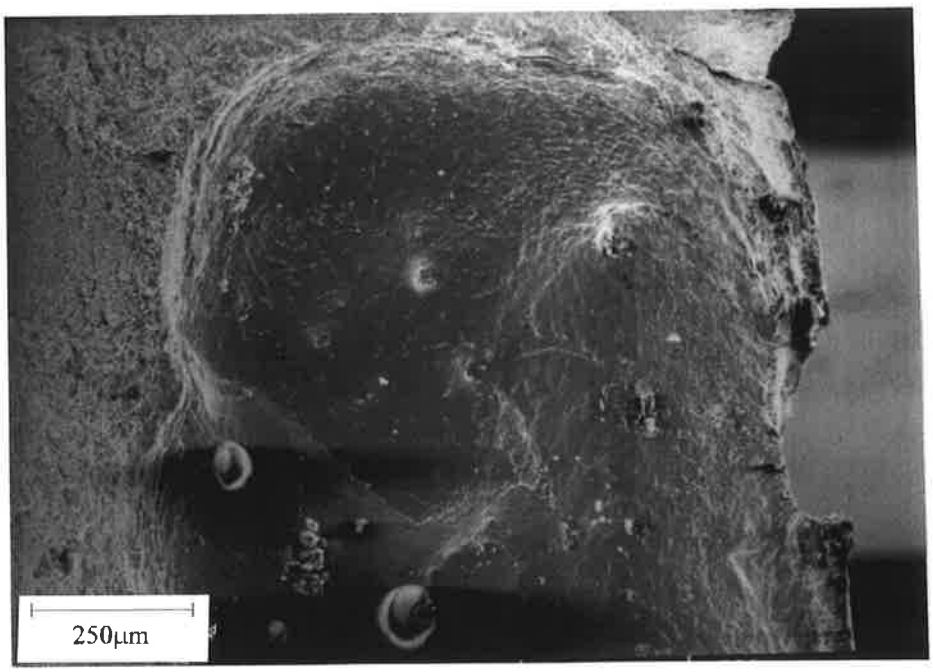

Figure 3.67: Higher magnification micrograph showing the cusp at (A) in Figure 3.63.

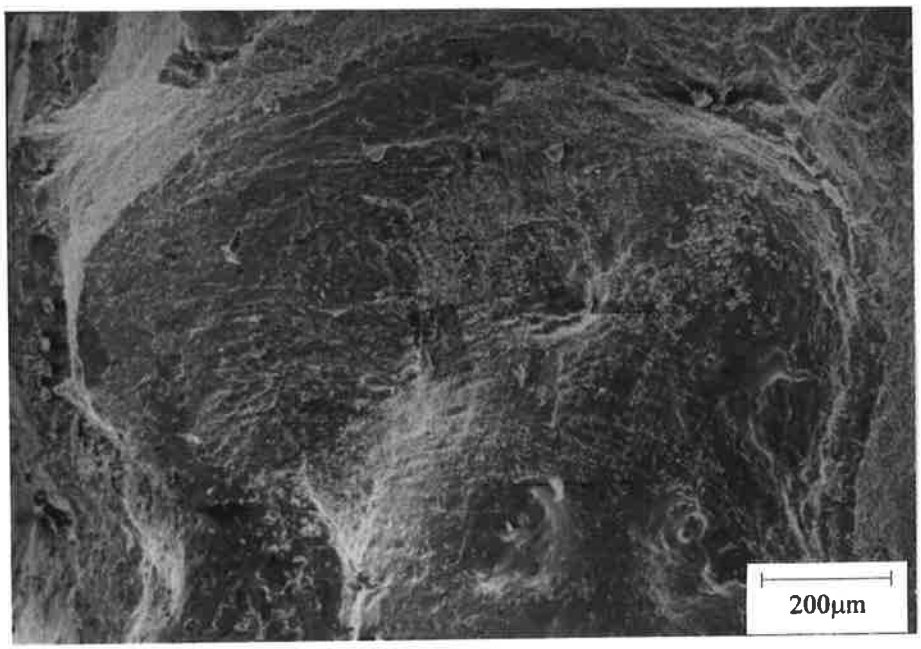

Figure 3.68: Higher magnification micrograph showing the cusp at (A) in Figure 3.64. Protrusions representing cellular dendritic growth are observed in the cusp.

The typical microstructure seen in the cusps are shown in Figures 3.69 and 3.70. Depending on the direction of growth of the cellular dendrites, the microstructure can show ridges resulting from microsegregation at their boundaries (Figure 3.69) or structures representing the ends of the cellular dendrites (Figure 3.70). The tips of cellular dendrites taper and thus have a smaller diameter than the main body (David and Vitek, 1989).

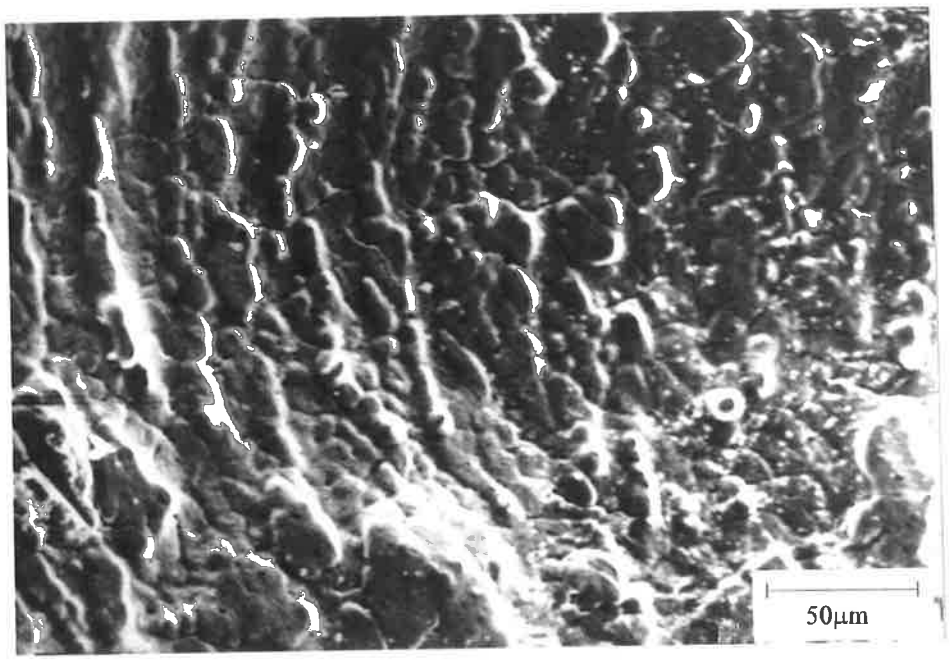

Figure 3.69 : Micrographs of the solidification microstructure of the initial cusp region of Figure 3.65. The oxide layer partially covers the microstructure.

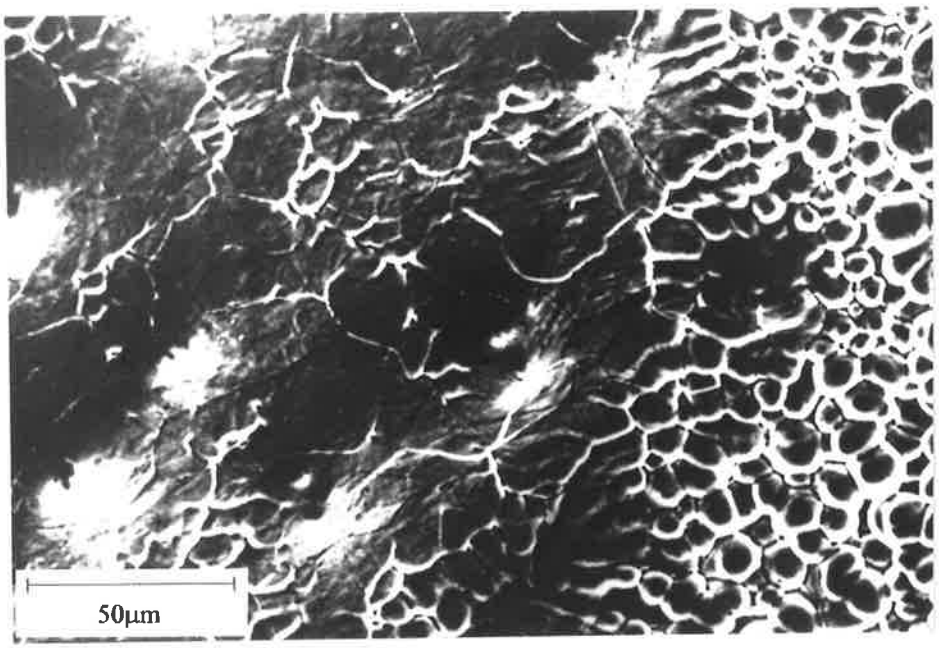

Figure 3.70 : Micrographs of the solidification microstructure of the initial cusp region of Figure 3.67. The oxide layer again partially covers the microstructure.

The micrographs in Figures 3.71 and 3.72 show the surface of two pores in regions approximately midway along their lengths. The surface shown in Figure 3.72 is oxidised to a much higher degree than the one in Figure 3.71 where the microstructure is partly visible at the top of the micrograph. The slag inclusions on the surface of hollow bead pores tend to be of the globular type shown in Figure 3.72.

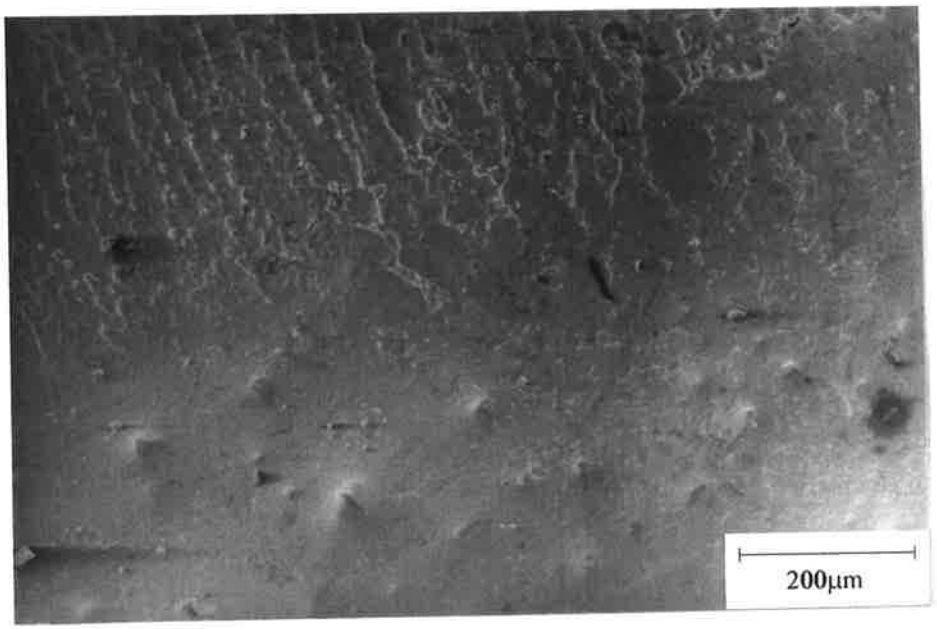

Figure 3.71: SEM micrograph showing the oxide layer partially covering the solidification microstructure of the hollow bead in Figure 3.61.

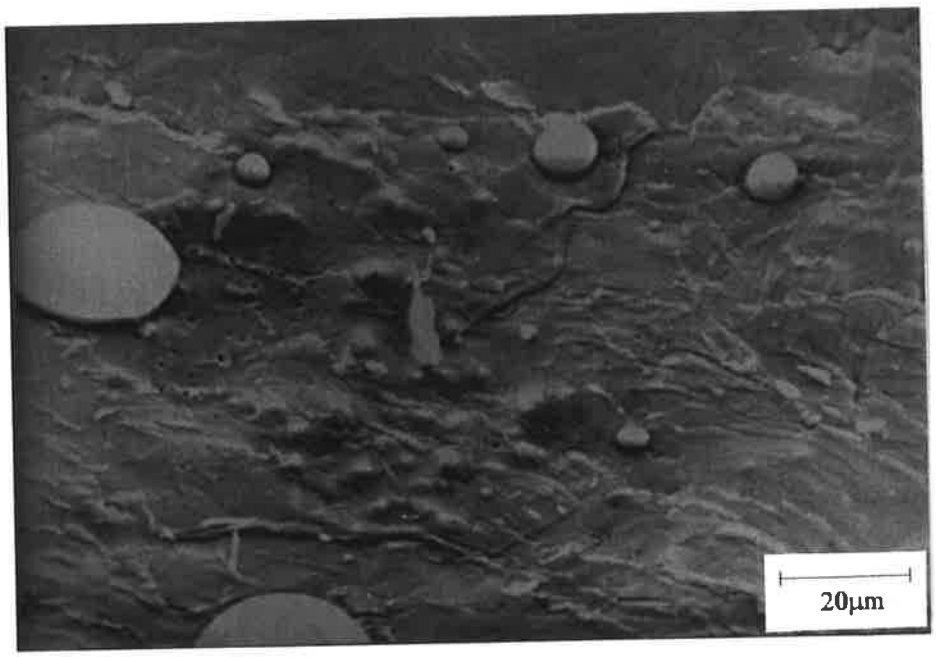

Figure 3.72: Micrograph of the completely oxidised surface of the pore in Figure 3.64 which also contains some slag fragments seen as bright rounded inclusions.

The slag observed at the termination end of pores is usually in the form of larger fragments as seen in Figure 3.73. This particular example also shows evidence of bubbles.

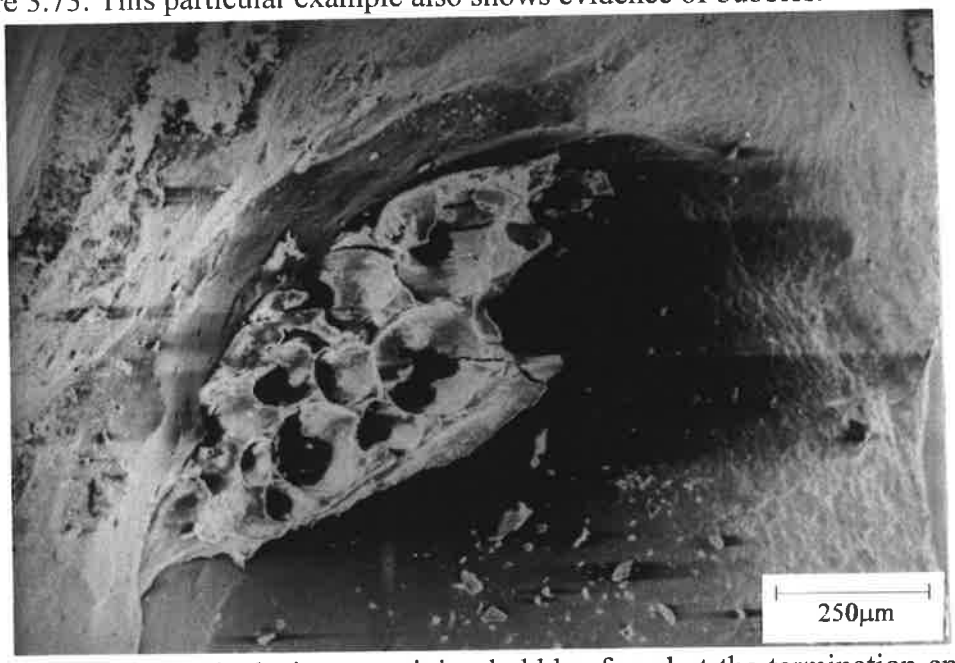

Figure 3.73: A slag inclusion containing bubbles found at the termination end of the hollow bead defect in Figure 3.61. The adjacent surface is oxidised and contains scattered non-metallic particles.

A large number of smaller fragments are present at the end of the pore in Figure 3.74.

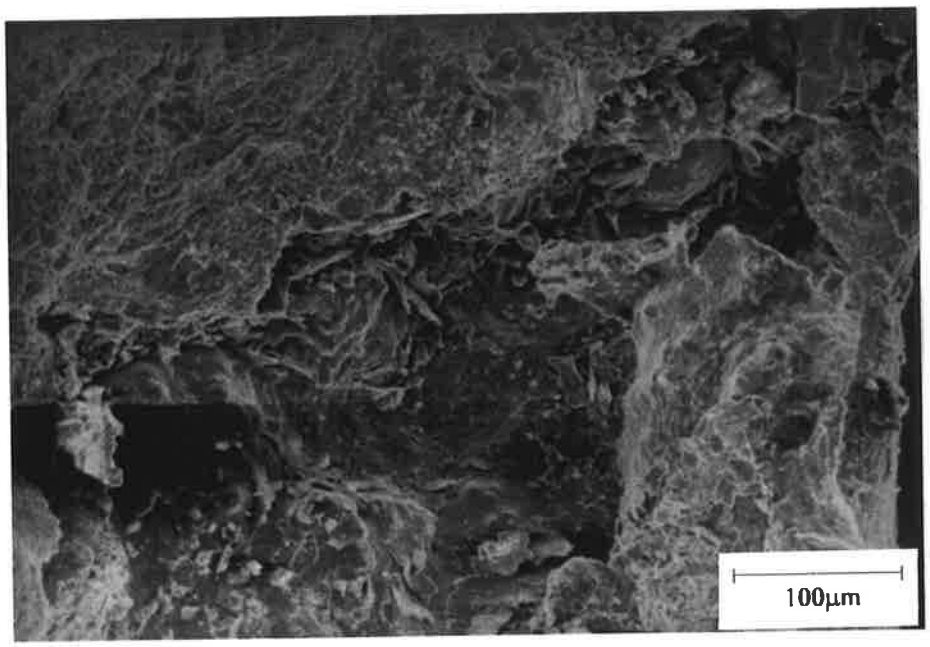

Figure 3.74: Micrograph of slag fragments which have accumulated at the end of the pore in Figure 3.62.

The slag can also accumulate as layers at the ends of pores (Figure 3.75). The cracked slag layer is seen at higher magnification in Figures 3.76 and 3.77.The very thick oxide layer surrounding the slag is evident in Figure 3.77. Small slag fragments can also be seen (Figure 3.78) towards the end of the pore shown in Figure 3.64.

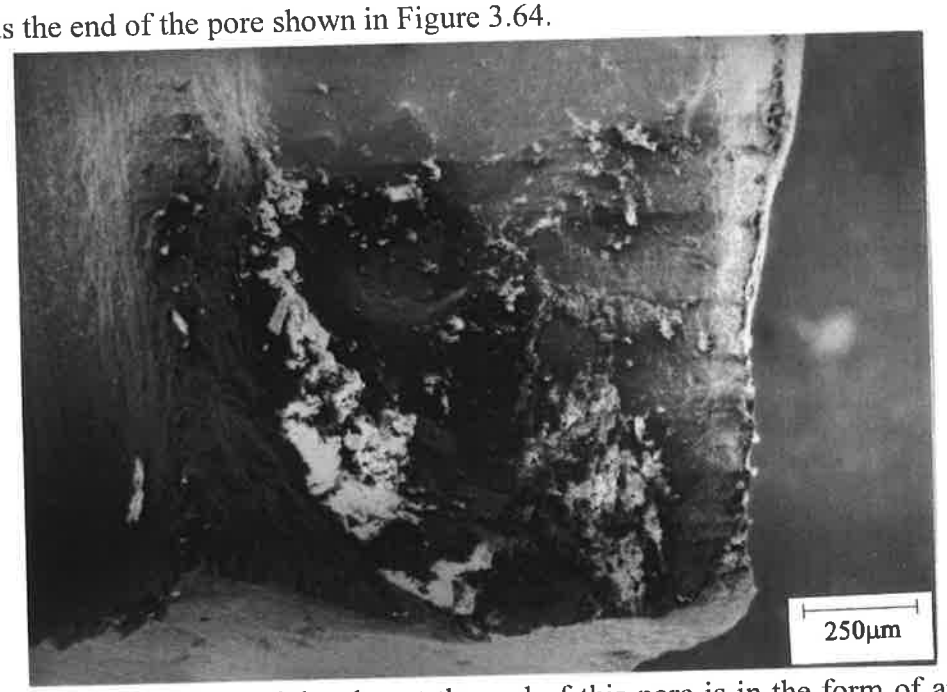

Figure 3.75: The structure of the slag at the end of this pore is in the form of an angular layer which is seen at higher magnification in the next figure.

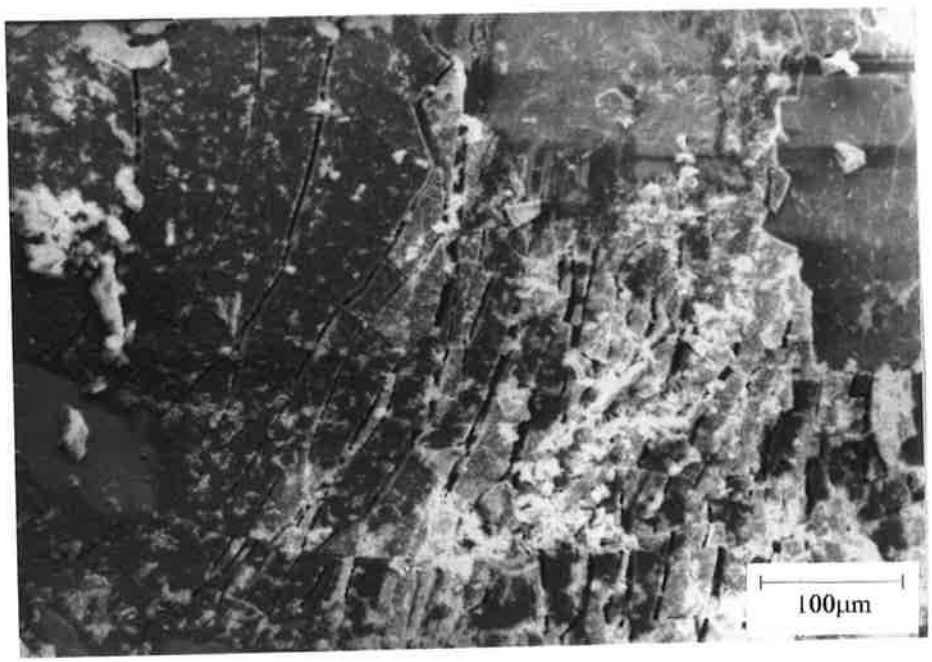

Figure 3.76: Higher magnification micrograph of Figure 3.75 showing structure of the slag as an angular and broken layer.

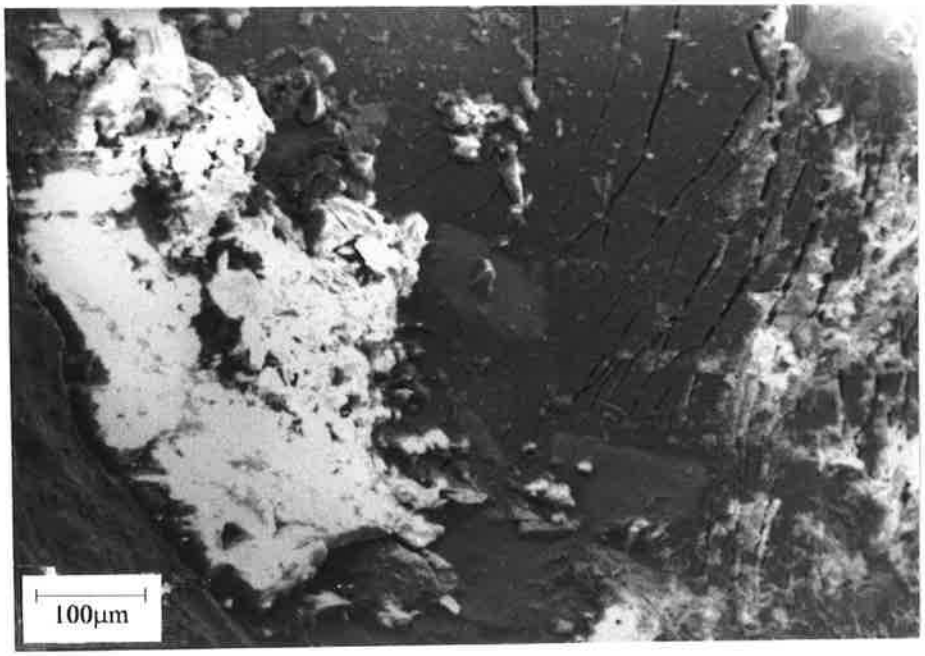

Figure 3.77: This micrograph is of the same area as in Figure 3.75 and reveals a very heavily oxidised surface surrounding the slag layer.

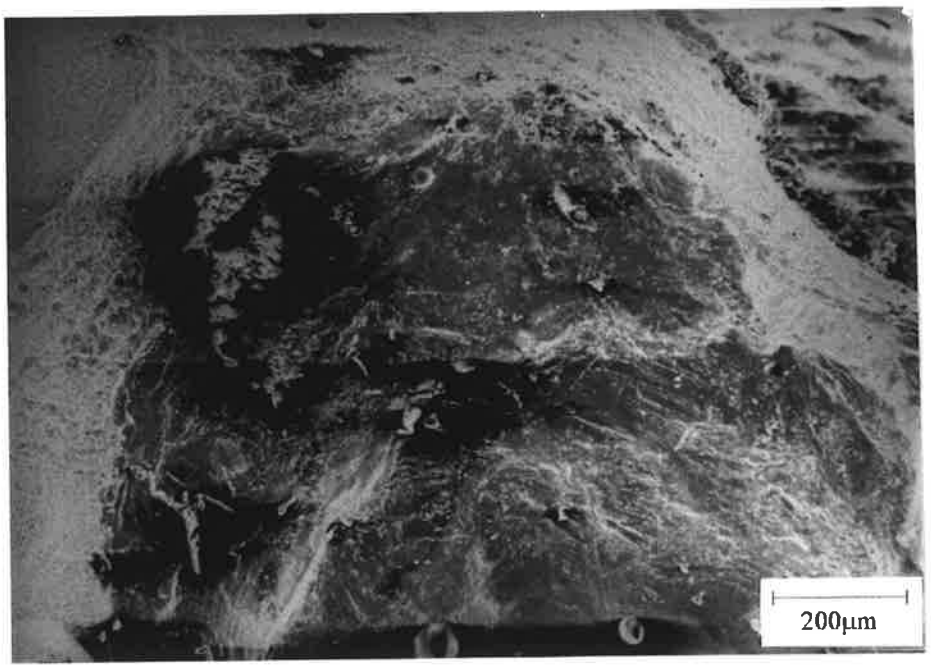

Figure 3.78: Micrograph of slag at the termination end of the pore in Figure 3.64.

An additional feature of hollow bead which is not shared by all samples but occurs frequently is the "ripples" or "steps" on the surface, indicated by arrows in Figure 3.79, which are associated with distinct changes in the diameter of the pore. Although only two examples are described here in detail, this characteristic was observed in most of the samples studied.

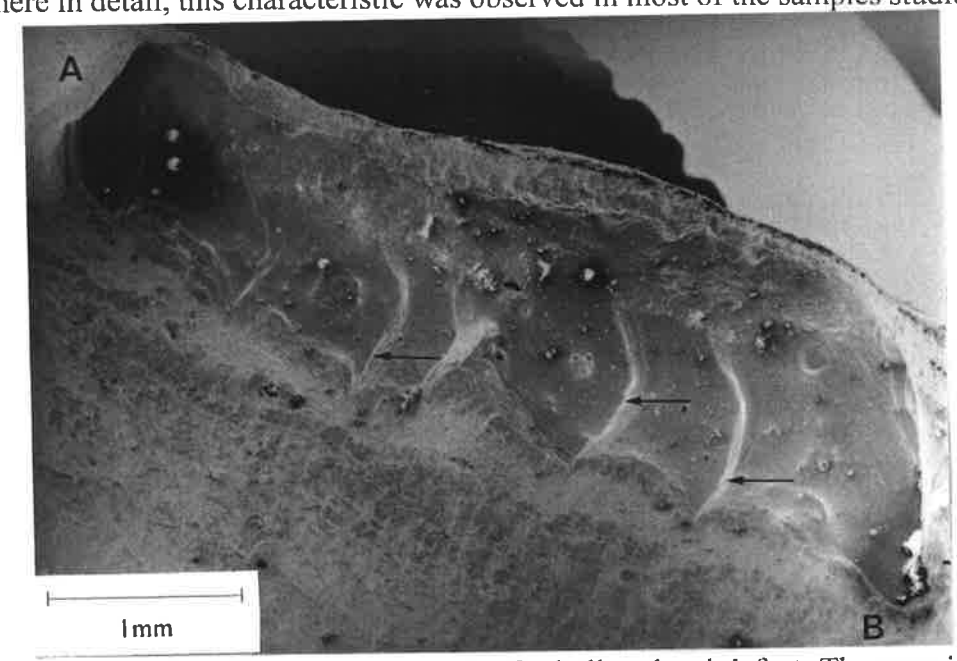

Figure 3.79 : Scanning electron micrograph of a hollow bead defect. The pore initiated at the cusp (marked A) and terminated at (B).

This particular pore is heavily oxidised and the oxide layer also covers the surface near the cusp (Figures 3.80 and 3.81) which is in most other cases the least oxidised region.

Figure 3.80 : Micrographs of the solidification microstructure of the initial cusp region. The oxide layer covers the microstructure. Some glassy slag fragments can also be seen.

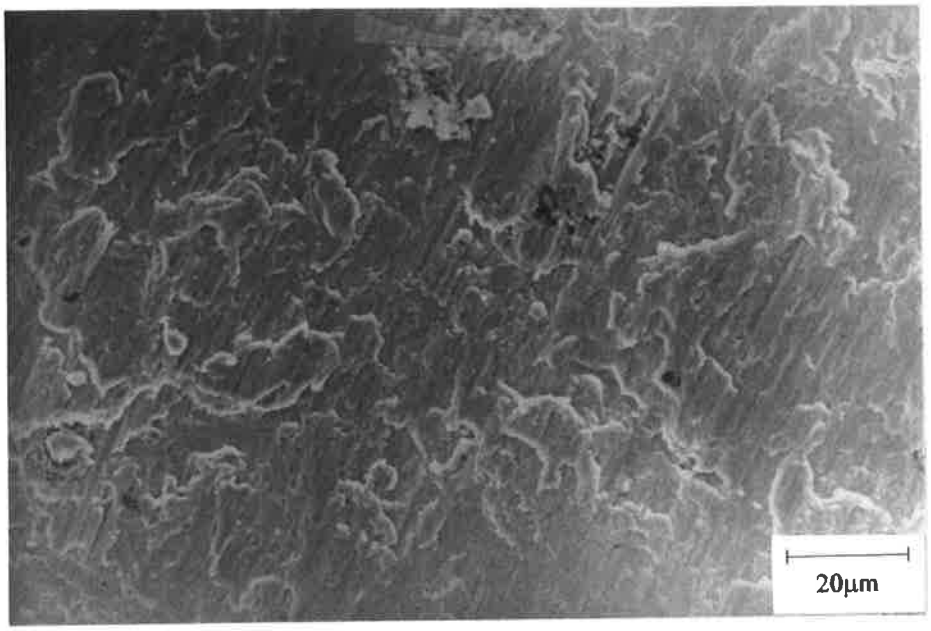

Figure 3.81: Higher magnification micrograph of the oxide layer near the cusp region.

Other features such as the oxidised surface which contains slag globules (Figure 3.82) and the slag fragments at the termination end of the pore (Figure 3.83) are similar to those described already.

Figure 3.82: Appearance of the surface in a region about midway along the pore.

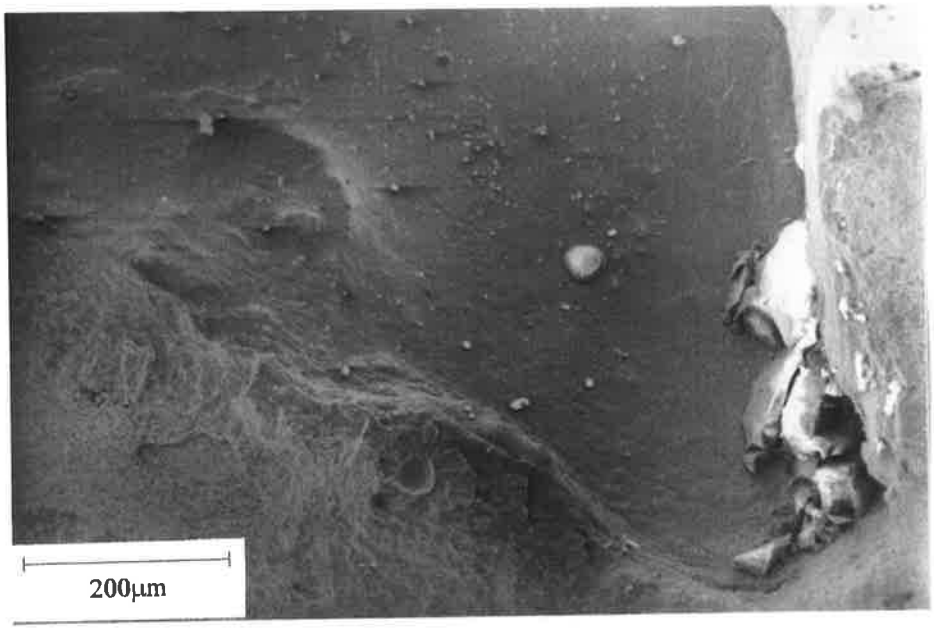

Figure 3.83: Micrograph showing the accumulation of slag at the termination end of the pore and the adjacent surface which is heavily oxidised.

Figure 3.84 is an SEM micrograph of another hollow bead pore where the ripples are again clearly visible on the surface. However, here the distribution of ripples is much less regular than in the previous example (Figure 3.79). This is presumably due to higher changes in growth rate. This pore is less oxidised than the previous one especially in the cusp (Figure 3.85) where there is evidence of cellular dendritic growth in the form of ridges due to microsegregation (Figure 3.86).

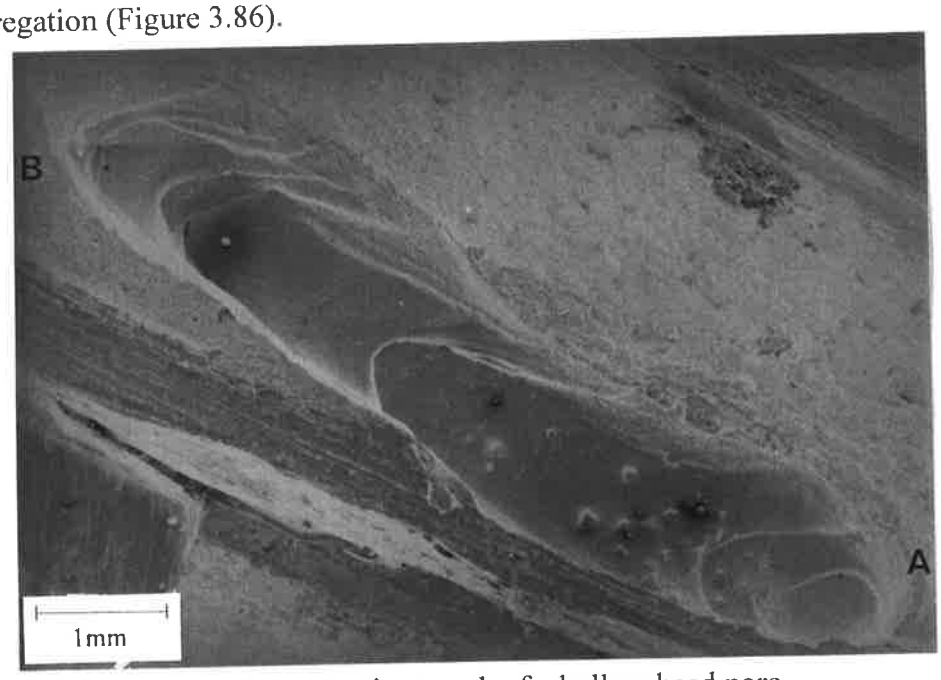

Figure 3.84 : Scanning electron micrograph of a hollow bead pore.

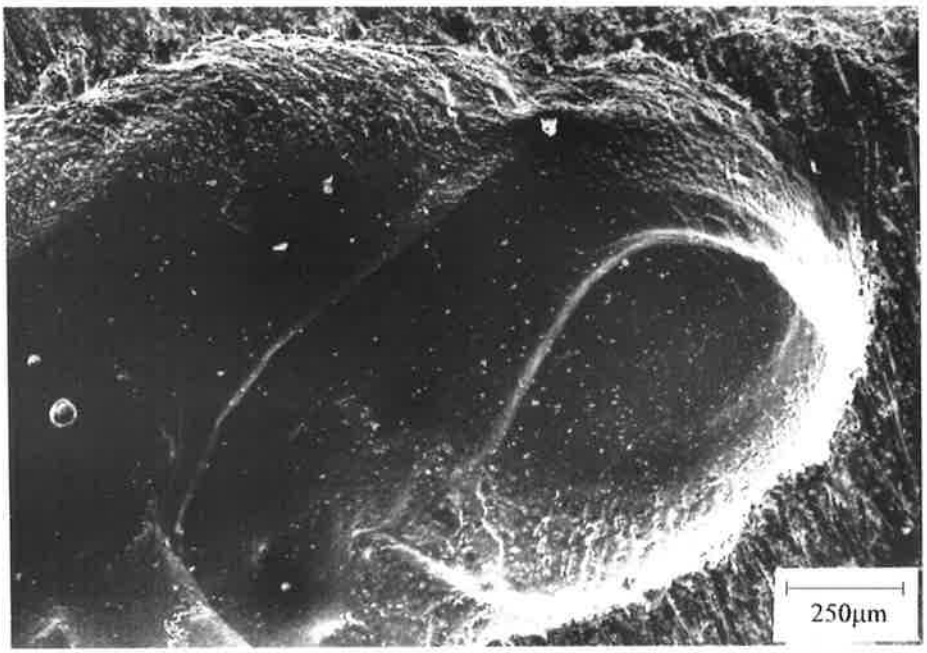

Figure 3.85: Higher magnification micrograph showing the cusp at (A) in Figure 3.84. The ridges resulting from microsegregation can be seen around the edges.

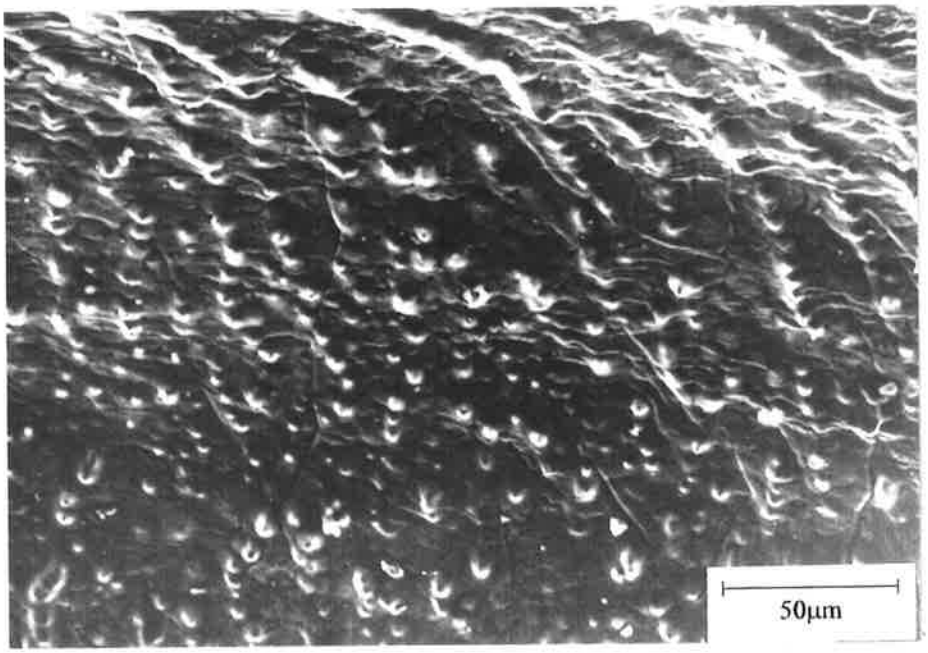

Figure 3.86: Micrograph of the ridges on the cusp surface. The distance between these ridges is about 20-25 microns.

The internal surface of the next hollow bead (Figure 3.87) is much more heavily oxidised than usual and is extensively covered by slag layers, which also cover most of the cusp region as seen in Figure 3.88.

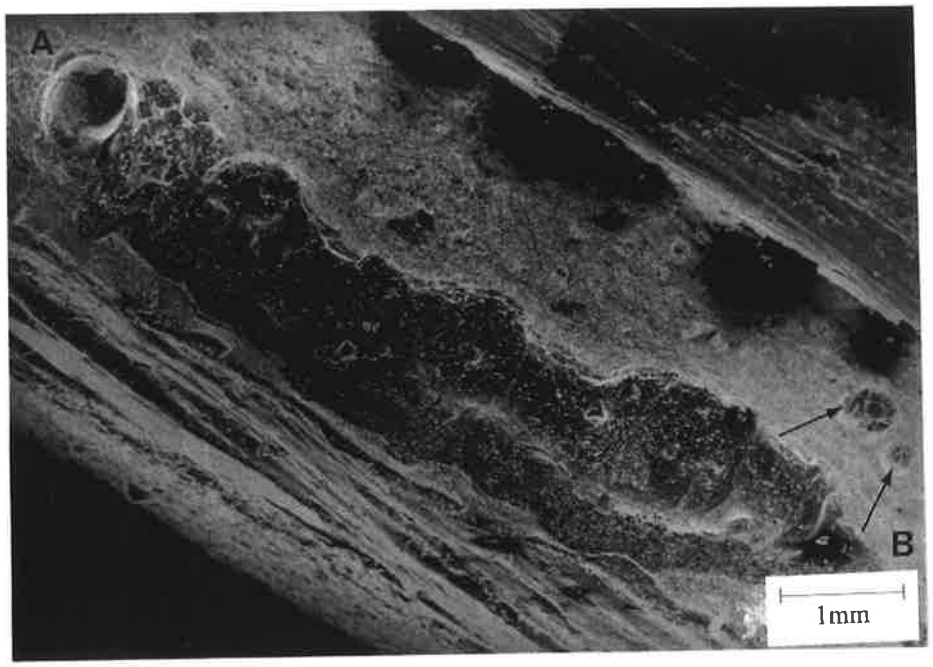

Figure 3.87: Scanning electron micrograph of the hollow bead pore.

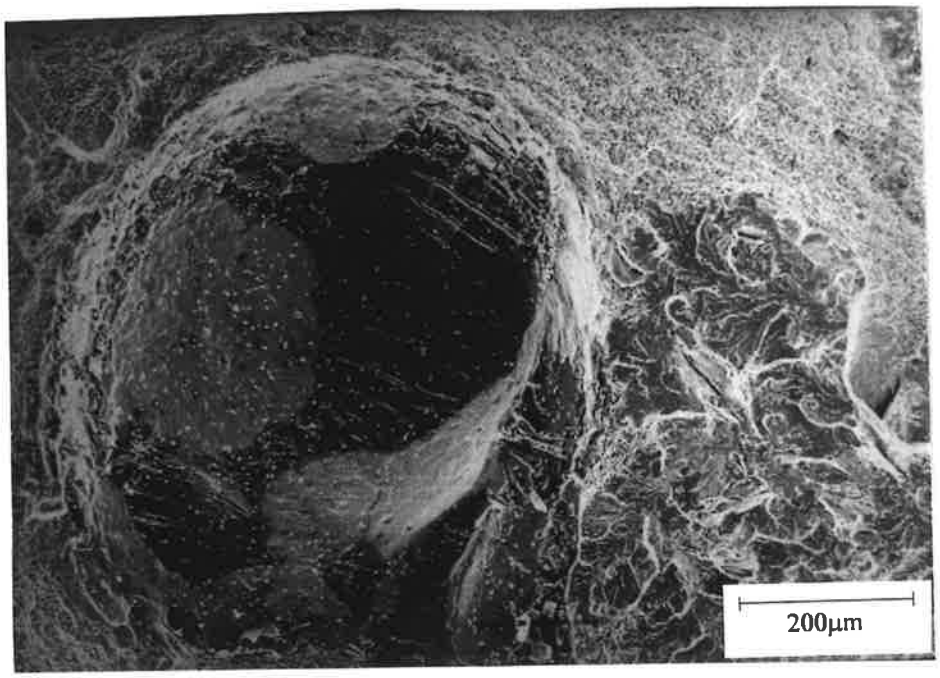

Figure 3.88: Higher magnification micrograph showing the cusp at (A) in Figure 3.87. The dark and broken regions are slag layers.

Slag inclusions (marked by arrows) can also be seen on the fracture surface of the weld metal outside the hollow bead (Figure 3.89). In Figure 3.87, they appear as round fragments (indicated by arrows) on the bottom right hand corner on the micrograph. An x-ray analysis confirmed their identity as slag inclusions rich in silicon, titanium and manganese.

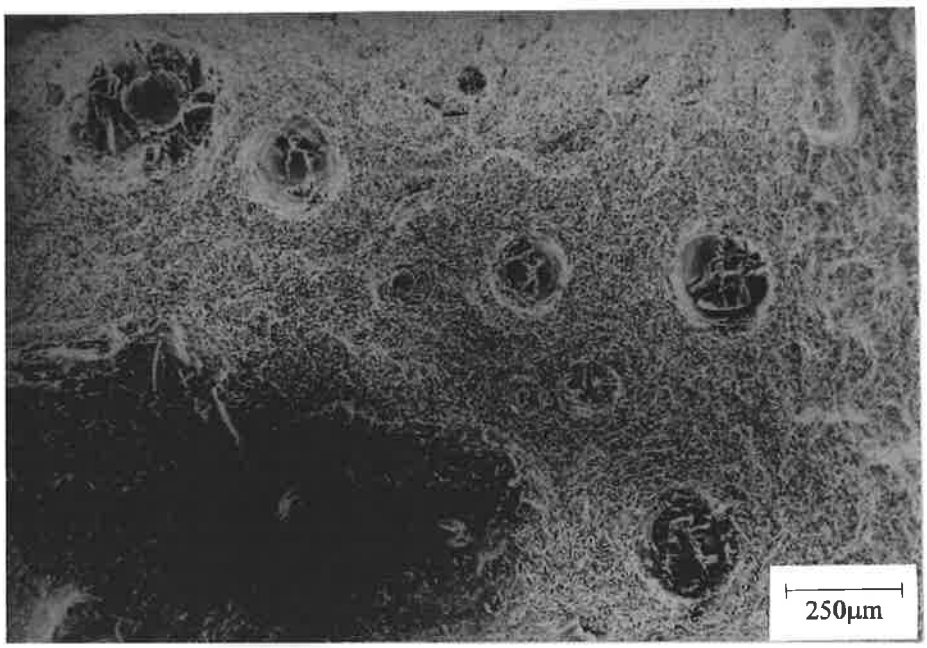

Figures 3.89: Higher magnification micrographs of slag inclusions outside the hollow bead pore.

In some pores, the internal surface has been oxidised to a much lesser degree especially near the region of nucleation: the cusp. These regions were used for a detailed study of the solidification microstructure. The other typical features are similar to the ones seen in other pores; an oxide layer forms and increases in thickness towards the end of the pore, small slag fragments are scattered along its entire length and larger inclusions located at the end.

For the hollow bead in Figure 3.90 the cusp is sparsely oxidised (Figure 3.91), especially its walls (marked I in Figure 3.91) where there is clear evidence of cellular dendritic growth as seen at higher magnification in Figure 3.92. The diameter of these protrusions suggests that they are likely to be the ends of the cellular dendrites.

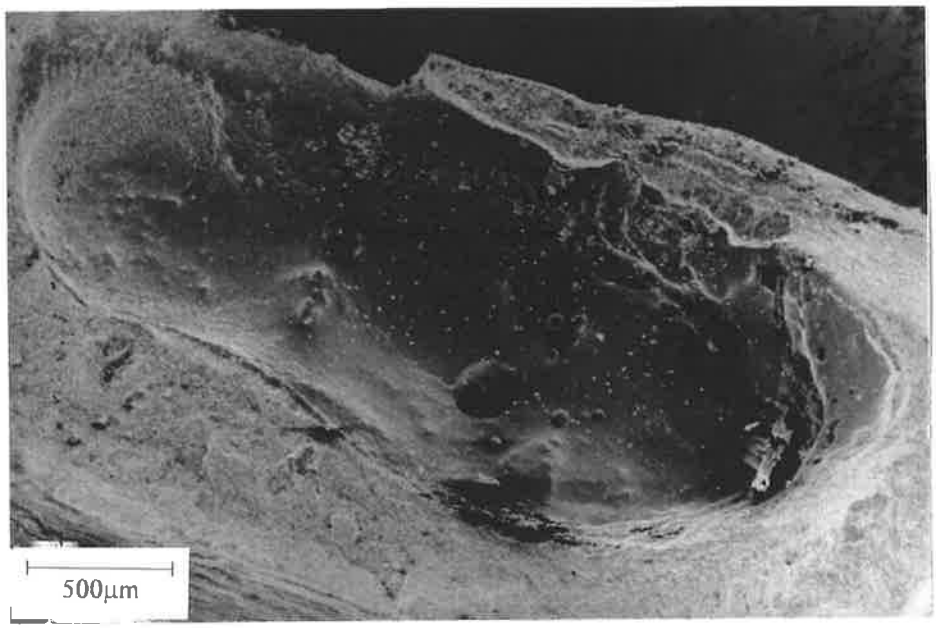

Figure 3.90 : Scanning electron micrograph of the hollow bead defect.

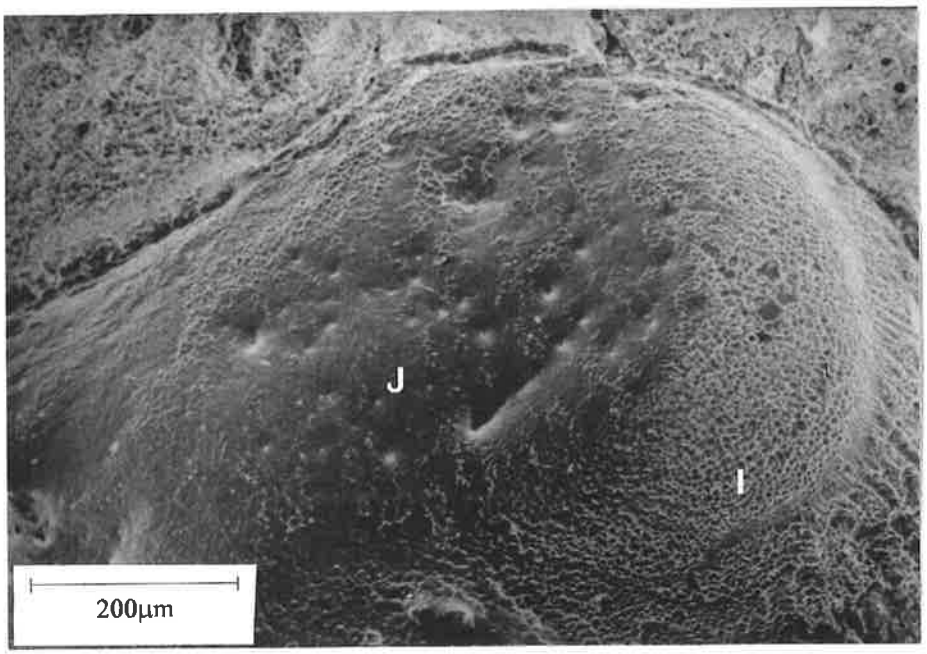

Figure 3.91: Higher magnification micrograph showing the cusp at (A) in Figure 3.90.

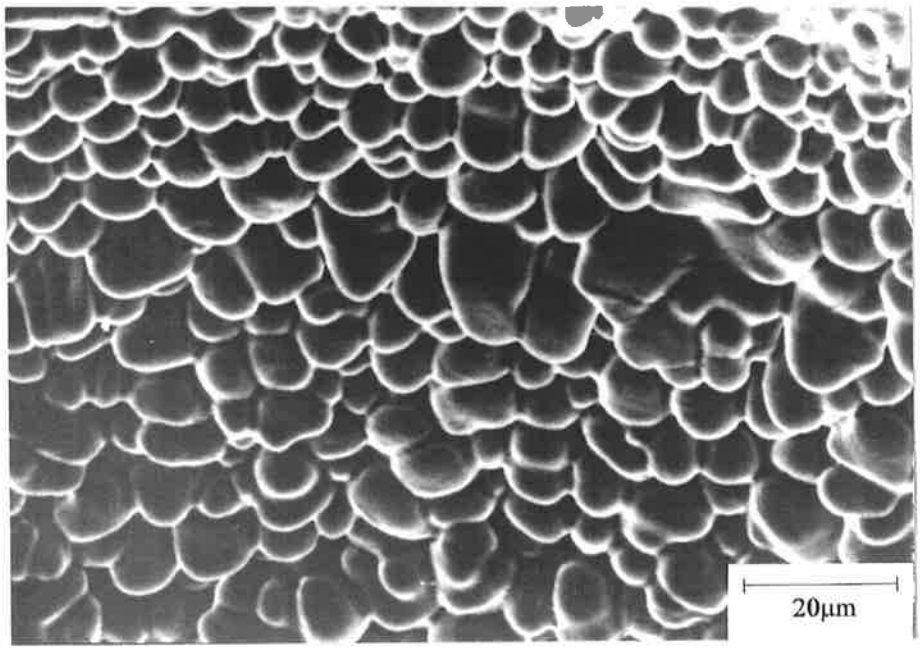

Figure 3.92: This higher magnification micrograph of the region near the tip of the cusp (marked I in Figure 3.91) reveals the tips of cellular dendrites which have protruded inside the pore.

In another area of the cusp (marked J in Figure 3.91) a thin oxide layer which partially masks the microstructure is also observed (Figure 3.93).

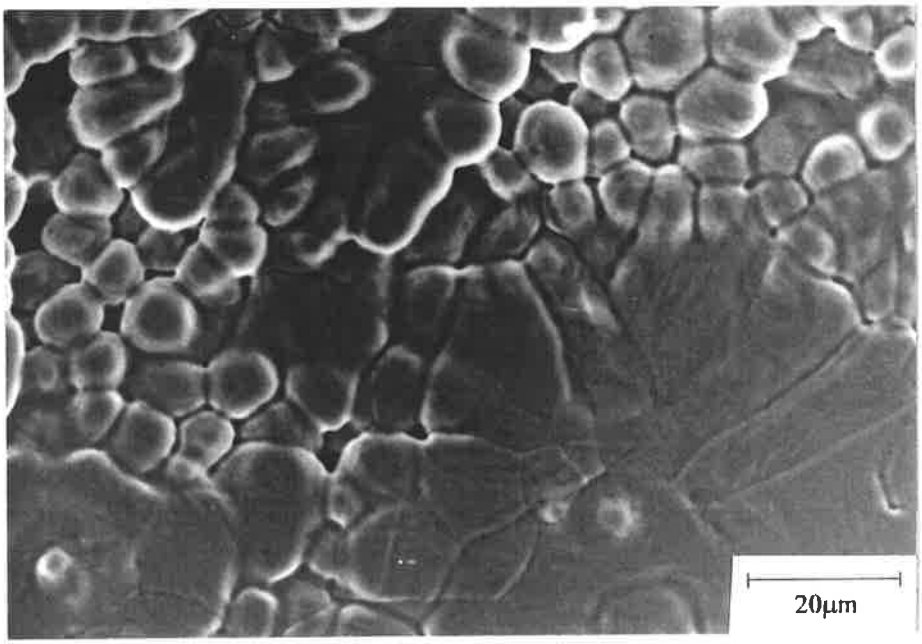

Figure 3.93: Micrograph of the solidification microstructure partially covered by a thin layer of oxide.

However, towards the end of the pore the degree of oxidation increases and angular particles of slag have accumulated (Figure 3.94).

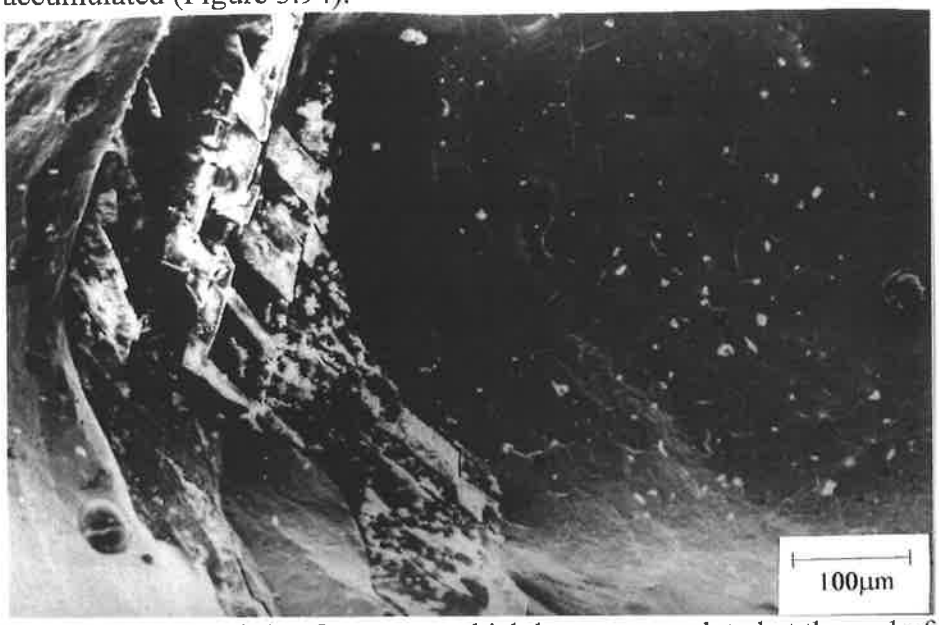

Figure 3.94: Micrograph of slag fragments which have accumulated at the end of this pore.

The hollow bead in Figure 3.95 has very similar features to the previous one. Evidence of cellular dendritic growth in the cusp (Figures 3.96 and 3.97) is in the form of ridges as previously described. The slag fragments in this pore are large (Figure 3.98). A large amount of slag, in the form of globules and fragments, and a thicker oxide layer are present at the termination end (Figure 3.99).

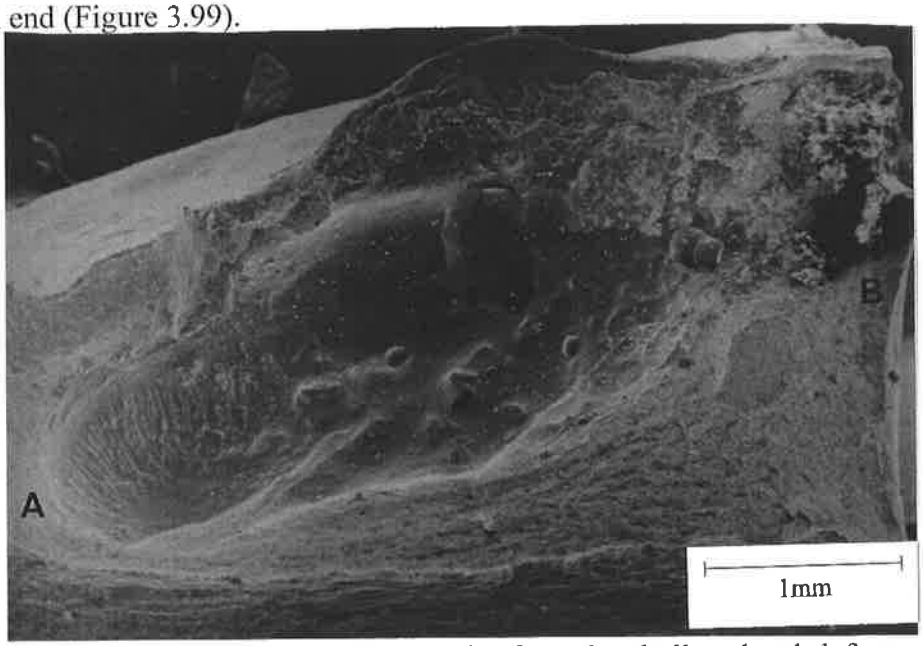

Figure 3.95 : Scanning electron micrograph of another hollow bead defect with a lower degree of oxidation. The pore initiated at the cusp (marked A) and terminated at (B).

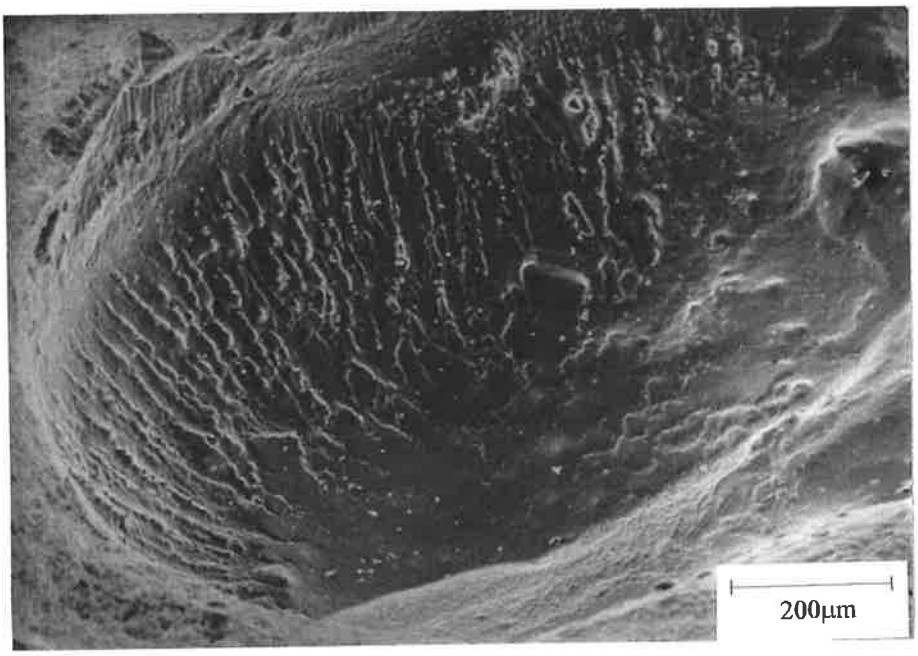

Figure 3.96: Higher magnification micrograph showing the cusp at (A) in Figure 3.95.

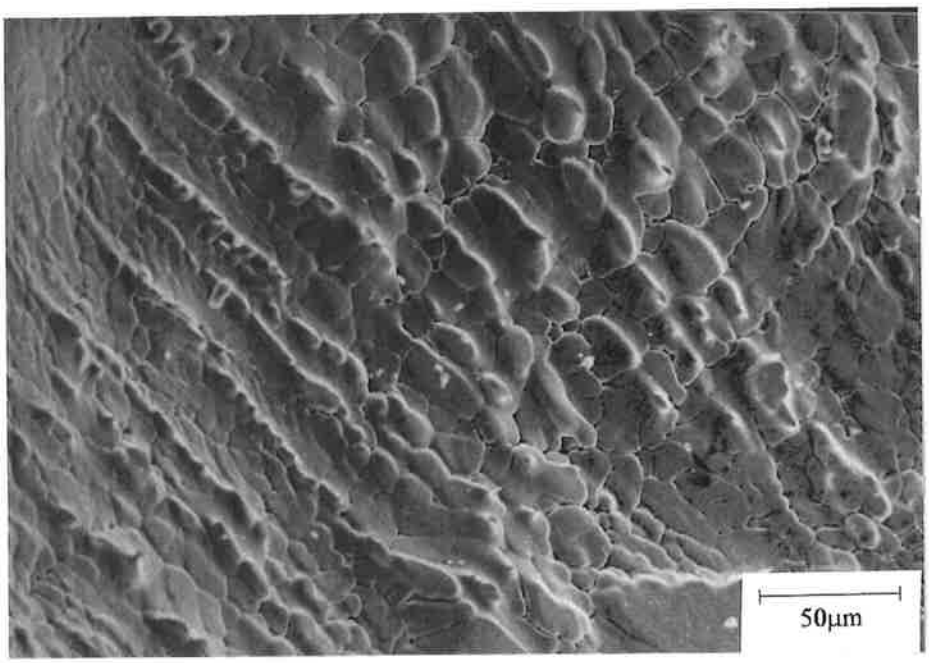

Figure 3.97: Micrograph of ridges observed along the cusp wall. It is thought that the rounded features seen between the ridges are the secondary arms of the main cellular dendrites.

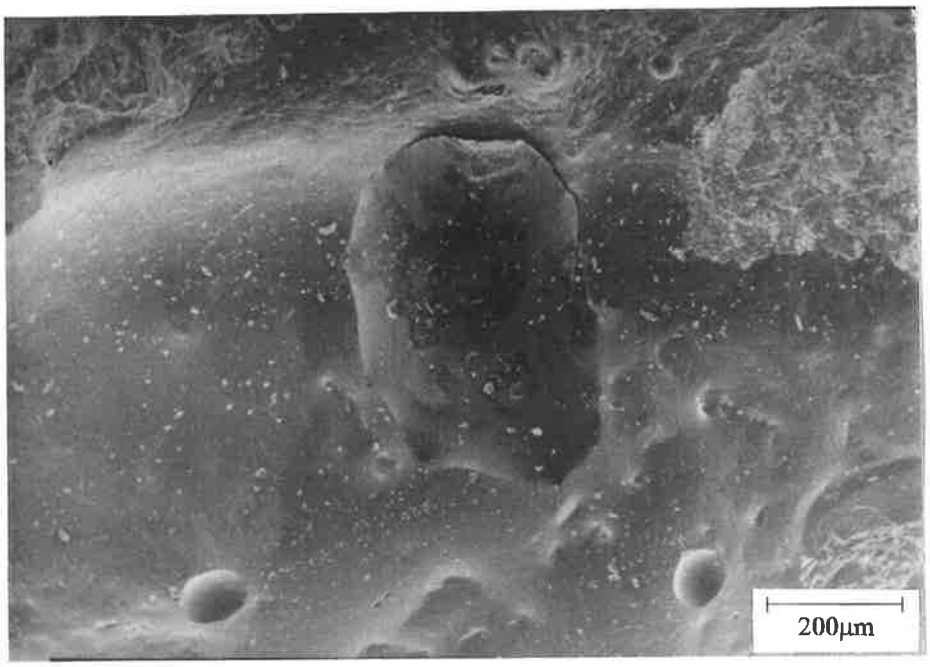

Figure 3.98: Micrograph of the oxidised surface. midway along the pore. containing large slag fragments.

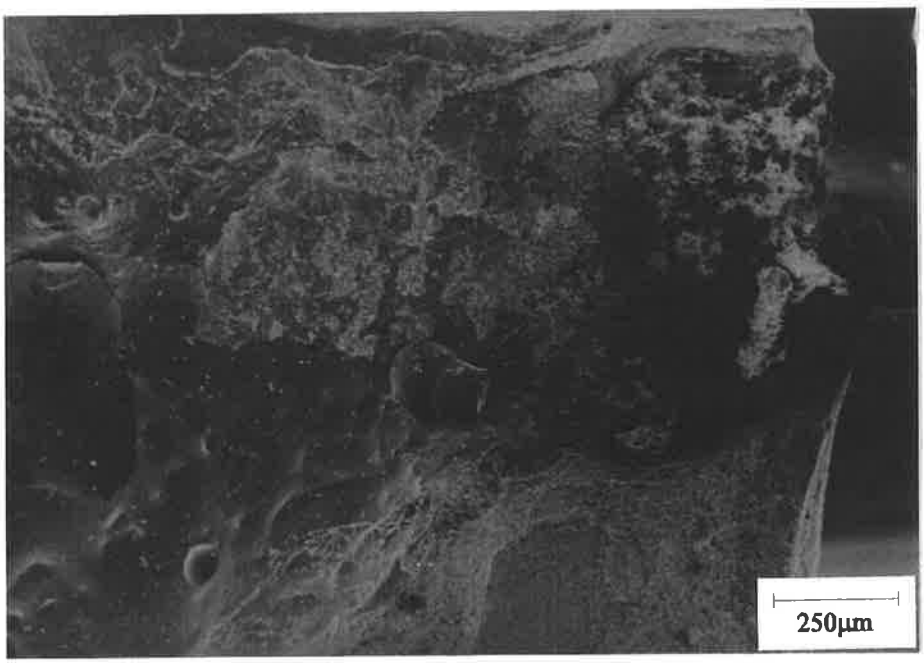

Figure 3.99: Micrograph showing the accumulation of slag at the end of the pore.

A slight anomaly is observed in the next example, where the hollow bead has not grown in a single horizontal plane. The pore has grown upwards, terminated and then formed another one (Figure 3.100). The reason for the upward growth is the presence of a tack weld between the two pores such that the first one is actually growing around the tack. The entire length of the hollow bead is not shown in Figure 3.101, however Figure 3.102 shows where the first pore terminates and then starts to propagate again (arrowed at the centre of the micrograph).

The cusp is seen in the Figure 3.103. Bright ridges can be seen along the boundary of the cusp which have been identified as segregation between cellular dendrites. A spacing of 20 to 25 microns has been measured from Figure 3.104.

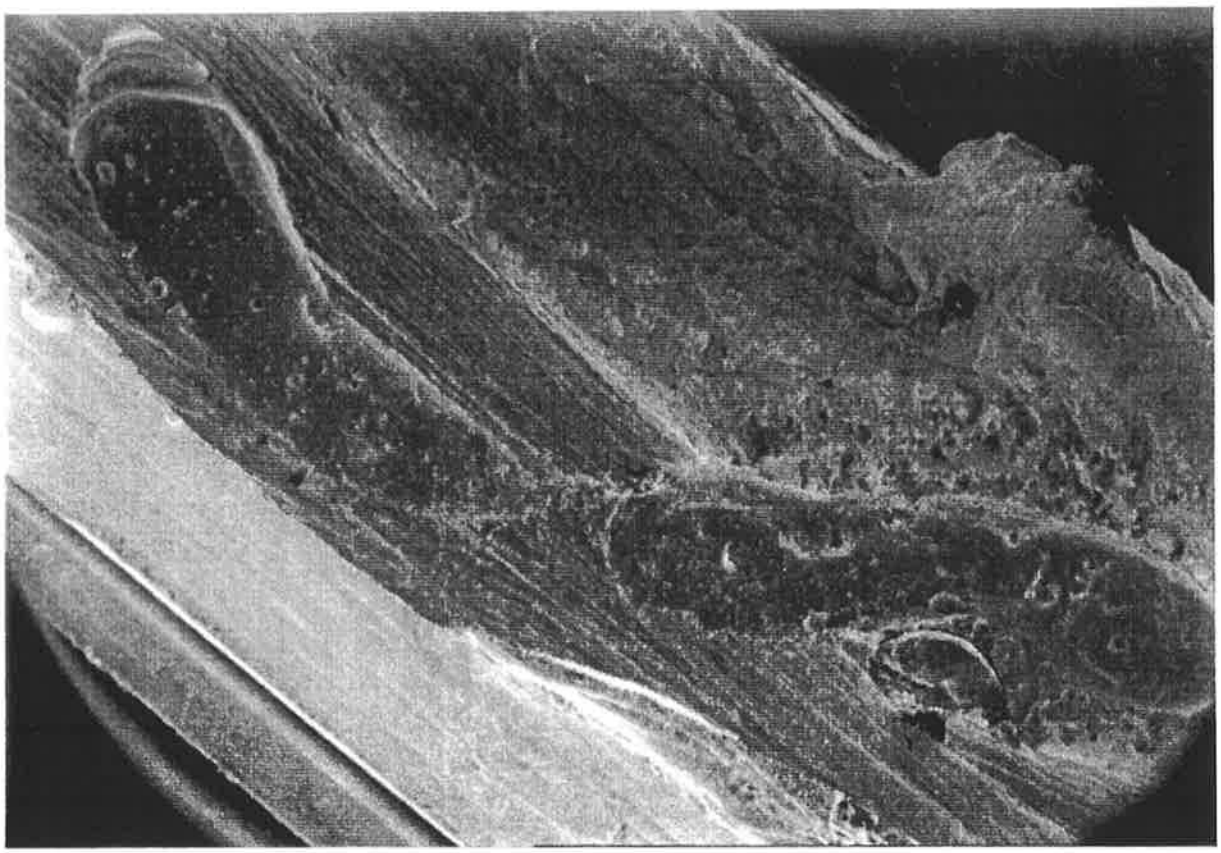

Figure 3.100: Scanning electron micrograph of the hollow bead pore described above.

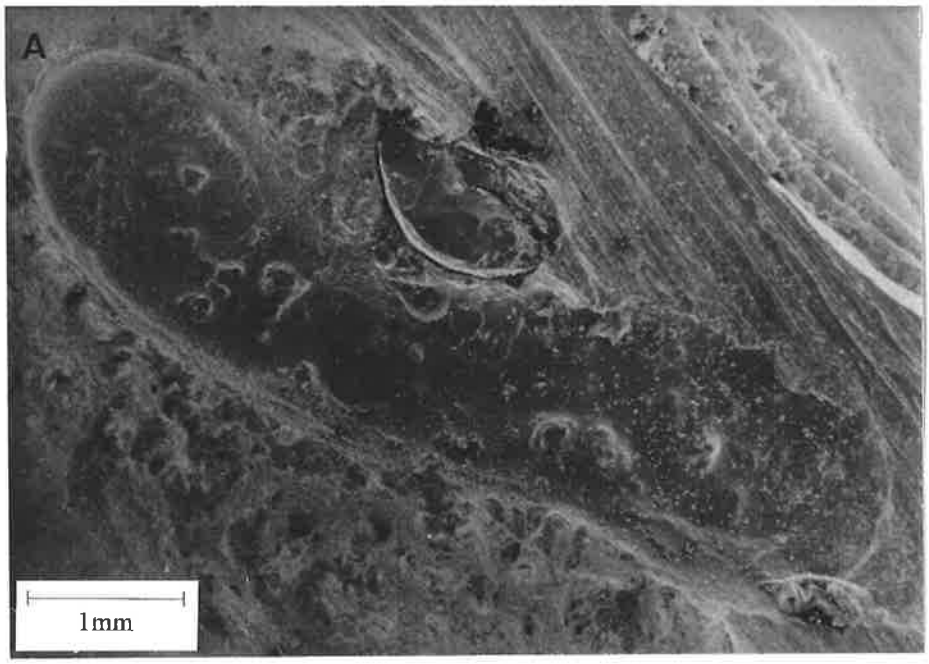

Figure 3.101 : Scanning electron micrograph of the first hollow bead defect. The pore initiated at a cusp (marked A). Midway along the length of this pore is a large slag fragment outside the pore itself.

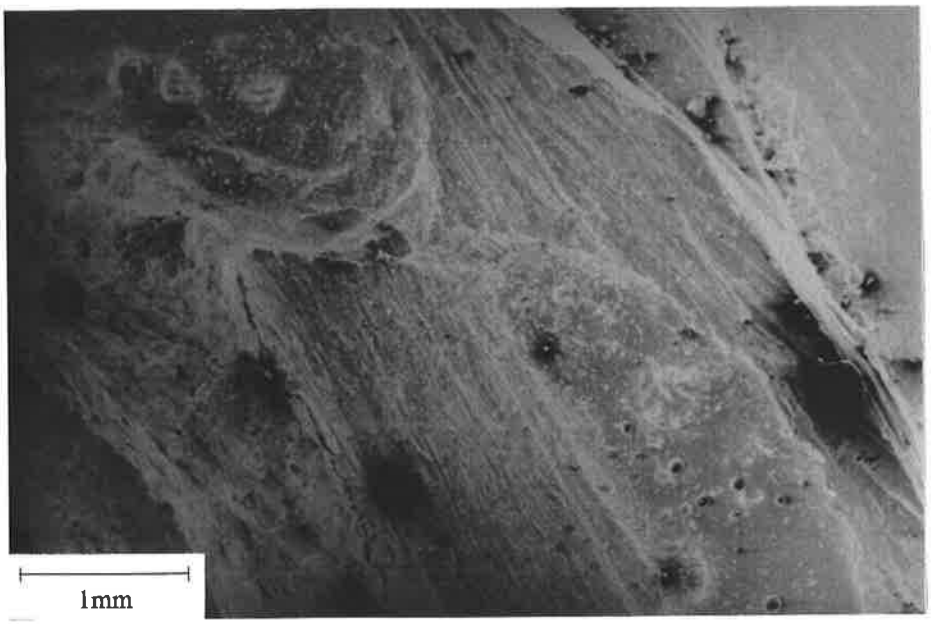

Figure 3.102: SEM micrograph showing the termination of the first pore, seen in Figure 3.101, which then starts to propagate again.

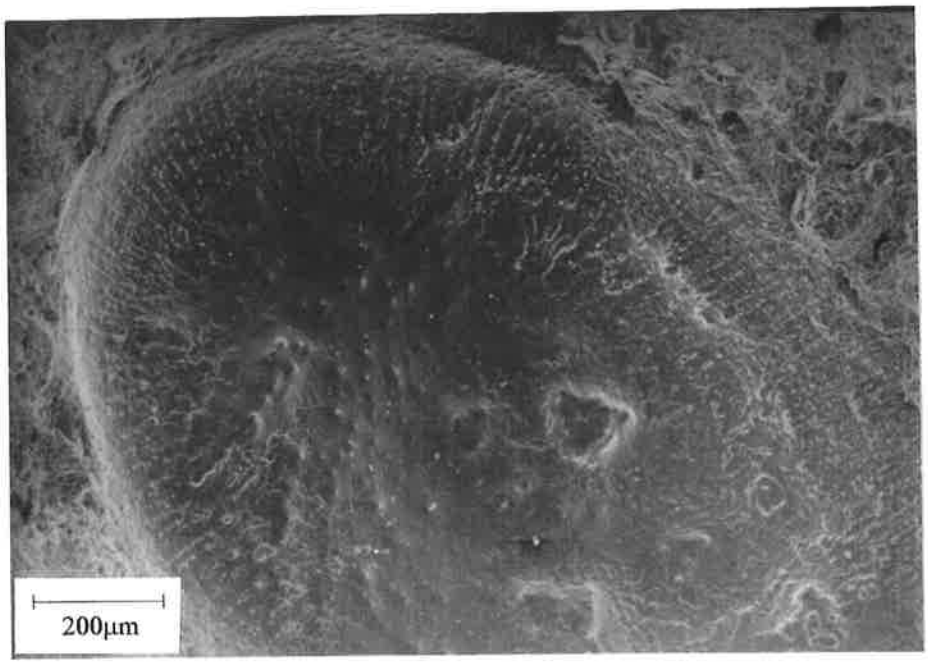

Figure 3.103: Higher magnification micrograph showing the cusp at (A) in Figure 3.100.

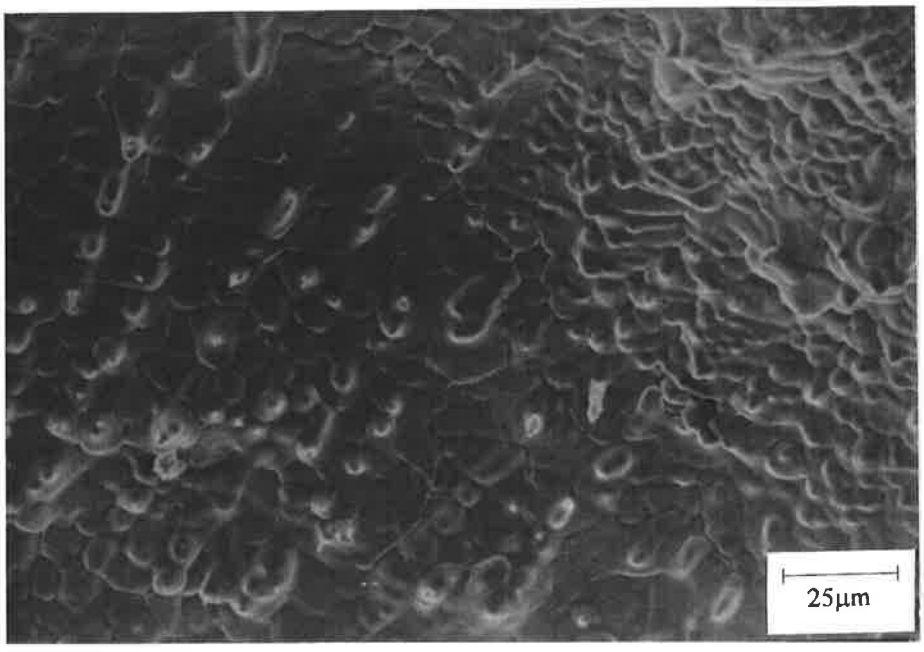

Figure 3.104: Micrograph of the ridges observed along the cusp wall.

The following examples deal with longer hollow bead pores which were studied to confirm that they exhibited the same characteristics as the ones discussed previously and to find out whether the length of the pore had any major effect on the common features of hollow beads, in particular the extent of oxidation of the surface.

Four samples of hollow bead with lengths ranging from approximately 9.5mm to 18mm are described. The hollow bead in Figure 3.105 exhibits all the common features previously discussed. The cusp seen in Figure 3.106 is well defined and reveals the solidification microstructure (Figure 3.107). Slag globules are present near the cusp but not in it.

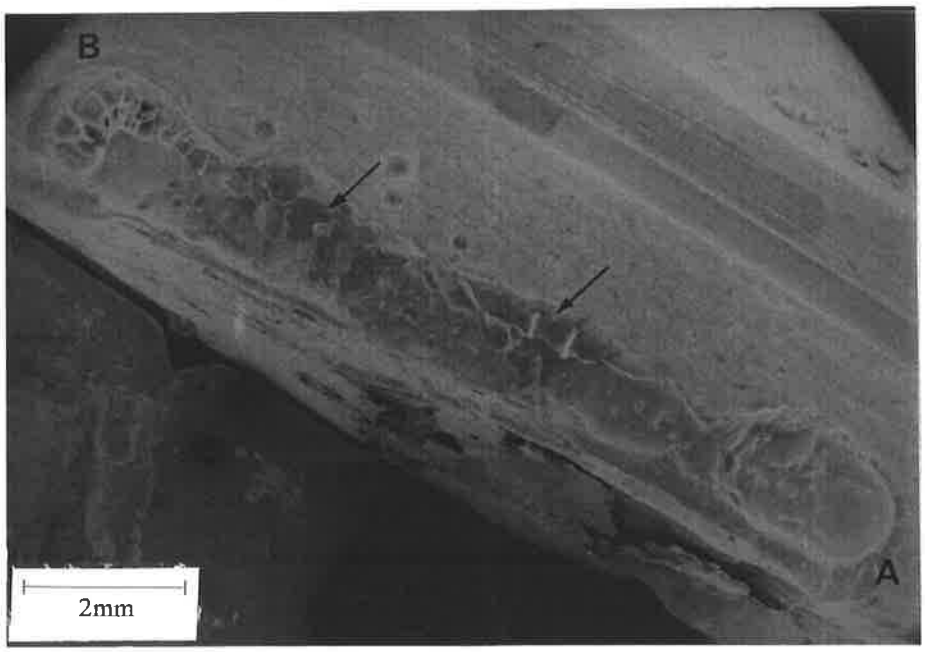

Figure 3.105 : Scanning electron micrograph of a 12mm long hollow bead defect.

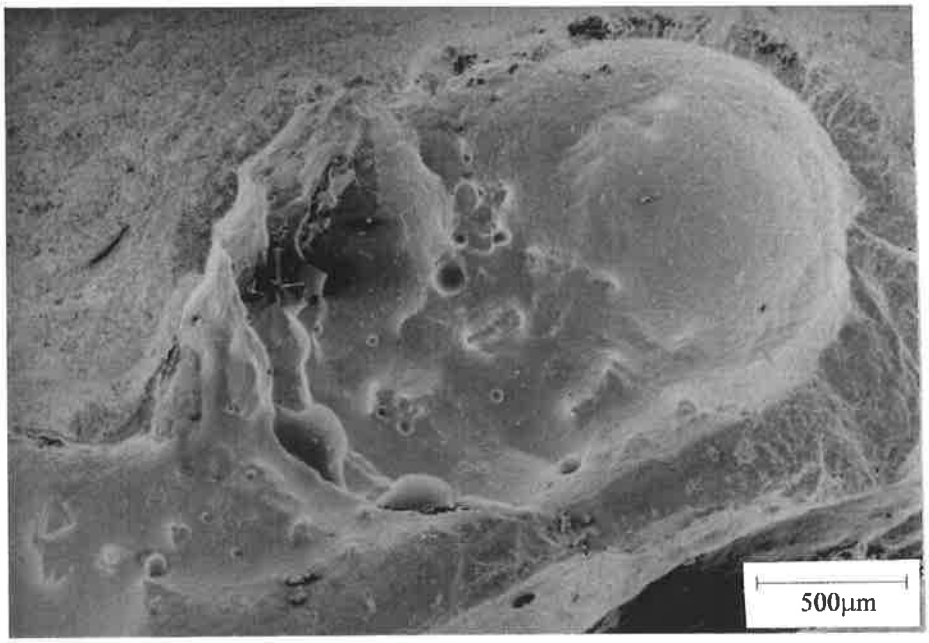

Figure 3.106: Higher magnification micrograph showing the cusp at (A) in Figure 3.105.

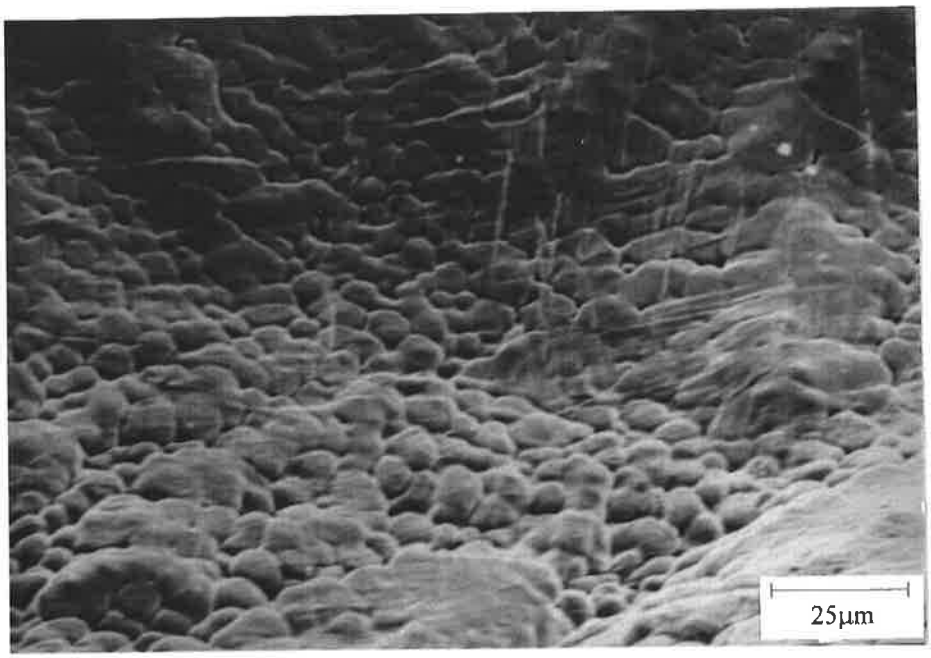

Figure 3.107 : Micrographs of the solidification microstructure of the initial cusp region. Due to their diameter, around 10 microns, the protrusions are thought to be the tips of the cellular dendrites.

The dark areas (shown by arrows in Figure 3.105) along the surface of the pore contain slag layers. A large slag fragment can be seen at the end of the pore and appears to contain bubbles (Figure 3.108). The surface near the slag fragment is again heavily oxidised.

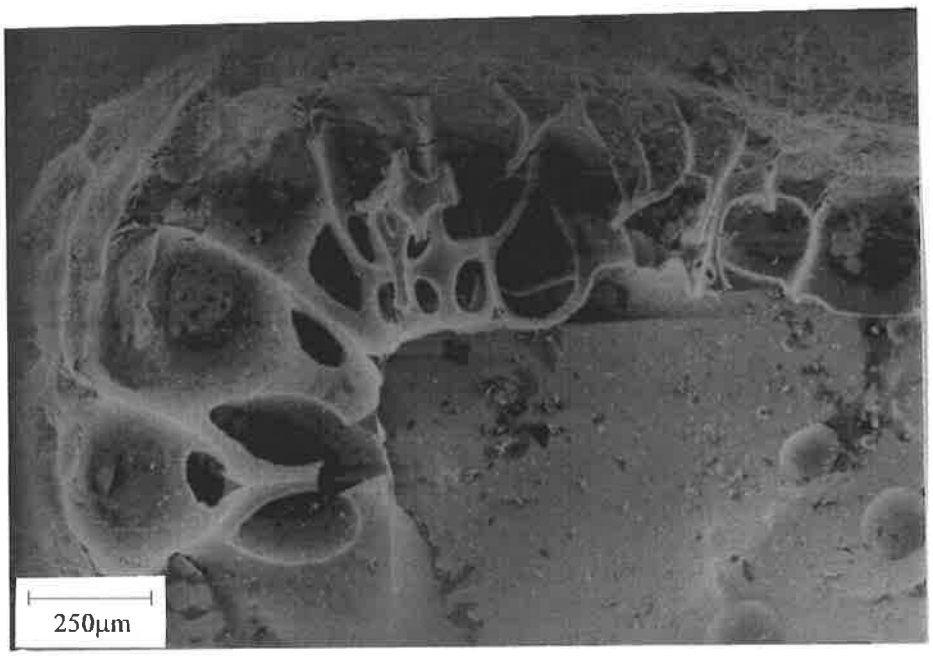

Figure 3.108: Micrograph of a large slag fragment containing bubbles at the end of the hollow bead.

An 18mm long pore is shown in Figure 3.109, although not in its entirety. The diameter varies irregularly along the length of the pore. The entire surface including the cusp (Figure 3.110) is heavily oxidised. Slag layers located near the cusp and along most of its surface have been observed (Figure 3.111).

Figure 3.109 : Scanning electron micrograph of an 18mm long hollow bead defect. The pore initiated at the cusp (marked A).

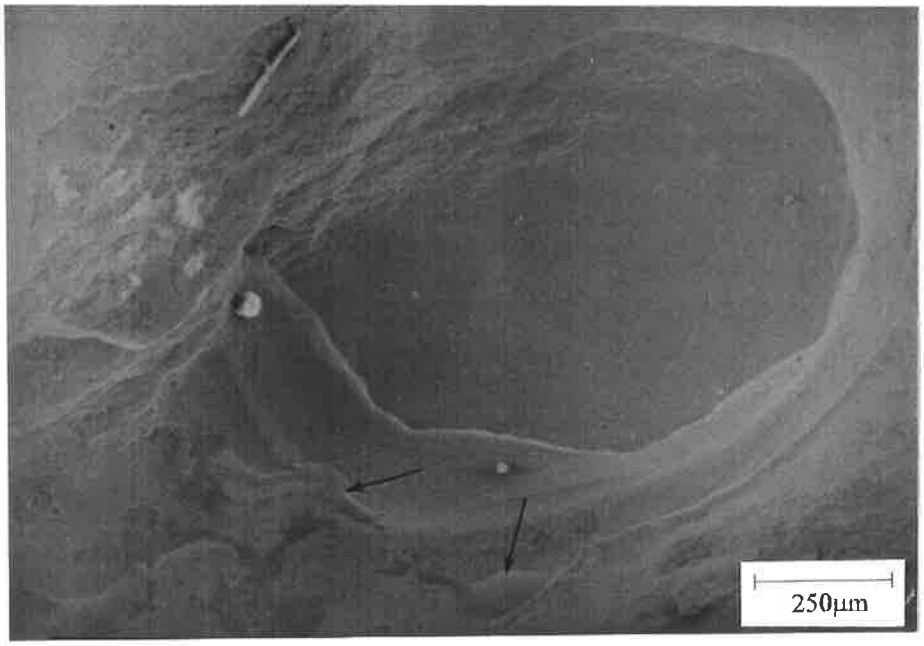

Figure 3.110: Higher magnification micrograph showing the cusp at (A) in Figure 3.109. Slag layers (shown by arrows) can be seen adjacent to the cusp.

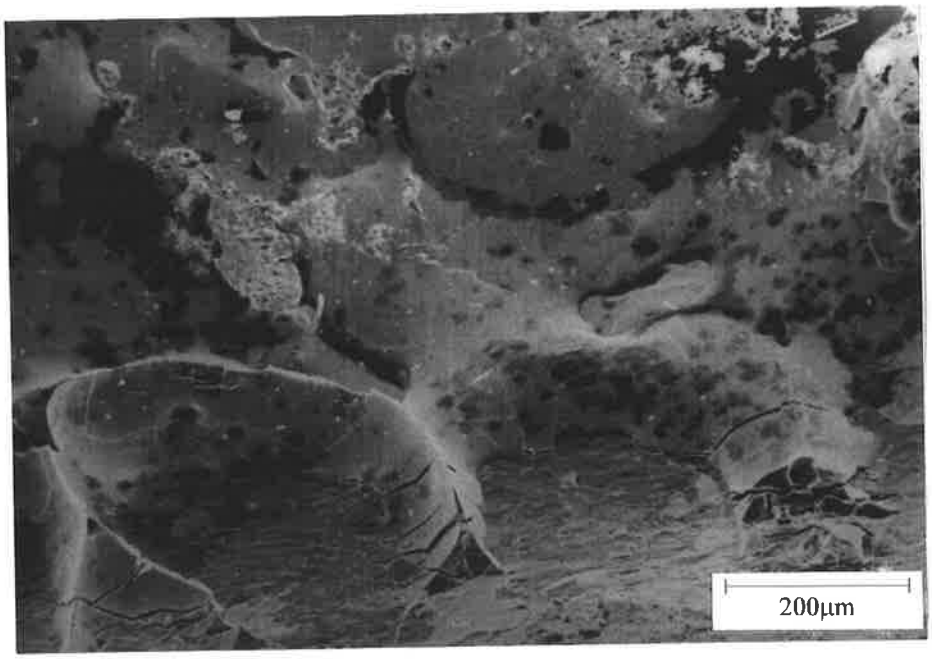

Figure 3.111: Micrograph of thick slag layers found along the pore length.

An 8mm long pore is shown in Figure 3.112. The diameter is irregular along its length, decreasing at mid length and then increasing towards the termination end. The cusp shown in Figure 3.113 is less heavily oxidised than the rest of the pore and the solidification microstructure is evident.

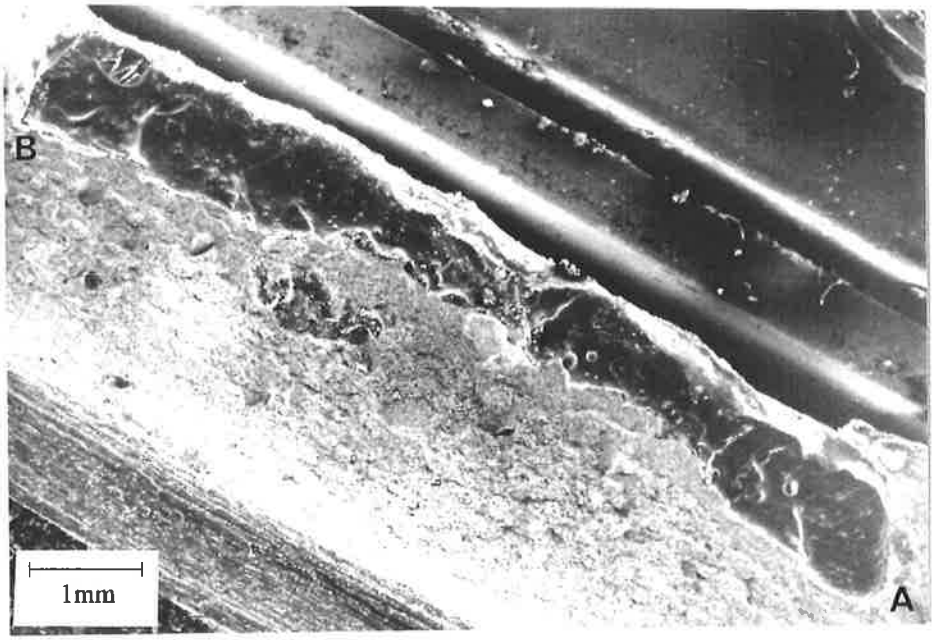

Figure 3.112 : Scanning electron micrograph of an 8mm long hollow bead defect. The pore initiated at the cusp (marked A) and terminated at (B). Ripples are evident on the pore surface.

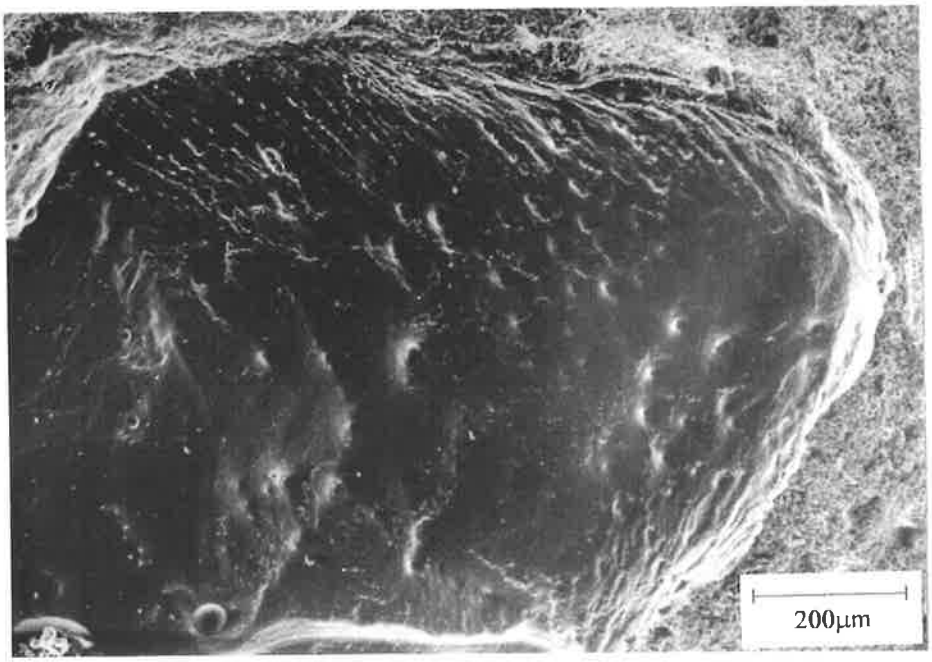

Figure 3.113: Higher magnification micrograph showing the cusp at (A) in Figure 3.112. The ridges resulting from microsegregation are present on the surface of this pore.

Another 18mm long pore is shown in Figure 3.114. As the pore is very long two micrographs are required to show it entirely. The pore diameter is very small at the start and increases irregularly towards the end. The cusp appears to be offset from the main axis of the pore and implies that it nucleated slightly higher than the body of the pore, further from the weld surface. The surface of the cusp is mostly covered by a layer of slag (Figure 3.115).The surface is also heavily oxidised and is extensively covered by slag layers and fragments (Figures 3.116 and 3.117). The surface at the termination end is shown in Figure 3.118 and is again observed to be heavily oxidised with slag layers and fragments.

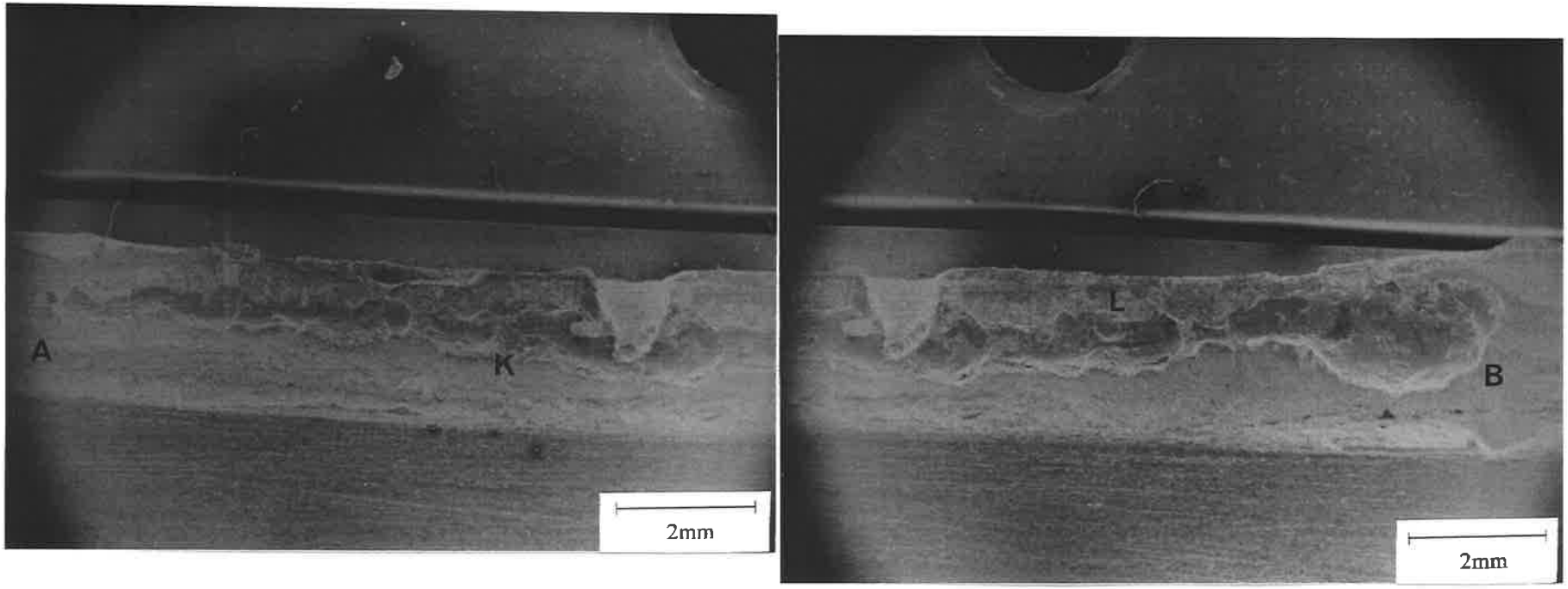

Figure 3.114 : Scanning electron micrographs of another 18mm long hollow bead defect. The pore initiated at the cusp (marked A) and terminated at (B).

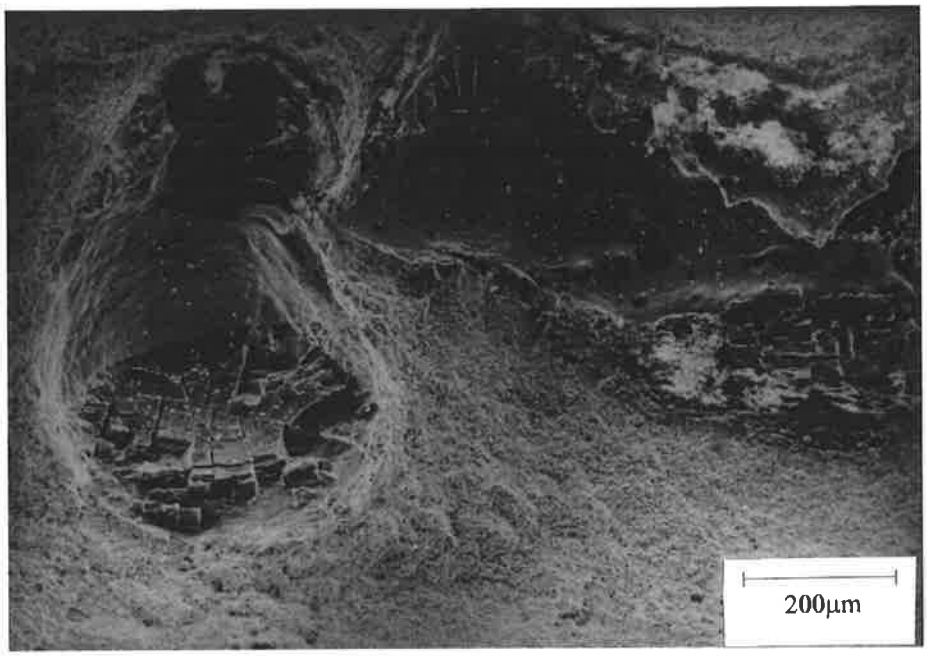

Figure 3.115: Higher magnification micrograph showing the cusp at (A) in Figure 3.114.

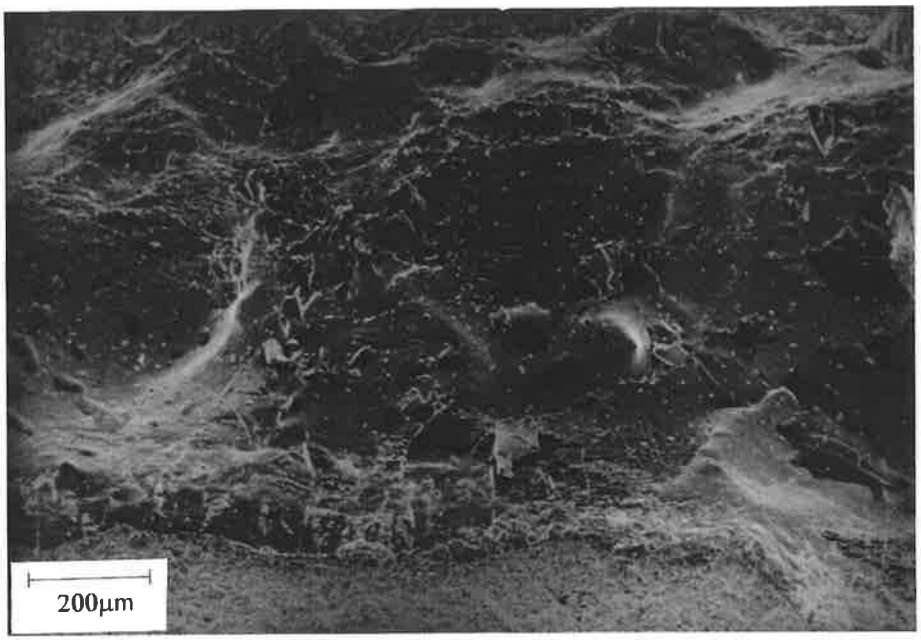

Figure 3.116: Micrograph of the pore surface at the area K in Figure 3.114.

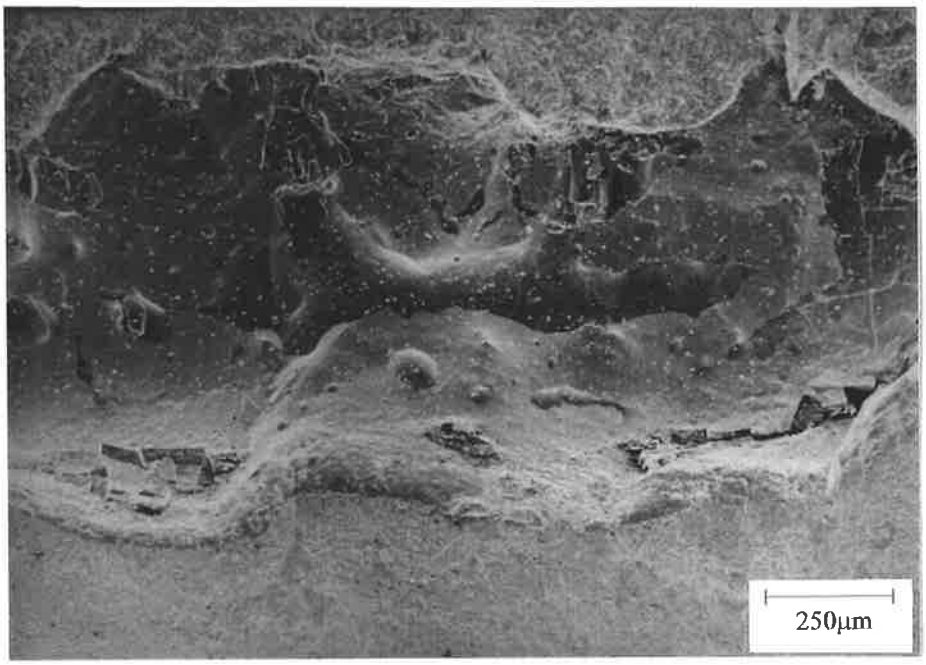

Figure 3.117: Micrograph of the pore surface at the area L in Figure 3.114.

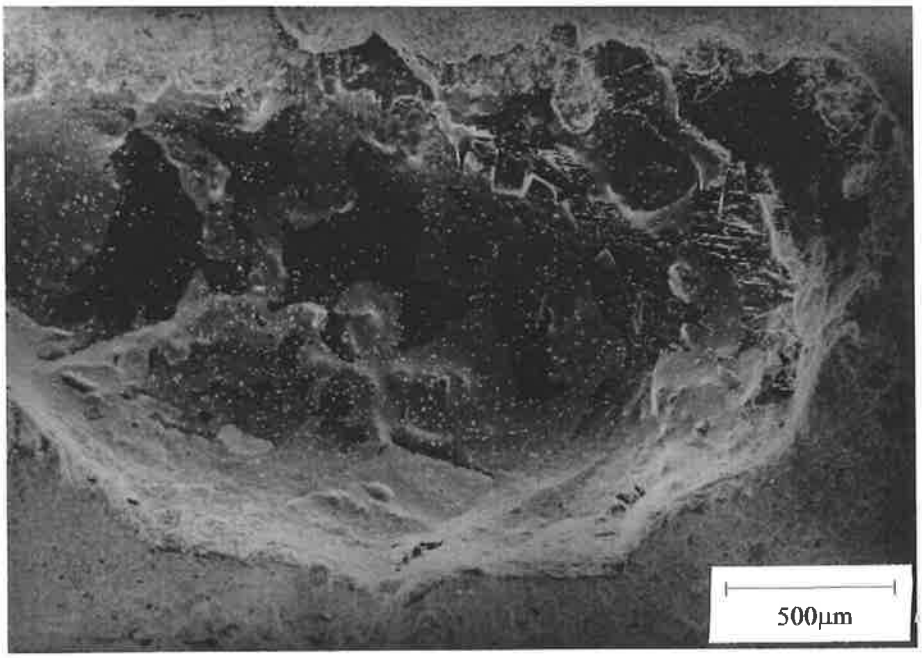

Figure 3.118: Micrograph of the pore surface at the termination end.

A pore measuring 1.5mm in length (Figure 3.119) was studied as these small pore have often been observed in radiographs of welds. This sample shows all the typical features attributed to hollow bead defects. The occurrence of these pores have been included in the experimental results as they have the same characteristics as longer ones. A start cusp (near the start of the pore marked A in Figure 3.119), ripples, and slag and oxide on the surface are evident on the surface. The dark patch at the top of the pore contains some slag.

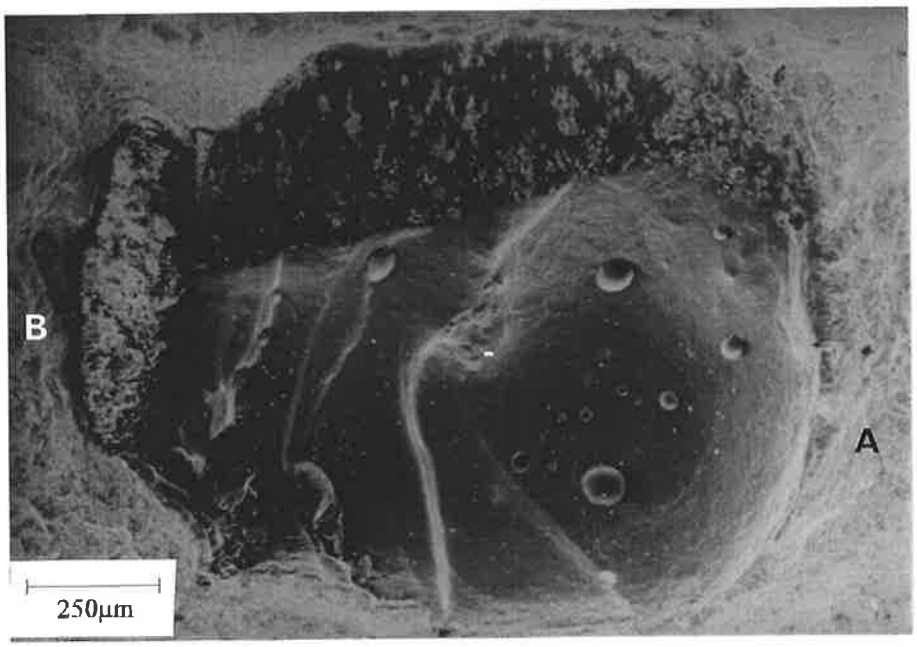

Figure 3.119: Micrograph of a small (1.5mm long) pore showing all the typical features of a hollow bead defect. The slag inclusion at the end is shown by an arrow. The pore starts at A and ends at B.

The following three specimens were used in the analysis of the gas present inside hollow bead pores. The composition of the gas inside the pores has been presented in Section 2.14. The composition of the gas in the third pore was different from the other two, containing a lower hydrogen content of 80% and a higher percentage of nitrogen and carbon monoxide. A study of their internal surfaces was thus undertaken to determine whether a difference in the gas

composition had affected the characteristics of the hollow beads. The first two samples described have a similar gas composition, with a hydrogen content around 95%.

The walls of the cusp of the first hollow bead (seen in Figure 3.120) are not oxidised and as a result the solidification structure is apparent with the protrusions representing cellular dendrites clearly visible the walls of the cusp (Figure 3.121). The protrusions (Figure 3.122) are about 12 microns in diameter and are therefore likely to be the ends of cellular dendrites. The darker region within the cusp is partially covered by oxide (Figure 3.124). The pore surface gradually becomes more oxidised; close to the cusp the solidification structure is still apparent (Figure 3.123), though masked in places by an oxide layer. The solidification structure resembles the one seen on the wall of the cusp with rounded features, or protrusions, about 15 microns in diameter. Further into the pore the oxide layer completely masks the solidification structure (figure 3.124). In addition the slag inclusions and layers become more numerous towards the end (Figure 3.125).

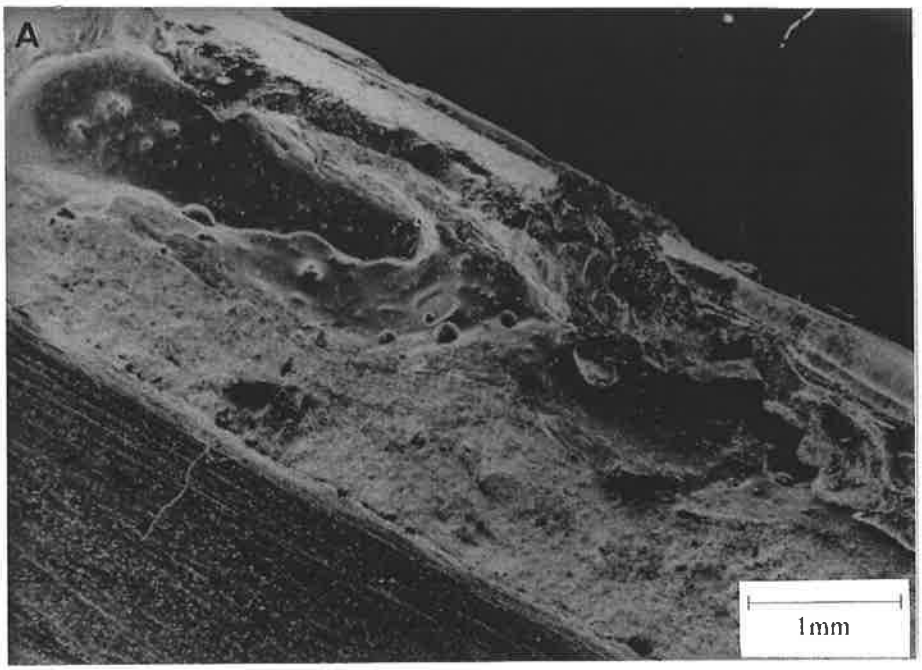

Figure 3.120 : Scanning electron micrograph of the hollow bead defect in the first gas analysis sample. The pore initiated at the cusp (marked A). Ripples are evident on the pore surface.

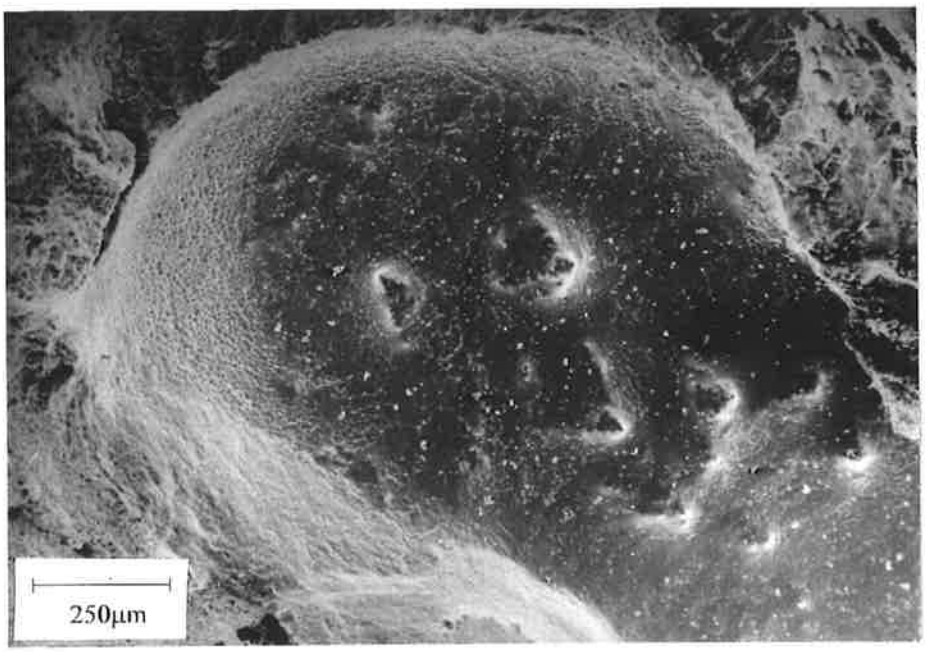

Figures 3.121: Higher magnification micrograph showing the cusp at (A) in Figure 3.120.

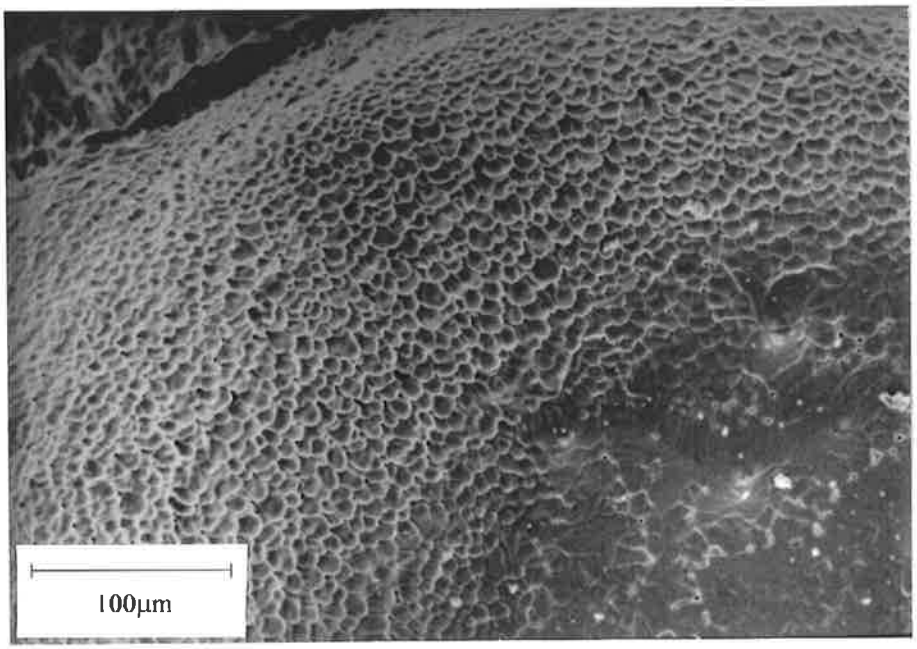

Figure 3.122: Higher magnification micrograph of the cellular dendrites seen along the cusp wall

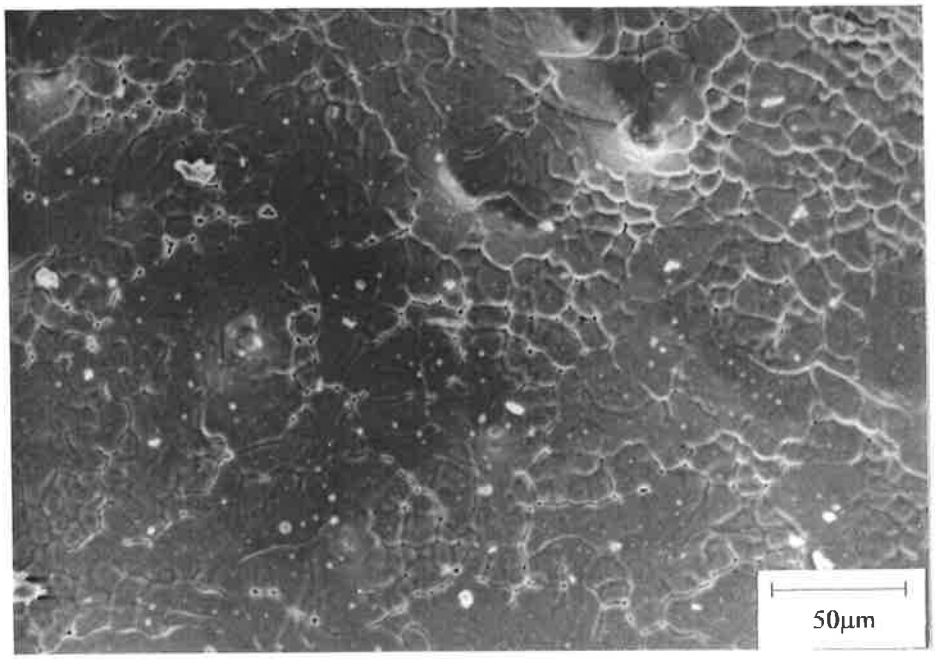

Figure 3.123: Micrograph showing an oxide layer in the cusp partially covering the microstructure.

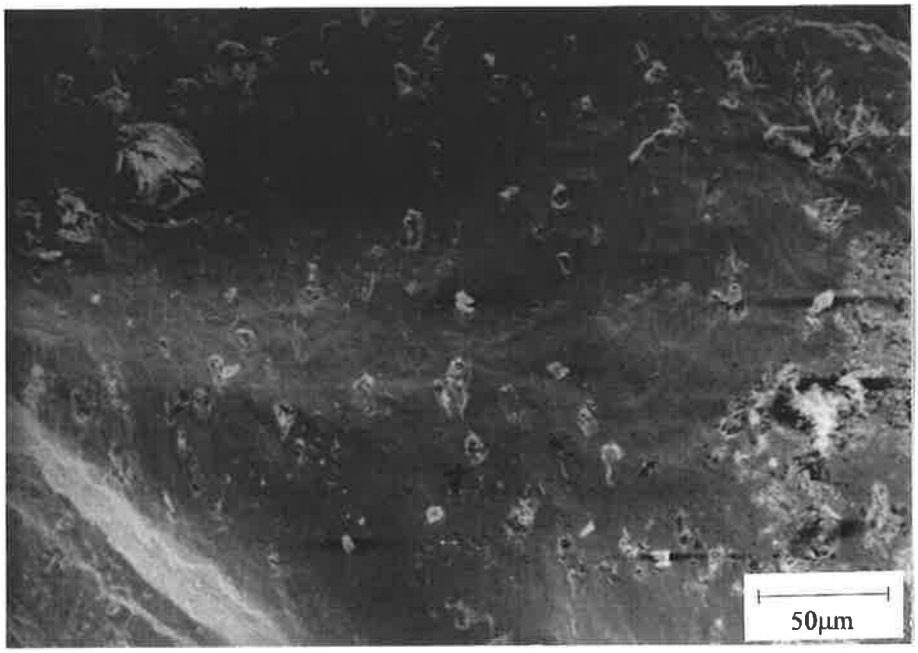

Figure 3.124: Micrograph of the surface in the second half of the pore.

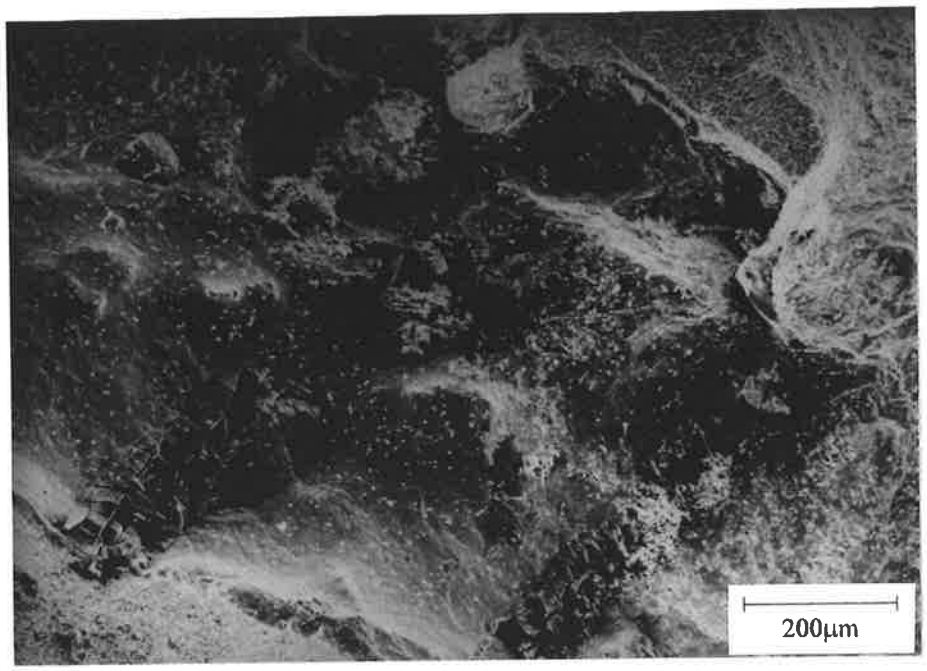

Figure 3.125: Micrograph of slag fragments at the termination end.

The surface of the second gas analysis sample (Figure 3.126) shows the initiation region of the pore at (A) where widely spaced ripples can be seen. The diameter of the pore becomes very small near its middle length. The termination end is not visible. The feature marked M on the micrograph in Figure 3.126 represents the surface created by the piercing operation to extract the gas.

The solidification structure is again more apparent at the cusp wall (Figure 3.127 and 3.128) where the oxide layer is thin and again it shows protrusions 10 to 15 microns in diameter. In an area close to the start the surface is heavily oxidised and remains in this condition to the end (Figure 3.129).

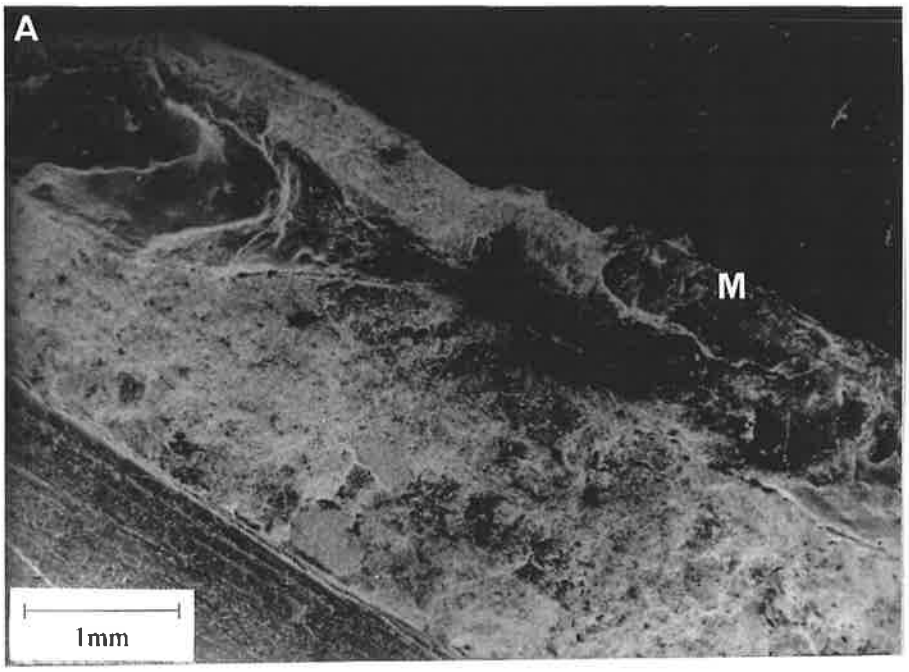

Figure 3.126 : Scanning electron micrograph of the hollow bead defect in the second gas analysis sample. The pore initiated at the cusp (marked A).

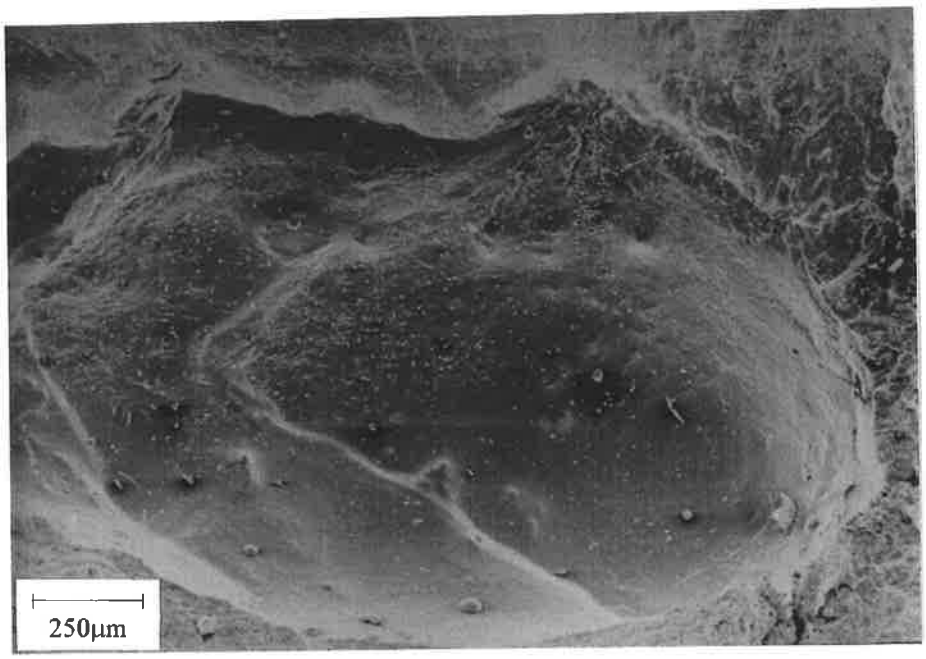

Figures 3.127: Higher magnification micrograph showing the cusp at (A) in Figure 3.126.

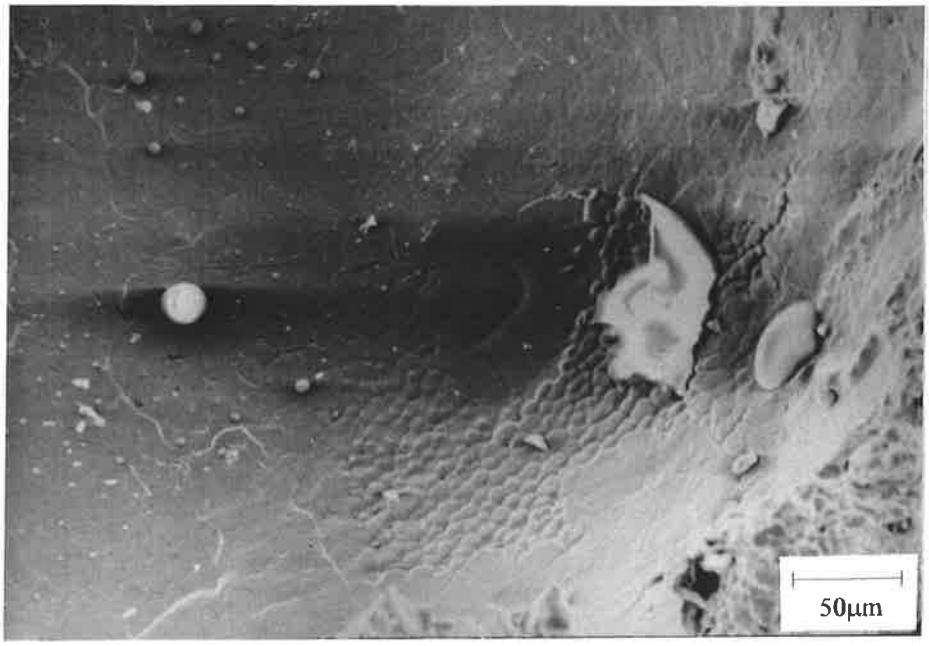

Figures 3.128: Higher magnification micrograph of the cusp surface and cusp wall.

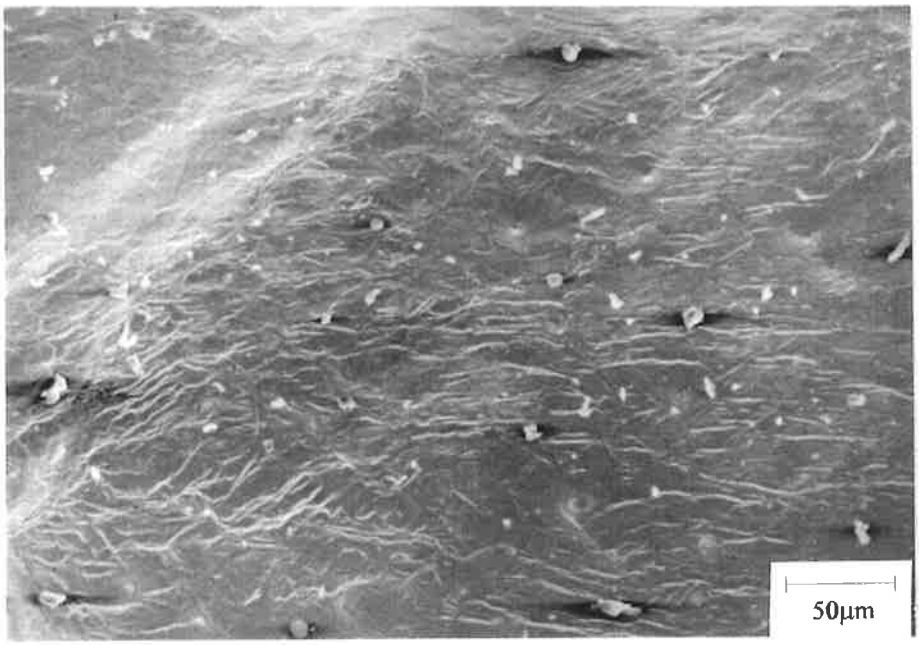

Figure 3.129: Micrograph of an oxidised surface typical of the entire pore surface.

The entire surface of the third gas analysis hollow bead pore (Figure 3.130) is oxidised, but again the cusp (Figure 3.131) to a lesser extent. There the solidification structure is only slightly apparent (Figure 3.132). Slag layers and fragments can also be seen around the cusp area and close to the start (Figure 3.133), and like the previous pore their occurrence increases towards the end of the pore. The oxide and slag layers cover the surface of this pore more extensively than the previous ones.

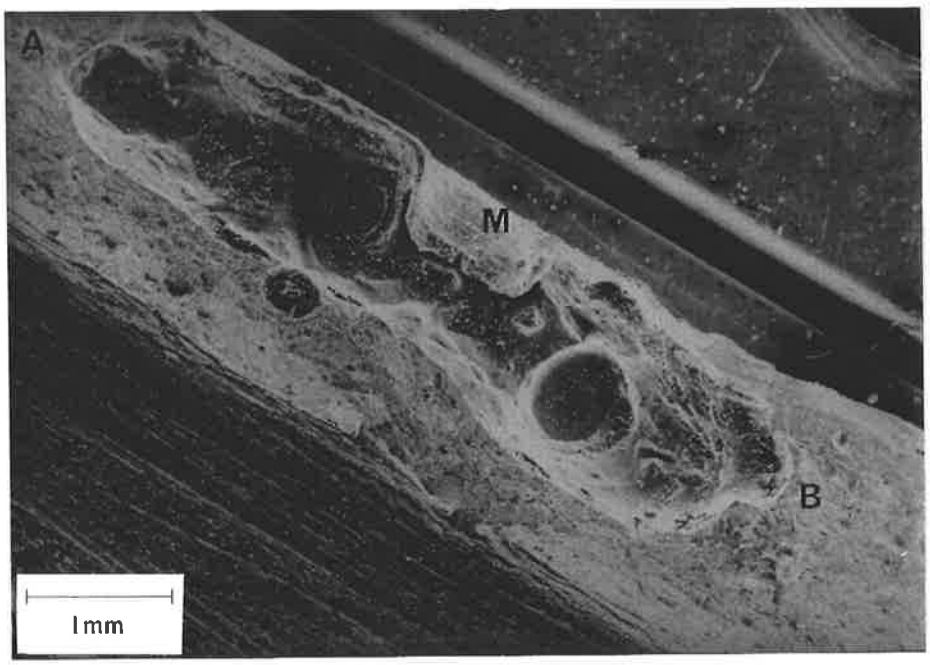

Figure 3.130 : Scanning electron micrograph of the third gas analysis hollow bead defect. The pore initiated at the cusp (marked A) and terminated at (B).

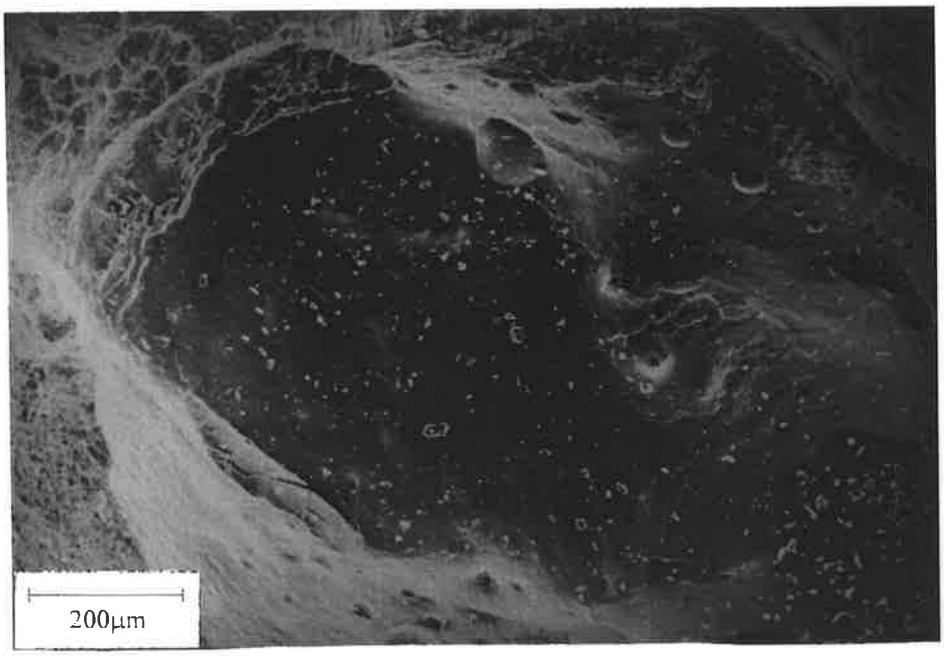

Figures 3.131: Higher magnification micrograph showing the cusp at (A) in Figure 3.130.

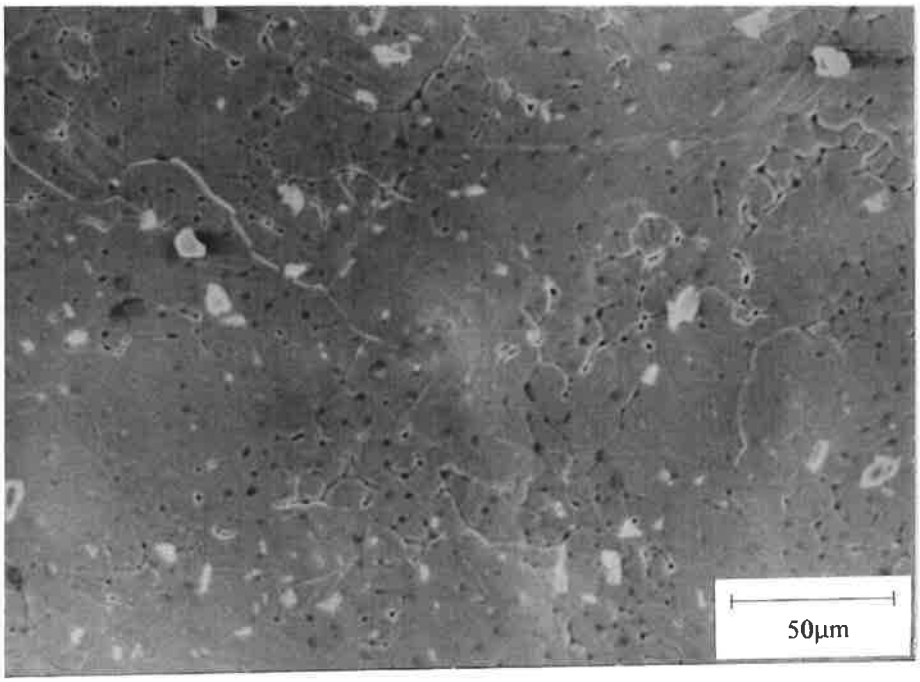

Figure 3.132: Micrograph of the cusp surface where the solidification structure is only just discernible.

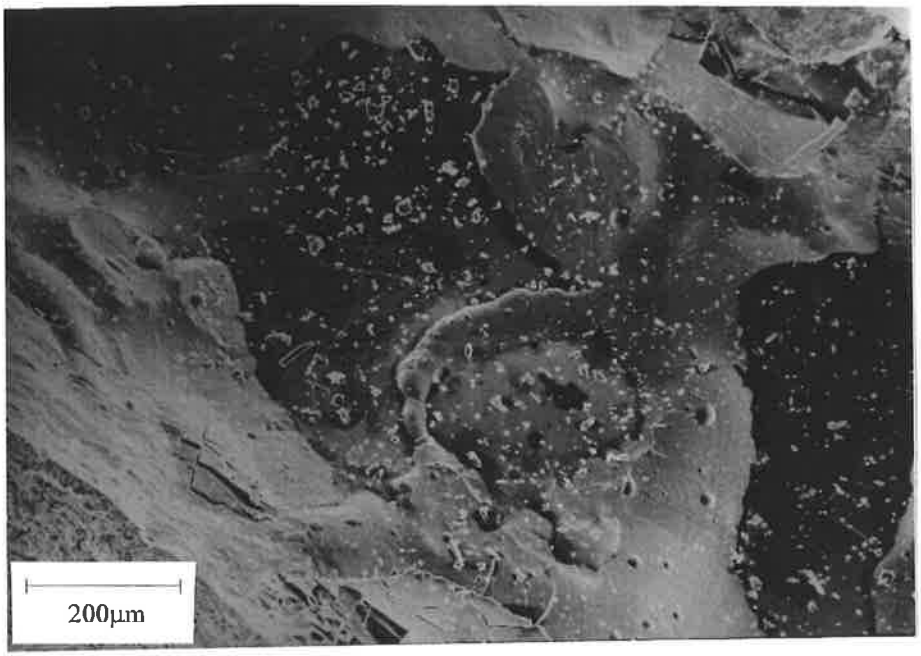

Figure 3.133: Slag seen as dark and cracked layers on the surface close to the start.

The two longest hollow bead pores, numbers 1 and 2, have a similar gas composition and similar internal features. The concentration of hydrogen is about 95%. The oxide layer on the inside surface is thin and sparse around the cusp, especially the cusp wall where the solidification structure is clearly seen. The oxide and slag layers gradually thicken towards the end of the pores. The smallest pore has a reduced hydrogen content compared with the previous ones. Its surface is more heavily oxidised and the slag fragments and layers cover the surface more extensively. The solidification structure is only very slightly apparent even around the cusp area. Large slag fragments can be seen along a region near the wall of the cusp. However, apart from some more oxidation, the gas content has not had a major influence on the observed features of hollow bead.

3.7.2 Scanning Electron Microscopy of Worm Hole Pores

3.7.2.1 Introduction

The test plates used in initial experiments to investigate the influence of the parent metal composition had a loose and powdery red oxide on the surface around the joint preparation. The welds made with this oxide left on the plate surface produced elongated pores which have different characteristics from hollow bead pores. The main difference is the location of the nucleation of the pores which is away from the weld centreline (nearer the fusion line) as well as closer to the centre of the weld bead (with respect to the weld cross section) (see Figure 3.134). The pores initially propagated in a direction perpendicular to the welding direction and then changed direction at the weld centreline to grow in the welding direction. The pores also grew from approximately the centre of the bead in the direction of the root or top surface of the bead. Due to these different characteristics these pores have been termed worm holes.

The worm holes were exposed in the same manner as hollow bead pores. The following SEM micrographs show in detail the internal surface features of these pores from longitudinal vertical sections.

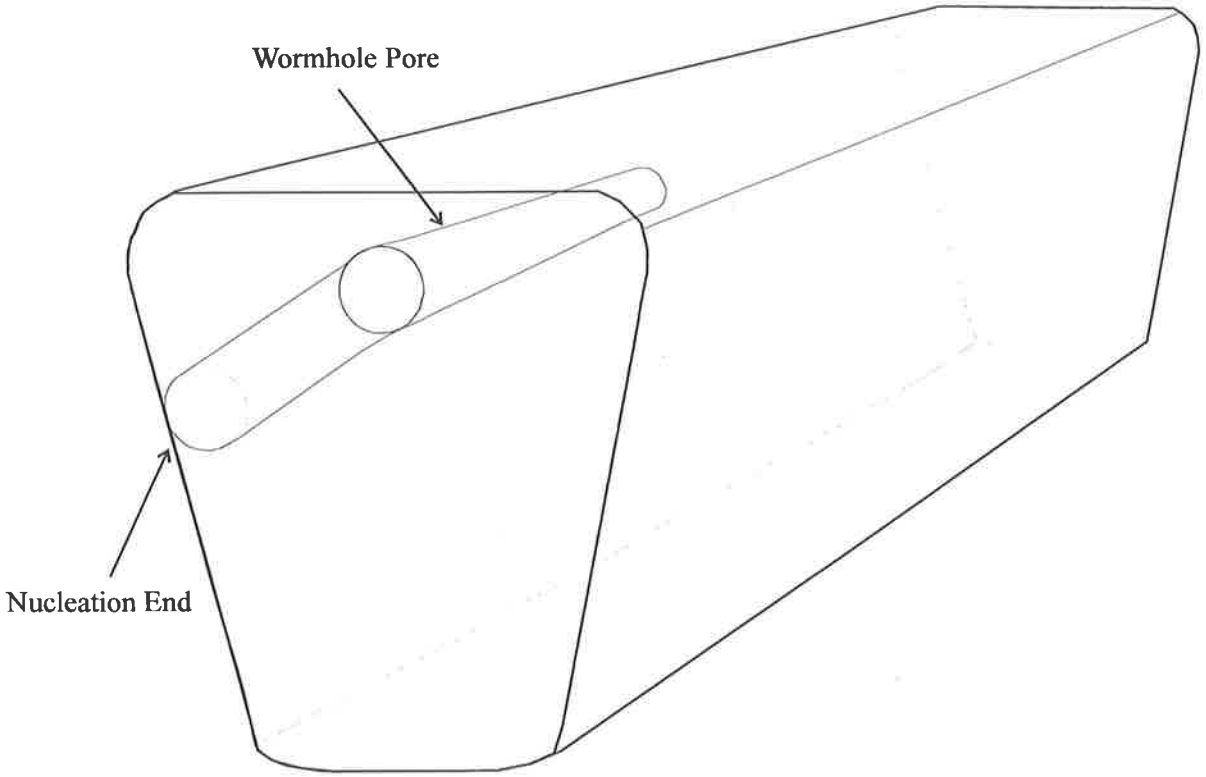

Figure 1.134: Schematic showing the nucleation and propagation of worm hole pores in a weld.

3.7.2.1 SEM Microscopy

The portion of a worm hole which has propagated along the weld centreline is shown in Figure 1.135 (also marked O in Figure 3.134). The initial section of the worm hole (marked N in Figure 1.135), which is at right angles to the welding direction, appears as the black region. The section at the weld centreline has similar features as observed in hollow bead pores such as the presence of the slag layers and fragments, an oxidised surface, ripples on the surface where the diameter of the pore changes (Figures 1.136 and 1.137) and slag fragments at the termination end (Figure 3.138). In this particular case the worm hole is growing towards the bottom surface of the weld bead.

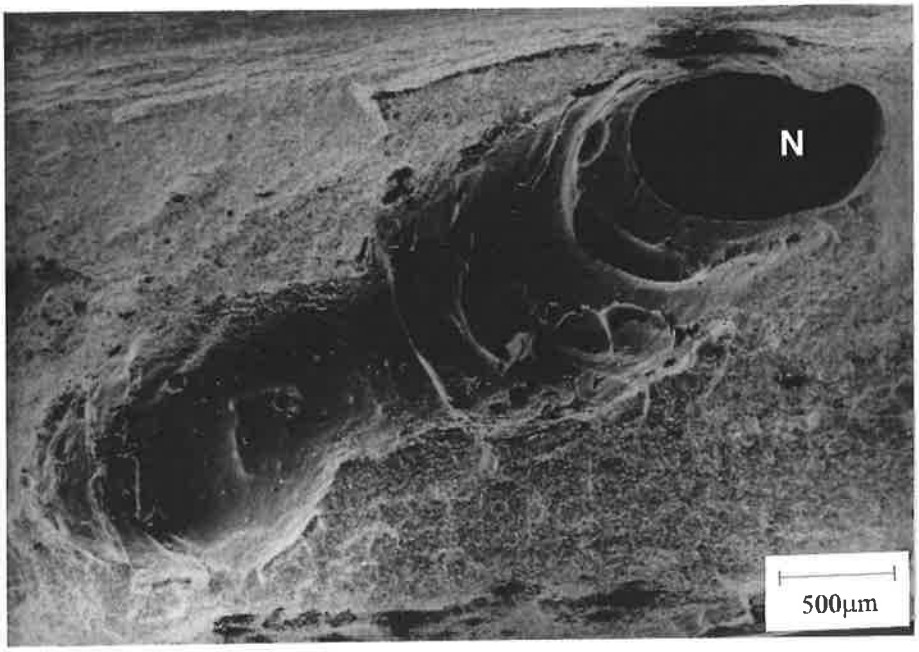

Figure 3.135: SEM micrograph of a worm hole pore showing the portion of the pore along the weld centreline (marked O in Figure 1.134).

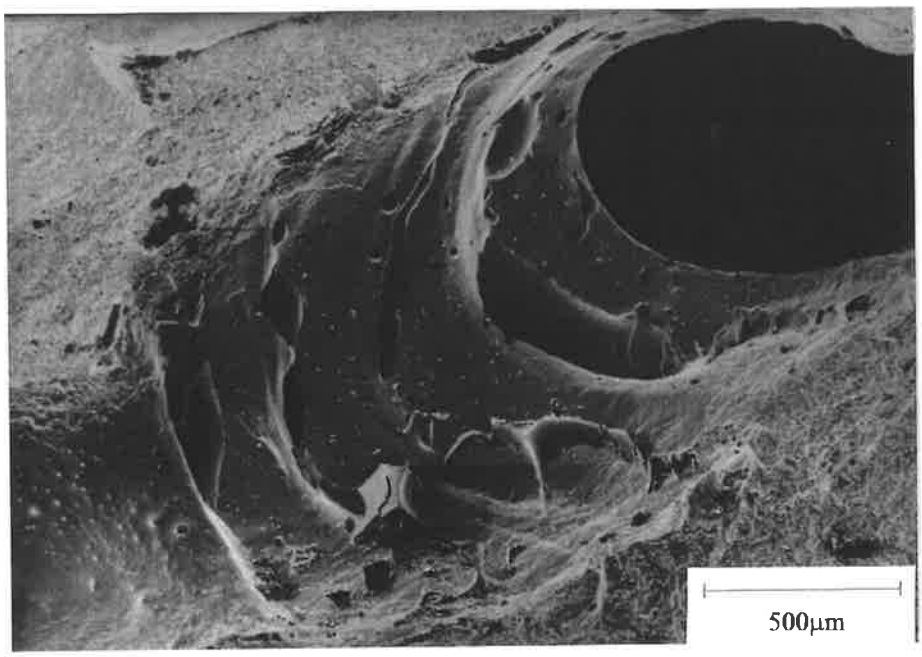

Figure 3.136: Higher magnification micrograph of the ripples and slag on the pore surface.

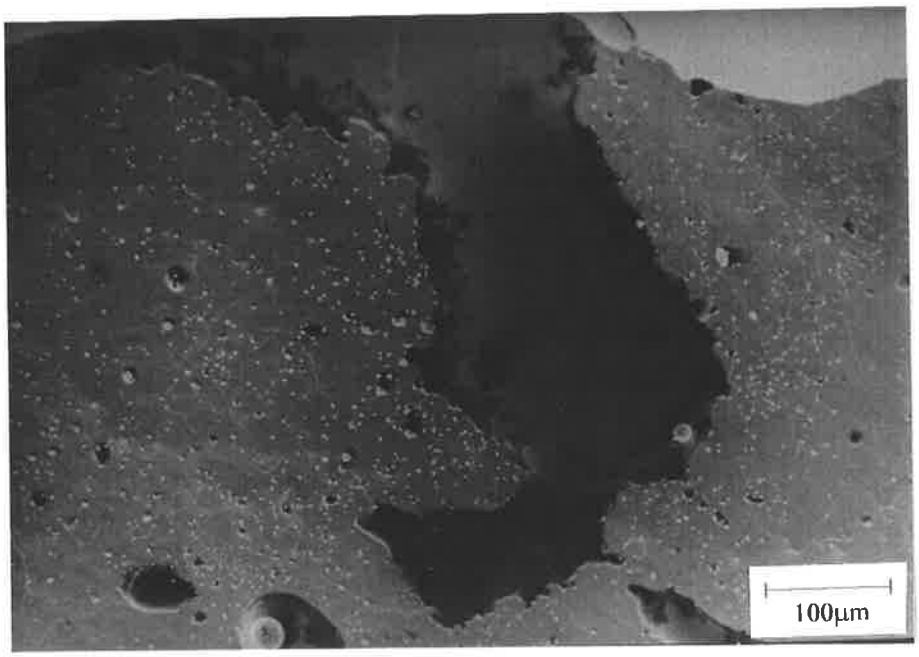

Figure 3.137: Higher magnification micrograph of slag fragments and layer.

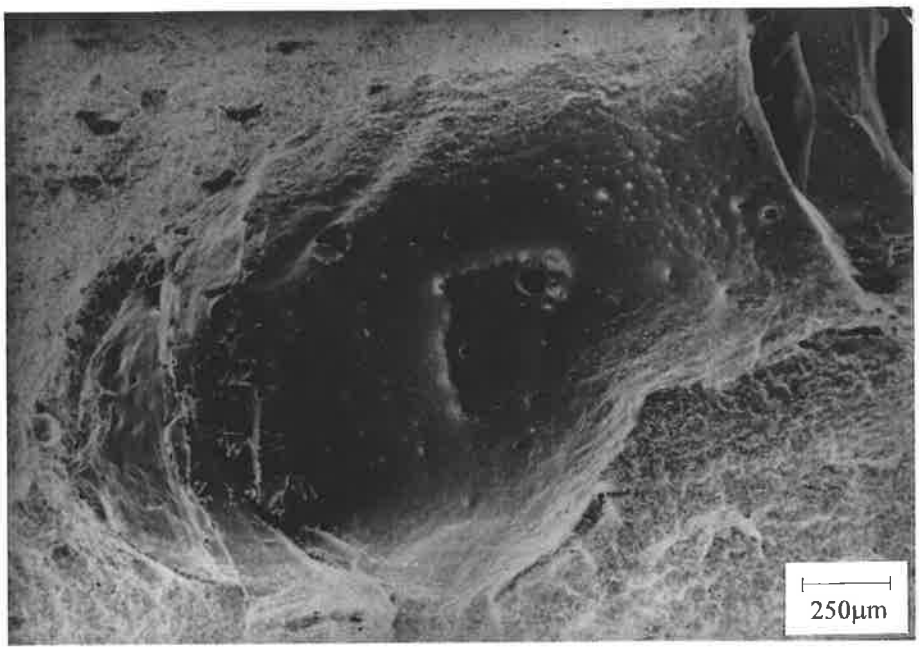

Figure 3.138: Micrograph showing slag fragments at the end of the pore.

The micrograph in Figure 3.139 is a section through the initial portion of the same worm hole. The weld was ground to reveal the section. The nucleation point is at the top of the micrograph.

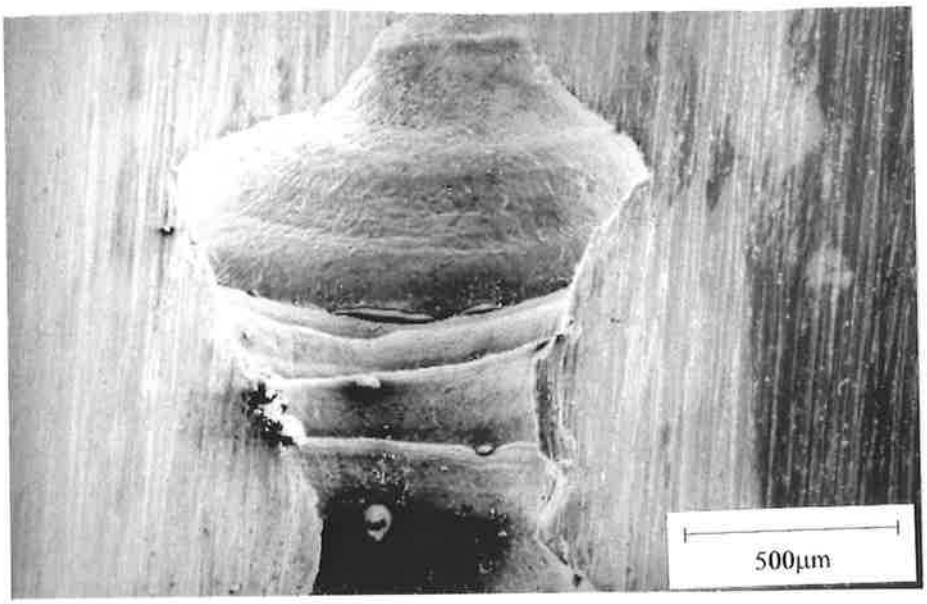

Figure 3.139: SEM micrograph of the initial portion of a worm hole.

Figures 3.140 and 3.141 are higher magnification micrographs of the area in Figure 3.139 showing the ripples and ridges on the surface due to the cellular dendritic growth respectively. The oxide layer, however, masks much of the detail of the solidification microstructure. Again slag particles are apparent on the surface.

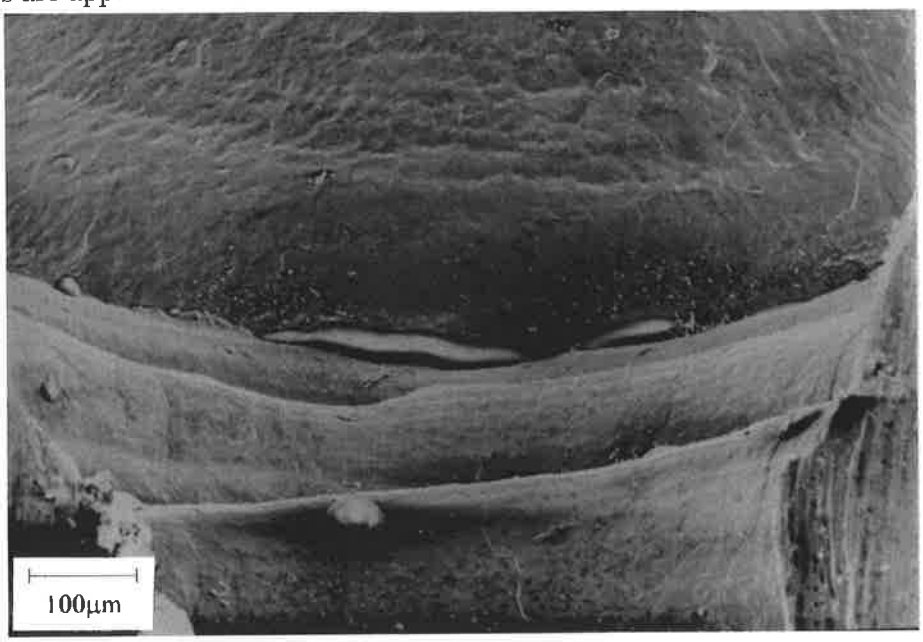

Figure 3.140: Micrograph of the surface ripples.

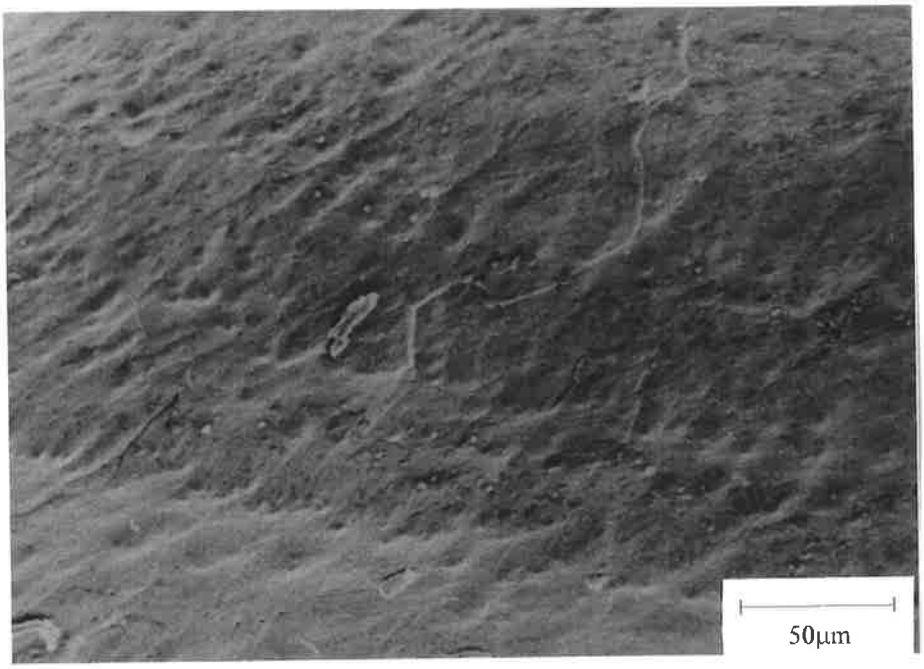

Figure 3.141: Micrograph of the ridges resulting from microsegregation.

The micrograph in Figure 3.142 is the other half of the longitudinal vertical section at the weld centreline. The shape and features are obviously similar although this half appears to have less slag on its surface and the slag is tends to be more globular

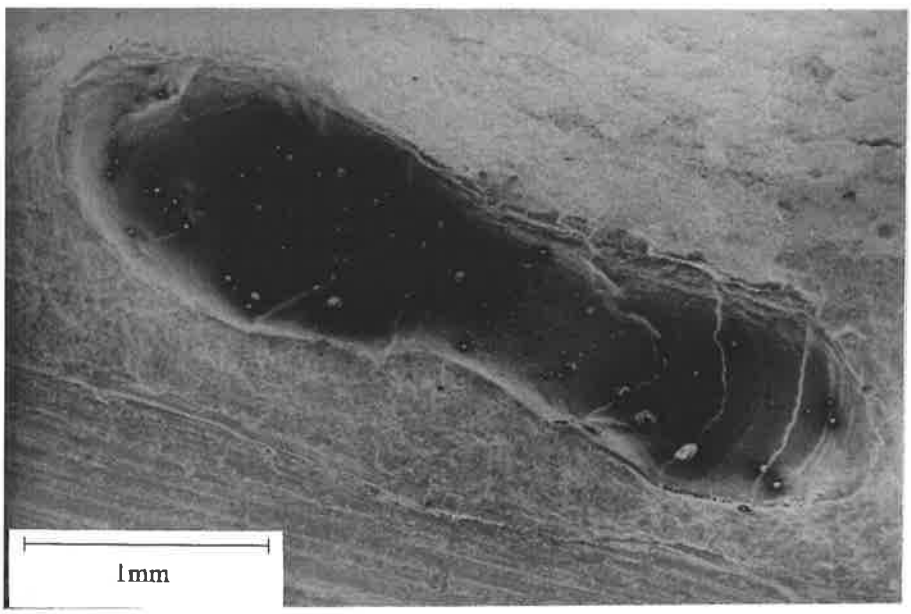

Figure 3.142: Micrograph of a longitudinal vertical section of a worm hole pore located at the weld centreline.

Another example of a worm hole is shown in Figure 3.143. The pore has propagated to the top surface of the weld bead. It was possible to look inside the initial portion of the pore (marked N in Figure 1.143). Figures 3.144 is a micrograph of this section which shows the surface at the start cusp. The hexagonal shaped features are likely to be the structures made by the oxide layer. The diameter of these shapes is larger than the diameter of the tips of cellular dendrites which protrude inside the pore.

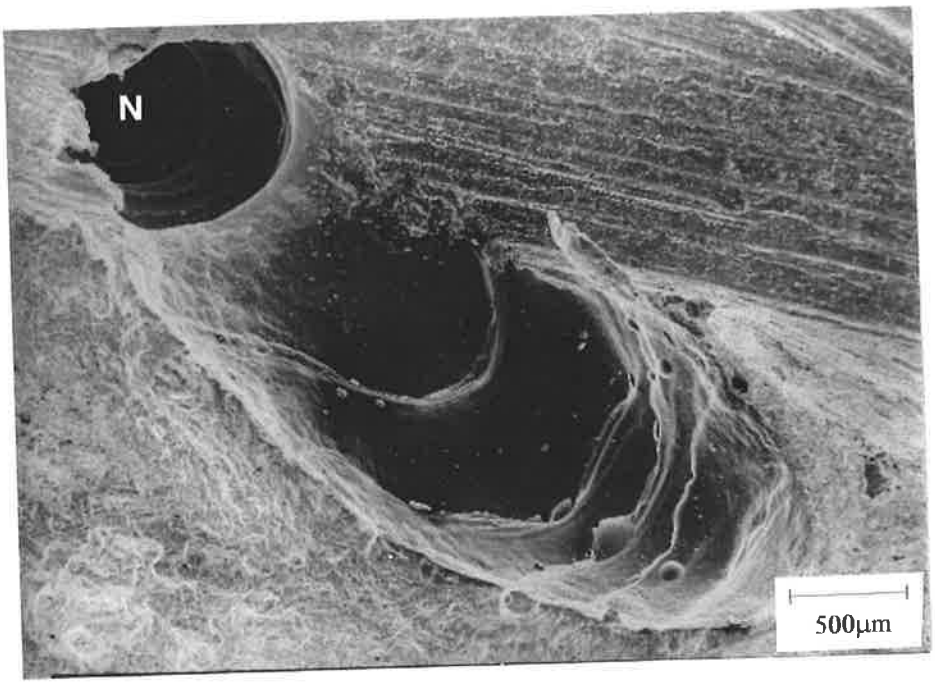

Figure 3.143: Micrograph of the initial portion of the worm hole.

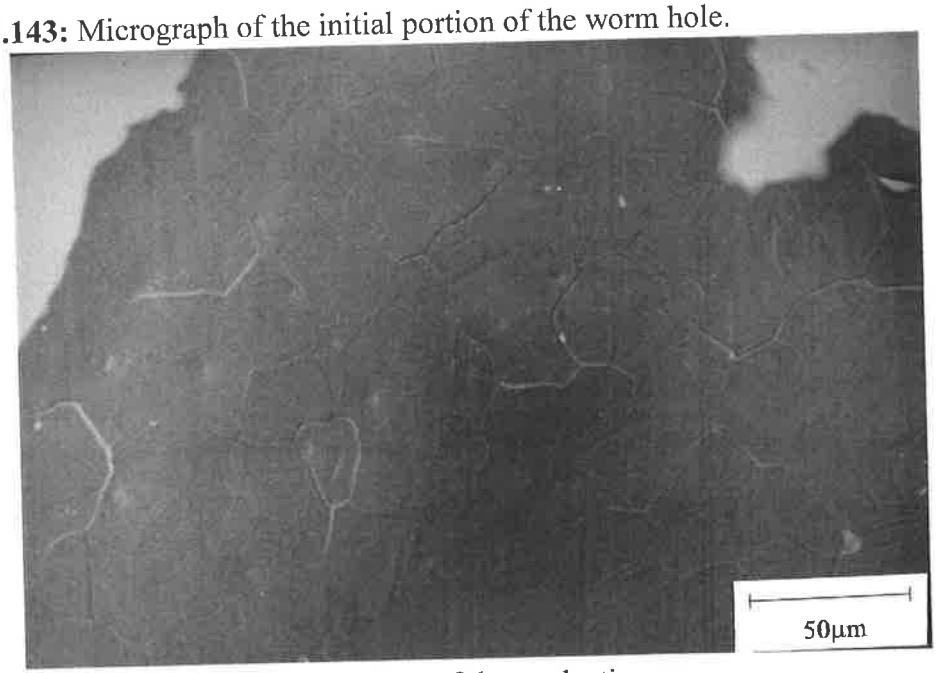

Figure 3.144: Micrograph of the surface of the nucleation cusp.

Further examples of worm hole pores are shown in Figures 3.145-3.147. These pores have nucleated close to the weld centreline. The oxide layer is sparse near the start region of the pore in Figure 3.145 and the tips of the cellular dendrites are apparent as seen in Figure 3.146. Another example of a worm hole is shown in Figure 3.147. The nucleation of this pore is at the weld centreline itself but not close to the surface of the bead.

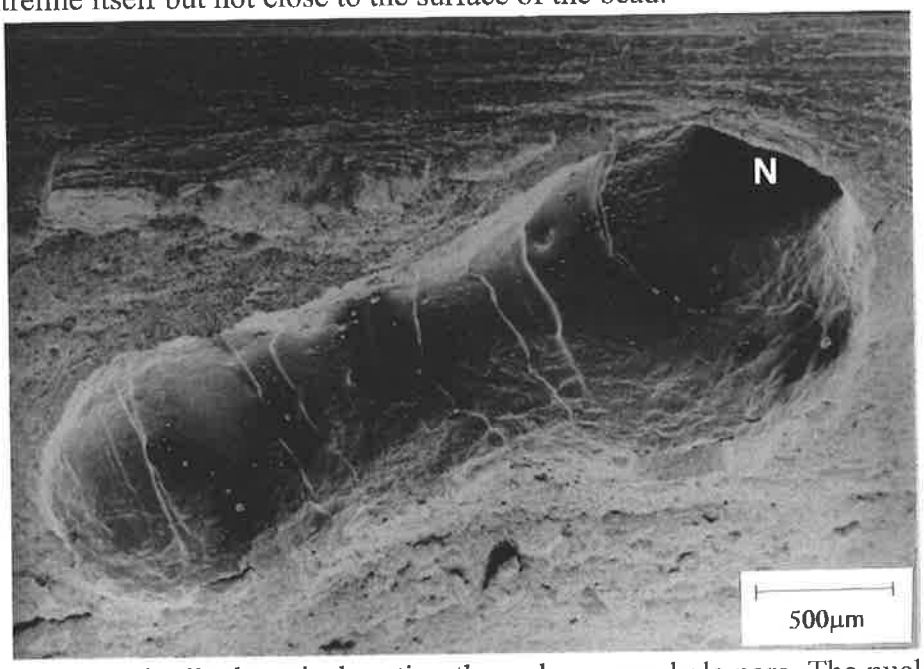

Figure 3.145: Longitudinal vertical section through a worm hole pore. The nucleation area is marked N.

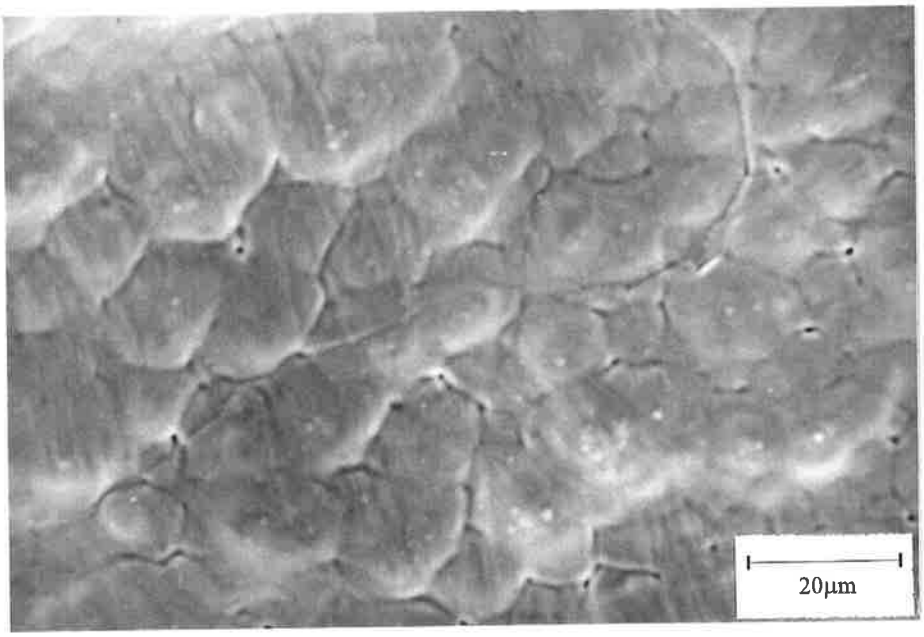

Figures 3.146: Micrograph of solidification microstructure seen inside pore.

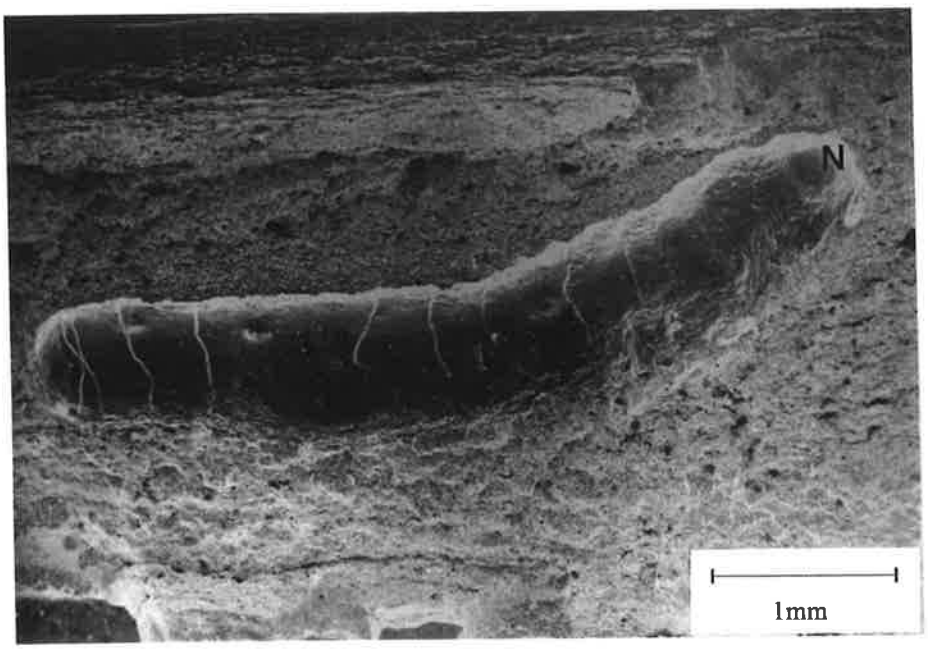

Figure 3.147: Longitudinal vertical section through a worm hole pore. The nucleation area is marked N.

3.8 Discussion

The development of the characteristic features of the hollow bead pore such as the cusp, the ripples and the oxidised surface is closely related to the mechanism of formation of hollow bead which is discussed in Chapter 5. Therefore a more thorough explanation for the formation of these features has also been reserved for that chapter. This section summarises the findings made in the study of hollow bead pores in the SEM and compares the characteristics of various pores.

The hollow bead pores initiate from a cusp, which is a feature common to all the samples examined. The cusp is in many cases approximately spherical in shape and smooth in appearance which suggests initially that the pores nucleated as bubbles and then grew with the solidification front while being continuously supplied with gas. This has been identified as predominantly hydrogen with some CO and N_2 However it is possible that other gases were

decreases further and the supply of gas into it increases. The pore stops when the amount of gas-forming solutes and thus gases at the solidification interface is depleted and is not sufficient to sustain the growth of the bubble at the same time as the motion of the interface.

SEM micrographs of the internal surface of some hollow bead pores show bright ridges on the surface, aligned in the direction of growth, over most of the length of the pore. The formation of these ridges has been explained as the result of microsegregation, at the cellular dendritic boundaries; the solute-enriched liquid at the boundaries between cellular dendrites which solidified after protruding inside the pore. The distance between these ridges is approximately 20 to 25 microns, the same value as measured from the cross sections etched in Le Pera's reagent.

Another microstructure is seen on the surface, where the diameter of the pore changes. Here the ridges are not present. The darker rounded features, approximately 10 microns in diameter, are thought to be the tips of the cellular dendrites. The change in diameter is the result of macrosegregation, which gives an increase in the amount of gas-forming solutes due to an increase in solidification rate. Similar rounded protrusions are seen in the cusp region and these could represent the tips of the main cellular dendrites which are usually tapered and therefore of a smaller diameter.

The inside surface of the pore is covered to various degrees by a thin layer of oxide. Slag fragments and globules of various sizes are seen on this oxide layer. The thickness of the layer varies within the pore, since in some regions the solidification structure is obscured. The oxide layer is usually very sparse and thin in the cusp where the solidification microstructure is clearly visible and tends to become thicker towards the end of the pore where the microstructure is totally obscured. The oxidation is thus an event which occurs after the nucleation of a bubble. Regions on the surface of the pore which contain slag fragments or

globules tend to be oxidised. In cases where slag was found inside the cusp, the surface there has also tended to be oxidised. There does not appear to be any correlation between the length of pores and the degree of oxidation of the surface. The examples shown in Figure 3.79 (approximately 3.5mm) and Figure 3.109 (approximately 18mm) vary significantly in length but are both heavily oxidised along most of their surfaces.

The formation of the oxide layer can be explained by the reaction of oxygen or water vapour with the iron. The main source of oxygen could be from the decomposition of the flux and moisture in the coating, while a smaller amount would be entrained from the atmosphere. The hollow bead pores used in the gas analysis have been described in Section 2.14 and it was found that the pore containing more nitrogen and less hydrogen is more heavily oxidised. The higher level of nitrogen suggests a greater degree of pick-up of gases from the atmosphere. The oxidation of the internal surface of hollow bead is discussed in greater detail in Chapter 5 (Sections 5.2.2 and 5.2.6) The possible oxidation of the surface due to oxygen, or oxygen radicals, and water vapour as well as the influence of the slag are argued.

Inclusions, identified by EDS analysis as oxides rich in titanium and silicon, typical of slag have been found at the termination of the pore of all the hollow bead samples studied. The size and shape of the slag varies from one pore to another. The most common form consists of angular fragments. However, some large inclusions which appear to contain bubbles have been found. This suggests that outgassing of the slag might also be a source of oxidising agents. In these regions the oxide layer is thick and completely obscures the solidification microstructure. In most cases, however, slag inclusions or layers are also found scattered along the length of the pore. The slag can also exhibit an angular, glassy surface.

The worm holes, as well as gas pores near the fusion line (see Section 2.11), have been observed in large numbers during one particular experiment only. The test plates used in that

experiment had a thick and powdery layer of red oxide on their surfaces, including the area adjacent to the joint preparation, which was however newly machined and cleaned. Once the oxide was removed, by grinding the bottom surface of the plates near the joint preparation, the worm holes and gas pores did not appear again in subsequent experiments. Single worm holes in other welds were observed only on rare occasions.

The worm holes share many common characteristics with hollow bead pores. The features on the internal surface of the worm holes such as slag fragments, an oxidised surface and ripples (or steps) are similar to the ones observed inside hollow bead pores. The shape of the slag fragments (the globular and angular inclusions) have also been observed inside hollow bead. The major difference between the two types of porosity is the location of their nucleation and growth in the weld. Hollow bead always nucleates at the weld centreline close to the top and bottom surfaces of the bead. Worm holes, however, nucleate closer to the fusion line and then grow in the direction of solidification toward and then along the centreline, either towards the top or bottom surfaces.

Chapter 4

FINITE ELEMENT MODELLING OF WELD POOLS.

4.1 Introduction

The main objective of this work was to attempt the modelling of the solidification sequence and temperature gradients in welds pools made using the manual stovepipe welding technique. Another aim was to confirm the observations stated in the Sections 3.2 and 3.3 relating to the existence of two regions close to the top and root surfaces at the weld centreline which solidify last. This information was considered an important factor in the hypothesis on the formation of hollow bead presented in this thesis which includes a statement regarding the location of the nucleation of hollow bead in the last regions to solidify.

The modelling of weld pools using finite element methods is well established in the area of gas tungsten arc (GTA) and gas metal arc (GMA) welding and is currently the object of various research projects at CSIRO - Division of Manufacturing Science and Technology in Adelaide, South Australia. Recourse was therefore made to some of the computer programmes and techniques used at CSIRO for this work. It was decided that the main components of the programmes such as the equations governing heat input and heat transfer in welds pools could be used with modifications made to model characteristics particular to the manual metal arc welding of pipeline joints.

4.2 Background and Theory

The finite element model developed at CSIRO applies to the GMA welding process, in particular direct current, electrode positive, argon-rich GMAW with a free flight drop transfer mode. In this particular section, reference was made to the work of researchers at CSIRO and The University of Adelaide (Davies, 1995). Further information on the computer modelling of welding heat sources and heat flow in weld pools can be obtained from the work of Goldak et al.(1984, 1986).

A three dimensional quasi static, steady state model of the arc is used since it can be assumed that the welding speed is very low in comparison to the speed of electrical conduction. The parent plate is considered to be at a temperature of 20°C and travels past the stationary arc or heat source at the weld travel speed.

A Gaussian distribution of the heat source is applied to the top surface of the weld pool since the current distribution in an arc over the upper surface of a workpiece has been shown experimentally to be Gaussian. In addition the absence of sharp steps in the heat input reduces the computational time.

This particular model was developed to include the effects of convective flows in the weld pool to increase the accuracy of predictions. The flow within the weld pool transfers heat from the surface of the pool to the base metal much more efficiently than conduction alone. Although the convection model provides a more general solution to the problem, the computational resources required for the analyses are extensive. An analytical technique was thus used to produce a model that simulates convection in the weld pool based on the most important driving forces within the pool. This modified model uses an enhanced thermal conductivity within the weld pool and gives similar accuracy to the full convection solution.

An artificially high value of 10 times the real value of the liquid metal conductivity was used.

Another way of simulating convection was the use of a double ellipsoid Gaussian heat source where heat is non-uniformly distributed within a volume of the base metal. Heat is applied directly to the base metal at some depth below the surface which effectively simulates the enhanced heat transfer due to convection within the weld pool. The parameters which describe a double ellipsoid heat source are the arc efficiency, η, the total energy input from the arc, Q_{in} = ηIV (where η = 0.8 for MMAW) and the ellipsoid axis width, **a** and depth, **b** and the length in front and behind the arc centre $\mathbf{c_f}$ and $\mathbf{c_b}$ respectively which are related to the size of the weld pool.

The amount of heat upstream and downstream of the source is unequally divided by using the factors r_f and r_b where $r_f + r_b = 2$. The heat content of the distribution downstream of the source is assumed to be larger as the flow of material tends to be towards the top of the pool. In this case r_f was given a value of 0.6 and r_b a value of 1.4.

The heat losses from the workpiece are simulated by convective and radiative boundary conditions, except in the weld pool area where the heat output is zero. The convective heat loss from the surfaces is given by:

$$q = -h\,(T - T_o)\ (W/mm^2)$$

where the heat transfer coefficient, h = 0.12 x10^{-4} (W/mm^2. °C) and T_o is the ambient temperature of the surrounding air.

The temperature of the metal droplet in the arc is assumed to be 2400°C which is reasonable for MMAW. It is also assumed that there is no temperature flux across the surface at the back end of the plate such that $\frac{dT}{dx} = 0$ and that the temperature at the front end, T = 20°C (ambient

temperature).

4.3 Modelling the Weld Pools Produced by MMA Stovepipe Welding

4.3.1 Double Ellipsoid Heat Source.

The same modelling strategy as described above was employed, together with some modifications to adapt the model to the MMAW of pipeline joints. Initially only the joint geometry was changed such that a root gap of 1.5mm was added to the joint configuration. The rate of weld metal deposition, or burn off rate, was calculated for particular conditions by knowing the length of the electrode used, the length of the weld and the weld travel speed.

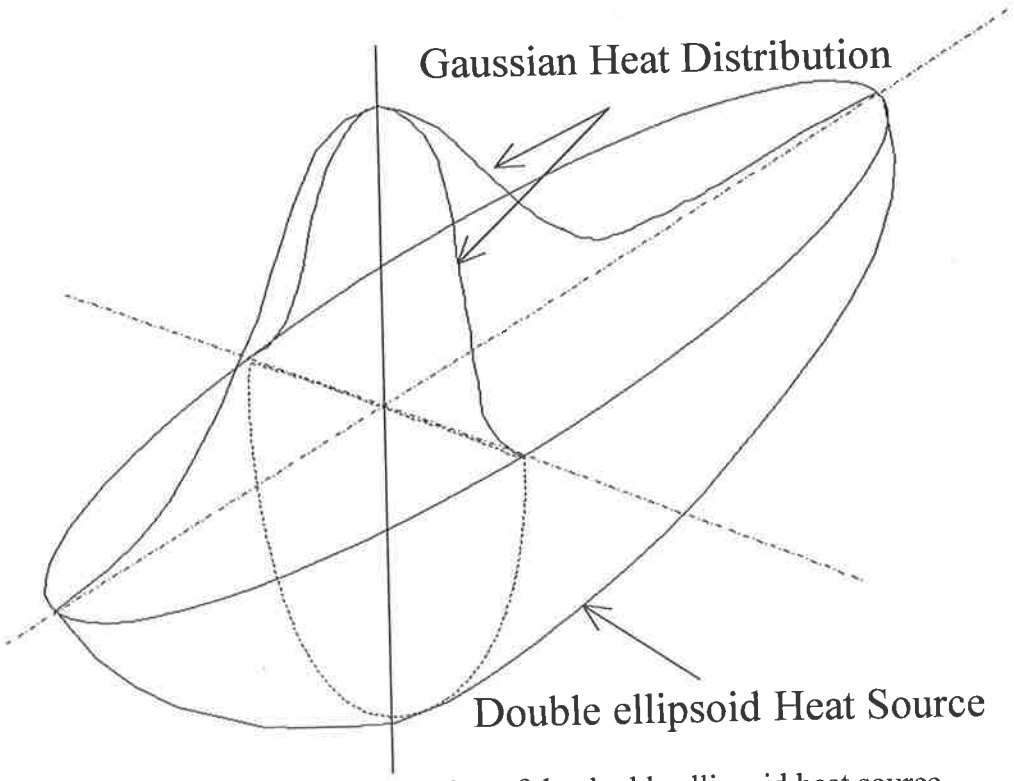

Figure 4.1: Schematic representation of the double ellipsoid heat source.

4.3.2 Cylindrical Heat Source.

The first model was refined in an attempt to better simulate the real process and to obtain a weld bead shape closer to the actual ones seen in macrographs. In order to justify any modifications a high speed film of the welding process was studied. Figure 2.23a-f are still

frames of the film. The most pertinent observation relates to the transfer of metal in the arc plasma from the electrode to the weld pool. The metal is transferred to the sides of the weld pool, that is on either side of the root gap. This gives the impression that the arc is rotating when in fact it is moving from one side of the bevel to the other. This characteristic was accounted for by modelling the heat distribution of the arc as a cylindrical heat source (see Figure 4.2) with the heat normally distributed on either side of a central hollow region where no heat was added. As the flow of material is assumed to be towards the back of the weld pool the heat distribution at the back of the source was given a value of 1.4 and in front of the source a factor of 0.6. The height of the cylindrical source is equal to the full depth of deposited metal volume as determined by the burn off rate.

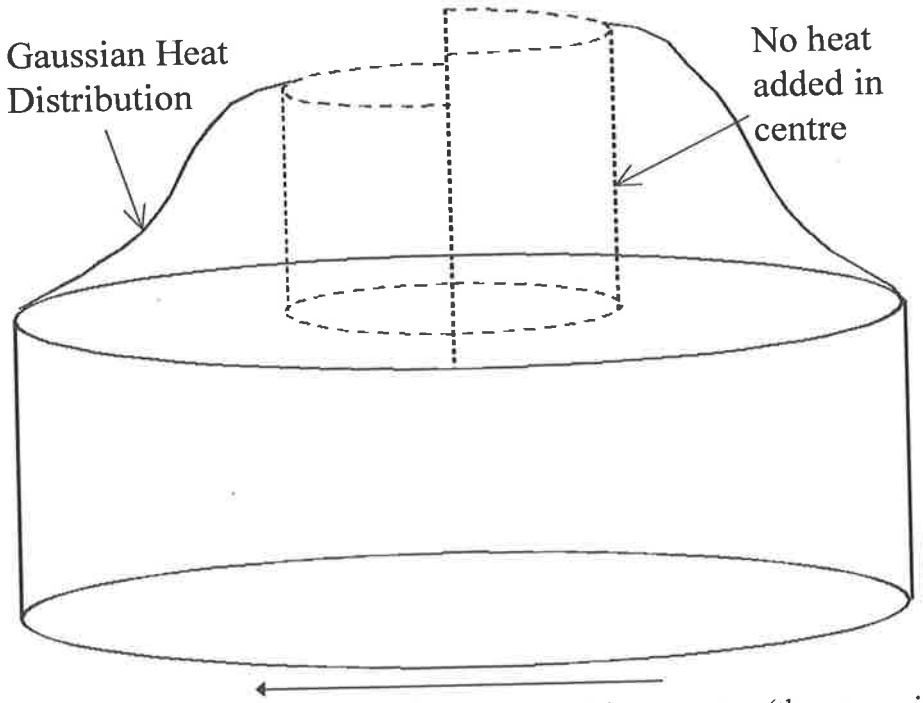

Figure 4.2: Schematic representation of the cylindrical heat source (the arrow indicates the direction of welding).

4.3.3 Results and Discussion

The output weld pool shapes from the finite element analysis are shown in Figures 4.3a-c. These figures show the weld pool obtained from the analysis using a cylindrical heat source at three welding currents, 134, 188 and 204A, and a constant weld travel speed of 400mm/min.

The real weld pools are seen in the macrographs in Figures 3.26-3.28. The black region in Figures 4.3a-c represents the molten metal and the last blue temperature contour represents the extent of the heat affected zone (HAZ) at a temperature of 720°C. A comparison of the dimensions of the two modelled weld pools (double-ellipsoid and cylindrical) and the real welds have been recorded in Table 4.1 and 4.2 and reveals good correlations. The cylindrical heat source has produced slightly better results than the double ellipsoid one which supports the justification of using such a heat source to model this particular welding process.

Welding Current		Weld Pool Width (mm)		Height (mm)
		Top	Bottom	
214A				
	Real	5.2	8.0	4.7 - 5.8
	Model	5.3	6.9	4.6
188A				
	Real	4.4	6.0	5.7
	Model	4.6	5.7	4.3
134A				
	Real	4.2	2.4	4.7
	Model	3.9	2.9	2.9

Table 4.1a: Comparison of the weld pool dimensions from the double ellipsoid heat source finite element model and real weld pools (as seen in the macrographs in Figures 3.26-3.28).

Welding Condition		Weld Pool Width (mm)		HAZ Width (mm)		Height (mm)
		Top	Bottom	Top	Bottom	
214A						
	Real	5.2	8	6.1	10.7	4.7-5.8
	Model	5.3	7.4	6.8	10.0	4.9
188A						
	Real	4.4	6.0	5.5	8.9	5.7
	Model	4.9	6.4	6.3	9.2	4.7
134A						
	Real	4.2	2.4	5.2	5.9	4.7
	Model	3.5	3.7	4.8	6.7	3.8

Table 4.2: Comparison of the weld pool dimensions from the cylindrical heat source finite element model and real weld pools (as seen in the macrographs in Figures 3.26-3.28).

The main differences observed when comparing only the shape of the modelled and real weld pools are the absence of tapering in the height of the bead and the wagon tracks at the top of the modelled weld beads. The former disagreement probably arises from the fact that convection in the pool is modelled to a limited extent and that the keyhole and the action of gravity on the molten pool have not been taken into account. Experimental data on the radiation and convection losses from the bottom surface of the weld for the stovepipe welding process would also be required to improve the results.

The three dimensional profiles in Figures 4.4a-c show the temperature distribution along the weld pool. At the back end of the pool the cross section shows the last region to solidify as the black ellipsoid shape at the centreline and offset towards the root surface. This feature is seen more clearly from the weld cross sections in Figures 4.5a-c. It can thus be inferred that the main direction of heat extraction is from the top portion of the parent plate on either side of the weld bead. These two portions represent the largest volumes of cooler material adjacent to the weld. The shape of the heat affected zone, which closely matches the shape from real

weldments, also supports this idea since its width at the top of the bead is narrower where the cooling rate was faster. The time interval between the observation of the last region to solidify within the weld and complete solidification increases from 0.018s at 134A to 0.14s at 188A to 0.18s at 214A.

It has been inferred, however, from the direction of grain growth in real weld microstructures that there exist two regions which are last to solidify. These are located along the weld centreline but are offset to the top and root surfaces of the bead. The finite element models only partially support this hypothesis as they reveal just one last region to solidify near the root surface. An explanation for this discrepancy is probably due to the following factors. The interface at the back of the weld pool as seen in Figure 4.6 is relatively flat (compared with weld pools from bead-on-plate welds), the delay in solidification near the bottom of the bead is represented by the curve in the bottom part of the longitudinal horizontal sections. It is proposed that the pattern and direction of convective flows and thus heat distribution in the weld pool, absent from the model, are responsible for producing the two regions where solidification is delayed. That is, since the interface is flat, disturbances in the heat distribution and turbulence would be responsible for fluctuations in its the shape and could result in two maxima along the interface. This is shown schematically in Figure 4.7.

The three dimensional models also show a longitudinal view of the weld pool which is generally elliptical in shape. The length of the weld pool is observed to elongate as the heat input increases.

The finite element models show that the formation of a "skin" on the bottom surface which solidifies prior to the region corresponding to the location of hollow bead could be possible. This is not unreasonable since surface dendrites produced by atmospheric cooling of a molten ribbon in rapid solidification processing have been observed experimentally (Wood et al., 1979).

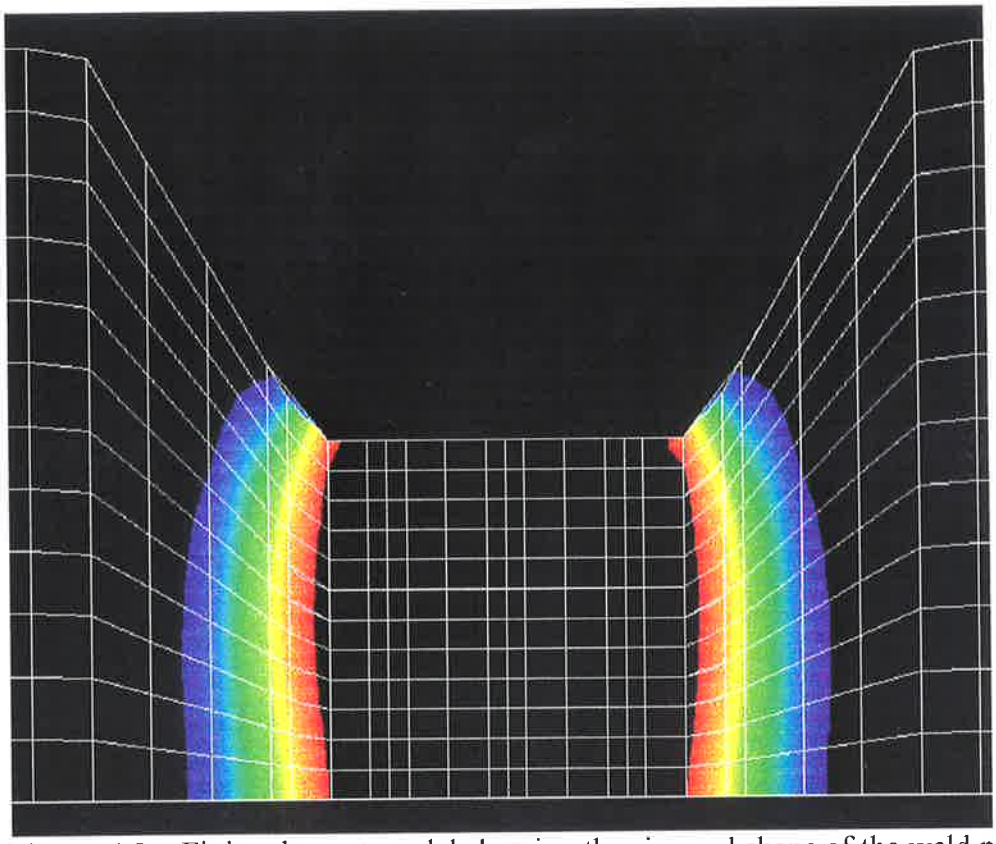

Figure 4.3a: Finite element model showing the size and shape of the weld pool cross section (weld travel speed : 400mm/min and welding current: 134A).

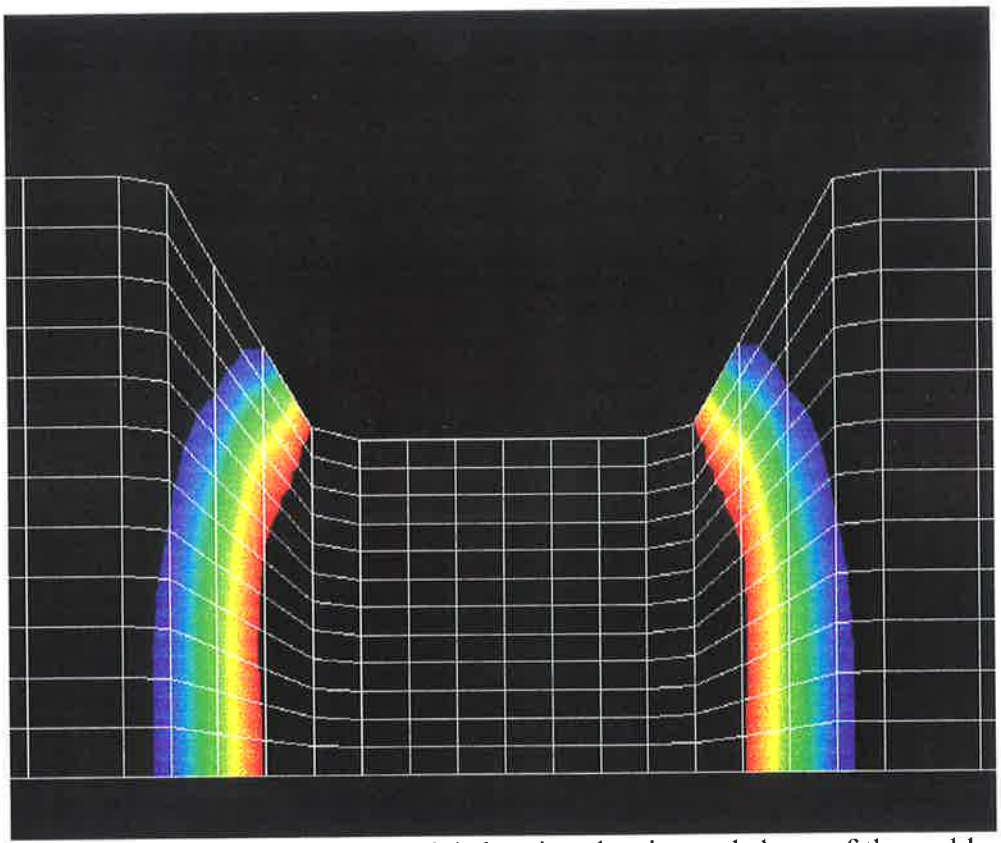

Figure 4.3b: Finite element model showing the size and shape of the weld pool cross section (weld travel speed : 400mm/min and welding current: 188A).

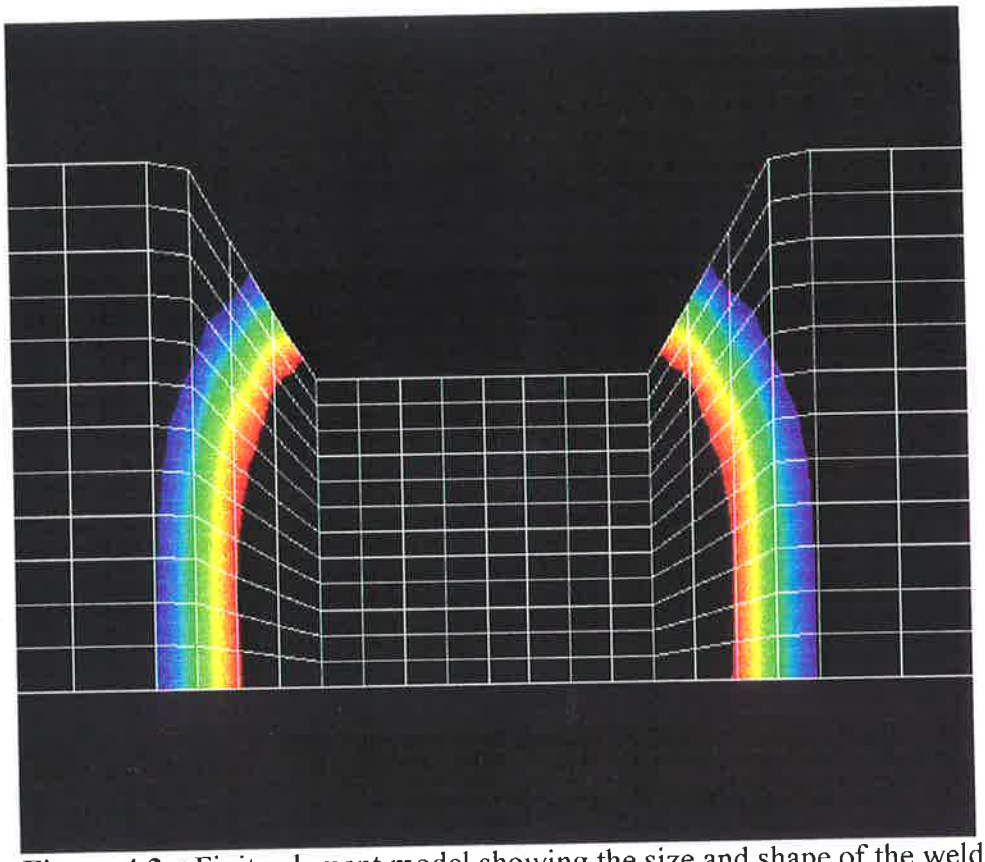

Figure 4.3c: Finite element model showing the size and shape of the weld pool cross section (weld travel speed : 400mm/min and welding current: 214A).

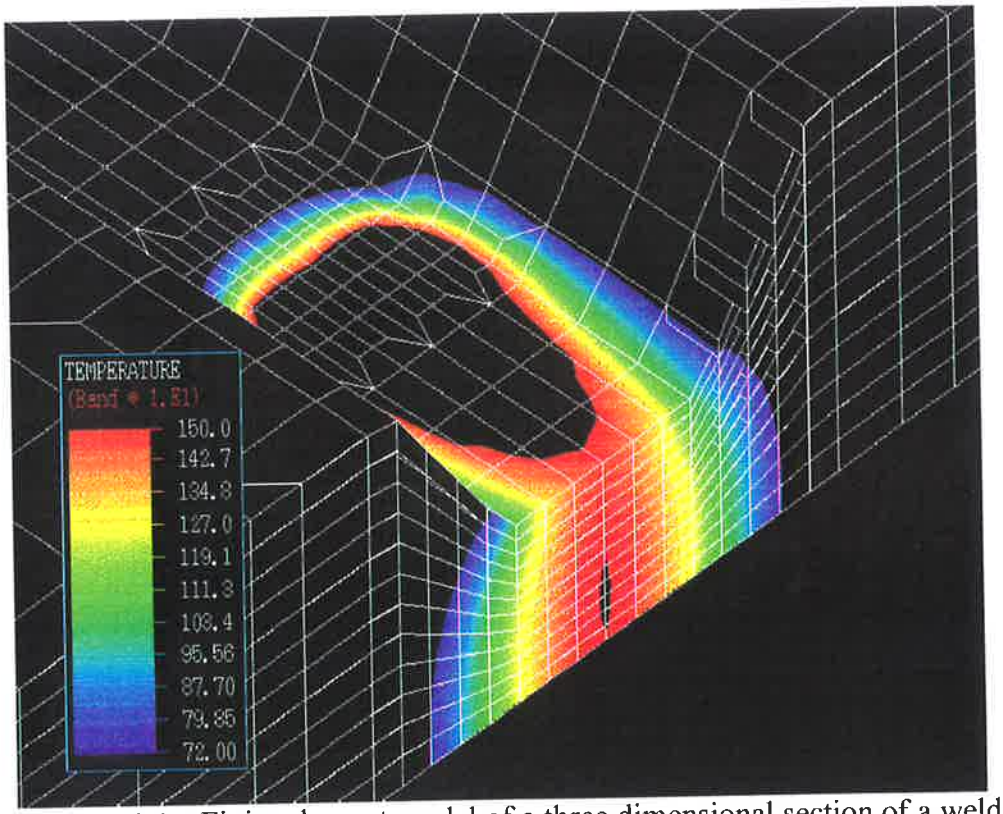

Figure 4.4a: Finite element model of a three dimensional section of a weld pool showing the solidification at the back end of the pool (weld travel speed: 400mm/min and welding current: 134A).

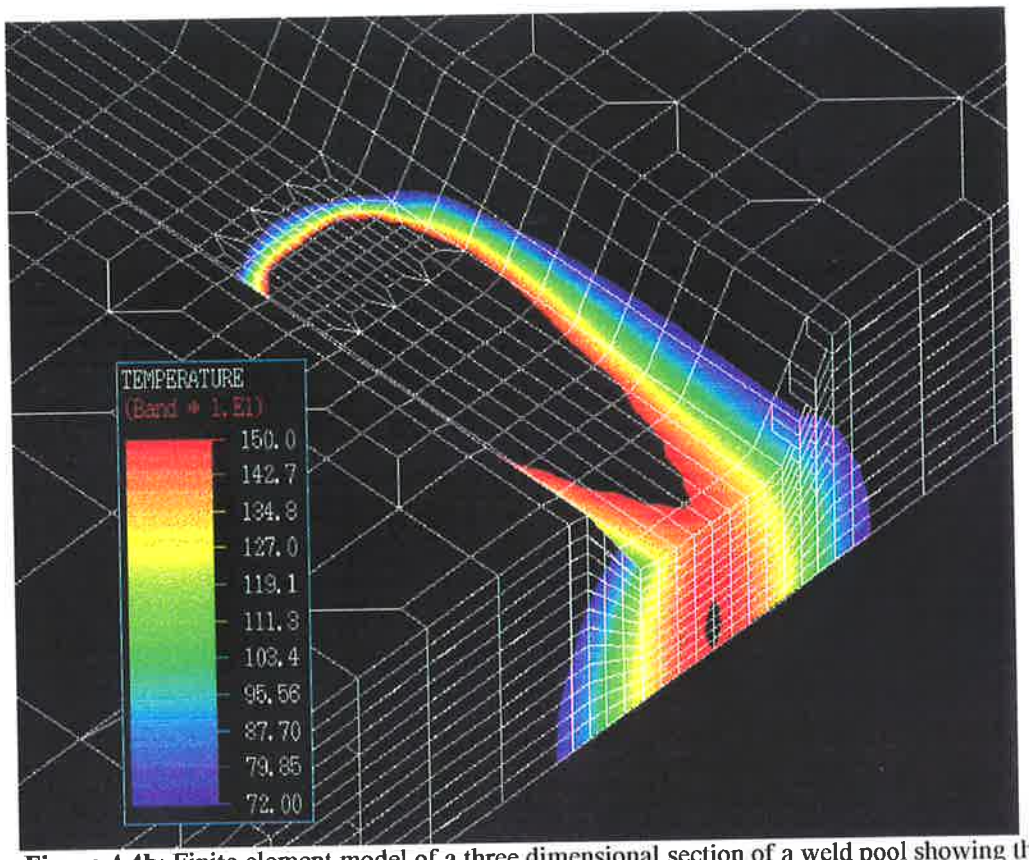

Figure 4.4b: Finite element model of a three dimensional section of a weld pool showing the solidification at the back end of the pool (weld travel speed: 400mm/min and welding current: 188A).

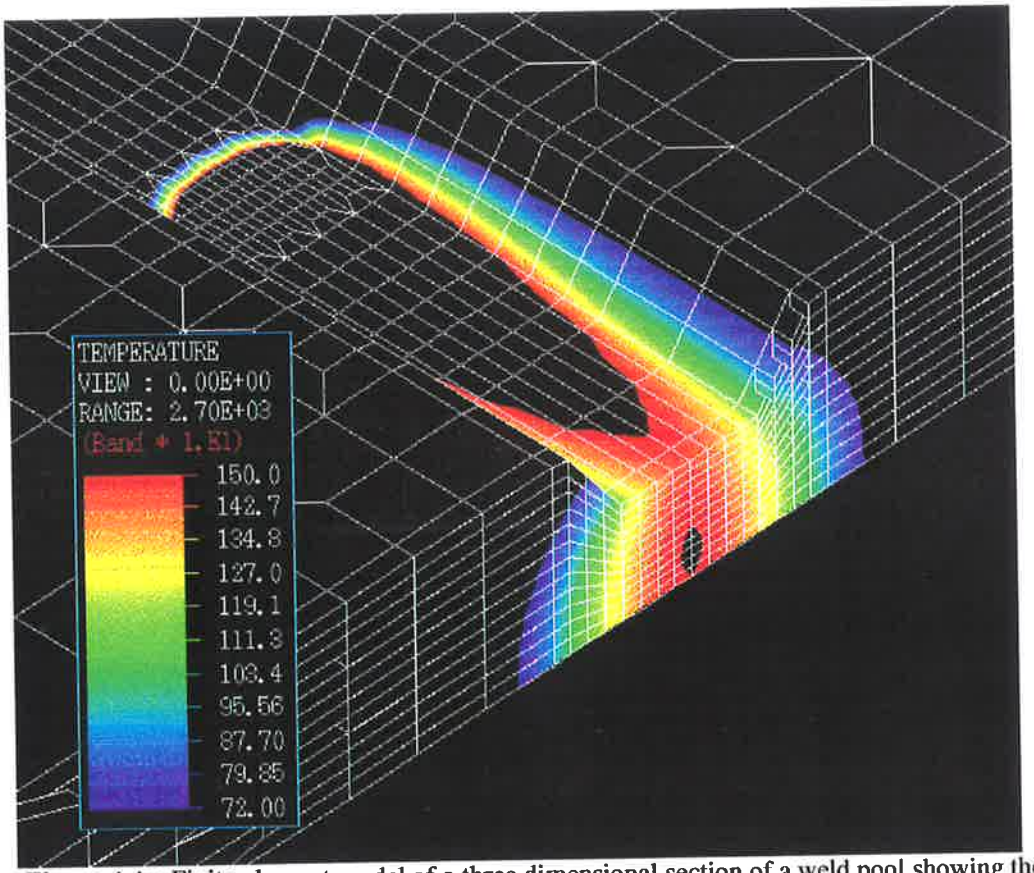

Figure 4.4c: Finite element model of a three dimensional section of a weld pool showing the solidification at the back end of the pool (weld travel speed: 400mm/min and welding current: 214A).

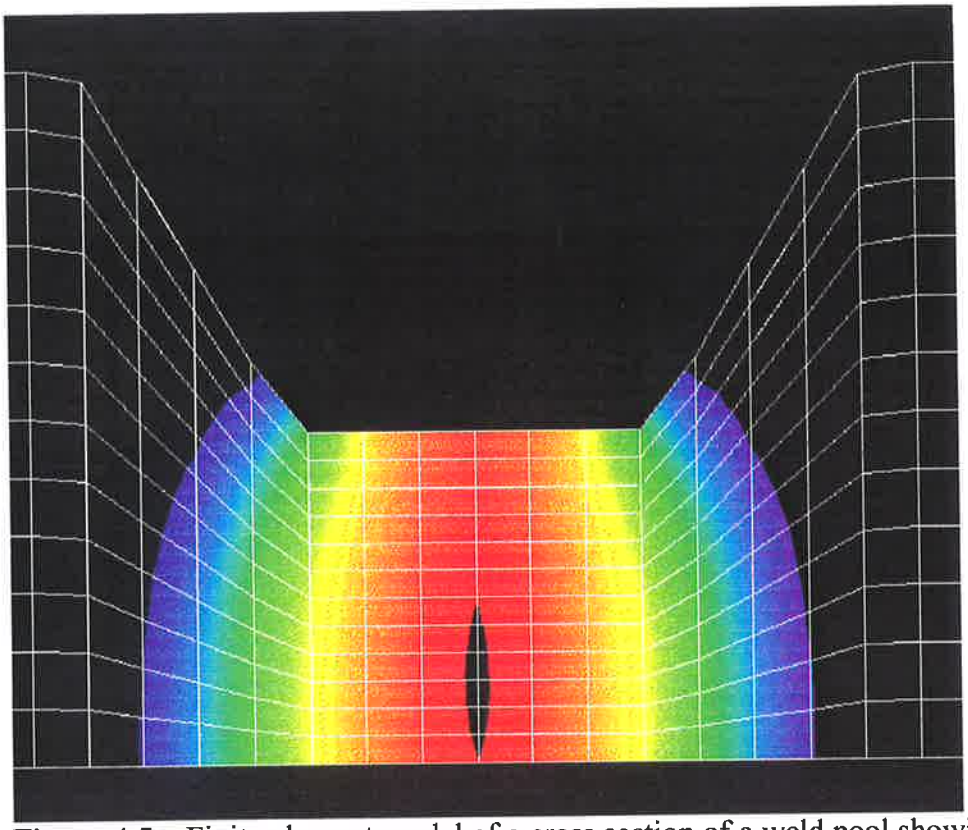

Figure 4.5a: Finite element model of a cross section of a weld pool showing the solidification at the back end of the pool (weld travel speed: 400mm/min and welding current: 134A).

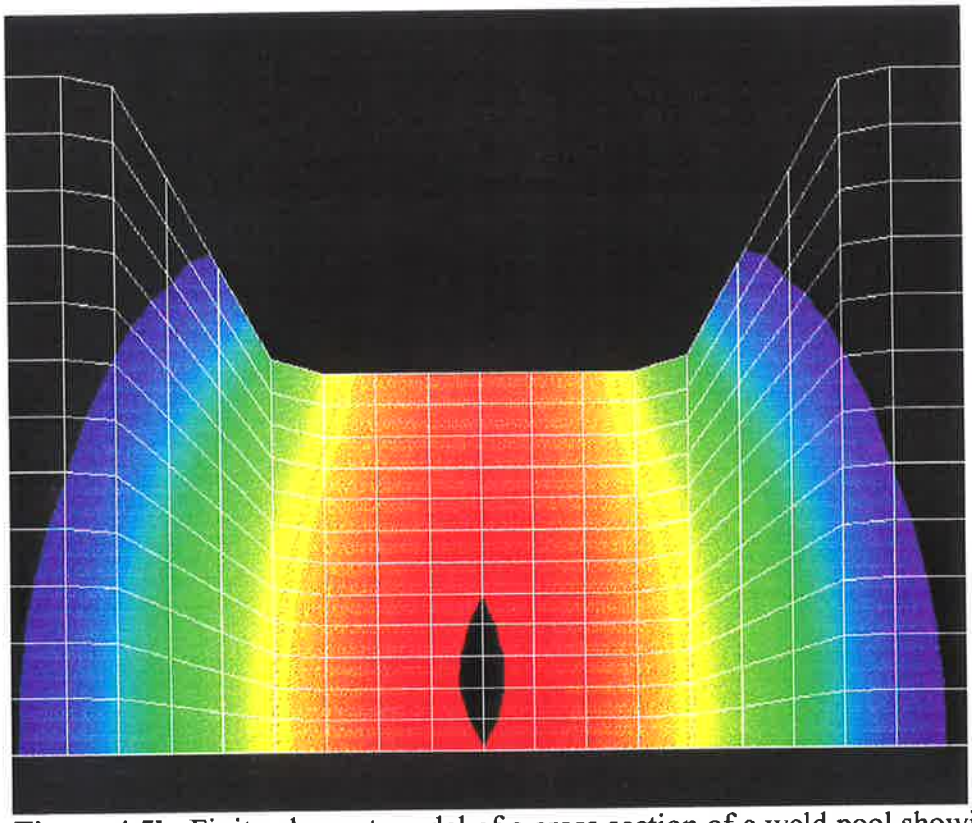

Figure 4.5b: Finite element model of a cross section of a weld pool showing the solidification at the back end of the pool (weld travel speed: 400mm/min and welding current: 188A).

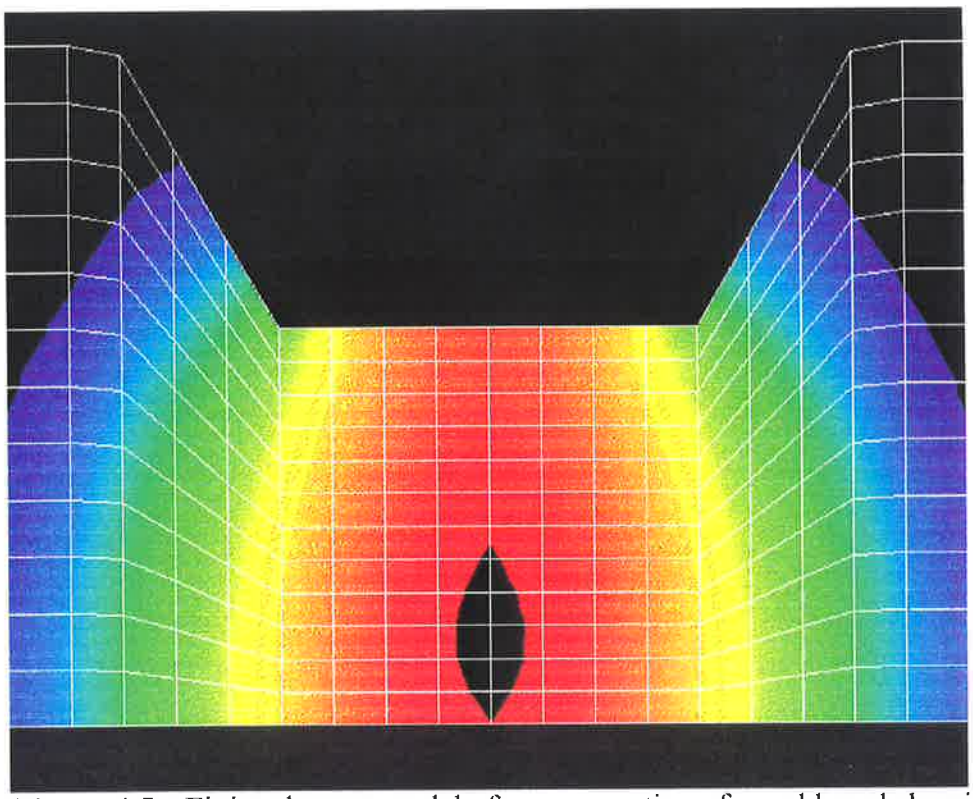

Figure 4.5c: Finite element model of a cross section of a weld pool showing the solidification at the back end of the pool (weld travel speed: 400mm/min and welding current: 214A).

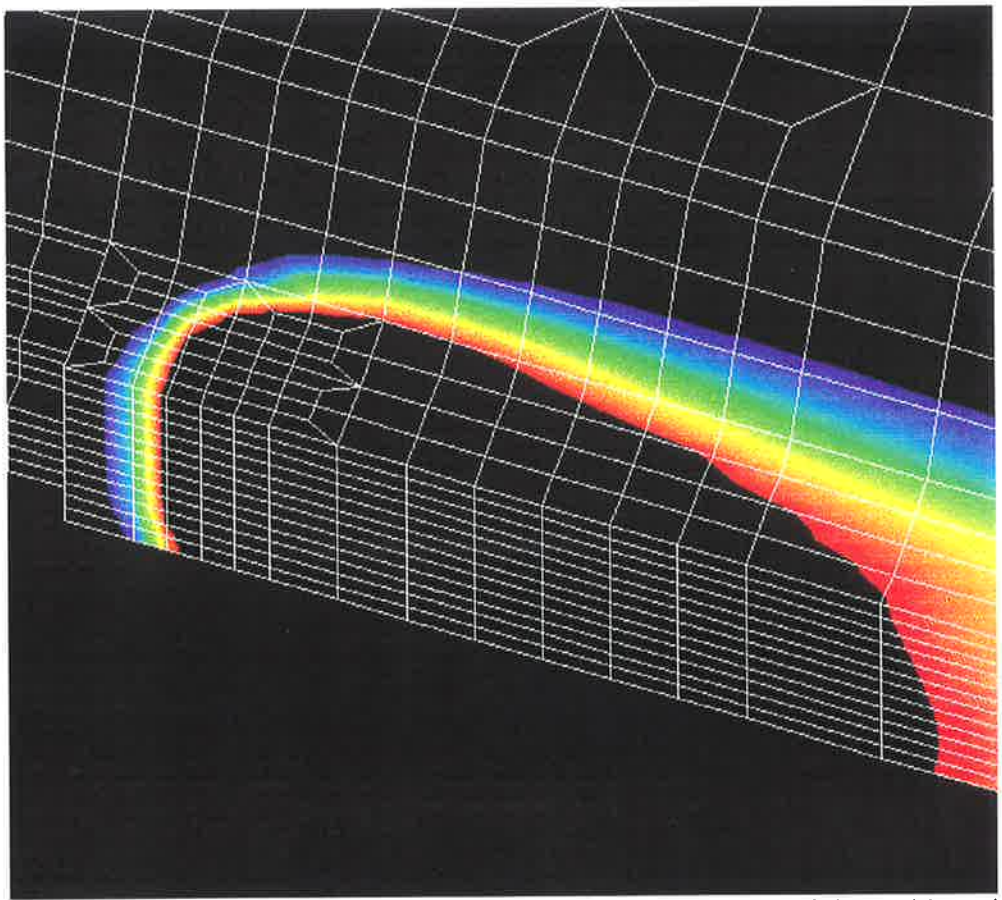

Figure 4.6: Finite element of a longitudinal vertical section of the weld pool along the weld centreline (weld travel speed: 400mm/min and welding current: 188A).

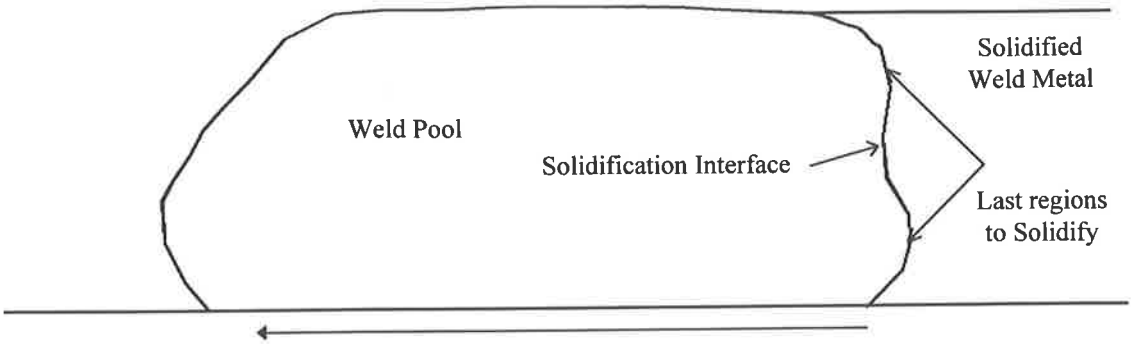

Figure 4.7: Schematic of a longitudinal vertical section of a weld pool showing two maxima, representing the two last regions to solidify, at the solidification interface (back end of the pool). The arrow indicates the indication of welding.

Chapter 5

A MODEL FOR THE FORMATION OF HOLLOW BEAD

5.1 Introduction

In this section a model for hollow bead formation is presented. The experimental section of this thesis has established the welding conditions which are most likely to give rise to hollow bead. These experiments, along with investigations into solidification microstructure, high speed filming of welding, pore gas analysis, finite element analysis of the weld pool and key results from the literature will be brought together to develop a plausible and consistent model for the formation of the defect.

5.2 The Model

5.2.1 Overview

It is proposed that hollow bead is initiated by the formation of hydrogen bubbles in the melt, at or near the solidification front, which are then subsequently captured by the advancing solidification front. The axial growth of the pore is effected by the diffusion of gases (mostly hydrogen) from the melt into the bubble/pore causing an elongated pore parallel to the welding axis. The decomposition of the cellulosic electrodes and moisture in the electrodes supply the hydrogen. The high temperature of the arc and melt combined with the high diffusivity of hydrogen facilitate its absorption into the melt. While other gases are also

absorbed from the arc it will be argued that hydrogen is the primary agent responsible for hollow bead. The capture of the hydrogen bubble by the solidification front produces the customary cusp found at the beginning of all hollow bead pores.

5.2.2 Hydrogen as the Principle Agent in Hollow Bead Formation

The pore gas analysis (Section 2.14) revealed hydrogen as the principal constituent. This suggests a strong role is played by hydrogen, but is not conclusive, as the analyses were conducted at room temperature and up to 30 days subsequent to welding and therefore does not reveal the identity of the original gas of formation. Also any voids in weld metal which contains hydrogen, as cellulosic deposits are, will become traps for hydrogen.

Oxidising gases producing the pore might also produce a similar result, as those gases might be consumed in oxidising the pore surface over time, leaving the hydrogen as a remnant. Hydrogen is often liberated from iron oxidation reactions. For instance:

$$Fe_{(s)} + H_2O_{(g)} \rightarrow FeO_{(s)} + H_{2(g)} \qquad (5.1)$$

Experimental evidence however suggests that oxidising gases play only a minor role in hollow bead formation. Principally, it has been shown (Section 2.11) that high concentrations of silicon in the parent metal increases the incidence of hollow bead (total length and number), and that a change in aluminium content, at constant silicon levels, does not produce any significant variation in the occurrence of hollow bead. As these elements are deoxidising agents that bind oxidising gases into silicate and aluminate complexes they would be expected to reduce the amount of gas available for pore formation and hence decrease the average length of pore, if the oxidising gases played a significant role.

Further evidence of the minor role played by oxidising gases in the formation of hollow bead is found in the pattern of oxidation observed on the internal surfaces of the beads. Oxidation

of the pore may occur anywhere along its length, although it was found to be far more prevalent at the end of the pores than at the beginning. If an oxidising gas, such as carbon monoxide, were responsible for the formation of the pore extensive oxidation would be expected along the entire length of the pore, including the cusp region. That this does not occur suggests that the pore is formed initially by a reducing gas such as hydrogen, and that the extensive oxidation of the pore along its length is the result of some other mechanism. Kudrin (1985) suggests that acidic slags in contact with liquid iron will oxidise the surface of the iron, according to the following reaction (Equation 5.2).

$$SiO_2 + 2Fe_{(s)} = 2FeO + Si \qquad (5.2)$$

with $\Delta G^o = 367.1 - 44.1 \times 10^{-6} T$ (kJ)

where ΔG^o is the standard Gibb's free energy and T is the temperature in Kelvin.

If this is the case then the increase in oxidation along the length of the pore could be explained by the pore attracting slag to its surface, which then subsequently oxidises that surface. The amount of slag collected on the pore surface would be expected to increase along the length of the pore due to the finite time required for slag to collect. This increase in slag along the length would result in increased oxidation, as observed. On initial inspection of the free energy change for the oxidising reaction this mechanism does not seem to be plausible. However, this is a surface reaction between the slag and the iron. If there is sufficient flux of oxygen atoms between the two materials, there could be a significant chemical leaching effect which results in a transfer of oxygen from the slag into the iron. This could continue to occur at a significant rate after solidification.

Cellulosic electrodes can produce a shielding gas with a very high hydrogen content, a

significant component of which will be in elemental form, and also yield a weld metal diffusible hydrogen content of up to 100 mL/100g of deposited metal (Boniszewski, 1992). The hydrogen results from the decomposition of the hydrogen-containing compounds (mainly cellulose) and moisture at the high temperatures existing in the welding arc. These processes also give rise to other gaseous elemental forms such as carbon and oxygen. Atmospheric contamination of the shielding gas can also give rise to the presence of nitrogen, although the high rate of production of the shielding gas and its high temperature and pressure limit atmospheric contamination to low levels. Although molecular nitrogen has been detected inside the hollow bead pores (at levels less than 5% partial pressure), it is very unlikely that it plays a dominant role in the formation of hollow bead. It does suggest, however, that a hollow bead growing in a weld becomes a low pressure "sink" which gases at the solidification interface can enter.

In addition Lancaster (1993) reports on a case where the energy required to dissociate hydrogen is lower than that for oxygen and nitrogen. The temperature for 90% dissociation of these gases are given as: 4575K for hydrogen, 5100K for oxygen and 8300K for nitrogen. Although these values have been calculated for a particular total pressure and composition of the plasma, they can be used to compare the dissociation potential of the gases. The values for hydrogen and oxygen are much lower than that for nitrogen. Since the concentration of a gas in the weld will increase when exposed to a monatomic gas, it is expected that hydrogen will be much more highly soluble than nitrogen.

5.2.3 Mechanism of Hydrogen Absorption in the Molten Weld Pool

5.2.3.1 Introduction

Previous research using GMA and GTA welding and arc melting (Woods, 1974, Howden and Milner, 1963, Salter, 1963) has established the existence of an annular region (or hot zone)

below the welding arc where most of the absorption of hydrogen occurs. The temperatures reached at the centre of the annular zone is high enough to cause vaporisation of the molten metal and thus reduce the absorption of gases in the molten pool. Although the temperature of the molten metal at the annular region is lower, it is still above the melting point of the metal, typically around 2100°C. The model described by these authors have assumed that the absorption of hydrogen in the molten weld pool could be determined by Sievert's law, which states that the concentration of a gas in the melt, [H], is proportional to the square root of the partial pressure, P_{H2}, of the gas above the melt at a particular temperature:

$$[H] = K\sqrt{P_{H_2}} \qquad (5.3)$$

where K is the equilibrium constant which is dependent on temperature.

The model for the absorption of hydrogen based on Sievert's law does not, however, take into account that hydrogen is dissociated in the arc and that absorption of monatomic hydrogen will occur. Recent research (Palmer and DebRoy, 1996, DebRoy, 1992, Gedeon and Eagar, 1990) in this area have identified the shortcomings of Sievert's law for predicting the absorption of hydrogen in welding.

Gedeon and Eagar (1990) conducted a systematic review of previous research and analysed the data on hydrogen absorption and diffusible hydrogen measurements. They demonstrated that the use of Sievert's law to calculate the hydrogen absorption reaction temperature (which they found to be in the range from 2500 to 2800°C) in the weld pool was invalid. The authors mentioned that these temperatures were unrealistically high and have now been shown to be unachievable in practice. In addition the assumption of a one step absorption process which neglects the effects of dissociation, solute rejection on solidification, and diffusion of

hydrogen away from the weld region, was too simplistic to provide realistic values of the absorption temperature.

A model which assumed a two-step process where diatomic hydrogen was dissociated in the high temperature regions of the arc, and then both diatomic and monatomic hydrogen were absorbed into the weld pool was proposed. The maximum weld pool temperature was limited by the vaporisation of iron, which occurs at approximately 3000K. The absorption was then considered to occur at a "reaction temperature" - a concept which is not accurately defined by Gedeon and Eagar. The main findings of their investigation are summarised below.

A plot of the amount of hydrogen absorbed as a function of the partial pressure of monatomic hydrogen at the reaction temperatures shows an opposite trend to diatomic hydrogen. The amount of monatomic hydrogen absorbed decreases with temperature while the absorption of diatomic hydrogen increases.

Investigating the degree of dissociation of hydrogen in an arc containing a mixture of diatomic and monatomic hydrogen and argon at 1 atmosphere of pressure it was found that changes in the partial pressure of diatomic hydrogen could result in a large variation in the dissociation fraction. For example at 3000K, the dissociation rose from 8 to 32% by reducing the pressure of hydrogen from 1 to 0.05 atmosphere. Thus the amount of dissociation occurring in the high temperature region of the welding arc plasma, which is dependent on the composition and temperature of the arc gases, could have a significant effect on the amount of hydrogen available for absorption. The percent dissociation was observed to increase with increasing temperature. It was suggested that the hydrogen molecules that dissociate in the high temperature region of the arc may not completely recombine before striking the weld pool. Gedeon and Eagar believed that the absorption occurred at the temperature of the liquid

weld pool surface.

The amount of hydrogen absorbed from monatomic gas at various locations in the weld pool was determined (see Figure 5.1). The results showed that monatomic hydrogen absorption dominated the contribution to the total hydrogen content and that the majority of the absorption would take place around the outer edges of the weld pool where the surface temperatures are lower. This contradicts the observations made in previous research on the absorption of diatomic hydrogen where most of the gas is thought to be absorbed in the high temperature central region of the pool.

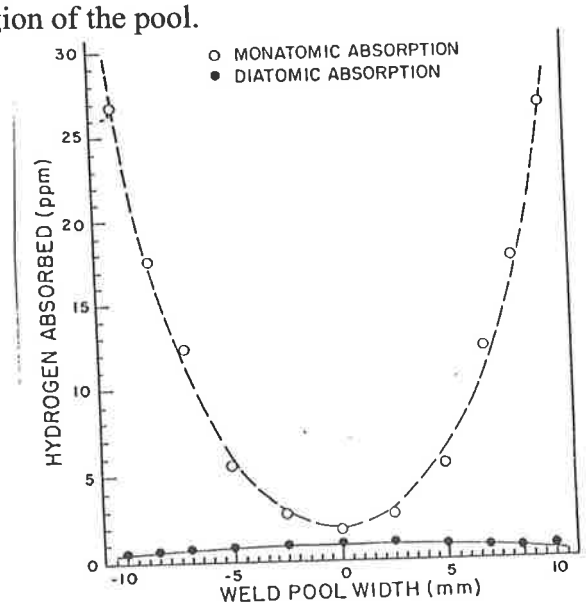

Figure 5.1: Theoretical hydrogen absorption due to both monatomic and diatomic hydrogen as a function of weld pool location. The calculated points assume a dissociation temperature of 2500°C, 0.01 atmosphere hydrogen added to the argon shielding gas and an absorption temperature equivalent to the surface temperature of the weld pool (Gedeon and Eagar, 1990).

Similar comments are made by DebRoy (1992) and Palmer and DebRoy (1996) who attributed the enhanced solubility of gases (that is at concentrations significantly higher than the value predicted by Sievert's law) to the decomposition of molecules to excited neutral atoms and ions. Palmer and DebRoy (1996) reported on the effects of nitrogen absorption in welds and pointed out that in welding the weld metal came into contact with a plasma formed

from a diatomic source gas. When the diatomic gas was transformed to a plasma phase it could dissociate, ionise or become excited. The formation of atomic nitrogen atoms in the plasma was a consequence of the collision of fast electrons with the nitrogen molecules and was therefore dependent on the electron density. Since the electron density decreased with increasing pressure, the partial pressure of atomic nitrogen also decreased with pressure.

The author of this thesis believes, however, that the dissociation fraction of gases and hence the partial pressure of the atomic form is dependent on the rate of dissociation and recombination as well as the density of electrons. Alternatively, it could be simply stated that the partial pressure of atomic nitrogen decreases with total pressure as a consequence of Le Chatelier's Principle.

Banerjee et al. (1992) discussed this issue with respect to the dissolution of nitrogen in the weld pool. Characterisation of the species present in a plasma in a series of gas-metal systems showed that the monatomic N and ionic N^+ species were principal components in the plasma atmosphere above a weld pool. It was stated that in arc welding, where a plasma was present, the solubility of nitrogen and hence the nitrogen contents of metals were observed to be significantly higher than those predicted using Sievert's law. In addition, similar to the behaviour of hydrogen, the solubility of monatomic nitrogen in iron was found to decrease with increasing temperature. In that case the amount of nitrogen in solution was proportional to the first power of the nitrogen pressure above the melt. A calculated profile of the nitrogen solubility across the surface of a molten pure iron weld pool showed that the absorption was higher at the edge of the pool (where the temperatures are lower) than at the centre of the pool.

It was also observed that an increase of 200K in the reaction temperature increased the

solubility of nitrogen by about 0.05weight% at the centre of the pool and by about 0.3weight% at the edges. The overall conclusions made by Banerjee et al. (1992) was that the nitrogen content of a weld pool in the presence of a plasma was influenced significantly by the amount of monatomic nitrogen and the local temperatures, and that the properties and composition of the plasma present during welding would play a fundamental role in governing the concentration of nitrogen in a weld pool.

These investigations have shown that the accurate determination of the amount of hydrogen absorbed in a liquid weld pool during welding is a very complicated task. The modelling process requires a detailed characterisation of the plasma which involves knowledge of the temperature gradients within the arc, the partial pressures of the molecular gases and any metal vapours, as well as the extent of dissociation and ionisation of these gases at various temperatures. The change in arc temperature for various welding conditions is therefore also required. In addition the spatial variations in the surface temperature of the weld pool are required to calculate the rate of dissolution of the gases into the weld pool.

The work performed in this thesis has built upon these recent ideas, applying them to MMA welding, and also taken into account the influence of the keyhole.

5.2.3.2 The Absorption of Hydrogen from Cellulosic Electrodes

5.2.3.2.1 Introduction

In manual metal arc (MMA) welding the gas absorption problem is aggravated further since the generation of the shielding gases is the result of decomposition of the flux constituents as well as the ionisation of metal. It was difficult to find information in the literature regarding the temperature gradients which exist in the arcs of MMA electrodes and the changes in temperature at various welding currents. Lancaster (1993) states temperatures (close to the

cathode) for arc columns generated by metal vapours ranging from 4000 to 6000K for alkali metal and iron vapours respectively.

5.2.3.2.2 Analytical Work

Although the approximate composition of the cellulosic flux is known (approximate because x-ray fluorescence cannot measure the carbon content), values for the partial pressures of the various gases and metal vapours which are generated are difficult to determine accurately.

An attempt has been made, however, to calculate the amount of monatomic and diatomic forms of hydrogen in the arc based on an estimate of the composition of the gases in the plasma. It is assumed that in the case of a cellulosic electrode, the cellulose will be the major contributor of gases to the shielding gas, and that the total pressure of the gases in the arc will be one atmosphere (it is expected, however, that the pressure will be marginally higher than this). The other major constituents are the oxides of silicon, calcium and titanium and iron powder. The carbonates present in the flux were not detected by the method of analysis.

A computer programme developed at CSIRO (Commonwealth Science and Industrial Research Organisation, Sydney, NSW) which calculates the equilibrium composition of the plasma from a given source gas composition using a method of minimisation of the Gibb's free energy of the system (Murphy and Arundell, 1994, Kovitya, 1985), has generated results which are in units of number of particles per metre cube. The partial pressure of all the components was calculated using the following equations, assuming ideal gas behaviour.

$$PV = NkT \qquad (5.4)$$

where P is the pressure in atmosphere, V is the volume in litres, N is the number of particles, k is Boltzmann's constant and T is the temperature in Kelvin.

$$k = \frac{R}{N_a} \qquad (5.5)$$

$$=1.363\text{x}10^{-25} \text{ L.atm/mole.}$$

where R is the Gas constant which is equal to $8.2053\text{x}10^{-2}$ L.atm/K.mole and N_a is Avogadro's number which is equal to $6.023\text{x}10^{23}$

An arc composition with 50% hydrogen and 50% carbon monoxide was initially proposed but could not be analysed by the software due to the numerous and complex interactions which resulted. A composition with 75% hydrogen and 25% carbon monoxide was used instead in the calculations. The contribution to the plasma from the metal vapours and dissociation products from the oxide and carbonates compounds were not added, again due to the increase in complexity of the calculations. It is expected that the elements and compounds in the flux as well as atmospheric gases will be dissociated and ionised in the arc and thus make a significant contribution to the composition of the shielding gas. It is, however, beyond the scope of this work to carry out further analyses.

In this research only an approximate analysis has been undertaken due to the difficulties in determining accurately the concentration of the various species in the plasma and its the temperature. As a result many assumptions had to be made. The information obtained has been used, however, in relating the results of the experimental work to the formation of hollow bead.

5.2.3.2.3 Results

The results of the analysis in the form of particles per cubic metre and the corresponding partial pressures in atmosphere are presented in detail in Tables A10a and A10b and Tables A10c and A10d respectively in Appendix A. The data pertaining to the dissociation of

hydrogen was extracted from Tables A10c and A10d and plotted in Figure 5.2. The graph shows the partial pressure of diatomic and monatomic hydrogen at temperatures ranging from 1000 to 10000K. The temperature gradients in the arc and the changes in temperature with welding current are not known. It is known, however, that the flux contains elements such as sodium and manganese which ionise at approximately 4000 and 5000K respectively (Physics of Welding, 1984), such that based on the information by Lancaster (1993) it can be deduced that the temperature of the arc column close to the cathode is probably in the range 4000 to 6000K.

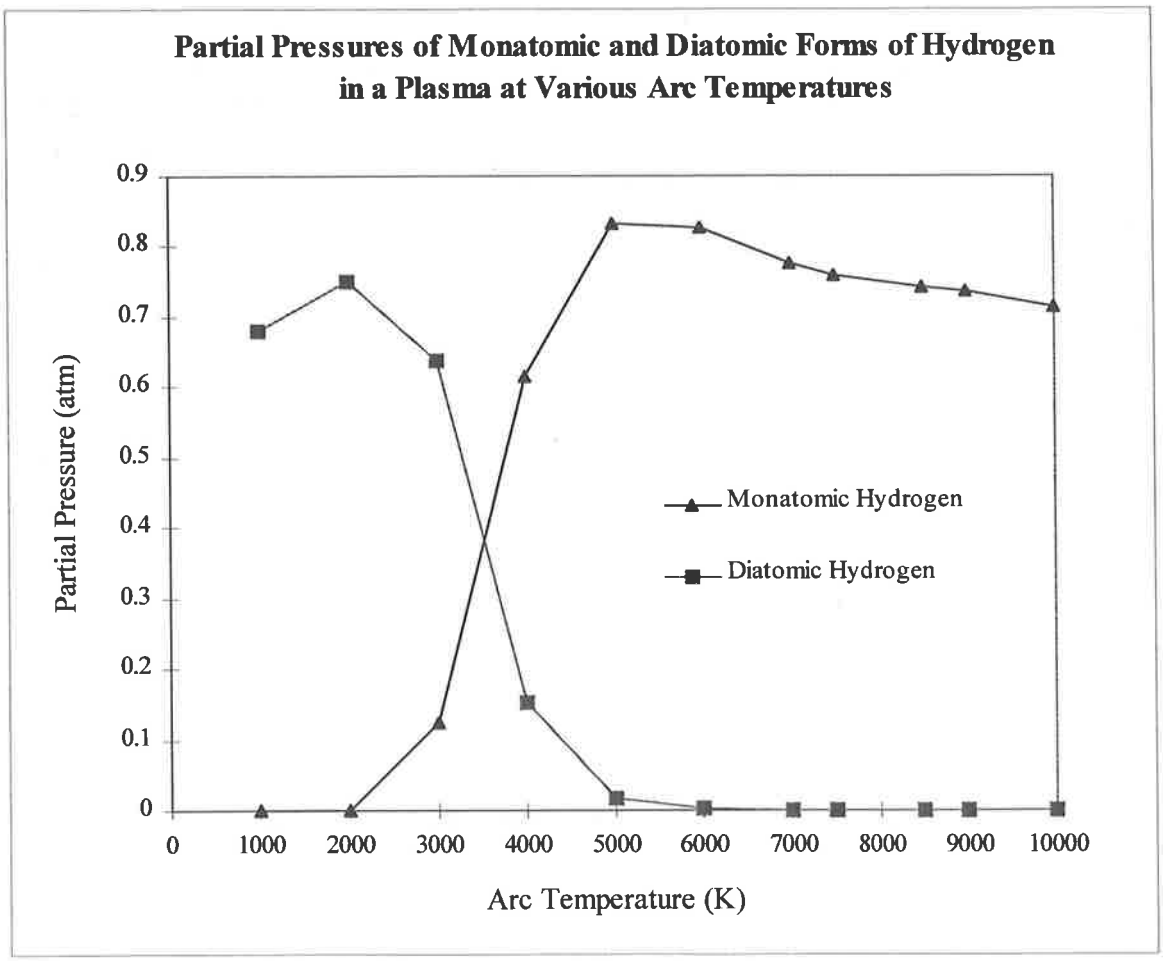

Figure 5.2: Graph of the partial pressures of diatomic and monatomic hydrogen in a plasma at various arc temperatures.

The results in Figure 5.2 indicate that the hydrogen begins to dissociate from 2000K. The partial pressure of monatomic hydrogen increases from 2000 to 5000K, then starts to decrease due to ionisation at higher temperatures (the results in Table A10c and A10d show that the

partial pressure of H^+, H^- and the density of electrons gradually increases with temperature). The partial pressure of diatomic hydrogen decreases from 2000 to 5000K after which it becomes negligible.

The thermochemical analysis for the absorption of monatomic hydrogen into liquid iron considers the following reactions. Equation 5.6 represents the absorption of hydrogen in the melt from a diatomic hydrogen gas above the melt and Equation 5.8 the dissociation of diatomic hydrogen gas to monatomic hydrogen gas.

$$\frac{1}{2}H_{2(g)} \rightarrow [H] \qquad (5.6)$$

$$\Delta G^o = -51977 + 11.62\ T\ (cal/mole) \text{(Elliot et al., 1963)} \qquad (5.7)$$

$$H_{2(g)} \rightarrow 2H_{(g)} \qquad (5.8)$$

$$\Delta G^o = 8720 - 11.02\ T\ (cal/mole) \text{(Handbook of Chemistry and Physics, 1971)} \qquad (5.9)$$

where [H] is the hydrogen absorbed in the melt and ΔG_o is the standard Gibb's free energy (calculated at standard conditions of 1 atmosphere partial pressure and 25°C).

These reactions can be combined to form the reaction in Equation 5.10 which represents the absorption of hydrogen into the melt from monatomic hydrogen above the melt.

$$H_{(g)} \rightarrow [H] \qquad (5.10)$$

The free energy associated with this reaction is:

$$\Delta G^o = -43257 + 0.60T\ (cal/mole) \qquad (5.11)$$

where T is the temperature. Equation 5.11 shows that although the equilibrium concentration

of hydrogen in metal will decrease with increasing temperatures the reaction is spontaneous at the arc temperatures assumed in MMA welding. Gedeon et al. (1990) obtained a different equation (Equation 5.12) for evaluating the free energy associated with the reaction in Equation 5.10.

$$\Delta G^{o} = -44780 + 3.38T \text{ (cal/mole)} \qquad (5.12)$$

Although the values for the enthalpy of formation of both Equations 5.11 and 5.12 are comparable, a discrepancy exists in the absolute entropy values (0.60 compared to 3.38). This dissimilarity may be because tables of thermochemical data may vary from one source to the next. The data used to derive Equation 5.7 was verified using two different sources (Brown et al., 1994 and Handbook of Chemistry and Physics, 1971).

The expression for the free energy given in Equations 5.11 and 5.12 and the data on the composition of the plasma obtained in the previous section (Section 5.2.3.2.2) were used to produce curves of equilibrium hydrogen solubility, [H], versus partial pressure of monatomic hydrogen, P_H, at various reaction temperatures, T, (Figure 5.3). The standard free energy was first calculated for a temperature range of 1000 to 10000K, in intervals of 100K, which was then used to evaluate the right hand side of Equation 5.13.

$$[H] = P_H \exp\left(\frac{-\Delta G^{o}}{RT}\right) \qquad (5.13)$$

where [H] is the solubility of hydrogen in the melt, P_H is the partial pressure of monatomic hydrogen, ΔG^{o} is the standard Gibb's free energy, T is the temperature in Kelvin and R is the gas constant (8.314J/mol K).

The data on the partial pressure of monatomic hydrogen extracted from Tables A10c and

A10d were plotted against temperature between 1000 and 10000K, in intervals of 1000K (see also Figure 5.2). The number of temperature increments within that range was increased by fitting a curve to the points and then re-evaluating the partial pressure. The solubility of hydrogen [H], in ppm, could then be calculated using Equation 5.13 and plotted against the reaction temperature (Figure 5.3). The concept of the reaction temperature is discussed in the following Section 5.2.3.2.4. It must also be pointed out that the curves shown in Figure 5.3 only apply to the particular composition estimated for the source gas, that is 75% hydrogen and 25% carbon monoxide.

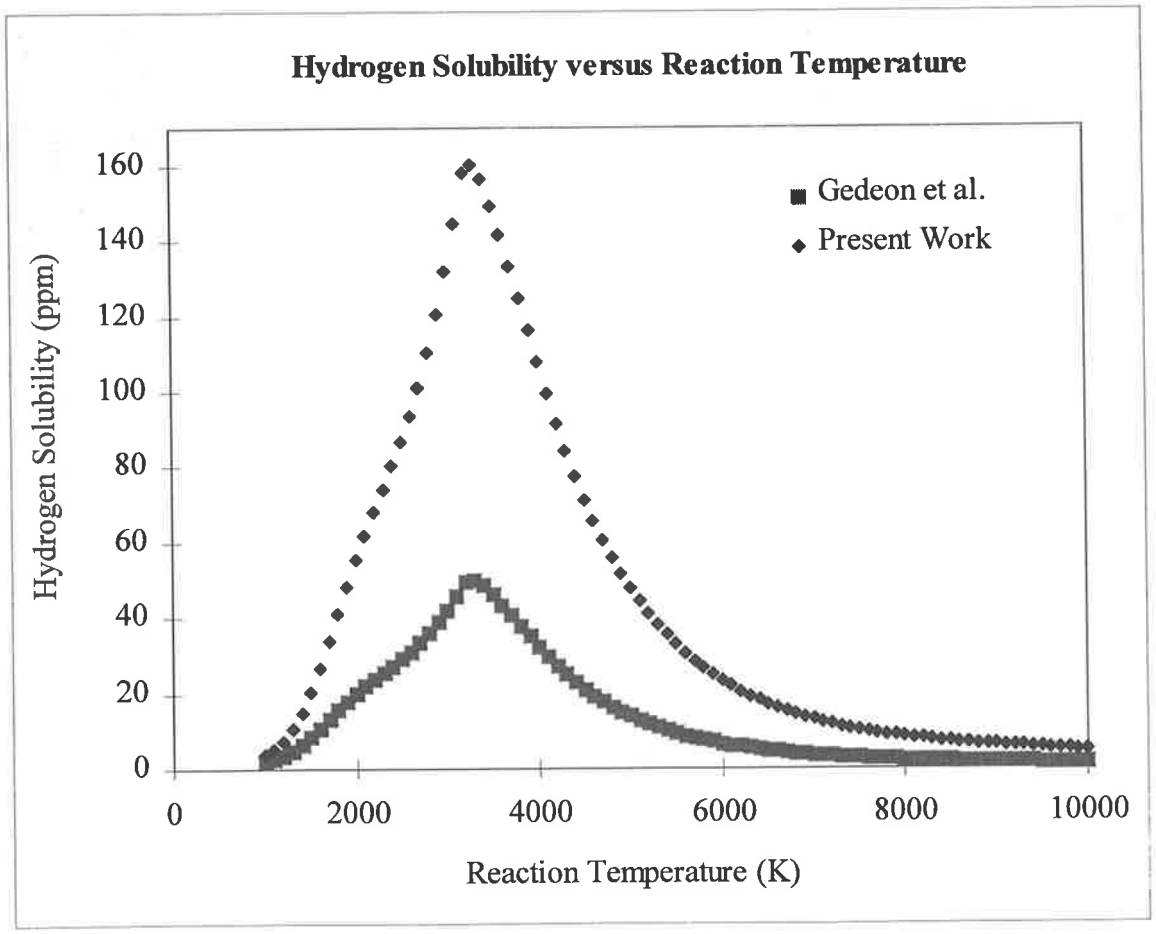

Figure 5.3: Graph of the solubility of hydrogen in the melt in ppm versus the reaction temperature calculated using the equation for the standard free energy derived in this work and the one derived by Gedeon and Eagar (1990).

Although the two curves predict different solubility values at particular temperatures, the peak

solubility occurs at approximately the same temperature for both curves.

5.2.3.2.4 Discussion

The work of researchers on the absorption of hydrogen in a weld pool discussed in Section 5.2.3.2 established that the determination of the amount of hydrogen absorbed in a weld pool must consider the contribution from monatomic hydrogen. However, the welding literature has given very little consideration to the problem of gas absorption into a molten weld pool where a keyhole is present between the arc and the weld pool. For a full quantitative understanding of the process accurate temperature profiles of the arc, shielding gases and weld pool are required, along with quantitative composition data. These data could only be reasonably obtained by experimental measurement. Temperature profiles of the gas and arc could be obtained from analysis of emission spectra, although the composition presents a more difficult problem. Neither were obtained in this work but are strongly recommended as future work in this area. The literature does contain data on hydrogen absorption in related applications.

Estimates of the arc temperature in the literature (Lancaster, 1993) place it between 4000K and 6000K for MMA welding. Figure 5.2 shows that at these temperatures the dissociation of hydrogen in the arc is expected to be quite high (60 - 85%). However, conditions will not be favourable for the absorption of hydrogen in the metal underneath the arc.

Calculations show that total hydrogen absorption peaks at a gas temperature of approximately 3300K and reduces dramatically with temperature increase thereafter (Figure 5.3). These calculations combine the hydrogen dissociation data of Figure 5.2 with hydrogen solubility curves.

This means that at the predicted arc temperatures total hydrogen absorption will be very small.

Because the boiling point of liquid iron is 2900K metal droplets produced in the arc will be far from thermal equilibrium with the surrounding plasma. It is anticipated that the surfaces of the metal droplets will be at 2900K and boiling vigorously. The outward flux of metal and slag vapour from the droplet surfaces will dramatically limit the absorption of arc gases in this region.

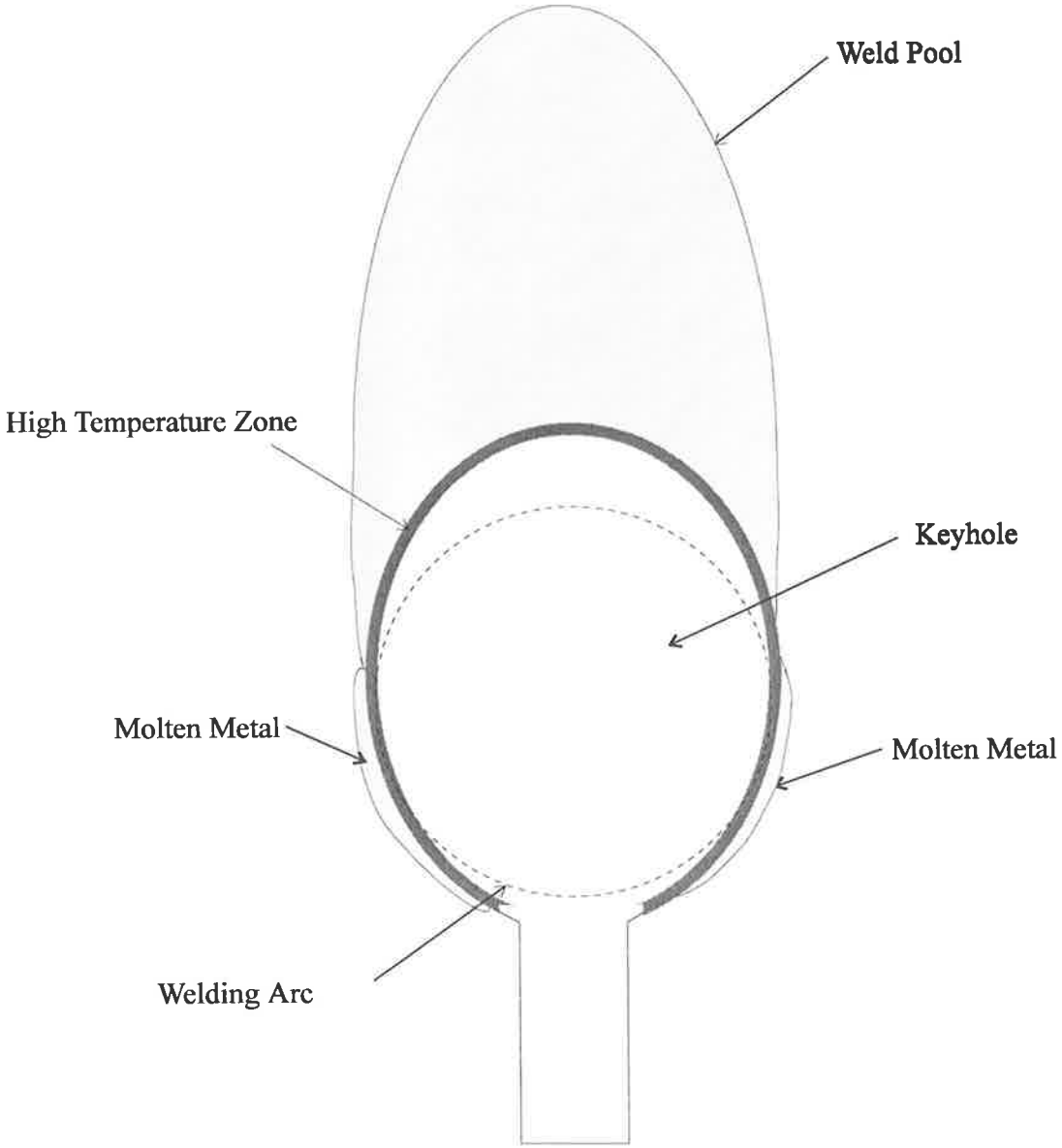

Figure 5.4: Schematic of showing the position of the keyhole, weld pool and welding arc, and the transfer of metal from the electrode to the weld pool along the sides of the keyhole.

The mechanism for metal transfer to the weld pool for this welding process is a poorly

understood phenomenon that has not been addressed in the literature. It has been observed from high speed filming of the keyhole that the metal appears to be inducted around the sides of the keyhole into the weld pool (Figure 5.4) (see also Chapter 4). Some of the metal transfer is also likely to arise from the transfer of metal vapour across the keyhole and by spraying of metal droplets across the keyhole.

The most likely mechanism for the absorption of hydrogen is absorption from the hot shielding gas flowing from the arc over the surface of the weld pool. Conditions in this region will be optimal for hydrogen absorption, combining a lower melt temperature with a hot, highly dissociated gas. Even though the shielding gas temperature will be much higher than the boiling point of iron, the weld pool is in contact with the base metal which provides a large heat sink, and hence maintains a lower weld pool temperature. In addition, the weld pool is separated from the arc by the height of the keyhole, which typically ranges from 4mm to 7mm., thus diminishing the heating effect of the arc, and providing a distance over which the transferred molten metal cools in transit. Absorption of monatomic hydrogen occurs much more readily at these lower weld pool temperatures than at the higher temperatures of the arc. As monatomic hydrogen is more readily absorbed than diatomic hydrogen, absorption by this mechanism is favoured in the highly dissociated shielding gas.

The precise dissociation fraction for hydrogen near the surface of the weld pool will depend on the temperature of the shielding gas outside the boundary layer adjacent to the weld pool. It is likely to be higher than that predicted from the melt surface temperature because the gaseous species of monatomic and diatomic hydrogen are not in equilibrium at the surface of the melt. Gedeon and Eagar (1990) describe a cathodic boundary layer, approximately 0.2mm thick for electrode positive GMA welding, over which the temperature changes abruptly from the melt surface temperature to the arc temperature. If a boundary layer of comparable

thickness exists between the melt and the shielding gas in MMA welding then it is expected that the dissociation fraction at the surface of the melt will be closer to that predicted by the shielding gas temperature than that of the melt surface. This is because the mean free path of monatomic hydrogen, estimated to be of the order of 0.01mm under these conditions (Tabor, 1969), is quite large in comparison with the boundary layer thickness. This value was estimated assuming that only other hydrogen atoms were present. It is therefore likely that the actual mean free path will be less since other gaseous species are also present. This implies that a large proportion of monatomic hydrogen will reach the melt surface without recombining to form molecular hydrogen. The reaction temperature can thus be considered as the temperature of hydrogen atoms since the boundary layer is not in thermal equilibrium. By this it is meant that the energy of the gas in a small region will not be evenly distributed resulting in different gaseous species from the same region having different temperatures. Monatomic hydrogen with its long mean free path will be the hottest of the gaseous species.

The exact location on the surface of the weld pool (either near the sides of the keyhole or near the top of the keyhole) where the optimal conditions for the absorption of hydrogen into the melt exist cannot be suggested at this stage since the surface temperatures of the pool in contact with the keyhole are not known.

The main factor affecting the formation of hollow bead pores has been identified as the welding current. It was also argued in Section 5.2.2 that the main gas responsible for the porosity is hydrogen. The work of previous authors have shown the dependence of the weld metal hydrogen content on welding current (White, 1992, Woods, 1974, Pokhodnya and Yavdoshchin, 1969, Howden and Milner, 1963, Salter, 1963). It has also been found, however, that with MMA welding the diffusible hydrogen content of welds does not vary with welding current when expressed as a function of fused metal compared with deposited metal

(Kiefer, 1996, The Lincoln Electric Company, 1986). The weight of fused metal is equal to the weight of added metal plus the weight of base metal melted. The results obtained by White (1992), however, show an increase in diffusible hydrogen in both cases, that is when expressed in deposited or fused metal. It was suggested in Section 2.15 that the range of welding current may have to be sufficiently wide in order to observe any effects on the diffusible hydrogen content.

The experimental results in this research have revealed an increase in the diffusible hydrogen content of the weld (expressed in deposited metal) with increasing current. A hypothesis to explain the effect of welding current (as well as the weld travel speed) on the absorption of hydrogen into the weld pool and hence the incidence of hollow bead is now proposed.

An increase in welding current is expected to increase the temperature of the arc plasma. It has been shown in GTA welding that an increase in welding current from 140 to 160A, increases the temperature at the central part of the arc from 16000 to 18000K (Kobayashi and Suga, 1979). Although this correlation is not directly applicable to MMA welding, it is assumed that a rise in the temperature of the arc will occur at higher welding currents.

The data obtained on the composition of the plasma at various temperatures shows that the partial pressure of monatomic hydrogen gradually increases with temperature in the range of 3000 to 5000K. An increase in the partial pressure of monatomic hydrogen in the arc will significantly increase the hydrogen content of the weld metal since the contribution to the hydrogen content of the weld pool from diatomic hydrogen will be very small compared to the contribution from monatomic hydrogen. This is illustrated in Figure 5.1 above. Furthermore, work undertaken by Palmer and DebRoy (1996) on the absorption of nitrogen in iron under a plasma, has shown that the calculated dissociation (or reaction) temperatures are

approximately 100 to 215K higher than the sample temperature with the increase in temperature corresponding to an increase in the solubility of nitrogen from 40 to 200ppm. It can thus be suggested that relatively small increases in the dissociation temperature, which are related to higher arc temperatures, have a significant influence on the level of absorption. It is expected that similar correlations apply to the absorption of hydrogen in steel. In summary it is postulated that an increase in welding current will increase the temperature of the arc and hence the percentage of dissociation of hydrogen. This will result in an increase in the absorption of hydrogen into the weld pool since monatomic hydrogen is much more readily absorbed than diatomic hydrogen. Also, the curve of hydrogen solubility versus reaction temperature in Figure 5.3 shows that the solubility of hydrogen increases with temperature when the reaction temperature is lower than 3300K, and conversely decreases with temperature with the reaction temperature above this value. This leads to the conclusions that the reaction temperature has to be less than 3300K.

Another important factor, however, may be the rate of transfer of the drops. Information has been obtained on the diameter of the droplets and their transfer rate across the arc (Physics of Welding, 1984). For MMA welding with cellulosic electrodes the droplet diameter changes very slightly with current (from 1.8mm at 165A to 1.9mm at 180A), whereas the transfer rate varies significantly from 145 drops per second at 165A to 185 drops per second at 180A. The higher rate of transfer of the drops at a higher current can potentially increase the rate of absorption of hydrogen, although the influence of slag around the metal droplets may impede to an extent the absorption of hydrogen into the metal.

In addition to the welding current, high weld travel speeds were observed to have a significant influence on the incidence of hollow bead. An increase in travel speed decreases the heat input which has the effect of increasing the solidification rate and decreasing the size of the weld

pool. Both factors will influence the hydrogen content of the weld pool. At higher solidification rates, the hydrogen will have less time to desorb from the weld pool resulting in a higher concentration. The reduction in surface area of smaller weld pools can further reduce the rate of desorption of hydrogen from the weld pool.

The experimental study also revealed that increasing the moisture content of the flux increases the occurrence of hollow bead, and conversely decreasing it significantly reduces the incidence of hollow bead. It is probable that the levels of moisture in the flux result in a higher concentration (or partial pressure) of hydrogen in the arc which would lead to an increase in the amount of hydrogen entering the weld pool.

5.2.4 Nucleation of Gas Bubbles in the Weld Pool

The work of researchers in the area of bubble nucleation has established that gas bubbles in weld pools will nucleate heterogeneously. It has also been shown that the energy required for the nucleation of a gas bubble is least at the solidification interface due to the supersaturation of hydrogen.

The case of equilibrium solubility at standard conditions is considered here since it was not possible to determine accurately the concentration of hydrogen in the molten pool. The solubility of hydrogen in liquid iron at the melting point (1535°C) is 26.7cm^3/100g, and in the solid 13.4cm^3/100g (Smialowski, 1962). Crystallisation is thus accompanied by a sharp decrease in the solubility of hydrogen. Therefore some hydrogen will be evolved as gas-forming solutes at the freezing point if the liquid iron is saturated with hydrogen, which is typical in MMA welding. It is still possible for the solid to be saturated with hydrogen as results in the experimental section have shown.

It is expected that saturation of the weld pool with hydrogen will occur in the case considered in this work. This is because the diffusible hydrogen content of the welds, which is expected to be less than the concentration in the molten weld pool due to desorption, has been observed in this research to be in the range of 30 to 54mL/100g when cellulosic electrodes are used and are therefore much higher than the standard solubility at the melting point

Since the solidification rates in welding are high, the hydrogen may also be trapped in the solidifying metal. This hypothesis has been proposed by Howden (1982) and Gedeon and Eagar (1990) who suggest that is the reason why little porosity is found in steel welds. It is possible, however, that at high partial pressures of hydrogen in the arc and thus high concentrations of hydrogen in the weld pool, the drop in solubility and the further decrease due to the formation of δ–ferrite, which has a very low solubility for hydrogen, can cause rejection of gas solutes at the solidification interface. As mentioned by Chalmers (1964), since the solubility of hydrogen is lower in the solid phase than the liquid, it can be stated that it will behave like an element with an equilibrium partition coefficient (k) less than unity. An element with $k<1$ will be rejected at the solidification interface and cause an enriched layer of that solute in the molten weld metal ahead of the interface (Suga and Hasui, 1986, Savage, Lundin and Hrubec, 1968). This is the case even if a large proportion of the hydrogen is retained in the solidifying metal (Rakhmanov, 1978, Grigorenko, 1970). If, therefore, the liquid metal is saturated with hydrogen, it will become supersaturated as soon as an enriched layer forms at the interface. Due to the high solidification rates encountered in welding, the diffusion of gas from the interface is not sufficiently fast compared to the rate of rejection at the interface. Hence at the supersaturation point there will be more gas in solution than the equilibrium amount. In this situation, Chalmers (1964) proposes that there is a thermodynamic force tending to reduce the gas content. The decrease in gas content may be

by the escape of gas at a free surface or by the formation of a gas bubble in the liquid.

Recent papers by Simone and Gibson (1997, 1996) explain the nucleation of elongated pores in a manner which is comparable to the mechanism described above. They propose that the gas pores form from a eutectic reaction where the liquid metal solidifies to form a solid and a gas phase. The nucleation of hollow bead can be considered in the same light as an "intercellular-dendritic aligned divorced eutectic" where the eutectic reaction is as follows:

$$\text{liquid} \rightarrow \delta\text{–ferrite} + \text{hydrogen} \qquad (5.14)$$

The distribution of the concentration of hydrogen, $C_{liq(x)}$, in the liquid in front of the solidification interface can be expressed as (Grigorenko, 1970):

$$C_{liq(x)} = C^{o}_{liq} + C^{o}_{liq}\left(\frac{1-k}{k}\right)\left(1 - e^{\frac{-kVx}{D_L}}\right) \qquad (5.15)$$

where C^{o}_{liq} is the initial gas content in the liquid, k is the equilibrium partition coefficient, V is the velocity of the solidification front, x is the distance from the fusion line and D_L is the diffusion coefficient in the liquid phase. This equation assumes that the interface is planar and that no convective flows exist in the weld, but works well in the enriched layer in front of the solidification interface (Pokhodnya, 1980).

It is proposed here that a gas bubble will nucleate at or near the solidification interface in the layer enriched in gas-forming solutes. It is possible that the nucleus forms heterogeneously on the interface or on a slag inclusion since both types of surfaces will reduce the energy required for the nucleation of a bubble. It has been mentioned, however, (Rakhmanov, 1978, Zakharov and Lipodaev, 1976) that the probability of forming gas bubbles increases with the degree of saturation of the liquid metal and thus nucleation is most likely at the solidification interface.

The probability of nucleating gas bubbles will also increase at the interface at the last regions to solidify due to macrosegregation. Solutes with low equilibrium partition coefficients and gas-forming solutes can accumulate at the last regions to solidify, which for the welds studied are near the top and bottom of the weld bead centreline.

The stable nucleus will have a lens shape, as shown in Figure 5.5, with a radius greater than the critical radius.

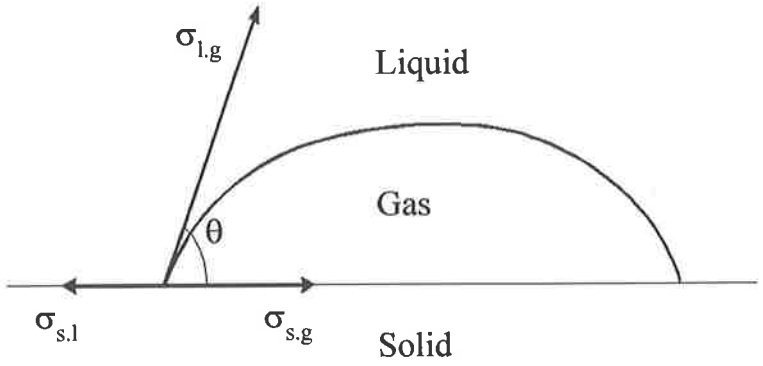

Figure 5.5: Schematic of a gas nucleus showing the three surface tension gradients between the solid, liquid and the gas phases.

The wetting angle, θ, for this system is given by (Kudrin, 1985):

$$\cos\theta = \frac{\sigma_{s.l} - \sigma_{s.g}}{\sigma_{l.g}} \qquad (5.16)$$

where $\sigma_{s.g}$ is the surface tension at the solid-gas boundary, $\sigma_{s.l}$ is the surface tension at the solid-liquid boundary and $\sigma_{l.g}$ is the surface tension at the liquid-gas boundary.

The welding conditions will have a strong influence on the probability of forming gas nuclei in a weld pool. Experimental data shows that high welding currents will increase the hydrogen content of the molten pool. Therefore according to Equation 5.15 the concentration of hydrogen ahead of the solidification interface (or the degree of supersaturation) will increase since the initial concentration of hydrogen in the liquid is higher, thus predicting that the

probability of forming gas bubbles will increase at high welding current.

The weld travel speed has also been observed to have an influence on the occurrence of hollow bead. Its effect is more pronounced at the very high travel speeds (500 and 600mm/min), but is still secondary to that of the welding current.

An increase in solidification rate due to higher welding speeds will, according to Equation 5.15, increase the concentration of hydrogen at the solidification interface while decreasing the thickness of the enriched layer. The higher degree of supersaturation should increase the probability of nucleating a gas bubble, although due to the reduction in the thickness of the enriched layer the rate of growth of the bubble should decrease (Suga and Hasui, 1986). The increase in the occurrence of hollow bead at high welding speed may also be explained as a result of the entrapment of a bubble at the solidification interface before it has time to grow and escape. This will be discussed further in the following Section 5.2.5.

Experimental data obtained in this work also shows that the diameter of hollow bead is not dependent on the welding current or weld travel speed which indicates that the solidification microstructure strongly influences its growth. The advancing cellular dendrites could be responsible for restricting the outward growth of the pores by solidifying around them. Some evidence for this hypothesis lies in the observation of ridges inside hollow bead pores which represent regions of microsegregation at the boundaries of cellular dendrites that have solidified after protruding inside the pores.

The next dominant factor in the formation of hollow bead is the silicon content of the parent metal. An extensive experimental study has established the role of high silicon contents in the promotion of hollow bead. The effect of silicon on the formation of porosity has not been extensively studied and information on the effect of silicon on gases in liquid metal is limited.

Pokhodnya and Yavdoshchin (1969, 1972) found that increasing the levels of surface active elements such as silicon and aluminium increases the occurrence of porosity in welds. It was proposed that silicon retards the desorption of gases from the weld pool thus increasing the degree of supersaturation of the liquid metal with gases. The data available in the literature (Smialowski, 1962) (see Figure 1.10 Section 1.2.8.2.3) shows that an increase in the silicon content (from 1% upwards) reduces the coefficient of hydrogen diffusion in iron. No information has been found, however, on the effect of smaller concentrations of silicon in the range used in pipeline steels (0.1 - 0.3%). If Equation 5.15 is considered again, a decrease in the coefficient of hydrogen diffusion in the liquid will increase the concentration of gas in the molten metal at the solidification interface and thus favour the formation of bubbles.

The information outlined above can be used to suggest that the increase in the occurrence of hollow bead at high silicon levels may be due to an increase in the degree of supersaturation at the solidification interface which increases the probability of forming gas bubbles.

The presence of a surface active element in greater concentrations can also influence the nucleation of a gas nucleus by changing the magnitude of the wetting angle (see Figure 5.3). A decrease in the wetting angle will result in a smaller spherical cap with the same radius of curvature (see Equation 5.16) which therefore requires less gas to form the cap. Silicon is known to reduce the surface tension of the liquid steel (and thus increase its fluidity) again due to its surface activity (Kudrin, 1985, The Lincoln Electric Company, 1984, Bukovinski, 1975). As a result it is possible that the reduction of the surface tension of the melt will decrease the component of the surface tension between the liquid and the gas and therefore, according to Equation 5.16, reduce the wetting angle. Unfortunately no data has been found in the literature on the effect of surface active elements on the three components of surface tension. This mechanism is, therefore, only speculative at this stage.

5.2.5 Factors Influencing the Location of Porosity in the Weld Pool

As explained above, macrosegregation will cause impurities in the weld (including gas-forming solutes) to accumulate in the last regions to solidify. Since the degree of supersaturation of hydrogen at the interface at these regions is expected to be highest, the probability of forming gas bubbles there is also high. It has been found in this research that porosity occurs almost exclusively in the form of hollow beads along the weld centreline. On only one occasion have small spherical gas pores at the fusion line and worm holes been observed. Since porosity occurs in the regions where the concentration of gas is highest, it can be suggested that steel is relatively resistant to porosity formation, due to the entrapment of the majority of the hydrogen in the solid metal during solidification, as proposed by Gedeon and Eagar (1990). Lancaster (1992) also mentions that steel can be welded using the MMA method without porosity with an arc atmosphere of up to 50% hydrogen. Howden (1982) found that for arc atmospheres consisting of up to 10% hydrogen in argon most of the hydrogen is retained in the solidified weld. However, as mentioned in Section 5.2.4 it is believed that at high concentrations of hydrogen in the weld pool, which is the case when welding with cellulosic electrodes, rejection of hydrogen in front of the solidification interface will occur. It is therefore suggested that hollow bead forms at the last regions to solidify where the concentration of hydrogen is sufficiently high to allow nucleation.

It is also expected that the flow patterns in the weld pool will have an influence on the location of hollow bead. Convective heat flow and fluid flow in a weld pool are controlled by three major factors, namely the buoyancy force, electromagnetic forces and surface tension effects. A brief description of the flow resulting from these forces is now given (Matsunawa, 1992, David and Vitek., 1989, Wang and Kou, 1986). The direction of flow is described for a bead-on-plate weld made in the horizontal downhand position.

The direction of the buoyancy force is vertically upwards. The resulting flow pattern is upwards towards the top surface at the weld centreline, across the surface and then down along the fusion line. The forces generated by electromagnetic effects are roughly opposite in nature to the buoyancy force, they point downward and inward. Consequently, the convective flow that results is also opposite to that produced by buoyancy effects.

The effect of surface tension on the flow is more complex. The surface tension gradients can develop as a result of temperature variations on the weld pool surface combined with the temperature dependence of the surface tension. The temperature coefficient of surface tension can be either positive or negative depending on the composition and temperature. For a negative coefficient gradient of surface tension, the surface tension force is across the surface away from the centreline. The resulting flow is upwards and across the surface away from the centreline.

Comparing the relative magnitudes of the convective flows, the buoyancy force is the weakest and the electromagnetic forces are considerably larger and can be either reinforced or opposed by surface tension effects. In consequence, although buoyancy is a force acting on bubbles in the weld pool, the resultant of the electromagnetic, surface tension and drag forces is likely to be the dominant factor affecting the motion of bubbles in a weld pool. These effects will be further discussed by considering a particular example where the location of hollow bead pores in a weld bead was determined. In addition, it is evident that the component of convective flows directed outwards toward the surfaces of the weld pool will allow hydrogen and other gases to be desorbed from the liquid pool.

An important feature of the shape of the weld pools obtained in the stovepipe welding process has been observed and described in the finite element modelling (Chapter 4). The analysis was

relatively crude in that it did not fully model the convective flows in the weld pool nor the influence of gravity and a keyhole. It nevertheless produced very good results pertaining to the size and shape of the weld pool, and it can thus be accepted that the predictions of the models describing the shape of the weld pool are reasonably accurate.

A particular feature is a relatively "bulbous" solidification interface at the back of the weld pool as shown in Figure 5.6 (on the right hand side). This should be compared with a typical bead-on-plate weld pool which has a sharply tapered interface (Figure 5.7). In these pools the last region to solidify is at the back of the weld pool (right hand side) near the top surface of the bead (or at the centreline near the top surface if a cross section is considered).

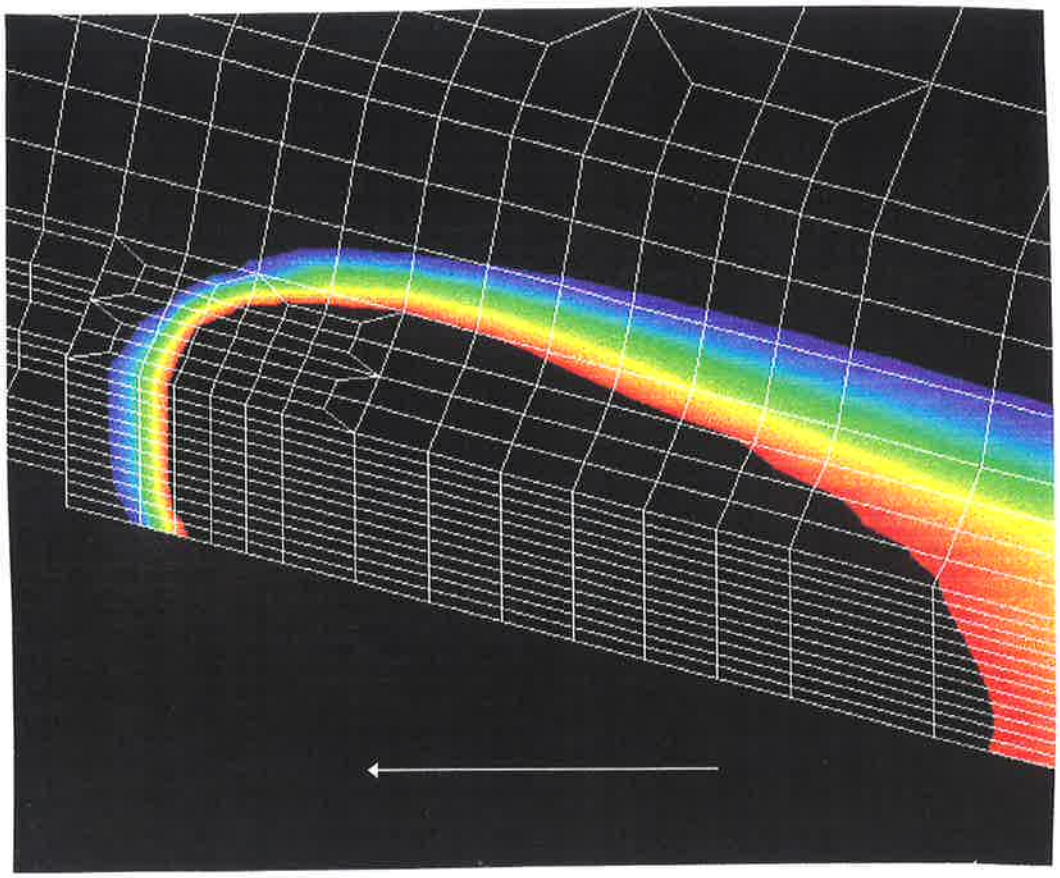

Figure 5.6: Finite element model of the longitudinal vertical section of the weld pool showing the a relatively flat interface at the back of the pool. The arrow shows the direction of welding.

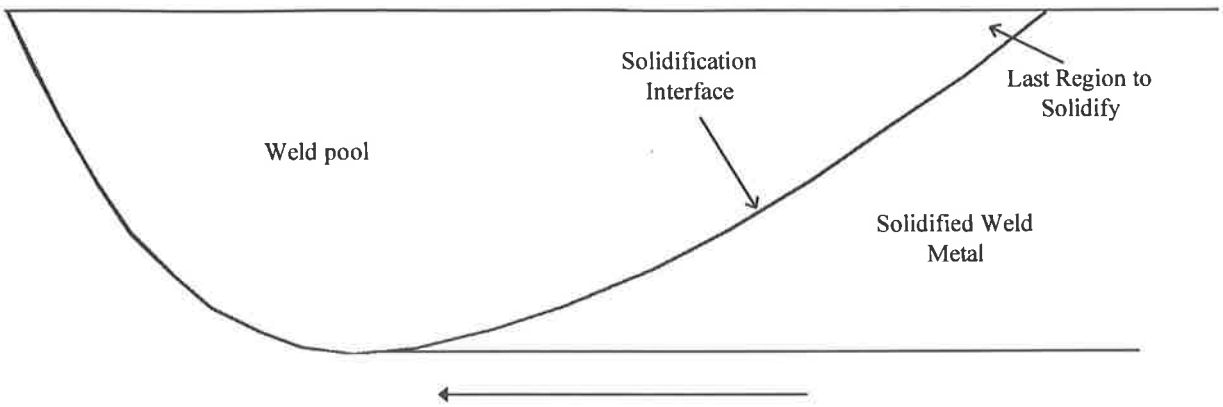

Figure 5.7: Shape of a typical longitudinal vertical section of a bead-on-plate weld pool. The arrow shows the direction of welding.

The study of the solidification microstructure of the welds (Chapter 3) has concluded that there exist two regions in the weld bead which are last to solidify. The finite element analysis only predicts one region which is last to solidify which is probably due to the limitations in the model. However, the model also indicates that the solidification interface is angled only very slightly to the vertical which tends to suggest that changes in the model such as the inclusion of actual convective and heat flow could affect its shape.

On this basis and using the evidence given above a model of the shape of the solidification interface has been constructed. This model is based on an approximately vertical interface with two curves on each side representing the delay in solidification (Figure 5.8). The model also assumes, based on information from the finite element analysis, that the surface of the weld bead solidifies prior to the adjacent regions. This feature is represented in the model by the dip in the curves at weld surfaces.

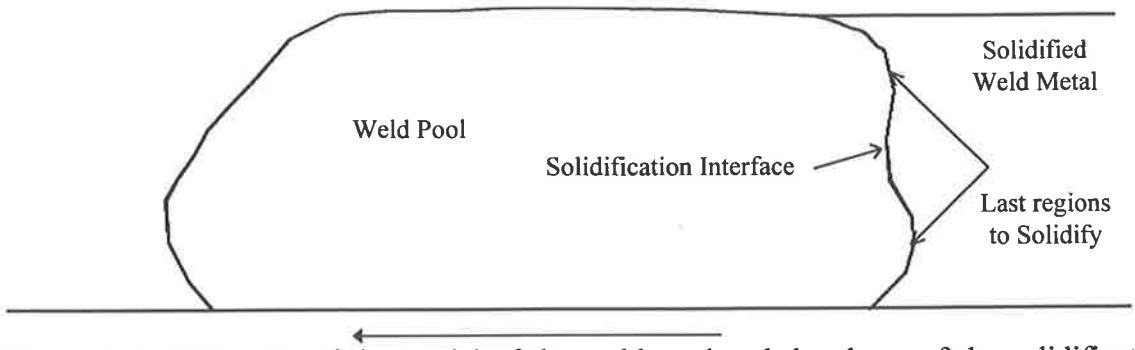

Figure 5.8: Schematic of the model of the weld pool and the shape of the solidification interface. The arrow shows the direction of welding.

This model will now be used to propose an explanation for the location of the nucleation and propagation of hollow bead.

A gas bubble which nucleates at the solidification interface will grow in the liquid as a result of the diffusion of gases from the surrounding supersaturated liquid into it. For this diffusion-controlled process, the time dependence of the bubble radius, r_g, is given by (Grong, 1991):

$$r_g = 2\Omega \sqrt{D_L t} \qquad (5.17)$$

Ω is the growth constant, defined as:

$$\Omega \approx \frac{C_L - C_e}{\rho_g} \text{, for } \Omega > 10 \qquad (5.18)$$

where C_L is the molar concentration of solute in the supersaturated liquid, C_e is the equilibrium molar concentration of the solute at the solidification interface and ρ_g is the gas density. Therefore, the higher the concentration of hydrogen in the melt the higher the rate of growth of a bubble.

When the radius reaches a critical value as determined by Equation 5.17 the buoyancy force will exceed the surface tension force and the bubble will become detached from the interface. Under the action of the buoyancy force the motion of a bubble will be in the upward direction.

Two cases will be considered next: the first for a weld proceeding along a single vertical axis which was the case in the current experiments, and the second for a weld proceeding along a continually changing axis as is the case of a pipeline girth weld.

In the first case the solidification interface will be assumed to be approximately perpendicular to the welding direction (although changes in the convective flow in the weld pool, which were not investigated, could possibly change the shape of this interface). A bubble moving upward towards the interface will travel to the highest point along the interface which are the last two regions to solidify.

The maxima at the interface may be of different magnitudes depending possibly on the flow within the pool. Of 27 samples of hollow bead in plate welds studied, 25 were found to be located at the root of the weld bead compared to 2 at the top. This suggests that the maximum on that side of the interface could have a larger magnitude and/or exist for a longer time interval. The finite element analysis has showed that as the welding current increases, the time period during which the last region to solidify remains molten, as well as its size, increases. It can be speculated that the heat distribution within the weld pool also strongly influences the size and duration of these regions, and thus the location of the nucleation of hollow bead.

In the case of welding around a pipe circumference the highest point along the interface will change continuously. The variation in the position of hollow bead, at the top or root of the bead, at different positions around the pipe circumference of one weld has been determined.

A survey of the location of hollow bead, with respect to the top and root of a weld bead, was carried out. In one particular circumferential weld 7 out of 10 pores were located at the top of the bead and no correlation between the occurrence and the position around the pipe circumference was observed. Some of the pores at the top of the weld bead were located near

the bottom dead centre position. If buoyancy was the most dominant force acting on the bubbles, the hollow bead pores which formed near the bottom dead centre location would be expected to be found at the root of the weld bead. This was not found to be the case. A prominent feature of that particular weld is a high crown at the top of the bead (a macrograph of the weld is shown in Figure 3.2). This suggests a stronger dependence of the location of hollow bead with the heat distribution and convective flows in the weld pool. The direction of flow in the weld pool may have been responsible for increasing the amount of metal, as well as the concentration of hydrogen and other gases towards the top of the weld bead. In addition the surface tension forces would tend to force a gas bubble into the last regions to solidify where the curvature of the interface would lead to a reduction in the area of the gas/liquid interface and thus its surface energy.

The formation of an elongated pore will depend on other factors such as the frequency of oscillation of the solidification interface, the convective flow in the weld pool and the rate of diffusion of gases into the pore.

5.2.6 Formation of Hollow Bead or an Elongated Gas Pore at the Solidification Interface

It has been proposed that a gas bubble has the highest probability of nucleating in the layer at the solidification interface enriched with gas-forming solutes and also in the last regions to solidify. If a bubble forms at different locations along or near the interface than the last regions to solidify, the influence of buoyancy may force it upwards towards these regions since they are the highest points along the interface. It is proposed that one important factor in the formation of a hollow bead pore will the rate of advance of the solidification interface.

Once at the interface the bubbles may either be trapped or be pushed along by the interface

until they escape to the surface. It is proposed that the rate of advance of the solidification interface as well as the magnitude and frequency of the oscillation of the interface will be a determining factor in the entrapment of a bubble and thus the formation of a hollow bead. The filming of the welding process to study the fluctuations in the keyhole has been discussed in Section 2.13. It was reported that the severe occurrence of hollow bead coincided with instabilities in the size of the keyhole which are large and aperiodic. It has been inferred from these observations that the weld pool and hence the solidification interface would exhibit a similar behaviour to a certain extent, and most importantly that the velocity of the interface can be much higher than the welding speed for short periods. It is suggested that the rapid instabilities of the interface are conducive to the entrapment of gas bubbles in the last regions to solidify, while with smaller fluctuations the bubbles may have the tendency to be pushed ahead of the interface or have time to escape from the weld pool.

The formation of a hollow bead at the start of 50% of welds studied could also be the result of fluctuation in the weld pool. It was reported in Section 2.12 that welding conditions tend to be unstable at the start and this was observed in films of the keyhole during welding. Lancaster (1992) suggests that porosity may result from unsteady welding conditions, for example at stops and starts, where the metal solidifies suddenly.

The mechanism of formation of a hollow bead assumes that a bubble is trapped at the solidification interface in the last regions to solidify. The bubble trapped by the interface will start to grow if the rate of diffusion of gases into it coincides with or exceeds the rate of advance of the interface. It has been assumed throughout most of the literature that the gas enters the pore from the supersaturated liquid in front of the interface. Howden (1982) has found, however, that much of the hydrogen in the liquid phase is retained in the solid on solidification and that the diffusion of gas from the solid surrounding the pore is sufficient to

allow the pore to propagate.

Evidence found in the literature (Redchits, 1996, Trevisan, 1990, Rakhmanov, 1978, Grigorenko, 1970) suggests, however, that a critical factor in the nucleation of a gas bubble is the degree of supersaturation of hydrogen at the solidification interface. This is the result of the rejection of hydrogen during solidification. Powell and Lloyd (1995) have demonstrated metallographically that the nucleation and propagation of elongated pore depends on macrosegregation in the weld, which is due to the rejection at the interface of solutes with an equilibrium partition coefficient less than unity (including gas-forming solutes which decrease in solubility with decreasing temperature). Furthermore, hollow bead and other gas pores in welds (Suga, 1987, Jenkins and Coe, 1970) contain carbon monoxide which will form in the supersaturated layer at the interface and must therefore enter the pore from the liquid phase. The solubility of oxygen in the solid phase is very small, around 0.01weight% (Fast, 1965), and cannot react with carbon in the solid phase to form carbon monoxide. It is thus suggested that, although some hydrogen can diffuse from the solid phase into the pore, the majority of the gases will enter from the solute-enriched layer at the interface. The main gas responsible for the growth of hollow bead is hydrogen.

The termination of the hollow bead pore occurs when the concentration of hydrogen in the liquid ahead of the interface is too low to provide the required diffusion rate of hydrogen into the pore to allow growth at a similar rate to the interface. In the studies of the growth of gas bubbles by Pokhodnya (1980) and Grigorenko (1970), it is mentioned that the layer of gas-forming solutes at the interface becomes depleted during the growth of a gas pore due to diffusion of the gas into the pore. It is possible that the growth of a hollow bead ends during a period of decrease in the rate of solidification, where the decrease in the accumulation of solutes at the interface further reduces the concentration of gas-forming solutes in the layer.

The decrease in the solidification rate is a consequence of fluctuations in the size of the keyhole and thus the weld pool.

The remainder of this section attempts to explain the structural and microstructural features of hollow bead in terms of the hypothesis presented above for the mechanism of its formation.

The direction of the growth microstructure will strongly influence the propagation of hollow bead. It has been established that the growth of the primary solidification microstructure proceeds in a similar direction to that of the solid transformation. The solidification at the weld centreline is parallel to the welding direction. Therefore, since hollow bead nucleates at the centreline, it will grow with the solidification interface also in the direction of welding. Simone and Gibson (1997, 1996) found that elongated pores which formed in unidirectionally solidified metal also grew in the direction of solidification.

The characterisation of hollow bead in the scanning electron microscope has revealed features which are typical of hollow bead pores. The start of a hollow bead forms a spherical cusp and in some cases the diameter of the pore in the region immediately next to the cusp is greatly reduced (see Figures 3.44, 3.54 and 3.64). One explanation for this is that hollow bead forms initially as a gas bubble which is then trapped by the cellular dendrites solidifying rapidly around it. Evidence of cellular dendritic growth inside the cusp of hollow bead pores, such as the tips and secondary branches of cellular dendrites, has been observed and discussed in Chapter 3. At this point the diffusion of gases, mainly hydrogen, is sufficient to start an elongated pore. It is proposed that when the velocity of the interface is high the cellular-dendrites solidify around a greater area of the bubble and the rate of diffusion of hydrogen is just sufficient to maintain growth of the pore. When the velocity of the interface at the time of entrapment is lower the pore is allowed more time to grow and the reduction in cross sectional

area near the cusp is less pronounced , or not seen, as shown in Figures 3.48, 3.63 and 3.84.

Another characteristic of hollow bead is the oxidation of the internal surface. In the majority of the pores studied the cusp is oxidised to a much lesser degree than the rest of the pore. The degree of oxidation tends to increase towards the termination end. This implies that the initial bubble contains only reducing gases, mainly hydrogen and perhaps small amounts of carbon monoxide and nitrogen. As mentioned earlier in this chapter the composition of the gas inside the pore during its formation and during the analysis is likely to be different. The gases which could be responsible for the oxidation of the surface, such as oxygen and its radicals and water vapour may only be present during the growth of the pore. This oxidation can be represented by the following equilibrium reactions:

$$Fe_{(s)} + H_2O_{(g)} \rightarrow FeO_{(s)} + H_{2(g)} \qquad (5.19)$$

$$2Fe_{(s)} + O_{2(g)} \rightarrow 2FeO_{(s)} \qquad (5.20)$$

At a high temperature (1400°C) the forward reaction (Equation 5.19) is unlikely to occur since the Gibb's free energy is positive (ΔG^o = 10.97kJ) (Brown et al., 1994). The reverse reaction (ΔG^o = -10.97kJ) is therefore favoured and the hydrogen present in the pore will tend to reduce the iron oxide. The forward reaction in 5.20, however, has a free energy, ΔG^o, of -312.5kJ at 1400°C (Brown et al., 1994). This suggests that the oxidation of the internal surface by oxygen is possible. Furthermore, the oxidation of hydrogen to water vapour given by the reaction in 5.21 has a free energy of -335.1kJ at 1400°C which is close to the value for the oxidation of iron and is therefore not much more highly favoured.

$$2H_{2(g)} + O_{2(g)} \rightarrow 2H_2O_{(g)} \qquad (5.21)$$

Considering these equilibrium cases, it is proposed that the internal surface of hollow bead

pores could be oxidised by oxygen and oxygen radicals during its formation and that the oxidation reaction (Equation 5.20) which has a more negative free energy will be more highly favoured than the reduction reaction (the reverse of Equation 5.19).

The argument above does not, however, explain the variation in the degree of oxidation along the length of the pores. The oxidation reaction in Equation 5.20 has a free energy which becomes more negative at lower temperatures which suggests that the cusp should be more oxidised. The reverse is observed in all cases studied. A possible mechanism, described in Section 5.2.2, involving the oxidation of the iron by the SiO_2 present in slag should be considered in more detail as part of a programme of future work in this area.

The presence of slag on the internal surface can be explained in terms of "particle pushing" by the interface. The fluid flow velocity acting on the particles at a solidification interface (Han and Hunt, 1995), which can be found from a balance of forces (viscous drag and normal, frictional and gravitational force), can be responsible for pushing particles ahead of the interface. In many cases the particles can end up in the last liquid to freeze. Slag particles could in this way be pushed ahead of the interface and enter the pore in the liquid phase. Once on the pore surface the slag will solidify. The solidification of liquid slag on the pore surface can be compared with the solidification of the liquid at the cellular dendritic boundaries solidifying after it protrudes into the pore. A few of the slag inclusions show evidence of bubbling (see Figures 3.73 and 3.108). The slag could thus be outgassing into the pore.

The ripples on the surface of the hollow bead, as well as banding in the weld microstructure, can be explained as a result of oscillations of the weld pool (as observed from the motion of the keyhole) as well as macrosegregation. It is known that at high rates of solidification the accumulation of solutes at the solidification interface increases. The enriched layer solidifies

just after the growth velocity increases and leads to banding. Since gas solutes will also segregate, an increase in their concentration at the interface will increase the amount that diffuses into the pore and thus increase its size. The converse also applies. This phenomenon has been demonstrated by Powell and Lloyd (1995) where the occurrence of banding in the microstructure has been correlated with the nucleation and the increase in diameter of a pore.

5.3 Summary

It is proposed that a hollow bead nucleates in the form of a hydrogen bubble which is subsequently trapped by the solidification interface where it grows as the result of the diffusion of gases, primarily hydrogen, into it. The influence of welding variables has been explained in terms of both their effects on the amount of hydrogen absorbed into the melt and the role of fluctuations in the solidification rate. The absorption of hydrogen into the weld pool from monatomic hydrogen in the arc as opposed to diatomic hydrogen was discussed. It is suggested that the hydrogen content of a weld pool increases with welding current due to higher levels of dissociation of hydrogen in the arc. This leads to a higher concentration of monatomic hydrogen and thus increased absorption.

The next major factor in the formation of hollow bead was found to be related to the fluctuations of the keyhole. At conditions which promote hollow bead, these fluctuations tend to be more rapid. This observation suggests that the rate of solidification of the weld pool and thus the rate of movement of the solidification interface are high leading to an increase in the probability of entrapment of gas bubbles at the interface.

It was also suggested that the convective flows and the distribution of heat in the weld pool could have a significant influence on the location of porosity in the weld.

Chapter 6

6.1 Summary and Conclusions

The objectives originally proposed by the project team and industry advisors with the Welding Technology Institute of Australia and the CRC for Materials Welding and Joining have been summarised in the Introduction (Section 1.1). The aims of the research presented in this thesis were to identify the major welding and metallurgical variables responsible for the formation of hollow bead and to obtain an understanding of the mechanism of its formation. This would in turn allow specific practical recommendations to be made concerning desirable changes in operating procedures which would minimise the problem.

A review of the literature showed that little research had been carried out in this field. Some factors, however, were highlighted as contributing to the formation of hollow bead. High welding currents and high travel speeds were identified as the most influential factors. The elements carbon, silicon and aluminium were also suggested as variables contributing to the incidence of hollow bead, although in this area no systematic experimental validation had been undertaken. In addition, other minor factors such as a reduction in the flux moisture content, thin walled pipes and narrow root gaps were suggested. The latter may have been related to high welding currents which would be required to obtain adequate penetration.

The literature on other types of porosity, namely worm hole and tunnel pores, was also reviewed since some common characteristics between these elongated gas pores and hollow bead were found. These pores, like hollow bead, show evidence of the cellular dendritic

growth on their internal surface which was identified from microsegregation and the tips of the dendrites. The pores also grow with the solidification microstructure. The welding current has a similar effect on these types of elongated pores, such that high levels increase their incidence. In the cases where hydrogen is the main gas responsible for the nucleation and propagation of gas pores, an increase in the silicon content of the weld increases their formation, as has been observed in this work on hollow bead.

Models describing the mechanism of formation of gas pores and the absorption of gases (mainly hydrogen) in the weld pool were also studied.

The experimental procedures and results have been reported in Chapter 2. All of the experimental work performed to study the effect of welding and metallurgical variables was performed using an automated manual metal arc welding machine capable of simulating the stovepipe technique. It allowed welds to be made under controlled conditions while the welding parameters could be continuously monitored.

Initially the welds and hollow bead pores produced using the automated equipment were validated by studying the welds and defects made using the manual stovepipe technique. The following variables were then investigated in a systematic and controlled procedure: the welding parameters including welding current, travel speed and heat input, the dimensions of the joint geometry and its surface condition, the brand of electrode and the flux moisture content, the composition of the parent metal and the diffusible hydrogen content.

The experimental results have clearly identified the impact of these welding variables on the formation of hollow bead defects. A list of conclusions is presented below and then expanded upon in the remainder of this section.

1. High levels of welding current and travel speed were found to have a major influence on hollow bead.
2. The silicon content of the parent metal and the flux moisture content of the electrode had a minor effect on the occurrence of the defect.
3. The dimensions of the joint geometry, the presence of rust and paint on the joint and the concentration of aluminium and carbon in the parent metal had no significant effect.

An increase in the welding current was found to be the major factor influencing the formation of hollow bead. The results have been summarised in the Table 6.1.

Weld Travel Speed (mm/min)	**Welding Current ≤ 160A**	**Welding Current 170 - 215A**
	Occurrence of Hollow bead (170mm of weld)	Occurrence of Hollow bead (170mm of weld)
250	No hollow bead forms	Total length < 20mm
300	No hollow bead forms	Total length < 20mm
400	No hollow bead forms	Total length increases from 10 - 40mm
500	No hollow bead forms	Total length increases from 10 - 40mm
600	Total length varies between 5 - 10mm	Total length increases from 15 - 95mm

Table 6.1: Summary of experimental results on the effect of weld travel speed and welding current on the occurrence of hollow bead in an API 5L X70 steel and 8.3mm thick welded with Lincoln Fleetweld 5P+ electrodes, 4.0mm in diameter and E6010 specification.

The acceptance criteria in Tier 1 of the Australian Standard 2885.2 - 1995 specify that hollow bead is acceptable when it does not reduce the weld thickness to less than that of the thinner parent metal, and is unacceptable when this limit is exceeded and when any of the following

conditions exist:

(i) The length of an individual indication of hollow bead exceeds 13mm.

(ii) The aggregate length of indication of hollow bead in any continuous 300mm of weld exceeds 50mm.

(iii) Individual indications of hollow bead, each greater than 6mm in length, are separated by less than 50mm.

(iv) The aggregate length of all indications of hollow bead exceeds 20% of the weld length.

The Lincoln Electric electrodes used in the experiments were 4mm in diameter with a recommended current rating of 90 to 175A. In general, therefore. it is not expected that hollow bead will cause welds to be rejected during the construction of pipelines when the welding conditions are maintained within the limits recommended by the electrode manufacturer. The results show that above 200A (from 400mm/min) and above 180A (from 500mm/min) the occurrence of hollow bead may lead to welds which do not meet the above criterion and therefore must be repaired. The influence of the weld travel speed is, however, secondary to that of the welding current.

When welding a cross country pipeline, however, all of the emphasis is placed on welding as many joints per day as possible. The productivity rates are mainly dependent on the speed of welding of the root pass which is thus desired to be as high as possible while still maintaining a minimum level of heat input for adequate root penetration and metallurgical considerations. Therefore, an increase in welding speed must be accompanied by an increase in welding current. Since this increase may result in the formation of hollow bead, guidelines are required which determine the levels of welding at particular heat inputs where the occurrence of hollow bead will remain below the acceptance criteria specified in the standard. A set of graphs of the

total length of hollow bead (normalised to 100mm of weld for more convenient comparison with the limits set out in the standard) against the heat input at particular weld travel speeds has been included in Figure F1 in Appendix F. The levels of welding current are also shown on the graphs. The heat input at a particular welding current and travel speed will not always be exactly the same because the voltage will change for particular conditions such as the joint geometry and the arc length (determined by the pressure the electrode on the bevel). The change, however, will not be great, as was observed during the experiments carried out in this work. These graphs can be used to determine a range of welding conditions which will provide the required minimum heat input and acceptable levels of hollow bead in welds. For example if a weld travel speed of 500mm/min is desired and the minimum heat input is approximately 0.5kJ/mm, the welding current can be maintained at levels which will not promote hollow bead. If a higher heat input is required, however, the higher welding currents may lead to the incidence of hollow bead above the specified limits.

It is proposed that the increase in hollow bead observed at high welding currents is due to an increase in the hydrogen content of the welds which leads to higher levels of saturation and supersaturation of the weld pool. This is caused by an increase in the concentration of monatomic hydrogen in the arc since at higher currents it is expected that the temperature of the arc will increase, resulting in higher levels of dissociation of gases.

This work has also shown that the formation of porosity is related to large fluctuations in the rate of solidification. The behaviour of the weld pool and the solidification interface was inferred from the motion of the keyhole and a correlation was observed between the incidence of hollow bead and fluctuations in the size of the keyhole. It is believed that rapid changes in the solidification rate result in macrosegregation as well as possibly being conducive to the entrapment of bubbles at the solidification interface.

The reduction in heat input and volume of the weld pool and the resulting increase in solidification rate at the very high travel speeds (between 500 and 600mm/min) is believed to have increased the occurrence of hollow bead due to a decrease in the rate of desorption of hydrogen from the weld pool.

The decrease in heat input with increasing weld travel speed is not believed to result in an insufficient amount of metal required to fill the joint and hence the formation of hollow bead pores at the last region to solidify, as was suggested by early researchers.

The investigation on the effect of the alloying elements silicon, aluminium and carbon revealed that increasing the concentration of silicon does influence the occurrence of hollow bead. Changes in the levels of aluminium and carbon were not observed to have a significant effect. A significant increase in hollow bead occurred when the silicon levels were increased from 0.22% to 0.33% in the parent plate, although no significant change was observed in the range of 0.33 to 0.37%. The results also showed, however, that the welding current is still the major influence since no hollow bead pores formed at the lowest current of 150A but were present at 180A and increased at 200A. This suggests that welding normal fully killed steels having silicon contents in the range 0.12 to 0.33% does not pose problems when the welding current levels are maintained within the manufacturer's recommended limits.

The mechanism by which the changes in the concentration of silicon affects the formation of hollow bead has not been fully investigated in this work. It is suggested at this stage, from information obtained in the literature survey, that an increase in silicon decreases the rate of diffusion of hydrogen within the melt and thus increases the level of supersaturation which can cause porosity. There is, however, insufficient data available on the changes in the diffusivity of hydrogen in steel at the concentrations of silicon considered here. Suggestions

for further research in this area are discussed in Section 6.2.

Changes in the moisture content of the flux were found to affect the occurrence of hollow bead to a limited extent. The increase in hollow bead at the higher moisture content is probably due to an increase in the concentration of hydrogen in the arc and hence in the weld pool.

The brand of electrode (in this case The Lincoln Electric Company and Böhler), contaminants, such as rust and paint on the joint preparation and adjacent surfaces, and the dimensions of the joint geometry, in the range of 1.5 to 2.4mm for the root face and 1.0 to 1.8mm for the root gap, did not have significant effects on the occurrence of hollow bead. The joint geometry may, however, have an indirect influence in the cases where high currents are used to achieve adequate penetration, for example when the root face is large. In such cases, however, adequate penetration can be obtained by widening the root gap and/or decreasing the weld travel speed to increase the heat input.

A detailed characterisation of hollow bead and the weld microstructure was carried out using optical and scanning electron microscopy and has been presented in Chapter 3. The typical, as well as the more uncommon, features of hollow bead have been described and illustrated in detail. The length of the pores studied in this work ranged from 1 to 18mm. The initial portion of most hollow bead pores were observed to start from a cusp, a smooth and almost spherical feature, which tends to indicate that they originated as gas bubbles. This cusp is in some cases not well defined and is more elliptical in shape which could be the result of a change in the solidification rate and thus the rate of motion of the solidification interface. In many cases the diameter of the hollow beads increases gradually with growth, although pores with varying as well as more uniform cross section were also observed. Again these effects are likely to

depend on the motion of the solidification interface since the pores are expected to grow at the same rate as the solidification interface. The internal surface reveals the solidification microstructure, oxide layers and slag fragments and layers which typically increase in thickness and number towards the termination end.

The weld microstructure shows that hollow bead nucleates in the last regions of the weld to solidify and then propagates in the direction of growth of the microstructure. The direction of the growth of the cellular dendrites and the columnar grains indicates that these two regions are located at the top and root of the weld bead, close to the surfaces. A finite element model of the solidification sequence of the welds partially supports this observation. The model shows only one last region to solidify, located at the root of the bead again close to the surface.

An hypothesis for the formation of hollow bead is presented in Chapter 5. It is first argued that hollow bead is nucleated in the form of a hydrogen bubble as a result of the supersaturation of hydrogen in a layer in front of the solidification interface. The pores nucleate at the last regions to solidify since the degree of supersaturation will be highest in these regions and the forces of buoyancy and surface tension will also tend to force bubbles there. It is also expected that the convective flow and the distribution of heat in the weld pool will have a stronger influence on the location of nucleation of bubbles and their motion in the weld pool.

It is also proposed that the degree of dissociation of hydrogen in the arc will be the major factor affecting the concentration of hydrogen in the melt. Previous work in the area of porosity have suggested that diatomic hydrogen is present above the weld pool and that the welding current increases the absorption due to a resulting increase in the surface temperature

of the melt. An analysis of the composition of the plasma carried out in this work has shown, however, that at the temperatures of the plasma most of the hydrogen exists in its monatomic form. It is proposed that an increase in welding current will increase the temperature of the plasma and hence the degree of dissociation of hydrogen and its absorption into the melt.

6.2 Future Work

6.2.1 Introduction

The extent to which this work has been carried out has been obviously constrained by the amount of time and resources available. An extensive programme of experimental work was carried out to identify the conditions which promote the formation of hollow bead. However, further experiments in conjunction with some theoretical work are required to clarify the mechanism of formation of hollow bead. The following section is a summary of these suggested extensions.

6.2.2 The Influence of Silicon

The silicon content of the parent metal was found to affect the formation of hollow bead and should be more extensively studied. The objective of future work in this area would clarify the role of silicon in the mechanism of formation of hollow bead.

Further experiments are required to determine the critical concentration of silicon in the parent metal at which the increase in the occurrence of hollow bead is detected. Steels with a range of silicon contents between 0.2 and 0.3% would first be required to be tested. It would also be necessary to determine whether any increases in silicon content over 0.3% still influence hollow bead. The concentration of silicon in the weld metal could be varied by either changing the concentration of silicon in the parent plate, as was done in this work, or in the

electrode flux.

The mechanism of formation of hollow bead proposed in this work involves the absorption of hydrogen in the weld metal and its rejection at the solidification interface where it reaches supersaturation levels sufficient to nucleate gas pores. Factors, therefore, influencing the absorption and desorption of hydrogen in the weld pool will be directly related to the formation of hollow bead. Determining the mechanisms by which silicon promotes a higher incidence of hollow bead requires that first its role in affecting the levels of hydrogen in the weld pool is known. There is evidence in the literature that the diffusivity of hydrogen in steel decreases with increasing silicon content. Data on diffusivity has been given by Smialowski (1962) and Boniszewki (1992). The silicon levels studied by these authors were, however, much higher than the ones which need to be considered for pipeline steels (in the range of 1 to 4%). The critical concentration of silicon in the weld metal at which hollow bead increases is first required to be determined as mentioned above. A comparison of the effect of silicon on the diffusivity of hydrogen at this critical value and above and below the value would then have to be made.

Measurements of the diffusible hydrogen content of welds containing varying concentrations of silicon between 0.1 and 0.4% would give an indication of the change in diffusivity with silicon content. Other procedures could be devised to determine the changes in the concentration of hydrogen in the molten weld pool due to diffusion from the pool before solidification.

The extent of macrosegregation and microsegregation of silicon in the weld would also have to be assessed. If macrosegregation is large, then the effect of silicon will be more pronounced towards the last regions of the weld to solidify. There is evidence in austenitic stainless steel

and nickel-base alloy welds that silicon, and other elements such as sulphur and manganese, have a high propensity to segregate on solidification (Castro and de Cadenet, 1974). As a result, solute enrichment of the interdendritic regions occurs and leads to a reduction in the solidification temperature of the interdendritic liquid. This causes high temperature or interdendritic cracking (in the presence of high stresses). Analyses in a microprobe could determine the levels of segregation of silicon in the welds produced in pipeline steels, as well as the distribution of this element around hollow bead pores. This method was successful in assessing the segregation of manganese and nickel in the welds produced in this work. Determining the distribution of silicon is, however, more difficult since its concentration is much lower. A larger number of higher magnification maps would be required in this case.

The silicon may also affect the nucleation of pores in the weld. Elements which are surface active, such as silicon, lower the surface tension of metals. It is possible that if the components of surface tensions between solid and gas and liquid and gas decrease, or the component between solid and liquid increases (see Figure 5.3), then the chance of nucleating a gas pore is increased since the gas nucleus is smaller (due to a smaller angle) and thus requires less gas for its formation. A knowledge of the change in the components of surface tension is required and would have to be obtained experimentally.

6.2.3 The Modelling of the Weld Pool

An extension of the modelling of the weld pool to include the effects of convection, gravity, a keyhole and the force of the arc would give an understanding of the flow patterns and thus the direction of heat flow in the weld pool. This could be used in part to explain the position of hollow bead in the weld bead since the direction of flow of hydrogen and gas bubbles in the pool as well as the rate of solidification depend on the convective flows.

6.2.4 Characterisation of the Plasma and Determination of Hydrogen Absorbed by the Weld Pool

A more detailed analysis of the type and concentration of the gases absorbed in the weld pool than the one presented in this thesis is required. The type of gases and metal vapours liberated by the cellulosic flux and the wire during decomposition, the change in the gas composition at different moisture levels and the change in the temperature of the arc with current would have to be determined. This information would be used to characterise the plasma in terms of its constituents and their concentration. An analysis similar to the one presented in Section 5.2.3.3.2 could be used for this purpose. A method to calculate the concentration of hydrogen in the liquid weld pool depending on the composition of the plasma and at different welding currents would then have to be devised.

References

All-American Pipeline Company, 'Pipe Weld Procedure AAPL-5A', 1993.

All-American Pipeline Company, 'Pipe Weld Procedure AAPL-24', 1993.

Banerjee, A., David, S. A. and Vitek, J. M., 'Nitrogen Dissolution in the Weld Pool', International Trends in Welding Science and Technology, Proceedings, 3rd International Conference, Gatlinburg TN USA, 1-5 June, 1992, ASM International, Materials Park, Ohio 44073-0002, p. 387-391.

Barbaro, F. J., Meta, A., Williams, J. G. and Fletcher, L. 'Weldability of X80 Linepipe', Welding of High Strength Thin Walled Pipelines, WTIA/APIA Research Panel 7 Joint Research Seminar, Wollongong, 26 October, 1995, Paper 11, p. 1-19.

Barkow, A. G., 'Hollow Bead: New Welding Problem for Pipeliners', The Oil and Gas Journal, July 23, 1973, **71**, p. 40-47.

Biddle, S., 'Junee-Griffith Natural Gas Pipeline Production Welding', C. W. Pope and Associates Pty Ltd, Waratah, NSW, Australia, August, 1993.

Bilston, K. Dietsch, A. and Fletcher, L., 'Performance Requirements for Onshore Pipeline Girth Welds in Australia - A Discussion Paper', Welding of High Strength Thin Walled Pipelines, WTIA/APIA Research Panel 7 Joint Research Seminar, Wollongong, 26 October, 1995, Paper 8, p. 1-12.

Böhler Welding Technology, 'Böhler Electrodes for Pipeline Welding'.

Boniszewski, T., 'Self-Shielded Arc Welding', Abington Publishing, Abington Hall, Abington, Cambridge CB1 6AH, England, 1992.

Brown, T. L., LeMay, H. E. and Bursten, B. E, 'Chemistry The Central Science', Sixth Edition, Prentice-Hall Inc., New Jersey, U.S., 1994.

Bukovinski, S., 'Some Metallurgical Aspects on Austenitic Stainless Welding Wire,

Australian Welding Journal, November/December, 1975, p. 57-64.

Castro, R and de Cadenet, J. J., 'Welding Metallurgy of Stainless and Heat-Resisting Steels', Cambridge University Press, Bentley House, 200 Euston Road, London, NW1 2DB, 1974.

Chalmers, B., 'Physical Metallurgy', John Wiley & Sons Inc., 2nd. Edition, 1962, p. 234-235.

Chalmers, B., 'Principles of Solidification', John Wiley & Sons Inc., 1964, p. 190-192.

D'Annessa, A. T., 'Characteristic Redistribution of Solute in Fusion Welding', Welding Journal, December, 1966, **45**, Welding Research Supplement, p. 569s-576s.

David, S. A and Vitek, J. M., 'Correlation between Solidification Parameters and Weld Microstructures', International Material Reviews, 1989, **34**(5), p. 213.

Davies, G. J. and Garland J. G., 'Solidification Structures and Properties of Fusion Welds', International Material Reviews, 1975, **20**(196), p. 83-106.

Davies, M., 'Numerical Modelling of Weld Pool Convection in Gas Metal Arc Welding', Ph. D. Thesis, Department of Mechanical Engineering, The University of Adelaide, 1995.

DebRoy, T., 'Mass Transfer in Welding', International Trends in Welding Science and Technology, Proceedings, 3rd International Conference, Gatlinburg TN USA, 1-5 June, 1992, ASM International, Materials Park, Ohio 44073-0002, p. 387-391.

Devletian, J. H. and Wood, W. E., 'Factors Affecting Porosity in Aluminium Welds - A Review', WRC Bulletin 290, 1983, p. 1-18.

Elliot, J. F., Gleiser, M. and Ramakrishna, V., 'Thermochemistry for Steelmaking', **2**, Addison-Wesley Publishing Company, Reading, Massachusetts, 1963.

Fast, J. D., 'Interaction of Metals and Gases', **1,** Philips Technical Library, Eindhoven, The Netherlands, 1965.

Fletcher, L. and Morrison, R. 'The Effect of Different Pipe Steels on the Cellulosic Manual Metal Arc Stovepipe Welding Process' Weld Pool Chemistry and Metallurgy, Proceedings, International Conference, London, 15-17 April, 1980, The Welding Institute, Abington, Cambridge CBI 6AL, UK, Session 2, Paper 5, p. 55-64.

Gedeon, S. A. and Eagar, T. W., 'Thermochemical Analysis of Hydrogen Absorption in Welding', Welding Journal, July, 1990, Welding Research Supplement, p. 264s-271s.

Goldak, J. A., Bibby, M. J., Moore, J., House, R. and Patel, B. 'Computer Modelling of Heat Flow in Welds', Transactions AIME, September, 1986, **17B**, p. 587-600.

Goldak, J. A., Chakravarti, A. and Bibby, M. J., 'A New Finite Element Model for Welding Heat Sources', Metallurgical Transactions B, June, 1984, **15B**, p. 299-305.

Granjon, H., 'Fundamentals of Welding Metallurgy', Abington Publishing, UK, 1991, p. 115-117.

Grigorenko, G. M., 'Formation of Pores in Welds', Automatic Welding, 1970, 10, p. 13-17.

Grong, O. and Matlock, D. K., 'Microstructural Development in Mild and Low-Alloy Steel Weld Metals', International Material Reviews, 1986, **31**(1), p. 27-48.

Han, Q and Hunt, J. D., 'Redistribution of Particles during Solidification', ISIJ International, 1995, 35(6), p. 693-699.

Harris, I. D., ' A Review of Porosity Formation and Recommendations on the Avoidance of Porosity in TIG Welding', Welding Institute Members Report 387, December, 1988, p 1-26.

Hinkel, J. E., 'Pipeline Welding - Meeting Today's Quality Requirements for Manual Vertical Down Techniques', The Lincoln Electric Company, Cleveland, Ohio, USA, January, 1984.

Hooijmans, J. W. and den Ouden, G., 'Hydrogen Absorption during Arc Melting', Materials Science and Technology, January, 1996, **12**, p 81-85.

Houldcroft, P. T., 'Welding Processes', Cambridge University Press, Bentley House, 200 Euston Road, London, NWI 2BD, 1967.

Howden, D. G. and Milner, D. R., 'Hydrogen Absorption in Arc Melting', British Welding Journal, June, 1963, **10,** p. 304-316.

Howden, D. G. and Yen, L. S., 'Hydrogen Induced Worm Hole Porosity in Stainless Steel Weld Metal', Advances in Welding Science and Technology, Proceedings, International Conference, Gatlinburg TN USA, 18-22 May, 1986, ASM International, Metals Park, p. 251-

260.

Howden, D. G., ' Behaviour of Hydrogen in Arc Weld Pools', Welding Journal, April, 1982, **61**, p. 103s-108s.

Ibarra, S. L. and Olson, D. L., 'Underwater Wet Welding of Steel', WRC Bulleting 401, May, 1995, p. 27.

Japan Welding Society, Tokyo 'Blow Holes, Slag Inclusions and Other Phenomena', Fractographic Atlas of Steel Weldment', 1982, p. 236-247.

Jenkins, N. and Coe, F. R., 'Extraction and Analysis of Gases from Pores in Weld Metal', Metal Construction and British Welding Journal, January, 1970, p. 27-31.

Kiefer, J. H., 'Effects of Moisture Contamination and Welding Parameters on Diffusible Hydrogen', Welding Journal, May, 1996, Welding Research Supplement, p. 155s-161s.

Kluken, A. O., Grong, Ø., Rørvik, G., 'Solidification Microstructures and Phase Trnasfromations in Al-Ti-Si-Mn Deoxidised Steel Weld Metals', Metallurgical Transactions A, **21A**, July, 1990, p. 2047-2058.

Kobayashi, M. and Suga, T., 'A Method for the Spectral Temperature Measurement of a Welding Arc', Arc Physics and Weld Pool Behaviour, Proceedings, International Conference, London, 8-10 May, 1979, The Welding Institute, Abington Hall, Abington, Cambridge CB1 6AL, p. 25-38.

Kovitya, P., 'Physical Properties of High-Pressure Plasmas of Hydrogen and Copper in the Temperature Range 5000-60000K', IEEE Transactions on Plasma Science, PS-13(6), December, 1985, p. 587-594.

Kudrin, V., 'Steelmaking', Mir Publishers, Moscow, I-110, GSP, USSR, 129820, 1985.

Kwiatkowski, J., 'Private Communication', Mc Connell Dowell Constructors (Aust.) Pty. Ltd., 1993.

Lancaster, J. F, 'Handbook of Structural Welding', Abington Publishing, Abington Hall, Abington, cambridge CB1 6AH, England, 1992.

Lancaster, J. F., 'Metallurgy of Welding', 3rd Edition, George Allen and Unwin Ltd, 40 Museum St, London WCIA ILU, 1980, p. 198-199 .

Lancaster, J. F., 'Metallurgy of Welding', 5th Edition, Chapman and Hall, London, 1993.

Lin, M. L. and Eagar, T. W., 'Influence of Surface Depression and Convection on Arc Weld Pool Geometry', Transport Phenomena in Materials Processing, ASME Publication PED **10**, HTD **39**, Proceedings, Conference, Boston, MA, 13-18 November, 1983, p. 63-69.

Lundin, C. D., 'Fundamentals of Weld Discontinuities and their Significance', WRC Bulletin 295, June, 1984, p. 7-8.

Lundin, C. D., Kuroda, T., Zhou, G., Wang, Y., Qiao, P. and Khan, K. K., 'Measurement of Diffusible Hydrogen and Hydrogen Effects on the Weldability of 2205/2209 Duplex Stainless Steel', International Trends in Welding Science and Technology, Proceedings, 3rd International Conference, Gatlinburg TN USA, 1-5 June, 1992, ASM International, Materials Park, Ohio 44073-0002, p. 743-747.

Mathias, T., 'Pipeline across the Zagros Mountains', Metal Construction, **12**, January, 1980, p. 24-28.

Matsunawa, A., 'Modelling of Heat and Fluid Flow in Arc Welding', International Trends in Welding Science and Technology, Proceedings, 3rd International Conference, Gatlinburg TN USA, 1-5 June, 1992, ASM International, Materials Park, Ohio 44073-0002, p. 387-391.

McKeown, D.,'Hydrogen and its Control in Weld Metal', Metal Construction, October, 1985, **17**(10), p. 655 - 661.

Morrison, R., 'Private Communication', Tubemakers of Australia Ltd. Pipelines Research Centre, Melbourne, Victoria, 1993.

Murphy, A. B. and Arundell, C. J., 'Transport Coefficients of Argon, Nitrogen, Oxygen, Argon-Nitrogen, and Argon-Oxygen Plasmas', Plasma Chemistry and Plasma Processing, **14**(4), 1994, p. 451-490.

Okuda, N., 'Characteristics and Selection of Various Welding Consumables', Welding International, November, 1987, **56**, p. 15-27.

Palmer, T. A and DebRoy, T., 'Physical Modelling of Nitrogen Partition between the Weld Metal and its Plasma Environment', Welding Journal, July, 1996, Welding Research Supplement, p. 197s- 207s.

Pokhodnya, I. K. and Demchenko. V. F., 'Mathematical Simulation of Gas Redistribution in Welding', Weld Pool Chemistry and Metallurgy, Proceedings, International Conference, London, 15-17 April, 1980, The Welding Institute, Abington Cambridge CBI 6AL, UK, Paper 2, p. 107-119.

Pokhoydna, I. K. and Yavdoshchin, I. R., ' Pores in Welds Made Using Rutile Coated Electrodes', Automatic Welding Journal, 1969, **22**(2), p. 11-16.

Pokhoydnya, I. K. and Yavdoshchin, I. R., 'Reasons for the Formation of Pores when Welds are Made Using Electrodes with Acid Ore Coatings', Automatic Welding Journal, 1972, 3, p. 9-12.

Powell, G. L. F. and Lloyd, P. G., 'Characterisation of an Elongated Gas Pore in a Weld in Terms of Solidification Mechanics', Practical Metallography, 1995, **32**(1), p. 25.

Rakhmanov, A. D., 'On the Conditions of the Nucleation of Gas Pores in Arc Welding', Welding Production, January, 1978, **25**(1), p. 48-53.

Redchits, V. V. and Froloc, V. A., 'Calculation and Analytical Evaluation of the Gas Pore Formation Susceptibility of Metals and Alloys in Fusion Welding', Welding International, 1996, **10**(1), p. 76-79.

Salter, G. R., 'Hydrogen Absorption in Arc Welding', British Welding Journal, June, 1963, **10**, p. 316-325.

San-Martin, A. and Manchester, F. D., 'Phase Diagrams of Binary Iron Alloys', Monograph Series on Alloy Phase Diagrams, 1993, ASM International, Materials Park, Ohio, USA, p. 161.

Saperstein, Z. P., Prescott, G. R.. and Monroe, E. W., 'Porosity in Aluminium Welds', Welding Journal, October, 1964, Welding Research Supplement, p. 443s-453s.

Savage, W. F. and Aronson, A. H., 'Preferred Orientation in the Weld Fusion Zone', Welding

Journal, February, 1966, **45**, p 85s-89s.

Savage, W. F. Lundin, C. D. and Hrubec, R. J., 'Segregation and Hot Cracking in Low-Alloy Quench and Tempered Steels', Welding Journal, September, 1968, Welding Research Supplement, p. 420-425.

Savage, W. F., Nippes, E. F. and Erickson, J. S., 'Solidification Mechanics in Fusion Welds', Welding Journal, August, 1976, **55,** p. 213s-221s.

Savage, W. F., Nippes, E. F. and Miller, T. W., 'Microsegregation in 70Cu-30Ni Weld Metal', Welding Journal, June, 1976, **55**, p. 165s-173s.

Simone, A. E. and Gibson, L. J., 'The Tensile Strength of Porous Copper Made by the GASAR Process', Acta Metallurgica, 1996, **44**(4), p. 1437-1447.

Simone, A. E. and Gibson, L. J., 'The Compressive Behaviour of Porous Copper Made by the GASAR Process', Journal of Materials Science, 1997, **32**, p. 451-457.

Smialowski, M., 'Hydrogen In Steel - Effect of Hydrogen on Iron and Steel During Production, Fabrication and Use', Pergamon Press Ltd., Headington Hill Hall, Oxford, London, 1962.

Stewarts and Lloyds (Australia) Pty. Ltd. (Kembla Grange Works), 'Test Certificate 6/67', 1967.

Stewarts and Lloyds (Australia) Pty. Ltd. (Kembla Grange Works), 'Test Certificate 9/68', 1968.

Suga, Y. and Hasui, A., 'On Formation of Porosity in Underwater Weld Metal (The 1st Report) - Effect of Water Pressure on Formation of Porosity', Transactions of the Japan Welding Society, 1986, **17**, April, p. 58-64.

Suga, Y., 'Study on the Mechanism of Blow Hole Formation by Hydrogen - On Formation of Porosity in Underwater Weld Metal (the 2nd Report)', Transaction of the Japan Welding Society, April, 1987, 18(1), p. 61-68.

Sugden, A. A. B. and Bhadhesia, H. K. D. H., 'The Nonuniform Distribution of Inclusions in

Low-Alloy Steel Weld Deposits', Metallurgical Transactions A, **19A**, March, 1988, p. 669-674.

Svensson, L-E., 'Control of Microstructures and Properties in Steel Arc Welds', CRC Press Inc., 1994, p 44-45.

Tabor, D., 'Gases, Solids and Liquids', Penguin, Middlesex, England, 1969.

Tenneco Energy Operations and Maintenance Pty Ltd, 'Weld Procedure Number CP2', 1988.

The Lincoln Electric Company (Australia) Pty. Ltd., 'Lincoln Cellulose Electrodes', 1986.

The Lincoln Electric Company, 'Technical Information Bulletin - Welding Parameters and Evolved Hydrogen", 1986.

The Lincoln Electric Company, 'Welding Pressure Pipelines and Piping Systems', Cleveland, Ohio, USA, February, 1991.

'The Physics of Welding', edited by J. F. Lancaster, Oxford Pergamon, 1984.

Trevisan, R. E, Schwemmer, D. D. and Olson, D. L., 'The Fundamentals of Weld Metal Pore Formation', Welding: Theory and Practice, Elsevier Science Publishers B. V., 1990, p. 79-115.

Tubemakers of Australia Ltd. (Stewarts and Lloyds Division - Kembla Grange Works), 'Test Certificate', September 24, 1975.

Tubemakers of Australia Ltd , 'Test Certificate No. 180-93', 1993.

Tubemakers of Australia Ltd. (Steel Pipe Division - Kemble Grange Works), 'Test Certificate No. N82-85', 1985.

Tweedale, J. G., 'Welding Fabrication', London Iliffe Books Ltd, American Elsevier Publishing Company Inc, New York, NY, **2**, 1969, p. 36.

Venton, P., 'Pipeline Construction Costs in Australia', WTIA/APIA Research Panel 7 Joint Research Seminar, Welding of High Strength Thin-Walled Pipelines, Wollongong, Australia, 26 October, 1995, p. 21_1 - 21_12.

Wang, Y. H. and Kou, S., 'Driving Forces for Convection in Weld Pool', International Conference on Trends in Welding Research, Advances in Welding Science and Technology, Proceedings, Gatlinburg, Tennessee, USA, 18-22 May, 1986, ASM International, p. 65-70.

Weinstein, M. and Elliott, J. F., 'Solubitity of Hydrogen in Liquid Iron Alloys', Transactions of the Metallurgical Society of AIME, April, 1963, **227**, p. 382.

White, D., Pollard, G. and Gee, R, 'The Effect of Welding Parameters on Diffusible Hydrogen Levels in Steels Produced with Cored Wires', International Trends in Welding Science and Technology, Proceedings, 3rd International Conference, Gatlinburg TN USA, 1-5 June, 1992, ASM International, Materials Park, Ohio 44073-0002, p. 387-391.

Willgoss, R. A. and Atthey, M. A., 'The Tunnel Pore in BS 1501, Type 316, Stainless Steel', Weld Pool Chemistry and Metallurgy, Proceedings, International Conference, London, 15-17 April, 1980, The Welding Institute, Abington, Cambridge CBI 6AL, UK, Session 3, Paper 10, p. 133-135.

Willgoss, R. A., ' Weld Pool Profile and Porosity in the TIG Welding of BS 1501, Type 316, Stainless Steel', Weld Pool Chemistry and Metallurgy, Proceedings, International Conference, London, 15-17 April, 1980, The Welding Institute, Abington Cambridge CBI 6AL, UK, Session 3, Paper 9, p. 121-131.

Williams, J. G., 'Recent Developments in Steel Production for SAW and ERW Linepipe Manufactured in Australia', International Conference on Pipe technology, Rome, Italy, November, 1987, p. 337-355.

Williams, J. G., Killmore, C. R., Barbaro, F. J., Piper, J.and Fletcher, L., 'High Strength ERW Linepipe Manufacture in Australia', Materials Forum, **20**, The Materials Society of the Institution of Engineers Australia, 21 Bedford Street, North Melbourne, Victoria, 3051, Australia, p. 13-28.

Williams Pipe Line Company, 'Pipe Welding Procedure 1C-S', 1988.

Wood, J. V., Mills, P. F., Bingham, J. K. and Bee J. V., ' Structure and the Initial Precipitation in a Rapidly Solidified Nickel Superalloy', Metallurgical Transactions A, 1079, **10A**, p. 575-584.

Woods, R. A., 'Porosity and Hydrogen Absorption in Aluminium Welds', Welding Journal, March, 1974, **53**(3), Welding Research Supplement, p. 97s-108s.

Wright, M. D., 'Hollow Bead - A Question of Technique?', TWI Bulletin, May/June, 1993, 3, p. 53-55.

Zakharov, L. S. and Lipodaev, V. N., 'Concerning the Formation of Pores in Welds', Welding Production, August, 1976, **23**(8), p. 54-56.

Publications Originating from this Thesis Work

Cantin, G. M. D. and Bee, J. V., 'An Investigation of the Formation of Hollow Bead Defects', Welding Technology in Action, Proceedings, National Conference, Melbourne, October 1994, WTIA, Session 1, 1, Paper 1, p. 1-14.

Bee, J. V. and Cantin, G. M. D., 'An Investigation of the Formation of Hollow Bead Defects in Pipeline Field Welds', Pipeline Technology, Proceedings, International Conference, Ostend, Belgium, 11-14 September, Elsevier Publishers, 1995, 1, p. 513-528.

Cantin, G. M. D. and Bee, J. V., 'The Causes and Control of Hollow Bead in Pipeline Girth Welds', Welding of High Strength Thin Walled Pipelines, WTIA/APIA Research Panel 7 Joint Research Seminar, Wollongong, 26 October, 1995, Session 4, Paper 12, p. 1-25.

Cantin, G. M. D. and Bee, J. V., 'Hollow Bead: Causes and Practical Control in Pipeline Girth Welds, APIA International Convention, Wollongong, 21-26 October, 1995.

Cantin, G. M. D. and Bee, J. V., 'A Literature Review on: An Investigation of the Formation of Hollow Bead Defects in Pipeline Field Welds', Australian Welding Research, February, CRC for Materials Welding and Joining and WTIA, 1996, 14, p. 1-12.

Cantin, G. M. D. and Bee, J. V., 'An Experimental Study of Hollow Bead Defects', Australasian Welding Journal, WTIA, 1996, **41**(1), p. 18-20.

Appendix A

Tables of Experimental Results and Welding Conditions

Pipe Number	Position	Hollow Bead Length (mm)	Hollow Bead Width (mm)	Number of Hollow Bead	Total Length (mm)	Average Length (mm)	Maximum Length (mm)
P1	0-1	5	1				
		3	0.5				
		2	0.5				
		2	0.5	4	12	3	5
	1-2	6	1				
		2.5	1				
		1.5	1	3	10	3.3	6
	2-3	2	0.5				
		4	0.8				
		3.5	1	3	9.5	3.2	4
	3-0	2.5	1				
		1	0.5				
		4	1				
		5	1				
		2	0.8				
		1	0.5	6	15.5	2.6	5
P2	2-3	2	0.8				
		3	0.5				
		2	0.5				
		1.5	0.5	4	8.5	2.1	3
	1-2	1	0.5				
		2	1				
		1.5	1	3	4.5	1.5	2
	0-1	0	0	0	0		
	3-0	0	0	0	0		
P3	0-1	1	0.5				
		1	0.5				
		3	1				
		3.5	1				
		1.5	1				
		5	1				
		4	1	7	19	2.7	5
	1-2	0	0	0	0	0	
	2-3	9	0.8				
		1.5	1	2	10.5	5.3	9
	3-0	13	0.8				
		1	0.8				
		2	1				
		5	0.8	4	21	5.3	13

Table A1: Data on the length, number and position of all hollow bead defects detected in pipe sample welds.

Pipe Number	Position	Hollow Bead Length (mm)	Hollow Bead Width (mm)	Number of Hollow Bead	Total Length (mm)	Average Length (mm)	Maximum Length (mm)
P5	0-1	5	1				
		3.5	1				
		5	1	3	13.5	4.5	5
	1-2	5	1	1	5	5	5
	2-3	5	1.5				
		4	1	2	9	4.5	5
	3-0	2	1.5				
		3	1				
		4	1				
		5	1				
		4	1				
		3	1				
		3	1	7	24	3.4	5
P6	0-1	3.5	1				
		3	1				
		4	1				
		3	1				
		5	1	5	18.5	3.7	5
	1-2	6.5	1				
		4.5	1				
		3	1				
		7	1				
		4.5	1				
		5	1				
		4	1				
		9	1	8	15.5	5.4	9
	2-3	2.5	1				
		3.5	1				
		2	1				
		3	1	4	11	2.8	3.5
	3-0	3	1				
		5	1.5	2	7	3.5	5

Table A1(continued): Data on the length, number and position of all hollow bead defects detected in pipe sample welds.

Pipe Number	Position	Hollow Bead Length (mm)	Hollow Bead Width (mm)	Number of Hollow Bead	Total Length (mm)	Average Length (mm)	Maximum Length (mm)
P7	0-1	5	1				
		3	1				
		4	1				
		4	1	4	16	4	5
	1-2	6	1				
		7	1.2				
		9	1.2	3	22	7.3	9
	2-3	5	1				
		4.5	1				
		5	1				
		3	1	4	17.5	4.4	5
	3-0	3.5	1				
		5	1				
		5	1	3	13.5	4.5	5
P8	0-0	0	0	0	0		
P10	0-1	2	1	1	2	2	2
	1-2	6	0.8				
		3	1				
		7	1				
		5	0.8				
		3	1	5	24	4.8	7
	2-3	0	0	0	0		
	3-0	5	0.5				
		3	1				
		1	0.8				
		2	1				
		4	1	5	15	3	5
P11	0-1	10	0.8	1	10	10	10
	1-2	2	0.8				
		6	0.5				
		4	1				
		3	1				
		1	1				
		9	1	6	25	4.2	9
	2-3	8	1				
		2	1	2	10	5	8
	3-0	3.5	1	1	3.5	3.5	3.5

Table A1(continued): Data on the length, number and position of all hollow bead defects detected in pipe sample welds.

Pipe Number	Position	Hollow Bead Length (mm)	Hollow Bead Width (mm)	Number of Hollow Bead	Total Length (mm)	Average Length (mm)	Maximum Length (mm)
P12	1-2	3	1				
		3	1	2	6	3	3
	0-1	0	0	0	0		
	2-3	3	1				
		1	1	2	4	2	3
	3-0	5	1	1	5	5	5
P13	0-1	2.5	1				
		3	1				
		5	1				
		3	0.8				
		2	0.5				
		2	1	6	17.5	2.9	5
	1-2	1	0.5				
		2	1				
		1	1				
		5	0.8				
		7	1				
		2	0.8				
		3.5	1				
		2	1				
		5	1				
		9	1				
		2	1				
		3	1				
		3	1				
		7	1				
		4	2	15	56.5	3.8	9
	2-3	3	0.8				
		12	1				
		3	1				
		2	1				
		2.5	1				
		3	1				
		5	1				
		3	1				
		1	1				
		10	1				
		5	1				
		2.5	1				
		2	0.8				
		2	0.8				
		2	0.8	15	58	3.9	12

Table A1(continued): Data on the length, number and position of all hollow bead defects detected in pipe sample welds.

Pipe Number	Position	Hollow Bead Length (mm)	Hollow Bead Width (mm)	Number of Hollow Bead	Total Length (mm)	Average Length (mm)	Maximum Length (mm)
P13	3-0	12	1.5				
		4	1.2				
		10	1				
		2	1				
		3	1				
		1	1	6	32	5.3	12
P14	0-1	1	1				
		2	1				
		2	1	3	5	1.7	2
	1-2	12	1	1	12	12	12
	2-3	1.5	1				
		1	1				
		1.5	1	3	4	1.3	1.5
	3-0	1	1				
		4	1	2	5	2.5	

Table A1(continued): Data on the length, number and position of all hollow bead defects detected in pipe sample welds.

Pipe Number	Position	Number of Hollow Bead	Total Length of Hollow Bead	Number of Hollow Bead	Total Length of Hollow Bead
		50mm from start		50mm from stop	
P1	0-1	3	7		
	1-2	1	6		
	2-3	2	6	1	3.5
	3-0			3	7.5
Total		**6**	**19**	**4**	**11**
P2	2-3			2	5
	1-2	1	2		
Total		**1**	**2**	**2**	**5**
P3	0-1	2	1	3	10.5
	2-3	1	1.5		
	3-0			1	13
Total		**3**	**2.5**	**4**	**23.5**
P5	0-1	1	5		
	1-2				
	2-3			2	9
	3-0	2	7	2	9
Total		**3**	**12**	**4**	**18**
P6	0-1	1	5	2	7
	1-2			4	22.5
	2-3	3	8	1	3
	3-0	1	5		
Total		**4**	**18**	**7**	**32.5**

Table A2: Data on the length, number and position of all hollow bead defects at the start and end of weld runs.

Pipe Number	Position	Number of Hollow Bead	Total Length of Hollow Bead	Number of Hollow Bead	Total Length of Hollow Bead
		50mm from start		50mm from stop	
P7	0-1			2	8
	1-2			1	9
	2-3	1	4.5	3	13
	3-0	2	10		
Total		**3**	**14.5**	**6**	**30**
P10	1-2			3	15
	3-0	2	3		
Total		**2**	**3**	**3**	**15**
P11	1-2			1	9
	2-3			1	8
Total				**2**	**17**
P12	1-2	1	3	1	3
	2-3	1	3		
Total		**2**	**6**	**1**	**3**
P13	0-1	1	2.2		
	1-2			2	11
	2-3	2	15		
	3-0	1	1	1	12
Total		**4**	**18.5**	**3**	**23**
P14	0-1				
	1-2				
	2-3				
	3-0	1	4		
Total		**1**	**4**		

Table A2(continued): Data on the length, number and position of all hollow bead defects at the start and end of weld runs.

Plate Number	Root Face (mm)	Root Gap (mm)	Travel Speed (mm/min)	Average Current (A)	Average Voltage (V)	Average Force (N)	Average Heat Input (kJ/mm)	Total Number of Hollow bead	Total Length of Hollow bead (mm)	Average Length of Hollow bead (mm)
3	1.6	1.4	300	204	25	16	1.03	3	12	4
5	1.6	1.5	300	163	22	16	0.70	1	1	
7	1.6	1.5	300	143	22	6	0.64	0	0	0
8	1.6	1.5	300	128	22	3	0.57	0	0	0
10	1.6	1.4	250	186	24	13	1.09	3	15	5
11	1.6	1.5	250	170	22	13	0.91	1	2	
12	1.6	1.4	250	131	22	5	0.68	0	0	0
14	1.6	1.4	350	191	27	4	0.87	1	7	
15	1.6	1.5	350	162	25	3	0.69	0	0	0
16	1.6	1.6	350	144	23	3	0.58	1	1	
17	1.6	1.5	400	134	22	3	0.44	0	0	0
18	1.6	1.5	400	162	25	3	0.61	0	0	0
20	1.6	1.1	400	188	26	4	0.74	2	12	6
21	1.6	1.4	400	214	28	4	0.89	10	42	4.2
23	1.6	1.5	500	160	25	3	0.47	0	0	0
24	1.6	1.5	500	203	29	3	0.70	9	30	3.3
26	1.6	1.5	550	184	28	3	0.55	6	26	4.3
27	1.6	1.5	550	150	24	3	0.39	0	0	0
28	1.6	1.4	400	147	25	3	0.55	0	0	0
30	1.6	1.4	500	139	25	2	0.41	0	0	
31	1.6	1.4	550	170	28	3	0.51	3	11	3.7
32	1.6	1.4	600	159	26	2	0.42	5	16	3.2
33	1.6	1.3	600	193	29	3	0.56	9	45	5
34	1.6	1.3	600	216	30	4	0.64	7	61	8.7
35	2.1	0.9	350	219	29	4	1.08	3	15.5	5.1

Table A3: Results and welding conditions of the experiments on the effect of welding conditions.

Plate Number	Root Face (mm)	Root Gap (mm)	Travel Speed (mm/min)	Average Current (A)	Average Voltage (V)	Average Force (N)	Average Heat Input (kJ/mm)	No. of Hollow Bead Defects	Total Length of Hollow Bead (mm)	Average Length of Hollow Bead (mm)
36	2.1	0.9	250	184	26	3	1.16	0	0	0
37	2.1	1	300	216	28	4	1.20	2	13	6.5
38	1.6	1.4	300	187	27	3	1.01	5	20	4
43	1.6	1.6	600	131	25	3	0.32	0	0	0
wc1	2.1	1.4	600	215	30	4	0.65	10	91.5	9.2
wc3	1.6	1.5	300	141	26	3	0.72	0	0	
wc4	1.6	1.5	400	148	26	3	0.58	0	0	
wc5	1.6	1.45	400	158	27	3	0.63	0	0	
wc6	2	1.5	400	188	29	4	0.80	3	11	3.7
wc7	1.6	1.4	500	161	27	3	0.52	0	0	
wc8	1.8	1.4	500	182	29	4	0.62	3	8.5	2.8
wc9	1.8	1.45	600	187	29	4	0.55	10	60.5	6.1
wc11	1.8	1.5	250	173	27	3	1.11	2	8	4.0
wc13	1.6	1.5	250	152	25	4	0.91	0	0	
wc15	1.6	1.45	300	165	26	3	0.86	0	0	
wc17	1.6	1.5	500	143	25	4	0.43	0	0	
wc18	2	1.5	500	205	30	4	0.74	8	32	4.0
wc19	1.6	1.5	600	140	N/A	N/A		0	0	
wc21	2	1.5	600	194	30	4	0.58	8	34.5	4.3
wts1	1.6	1.5	400	142	26	3	0.54	0	0	
wts2	1.8	1.45	400	171	27	3	0.70	1	2	2.0
wts3	1.8	1.4	300	171	27	3	0.91	1	5	5.0
wts4	2	1.5	500	188	29	4	0.66	4	28.5	7.1
wts5	1.6	1.5	500	142	26	3	0.44	0	0	
wts6	1.6	1.5	600	140	25	3	0.35	3	6.5	2.2
wts7	2	1.5	600	182	29	4	0.53	4	23.5	5.9

Table A3(continued): Results and welding conditions of the experiments on the effect of welding conditions.

Plate Number	Root Face (mm)	Root Gap (mm)	Travel Speed (mm/min)	Average Current (A)	Average Voltage (V)	Average Force (N)	Average Heat Input (kJ/mm)	No. of Hollow Bead Defects	Total Length of Hollow Bead (mm)	Average Length of Hollow Bead (mm)
wts8	1.8	1.5	600	172	28	3	0.49	4	15	3.8
wts9	1.8	1.55	300	165	27	3	0.89	0	0	
wc22	1.7	1.4	400	162	27	3	0.65	0	0	
wc23	2.1	1.4	400	215	29	4	0.94	5	31	6.2
wc26	1.8	1.4	250	172	26	3	1.07	1	10	
wc27	1.6	1.5	500	163	27	3	0.53	0	0	
wc28	1.8	1.4	500	181	29	3	0.64	5	24.5	4.9
wc30	2.1	1.4	500	202	N/A	N/A		10	38	3.8
wc31	2.1	1.55	400	147	26	3	0.58	0	0	
wc32	2.1	1.55	400	134	25	3	0.50	0	0	
wc33	1.9	1.5	600	159	N/A	N/A		1	5	
wc34	2	1.5	600	186	N/A	N/A		3	13	4.3
wc35a	2.1	1.5	600	159	N/A	N/A		3	6	2.0
wc35	2.1	1.5	400	212	30	3	0.95	4	42.5	10.6
wc36	2	1.5	300	187	27	3	1.02	2	9	4.5
wc37	2	1.5	300	207	27	3	1.11	4	13.5	3.4
wc38	2	1.5	250	190	28	3	1.25	2	12	6.0
wc39	1.8	1.5	250	204	28	3	1.35	1	9	
wc40	2	1.5	300	188	28	3	1.04	2	11	5.5
wc41	2	1.5	600	185	29	3	0.54	6	21.5	3.6
wc42	2.1	1.45	600	215	31	3	0.66	12	95.5	8.0

Table A3(continued): Results and welding conditions for the experiments on the effect of welding conditions.

Plate Number	Root Face (mm)	Root Gap (mm)	Travel Speed (mm/min)	Average Current (A)	Average Voltage (V)	Average Force (N)	Average Heat Input (kJ/mm)	Total Number of Hollow Bead	Total Length of Hollow Bead (mm)	Average Length (mm)
2	1.6	1.4	300	162	27	2	0.87	1	1	
6	1.6	1.4	400	160	26	3	0.63	0	0	
9	1.6	1.4	600	162	28	2	0.45	4	7.5	1.9
10	1.6	1.4	600	195	31	3	0.60	9	42	4.7
11	1.6	1.5	600	131	23	3	0.30	0	0	
17	1.8	1.3	300	181	29	4	1.05	4	15	3.8
19	1.6	1.5	300	130	25	2	0.64	0	0	
23	1.6	1.4	400	136	25	3	0.50	0	0	
25	1.8	1.3	400	179	29	3	0.78	2	15	7.5

Table A4(a): Welding conditions and results for experiments on the effect of Bohler electrodes.
All welds were made using Bohler Fox Cel electrodes 4.0mm in diameter and E6010 specification.

Plate Number	Root Face (mm)	Root Gap (mm)	Travel Speed (mm/min)	Average Current (A)	Average Voltage (V)	Average Force (N)	Average Heat Input (kJ/mm)	Total Number	Total Length of Hollow Bead (mm)	Average Length (mm)
12B	1.6	1.5	600	131	25	3	0.32	0	0	
26B	1.8	1.25	400	181	28	3	0.75	2	9.5	4.8
28B	1.8	1.3	300	181	27	3	0.97	0	0	
5	1.6	1.5	300	163	22	6	0.7	1	1	
18	1.6	1.5	400	162	25	3	0.6	0	0	
32	1.6	1.4	600	159	26	2	0.6	5	16	3.2
33	1.6	1.3	600	193	29	3	0.6	9	45	5
43	1.6	1.6	600	131	25	3	0.3	0	0	
8	1.6	1.5	300	128	22	3	0.6	0	0	
17	1.6	1.5	400	134	22	3	0.4	0	0	

Table A4(b): Welding Conditions and results of the experiments on the effect of Bohler electrodes (continued).
All welds recorded in this table were made using Lincol Electric 5P+ electrodes. The first three welds were made in conjunction with the welds in Table A4(a) and the remainder of the welds made during experiments on the effect of the welding conditions.
The plate numbers for these correspond to the ones in Table A3.

Plate Number	Root Face (mm)	Root Gap (mm)	Travel Speed (mm/min)	Average Current (A)	Average Voltage (V)	Average Force (N)	Average Heat Input (kJ/mm)	Total Number of Hollow Bead	Total Length of Hollow Bead (mm)	Average Length (mm)
1	1.6	1.8	400	151	26	3	0.58	0	0	
2	1.6	1	400	152	25	3	0.57	0	0	
3	1.5	1.6	400	150	26	3	0.58	2	10	5.0
4	2.4	1.6	400	153	25	3	0.57	0	0	
5	1.6	1.8	500	180	28	3	0.60	8	28	3.5
6	1.6	1	500	182	28	3	0.62	4	14	3.5
7	1.5	1.6	500	178	28	3	0.60	2	8.5	4.3
8	2.4	1.6	500	180	N/A			1	8	
9	1.6	1	400	152	26	4	0.59	0	0	
10	1.5	1.6	400	150	26	4	0.59	0	0	
11	1.6	1.8	400	151	26	4	0.60	0	0	
12	2.4	1.6	400	152	26	4	0.59	0	0	
13	1.5	1.6	500	181	28	3	0.61	1	7	
14	1.6	1.8	500	180	28	3	0.61	3	6	2.0
15	1.6	1.8	500	179	28	3	0.60	4	21	5.3
16	1.5	1.6	500	183	29	3	0.63	5	10	2.0
17	1.6	1	500	180	N/A			4	18.5	4.6
18	1.6	1	500	178	28	3	0.61	5	12	2.4
19	2.4	1.6	500	181	29	3	0.62	4	17	4.3
20	2.4	1.6	500	182	29	3	0.63	3	8	2.7
21	1.6	1	400	151	25	3	0.58	0	0	
22	1.6	1.8	400	150	26	3	0.59	0	0	
23	1.5	1.6	400	150	27	3	0.60	0	0	
24	2.4	1.6	400	150	03	26	0.07	0	0	

Table A5: Welding conditions and results of experiments on the effect of joint geometry.

Plate Number	Root Face (mm)	Root Gap (mm)	Travel Speed (mm/min)	Average Current (A)	Average Voltage (V)	Average Force (N)	Average Heat Input (kJ/mm)	Total Number of Hollow Bead	Total Length of Hollow bead (mm)	Average Length (mm)
scr1	2.1	1.4	500	198	30	4	0.72	8	33	4.1
scr2	2.0	1.45	500	180	29	4	0.62	3	8	2.7
scr3	1.8	1.45	500	142	26	4	0.43	0	0	
scp1	1.8	1.4	500	140	26	3	0.44	0	0	
scp2	2.0	1.4	500	184	29	3	0.64	4	14	3.5
scp3	2.1	1.4	500	202	30	3	0.73	9	33	3.7

Table A6: Results and welding conditions of experiments on the effect of joint preparation surface contamination.

Plate Number	Composition Number	Root Face (mm)	Root Gap (mm)	Travel Speed (mm/min)	Average Current (A)	Average Voltage (V)	Average Force (N)	Average Heat Input (kJ/mm)	Total Number of Hollow Bead	Total Length of Hollow Bead (mm)	Average Length (mm)	Length of Weld (mm)
PMC13	2	2.0	1.5	400	183	29	4	0.79	4	12	3.0	170
PMC14	2	2.0	1.5	400	180	28	4	0.74	4	11.5	2.9	170
PMC15	3	2.0	1.5	400	182	28	4	0.77	0	0		170
PMC16	3	2.0	1.5	400	180	29	4	0.77	6	6	1.0	170
PMC17	1	2.0	1.5	400	181	28	4	0.76	1	1		170
PMC18	1	2.0	1.5	400	181	28	4	0.75	0	0		170
PMC19	4	2.1	1.5	400	179	28	4	0.76	0	0		170
PMC 20	4	2.1	1.5	400	183	28	4	0.76	2	2	1.0	170
PMC 21	5	2.0	1.5	400	180	28	4	0.76	1	1		170
PMC 22	5	2.0	1.5	400	181	28	4	0.76	0	0		170
PMC 23	5	2.0	1.5	400	183	28	4	0.77	0	0		170
PMC 24	2	1.7	1.5	400	150	26	4	0.59	0	0		170
PMC 25	2	1.7	1.55	400	150	26	4	0.58	0	0		170
PMC 26	2	2.1	1.5	400	203	30	4	0.91	10	30.5	3.1	170
PMC 27	3	1.7	1.5	400	152	26	4	0.59	0	0		170
PMC 28	3	1.8	1.5	400	150				0	0		170
PMC 29	3	2.2	1.5	400	202	29	4	0.87	1	6		170
PMC 30	1	1.7	1.5	400	152	36	4	0.82	0	0		170
PMC 31	1	1.7	1.5	400	151	27	4	0.60	0	0		170
PMC 32	1	2.1	1.5	400	198	28	4	0.84	2	4	2.0	170
PMC 33	4	2.1	1.5	400	201	29	4	0.87	5	17	3.4	170
PMC 34	4	1.7	1.5	400	150	26	3	0.59	0	0		170
PMC 35	5	2.0	1.5	400	203	30	4	0.90	0	0		170

Table A7a: Welding conditions and results of the experiments on the effect of parent metal composition.

Plate Number	Melt Number	Root Face (mm)	Root Gap (mm)	Travel Speed (mm/min)	Average Current (A)	Average Voltage (V)	Average Force (N)	Average Heat Input (kJ/mm)	Total Number of Hollow Bead	Total Length of Hollow Bead (mm)	Average Length (mm)	Length of Weld (mm)
PMC 39	3	2.1	1.4	400	203	29	4	0.89	1	3		170
PMC 41	1	2.1	1.4	400	202	29	4	0.89	0	0		170
PMC 42	1	2.1	1.4	400	203	29	4	0.88	0	0		170
PMC 43	1	2.0	1.45	400	182	29	4	0.79	0	0		170
PMC 45	5	2.1	1.4	400	202	30	4	0.89	0	0		170
PMC 46	5	2.1	1.4	400	200	29	4	0.88	1	3		170
PMC 47	5	1.8	1.4	400	152	26	4	0.60	0	0		170
PMC 48	5	1.8	1.5	400	152	25	4	0.58	0	0		170
PMC 49	5	2.0	1.45	400	184	28	4	0.78	1	2.5		170
PMC 50	5	2.0	1.45	400	182	28	4	0.77	1	2		170
PMC 51	4	2.1	1.4	400	201	29	4	0.88	1	1		170
PMC 52	4	2.1	1.4	400	203	29	4	0.87	1	1		170
PMC 53	4	2.0	1.45	400	182	28	4	0.77	0	0		170
PMC 54	4	2.0	1.45	400	182	28	4	0.77	0	0		170
PMC 55	3	2.0	1.45	400	182	28	4	0.76	1	3		170
PMC 56	3	2.0	1.45	400	180	28	4	0.75	0	0		170
PMC 57	3	2.1	1.4	400	200	28	4	0.84	2	10	5.0	170
PMC 58	3	2.1	1.4	400	200	29	4	0.87	1	10		170
PMC 59	2	2.1	1.4	400	200	29	4	0.88	7	30	4.3	170
PMC 60	2	2.1	1.4	400	198	29	4	0.85	4	26	6.5	170
PMC 61	2	2.0	1.45	400	182	29	4	0.78	10	21.5	2.2	170
PMC63	4	1.8	1.5	400	150	26	3	0.59	0	0		170
PMC64	4	2.0	1.5	400	174	27	3	0.71	0	0		170

Table A7a(continued): Welding conditions and results of the experiments on the effect of parent metal composition.

Plate Number	Melt Number	Root Face (mm)	Root Gap (mm)	Travel Speed (mm/min)	Average Current (A)	Average Voltage (V)	Average Force (N)	Average Heat Input (kJ/mm)	Total Number of Hollow Bead	Total Length of Hollow Bead (mm)	Average Length (mm)	Length of Weld (mm)
PMC68	2	2.0	1.5	400	184	28	3	0.78	2	7.5	3.8	170
PMC69	2	2.0	1.5	400	183	28	3	0.78	5	13	2.6	170
PMC70	2	2.0	1.45	400	204	28	3	0.87	6	29	4.8	170
PMC71	2	2.0	1.45	400	200	28	3	0.85	9	30.5	3.4	170
PMC72	6	2.1	1.5	400	202	30	3	0.89	11	48	4.4	130
PMC74	6	2.1	1.5	400	201	30	3	0.90	7	32	4.6	135
PMC75	6	2.1	1.5	400	200	29	3	0.88	8	40	5.0	150
PMC76	6	2.1	1.55	400	182	29	3	0.78	5	10.5	2.1	130
PMC77	6	2.1	1.5	400	180				9	22.5	2.5	150
PMC78	6	2.1	1.5	400	181	00	3	0.01	7	13.5	1.9	150
PMC79	7	2.1	1.5	400	180			0.00	9	18.5	2.1	170
PMC80	7	2.1	1.5	400	182	28	3	0.78	11	24	2.2	170
PMC81	7	2.1	1.5	400	178	28	3	0.75	0	0		170
PMC82	7	2.1	1.45	400	205	30	3	0.91	7	28.5	4.1	145
PMC83	7	2.1	1.45	400	200				11	32	2.9	145
PMC84	7	2.1	1.45	400	203	30	3	0.91	7	19.5	2.8	100
PMC85	8	2.1	1.5	400	202	29	3	0.89	13	47.5	3.7	155
PMC87	8	2.1	1.45	400	205	30	3	0.91	10	28	2.8	150
PMC89	8	2.1	1.5	400	181	29	3	0.77	7	18.5	2.6	170
PMC90	8	2.0	1.5	400	180	28	3	0.76	7	20.5	2.9	120

Table A7(continued): Welding conditions and results of the experiments on the effect of parent metal composition.

Plate Number	Melt Number	Root Face (mm)	Root Gap (mm)	Travel Speed (mm/min)	Average Current (A)	Average Voltage (V)	Average Force (N)	Average Heat Input (kJ/mm)	Total Number of Hollow Bead	Total Length of Hollow Bead (mm)	Average Length (mm)	Length of Weld (mm)
PMC92	9	2.1	1.45	400	199	29	3	0.86	5	25	5.0	130
PMC93	9	2.1	1.45	400	202	29	3	0.89	5	25.5	5.1	150
PMC94	9	2.1	1.45	400	201	30	3	0.91	8	66.5	8.3	140
PMC95	9	2.1	1.5	400	179	29	3	0.79	3	13	4.3	145
PMC96	9	2.1	1.5	400	182	29	3	0.80	2	4	2.0	170
PMC97	9	2.1	1.5	400	181	29	3	0.79	3	5.5	1.8	170
PMC98	10	2.1	1.55	400	150				0	0		170
PMC99	10	2.1	1.5	400	180	29	3	0.77	0	0		170
PMC100	10	2.1	1.5	400	181	29	3	0.79	1	2		130
PMC101	10	2.1	1.5	400	200	29	3	0.88	0	0		120
PMC102	10	2.1	1.45	400	200	29	3	0.86	0	0		120
PMC103	10	2.1	1.45	400	201	29	3	0.87	1	3	3.0	150

Table A7a(continued): Welding conditions and results of the experiments on the effect of parent metal composition.

Plate Number	Melt Number	Length of Hollow Bead in 100mm of Weld	Number of Hollow Bead in 100mm of Weld
PMC13	2	2.4	7.1
PMC14	2	2.4	6.8
PMC15	3	0.0	0.0
PMC16	3	3.5	3.5
PMC17	1	0.6	0.6
PMC18	1	0.0	0.0
PMC19	4	0.0	0.0
PMC 20	4	1.2	1.2
PMC 21	5	0.6	0.6
PMC 22	5	0.0	0.0
PMC 23	5	0.0	0.0
PMC 24	5	0.0	0.0
PMC 25	5	0.0	0.0
PMC 26	2	5.9	17.9
PMC 27	3	0.0	0.0
PMC 28	3	0.0	0.0
PMC 29	3	0.6	3.5
PMC 30	1	0.0	0.0
PMC 31	1	0.0	0.0
PMC 32	1	1.2	2.4
PMC 33	4	2.9	10.0
PMC 34	4	0.0	0.0
PMC 35	5	0.0	0.0

Table A7b: Data on the total length and number of hollow bead normalised to 100mm of weld length.

Plate Number	Melt Number	Length of Hollow Bead in 100mm of Weld	Number of Hollow Bead in 100mm of Weld
PMC 38	3	0.0	0.0
PMC 39	3	0.6	1.8
PMC 41	1	0.0	0.0
PMC 42	1	0.0	0.0
PMC 43	1	0.0	0.0
PMC 45	5	0.0	0.0
PMC 46	5	0.6	1.8
PMC 47	5	0.0	0.0
PMC 48	5	0.0	0.0
PMC 49	2	0.6	1.5
PMC 50	5	0.6	1.2
PMC 51	4	0.6	0.6
PMC 52	4	0.6	0.6
PMC 53	4	0.0	0.0
PMC 54	4	0.0	0.0
PMC 55	3	0.6	1.8
PMC 56	3	0.0	0.0
PMC 57	3	1.2	5.9
PMC 58	3	0.6	5.9
PMC 59	2	4.1	17.6
PMC 60	2	2.4	15.3
PMC 61	2	5.9	12.6
PMC63	4	0.0	0.0

Table A7b (cont.): Data on the total length and number of hollow bead normalised to 100mm of weld length.

Plate Number	Melt Number	Length of Hollow Bead in 100mm of Weld	Number of Hollow Bead in 100mm of Weld
PMC64	4	0.0	0.0
PMC65	4	0.0	7.6
PMC68	2	1.2	4.4
PMC69	2	2.9	7.6
PMC70	2	3.5	17.1
PMC71	2	5.3	17.9
PMC72	6	8.5	36.9
PMC74	6	5.2	23.7
PMC75	6	5.3	26.7
PMC76	6	3.8	8.1
PMC77	6	6.0	15.0
PMC78	6	4.7	9.0
PMC79	7	5.3	10.9
PMC80	7	6.5	14.1
PMC81	7	0.0	0.0
PMC82	7	4.8	19.7
PMC83	7	7.6	22.1
PMC84	7	7.0	19.5
PMC85	8	8.4	30.6
PMC87	8	6.7	18.7
PMC89	8	4.1	10.9
PMC90	8	5.8	17.1
PMC91	8	0.0	12.9
PMC92	9	3.8	19.2
PMC93	9	3.3	17.0
PMC94	9	5.7	47.5
PMC95	9	2.1	9.0
PMC96	9	1.2	2.4
PMC97	9	1.8	3.2
PMC98	10	0.0	0.0
PMC99	10	0.0	0.0
PMC100	10	0.8	1.5
PMC101	10	0.0	0.0
PMC102	10	0.0	0.0
PMC103	10	0.7	2.0

Table A7b (cont.): Data on the total length and number of hollow bead normalised to 100mm of weld length.

Plate Number	Length of Hollow Bead at Start (mm)	Average Current for Weld (A)	Average Current at Start (A)	Total Number of Hollow Bead	Total Length of Hollow Bead (mm)
PLT3	13	204	150-198*	3	12
PLT10	4	186	147-190*	3	15
PLT14	7	191	196*	1	7
PLT20	11	188	207	2	12
PLT21	14	214	227	10	42
PLT26	9	184	170	6	26
PLT27	5	150	164	0	0
PLT31	2	170	164	3	11
PLT32	5	159	145	5	16
PLT37	9	216	200	1	2
WC3	5	141	140	0	0
WC5	3	158	150	0	0
WC6	10	188	193	3	11
WC7	4	161	160	0	0
WC8	8	182	180	3	8.5
WC9	11	187	177	10	60.5
WC11	3	173	146-184*	2	8
TS8	3	172	170	4	15
TS9	2	165	168	0	0
TS1	2	142	140	0	0
TS3	5	171	165-170	1	5
TS4	10	188	170-200	4	28.5
TS7	7	182	170-200	4	23.5
WC15	3	165	170	0	0
WC17	3	143	160	0	0
WC18	7	205	200	8	32
WC21	15	194	200	8	34.5
WC22	7	162	164	0	0
WC27	4	163	141-187*	0	0
WC28	5,5	181	181	5	24.5
WC30	8	202	N/A	10	38
PMC13	10	183	190-200	4	12
PMC15	6	182	200*	0	0
PMC18	10	181	190*	0	0
PMC19	6	179	190-200	0	0

Table A8: Data from the survey of hollow bead defects at the start of welds. A total of 122 radiographs were surveyed.
*current unstable at the start of the weld run.

Plate Number	Length of Hollow Bead at Start (mm)	Average Current for Weld (A)	Average Current at Start (A)	Total Number of Hollow Bead	Total Length of Hollow Bead (mm)
PMC21	3	180	177	1	1
PMC23	8	183	185	0	0
PMC24	6	150	152	0	0
PMC26	5,4	203	195	10	30.5
PMC27	6	152	160	0	0
PMC28	2	150	170	0	0
PMC32	10	198	204	2	4
PMC35	12,4	203	195	0	0
PMC39	11	203	190	1	3
PMC43	1.5	182	188	0	0
PMC46	12	200	210	1	3
PMC48	4	152	150	0	0
PMC49	7	184	185	1	2.5
PMC50	7	182	190	1	2
PMC57	6	200	175	2	10
PMC58	6	200	190	1	10
PMC60	13	198	197*	4	26
PMC52	4	203	190	1	1
PMC54	4	182	190*	0	0
PMC56	10	180	185	0	0
SHG4	10	182	190*	3	5.5
SHG5	3.5	182	175	3	10
SHG6	8	180	170-200	1	9
SHG7	5,5	184	180-200	5	8.5
SHG8	10	180	190	7	17
SHG10	6	179	190	3	3.5
SHG11	8	182	190	0	0
JG6	5	182	180	4	14
JG9	4	152	150	0	0
JG11	2	151	150	0	0
JG12	2.5	152	150	0	0

Table A8 (continued): Data from the survey of hollow bead defects at the start of welds. A total of 122 radiographs were surveyed.
*current unstable at the start of the weld run.

Plate WTS 9	Frame	15th second			26th second			35th second		
	Number	Length	Width	Area	Length	Width	Area	Length	Width	Area
		of Keyhole (mm) [x10]			of Keyhole (mm) [x10]			of Keyhole (mm) [x10]		
	1	55	45	1943	60	50	2355	45	35	1236
	2	45	50	1766	45	40	1413	40	45	1413
	3	55	45	1943	45	40	1413	50	45	1766
	4	55	50	2159	30	30	707	40	30	942
	5	55	50	2159	45	50	1766	50	40	1570
	6	60	45	2120	50	40	1570	55	50	2159
	7	55	50	2159	50	45	1766	50	30	1178
	8	50	45	1766	50	35	1374	45	45	1590
	9	55	45	1943	35	40	1099	45	40	1413
	10	45	40	1413	50	40	1570	50	45	1766
	11	60	50	2355	35	30	824	45	50	1766
	12	60	45	2120	60	55	2591	45	40	1413
	13	65	55	2806	50	40	1570	50	50	1963
	14	60	45	2120				45	35	1236
	15	60	55	2591				45	40	1413
	16	60	45	2120				55	40	1727
	17	55	45	1943				45	40	1413
	18	50	50	1963				50	50	1963
	19	55	50	2159				40	30	942
Average		**56**	**48**	**2081**	**47**	**41**	**1540**	**47**	**41**	**1519**
Standard Deviation		**5**	**4**	**301**	**9**	**7**	**527**	**4**	**7**	**336**
Total Average for the Length				50						
Total Standard Deviation for the Length				7						
Total Average for the Area				1733						
Total Standard Deviation for the Area				461						

Table A9a: Data on the dimensions of the keyhole in periods of approximately 1 second for weld WTS 9.
Welding current 162A, weld travel speed 300mm/min. No hollow bead.

Plate WTS 7	Frame	8th second			16th second			24th second			20th second			10th second		
	No.	Length	Width	Area	Length	Width	Area	Length	Width	Area	Length	Width	Area	Length	Width	Area
		of Keyhole (mm) [x10]			of Keyhole (mm) [x10]			of Keyhole (mm) [x10]			of Keyhole (mm) [x10]			of Keyhole (mm) [x10]		
	1	75	45	2649	55	40	1727	40	30	942	60	35	1649	45	40	1413
	2	65	40	2041	60	45	2120	50	40	1570	55	35	1511	65	40	2041
	3	55	40	1727	40	35	1099	60	40	1884	60	35	1649	45	35	1236
	4	65	45	2296	40	30	942	60	40	1884	70	40	2198	45	40	1413
	5	55	40	1727	65	35	1786	45	35	1236	45	30	1060	80	40	2512
	6	90	40	2826	60	40	1884	40	35	1099	50	35	1374	50	35	1374
	7	60	45	2120	40	35	1099	50	40	1570	35	25	687	35	30	824
	8	60	40	1884	40	30	942	30	25	589	45	35	1236	65	35	1786
	9	75	45	2649	45	35	1236	60	40	1884	65	40	2041	55	40	1727
	10	55	40	1727	45	35	1236	65	40	2041	40	30	942	40	35	1099
	11	45	40	1413	65	40	2041	50	40	1570	50	35	1374	60	40	1884
	12	65	40	2041	50	35	1374	60	40	1884	40	30	942	50	40	1570
	13	55	40	1727	35	30	824	55	40	1727	55	40	1727	40	35	1099
	14	60	45	2120	60	40	1884	60	40	1884	50	40	1570	65	35	1786
	15	40	35	1099	45	40	1413	35	25	687	35	30	824	45	35	1236
	16	65	40	2041	50	30	1178				40	35	1099	60	40	1884
	17	50	40	1570	40	35	1099				65	40	2041	45	35	1236
	18	75	40	2355							55	40	1727	65	35	1786
	19	60	35	1649							40	35	1099	45	30	1060
Average		**62**	**41**	**1982**	**49**	**36**	**1405**	**51**	**37**	**1497**	**50**	**35**	**1408**	**52**	**37**	**1525**
Standard Deviation		**12**	**3**	**444**	**10**	**4**	**417**	**11**	**6**	**473**	**11**	**4**	**436**	**12**	**3**	**416**
Total Average for the Length					53											
Total Standard Deviation for the Length					12											
Total Average for the Area					1569											
Total Standard Deviation for the Area					480											

Table A9b: Data on the dimensions of the keyhole in periods of approximately 1 second for weld WTS 7.
Welding current 186A, weld travel speed 600mm/min. Total number of hollow bead 4 and total length 24mm.

Plate WTS 6	Frame	12th second			20th second			27th second		
	No.	Length	Width	Area	Length	Width	Area	Length	Width	Area
		of Keyhole (mm) [x10]			of Keyhole (mm) [x10]			of Keyhole (mm) [x10]		
	1	45	35	1236	40	35	1099	40	30	942
	2	65	30	1531	40	35	1099	45	30	1060
	3	35	30	824	40	35	1099	35	30	824
	4	50	30	1178	40	35	1099	40	25	785
	5	35	35	962	45	35	1236	35	25	687
	6	50	30	1178	45	35	1236	30	30	707
	7	60	35	1649	50	35	1374	30	25	589
	8	55	35	1511	30	30	707	35	30	824
	9	65	35	1786	45	30	1060	40	30	942
	10	50	30	1178	45	35	1236	30	25	589
	11	50	30	1178	45	35	1236	30	25	589
	12	65	25	1276	50	35	1374	40	30	942
	13	75	25	1472	40	35	1099	25	25	491
	14	70	20	1099	55	35	1511	30	30	707
	15	75	20	1178	40	35	1099	40	30	942
	16	80	20	1256	55	35	1511	45	30	1060
	17				35	30	824	40	30	942
	18				55	35	1511			
	19				45	35	1236			
Average		**58**	**29**	**1281**	**44**	**34**	**1192**	**36**	**28**	**801**
Standard Deviation		**14**	**6**	**251**	**7**	**2**	**214**	**6**	**2**	**176**
Total Average for the Length				46						
Total Standard Deviation for the Length				12						
Total Average for the Area				1091						
Total Standard Deviation for the Area				296						

Table A9c: Data on the dimensions of the keyhole in periods of approximately 1 second for weld WTS 6.
Welding current 140A, weld travel speed 600mm/min. Total number of hollow bead 3 and total length 7mm.

Plate WTS 8	Frame	10th second			15th second			20th second				6th second	
	No.	Length	Width	Area	Length	Width	Area	Length	Width	Area	Length	Width	Area
		of Keyhole (mm) [x10]			of Keyhole (mm) [x10]			of Keyhole (mm) [x10]			of Keyhole (mm) [x10]		
	1	35	35	962	65	45	2296	45	35	1236	45	45	1590
	2	55	40	1727	55	45	1943	65	35	1786	50	40	1570
	3	60	45	2120	65	40	2041	50	40	1570	40	40	1256
	4	30	30	707	60	45	2120	30	30	707	60	40	1884
	5	60	40	1884	30	30	707	25	25	491	40	40	1256
	6	35	35	962	30	30	707	30	30	707	40	40	1256
	7	60	40	1884	60	45	2120	45	30	1060	60	40	1884
	8	40	35	1099	50	40	1570	50	35	1374	40	35	1099
	9	65	35	1786	50	40	1570	30	30	707	40	35	1099
	10	55	35	1511	30	30	707	60	30	1413	45	30	1060
	11	30	30	707	50	40	1570	50	35	1374	65	40	2041
	12	45	30	1060	45	40	1413	45	35	1236	35	35	962
	13	45	35	1236	80	45	2826	40	35	1099	55	35	1511
	14	35	30	824	55	45	1943	65	30	1531	60	40	1884
	15				50	40	1570	40	35	1099	60	40	1884
	16				35	35	962	40	30	942			
Average		**46**	**35**	**1319**	**51**	**40**	**1629**	**44**	**33**	**1146**	**49**	**38**	**1482**
Standard Deviation		**12**	**5**	**486**	**14**	**6**	**621**	**12**	**4**	**364**	**10**	**4**	**366**
Total Average for the Length				48									
Total Standard Deviation for the Length				12									
Total Average for the Area				1395									
Total Standard Deviation for the Area				496									

Table A9d: Data on the dimensions of the keyhole in periods of approximately 1 second for weld WTS 8.
Welding current 170A, weld travel speed 600mm/min. Total number of hollow bead 4 and total length 15mm.

Plate WC 3	Frame	12th second			19th second			26th second			35th second			42th second		
	No.	Length	Width	Area	Length	Width	Area	Length	Width	Area	Length	Width	Area	Length	Width	Area
		of Keyhole (mm) [x10]			of Keyhole (mm) [x10]			of Keyhole (mm) [x10]			of Keyhole (mm) [x10]			of Keyhole (mm) [x10]		
	1	45	40	1413	50	40	1570	55	50	2159	60	45	2120	50	35	1374
	2	45	40	1413	35	35	962	55	45	1943	55	45	1943	45	40	1413
	3	55	45	1943	40	40	1256	55	40	1727	60	40	1884	30	30	707
	4	50	45	1766	45	35	1236	60	40	1884	50	45	1766	45	40	1413
	5	40	35	1099	40	40	1256	50	45	1766	55	45	1943	40	45	1413
	6	60	50	2355	40	40	1256	50	40	1570	45	40	1413	50	40	1570
	7	55	35	1511	55	45	1943	50	40	1570	50	45	1766	50	40	1570
	8	55	45	1943	40	40	1256	45	45	1590	50	45	1766	40	35	1099
	9	55	45	1943	45	45	1590	50	40	1570	45	45	1590	50	45	1766
	10	65	40	2041	45	40	1413	50	50	1963	50	40	1570	45	40	1413
	11	55	45	1943	40	40	1256	50	45	1766	60	40	1884	55	40	1727
	12	45	40	1413	50	45	1766	70	35	1923	50	50	1963	50	40	1570
	13	45	45	1590	45	40	1413	50	45	1766	50	40	1570	45	40	1413
	14	65	35	1786	40	40	1256	50	40	1570	60	40	1884	60	45	2120
	15	55	50	2159	50	35	1374	55	50	2159	45	45	1590	50	40	1570
	16	45	40	1413	50	40	1570	60	35	1649	45	40	1413	45	45	1590
	17	55	45	1943	45	45	1590	50	50	1963	65	40	2041	60	45	2120
	18	50	45	1766	40	40	1256	50	45	1766	55	45	1943	40	40	1256
	19				55	40	1727	60	40	1884				50	50	1963
	20				50	45	1766									
Average	21	**52**	**43**	**1747**	**45**	**41**	**1436**	**53**	**43**	**1799**	**53**	**43**	**1780**	**47**	**41**	**1530**
Standard Deviation		7	**5**	**322**	**6**	**3**	**245**	**6**	**5**	**190**	**6**	**3**	**211**	7	**4**	**335**
Total Average for the Length					50											
Total Standard Deviation for the Length					7											
Total Average for the Area					1654											
Total Standard Deviation for the Area					301											

Table A9e: Data on the dimensions of the keyhole in periods of approximately 1 second for weld WC 3.
Welding current 170A, weld travel speed 600mm/min. No hollow bead.

Plate WTS 5	Frame	11th second			20th second			25th second			22nd second			26th second			15th second		
	No.	Length	Width	Area	Length	Width	Area	Length	Width	Area	Length	Width	Area	Length	Width	Area	Length	Width	Area
		of Keyhole (mm) [x10]			of Keyhole (mm) [x10]			of Keyhole (mm) [x10]			of Keyhole (mm) [x10]			of Keyhole (mm) [x10]			of Keyhole (mm) [x10]		
	1	50	35	1374	55	40	1727	35	30	824	55	35	1511	35	30	824	50	35	1374
	2	40	30	942	50	35	1374	40	30	942	40	35	1099	15	15	177	25	30	589
	3	40	30	942	40	35	1099	45	30	1060	40	30	942	35	25	687	40	35	1099
	4	35	30	824	55	40	1727	25	25	491	45	40	1413	25	25	491	40	30	942
	5	35	35	962	45	40	1413	45	30	1060	60	35	1649	20	20	314	60	30	1413
	6	40	35	1099	60	35	1649	35	30	824	40	30	942	30	25	589	40	35	1099
	7	40	35	1099	55	40	1727	45	30	1060	50	40	1570	20	20	314	40	35	1099
	8	45	35	1236	55	40	1727	35	30	824	50	35	1374	35	25	687	35	30	824
	9	35	30	824	50	40	1570	45	35	1236	40	35	1099	20	20	314	45	35	1236
	10	45	30	1060	65	40	2041	40	30	942	40	40	1256	30	25	589	35	35	962
	11	40	35	1099	45	40	1413	40	30	942	45	35	1236	15	15	177	45	35	1236
	12	45	40	1413	60	40	1884	40	30	942	35	40	1099	25	20	393	35	35	962
	13	45	35	1236	60	40	1884	40	30	942	40	30	942	25	25	491	45	35	1236
	14	25	30	589	40	35	1099	45	30	1060	50	35	1374	20	20	314	40	35	1099
	15	45	35	1236	65	40	2041				45	35	1236	35	25	687	55	35	1511
	16	50	40	1570	45	40	1413				25	30	589	35	25	687	40	40	1256
	17	55	35	1511	35	35	962				45	35	1236	25	20	393	45	35	1236
	18	35	40	1099	55	40	1727				25	35	687	30	20	471	35	35	962
	19	50	35	1374	50	40	1570				35	35	962	35	25	687	45	35	1236
Average		**42**	**34**	**1131**	**52**	**39**	**1581**	**40**	**30**	**939**	**42**	**35**	**1169**	**27**	**22**	**489**	**42**	**34**	**1125**
Standard Deviation		**7**	**3**	**254**	**9**	**2**	**1573**	**6**	**2**	**173**	**42**	**35**	**1150**	**26**	**22**	**470**	**41**	**34**	**1111**
Total Average for the Length					41														
Total Standard Deviation for the Length					11														
Total Average for the Area					1078														
Total Standard Deviation for the Area					410														

Table A9f: Data on the dimensions of the keyhole in periods of approximately 1 second for weld WTS 5.
Welding current 170A, weld travel speed 600mm/min. No hollow bead.

Plate WC 1	Frame	13th second			19th second			11th second		
	No.	Length	Width	Area	Length	Width	Area	Length	Width	Area
		of Keyhole (mm) [x10]			of Keyhole (mm) [x10]			of Keyhole (mm) [x10]		
	1	85	45	3003	90	50	3533	70	45	2473
	2	60	45	2120	85	50	3336	75	45	2649
	3	55	45	1943	75	45	2649	65	40	2041
	4	45	40	1413	90	50	3533	50	40	1570
	5	55	40	1727	70	40	2198	55	40	1727
	6	70	40	2198	60	45	2120	45	25	883
	7	65	45	2296	70	45	2473	130	40	4082
	8	55	45	1943	85	45	3003	80	55	3454
	9	80	50	3140	65	50	2551	75	50	2944
	10	60	45	2120	65	45	2296	60	50	2355
	11	70	50	2748	100	40	3140	110	45	3886
	12	85	50	3336	85	50	3336	90	45	3179
	13	70	45	2473	65	50	2551	85	45	3003
	14	65	50	2551	60	45	2120	50	75	2944
	15	55	45	1943	60	45	2120	110	50	4318
	16	95	40	2983	65	45	2296	100	45	3533
	17	75	45	2649	100	45	3533	100	45	3533
	18	65	50	2551	80	45	2826	125	45	4416
	19							115	35	3160
	20							115	40	3611
	21							110	40	3454
Average		**67**	**45**	**2396**	**76**	**46**	**2756**	**86**	**45**	**3010**
Standard Deviation		**13**	**4**	**522**	**14**	**3**	**533**	**27**	**9**	**922**
Total Average for the Length				77						
Total Standard Deviation for the Length				21						
Total Average for the Area				2736						
Total Standard Deviation for the Area				733						

Table A9g: Data on the dimensions of the keyhole in periods of approximately 1 second for weld WC 1.
Welding current 216A, weld travel speed 600mm/min. Total number of hollow bead 10 and total length 92mm.

Plate WTS 3	Frame	14th second			19th second		
	No.	Length	Width	Area	Length	Width	Area
		of Keyhole (mm) [x10]			of Keyhole (mm) [x10]		
	1	55	45	1943	60	50	2355
	2	45	45	1590	60	50	2355
	3	50	50	1963	55	50	2159
	4	55	50	2159	55	45	1943
	5	50	55	2159	45	45	1590
	6	55	50	2159	65	45	2296
	7	55	45	1943	55	45	1943
	8	55	55	2375	55	50	2159
	9	55	50	2159	60	50	2355
	10	60	50	2355	55	40	1727
	11	60	50	2355	60	50	2355
	12	60	50	2355	55	45	1943
	13	60	50	2355	60	45	2120
	14	60	45	2120			
	15	60	40	1884			
	16	70	50	2748			
	17	60	45	2120			
	18	55	45	1943			
	19	75	45	2649			
	20						
	21						
Average		**58**	**48**	**2175**	**57**	**47**	**2100**
Standard Deviation		**7**	**4**	**275**	**5**	**3**	**255**
Total Average for the Length					57		
Total Standard Deviation for the Length					6		
Total Average for the Area					2145		
Total Standard Deviation for the Area					266		

Table A9h: Data on the dimensions of the keyhole in periods of approximately 1 second for weld WTS 3. Welding current 170A, weld travel speed 300mm/min. Total number of hollow bead 1 and total length 5mm.

Plate WTS 2	Frame	36th second			28th second			22nd second		
	No.	Length	Width	Area	Length	Width	Area	Length	Width	Area
		of Keyhole (mm) [x10]			of Keyhole (mm) [x10]			of Keyhole (mm) [x10]		
	1	60	50	2355	50	40	1570	45	35	1236
	2	55	45	1943	40	35	1099	55	40	1727
	3	65	50	2551	45	40	1413	45	35	1236
	4	55	45	1943	35	35	962	40	35	1099
	5	55	35	1511	50	40	1570	50	35	1374
	6	60	45	2120	45	35	1236	45	35	1236
	7	50	40	1570	40	35	1099	50	35	1374
	8	60	45	2120	55	45	1943	45	35	1236
	9	60	40	1884	40	30	942	45	40	1413
	10	55	40	1727	55	45	1943	55	45	1943
	11	50	35	1374	45	40	1413	45	40	1413
	12	60	45	2120	50	40	1570	45	40	1413
	13	55	45	1943	40	35	1099	50	40	1570
	14	65	40	2041	35	40	1099	45	40	1413
	15	45	45	1590	50	40	1570	45	45	1590
	16	60	45	2120	45	40	1413	45	45	1590
	17	70	45	2473	45	40	1413	40	35	1099
	18	50	45	1766				55	45	1943
	19	70	45	2473						
	20									
	21									
Average		**58**	**43**	**1980**	**45**	**39**	**1374**	**47**	**39**	**1439**
Standard Deviation		7	**4**	**339**	**6**	**4**	**305**	**5**	**4**	**250**
Total Average for the Length				50						
Total Standard Deviation for the Length				8						
Total Average for the Area				1609						
Total Standard Deviation for the Area				405						

Table A9i: Data on the dimensions of the keyhole in periods of approximately 1 second for weld WTS 2.
Welding current 170A, weld travel speed 400mm/min. Total number of hollow bead 1 and total length 2mm.

Plate WTS 1	Frame	12th second			18th second			23rd second		
	No.	Length	Width	Area	Length	Width	Area	Length	Width	Area
		of Keyhole (mm) [x10]			of Keyhole (mm) [x10]			of Keyhole (mm) [x10]		
	1	30	30	707	35	40	1099	50	40	1570
	2	25	25	491	50	35	1374	35	30	824
	3	40	35	1099	55	40	1727	35	40	1099
	4	40	30	942	50	35	1374	45	40	1413
	5	35	30	824	35	35	962	30	30	707
	6	35	30	824	50	45	1766	45	40	1413
	7	35	35	962	45	45	1590	35	35	962
	8	25	30	589	50	40	1570	50	35	1374
	9	25	30	589	40	35	1099	40	40	1256
	10	35	35	962	40	45	1413	40	40	1256
	11	40	30	942	50	40	1570	30	35	824
	12	35	35	962	50	40	1570	60	40	1884
	13	35	30	824	40	40	1256	45	35	1236
	14	45	40	1413	55	35	1511	45	35	1236
	15	40	35	1099	50	45	1766	40	45	1413
	16	35	35	962	50	40	1570	40	35	1099
	17	40	35	1099	50	40	1570	40	35	1099
	18	40	35	1099	45	45	1590	45	40	1413
	19	30	30	707	45	35	1236	40	40	1256
	20	40	40	1256	60	40	1884	50	45	1766
	21	30	30	707	45	40	1413	50	40	1570
	22	40	35	1099	45	40	1413	55	50	2159
	23	30	30	707	50	40	1570			
	24	40	40	1256						
Average		**35**	**33**	**922**	**47**	**40**	**1474**	**43**	**38**	**1310**
Standard Deviation		**6**	**4**	**233**	**6**	**4**	**230**	**8**	**5**	**348**
Total Average for the Length				42						
Total Standard Deviation for the Length				8						
Total Average for the Area				1230						
Total Standard Deviation for the Area				359						

Table A9j: Data on the dimensions of the keyhole in periods of approximately 1 second for weld WTS 1.
Welding current 140A, weld travel speed 400mm/min. No hollow bead.

Plate WTS 4		7th second			14th second			18th second			22nd second			27th second		
	Frame No.	Length of Keyhole (mm) [x10]	Width	Area	Length of Keyhole (mm) [x10]	Width	Area	Length of Keyhole (mm) [x10]	Width	Area	Length of Keyhole (mm) [x10]	Width	Area	Length of Keyhole (mm) [x10]	Width	Area
		55	50	2159	65	45	2296	60	40	1884	45	30	1060	55	40	1727
	1	60	50	2355	60	45	2120	50	40	1570	45	35	1236	60	40	1884
	2	55	40	1727	55	40	1727	55	35	1511	50	40	1570	60	40	1884
	3	60	40	1884	70	50	2748	55	40	1727	40	30	942	45	35	1236
	4	60	40	1884	60	50	2355	70	40	2198	45	35	1236	70	40	2198
	5	70	50	2748	55	40	1727	50	40	1570	70	35	1923	50	40	1570
	6	55	40	1727	55	40	1727	50	40	1570	45	35	1236	55	40	1727
	7	45	40	1413	60	45	2120	70	40	2198	45	40	1413	75	35	2061
	8	70	45	2473	50	50	1963	50	45	1766	60	45	2120	65	40	2041
	9	60	45	2120	55	40	1727	50	40	1570	40	35	1099	60	35	1649
	10	50	40	1570	40	30	942	50	40	1570	20	20	314	75	40	2355
	11	75	40	2355	65	45	2296	45	40	1413	45	35	1236	55	35	1511
	12	60	45	2120	50	40	1570	45	35	1236	40	35	1099	50	40	1570
	13	50	45	1766	60	45	2120	40	35	1099	55	40	1727	65	35	1786
	14	55	45	1943	50	40	1570	50	35	1374	70	40	2198	50	40	1570
	15	55	40	1727	35	35	962	30	30	707	50	35	1374	55	45	1943
	16	60	45	2120	70	40	2198	70	35	1923	35	35	962	70	40	2198
	17	55	40	1727	55	40	1727	45	35	1236	75	35	2061	65	40	2041
	18	50	40	1570	40	35	1099	55	35	1511	40	35	1099	50	40	1570
	19										55	40	1727	60	40	1884
	20										40	35	1099	65	40	2041
											55	40	1727	50	40	1570
											45	35	1236	70	40	2198
														50	35	1374
Average		**58**	**43**	**1968**	**55**	**42**	**1842**	**52**	**38**	**1560**	**48**	**36**	**1378**	**59**	**39**	**1816**
Standard Deviation		**8**	**4**	**348**	**10**	**5**	**484**	**10**	**3**	**360**	**12**	**5**	**447**	**9**	**3**	**291**
Total Average for the Length					55											
Total Standard Deviation for the Length					11											
Total Average for the Area					1700											
Total Standard Deviation for the Area					440											

Table A9k: Data on the dimensions of the keyhole in periods of approximately 1 second for weld WTS 4.
Welding current 186A, weld travel speed 600mm/min. Total number of hollow bead 4 and total length 29mm.

Pressure (atm)	1	1	1	1	1
Temperature(^{o}K)	300	1000	2000	3000	4000
C	0.00E+00	6.11E-05	2.63E+13	2.86E+17	4.37E-08
C_2	0.00E+00	2.92E-09	2.72E+11	2.83E+14	0.00E+00
CH	0.00E+00	5.63E-01	1.37E+14	1.14E+17	2.46E-09
CH_2	0.00E+00	3.15E+07	2.35E+16	2.47E+17	2.97E-10
CH_2O	2.07E+03	1.38E+18	4.46E+17	2.05E+17	3.10E-09
CH_3	3.24E-08	2.46E+16	7.91E+18	5.90E+17	3.09E-11
CH_4	1.22E+25	4.35E+23	1.71E+20	1.33E+17	3.75E-13
C_2H	0.00E+00	8.64E+06	2.50E+17	1.70E+17	0.00E+00
C_2H_2	0.00E+00	1.22E+16	1.12E+20	5.28E+17	0.00E+00
C_2H_4	1.71E+03	3.61E+18	5.06E+17	5.07E+13	0.00E+00
C_2H_6	6.74E+16	7.90E+18	2.24E+14	1.84E+09	0.00E+00
C_7H_8	0.00E+00	3.10E+08	8.37E+03	2.34E+20	5.48E+22
CH_4O	2.82E+08	2.12E+16	4.07E+10	3.20E-07	0.00E+00
CO_2	6.06E+20	1.31E+23	2.77E+19	7.40E+19	6.21E-04
CO	1.27E+12	1.49E+24	9.16E+23	5.72E+23	3.74E-02
e	3.69E+03	8.62E+11	2.68E+11	3.47E+15	1.32E+17
H	0.00E+00	1.37E+16	5.14E+21	3.07E+23	1.13E+24
H^+	0.00E+00	0.00E+00	2.22E+02	5.00E+11	3.84E+16
H^-	0.00E+00	2.47E+05	1.28E+08	1.25E+13	5.47E+14
H_2	2.42E+21	4.98E+24	2.75E+24	1.56E+24	2.78E+23
H_2O	1.22E+25	3.04E+23	3.76E+20	1.46E+21	3.93E+22
HCO	0.00E+00	7.57E+13	4.45E+17	5.52E+18	8.24E-07
HCO^+	0.00E+00	0.00E+00	2.68E+11	3.48E+15	5.89E-08
HCO_3^-	2.12E+16	5.30E+09	5.77E-01	1.02E+04	0.00E+00
O	0.00E+00	6.07E+03	9.62E+13	1.17E+19	2.23E+23
O^+	0.00E+00	0.00E+00	3.49E-06	1.63E+07	6.52E+15
O^-	0.00E+00	5.58E-04	1.97E+02	9.88E+09	1.13E+15
O_2	0.00E+00	2.07E+02	5.73E+09	4.42E+15	1.24E+22
O_2^+	0.00E+00	0.00E+00	3.63E-06	5.26E+06	6.70E+16
O_3	0.00E+00	0.00E+00	1.16E-05	1.79E+05	4.14E+15
OH	0.00E+00	1.82E+12	7.01E+16	9.66E+19	9.65E+22
OH^+	0.00E+00	0.00E+00	6.47E-02	1.55E+09	2.23E+16
OH^-	4.99E-11	4.75E+06	4.67E+05	1.29E+11	5.38E+14

Table A10a: Particle densities in particles/m^3 for a plasma containing 75% hydrogen and 25% carbon monoxide by mole for temperatures ranging from 300 to 5000K.

Pressure(atm.)	1	1	1	1	1	1	1
Temperature(°K)	5000	6000	7000	7500	8500	9000	10000
C	5.58E+21	3.74E+22	9.44E+22	1.06E+23	9.86E+22	8.98E+22	7.01E+22
C^+	4.35E+18	1.33E+20	1.14E+21	2.35E+21	6.65E+21	9.89E+21	1.83E+22
C^{++}	5.19E+01	1.19E+06	1.35E+09	2.20E+10	2.13E+12	1.42E+13	3.48E+14
C^-	1.70E+14	1.17E+16	1.37E+17	2.55E+17	4.84E+17	5.81E+17	7.05E+17
CH	4.69E+19	7.54E+19	6.48E+19	4.74E+19	2.20E+19	1.50E+19	7.01E+18
CHO	1.01E+19	3.82E+18	7.55E+17	2.40E+17	2.21E+16	7.36E+15	9.85E+14
CHO^+	3.49E+17	2.67E+17	1.02E+17	4.75E+16	9.35E+15	4.40E+15	1.10E+15
CH_2	1.26E+17	3.48E+16	7.99E+15	3.45E+15	6.85E+14	3.27E+14	8.24E+13
CH_2O	1.39E+15	1.46E+14	1.10E+13	2.40E+12	1.21E+11	3.13E+10	2.72E+09
CH_3	3.47E+15	1.39E+14	7.59E+12	1.85E+12	1.44E+11	4.65E+10	5.93E+09
CO	2.07E+23	1.32E+23	4.03E+22	1.52E+22	1.84E+21	6.85E+20	1.13E+20
CO_2	4.52E+18	2.97E+18	6.18E+17	1.58E+17	8.01E+15	2.01E+15	1.65E+14
C_2	1.20E+19	5.61E+19	7.29E+19	4.93E+19	1.52E+19	8.29E+18	2.48E+18
C_2^-	1.39E+14	2.30E+15	6.40E+15	5.23E+15	1.95E+15	1.12E+15	3.54E+14
C_2H	3.55E+18	1.62E+18	3.79E+17	1.29E+17	1.32E+16	4.51E+15	6.05E+14
C_2H_2	3.51E+16	2.51E+15	1.50E+14	2.98E+13	1.28E+12	3.07E+11	2.23E+10
C_2O	8.31E+17	1.32E+18	5.21E+17	1.71E+17	1.26E+16	3.64E+15	3.58E+14
C_3	3.89E+16	6.17E+16	2.39E+16	7.70E+15	5.34E+14	1.46E+14	1.24E+13
e	7.46E+18	1.61E+20	1.30E+21	2.71E+21	8.17E+21	1.27E+22	2.64E+22
H	1.22E+24	1.01E+24	8.14E+23	7.42E+23	6.41E+23	6.00E+23	5.24E+23
H^+	2.75E+18	2.69E+19	1.46E+20	3.21E+20	1.33E+21	2.47E+21	7.09E+21
H^-	1.51E+16	1.53E+17	6.46E+17	1.02E+18	1.92E+18	2.42E+18	3.40E+18
OH	2.09E+20	2.24E+20	1.41E+20	9.18E+19	3.57E+19	2.31E+19	1.04E+19
OH^+	2.35E+15	2.61E+16	1.02E+17	1.54E+17	2.74E+17	3.42E+17	4.87E+17
OH^-	1.09E+13	1.00E+14	2.55E+14	2.58E+14	1.84E+14	1.49E+14	9.56E+13
OH_2	5.54E+13	1.66E+14	1.43E+14	8.22E+13	2.07E+13	1.07E+13	3.20E+12
H_2	2.50E+22	3.18E+21	6.35E+20	3.32E+20	1.17E+20	7.55E+19	3.44E+19
H_2^+	1.21E+16	3.91E+16	9.05E+16	1.41E+17	3.36E+17	4.90E+17	9.16E+17
H_3^+	2.80E+15	6.97E+14	2.54E+14	1.92E+14	1.46E+14	1.35E+14	1.16E+14
H_2O	3.63E+18	5.04E+17	7.00E+16	2.48E+16	3.63E+15	1.56E+15	3.45E+14
O	5.45E+21	3.74E+22	9.55E+22	1.09E+23	1.05E+23	9.94E+22	8.73E+22
O^+	1.05E+16	8.57E+17	1.48E+19	4.05E+19	1.89E+20	3.55E+20	1.04E+21
O^{++}	2.16E-11	8.63E-05	3.87E+00	2.77E+02	3.16E+05	6.01E+06	9.25E+08
O^-	3.76E+14	2.48E+16	2.76E+17	5.04E+17	9.40E+17	1.14E+18	1.47E+18
O_2	4.20E+17	3.00E+18	5.19E+18	3.97E+18	1.59E+18	1.00E+18	4.27E+17
O_2^+	5.48E+13	2.44E+15	1.78E+16	2.72E+16	3.79E+16	4.12E+16	4.58E+16

Table A10b: Particle densities in particles/m3 for a plasma containing 75% hydrogen and 25% carbon monoxide by mole for temperatures ranging from 5000 to 10000K.

Temperature(°K)	300	1000	2000	3000	4000
Partial Pressure (atm)					
C	0.00E+00	8.33E-30	7.17E-12	1.17E-07	2.38E-32
C_2	0.00E+00	3.98E-34	7.41E-14	1.16E-10	0.00E+00
CH	0.00E+00	7.67E-26	3.73E-11	4.66E-08	1.34E-33
CH_2	0.00E+00	4.29E-18	6.41E-09	1.01E-07	1.62E-34
CH_2O	8.46E-23	1.88E-07	1.22E-07	8.38E-08	1.69E-33
CH_3	1.32E-33	3.35E-09	2.16E-06	2.41E-07	1.68E-35
CH_4	4.99E-01	5.93E-02	4.66E-05	5.44E-08	2.04E-37
C_2H	0.00E+00	1.18E-18	6.82E-08	6.95E-08	0.00E+00
C_2H_2	0.00E+00	1.66E-09	3.05E-05	2.16E-07	0.00E+00
C_2H_4	6.99E-23	4.92E-07	1.38E-07	2.07E-11	0.00E+00
C_2H_6	2.76E-09	1.08E-06	6.11E-11	7.52E-16	0.00E+00
C_7H_8	0.00E+00	4.23E-17	2.28E-21	9.57E-05	2.99E-02
CH_4O	1.15E-17	2.89E-09	1.11E-14	1.31E-31	0.00E+00
CO_2	2.48E-05	1.79E-02	7.55E-06	3.03E-05	3.39E-28
CO	5.19E-14	2.03E-01	2.50E-01	2.34E-01	2.04E-26
e	1.51E-22	1.17E-13	7.31E-14	1.42E-09	7.20E-08
H	0.00E+00	1.87E-09	1.40E-03	1.26E-01	6.16E-01
H^+	0.00E+00	0.00E+00	6.05E-23	2.04E-13	2.09E-08
H^-	0.00E+00	3.37E-20	3.49E-17	5.11E-12	2.98E-10
H_2	9.90E-05	6.79E-01	7.50E-01	6.38E-01	1.52E-01
H_2O	4.99E-01	4.14E-02	1.02E-04	5.97E-04	2.14E-02
HCO	0.00E+00	1.03E-11	1.21E-07	2.26E-06	4.49E-31
HCO^+	0.00E+00	0.00E+00	7.31E-14	1.42E-09	3.21E-32
HCO_3^-	8.67E-10	7.22E-16	1.57E-25	4.17E-21	0.00E+00
O	0.00E+00	8.27E-22	2.62E-11	4.78E-06	1.22E-01
O^+	0.00E+00	0.00E+00	9.51E-31	6.67E-18	3.55E-09
O^-	0.00E+00	7.61E-29	5.37E-23	4.04E-15	6.16E-10
O_2	0.00E+00	2.82E-23	1.56E-15	1.81E-09	6.76E-03
O_2^+	0.00E+00	0.00E+00	9.90E-31	2.15E-18	3.65E-08
O_3	0.00E+00	0.00E+00	3.16E-30	7.32E-20	2.26E-09
OH	0.00E+00	2.48E-13	1.91E-08	3.95E-05	5.26E-02
OH^+	0.00E+00	0.00E+00	1.76E-26	6.34E-16	1.22E-08
OH^-	2.04E-36	6.47E-19	1.27E-19	5.27E-14	2.93E-10

Table A10c: Calculated partial pressure of all constituents.

Temperature(°K)	5000	6000	7000	7500	8500	9000	10000
Partial pressure (atm)							
C	3.80E-03	3.06E-02	9.01E-02	1.08E-01	1.14E-01	1.10E-01	9.55E-02
C^+	2.96E-06	1.09E-04	1.09E-03	2.40E-03	7.70E-03	1.21E-02	2.49E-02
C^{++}	3.54E-23	9.73E-19	1.29E-15	2.25E-14	2.47E-12	1.74E-11	4.74E-10
C^-	1.16E-10	9.57E-09	1.31E-07	2.61E-07	5.61E-07	7.13E-07	9.61E-07
CH	3.20E-05	6.17E-05	6.18E-05	4.85E-05	2.55E-05	1.84E-05	9.55E-06
CHO	6.88E-06	3.12E-06	7.20E-07	2.45E-07	2.56E-08	9.03E-09	1.34E-09
CHO^+	2.38E-07	2.18E-07	9.73E-08	4.86E-08	1.08E-08	5.40E-09	1.50E-09
CH_2	8.59E-08	2.85E-08	7.62E-09	3.53E-09	7.94E-10	4.01E-10	1.12E-10
CH_2O	9.47E-10	1.19E-10	1.05E-11	2.45E-12	1.40E-13	3.84E-14	3.71E-15
CH_3	2.36E-09	1.14E-10	7.24E-12	1.89E-12	1.67E-13	5.70E-14	8.08E-15
CO	1.41E-01	1.08E-01	3.85E-02	1.55E-02	2.13E-03	8.40E-04	1.54E-04
CO_2	3.08E-06	2.43E-06	5.90E-07	1.62E-07	9.28E-09	2.47E-09	2.25E-10
C_2	8.18E-06	4.59E-05	6.96E-05	5.04E-05	1.76E-05	1.02E-05	3.38E-06
C_2^-	9.47E-11	1.88E-09	6.11E-09	5.35E-09	2.26E-09	1.37E-09	4.83E-10
C_2H	2.42E-06	1.32E-06	3.62E-07	1.32E-07	1.53E-08	5.53E-09	8.25E-10
C_2H_2	2.39E-08	2.05E-09	1.43E-10	3.05E-11	1.48E-12	3.77E-13	3.04E-14
C_2O	5.66E-07	1.08E-06	4.97E-07	1.75E-07	1.46E-08	4.47E-09	4.88E-10
C_3	2.65E-08	5.05E-08	2.28E-08	7.87E-09	6.19E-10	1.79E-10	1.69E-11
e	5.08E-06	1.32E-04	1.24E-03	2.77E-03	9.47E-03	1.56E-02	3.60E-02
H	8.31E-01	8.26E-01	7.77E-01	7.59E-01	7.43E-01	7.36E-01	7.14E-01
H^+	1.87E-06	2.20E-05	1.39E-04	3.28E-04	1.54E-03	3.03E-03	9.66E-03
H^-	1.03E-08	1.25E-07	6.16E-07	1.04E-06	2.22E-06	2.97E-06	4.63E-06
OH	1.42E-04	1.83E-04	1.35E-04	9.38E-05	4.14E-05	2.83E-05	1.42E-05
OH^+	1.60E-09	2.13E-08	9.73E-08	1.57E-07	3.17E-07	4.20E-07	6.64E-07
OH^-	7.43E-12	8.18E-11	2.43E-10	2.64E-10	2.13E-10	1.83E-10	1.30E-10
OH_2	3.78E-11	1.36E-10	1.36E-10	8.40E-11	2.40E-11	1.31E-11	4.36E-12
H_2	1.70E-02	2.60E-03	6.06E-04	3.39E-04	1.36E-04	9.26E-05	4.69E-05
H_2^+	8.25E-09	3.20E-08	8.63E-08	1.44E-07	3.89E-07	6.01E-07	1.25E-06
H_3^+	1.91E-09	5.70E-10	2.42E-10	1.96E-10	1.69E-10	1.66E-10	1.58E-10
H_2O	2.47E-06	4.12E-07	6.68E-08	2.54E-08	4.21E-09	1.91E-09	4.70E-10
O	3.71E-03	3.06E-02	9.11E-02	1.11E-01	1.22E-01	1.22E-01	1.19E-01
O^+	7.16E-09	7.01E-07	1.41E-05	4.14E-05	2.19E-04	4.35E-04	1.42E-03
O^{++}	1.47E-35	7.06E-29	3.69E-24	2.83E-22	3.66E-19	7.37E-18	1.26E-15
O^-	2.56E-10	2.03E-08	2.63E-07	5.15E-07	1.09E-06	1.40E-06	2.00E-06
O_2	2.86E-07	2.45E-06	4.95E-06	4.06E-06	1.84E-06	1.23E-06	5.82E-07
O_2^+	3.73E-11	2.00E-09	1.70E-08	2.78E-08	4.39E-08	5.05E-08	6.24E-08

Table A10d: Calculated partial pressure of all constituents.

Appendix B

Determination of Percentage Dilution of Base Metal

The amount of dilution from the base metal in the root bead was determined from a software package capable of calculating an area from input describing the contour of the surface. Macrographs of two welds cross sections etched in 2% nital were used to evaluate their surface area. The two welds were made at the same welding conditions - a welding current of 180A and a weld travel speed of 400mm/min. The initial joint preparation was drawn on the macrographs and the area of base metal melted ($A_1 + A_2$) was evaluated. The total weld area, A_w, was evaluated from the boundaries made by the top and bottom surfaces and the fusion lines.

The percentage dilution was calculated the following equation:

$$\% \text{ dilution} = \frac{A_1 + A_2}{A_w} \times 100$$

The % dilution for the two welds were 55% and 58%.

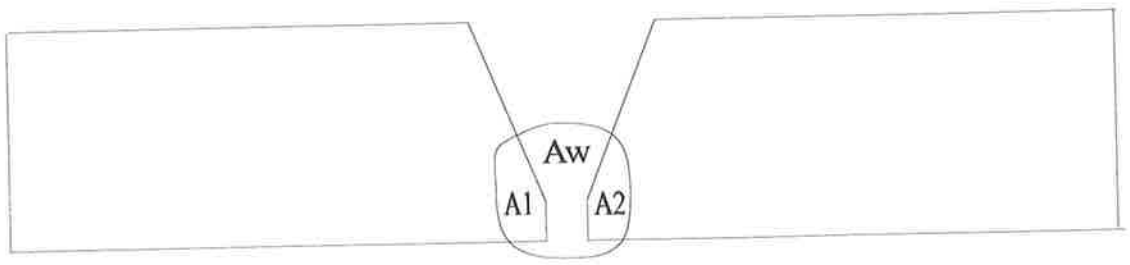

Figure B1: Schematic of the weld cross section showing the areas used in the calculation of the percentage dilution.

Appendix C

Report on Training Programme

Introduction

At the start of my postgraduate studies, in August 1993, I undertook a training programme designed to learn about the pipeline industry. It involved industry and pipeline construction site visits aimed at looking in detail into the various phases associated with the construction of a pipeline: steelmaking, linepipe production and coating, electrode manufacturing and pipelaying.

The main objectives of these activities were to learn about these processes and to identify the impact of any possible variables on the formation of hollow bead. The programme was also aimed at establishing contacts within all the organisations involved, to note their particular concerns and ideas on the project and also to gather information on experiences with hollow bead on particular pipeline projects.

The industrial visits included BHP - Slab and Plate Products Division (Port Kembla), BHP - Pipelines (formerly Tubemakers of Australia Ltd.) (Kembla Grange), Tubemakers of Australia Kwinana Submerged Arc Welding Line Pipe Plant (Western Australia) and the Shaw Coating Plant. The Lincoln Electric Company in Sydney was also visited to observe the manufacture of cellulosic electrodes and to learn about the stovepipe welding technique. Training on the automated manual metal arc welding machine was undertaken at Tubemakers - Pipelines Research Centre in Melbourne for a week during its refurbishment. The site visit included the observation of a pipeline construction site in Western Australia.

A study tour to the USA was also undertaken in July/August of 1994. It was aimed at gathering information on the welding and construction practices of the pipeline industry in the

USA and hence make the research on hollow bead defects also applicable to overseas pipeline projects. The objective was met in three ways.

1. By obtaining practical welding skills at the National Pipeline Welding School in Tulsa, Oklahoma under the supervision of a professional instructor.

2. By monitoring the welding techniques and parameters used during the construction of two pipelines in Florida.

3. Through discussions with David Howden at the Ohio State University, with Malcom Gray of Microalloying Inc., and with researchers at the Edison Welding Institute in Columbus, Ohio.

Notes on Industrial Visits

BHP - Slab and Plate Products Division (Port Kembla)

Steelmaking Plant

Hot Metal Pre-treatment (performed in transfer ladle)

Desulphurisation by the addition of magnesium and lime or aluminium. This reduces the risk of lamellar tearing and improves toughness in the transverse direction by globularising MnS (resulting inclusions are much harder than MnS and so do not deform on rolling and resist crack propagation).

Basic Oxygen Steelmaking (BOS)

The BOS furnace is a barrel-shaped steel shell with a refractory lining and supported on mechanism which allows it to tilt. The lining of the furnace is made of alkaline material (dolomite and magnesite) and the flux used in the process is primarily burnt lime. The vessel can swing through a vertical plane of 360^{o} in either direction and can be held in any position. A tap hole is located on one side of the vessel below the mouth to enable the steel to be poured from under the floating slag when the furnace is tilted. A brief description of the sequence of operations and approximate cycle times (in brackets) follows.

1. Scrap metal is charged into the furnace (2 minutes).

2. The molten iron and fluxes (burnt lime, dolomite and fluorspar) are charged (2 minutes).

3. Oxygen is blown via a lance to lower the carbon content of the iron and to remove other impurities in the form of oxides through the slag or in gaseous form (16 - 18 minutes). Argon is also introduced at the bottom of the vessel to create turbulence within the steel and assist homogenisation. It also helps reduce the inclusion content of the steel since impurities are swept up and contained in the slag. A steel sample is tested and the temperature is checked (6 minutes).

4. The steel is tapped and alloys are added in the ladle (some alloys due to their more rapid rate of oxidation must be added at this stage) (6 minutes).

5. Slagging operation (2 minutes).

Calcium Ladle Injection System and RH Vacuum Degassing

Calcium silicide is added at this point to globularise the alumina stringers by forming calcium aluminate inclusions and to add the amount of silicon required for strength. During the calcium treatment the sulphur content, the dissolved oxygen and the total oxygen content (due to the reduction in the concentration of inclusions) of the heat decreases.

Degassing and Vacuum Degassing

Ladle degassing (CAS (SAB) - Composition Adjustment by Sealed Argon Bubbling): inert gas introduced at the bottom of the ladle creates convective currents (or stirring) in the molten metal which bring new metal to the surface where the vacuum degasses the metal.

RH Degassing: a twin-legged evacuated vessel is used to degas the steel. The injection of inert gas into one of the legs reduces the density of the steel which flows upwards into the egassing chamber. There the liquid steel is exposed to a vacuum creating turbulence which frees dissolved gases. When degassed, the steel returns to the ladle via the other leg and

circulation of the steel from the ladle to the vessel ensures complete degassing of the steel. Vacuum degassing is used in the making of line pipe steel, which requires a higher degree of cleanliness and the removal of dissolved gases particularly oxygen, nitrogen and hydrogen. This process also assists in the floating out of calcium aluminate and oxides to the slag. Vacuum degassing allows alloys to be added to the molten steel in the absence of oxygen so that oxides cannot form.

Continuous Casting

This technique involves pouring the molten steel into a water cooled reciprocating bottomless mould. Steel is poured into the mould just enough to harden the surface so forming a shell to contain the remaining liquid metal. A dummy bar which closes the bottom to begin a cast is slowly pulled downward, drawing the steel with it. The rate at which the steel is poured in at the top of the mould is matched by the rate of withdrawal of the partly solidified steel slab at the bottom. Water is sprayed on the casting as it emerges from the mould until all the metal solidifies.

During casting electromagnetic stirring is applied to the steel to reduce segregation. Other features which reduce the occurrence of centreline segregation in the slab are closely split rolls up to the region of final solidification, internally water cooled rolls which keep their rigidity and reduce roll bending and air mist cooling for uniform cooling across the strand.

Hot Strip Mill

Walking beam furnace: this furnace reheats the slab to the appropriate rolling temperatures (approximately 1225°C). The walking beam carries the slab through the furnace thereby eliminating surface gouging. An extractor slab discharge replaces the gravity discharge eliminating damage to the edges of the slab.

Reversing roughing mill: this area extends from the furnace discharge to the entry of the coilbox. Primary equipment includes a descaling station, which uses water jets, a vertical edger to control the width of the strip, reversing roughing rolls and related table rolls.

Coilbox: on leaving the mill after the last pass, the strip is directed into the coilbox where it is formed into a tight coil. The coiling operation is then reversed and the new head end strip is fed into the finishing mill. The tail end becomes the new head and the bottom of the strip from the roughing mill becomes the top.

Cropshear: a stop/start rotary drum type shear is used for cutting crops from the head and tail ends of the transfer strip before it enters the finishing mill. The ends are cut to a curved shape.

Finishing mill: this mill takes the strip with an intermediate thickness from the roughing mill and coilbox and rolls it to the final desired thickness.

Run-out table: this section provides controlled cooling of the rolled strip in order to produce the desired mechanical properties prior to coiling. Automated spray banks and close-centred table rolls ensure that the strip is delivered to the coilers at a constant temperature and with minimal defects.

Coiling: after being conveyed from the finishing mill to the downcoilers, the strip is deflected by pinch rolls into a chute which guides it into a gap between the wrapper rolls and the mandrel to form a coil. An automatic strapping machine then ties the coils with steel strapping.

Plate Mill

Reheat furnace: slabs from the casting are placed in the furnace to reheat to the appropriate rolling temperature.

Roughing mill: slab is rolled in two directions until the desired dimensions are obtained. Scales are removed by water jets as the slab enters the mill.

Finishing mill: again the slab is rolled until the required dimensions are achieved.

Thermo Mechanical Controlled Process (Hot Strip Mill and Plate Mill)

Slab Reheating Furnace

The slab reheat temperature (SRT) must be high enough for all the Nb to dissolve in the austenite. High slab reheat temperatures increases the yield and tensile strength of the steel. At a high SRT control of the austenite grain size can be achieved in continuous cast steel by suitable dispersion of Ti(C, N). This allows the achievement of a fine and uniform austenite grain size during rough rolling.

Rough Rolling (γ (austenite) recrystallisation)

The rolling reduction is performed at high temperatures. Grain coarsening, however, must be avoided by controlling the roughing passes (final passes must not be too light). The purpose of deformation in the austenite recrystallisation region is to reduce the austenite grain size as much as possible by repeated deformation and recrystallisation. Grain growth in transfer holding is controlled by Ti(N, C).

Finish Rolling (γ non-recrystallisation regime/γ+α(ferrite) regime)

Starts below T_{nr} (approximately 950°C) to increase nucleation sites for ferrite.

1. Deformation in γ non-recrystallisation region, in which the deformation bands are formed in elongated unrecrystallised γ grains, and the α nucleates on the deformation bands as well as γ grain boundaries, giving fine a grain structure. Niobium suppresses recrystallisation of the austenite at this relatively low rolling temperature.

2. Deformation in the $\alpha+\gamma$ two-phase region, in which both the $\gamma+\alpha$ grains are deformed simultaneously, produce a microstructure consisting of equiaxed soft ferrite grains and hard α grains containing substructure. During cooling after deformation, unrecrystallised γ transforms to equiaxed α grains, while deformed α changes into α subgrains, causing an even finer structure.

The finish roll temperature is approximately equal to the Ar_3 temperature. During and immediately after transformation, precipitation of finely dispersed niobium carbonitride occurs, restricting grain growth of the ferrite.

In niobium steels, lower coiling temperatures promote higher strength for the following reasons. A finer ferrite grain size due to the lowered transformation temperature and reduced ferrite grain growth, hardenability effects of solute Nb on the transformation products (such as promotion of acicular ferrite and fine pearlite/bainite second phase), higher dislocation density and finer and more effective Nb(C,N) precipitation.

Accelerated cooling prevents the coarsening of austenite grain boundaries by water cooling from the temperature of the austenite region and allows the formation of fine grained ferrite by water cooling from the temperature of austenite/ferrite dual phases region.

The coil temperature is about 570^{o}C which results in finer grain size due to lowered transformation temperature and reduced ferrite grain growth.

Contacts

Frank Barbaro	Greg Oats	Ian Squires	Bing Feng
Tony Stamp	Eric Bradley	Paul Kelly	Ian Simpson
Jim Williams	Phil Drapper	Peter Edwards	Ceasar Zamunar

BHP - Pipelines (Kembla Grange Electric Resistance Welding (ERW) Line Pipe Plant)

Plant Layout and Notes on Sequence of Operations

1. Storage yard: the coils are stored in a yard and are selected and lifted by crane when required in the plant.
2. The steel coils are uncoiled.
3. Leveller rolls flatten the front end of the steel coil.
4. Continuous rotary shears set the correct width and prepare the edges for welding.
5. Break down, cage forming and fin rolls form the flat strip to a near circular shape prior to the welding operation.
6. ERW of the seam weld: high frequency low voltage electricity flows from one contact along the edge of the strip to an apex where it turns around and flows to the other contact along the opposite edge (Figure C1). The current heats the edges by resistance heating to the welding temperature (at the apex). The hot metal is then squeezed together by squeeze rolls on either side of the pipe. Some current will flow from one contact to another inside the pipe; however since high frequency current will always take the path of least inductance, less current will flow in this longer path (the internal pipe diameter) than in the shorter vee path. Internal and external cutters smooth the weld after welding.

Figure C1: Schematic representing the principle of high frequency electric resistance welding of linepipe (Lancaster, 1992).

7. Induction heating of the seam weld achieves optimal properties.
8. The weld is cooled to ambient temperature using air and water.
9. The final size, shape and straightness of the pipe is produced using a final set of rolls.
10. The seam weld is ultrasonically tested.
11. An on-line cutter cuts the pipe to the length specified by the customer.
12. The loose weld flash inside the pipe is removed.
13. The pipes are number sequentially such that they are traceable to each steel coil.
14. Control inspection of the mill operations is made and the pipes are sorted.
15. An online cutter cuts a weld sample for testing
16. The sample is flattened and a weld ductility test is conducted.
17. The root face and bevel at both pipe ends are machined.
18. The pipe is pressure tested using water.
19. The dimensions of the pipe end geometry and roundness are inspected.
20. A final ultrasonic test of the seam weld is made.

Contacts

Chris Polhill

Robin Buckham

Kosta Kontopoulos

Shaw Coating Plant (Kembla Grange)

Notes on Sequence of Operation

1. The inside surface of the pipe is painted to prevent rusting.

2. The pipe is heated and shot blasted with a mixture containing copper to remove moisture, scale, rust, oil and dirt and so that the mastic (a 0.2mm thick coat which acts as a corrosion barrier) can bond properly to the pipe surface.

3. The yellow jacket (a 1mm plastic cover) is extruded around the pipe using an injection moulding technique.

4. The ends of the pipe are primed and painted.

The Lincoln Electric Company (Sydney)

Notes on the Sequence of Operations in the Manufacture of Cellulosic Electrodes

Preparation of the Electrode Coating

1. The cellulose (or wood pulp) is crushed.
2. A dye and the alloys are added to the cellulose.
3. The ingredients are mixed to form a paste.
4. The coating mix is fed to the extruder.

Preparation of Core Wire

1. Coiled wire (from BHP) is drawn to obtain the required diameter and cut to the desired length.

Production of Coated Electrode

1. The wire and coating mix are fed together to an extruder which produces the finished electrodes.
2. The production line is inspected.
3. The electrodes are baked in an oven.
4. The finished electrodes are inspected (tests for eccentricity and chemical analyses of weld buttons are performed).
5. The electrodes are packed and stored.

Contacts

Jim Magnusson

Bob Sim

Tubemakers of Australia (TOA) Ltd. Pipelines Research Centre (Melbourne)

A week was spent at TOA Pipelines Research Centre in Melbourne working mainly with Bob Morrison who was modifying and refurbishing the automated manual metal arc welding machine. The machine was originally designed and built by TOA in 1976 and was being upgraded for the project on hollow bead. I was taught the system design of the machine and how to operate it.

Contacts

Leigh Fletcher
Bob Morrison

Tubemakers of Australia Ltd. (Kwinana Submerged Arc Welding and Spiral Pipe)

Notes on Sequence of Operation

1. The edges of the steel plate are prepared for the submerged arc welding (SAW) process.
2. The steel plate is formed from flat to a circular shape using an edge press.
3. The SAW process is carried out.
4. The seam weld is ultrasonically tested.
5. The welded pipe is cold expanded to improve roundness and to achieve a constant internal diameter.
6. The ends of the pipe are machined.
7. The pipes are coated and labelled.

Contact

David Clark

Notes on Visits to Pipeline Construction Sites

Tubridgi Pipeline (Western Australia - Constructed by Mc Connell Dowell)

Introduction

This pipeline spread was located in the north west of Western Australia and was built to carry gas from a gas field near the coast to the main Dampier - Perth pipeline (Figure C2). The linepipe was API 5L X70, with an outer diameter of 273.1mm and a wall thickness of 5mm. A week was spent observing all aspects of the construction process, although attention was focused on the welding operations, especially welding of the root pass.

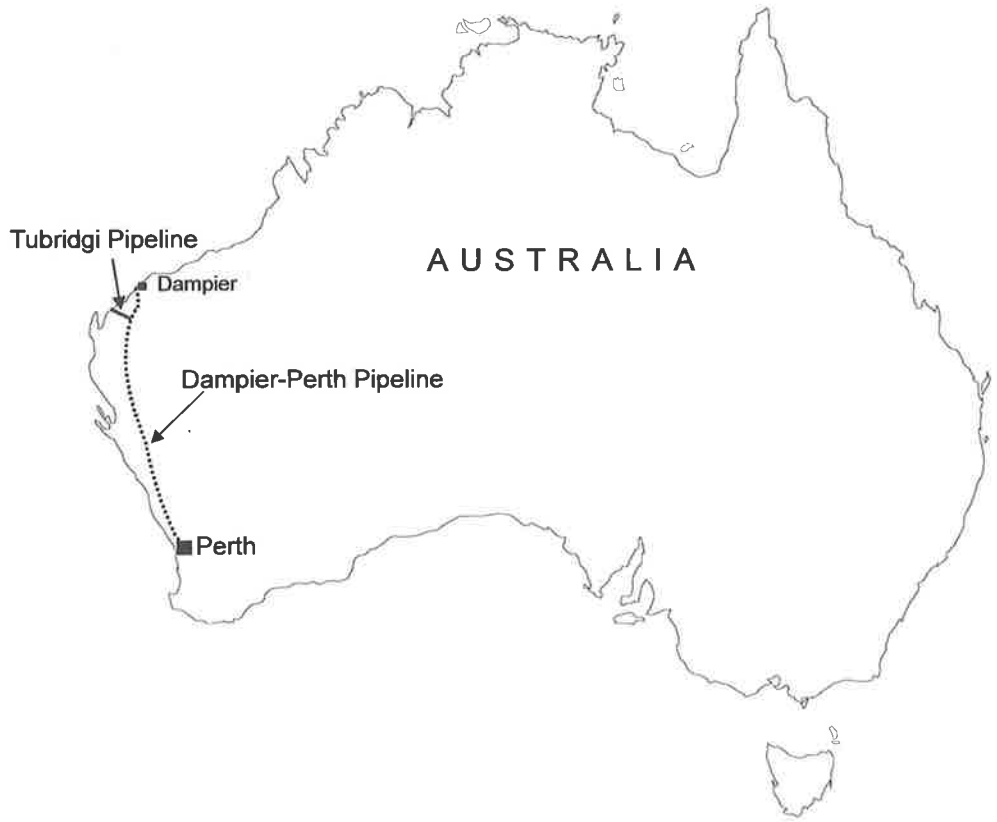

Figure C2: Location of the Tubridgi pipeline in Western Australia.

Sequence of Operations for the Construction of the Tubridgi Pipeline

The general features of the procedure described below are typical of the ones used for the construction of most cross country pipelines in Australia. The procedure is designed to allow the welders of the root pass (or front end welders) to complete this pass as quickly as possible since the rate of construction of the pipeline is dependent primarily on this operation. These practices have been promoted for two main reasons: in Australia, the majority of pipelines are built in remote areas which tend to have flat and bare terrains and the trend towards using small diameter and thin wall pipe. The processes are described below.

A "right-of-way", a strip of land where the pipeline is built and which allows the movement of vehicles, was cleared and graded, and wooden stiles were put in place (Figure C3).

Figure C3: Photograph showing the right-of-way which is graded and cleared prior to digging the trench and laying the pipe.

The linepipe was transported by truck and lifted and laid on the wooden stiles by a sideboom (Figure C4). The length of the pipes was 18m. A trench about 1.2m deep was made by the of the pipes (Figure C5).

Figure C4: Photograph showing a sideboom lifting a pipe from the truck and laying it on the stiles.

Figure C5: Photograph showing the trench being dug.

The pipe was bent (cold field bends) where required by the terrain (such as river crossings, turns in the right-of-way...).

The rate of progress of the pipeline is dependent on the speed of the "front end" crew who weld the root pass. The team thus consists of workers who have very dedicated tasks, which are performed as quickly as possible.

The first operation consisted of bringing a pipe, supported at its centre by a side boom, to the end of one being welded and holding them in place using a pneumatically activated internal line-up clamp (Figure C6). After the proper alignment was obtained and the root gap had been set (and spacers are left to hold the gap) (Figure C7), the line-up clamp was activated and the two welders began welding (Figure C8 and C9). The electrodes used for welding the root pass were Lincoln Electric Fleetweld 5P+ and 3.2mm in diameter.

Figure C6: Photograph showing two pipes being brought together over the internal clamp. The pipe on the left hand side of the photograph is held and moved by a sideboom.

Figure C7: Photograph showing setting of the root gap using spacing tools (or spacers) which are hammered into the joint. The spacers are left into the joint until during the welding operation when they are removed.

Figure C8: Photograph showing, in the foreground, the two front end welders working opposite each other and, in the background, the pipe being held by the sideboom.

Figure C9: Photograph showing the two front end welders welding the root pass in more detail.

The time at which the line-up clamp is released to permit the set up of a new joint is dependent on the welding procedure and may vary between release after 100% of the root pass is completed or after 70% (which was the case for this project). After the clamp was released, the pipe was lifted to allow more wooden stiles and a sand bag to be placed under the pipe (the pipe is further raised from the ground prior to welding to allow welding underneath the pipe). The sideboom then released the pipe and advanced to the next length of pipe which was lifted to permit the set up of the next joint.

After cleaning the root pass with a grinder the hot pass was deposited by one welder. Two welders are sometimes used to increase productivity. The hot pass is usually welded within ten minutes of the completion of the root pass to minimise the occurrence of hydrogen assisted cracking by allowing hydrogen to diffuse away from the weld. A capping pass then followed. Filling passes are required for larger wall thicknesses.

The welded joints were then radiographed using a gamma ray source. The surface of the capping passes were also inspected using a mirror. The joints were then sand blasted and coated with molten tar and a plastic sleeve. The pipe strings (about 1 - 1.5km of welded pipes) were lowered into the ditch by side booms and then tied-in by one welder. Finally the trench was filled with dirt and the right-of-way restored as closely as possible to its original condition.

Contact

Jim Kwiatkowski

Notes on Trip to the USA

National Pipeline Welding School, Tulsa, Oklahoma

I spent the first week at the National Pipeline Welding School in Tulsa and under the instruction of John Balch learned the stovepipe welding technique. Although we concentrated on welding of the root bead, I also practiced the hot pass, filler pass and capping pass. I learned to cope with changes in the root gap and root face and observed the influence of varying the levels of welding current and travel speed. I also had the opportunity to observe pipeline welders at the school and monitor the welding parameters they employed. Weld travel speeds up to about 450mm/min were used, but were usually maintained between 300 and 350mm/min. The welding currents were between approximately 160 and 170A. During discussions with John Balch relating to his experiences with the occurrence of hollow bead, he suggested that high currents and weld travel speeds were the most influential factors in the formation of hollow bead.

Sites Visits to Pipeline Construction Sites in Florida

A network of pipelines and compressor stations were being constructed by the Florida Gas Transmission Company next to the existing pipelines to increase the capacity of the system. Two of the pipeline spreads (see Figure C10) were visited as different welding procedures were being used. The linepipe was, in both cases, made from API 5L X70 steel, 8.9mm thick and the diameter was 762mm. The weld travel speed on Spread 8 (near Fort Pierce) were generally slower (an average of 365mm/min) and the front end welders were welding both the

root and hot passes such that the rate of advance of the pipeline was slowed down. This was mainly because the pipeline was being built next to a highway where many road and stream crossings had to be made. The travel speeds on Spread 7 (near Spring Hill) were, on the other hand, faster (456mm/min on average) and the front end welders were only welding the root pass. This spread was proceeding at a faster pace as the area was in the countryside where less obstacles were present. I had the opportunity to observe most of the activities taking place along the spreads, although I spent most of the time monitoring the front end welders.

Figure C10: Schematic showing the locations where the two pipeline spreads were visited.

The information on the procedure for welding of the root bead was gathered for both spreads and are presented in Tables C1 and C2. The root pass was welded by two welders in both cases. The internal line up clamp was released after completion of 100% of the root pass on both spreads. A preheat temperature of 93°C was employed on Spread 7 while no preheat was required on Spread 8. An average weld travel speed was obtained by recording the time taken

by the welders to weld each bead which was approximately equal to a sixth of the pipe circumference (three electrodes were used by each welder to weld one half of the pipe). The average welding current and voltage were measured using a tong tester.

Location	Number of Welders	Type of Electrode	Weld Travel Speed Range (mm/min)	Average Weld Travel Speed (mm/min)	Average Welding Current (A)	Average Welding Voltage (V)
Spread 7	2	Lincoln 5P+ 4.0mm Diameter	330 - 405	365	175	26

Table C1: Details of the welding parameters for the root pass.

As well as measuring the welding current and travel speed, information on these parameters were obtained from the daily inspection sheets. The inspections sheets showed that the travel speed varied between 18 and 22in/min (457 - 559mm/min) and the welding current and voltage varied between 140 and 180A and 23 to 33V respectively.

Location	Number of Welders	Type of Electrode	Weld Travel Speed Range (mm/min)	Average Weld Travel Speed (mm/min)	Average Welding Current (A)	Average Welding Voltage (V)
Spread 8	2	Lincoln 5P+ 4.0mm Diameter	399 - 480	456	170	28

Table C2: Details of the welding parameters for the root pass.

During discussions with the non-destructive testing personnel on Spread 8 I was able to observe radiographs of welds containing hollow bead defects. As only a few radiographs were available for observation only three cases are described here. These do not represent the total occurrence of hollow bead defects for that pipeline.

Case 1: Tie-in weld

Location: 3 indications of hollow bead near the 10 and 12 o'clock position.

Length of Hollow Beads: 2.5mm, 3.0mm and 14mm.

Comments: The weld was repaired, due to the incidence of hollow bead, by grinding the affected region.

Case 2: Main line weld

Location: 2 indications of hollow bead near the 1 and 2 o'clock position.

Length of Hollow Beads: 1.5mm and 2.5mm.

Comments: The weld was not repaired.

Case 3: Main line weld

Location: 2 indications of hollow bead near the 10 o'clock position.

Length of Hollow Beads: 2.0mm and 5.0mm.

Comments: The weld was not repaired.

Overall most of the hollow bead defects were quite short in length.

The other activities observed along Spread 8 are described below.

Due to the height of the water table in Florida, the soil in some regions had to be dewatered before commencing particular operations such as dewatering of a trench prior to a tie-in and dewatering before digging and boring (Figure C11). The trench was dug with a back-hoe as shown in Figure C12. A boring operation underneath a road is shown in Figure C13 where a pulley system is attached to the pipe and to a fixed structure, seen in the foreground, which pushes the pipe into the ground.

Figure C11: Water and sediment are pumped through pipes installed in the ground and through the ones above ground as seen in this figure. This particular area was being dewatered prior to boring operation underneath the railway tracks seen in the foreground.

Figure C12: Digging of the trench with a back-hoe. The existing pipeline can also be seen.

Figure C13: A boring operation underneath a road.

Where necessary the pipes had to be bent to fit the slope and bends of the right-of-way as well as the road and river crossings (Figure C14).

Figure C14: Equipment for field bending of pipes.

Figure C15 below shows the two front end welders on Spread 8. The preparation for the welding of a tie-in is shown in Figure C16. An external clamp was used to fix the end of the two pipes.

Figure C15: Welding of the root pass on Spread 8.

Figure C16: Preparation for a tie-in weld.

The lowering-in of a pipe string is shown in Figure C17. The pipe string was held using slings by a number of booms which gradually lower the whole string into the trench where it could be tied-in to the next one.

Figure C17: The lowering-in process of a pipe string.

Discussion Relating to Site Visits

The observations made on the pipeline construction sites in Australia and in the USA have shown primarily that the practices used for building pipelines in both countries are generally the same. The stovepipe technique which is used to weld the root pass is used in both countries with the same types of electrodes and similar welding parameters. The sequence of operations as well as some of the equipment and techniques used to construct the pipeline are also similar.

Contacts

Malcom Gray
David Howden
John Balch
Louis Kinztl

Visits to the Edison Welding Institute (EWI) and the Ohio State University

A tour of the laboratories and discussions with researchers at the EWI was also organised. The discussions included introductions to some of the pipeline related projects being undertaken and a short presentation on the hollow bead project. The projects discussed were:

1. A laser-based pipeline inspection system.
2. Testing the structural integrity of girth welds containing lack of fusion and lack of penetration.
3. Methods for hardness testing and analysing of weld heat affected zones.

The researchers from EWI involved in the discussions were:

Davis Yapp, Troy Paskell (Senior Research Engineer), Fabian Orth (Senior Research Engineer) and Lawrence Friedman (Principal Research Engineer).

This was followed by a meeting with Professor David Howden from the Ohio State University, where an overview of the hollow bead project was presented including the objectives of the program, the experimental methods and results obtained to date. David Howden had undertaken research on hollow bead where root beads were welded on pipe segments attached to a lathe in order to keep the welding speed constant. The experiments, however, failed to produce hollow bead and it was suggested that the weld travel speed may not be an influential factor.

Contact

David Howden

Appendix D

TRACES OF WELDING CURRENT, VOLTAGE AND ELECTRODE FORCE FROM DATA LOGGER

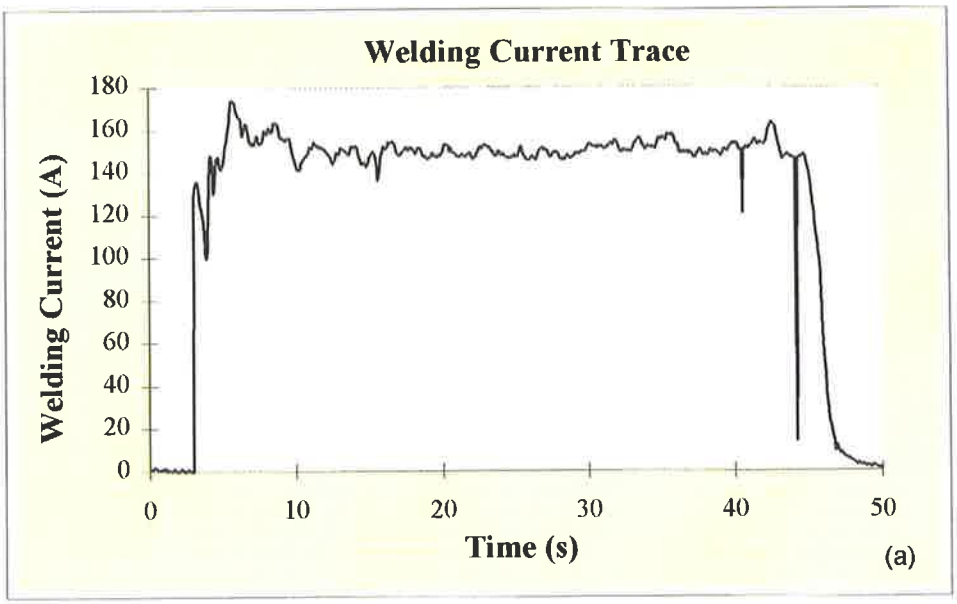

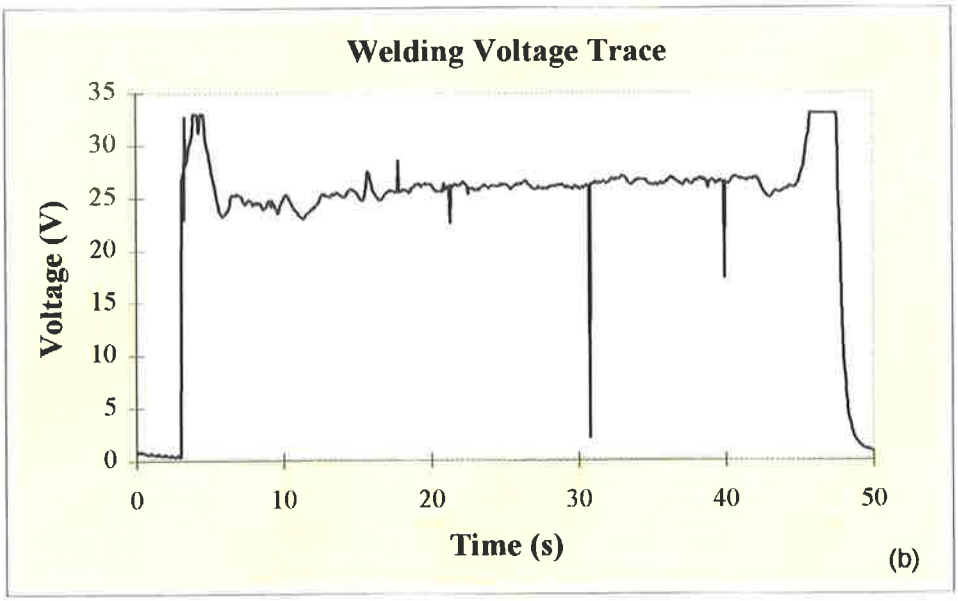

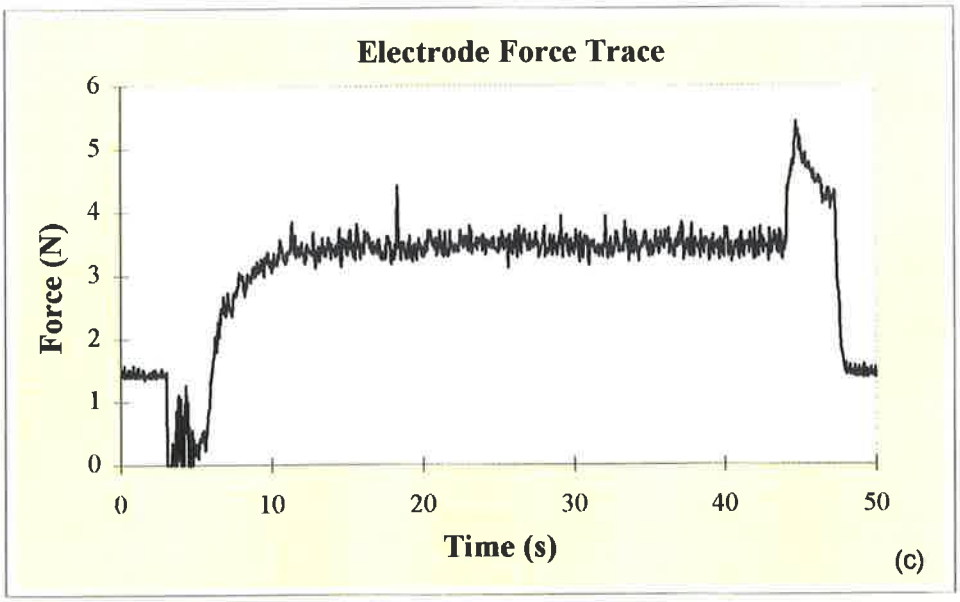

Figure 1Da, b and c: Graphs of (a) welding current, (b) voltage and (c) electrode force during a welding run.

Appendix E

MACROGRAPHS OF HOLLOW BEAD IN X80 STEEL

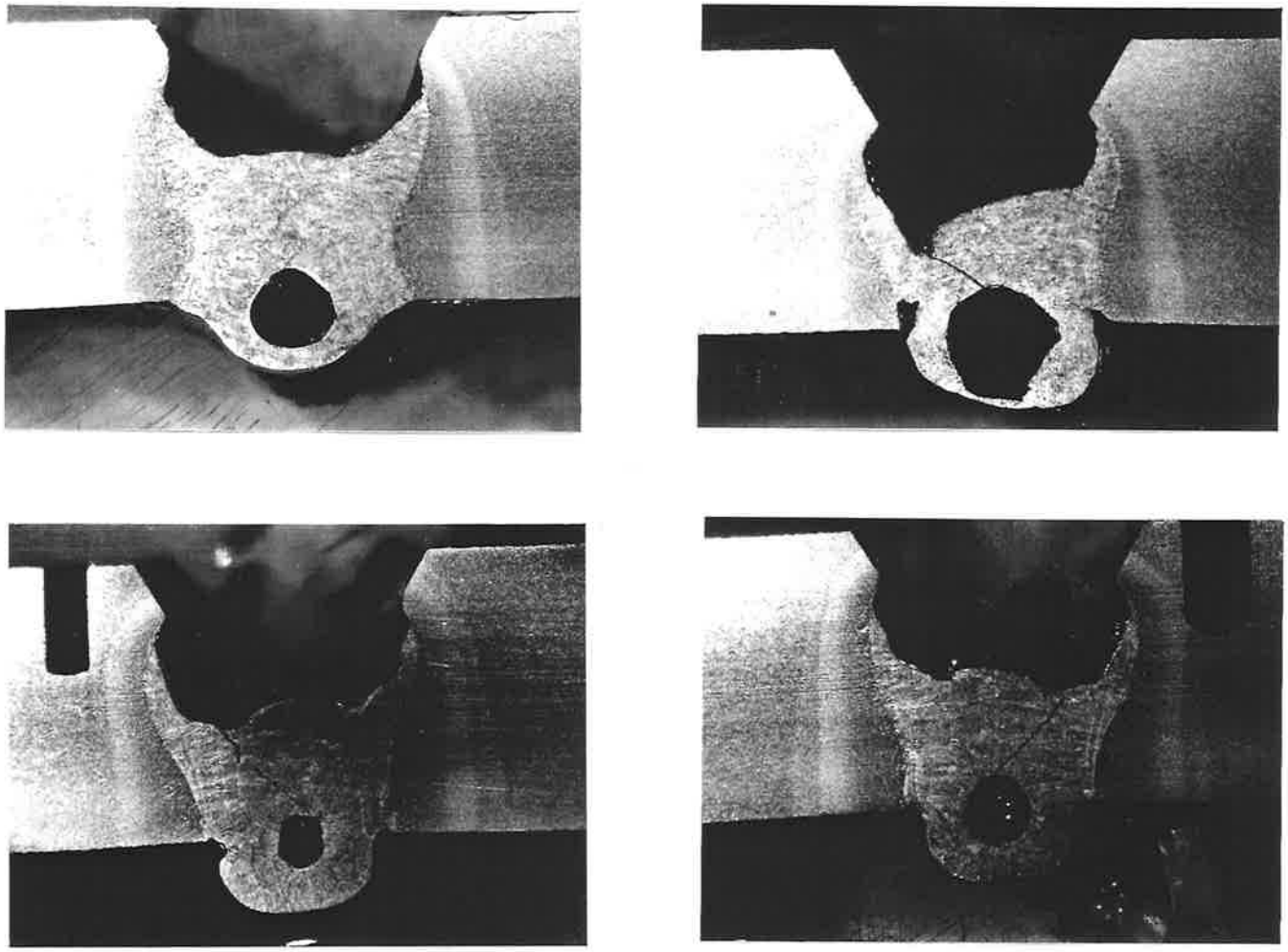

Figure E1: Macrographs of weld cross sections showing hollow bead pores in the reinforcement region. The welds were made in API X80 steel using cellulosic electrodes 4.0mm in diameter and E9010 specification during WIC cracking tests.

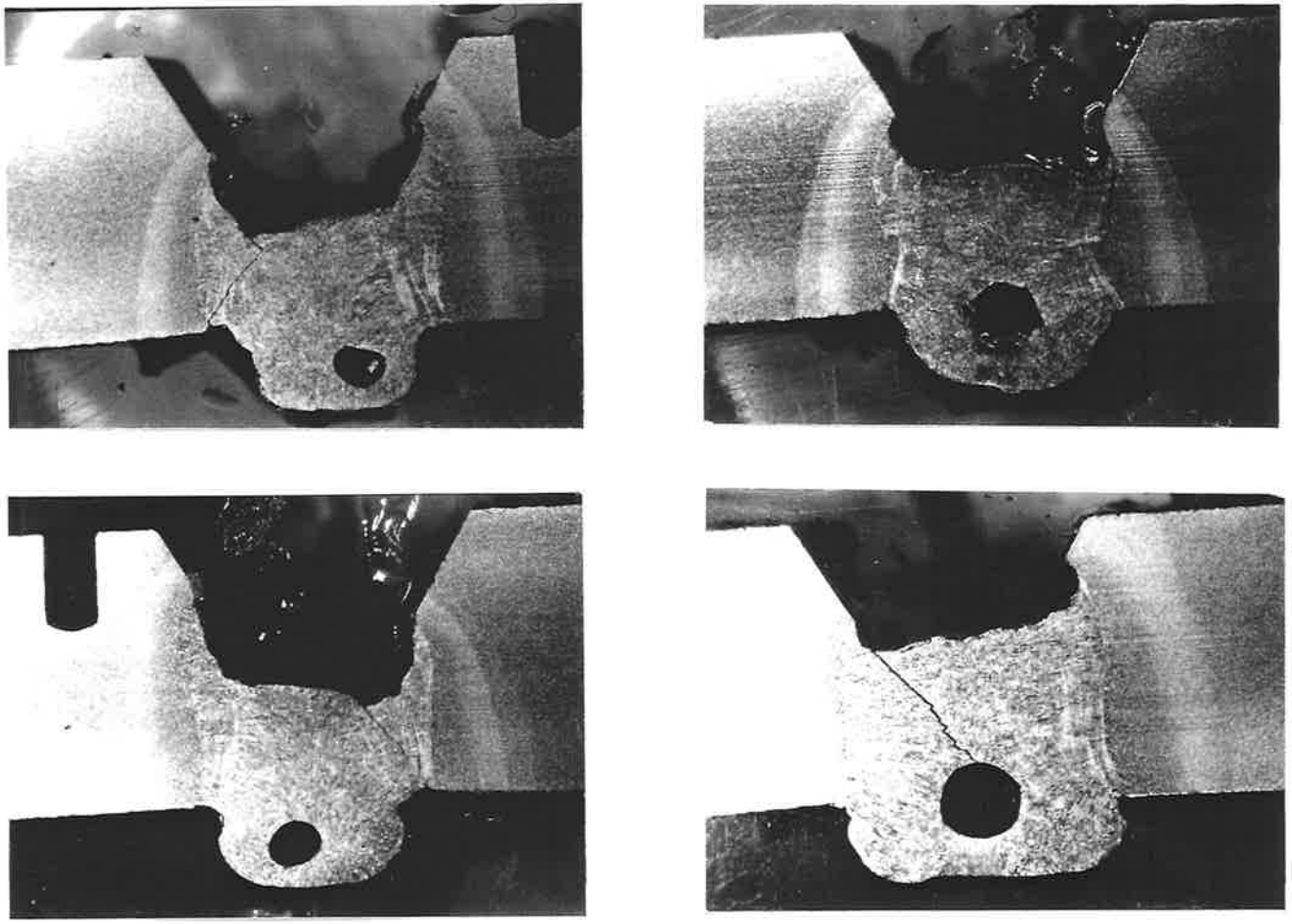

Figure E1 (continued): Macrographs of weld cross sections showing hollow bead pores in the reinforcement region. The welds were made in API X80 steel using cellulosic electrodes 4.0mm in diameter and E9010 specification during WIC cracking tests.

Appendix F

GRAPHS OF THE OCCURRENCE OF HOLLOW BEAD AGAINST HEAT INPUT AT CONSTANT WELD TRAVEL SPEED

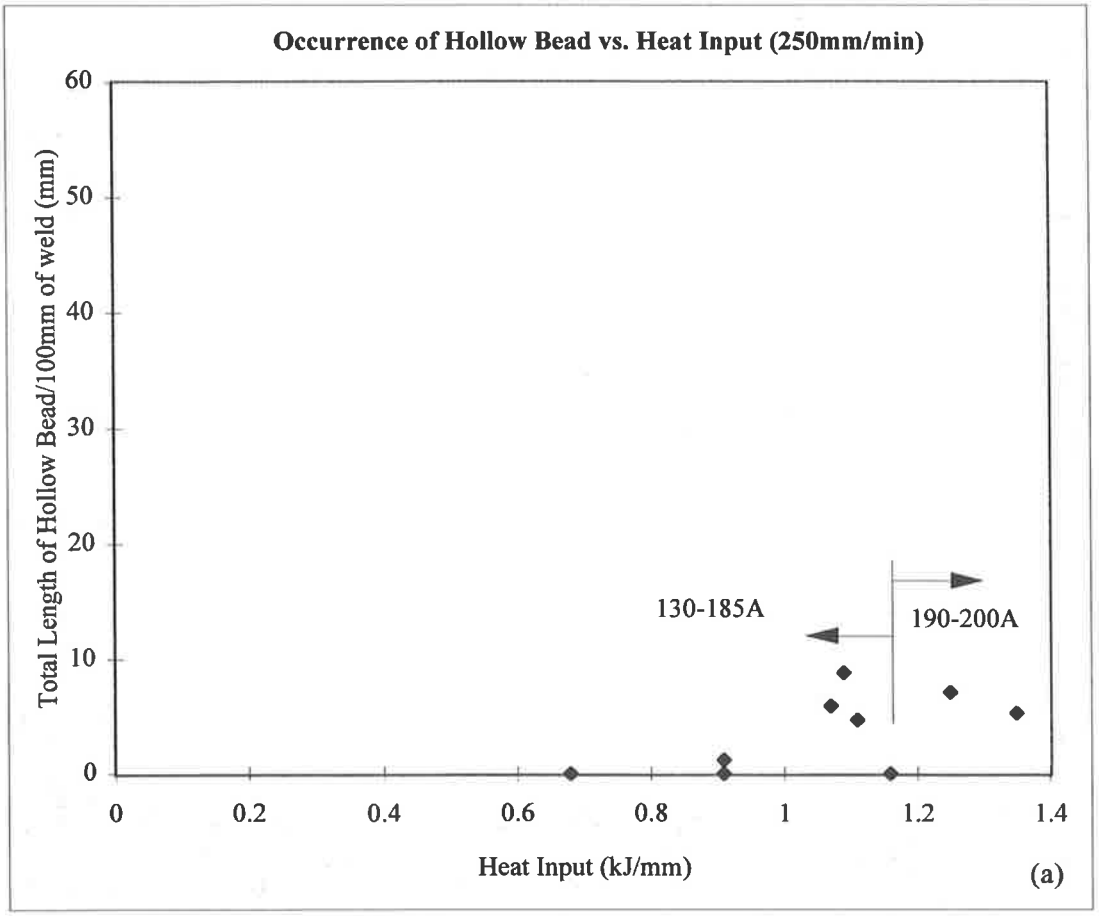

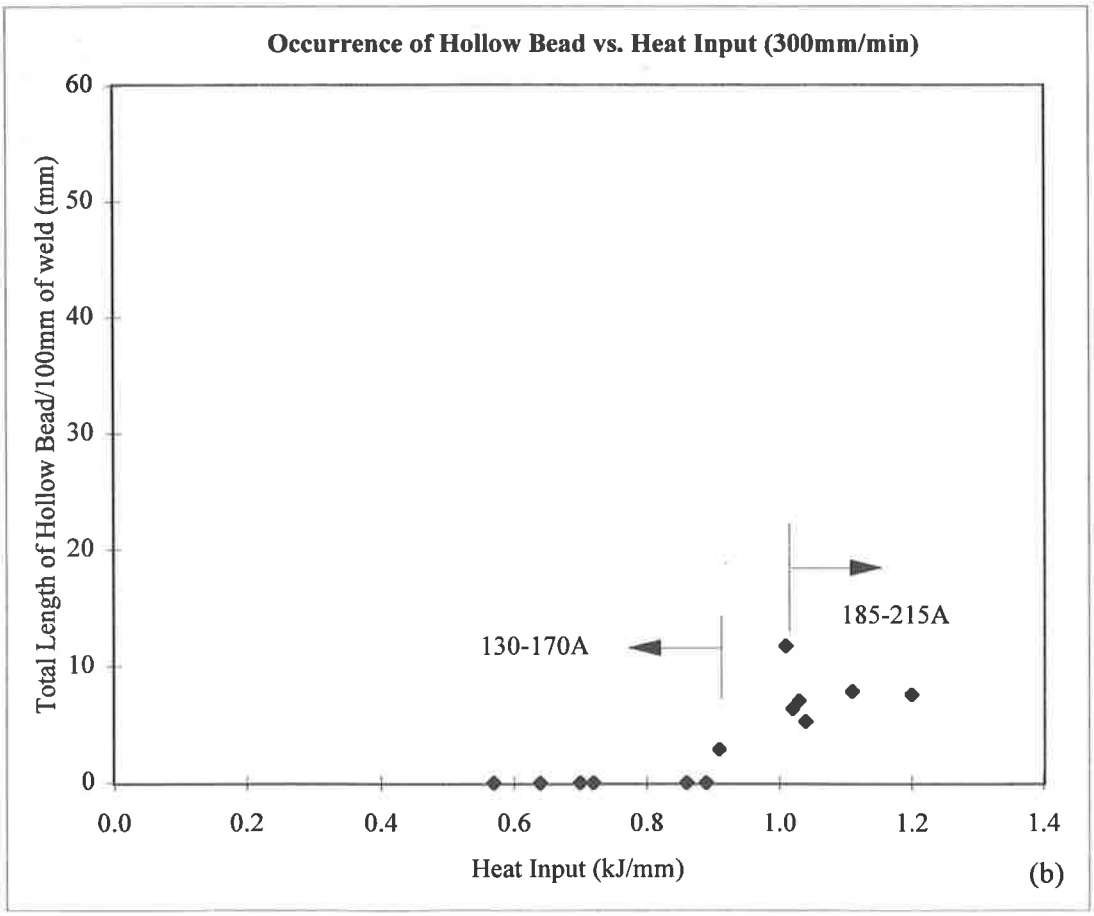

Figure F1a and b: Total length of hollow bead against heat input at (a) 250mm/min and (b) 300mm/min) for a weld made with an X70 steel 8.3mm thick and with a 4.0mm ϕ 5P+ electrode

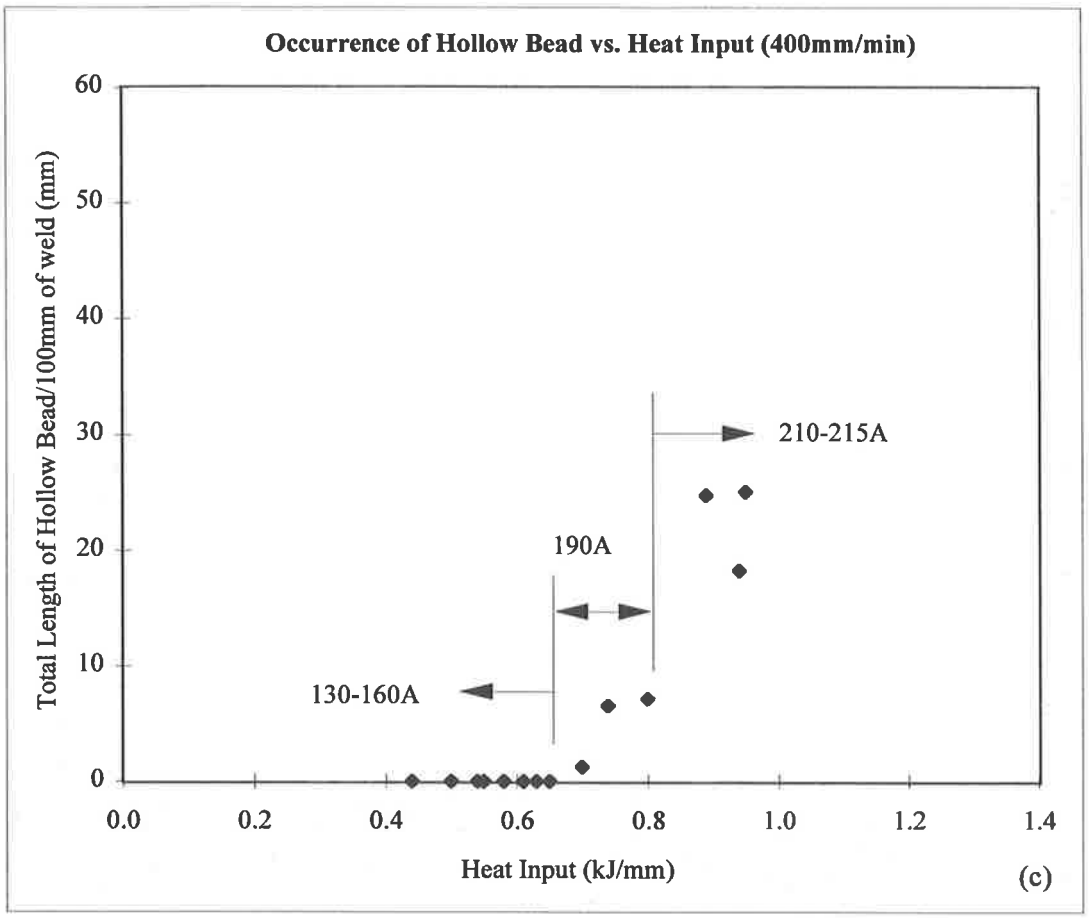

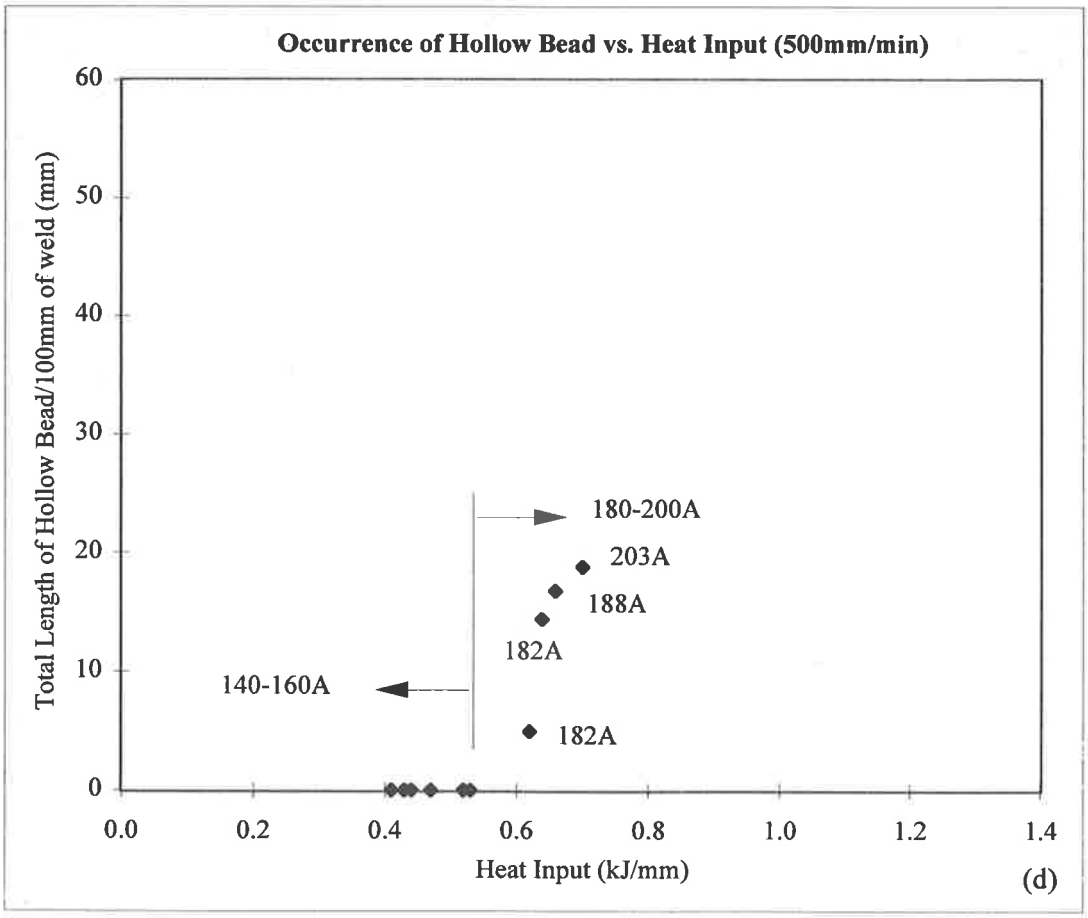

Figure F1c and d: Total length of hollow bead against heat input at (c) 400mm/min and (d) 500mm/min) for a weld made with an X70 steel 8.3mm thick and with a 4.0mm ϕ 5P+ electrode.

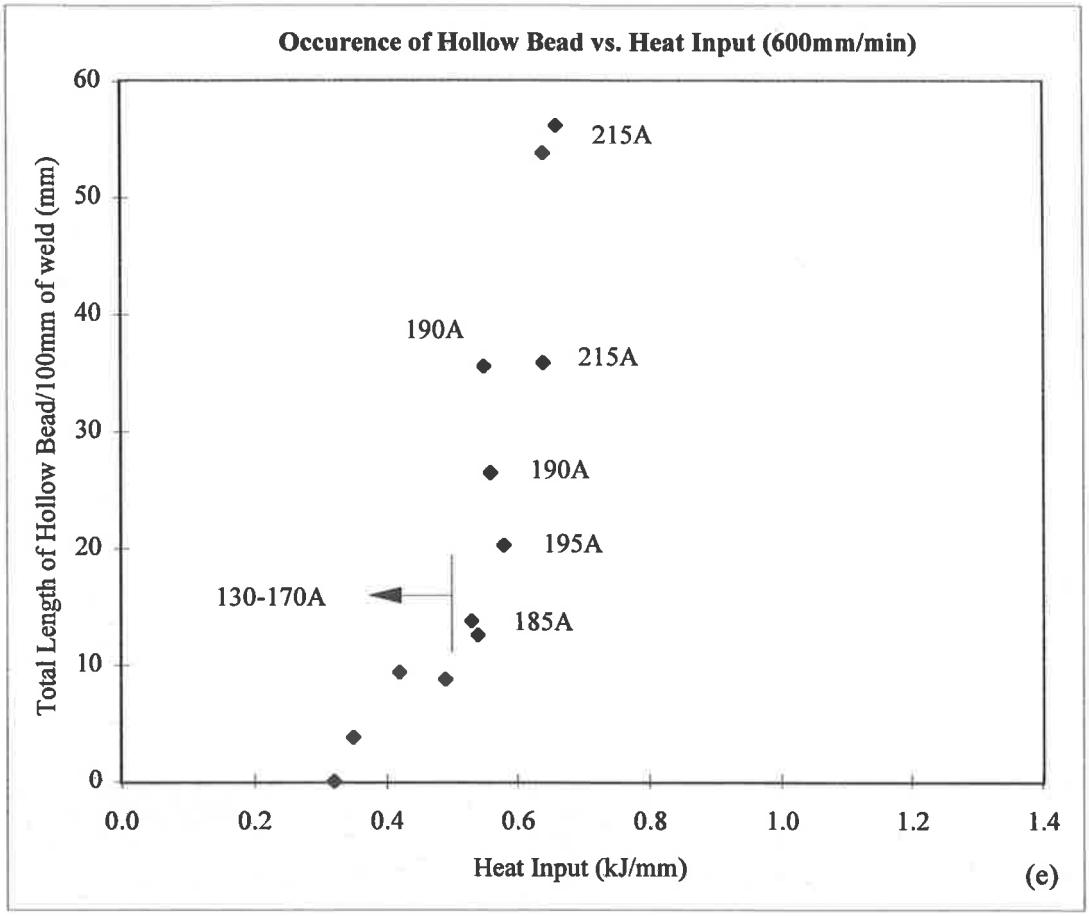

Figure F1e: Total length of hollow bead against heat input at 600mm/min
for a weld made with an X70 steel 8.3mm thick and with a 4.0mm ϕ 5P+ electrode.